Physics of Atomic Nuclei, Vol. 68, No. 3, 2005, pp. 359–371. Translated from Yadernaya Fizika, Vol. 68, No. 3, 2005, pp. 388–400.

Investigation of Hybrid States in the VES Experiment at the Institute for High Energy Physics (Protvino)

D. V. Amelin, Yu. G. Gavrilov, Yu. P. Gouz*, V. A. Dorofeev, R. I. Dzhelyadin, A. M. Zaitsev, A. V. Zenin, A. V. Ivashin, I. A. Kachaev, V. V. Kabachenko, A. N. Karyukhin, A. N. Konoplyannikov, V. F. Konstantinov, V. V. Kostyukhin, V. D. Matveev, V. I. Nikolaenko, A. P. Ostankov, B. F. Polyakov, D. I. Ryabchikov, A. A. Solodkov, A. V. Solodkov, O. V. Solovianov, E. A. Starchenko, A. B. Fenyuk, and Yu. A. Khokhlov

Institute for High-Energy Physics, Protvino, Moscow oblast, 142284 Russia

Received May 24, 2004; in final form, September 27, 2004

Abstract—Experimental investigations of candidates for hybrid mesons in the VES experiment at the Institute for High Energy Physics (Protvino) are surveyed. The data in question concern $\pi_1(1400)$ characterized by the exotic quantum numbers of $J^{PC} = 1^{-+}$ and observed in the $\eta\pi^-$ final state; $J^{PC} = 1^{-+}$ $\pi_1(1600)$ in the $\eta'\pi^-$, $b_1(1235)\pi$, and $f_1(1285)\pi^-$ final states; and $J^{PC} = 0^{-+}$ $\pi(1800)$ in the $f_0(980)\pi^-$, $f_0(1300)\pi^-$, $f_0(1500)\pi^-$, and $a_0^-(980)\eta$ final states. New results are given along with data published previously. *© 2005 Pleiades Publishing, Inc.*

INTRODUCTION

Although the validity of QCD as the theory of strong interactions is presently unquestionable, its equations cannot be directly applied to describing processes at low and intermediate energies, because relevant calculations are very involved. In calculating the properties of hadron resonances consisting of light quarks, use is usually made of various phenomenological models, including the bag model, potential models, and the current-tube model. Phenomenological models successfully describe the properties of the majority of known hadrons (see, for example, [1]), interpreting them as a bound state of a quark and an antiquark ($q\bar{q}$) in the case of mesons or as a bound state of three quarks (qqq) in the case of baryons.

All of these models admit the existence of hadrons whose structure is more complicated than $q\bar{q}$ or qqq. Such hadrons are referred to as exotic ones. They include multiquark states ($q\bar{q}q\bar{q}$, $q\bar{q}q\bar{q}q\bar{q}$, etc.). There can also exist hadron states where gluons manifest themselves not only as quanta of a field that binds quarks but also as an important constituent part of the structure of hadrons. In particular, a number of theoretical studies performed in the late 1970s (see, for example, [2]) predicted the existence of quark—antiquark mesons involving excited gluon degrees of freedom. Such objects were called hybrid mesons.

Data indicating that diffractive processes in pion beams can lead to the production of hybrid mesons involving light quarks (u, d) were obtained in the early 1990s, first in the VES experiment at the Institute for High Energy Physics (IHEP, Protvino) and later in the E852 experiment at the Brookhaven National Laboratory (BNL). In the present article, we describe the current state of investigations of candidates for hybrid mesons in the IHEP VES experiment.

The properties of hybrid mesons formed by light quarks were predicted on the basis of the bag model [3], potential models [4], sum rules [5, 6], and the current-tube model [7–9]. Despite considerable successes of QCD lattice calculations [10, 11], realistic calculations of the properties of hybrid mesons consisting of light quarks can hardly be performed at the present time.

In the bag model and in potential models, the excitation of gluon degrees of freedom is represented in the form of an additional (constituent) gluon in the composition of a meson, while, in the current-tube model, this is an excitation of the massive string (tube) that connects the quark and the antiquark involved.

The quantum numbers of ordinary ($q\bar{q}$) mesons are given by $P = (-1)^{L+1}$ and $C = (-1)^{L+S}$, where L is the relative orbital angular momentum and S is the total spin of the quark and the antiquark. There exist combinations of J^{PC} that are impossible for ($q\bar{q}$) mesons: 0^{--}, 0^{+-}, 1^{-+}, 2^{+-}, and 3^{-+}; these

---

[*] E-mail: `Yury.Guz@ihep.ru`

1063-7788/05/6803-0359$26.00 © 2005 Pleiades Publishing, Inc.

Table 1. Predictions of various models for the mass of the lightest hybrid meson

Model	Mass, GeV/c^2	References
Bag model	1.3–1.8	[3]
Current-tube model	1.8–2.0	[7–9]
Sum rules	1.3–1.5	[5]
Sum rules	2.1–2.5	[6]
Lattice QCD	1.8 ± 0.2	[10]

are referred to as exotic combinations. For hybrid mesons, any combinations of quantum numbers, including exotic ones, are possible.

In the bag model, the lightest hybrid meson is the combination including $(q\bar{q})$ of total spin 0 or 1 and a transverse electric gluon ($J^{PC} = 1^{+-}$) [3]. Thus, the existence of four multiplets close in mass that are characterized by the quantum numbers $J^{PC} = 1^{--}$, $(0, 1, 2)^{-+}$ is predicted. In other models, multiplets of hybrid mesons having these quantum numbers are also the lightest ones.

Theoretical predictions of various models for the mass of the lightest hybrid meson formed by (u, d) quarks are given in Table 1.

In the bag model, potential models, and the current-tube model, the $^3P_0$ model [12] or its modifications from [13, 14] are used to calculate two-body meson decays. The decay of a meson is described as the process where the production of a quark–antiquark pair $(q\bar{q})$ in the $J^{PC} = 0^{++}$ state is followed by the separation of the quark and the antiquark constituting it between different reaction products. It is assumed that decay schemes where the product $(q\bar{q})$ pair forms one of the final mesons instead of being separated [that is, a decay process violating the Okubo–Zweig–Iizuki (OZI) rule] make a negligible contribution.

The suppression of the decays of light hybrid mesons to two S-wave mesons (π, ρ, K, K^*) is one of the results obtained on the basis of this model. The most detailed analysis of hybrid-meson decays was performed within the current-tube model [7–9].

It is expected that hybrid states must be vigorously produced in diffractive processes, weak decays, and electro- and photoproduction processes [7]: an “impact” on one of the quarks in a meson should lead, with a high probability, to the excitation of gluon degrees of freedom.

It should be noted that one of the lightest hybrid multiplets has exotic quantum numbers, $J^{PC} = 1^{-+}$. For such states, there is no mixing with ordinary $(q\bar{q})$ mesons, and this facilitates their experimental identification. However, they can be mixed with four-quark states, for which the quantum numbers $J^{PC} = 1^{-+}$ are also possible.

Hybrid states characterized by conventional quantum numbers can be identified on the basis of the branching ratios for their decays to various final states, since these branching ratios can differ from those for the radial excitations of ordinary meson states [15].

We note that, in performing experimental investigations, it is necessary to verify, in any case, that one observes precisely a resonance—that is, its amplitude and phase feature the respective dependences on the effective mass.

VES FACILITY

The layout of the VES facility is depicted in Fig. 1. A target featuring a veto system, a wide-aperture magnetic spectrometer equipped with a system of proportional and drift chambers, a triggering scintillation hodoscope, a multichannel Cherenkov counter, and a lead-glass electromagnetic calorimeter are the main units of this apparatus. A more detailed description of the facility is given elsewhere [16].

The facility operates in a 28- to 43-GeV beam of negatively charged pions that is extracted from the IHEP U-70 accelerator. The VES experiment is devoted to studying reactions of the type

$$\pi^- A \to n(\pi, K)^{\pm} m\gamma A'. \qquad (1)$$

The triggering condition for logging events on a tape consists in requiring the presence of two or more charged particles in the final state and the absence of signals from charged particles in the veto system of the target. This condition makes it possible to study a wide class of final states in reactions of the type in (1). Throughout the experimental time, we were able to accumulate about 10^9 events. We have studied various final states including $\pi^+\pi^-\pi^-$, $\pi^+\pi^-\pi^-\eta$, $\eta\pi^-$, $\eta'\pi^-$, $\omega\pi^-\pi^0$, $\eta\eta\pi^-$, $\eta'\eta\pi^-$, $K^+K^-\pi^-$, $\pi^+\pi^-K^-$, $\pi^+\pi^-$, $\pi^+\pi^-\pi^0$, $\pi^+\pi^-\eta$, and $\eta'\pi^0$.

INVESTIGATION OF THE $J^{PC} = 1^{-+}$ STATES

The predictions of the current-tube model [8] for the widths of $J^{PC} = 1^{-+}$ light hybrid mesons with respect to decays to various final states are summarized in Table 2.

A $J^{PC} = 1^{-+}$ exotic wave of significant intensity was observed by several experimental groups in a partial-wave analysis of various two-meson systems produced in the diffraction of a beam of negatively

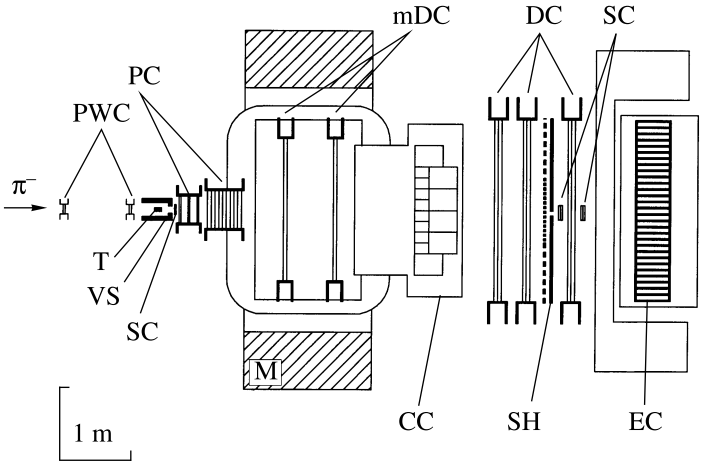

Fig. 1. Layout of the VES facility: (T) target, (VS) veto system, (PWC) proportional wire chambers, (PC) proportional chambers, (SC) scintillation counters, (M) magnet, (mDC) microdrift chambers, (CC) multichannel Cherenkov counter, (SH) scintillation hodoscope, (DC) drift chambers, (EC) electromagnetic calorimeter.

charged pions on nuclei. The intensity spectra of this exotic wave have different shapes in different final states; therefore, they cannot be described in terms of a universal amplitude. Sometimes, the spectrum features a peak that is characterized by a mass of $M \sim$ 1.4 GeV and a width of about 400 MeV and which can be interpreted as the exotic meson $\pi_1(1400)$. In other cases, there is a peak at $M \sim 1.6$ GeV such that its width is about 350 MeV and that it can associated with the exotic meson $\pi_1(1600)$.

The 1^{-+} wave was studied experimentally by using various facilities: VES (IHEP), E179 (KEK), GAMS/NA12 (IHEP–CERN), Crystal Barrel (CERN), and E852 (BNL) (see Table 3).

The first reliable observation of a wave characterized by the exotic quantum numbers of $J^{PC} = 1^{-+}$ was made in the VES experiment by means of a partial-wave analysis of diffraction-like reactions producing the $\eta\pi^-$ and $\eta'\pi^-$ final states [17, 18]. Later on, the VES experiment included studying a 1^{-+} wave in the $f_1\pi^-$, $b_1\pi^-$, $\rho\pi^-$, $\eta\pi^0$, and $\eta'\pi^0$ final states.

In the E-173 experiment at KEK, a significant P wave was also observed in the $\eta\pi^-$ system by means of a partial-wave analysis of $\pi^-A \to \pi^-\eta A$ reactions at a beam energy of 6.3 GeV [25], the spectrum in that case being substantially different from that which was obtained in the VES experiment at 37 GeV.

In the GAMS/NA12 experiment, an analysis of the charge-exchange reaction $\pi^-p \to \eta\pi^0 n$ revealed that the exotic-wave contribution is quite sizable, 20% of the total intensity.

In the Crystal Barrel experiment, a P-wave resonance at ~1.4 GeV in the $\eta\pi$ system was found from an analysis of the Dalitz plots of the $\eta\pi^+\pi^-$ and $\eta\pi^0\pi^0$ final states that are produced in $p\bar{p}$ annihilation.

Subsequently, the main results obtained in the VES and GAMS experiments from an analysis of the above exotic wave in various final states were confirmed in the E852 experiment at BNL.

$\eta\pi^-$ and $\eta'\pi^-$ Systems

Waves characterized by the orbital angular momenta of $L = 0$, 1, and 2 and the orbital-angular-momentum projections of $M = 0$ and 1 onto the Gottfried–Jackson axis were included in the analysis [18, 19]. It turned out that waves in which the naturality of exchange is negative are insignificant in both reactions.

Figure 2 shows the intensities of waves whose exchange naturality is positive, (*a*) D_+ ($L = 2$, $M = 1$) and (*b*) P_+ ($L = 1$, $M = 1$), and (*c*) the phase difference between the P_+ and D_+ waves. The D_+ wave, which displays a $a_2(1320)$-meson peak, is dominant. The P_+ wave is also significant—it is about 4% of the maximum of the D_+-wave intensity.

The graph representing the dependence of the phase difference between the P_+ and D_+ waves on the effective mass of the $\eta\pi^-$ system (Fig. 2*b*) exhibits a decrease in the mass region around 1.3 GeV/c^2

Table 2. Theoretical predictions for the decays of a $J^{PC} = 1^{-+}$ light hybrid meson

Decay mode	$b_1(1235)\pi$	$f_1(1285)\pi$	$\rho\pi$	$f_2\pi$	$\eta(\eta')\pi$
Width, MeV	170	60	5–20	0	0–10

Table 3. Experimental investigations of 1^{-+} states

Experiment	Reaction	Final state	References
VES	Diffraction; charge exchange; 28-, 37-, 43-GeV/c π^- beam	$\eta\pi^-$, $\eta'\pi^-$, $\rho\pi^-$ $f_1\pi^-$, $b_1\pi^-$, $\eta'\pi^0$	[17–24]
E179 (KEK)	Diffraction, 6.3-GeV/c π^- beam	$\eta\pi^-$	[25]
Crystal Barrel	$p\bar{p}$ annihilation, analysis of Dalitz plots for $\eta\pi^+\pi^-$, $\eta\pi^0\pi^0$, $\eta'\pi^+\pi^-$	$\eta\pi^\pm$, $\eta\pi^0$, $\eta'\pi^\pm$	[26]
GAMS/NA12	Charge exchange; 32-, 38-, 100-GeV/c π^- beam	$\eta\pi^0$	[27, 28]
E852 (BNL)	Diffraction; charge exchange; 18-GeV/c π^- beam	$\eta\pi^-$, $\eta'\pi^-$, $\rho\pi^-$ $f_1\pi^-$, $b_1\pi^-$, $\eta'\pi^0$	[29–34]

due to the $a_2(1320)$ meson and a slight increase for $M > 1.4$ GeV/c^2. For $M > 1.5$ GeV/c^2 [this is beyond the mass region of $a_2(1320)$], the D_+ wave shows a significant intensity, which may be associated either with the nonresonance production of the $\eta\pi^-$ system or with the production of an $a_2(1700)$ meson [$a_2(1700)$ is not yet a reliably established resonance].

The spectrum of the P_+ wave and the behavior of its phase with respect to the dominant D_+ wave can be described either as a nonresonance background or, within any possible hypothesis on the nature of the D_+ wave for $M > 1.5$ GeV/c^2, under the assumption that there exists the exotic resonance $\pi_1(1400)$. Versions of the description involving the resonance and the nonresonance background in the P_+ wave are represented by curves in Figs. 2*a*–2*c*. The D_+-wave spectrum is represented, in this case, as the $a_2(1320)$ resonance and a polynomial background.

In the $\eta'\pi^-$ system (Fig. 3), the situation is qualitatively different: an exotic wave is dominant here. As in the case of the $\eta\pi^-$ system, the D_+-wave spectrum for $M > 1.6$ GeV/c^2 can be due either to a resonance or to a nonresonance background. The resonance interpretation of the signal in the P_+ wave is possible in either case. The curves in Fig. 3 correspond to the version of description where the D_+ wave is represented as the sum of the $a_2(1320)$ and $a_2(1700)$ resonances, while the P_+ wave is represented as the $\pi_1(1600)$ resonance.

The seeming paradox—the strongly different P_+-wave spectra in the $\eta\pi^-$ and $\eta'\pi^-$ systems—can be explained as follows: the P-wave states in the $\eta_8\pi^-$ and $\eta_0\pi^-$ systems are substantially different (η_8 and η_0 stand for, respectively, the octet and the singlet member of the nonet of pseudoscalar mesons). Specifically, $\eta_0\pi^-$ is an $SU_f(3)$ octet, while the P_+-wave state in the $\eta_8\pi^-$ system can belong only to the $\mathbf{10}$–$\overline{\mathbf{10}}$ representation.

Of two hypothetical resonance states—$\pi_1(1400)$ in the $\eta\pi^-$ system and $\pi_1(1600)$ in the $\eta'\pi^-$ system—only the $\pi_1(1600)$ state can therefore be a hybrid meson, while the $\pi_1(1400)$ state must be a more complicated object—for example, a four-quark state [35].

The P-wave decuplet must also contain a state that decays to $K^+\pi^+$. Therefore, the experimental limit that was obtained in the effective-mass range 0.9–1.9 GeV/c^2 for the production of a P wave in the $K^+\pi^+$ system in the K beam [36] and which is indicative of the absence of the spin-1 meson decuplet in this mass region can be an argument against the resonance interpretation of the peak in the $\eta\pi^-$ system at $M \approx 1.4$ GeV/c^2.

The decay of the $J^{PC} = 1^{-+}$ hybrid state to $\eta\pi$ and $\eta'\pi$ cannot proceed according to the scheme in Fig. 4*(*a) [37]; only processes violating the OZI rule (Fig. 4*b*) and involving the production of an $SU_f(3)$ singlet in the final state—that is, predominantly η'—can contribute. A comparison of the squares of the matrix elements (intensity divided by the phase-space volume) for the exotic wave in the $\eta\pi^-$ and $\eta'\pi^-$ systems corroborates its predominantly hybrid character at $M > 1.4$ GeV/c^2 (Fig. 4*c*).

$b_1(1235)\pi$ System

In the VES experiment, an exotic wave in the $b_1\pi$ final state was investigated by means of a partial-wave analysis of $\pi^-A \to \omega\pi^-\pi^0A$ reactions [19, 20].

In Fig. 5, which was borrowed from [19], the intensities of (*a*) the $J^{PC} = 2^{++}$ wave in the $\omega\rho$ channel and (*b*) the $J^{PC} = 1^{-+}$ wave in the $b_1\pi$ channel are shown along with the difference of their phases (*c*).

In the 2^{++} wave, one can observe the $a_2(1320)$ peak and a peak at $M \approx 1.7$ GeV/c^2, which, as in the case of $\eta'\pi^-$, can be described either in terms

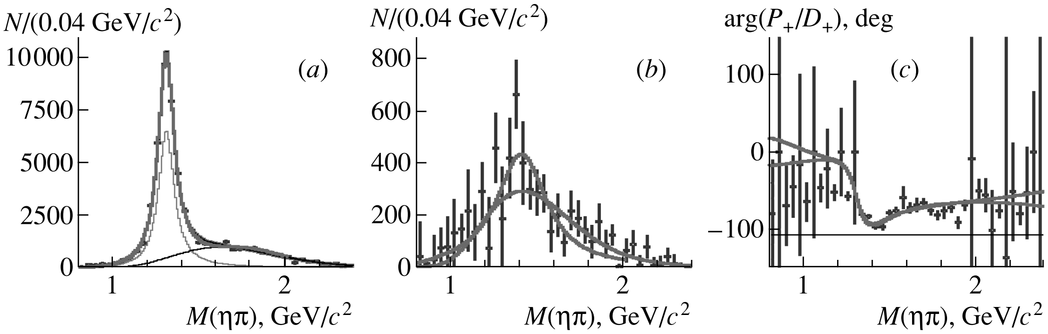

Fig. 2. Results of a partial-wave analysis of the $\eta\pi^-$ system: intensities of the (a) D_+ and (b) P_+ waves and (c) behavior of the phase difference between them.

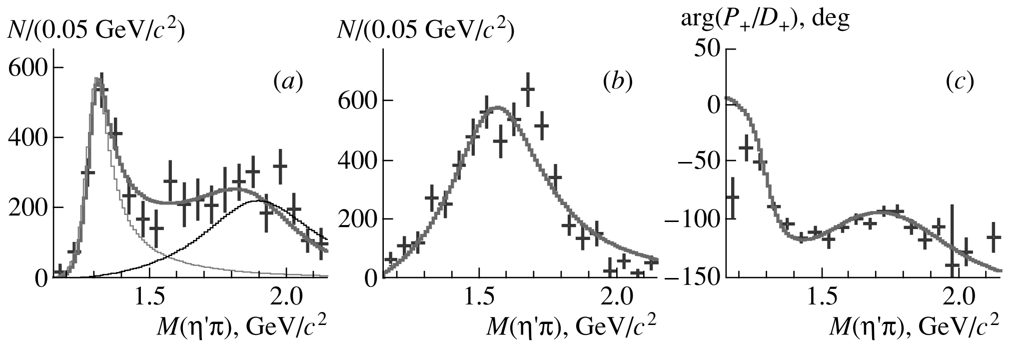

Fig. 3. Results of a partial-wave analysis of the $\eta'\pi^-$ system: intensities of the (a) D_+ and (b) P_+ waves and (c) behavior of the phase difference between them.

of a nonresonance background or in terms of the production of the $a_2(1700)$ resonance. In the exotic wave, there is also a broad peak at $M \approx 1.6$ GeV/c^2. In order to describe the spectrum of the 1^{-+} wave and its phase shift with respect to the 2^{++} wave, the contribution of an exotic resonance is required for any hypothesis on the nature of the peak in the 2^{++} wave for $M > 1.5$ GeV/c^2 . The curves in Fig. 5 correspond to the version of description where the 2^{++} wave is represented as the sum of the $a_2(1320)$ resonance and a nonresonance background, while the 1^{-+} wave is represented as the $\pi_1(1600)$ resonance and a nonresonance background.

A global fit of the $b_1\pi$ and $\eta'\pi^-$ spectra in terms of a resonance and an incoherent background yields the following values of the resonance parameters [21]: $M \approx 1.56 \pm 0.06$ GeV/c^2 and $\Gamma \approx 0.34 \pm 0.06$ GeV/c^2.

$f_1(1285)\pi^-$ System

An exotic wave in the $f_1\pi^-$ system was studied by means of a partial-wave analysis of the $\pi^- A \rightarrow \eta\pi^+\pi^-\pi^- A$ reactions in [17, 21].

In these reactions, the $J^{PC} = 1^{++}$ wave in the $f_1\pi^-$ system (at $L = 1$, $M = 0$) has a maximum intensity, forming a broad peak at a mass value of $M \sim 1.7$ GeV/c^2. The S wave in the $f_1\pi^-$ system has the exotic quantum numbers of $J^{PC} = 1^{-+}$ and is the second in intensity.

Figure 6 presents the results of new analysis of this reaction, which were obtained on the basis of vaster statistics by using a wider set of waves. Specifically given in this figure are the intensities of the (a) $J^{PC} = 1^{++}$ and (b) $J^{PC} = 1^{-+}$ waves in the $f_1\pi^-$ system and (c) the difference of their phases.

The total intensity of the exotic wave can be described under the assumption that it is due to the production of the $\pi_1(1600)$ resonance in the presence of a low nonresonance background. The parameters of this resonance, $M \approx 1.64 \pm 0.03$ GeV/c^2 and $\Gamma \approx 0.24 \pm 0.06$ GeV/c^2, are compatible with the parameters of the exotic resonance in the $\eta'\pi^-$ and $b_1\pi$ channels. This result differs from that obtained in [29] by the absence of significant structures in the exotic wave in the mass region $M > 1.9$ GeV/c^2.

A broad peak in the 1^{++} dominant wave in the $f_1\pi$ channel can be caused either by a nonresonance

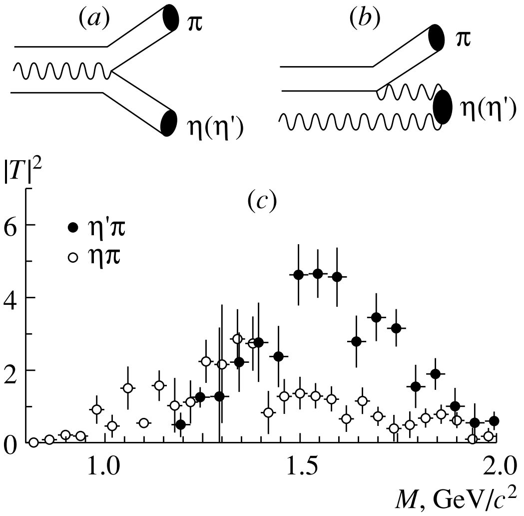

Fig. 4. (*a*) OZI-allowed and (*b*) OZI-forbidden diagrams for the decay of a hybrid meson and (*c*) squares of the matrix elements for the 1^{-+} wave in the $\eta\pi^-$ and $\eta'\pi^-$ systems.

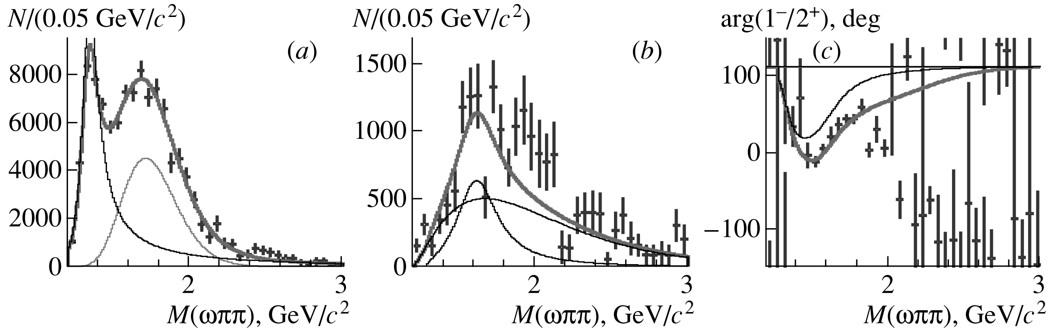

Fig. 5. Results of a partial-wave analysis of the $\omega\pi^-\pi^0$ system: intensities of (*a*) the $J^{PC}M\eta LS = 2^{++}1{+}S2$ wave in the $\omega\rho$ channel and (*b*) the $1^{-+}1{+}S1$ wave in the $b_1\pi$ channel and (*c*) the difference of their phases. Here, J, P, and C are, respectively, the spin, parity, and charge parity; M is the spin projection onto the Gottfried–Jackson axis; η is the exchange naturality; and L and S are, respectively, the orbital angular momentum and the total spin of the final state.

background or by the production of the $a_1(1640)$ resonance, which, just as the $a_2(1700)$ resonance, has not yet been reliably established.

Variations of the relative phase of the 1^{-+} and 1^{++} waves are modest (Fig. 6*c*); therefore, the interpretation of the peak in the exotic wave is completely determined by the interpretation of the 1^{++} wave: if a resonance is seen in the 1^{++} wave, the peak in the 1^{-+} wave is also a resonance, and vice versa.

$\pi^+\pi^-\pi^-$ *System*

The partial-wave analysis of the $\pi^+\pi^-\pi^-$ system involves a significant $J^{PC} = 1^{-+}$ exotic wave in the $\rho\pi^-$ channel, its intensity being 2 to 3% of the total intensity of the $\pi^+\pi^-\pi^-$ system (Fig. 7). The application of some models in the partial-wave analysis [17, 30] leads to the appearance of a peak at $M \sim 1.6$ GeV in its spectrum, this peak resembling the $\pi_1(1600)$ peak. The dependence of the magnitude of this peak on the model used was proven in [23]: it is maximal under the assumption of total coherence of waves ("tight model," Fig. 7*b*) and decreases strongly if this assumption is not used ("loose model," Fig. 7*c*). Thus, the results of the direct search for exotic resonances by means of a partial-wave analysis of the diffractive production of the $\pi^+\pi^-\pi^-$ system are not reliable.

The limit on the branching fraction of $\pi_1(1600)$ decay to $\rho\pi$ can be obtained from an analysis of the production of the 1^{-+} wave in the charge-exchange reaction $\pi^-p \to \eta'\pi^0 n$ [24]. A $\pi_1(1600)$ signal is present in the spectrum of the $\eta'\pi^-$ system and is absent in the $\eta'\pi^0$ spectrum (Fig. 8*a*); hence, $\pi_1(1600)$ is not produced in ρ exchange. By using the

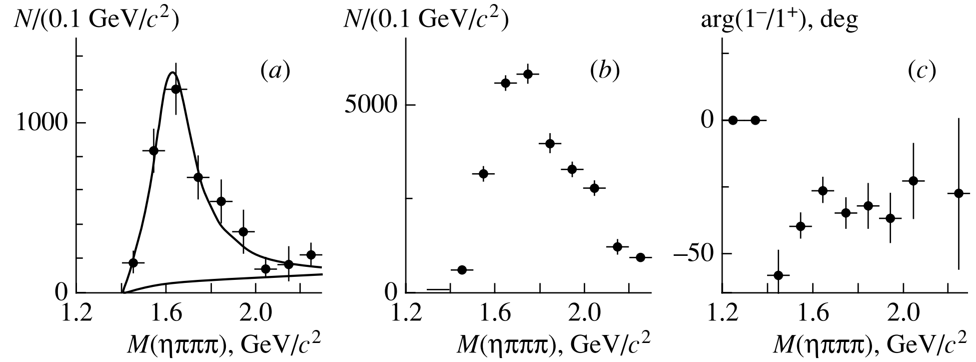

Fig. 6. Results of a partial-wave analysis of the $\pi^+\pi^-\pi^-\eta$ system: intensities of the $J^{PC}M\eta = (a)\ 1^{++}0+$ and $(b)\ 1^{-+}1+$ waves in the $f_1\pi^-$ channel and (c) the phase difference between them.

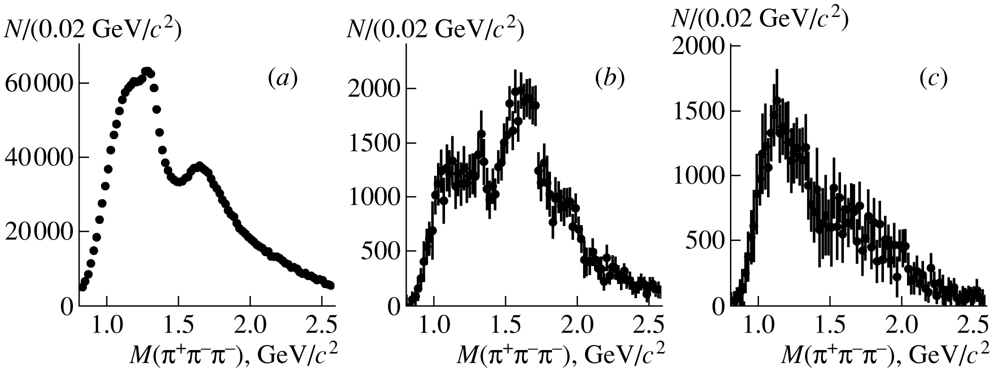

Fig. 7. Results of a partial-wave analysis of the $\pi^+\pi^-\pi^-$ system: (a) total intensity; intensity of the $J^PM\eta = 1^-1+$ wave in the $\rho\pi$ channel (b) under the assumption of full coherence and (c) in the case where this assumption is not used.

signal from an $a_2(1320)$ meson in the $\eta\pi^0$ spectrum (Fig. 8*b*) as a monitor of the intensity of ρ exchange, one can set a model-dependent limit: $\mathrm{Br}(\pi_1(1600) \to \rho\pi) < 3\%$ or $\Gamma(\pi_1(1600) \to \rho\pi) < 10$ MeV.

The 1^{-+} wave in the $f_2\pi^-$ final state was also included in the partial-wave analysis of the $\pi^+\pi^-\pi^-$ system. It turned out that its intensity is compatible with zero.

1^{-+} Wave in the VES Experiment: Discussion

In the VES experiment, a partial-wave analysis was performed for the $\eta\pi^-$, $\eta'\pi^-$, $\pi^+\pi^-\pi^-$, $\eta\pi^+\pi^-\pi^-$, and $\omega\pi^-\pi^0$ systems.

$\boldsymbol{\pi_1}$**(1400)**. In the wave characterized by the exotic quantum numbers of $J^{PC} = 1^{-+}$ in the $\eta\pi^-$ system, there is a broad peak at a mass value of $M \sim 1.4$ GeV$/c^2$. Since the P_+-wave state in the $\eta_8\pi^-$ system can belong only to the $SU_f(3)$ decuplet, the peak at a mass value of 1.4 GeV$/c^2$ cannot be a signal from a hybrid meson. Moreover, nonobservation of the production of a P-wave state in the K beam in the $K^+\pi^+$ system—it must present in this decuplet—casts some doubt on the resonance interpretation of this peak.

$\boldsymbol{\pi_1}$**(1600)**. In the $\eta'\pi^-$, $f_1(1235)\pi^-$, and $b_1(1235)\pi^-$ systems, there is a broad peak at a mass value of $M \sim 1.6$ GeV$/c^2$, which can be interpreted as an exotic resonance $\pi_1(1600)$ of width about 300 MeV. This peak is not observed in the $\rho\pi^-$ and $f_2\pi^-$ systems.

Strictly speaking, it is presently impossible to make a definitive conclusion on the resonance nature of this peak: the phase of the exotic wave is measured with respect to the $J^{PC} = 1^{++}$ and 2^{++} waves, whose origin has no unambiguous explanation in this mass region, since the $a_1(1640)$ and $a_2(1700)$ resonances have not yet been firmly established. In order to clarify the nature of this peak in the exotic wave, it is therefore necessary to study these resonances further. If we adopt the hypothesis that this peak is a signal from the hybrid resonance $\pi_1(1600)$, a comparison of the observable properties of this peak with theoretical predictions makes it possible to draw the following conclusions.

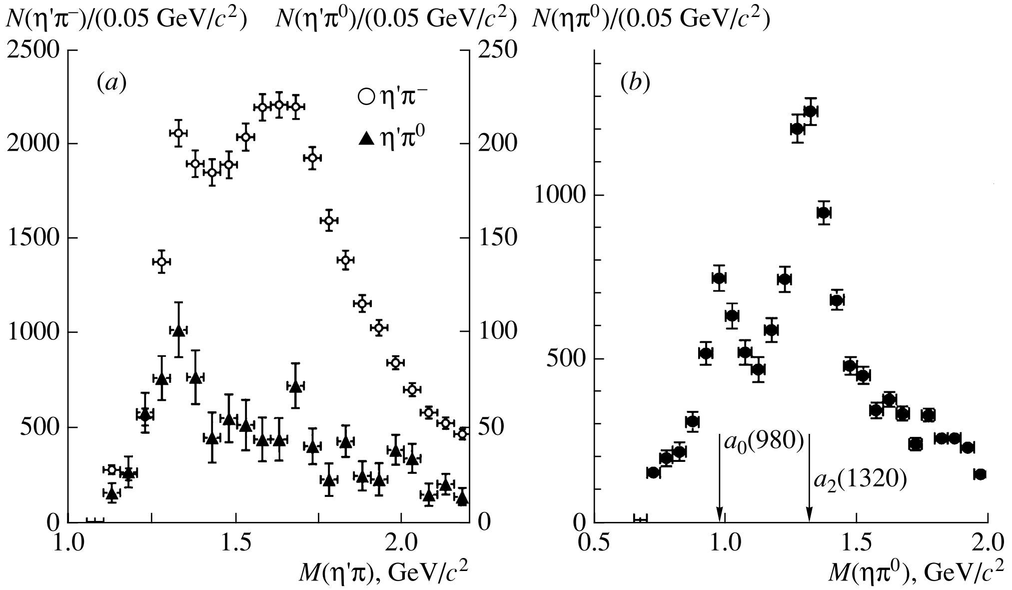

Fig. 8. Effective-mass distributions of the (*a*) $\eta'\pi^-$, $\eta'\pi^0$ and (*b*) $\eta\pi^0$ systems.

The mass value (1.6 GeV) is within the predictions of the bag model and somewhat below the predictions of the current-tube model [9] and lattice QCD [10].

The experimental relationship between the branching fractions of the $\pi_1(1600)$ decays is as follows:

$$b_1\pi : f_1\pi : \rho\pi : \eta'\pi$$
$$= (1.0 \pm 0.3) : (1.1 \pm 0.3) : <0.3 : 1.$$

The maximum deviation from the predictions of the current-tube model ([8], Table 2) is observed in the $\eta'\pi$ channel. This can be explained by the fact that the respective calculations disregard the contribution of OZI-forbidden processes (see Fig. 4*b*). Their contribution may be significant in hybrid-meson decays. For example, the calculations of the features of hybrid mesons from b quarks ($b\bar{b}g$) in lattice QCD [11] showed that, for them, the deexcitation of gluon degrees of freedom via the emission of the $SU_f(3)$-singlet state (f_0 mesons)—that is, a process of the type in Fig. 4*b*—is the main decay mode. Although the speed of modern computers is not yet sufficient for performing such calculations for hybrid mesons from light quarks, there is every reason to believe that, for them, the probability of OZI-forbidden decays accompanied by the emission of the $SU_f(3)$ singlet ($\eta'\pi$) is also significant. It seems that the same mechanism can lead to an increase in the branching fraction of decay to $f_1\pi^-$ with respect to the predictions of the current-tube model.

A similar effect is observed in the decays of the $\pi(1800)$ object, whose resonance nature is unquestionable and whose interpretation as a hybrid meson is highly probable.

INVESTIGATION OF THE $J^{PC} = 0^{-+}$ $\pi(1800)$ OBJECT

Since the quantum numbers of $J^{PC} = 0^{-+}$ are not exotic, an interpretation of states characterized by such quantum numbers as ordinary or exotic resonances is possible on the basis of their observable properties: mass, width, and decay branching fractions.

Calculations performed within the current-tube model [15] predict close mass values of $M \sim 1.8$–2.0 GeV/c^2 for $J^{PC} = 0^{-+}$ hybrid mesons (π_H) and ordinary mesons (π-meson radial excitation $3S$). Table 4 gives theoretical predictions for the π_H and $3S$ widths with respect to decays to various final states.

Thus, 0^{-+} hybrid and ordinary ($3S$) mesons have no common decay channels of high intensity; therefore, it is natural to expect that their mixing is modest. The hybrid state decays predominantly through the $f_0(1300)\pi$ channel, which is suppressed for the ordinary state ($3S$).

The features of the $J^{PC} = 0^{-+}$ meson state $\pi(1800)$ were studied in detail in the VES experiment. It was shown that the branching fraction of $\pi(1800)$ decay to $f_0(1300)\pi$ is large; therefore, this state can be considered as a candidate for hybrid mesons. However, its decay branching ratios differ somewhat from those predicted in [15].

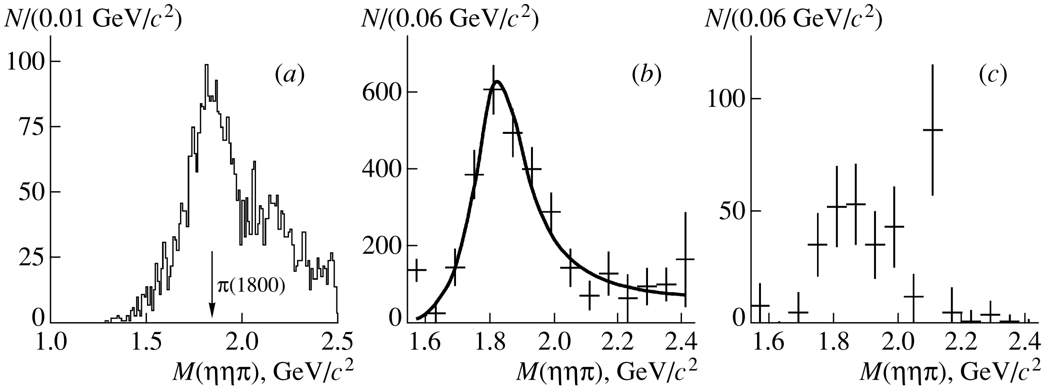

Fig. 9. (*a*) Effective-mass distribution of the $\eta\eta\pi$ system and intensities of (*b*) the $0^- S$ wave in the $a_0(980)\eta$ channel and (*c*) the $0^- S$ wave in the $f_0(1500)\pi$ channel.

The $\pi(1800)$ object was first observed with the Dubna–Milan spectrometer at the IHEP U-70 accelerator [38] in the $f_0(1300)\pi$ decay mode $f_0 \to \pi^+\pi^-$.

Its $f_0(980)\pi$, $f_0(1300)\pi$, $f_0(1500)\pi$, $a_0(980)\eta$, and $(K\pi)_S K$ decay channels were studied in the VES experiment in the $\pi^+\pi^-\pi^-$, $K^+K\pi^-$, $\eta\eta\pi^-$, and $\eta'\eta\pi^-$ final states [39–41]. It was shown that its decays to $\rho\pi$, K^*K, and $f_2\pi$ are suppressed.

In the E852 experiment (BNL), the $\pi(1800)$ object was observed in the $\pi^+\pi^-\pi^-$ final state in the $f_0(600)\pi$ and $f_0(980)\pi$ decay channels [42].

$\eta\eta\pi^-$ *System*

The effective-mass spectrum of the $\eta\eta\pi^-$ system and the results of the partial-wave analysis [16, 39] are presented in Fig. 9. The effective-mass spectrum (Fig. 9*a*) is dominated by the peak corresponding to $\pi(1800)$. In the partial-wave analysis, this peak is observed in the $J^{PC} = 0^{-+}$ waves in the $a_0(980)\eta$ and $f_0(1500)\pi$ channels (Figs. 9*b*, 9*c*). The resonance parameters of the peak in the $a_0(980)\eta$ channel are

$$M \approx 1840 \pm 10\,(\text{stat.}) \pm 10\,(\text{syst.})\ \text{MeV}/c^2,$$

$$\Gamma \approx 210 \pm 30\,(\text{stat.}) \pm 30\,(\text{syst.})\ \text{MeV}/c^2.$$

$\pi^+\pi^-\pi^-$ *System*

The results of the VES experiment devoted to studying $\pi(1800)$ in the $\pi^+\pi^-\pi^-$ final state were reported in [40]. Figure 10 presents the results of a new partial-wave analysis performed for the $\pi^+\pi^-\pi^-$ system on the basis of a vaster statistical sample by using a wider set of waves. Figures 10*a*–10*d* display the intensities of the $J^{PC} = 0^{-+}$ waves in the $f_0(1300)\pi^-$, $f_0(980)\pi^-$, $f_0(1500)\pi^-$, and $\rho\pi^-$ channels. Figures 10*e* and 10*f* show the phases of the 0^{-+} waves in the $f_0(980)\pi^-$ and $f_0(1500)\pi^-$ channels with respect to the $J^{PC} = 2^{-+}$ wave in the $f_2\pi$ channel. The 2^{-+} wave in the $f_2\pi$ channel was chosen as a reference one for phase measurements because this wave is dominated by the production of the $\pi_2(1670)$ meson, which has received adequate study.

The $\pi(1800)$ object is observed in the $f_0(980)\pi^-$, $f_0(1300)\pi^-$, and $f_0(1500)\pi^-$ decay channels, but it is not observed in the $\rho\pi^-$ channel. In the graphs representing the phase difference as a function of the effective mass (Fig. 10*e*, 10*f*), there are motion downward in the range 1500–1700 MeV due to the production of $\pi_2(1670)$ in the reference wave and motion upward in the range 1700–2000 MeV due to the production of the $\pi(1800)$ object. This proves unambiguously the resonance nature of $\pi(1800)$.

The parameters of the peak in the $0^- S$ $f_0(980)\pi^-$ and $0^- S$ $f_0(1300)\pi^-$ waves are

$$M \approx 1775 \pm 7\,(\text{stat.}) \pm 10\,(\text{syst.})\ \text{MeV}/c^2,$$

$$\Gamma \approx 190 \pm 15\,(\text{stat.}) \pm 15\,(\text{syst.})\ \text{MeV}/c^2.$$

The 0^{-+} wave in the $f_2\pi^-$ system was also included in the partial-wave analysis. It turned out that its intensity is compatible with zero.

Table 4. Decay widths (in MeV) of the $J^{PC} = 0^{-+}$ hybrid (π_H) and ordinary ($3S$) mesons according to the predictions of the current-tube model

	$\rho\pi$	$\rho\omega$	$\rho(1470)\pi$	$f_0(1300)\pi$	$f_2\pi$	K^*K	Total width
$3S$	30	74	56	6	29	36	231
π_H	30	0	30	170	6	5	240

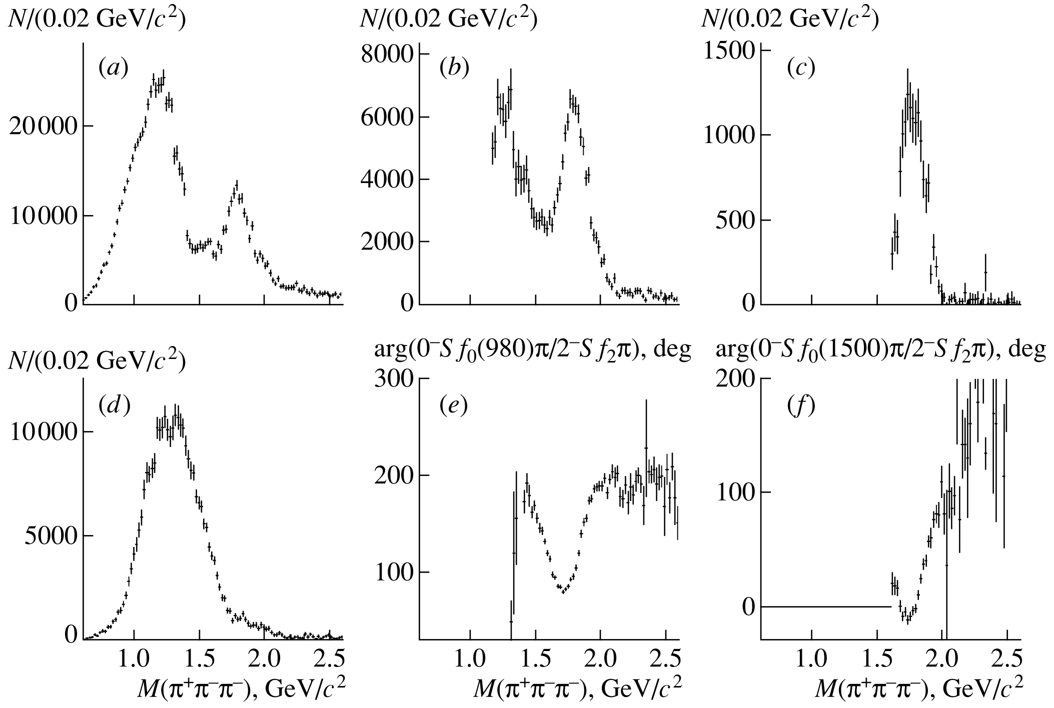

Fig. 10. Results of the partial-wave analysis of the $\pi^+\pi^-\pi^-$ system: intensities of the $J^{PC} = 0^{-+}$ wave in the (a) $f_0(1300)\pi$, (b) $f_0(980)\pi$, (c) $f_0(1500)\pi$, and (d) $\rho\pi$ channels; phases of the 0^{-+} waves in the (e) $f_0(980)\pi^-$ and (f) $f_0(1500)\pi^-$ channels with respect to the $J^{PC} = 2^{-+}$ wave in the $f_2\pi$ channel.

$K^+K^-\pi^-$ System

Figure 11 presents the results of the partial-wave analysis of the $K^+K^-\pi^-$ system [41]: the intensities of the $J^P = 0^-$ waves in the $f_0\pi^-$, κK^-, and $K^*(890)K^-$ channels (the isobars κ and f_0 represent a parametrization of S-wave $K^+\pi^-$ and K^+K^- scattering [43]). The expected intensity of the nonresonance production of the $K^+K^-\pi^-$ system in the corresponding waves is shown by the dashed curves against the background of the histograms.

The $\pi(1800)$ peak is present in the intensity spectra of the 0^-S wave in the $f_0\pi^-$ channel and the 0^-S wave in the κK^- channel, but it is absent in the 0^-S wave in the $K^*(890)K^-$ channel. Its resonance parameters in the 0^-S wave in the $f_0\pi^-$ channel and the 0^-S wave in the κK^- channel are

$$M \approx 1790 \pm 14\,(\text{stat.})\,\text{MeV}/c^2,$$

$$\Gamma \approx 210 \pm 70\,(\text{stat.})\,\text{MeV}/c^2.$$

$\pi(1800)$ in the VES Experiment: Discussion

The branching fractions of $\pi(1800)$ decays are given in Table 5 according to a global analysis of all decay channels observed in the VES experiment for this object [44].

The mass and the width of the observed resonance $\pi(1800)$ are close to the values predicted theoretically in [15] for the $J^{PC} = 0^{-+}$ hybrid resonance. It decays predominantly through the $f_0(1300)\pi$, $f_0(980)\pi$, and $f_0(1500)\pi$ channels; the branching fractions of decays to $\rho\pi$, $f_2\pi$, and K^*K are small.

A high branching fraction of decay to $f_0(1300)\pi$ and the suppression of decays to $\rho\pi$, $f_2\pi$, and K^*K favor the interpretation of this state as a hybrid meson. However, the set of decay branching fractions forms a more complicated pattern than that predicted by the theory. This object decays not only to $f_0(1300)\pi$ but has compatible branching fractions of decays to $f_0(980)\pi$ and $f_0(1500)\pi$. While $f_0(1300)$ is assumed to consist of u and d quarks, $f_0(980)$ and $f_0(1500)$ involve a large $s\bar{s}$ component. It can be seen from Table 5 that, on the whole, the branching fraction of $\pi(1800)$ decay to $KK\pi$ is commensurate with that for $\pi(1800)$ decay to 3π.

Thus, the OZI rule in $\pi(1800)$ decays is strongly violated, and the contribution of the deexcitation of gluon degrees of freedom via the emission of the $SU_f(3)$-singlet state (Fig. 4b) is rather high. It was shown in [11] that processes of this type are of importance for the decays of hybrid mesons from b quarks ($b\bar{b}g$); therefore, their contribution to the decay of hybrid mesons from light quarks can also be significant,

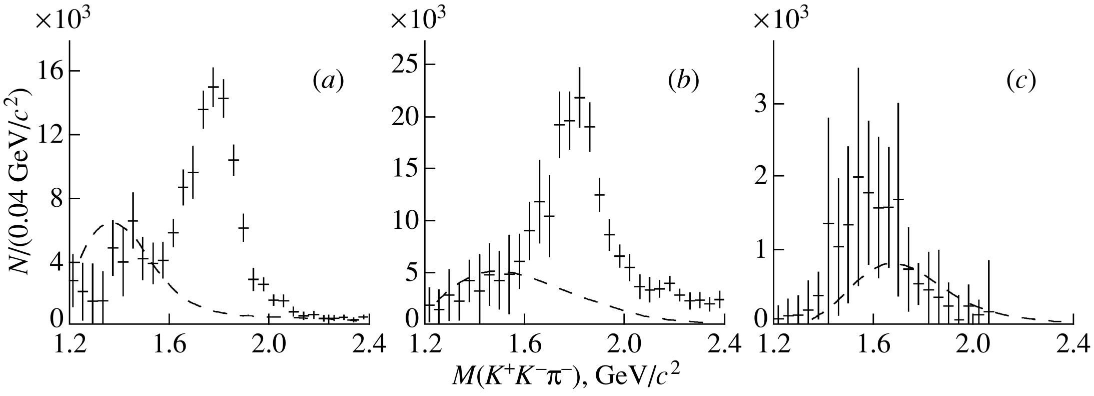

Fig. 11. Results of the partial-wave analysis of the $K^+K^-\pi^-$ system: intensities of the $J^P = 0^-$ wave in the (a) $f_0(980)\pi$, (b) κK, and (c) $K^{*(890)}K$ channels.

so that the hypothesis that the $\pi(1800)$ object is a hybrid does not contradict the experimentally observed branching fractions of its decay.

On the other hand, radial excitations in the $q\bar{q}$ system can also be considered as excitations of gluon degrees of freedom, and we cannot rule out the possibility that the $3S$ state (Table 4) also decays, with a high probability, via the emission of the $SU_f(3)$-singlet state (f_0 mesons). In this case, there will be a strong mixing of the hybrid (π_H) and the ordinary ($3S$) state, and the experimentally observed resonance $\pi(1800)$ will be their combination. In order to analyze in detail the nature of the $\pi(1800)$ object, one needs theoretical predictions for decay branching fractions within more realistic models that would take into account the contribution of OZI-forbidden processes.

CONCLUSION

The current state of investigations of the features of three candidates for exotic mesons—$\pi_1(1400)$ and $\pi_1(1600)$ characterized by the exotic quantum numbers of $J^{PC} = 1^{-+}$ and $\pi(1800)$ characterized by the quantum numbers of 0^{-+}—in the VES experiment has been presented.

In the $\eta\pi^-$ system, the $\pi_1(1400)$ object is observed in the P wave. Since the P_+-wave state in the $\eta\pi^-$ system must belong to the $SU_f(3)$ decuplet, the $\pi_1(1400)$ object cannot be a hybrid meson [35]. Moreover, there exists an experimental limit on the production of the P-wave state in the $K^+\pi^+$ system in this effective-mass region [36]. This is indicative of the absence of the spin-1 light meson decuplet and casts some doubt on the resonance interpretation of the $\pi_1(1400)$ object.

The $\pi_1(1600)$ object observed in the $\eta'\pi^-$, $b_1(1235)\pi^-$, and $f_1(1285)\pi^-$ systems is an $SU_f(3)$-octet state and can be interpreted as a hybrid meson. However, there are presently no model-independent methods for measuring the behavior of its phase; therefore, it is impossible, strictly speaking, to interpret it as a reliably established resonance.

If we assume that $\pi_1(1600)$ is a resonance, its experimentally observed properties correspond by and large to theoretical predictions for 1^{-+} hybrid mesons. The deviation from the predictions of phenomenological models—the branching fraction of the

Table 5. Branching ratios for the decays of $\pi(1800)$ according to measurements in the VES experiment

Final state	Decay channel	Branching ratio
$\pi^+\pi^-\pi^-$		1
	$f_0(1300)_{\pi^+\pi^-}\pi^-$	1.1 ± 0.1
	$f_0(980)_{\pi^+\pi^-}\pi^-$	0.44 ± 0.15
	$f_0(1500)_{\pi^+\pi^-}\pi^-$	0.11 ± 0.05
	$\rho\pi^-$	<0.02
	$f_2\pi^-$	0
$K^+K^-\pi^-$		0.29 ± 0.10
	$K^*(892)K^-$	<0.03
$\eta\eta\pi^-$		0.15 ± 0.06
	$a_0^-(980)_{\eta\pi^-}\eta$	0.13 ± 0.06
	$f_0(1500)_{\eta\eta}\pi^-$	0.012 ± 0.005
$\eta'\eta\pi^-$	$f_0(1500)_{\eta'\eta}\pi^-$	0.026 ± 0.010

decay $\pi_1(1600) \to \eta'\pi$ is large—can be explained by a significant contribution from OZI-forbidden processes (Fig. 4*b*), which are not taken into account in theoretical calculations.

The $\pi(1800)$ object is a reliably established resonance, which is observed in the $\pi^+\pi^-\pi^-$, $\eta\eta\pi^-$, $\eta'\eta\pi^-$, and $K^+K^-\pi^-$ final states in the $f_0(980)\pi$, $f_0(1300)\pi$, $f_0(1500)\pi$, and $a_0(980)\eta$ decay modes.

The current-tube model predicts the existence of a hybrid and an ordinary state close in mass that are characterized by the quantum numbers of $J^{PC} = 0^{-+}$.

The mass, width, and decay branching fractions of $\pi(1800)$ are in qualitative agreement with the predictions of the current-tube model for a hybrid state: the branching fraction of its decay to $f_0(1300)\pi$ is high, while its decays to $\rho\pi$, $f_2\pi$, and K^*K are suppressed.

However, $\pi(1800)$ also decays, with a high probability, to $f_0(980)\pi$ and $f_0(1500)\pi$, this being indicative of a strong violation of the OZI rule. We cannot rule out the possibility that OZI-forbidden processes, which are disregarded in the theoretical calculations, make a significant contribution to the decays of both the hybrid and the ordinary 0^{-+} state. In this case, the experimentally observed resonance $\pi(1800)$ is a combination of the hybrid and the ordinary state. In order to perform a thorough analysis of its nature, it is necessary to have theoretical predictions obtained with allowance for OZI-forbidden processes.

ACKNOWLEDGMENTS

This work was supported in part by the Russian Foundation for Basic Research (RFBR), project nos. 02-02-17479 and 00-15-96689, and by the RFBR program for support of leading scientific schools, project no. 1695.2003.2.

REFERENCES

1. T. DeGrand, R. L. Jaffe, K. Johnson, and J. E. Kiskis, Phys. Rev. D **12**, 2060 (1975); A. Chodos, R. L. Jaffe, K. Johnson, *et al.*, Phys. Rev. D **9**, 3471 (1974).
2. A. I. Vaĭnshteĭn and L. B. Okun', Yad. Fiz. **23**, 1347 (1976) [Sov. J. Nucl. Phys. **23**, 716 (1976)]; R. L. Jaffe and K. Johnson, Phys. Lett. B **60B**, 201 (1976).
3. T. Barnes, F. E. Close, F. de Viron, and J. Weyers, Nucl. Phys. B **224**, 241 (1983); M. S. Chanowitz and S. R. Sharpe, Nucl. Phys. B **222**, 211 (1983).
4. D. Horn and J. Mandula, Phys. Rev. D **17**, 898 (1978); S. Ishida, H. Sawazaki, M. Oda, and K. Yamada, Phys. Rev. D **47**, 179 (1993).
5. I. I. Balitsky, D. I. Diakonov, and A. V. Yung, Z. Phys. C **33**, 265 (1986).
6. J. I. Latorre, P. Pascual, and S. Narison, Z. Phys. C **34**, 347 (1987); J. Govaerts, L. J. Reinders, P. Francken, *et al.*, Nucl. Phys. B **284**, 674 (1987).
7. N. Isgur, R. Kokoski, and J. Paton, Phys. Rev. Lett. **54**, 869 (1985).
8. F. E. Close and P. R. Page, Nucl. Phys. B **443**, 233 (1995).
9. T. Barnes, F. E. Close, and E. S. Swanson, Phys. Rev. D **52**, 5242 (1995); P. R. Page, E. S. Swanson, and A. P. Szczepaniak, Phys. Rev. D **59**, 034016 (1999).
10. C. Bernard *et al.*, Phys. Rev. D **68**, 074505 (2003).
11. C. McNeile, C. Michael, and P. Pennanen, Phys. Rev. D **65**, 094505 (2002); C. Michael, hep-ph/0308293.
12. L. Micu, Nucl. Phys. B **10**, 521 (1969).
13. E. S. Ackleh, T. Barnes, and E. S. Swanson, Phys. Rev. D **54**, 6811 (1996).
14. R. Ricken, M. Koll, D. Merten, and B. C. Metsch, Eur. Phys. J. A **18**, 667 (2003).
15. T. Barnes, F. E. Close, P. R. Page, and E. S. Swanson, Phys. Rev. D **55**, 4157 (1997).
16. S. I. Bityukov *et al.*, Phys. Lett. B **268**, 137 (1991).
17. Yu. Gouz *et al.*, in *Proceedings of the XXVI International Conference on High Energy Physics "ICHEP 1992"*, Ed. by J. R. Sanford; AIP Conf. Proc. **272**, 572 (1992).
18. G. M. Beladidze *et al.*, Phys. Lett. B **313**, 276 (1993).
19. V. Dorofeev *et al.*, in *Proceedings of IX International Conference on Hadron Spectroscopy "HADRON 2001", Protvino, 2001*, Ed. by D. V. Amelin and A. M. Zaitsev; AIP Conf. Proc. **619**, 143 (2002).
20. D. V. Amelin *et al.*, Yad. Fiz. **62**, 487 (1999) [Phys. At. Nucl. **62**, 445 (1999)].
21. A. Zaitsev *et al.*, Nucl. Phys. A **675**, 155 (2000).
22. Yu. Khokhlov *et al.*, Nucl. Phys. A **663**, 596 (2000).
23. A. M. Zaitsev *et al.*, in *Proceedings of 7th International Conference on Hadron Spectroscopy (HADRON 97), Upton, N.Y., 1997*, Ed. by S. U. Chung and H. J. Willutzki; AIP Conf. Proc. **432**, 461 (1998).
24. D. V. Amelin *et al.*, Yad. Fiz. **67**, 1433 (2004) [Phys. At. Nucl. **67**, 1408 (2004)].
25. H. Aoyagi *et al.*, Phys. Lett. B **314**, 246 (1993).
26. A. Abele *et al.*, Phys. Lett. B **423**, 175 (1998); **446**, 349 (1999); J. Reinnharth *et al.*, Nucl. Phys. A **692**, 268 (2001).
27. D. Alde *et al.*, Yad. Fiz. **62**, 462 (1999) [Phys. At. Nucl. **62**, 421 (1999)].
28. S. Sadovsky *et al.*, Nucl. Phys. A **665**, 421 (1999).
29. J. Kuhn *et al.*, Phys. Lett. B **595**, 109 (2004).
30. G. S. Adams *et al.*, Phys. Rev. Lett. **81**, 5760 (1998).
31. D. R. Thompson *et al.*, Phys. Rev. Lett. **79**, 1630 (1997).
32. E. I. Ivanov *et al.*, Phys. Rev. Lett. **86**, 3977 (2001).
33. A. R. Dzierba *et al.*, Phys. Rev. D **67**, 094015 (2003).
34. A. Popov *et al.*, in *Proceedings of the IX International Conference on Hadron Spectroscopy "HADRON 2001", Protvino, 2001*, Ed. by D. V. Amelin and A. M. Zaitsev; AIP Conf. Proc. **619**, 565 (2002).
35. S. U. Chung, E. Klempt, and J. G. Korner, Eur. Phys. J. A **15**, 539 (2002).
36. P. Estabrooks *et al.*, Nucl. Phys. B **133**, 490 (1978).

37. F. E. Close and H. J. Lipkin, Phys. Lett. B **196**, 245 (1987).
38. G. Bellini *et al.*, Phys. Rev. Lett. **48**, 1697 (1982).
39. D. V. Amelin *et al.*, Yad. Fiz. **59**, 1021 (1996) [Phys. At. Nucl. **59**, 976 (1996)].
40. D. V. Amelin *et al.*, Phys. Lett. B **356**, 595 (1995).
41. D. V. Amelin *et al.*, Phys. Lett. B **337**, 219 (1994).
42. S. U. Chung *et al.*, Phys. Rev. D **65**, 072001 (2002).
43. D. L. Au, D. Morgan, and M. R. Pennington, Phys. Rev. D **35**, 1633 (1987); D. Aston *et al.*, Nucl. Phys. B **296**, 493 (1988).
44. V. Nikolaenko *et al.*, in *Proceedings of the 10th International Conference on Hadron Spectroscopy (HADRON 2003), Aschaffenburg, Germany, 2003.*

Translated by A. Isaakyan

Physics of Atomic Nuclei, Vol. 68, No. 3, 2005, pp. 372–377. Translated from Yadernaya Fizika, Vol. 68, No. 3, 2005, pp. 401–406.
Original Russian Text Copyright © 2005 by Amelin, Gavrilov, Gouz, Dorofeev, Dzhelyadin, Zaitsev, Zenin, Ivashin, Kachaev, Kabachenko, Karyukhin, Konoplyannikov, Konstantinov, Kostyukhin, Matveev, Nikolaenko, Ostankov, Polyakov, Ryabchikov, A.A. Solodkov, A.V. Solodkov, Solovianov, Starchenko, Fenyuk, Khokhlov.

Measurement of Form Factors for the Decay $\eta' \to \eta\pi^-\pi^+$

D. V. Amelin, Yu. G. Gavrilov, Yu. P. Gouz, V. A. Dorofeev, R. I. Dzhelyadin, A. M. Zaitsev, A. V. Zenin, A. V. Ivashin, I. A. Kachaev, V. V. Kabachenko, A. N. Karyukhin, A. N. Konoplyannikov, V. F. Konstantinov, V. V. Kostyukhin, V. D. Matveev, V. I. Nikolaenko, A. P. Ostankov, B. F. Polyakov, D. I. Ryabchikov*, A. A. Solodkov, A. V. Solodkov, O. V. Solovianov, E. A. Starchenko, A. B. Fenyuk, and Yu. A. Khokhlov

Institute for High-Energy Physics, Protvino, Moscow oblast, 142284 Russia

Received May 24, 2004; in final form, September 27, 2004

Abstract—Form factors measured for the decay $\eta' \to \eta\pi^-\pi^+$ in $\pi^- A \to \eta'\pi^- A^*$ reactions at a beam momentum of $p_\pi = 28$ GeV are presented. The distribution in Dalitz variables for 7000 decay events is described well within a linear and a nonlinear parametrization of the relavant matrix element. The slope parameter in the variable y differs from zero significantly. It is $\mathrm{Re}\alpha = -0.072 \pm 0.012\,(\text{stat.}) \pm 0.006\,(\text{syst.})$ in the linear and $a = -0.120 \pm 0.027\,(\text{stat.}) \pm 0.015\,(\text{syst.})$ in the nonlinear parametrization. In this decay, the C-violation parameter is compatible with zero, $c = 0.021 \pm 0.024$.

INTRODUCTION

Despite a long history, the decay $\eta' \to \eta\pi\pi$ has not yet been adequately studied and understood. Therefore, it is of importance to refine the form factors for this decay. Interest in this decay is first of all motivated by the nature of the η' meson itself: a high concentration of the gluon component there must strongly affect the dynamics of its decays [1], especially the dynamics of the dominant decay $\eta' \to \eta\pi\pi$ [2].

In a phenomenological description of the decays $\eta' \to \eta\pi^+\pi^-$ and $\eta' \to \eta\pi^0\pi^0$, it is convenient to employ the Dalitz variables

$$x = \frac{\sqrt{3}}{Q}(T_{\pi_1} - T_{\pi_2}), \quad y = \frac{m_\eta + 2m_\pi}{m_\pi}\frac{T_\eta}{Q} - 1, \quad (1)$$

where $\pi_1 = \pi^+/\pi^0$, $\pi_2 = \pi^-/\pi^0$, T stands for the kinetic energies of the η and π mesons in the η'-meson c.m. frame, and $Q = T_\eta + T_{\pi_1} + T_{\pi_2}$ is the energy deposition.

In the literature, the relevant matrix element is parametrized in a linear or a nonlinear form,

$$|M|^2 = |1 + \alpha y|^2 + cx + dx^2 \quad (2)$$

(α is a complex-valued parameter) or

$$|M|^2 = 1 + ay + by^2 + cx + dx^2, \quad (3)$$

respectively. In these formulas, the parameter c takes into account C violation. It should be noted that these parametrizations are not equivalent, that in (3) being more general than that in (2).

The decay $\eta' \to \eta\pi\pi$ was studied theoretically by many authors on the basis of effective chiral Lagrangians. The earliest studies dating back to the current-algebra period resulted in predicting a rather large value for the slope parameter in the variable y, $\alpha = -(0.41–0.45)$ [3], and an extremely low value for the partial width $\Gamma(\eta' \to \eta\pi\pi)$ [4]. Allowance for contact terms from operators of dimension higher than that of the minimal chiral Lagrangian and for loop corrections leads to a much more isotropic decay spectrum close to that in the phase-space model and increases severalfold the value of the partial width. For example, the values predicted in [5], which is one of the latest studies on the subject, for the parameters of the nonlinear matrix element for the decay $\eta' \to \eta\pi^+\pi^-$ are $a = -0.09$, $b = -0.06$, and $d = -0.003$. We note that these values are not compatible with the linear parametrization (2) ($b < 0$). The authors of that study took partly into account the final state interaction of the mesons—they summed diagrams involving any number of rescatterings of two final mesons, with the third meson issuing from the primary vertex without rescattering. The sensitivity of the matrix element to higher order corrections indicates that it is of importance to measure decay parameters precisely.

A large effect of final-state rescattering can also indicate that models assuming the dominance of the scalar-meson nonet [6] are valid for η'-meson decays. It follows that, in principle, investigation of the decay $\eta' \to \eta\pi\pi$ can also shed light on the nature of light scalar mesons and refine their features and interactions [7].

---

[*] E-mail: `ryabchikov@mx.ihep.su`

It should be emphasized that many theoretical studies, including that quoted in [5], predict values of the parameters a and b such that they are not compatible with the linear parametrization (2). Thus, it is necessary to use the parametrization in (3) in processing experimental data. However, experimental groups present the parameters of the linear matrix element because of the paucity of statistics accumulated for η' mesons.

The parameters describing the decay $\eta' \to \eta\pi^+\pi^-$ were determined by using the linear parametrization of the matrix element in [8] on the basis of 1400 events, $\mathrm{Re}\alpha = -0.08 \pm 0.03$, and in [9] on the basis of the statistics of 6700 events against a sizable background, $\mathrm{Re}\alpha = -0.021 \pm 0.025$.

There are no data in the literature on the C-violation parameter c.

The form factors for the decay $\eta' \to \eta\pi^0\pi^0$ were determined at the GAMS-2000 detector by using a statistical sample of 6000 events [10]. This yielded a value of $\mathrm{Re}\alpha = -0.058 \pm 0.013$.

A considerable number of events involving η'-meson production followed by decay to $\eta\pi^+\pi^-$ were detected in the VES experiment.

A run at a beam momentum of $p_\pi = 28$ GeV was dominated in accumulated statistics by the charge-exchange reaction (nearly 14 000 events)

$$\pi^- p \to \eta' n \tag{4}$$

and by the diffractive production of the $\eta'\pi^-$ system in the reaction (nearly 7000 events)

$$\pi^- A \to \eta'\pi^- A^*, \tag{5}$$

where A stands for a nuclear target and A^* is a recoil nucleus or nucleon.

In the present study, we explore the decay $\eta' \to \eta\pi^+\pi^-$ for the case where the η' mesons involved were produced in reaction (5). The choice of this reaction was motivated by the fact that, at the present time, it has been thoroughly investigated at the VES spectrometer [11, 12].

1. EVENT SELECTION AND QUALITY OF SIMULATION

The selection of events of reaction (5) obeyed, by and large, the standard requirements used in analyzing data obtained with the VES spectrometer. The description of this facility was presented elsewhere [13].

The presence of three reconstructed charged tracks and of two clusters in the electromagnetic calorimeter was required.

The invariant mass of two photons was restricted to be within the broad interval $0.461 < M(\gamma\gamma) < 0.643$ GeV, which corresponds to an experimentally resolved η meson. The photon parameters were subjected to the procedure of a kinematical fit to the η-meson mass.

Further, the reconstructed beam momentum was required to be within the range $26.8 < p_\pi < 29.5$ GeV (this corresponds to the momentum spectrum of the beam in this run and suppresses inelastic events). Finally, we selected events involving an η' meson and a vast background region, $0.900 < M(\eta\pi^-\pi^+) < 1.017$ GeV.

Numerous kinematical cuts were also used to improve the purity of data and to exclude regions where the detection efficiency was not known reliably. We excluded electrons, charged kaons, events in the kinematical region of target fragmentation, events for which the distance between the center of the photon cluster and the point of intersection of a track with the plane of the γ detector used was smaller than 13 cm, events involving photons of energy less than 1.0 GeV, and events where the total energy of two photons was less than 5.0 GeV.

In order to derive the form factors for η'-meson decay, it is necessary to know the event-detection efficiency as a function of variables x and y, this requiring a detailed parametrization of kinematical distributions.

The dynamics of the production of $\eta'\pi^-$ systems at the VES spectrometer was studied in detail in [11] (at a beam momentum of 37 GeV) and in [12], where the data used in the present study were analyzed.

The distribution of events in the phase space of the reaction was parametrized by a set of partial-wave amplitudes in the Gottfried–Jackson frame, which are determined independently in narrow intervals of the invariant mass $M(\eta'\pi^-)$. The kinematics of the production of an $\eta'\pi^-$ system is described by the t-channel squared-momentum-transfer distribution unified for all partial-wave amplitudes.

Thus, the selected events were subjected to a partial-wave analysis. On the basis of measured partial-wave amplitudes, we constructed a set of events simulated by the Monte Carlo method and used it further to determine the parameters of η'-meson decay.

We simulated the coordinate and energy resolution of photons and the momentum resolution of tracks, which leads to the broadening of the η'-meson spectrum, as well as to the redistribution of events in terms of the measured quantities x and y.

The experimental distributions and the quality of their description are illustrated in Figs. 1 and 2. The distributions of simulated events that were subjected to the same kinematical cuts as physical data are represented by the dashed curves.

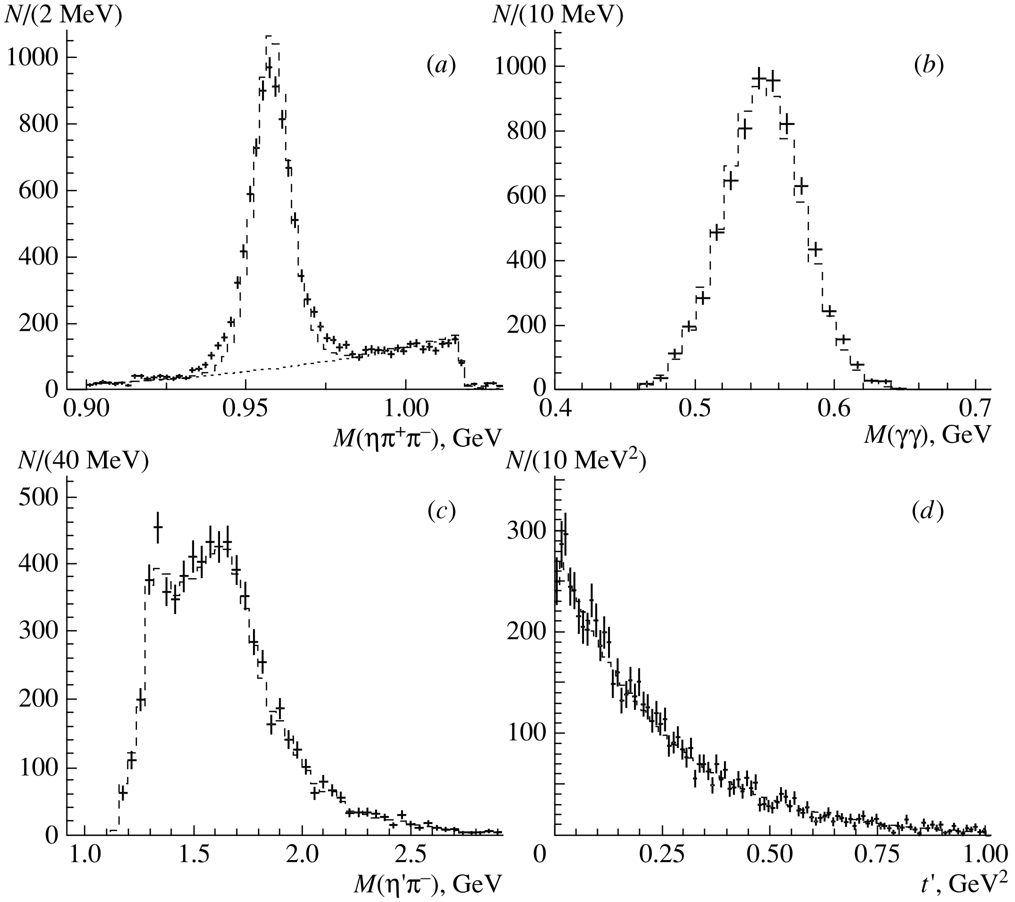

Fig. 1. Mass spectra of the (a) $\eta\pi^-\pi^+$ system, (b) $\gamma\gamma$ system from η-meson decay, and (c) $\eta'\pi^-$ system; (d) spectrum of the square of the momentum transfer from the π^- beam to the $\eta'\pi^-$ system.

Figure 1a shows the $M(\eta\pi^+\pi^-)$ spectrum upon a 1C fit to the η-meson mass, while Fig. 1b gives the $M(\gamma\gamma)$ mass spectrum for η-meson decay.

Both mass spectra are satisfactorily reproduced by a Monte Carlo simulation.

Figure 1a also shows the contribution of the background that was determined from a partial-wave analysis and which is described by a set of coherent amplitudes in the $\eta 3\pi$ system and an incoherent isotropic contribution. A comparison of the various spectra in sidebands of the η' meson also demonstrates that physical data are satisfactorily described.

The mass spectrum of the $\eta'\pi^-$ system and the absolute value of the square of the momentum transfer from the π^- beam to the $\eta'\pi^-$ system are shown in Figs. 1c and 1d, respectively.

The basic angular variables are given in Fig. 2. Figures 2a and 2b display the distributions in, respectively, the polar and the azimuthal angle of the η' meson with respect to the Gottfried–Jackson axes. These distributions determine the partial-wave amplitudes in the $\eta'\pi^-$ system, so that they are optimized by the procedure of our partial-wave analysis.

The distributions in the polar and azimuthal angles (specifically, in $\cos\theta$ and ϕ) of η-meson emission in the η' rest frame with respect to axes parallel to the Gottfried–Jackson axes are shown in Figs. 2c and 2d. The quality of their description characterizes the reliability of the simulation, since these distributions are isotropic in the full phase space.

Thus, the simulated events satisfactorily reproduce the mass and angular spectra of the physical data and the experimental resolution of the VES spectrometer.

2. METHOD FOR DETERMINING DECAY PARAMETERS

A rather wide mass interval—$(m_0 - 0.016) < M(\eta\pi^-\pi^+) < (m_0 + 0.016)$ GeV, where m_0 is the η'-meson mass—was used to separate the η'-meson signal. The background was subtracted from the sidebands of the $M(\eta\pi^-\pi^+)$ spectrum.

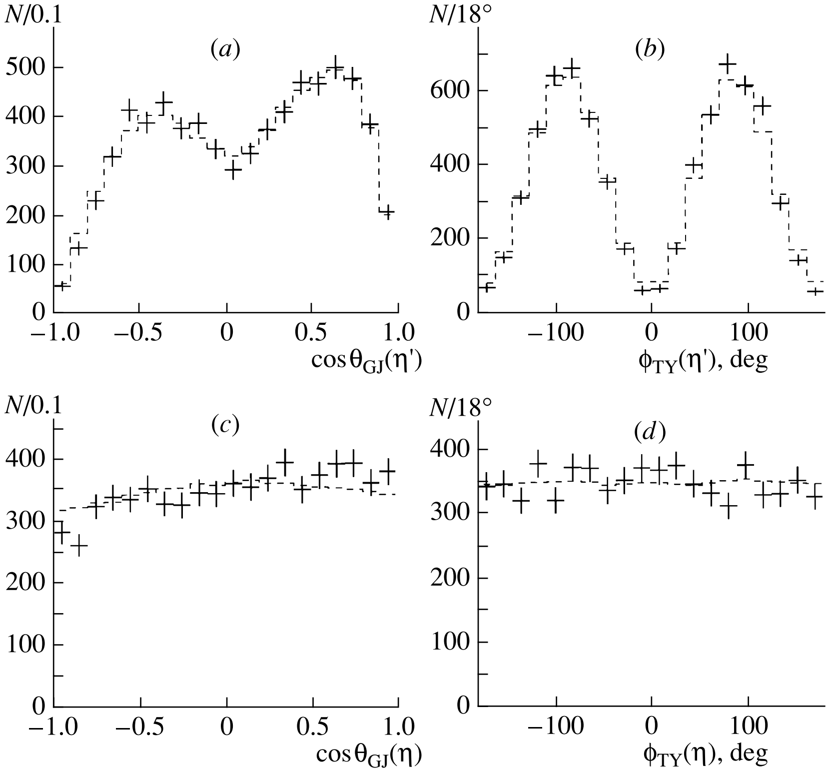

Fig. 2. Distributions with respect to (*a, b*) the cosine of the Gottfried–Jackson angle and the Treiman–Yang angle of the η' meson and (*c, d*) the polar and azimuthal angles of η-meson emission in the η' rest frame.

The distribution of experimental data with respect to the Dalitz variable y is displayed in Fig. 3 for eight intervals of the variable x.

The variation of the efficiency as a function of the variable y is illustrated by the description obtained within the isotropic-decay model (dotted histogram in Fig. 3).

A detailed analysis of the efficiency shows that its behavior as a function of x and y is highly uniform (its variation versus the variable y is one-third as great as the variation of the matrix element in the linear approximation). The mean value of the efficiency is 39%.

In order to determine the decay form factors, we varied the parameters of the matrix elements in (2) and (3) and optimized the experimental distributions in x and y by the χ^2 method.

Technically, the procedure was as follows: we weighed the isotropic decay of an η' meson with the densities $1, y, y^2, x$, and x^2; after a simulation of the detection efficiency and the detector resolution, we obtained two-dimensional distributions with respect to the variables x and y and, after that, summed these distributions with the weights $1, a, b, c$, and d, which we varied to attain the best description of the experimental data [14]. The effect of the background, which was simulated separately, was also taken into account.

3. RESULTS AND ESTIMATION OF SYSTEMATICAL ERRORS

Upon imposing the aforementioned kinematical cuts, we selected nearly 7000 events of η'-meson decay.

Upon optimization, we have

$$\begin{gathered}\mathrm{Re}\alpha = -0.072 \pm 0.012\,(\mathrm{stat.}) \pm 0.006\,(\mathrm{syst.}), \qquad (6)\\ \mathrm{Im}\alpha = 0.0 \pm 0.1\,(\mathrm{stat.}) \pm 0.0\,(\mathrm{syst.}),\\ c = 0.020 \pm 0.018\,(\mathrm{stat.}) \pm 0.004\,(\mathrm{syst.}),\\ d = -0.066 \pm 0.030\,(\mathrm{stat.}) \pm 0.015\,(\mathrm{syst.}),\\ \chi^2 = 62/(59-3)\end{gathered}$$

for the linear and

$$\begin{gathered}a = -0.120 \pm 0.027\,(\mathrm{stat.}) \pm 0.015\,(\mathrm{syst.}), \qquad (7)\\ b = -0.090 \pm 0.050\,(\mathrm{stat.}) \pm 0.030\,(\mathrm{syst.}),\\ c = 0.021 \pm 0.019\,(\mathrm{stat.}) \pm 0.005\,(\mathrm{syst.}),\\ d = -0.085 \pm 0.030\,(\mathrm{stat.}) \pm 0.020\,(\mathrm{syst.}),\\ \chi^2 = 58/(59-3)\end{gathered}$$

for the nonlinear parametrization of the matrix element. Thus, one can see that, for the statistical sample being considered, the slope in the variable y shows the most significant deviation from zero among

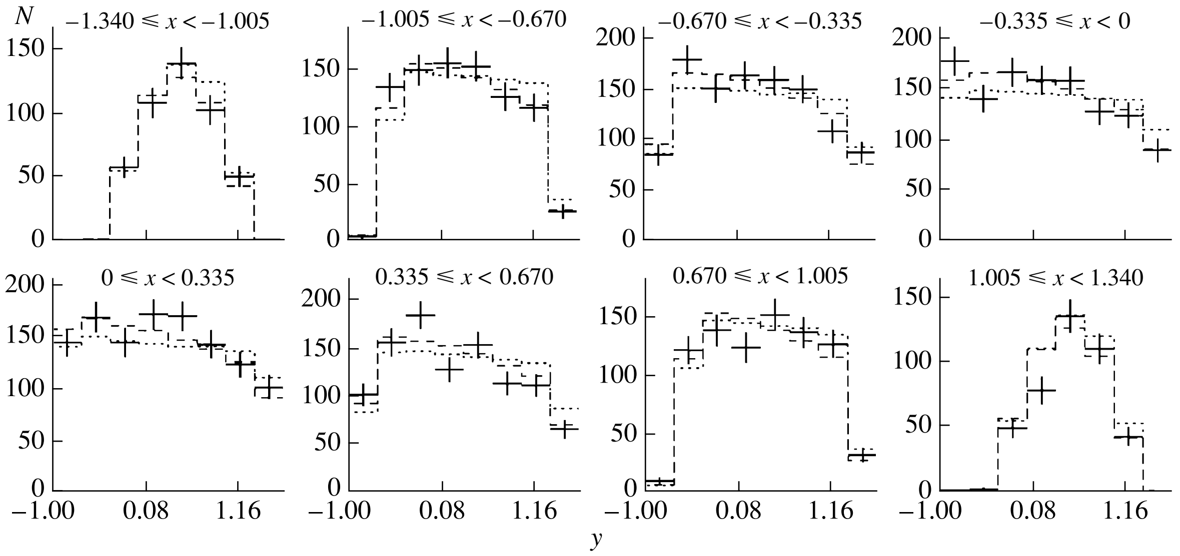

Fig. 3. Distributions in the variable y for various intervals of x: (histograms with displayed errors) experimental data, (dashed-line histogram) description on the basis of the nonlinear matrix element, and (dotted-line histogram) description within the isotropic-decay model.

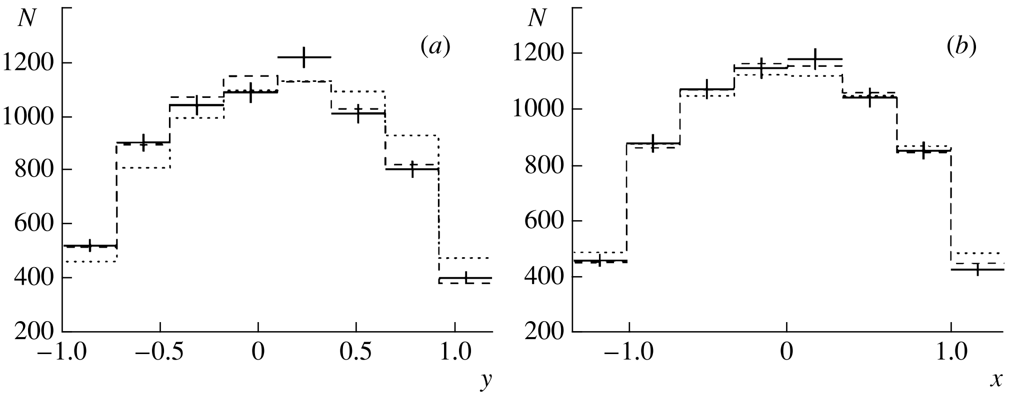

Fig. 4. Distributions with respect to the variables (a) y and (b) x. The notation for the histograms is identical to that in Fig. 3.

all parameters, both parametrizations, that in (2) and that in (3), providing a good description.

It should be noted that the result in (6) is compatible with the result obtained in [8] on the basis of a statistical sample that is severalfold smaller.

The measured parameters and the parameters of the decay $\eta' \to \eta\pi^0\pi^0$ that were obtained by the GAMS-2000 group in [10] are also compatible, which corresponds to isotopic symmetry.

The description of the data in terms of the nonlinear matrix element with the parameters given in (7) is shown in Figs. 3 and 4. Both figures also present the distributions that were obtained on the basis of the phase-space decay model, where the matrix element is set to a constant (dotted-line histograms). It can be seen from Fig. 4a that the use of the model of isotropic η'-meson decay leads to an unsatisfactory description.

In the present investigation, it was also found for the first time that, in the decay $\eta' \to \eta\pi^-\pi^+$, the C-violation parameter c is compatible with zero.

An insufficient knowledge of kinematics imbedded in the model and of the event-detection efficiency as a function of the Dalitz variables, an incomplete description of the resolution of tracks and photons, and an imperfect simulation of the background-subtraction procedure are sources of systematic errors in measuring parameters.

A detailed analysis of the detection efficiency shows that its variation as a function of y is one-third as large as the variation of the matrix element (7). The asymmetry of the efficiency in the variable x is negligible, while the contribution of the second-order term is five times less than the parameter d in the matrix element. In order to estimate systematic effects, we applied softer cuts on physical and simulated events and, on the contrary, more stringent cuts on the photon energy and on the acceptance of the γ detector. As a result, the values of the parameters a, b, and d changed by not more than $1/3$ of their statistical errors.

It was found that a pronounced systematic bias of the parameters a and b occurs upon varying the width of the $M(\eta\pi^-\pi^+)$ interval with the aim of η'-meson separation. This is because the exclusion of events from the sidebands of the η'-meson peak leads to a sizable distortion of the efficiency as a function of y, and this distortion is not quite precisely simulated. By varying the width of the gate for η'-meson separation from 24 to 50 MeV, we determined the contribution of the systematic effect. It should be noted that, in order to exclude this source of systematic effects, one must use an interval of η'-meson separation as wide as is allowed by background conditions.

The resolution in the variables x and y and the subtraction of the background under the η'-meson peak are not sources of significant systematic errors. The measured decay parameters changed insignificantly upon successively excluding both factors in our simulation.

CONCLUSION

The form factors for the decay $\eta' \to \eta\pi^+\pi^-$ have been measured in $\pi^- A \to \eta'\pi^- A^*$ reactions at a beam momentum of $p_\pi = 28$ GeV.

On the basis of the statistical sample of 7000 events chosen for analysis, it has been shown that both the linear and the nonlinear parametrization of the matrix element give a good description. Of all parameters, it is the slope in the variable y that differs from zero the most significantly. It is

$$\mathrm{Re}\alpha = -0.072 \pm 0.012\,(\text{stat.}) \pm 0.006\,(\text{syst.})$$

in the linear and

$$a = -0.120 \pm 0.027\,(\text{stat.}) \pm 0.015\,(\text{syst.})$$

in the nonlinear parametrization. We have also measured the parameter that takes into account C violation in this decay. It turned out to be compatible with zero; that is,

$$c = 0.021 \pm 0.019\,(\text{stat.}) \pm 0.005\,(\text{syst.}).$$

ACKNOWLEDGMENTS

This work was supported in part by the Russian Foundation for Basic Research (RFBR), project nos. 02-02-17479 and 00-15-96689, and by the RFBR program for support of leading scientific schools, project no. 1695.2003.2.

REFERENCES

1. M. K. Volkov, Fiz. Élem. Chastits At. Yadra **13**, 1070 (1982) [Sov. J. Part. Nucl. **13**, 446 (1982)].
2. V. A. Novikov *et al.*, Nucl. Phys. B **165**, 55 (1980); K. A. Milton *et al.*, Phys. Rev. D **22**, 1124 (1980); P. Di Vecchia *et al.*, Nucl. Phys. B **181**, 18 (1981).
3. J. Cronin, Phys. Rev. **161**, 1483 (1967); J. Schwinger, Phys. Rev. **167**, 1432 (1968); D. Majumdar, Phys. Rev. Lett. **21**, 502 (1968).
4. Riazuddin and S. Oneda, Phys. Rev. Lett. **27**, 548 (1971); P. Weisz, Riazuddin, and S. Oneda, Phys. Rev. D **5**, 2264 (1972).
5. N. Beisert and B. Borasoy, Nucl. Phys. A **716**, 186 (2003); hep-ph/0301058.
6. G. W. Intemann and G. K. Greenhut, Phys. Rev. D **22**, 1669 (1980).
7. A. H. Fariborz and J. Schechter, Phys. Rev. D **60**, 034002 (1999); hep-ph/9902238.
8. George R. Kalbfleisch, Phys. Rev. D **10**, 916 (1974).
9. R. A. Briere *et al.*, Phys. Rev. Lett. **84**, 26 (2000).
10. D. Alde *et al.*, Phys. Lett. B **177**, 115 (1986).
11. G. M. Beladidze *et al.*, Phys. Lett. B **313**, 276 (1993).
12. V. Dorofeev *et al.*, in *Proceedings of the IX International Conference on Hadron Spectroscopy "HADRON 2001", Protvino, 2001*, Ed. by D. V. Amelin and A. M. Zaitsev; AIP Conf. Proc. **619**, 143 (2002).
13. S. Bityukov *et al.*, Phys. Lett. B **268**, 137 (1991).
14. V. F. Obraztsov, private communication.

Translated by A. Isaakyan

Physics of Atomic Nuclei, Vol. 68, No. 3, 2005, pp. 378–384. Translated from Yadernaya Fizika, Vol. 68, No. 3, 2005, pp. 407–413.
Original Russian Text Copyright © 2005 by Vavilov, Antipov, Artamonov, Batarin, Victorov, Golovkin, Gorin, Eroshin, Kozhevnikov, Kolganov, Konstantinov, Kubarovsky, Kurshetsov, Landsberg, Leontiev, Lomkatsi, Molchanov, Mukhin, Nilov, Patalakha, Petrenko, Petrukhin, Smolyankin.

$\Lambda(1520) \to \Lambda\gamma$ Radiative-Decay Width

D. V. Vavilov[1)], **Yu. M. Antipov**[1)], **A. V. Artamonov**[1)], **V. A. Batarin**[1)], **V. A. Victorov**[1)], **S. V. Golovkin**[1)], **Yu. P. Gorin**[1)], **O. V. Eroshin**[1)], **A. P. Kozhevnikov**[1)], **V. Z. Kolganov**[2)], **A. S. Konstantinov**[1)], **V. P. Kubarovsky**[1)], **V. F. Kurshetsov**[1)], **L. G. Landsberg**[1)*], **V. M. Leontiev**[1)], **G. S. Lomkatsi**[2)], **V. V. Molchanov**[1)], **V. A. Mukhin**[1)], **A. F. Nilov**[2)], **D. I. Patalakha**[1)], **S. V. Petrenko**[1)], **A. I. Petrukhin**[1)], and **V. T. Smolyankin**[2)]
The SPHINX Collaboration (IHEP—ITEP)

Received June 3, 2004

Abstract—The radiative decay $\Lambda(1520) \to \Lambda\gamma$ was recorded in the exclusive reaction $p + N \to \Lambda(1520)K^+ + N$ at the SPHINX facility. The branching ratio for this decay and the corresponding partial width were found to be, respectively, $\mathrm{Br}[\Lambda(1520) \to \Lambda\gamma] = (1.02 \pm 0.21) \times 10^{-2}$ and $\Gamma[\Lambda(1520) \to \Lambda\gamma] = 159 \pm 35$ keV (the quoted errors are purely statistical, the systematic errors being within 15%).

1. INTRODUCTION

Investigation of radiative decays is an important part of hadron spectroscopy, since it enables one to obtain information about the electromagnetic structure of strongly interacting particles and about quark configurations within these hadrons. Numerous data on radiative decays of light mesons were summarized in [1, 2], while data on N and Δ baryons were compiled in [3, 4]. At the same time, radiative decays of hyperons have not yet received adequate study [5]. Among radiative hyperon decays that are rather easily accessible to investigation, we would like to mention the decay process

$$\Lambda(1520) \to \Lambda\gamma. \qquad (1)$$

Theoretical predictions for the respective partial-decay width within various models are highly sensitive to assumptions on the $SU(3)$ structure of the $\Lambda(1520)$-hyperon wave function, ranging between 30 and 215 keV (see [5] and references therein), and this point alone is of interest to experimentalists.

The width with respect to the radiative-decay process in (1) was determined in two experiments. The first measurement, which was reported in [6], was performed by using a bubble chamber to study the resonance production of $\Lambda(1520)$ hyperons in a separated beam of 270- to 470-MeV/c K^- mesons. Photons were not recorded in that experiment, and the radiative-decay process (1) was separated in the reaction $K^- + p \to \Lambda +$ (neutral particles) through an analysis of the spectrum of missing masses with respect to the product Λ hyperon. According to data from [6], the width with respect to the radiative-decay process (1) was $\Gamma[\Lambda(1520) \to \Lambda\gamma] = 134 \pm 25$ keV; the correction to the photon spectrum due to the different radiative decay $\Lambda(1520) \to \Sigma^0\gamma$ was introduced on the basis of theoretical considerations, was model-dependent, and was likely to result in an underestimation of $\Gamma[\Lambda(1520) \to \Lambda\gamma]$ in [6]. The second measurement, which yielded $\Gamma[\Lambda(1520) \to \Lambda\gamma] = 33 \pm 11$ keV for the same radiative width, was performed by directly recording the Λ hyperon and photon from the corresponding decay process in experiments aimed at studying the resonance production of $\Lambda(1520)$ hyperons. This result was presented at PANIC-84 [7] (see also [8]). So drastic a discrepancy between the results reported in [6] and in [7, 8] calls for pursuing further investigations into radiative decays of Λ hyperons.

In the present study, the width with respect to the radiative-decay process (1) was measured by directly recording all decay produets on the basis of an analysis of data obtained at the IHEP SPHINX facility.

2. SPHINX FACILITY

The SPHINX facility had operated in a proton beam of energy $E_p = 70$ GeV from the IHEP accelerator in the period between 1989 and 1999. Over this period, the facility was upgraded several times

---

[1)] Institute for High Energy Physics, Protvino, Moscow oblast, 142284 Russia.
[2)] Institute of Theoretical and Experimental Physics, Bol'shaya Cheremushkinskaya ul. 25, Moscow, 117259 Russia.
[*] E-mail: `lgl@mx.ihep.su`

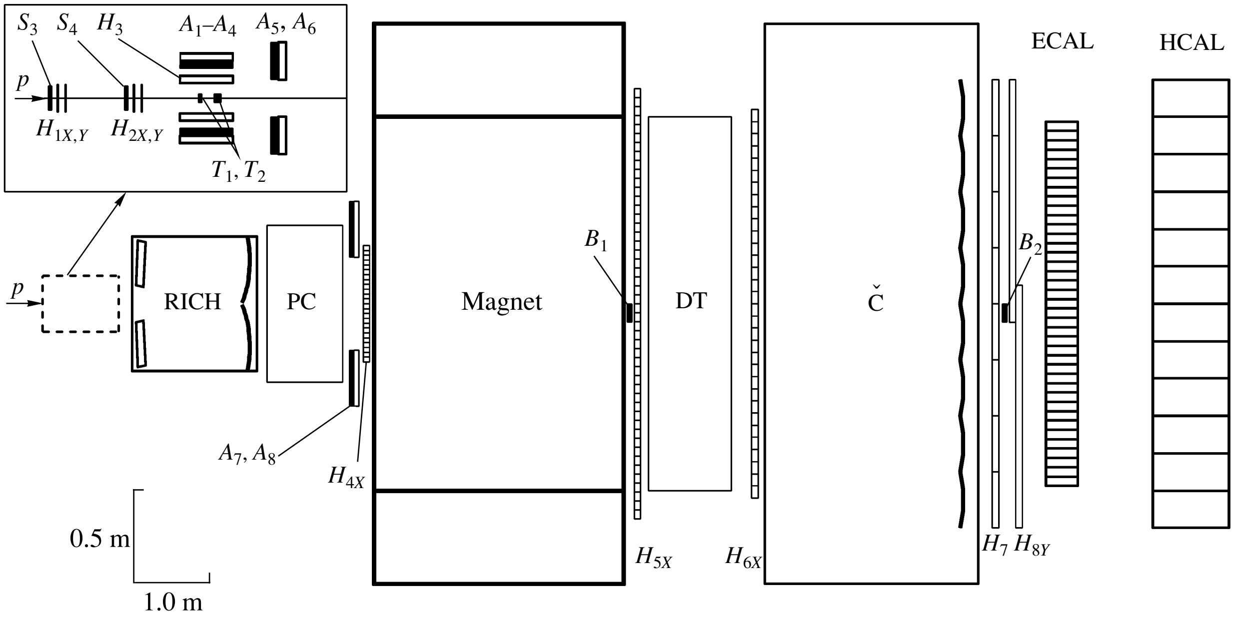

Fig. 1. Layout of the SPHINX facility: (S_1–S_4) scintillation counters (S_1 and S_2 are not shown); (T_1, T_2) copper and graphite targets, respectively; (A_1–A_8) counters of the veto system (lead/scintillator); (B_1, B_2) anticoincidence scintillation counters for suppressing beam particles that did not undergo interaction; (H_1–H_8) scintillation hodoscopic detectors; (RICH) ring-image Cherenkov detector; (PC) proportional chambers; (DT) drift tubes; (Č) multichannel threshold Cherenkov detector; (ECAL) electromagnetic calorimeter; and (HCAL) hadron calorimeter.

(see [9–11]). The data used in the present research were obtained with its last modification, referring to the period from 1996 to 1999 [11]. The layout of the facility is shown in Fig. 1. In its coordinate system, the z axis was aligned with the proton-beam axis, the y axis was directed vertically upward, and the x axis complemented these two axes to a right-hand system of coordinates, the origin of coordinates being chosen at the center of the magnet.

Upon being measured by scintillation counters (S_1–S_4) and scintillation hodoscopes ($H_{1X,Y}$, $H_{2X,Y}$), a primary proton beam was incident on a target surrounded by a side hodoscope (H_3) and a veto system. In the facility, use was made of a graphite target 11.3 g/cm^2 thick and a copper target 2.64 g/cm^2 thick. The targets were employed simultaneously and were separated by a distance of 25 cm. The veto system was sensitive both to charged particles and to photons and made it possible to separate exclusive reactions of the diffractive type.

Upon traversing a target, charged secondaries were recorded in the block of proportional chambers (PC). This block included five x planes and five y planes and had a sensitive area of 76.8×64.0 cm, the step being 2 mm. After the deflection in the horizontal plane by a wide-aperture magnet ($p_T = 0.588$ GeV/c), tracks were measured by a block of drift tubes (DT), the configuration of the electric field there being identical to that which was described in [12]. This block consisted of 18 planes oriented at angles of 0° and ±7.5° to the vertical direction. Each plane included 32 tubes of diameter 6.25 cm, the sensitivity of the central tube in the beam region being artificially reduced. With allowance for uncertainties of the calibration, the spatial resolution of the tubes at typical loads was about 300 μm. In reconstructing tracks, use was also made of scintillation hodoscopes positioned near the PC and DT blocks.

Charged particles were identified with the aid of the ring-image Cherenkov detector (RICH) and a multichannel threshold Cherenkov counter (Č). In the RICH counter, an insulating gas (SF$_6$) at a pressure slightly exceeding atmospheric pressure was used for a radiator; the threshold momenta there for pions, kaons, and protons were about 3.5, 12.4, and 23.6 GeV/c, respectively. More detailed information about this detector is given in [9, 13]. In the Č counter, air at atmospheric pressure served as a radiator; this corresponded to the thresholds of 6.5, 21.3, and 40.1 GeV/c for pions, kaons, and protons, respectively.

Neutral particles were measured with the aid of an electromagnetic and a hadron calorimeter (ECAL and HCAL, respectively). The electromagnetic calorimeter, which was made from lead-glass counters, had the form of a 39×27 matrix, its cells being 5×5 cm in dimension each. The central cell was removed in order to ensure the passage of the beam. Blocks of steel–scintillator sandwiches were used in the hadron calorimeter [14], the total thickness being $5L_{\text{abs}}$. The blocks had transverse dimensions of 20×20 cm and formed a 12×8 matrix.

In order to develop various triggers, use could be made of signals from scintillation counters positioned along the beam trajectory, which separated beam interactions; information from the side hodoscope H_3 and the veto system; the multiplicity in the scintillation hodoscopes and in the threshold Cherenkov detector Č; and the multiplicity of coincidences (anticoincidences) of signals from this detector with signals from the scintillation matrix hodoscope that was situated behind it and which was geometrically conjugate to it. Triggering electronics made it possible to realize eight different triggering solutions. The data-collecting system of the facility could record more than 3000 events per accelerator spill.

More than 10^9 events of various types were recorded on magnetic carriers over the time of measurements with the last modification of the SPHINX facility, and the analysis of these events is now under way.

3. DATA ANALYSIS

For a source of $\Lambda(1520)$, we used the exclusive production reaction

$$p + N \to \Lambda(1520)K^+ + N \qquad (2)$$

at the beam energy of $E_p = 70$ GeV. For the analysis of this process, we took the data sample that was formed by events involving the production of $[pK^-]K^+$ and $[(p\pi^-)\gamma]K^+$ systems and which was selected with the same trigger signal $T_{(3)}$ generated by the production of three charged particles in the final state (after the decay gap for Λ hyperons). Here, the decay process

$$\Lambda(1520) \to pK^-, \qquad (3)$$

which was studied quite thoroughly and which is characterized by a branching fraction of $\mathrm{Br}[\Lambda(1520) \to pK^-] = (22.5 \pm 0.5)\%$ [15], was employed to study the dynamics of reaction (2) and, as a normalization process, to determine the radiative width $\Gamma[\Lambda(1520) \to \Lambda\gamma]$.

The actuation of the scintillation counters that corresponds to a beam interaction in the targets of the facility and multiplicities in the scintillation hodoscopes such that they do not contradict the production of three charged particles in the final state are the main requirements for the generation of the triggering signal $T_{(3)}$. The requirement that three and only three elements of the hodoscope H_{6X}, which was situated immediately downstream of the block of drift tubes DT, be actuated was the most stringent triggering condition. The veto system was employed in anticoincidences; in the hodoscope H_3, not more than one soft charged particles (recoil proton) was allowed to travel aside with respect to a target. Thus, the detected events of reaction (2) included both those that were due to a coherent interaction on a target nucleus and those that were due to an interaction on a nucleon.

In order to separate the $\Lambda K^+\gamma$ final state, we selected events featuring reconstructed tracks of one negatively charged particle and two positively charged particles and one and only one cluster in the electromagnetic calorimeter such that it was not associated with charged-particle tracks. The minimum energy of this photon cluster was 1 GeV. Assuming that the tracks of positively charged particles are associated with a proton and a kaon and that the track of a negatively charged particle is associated with a pion, we further reconstructed interaction vertices and effective masses. On the basis of data on the p and π^- tracks, we reconstructed the momentum of the presumed Λ hyperon and its decay vertex, which we call, in the following, a secondary vertex. The primary vertex could be found by using the Λ track found in this way, the K^+ track, and the beam track.

An event was accepted as that which involved the exclusive production of the $\Lambda K^+\gamma$ system if the following conditions were satisfied:

(i) The primary vertex (Z_1) was in the region of the main graphite target ($-555 < Z_1 < -525$ cm), while the secondary vertex (Z_2) was upstream or at the very beginning of the block of proportional chambers PC ($Z_2 < -280$ cm); the distance between the secondary and primary vertices significantly exceeded the experimental inaccuracy in determining this quantity ($\sigma_{\Delta Z}$), the inaccuracy in question found for each event being about 8 cm ($Z_2 - Z_1 > 3\sigma_{\Delta Z}$).

(ii) Information from the RICH detector was compatible with above assumptions concerning the masses of the tracks, and the momenta of positively charged particles were not less than 5 GeV, which is above the threshold for Cherenkov radiation from a pion in this detector, so that the reliability of the identification of secondary particles is improved.

(iii) The effective mass of the $p\pi^-$ system was in the region of the Λ-hyperon mass ($1.106 < M(p\pi^-) < 1.126$ GeV).

(iv) The total energy of all secondary particles corresponded to the beam energy $68 < E_\Lambda + E_{K^+} + E_\gamma < 73$ GeV (this cut on the total energy was used to reduce the background from events featuring missing photons).

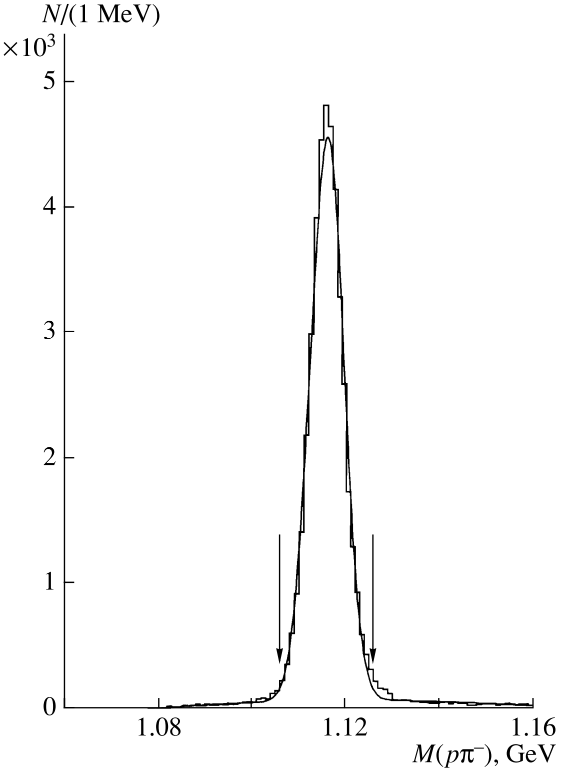

Fig. 2. Effective-mass spectrum of the $p\pi^-$ system in the reaction $p + N \to [(p\pi^-)\gamma]K^+ + N$ (for the separation of the reaction, see the main body of the text). The spectrum is dominated by the peak associated with the decay process $\Lambda \to p\pi^-$.

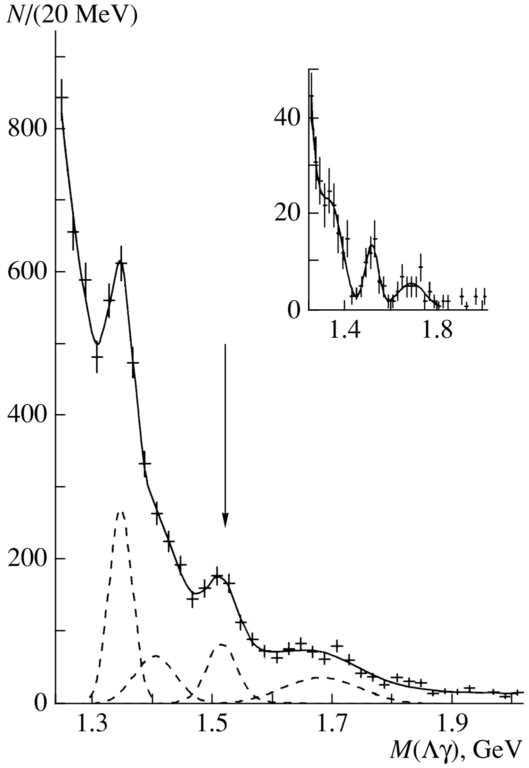

Fig. 3. Effective-mass spectrum of the $\Lambda\gamma$ system in the reaction $p + N \to [\Lambda\gamma]K^+ + N$. The spectrum was fitted in accordance with the procedure described in the main body of the text. The inset shows the analogous spectrum obtained for more stringent selection criteria for suppressing the background (see main body of the text). The arrow indicates the peak corresponding to the radiative-decay process $\Lambda(1520) \to \Lambda\gamma$.

Since the final state involves two tracks of positively charged particles, there is a two-valued ambiguity in deciding as to which of them is due to the proton and which is due to the kaon. The reconstruction of the kinematical features of an event and the subsequent selection were performed for either combination. The fraction of events where both combinations satisfied all selection criteria was negligible (owing to the conditions for the separation of the secondary vertex and a good identification of particles in the RICH counter).

The result obtained for the effective-mass spectrum of the $p\pi^-$ system after all selections, with the exception of the selection in the effective mass itself, is displayed in Fig. 2. It can be seen that Λ hyperon is isolated quite readily. The effective-mass spectrum of the $\Lambda\gamma$ system is shown in Fig. 3.

This spectrum clearly shows a peak at a mass value of 1520 MeV and two structures to the left and to the right of it. The structure in the region around 1.35 GeV corresponds to the decays $\Sigma(1385)^0 \to \Lambda\pi^0$ and $\Lambda(1405) \to \Sigma^0\pi^0$ featuring one missing photon in the former and two missing photons in the latter case. The structure in the region around 1.7 GeV corresponds to decays of heavier hyperon resonances. A smooth background receives contributions both from nonresonance-production processes involving one or a few missing photons and from spurious photons (noise and the interactions of charged tracks in the electromagnetic calorimeter).

The background level can be reduced by requiring that charged particles not interact in the electromagnetic calorimeter and by reducing the photon-detection threshold ($E_\gamma > 0.5$ GeV). The inset in Fig. 3 shows the $\Lambda\gamma$ mass spectrum obtained under these conditions. Despite a considerable decrease in statistics, the decay process in (1) is separated more clearly in this case. The displayed distribution is presently considered only as a demonstration of the reliability of the separation of the decay process in (1), but it was not used to determine its branching ratio, since the systematic uncertainties arising because of the more stringent selections have not yet received adequate study.

An analysis of known hyperon resonances and their decay modes revealed that, apart from the aforementioned processes, the decays $\Lambda(1520) \to \Sigma^0\pi^0$ and $\Lambda(1520) \to \Sigma^0\gamma$ involving two missing photons in the former and one missing photon in the latter case may also be sources of background to $\Lambda(1520)$. The possible contribution of these decays to the $\Lambda\gamma$ mass spectrum was studied by means of a Monte Carlo simulation. We note that the relative values of these contributions are determined by the efficiency of the facility and the branching ratios of the corresponding decays, but, of these, only the branching ratio for $\Lambda(1520) \to \Sigma^0\pi^0$ is well known. Under the assumption that $\mathrm{BR}[\Lambda(1520) \to \Lambda\gamma] = 1\%$ and $\mathrm{BR}[\Lambda(1520) \to \Sigma^0\gamma] = 1\%$, the distributions expected for the process being studied and for the background processes are displayed in Fig. 4. It can be seen that peaks associated with processes involving missing photons are quite modest and are shifted toward lower effective-mass values by about 100 MeV, but that they cannot be disregarded.

In order to determine the number of recorded events of the decay process in (1), the effective-mass distribution of the $\Lambda\gamma$ system was described by the sum of the resonance and a background. The background was represented as the sum of the smooth function $P_1 \exp(-P_2 M - P_3 M^2)$ and three normal distributions. Of these, two corresponded to peaks seen in Fig. 3 at 1.35 and 1.7 GeV, while the third corresponded to the presumed contribution of the decay processes $\Lambda(1520) \to \Sigma^0\pi^0$, $\Lambda(1520) \to \Sigma^0\gamma$, $\Sigma^*(1385)^0 \to \Lambda\gamma$, and $\Lambda(1405) \to \Lambda\gamma$. The parameters P_i and all of the parameters of the normal distributions were free. The $\Lambda(1520)$ resonance was described by the convolution of a Breit–Wigner distribution in the relativistic form with the resolution of the facility. The intrinsic resonance width was fixed at the world-average value of $\Gamma = 15.6$ MeV [15], while the resolution was set to the value of $\sigma = 26$ MeV, which was determined from our Monte Carlo simulation. The mass was a free parameter. In order to avoid a strong dependence on the parametrization of the resonance shape at the edges of the distribution, the number of resonance events was determined in the bounded effective-mass range 1.40–1.65 GeV. The possible effect of decay dynamics [the values of $L = 0$ and 2 are admissible for the orbital angular momentum in the decay process in (1)] on the results of fitting was found to be negligible (not greater than 2%). The resulting description of the effective-mass spectrum is shown by the solid curve in Fig. 3. The contributions corresponding to the decay process being studied and to the background processes are represented by the dashed curves. The number of detected events of the decay process in (1) was found to be 290 ± 60.

The probability of the decay process in (1) was measured with respect to the decay process in (3), which was also used to determine the features of the production of the $\Lambda(1520)K^+$ system in reaction (2) that were necessary for simulating the efficiencies of the detection of both decays. The procedures for the selection and reconstruction of the pK^-K^+ final state formed in the decay process (3) are similar in many respects to those that were used to select the $\Lambda K^+\gamma$ system; therefore, they are described schematically in the following.

For our analysis, we selected events such that they involved one reconstructed track of a negatively charged particle and two reconstructed tracks of positively charged particles and that, in them, there were no clusters in the electromagnetic calorimeter that were not associated with charged-particle tracks. Further, fulfillment of the following conditions was required:

(i) The primary vertex (Z_1), which was determined by using the beam track and three secondary tracks, should be within the main, graphite, target ($-550 < Z_1 < -528$ cm).

(ii) Actuations in the RICH detector should not contradict the assumptions adopted for the track masses, and the momenta of positively charged particles should not be less than 5 GeV/c.

(iii) The total energy of all secondary particles should correspond to the beam energy ($65 < E_p + E_{K^-} + E_{K^+} < 75$ GeV).

In choosing as to which of the tracks associated with positively charged particles is that of the proton and which is that of the kaon, there is a two-valued ambiguity. The two combinations in question satisfied the selection criteria very rarely (approximately in 1% of chosen events). In such cases, either was used in analyzing the pK^- system. A simulation revealed that this does not affect the extracted number of $\Lambda(1520)$ hyperons. The resulting distribution of the effective mass $M(pK^-)$ is shown in Fig. 5.

This spectrum exhibits a large peak that corresponds to $\Lambda(1520)$ production and two peaks at higher masses of 1.67 and 1.8 GeV. About ten hyperon resonances are known in this region, so that it is hardly possible to identify unambiguously the observed peaks with one of them. The spectrum of $M(pK^-)$ was described as the sum of three resonances and a smooth background that has the form $P_1(M - M_{\mathrm{thr}})^{P_2} \exp(-P_3 M - P_4 M^2)$ and which vanishes at the threshold $M_{\mathrm{thr}} = m_p + m_K$, P_i being free parameters. As in the case of the decay process in (1), the $\Lambda(1520)$ resonance was represented as the convolution of a relativistic Breit–Wigner distribution with the resolution of the facility, the

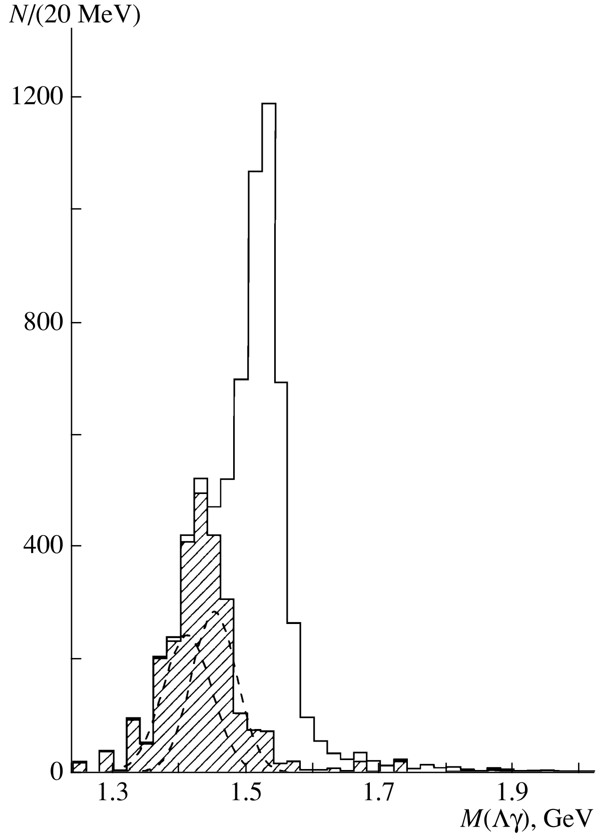

Fig. 4. Effective-mass spectrum of the $\Lambda\gamma$ system according to the Monte Carlo simulation by the method described in the main body of the text. The main peak corresponds to the decay process $\Lambda(1520) \to \Lambda\gamma$. The peaks to the left of it correspond to the decay processes $\Lambda(1520) \to \Sigma^0\pi^0$ and $\Lambda(1520) \to \Sigma^0\gamma$ involving two missing photons in the former and one missing photon in the latter case (the curves represent the contributions of the respective decays, while the shaded histogram shows the sum of these contributions).

width and the resolution being fixed. The resolution determined for the pK^- channel by means of Monte Carlo calculations was 8 MeV. The other two peaks were described in a similar way, but their widths and masses were treated as free parameters. In Fig. 5, the solid curve corresponds to the fitted mass spectrum, while the dashed curve represents the description of the background. In the effective-mass range 1.40–1.65 GeV, the number of $\Lambda(1520) \to pK^-$ events appeared to be $21\,200 \pm 300$.

The detection efficiencies for reaction (2) followed by the decay processes in (1) and (3) were taken into account by means of a Monte Carlo simulation. The simulation code used relied on the GEANT-3.21 package and contained a detailed description of the geometry of the facility and materials in it, as well as the efficiencies and resolutions of all instruments, including a reduced efficiency of the proportional chambers and drift tubes in the beam region. The simulation of the response of all detectors was performed up to digitization level, whereupon relevant events were reconstructed by the same codes as those that were used to analyze experimental data. The kinematical features of $\Lambda(1520)K^+$ production in reaction (2) (distributions with respect to momentum transfers, effective masses, and angles in the Gottfried–Jackson frame) were simulated in such a way that the resulting distributions were in agreement with experimental data, the ratio of the efficiencies of detection of decays (1) and (3) being 0.47.

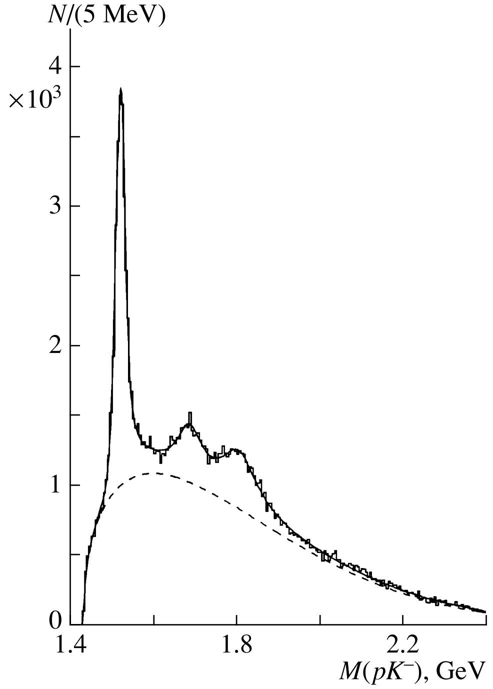

Fig. 5. Spectrum of effective masses $M(pK^-)$ in the reaction $p + N \to pK^-K^+ + N$. The spectrum is dominated by the peak associated with the decay process $\Lambda(1520) \to pK^-$. The solid curve represents the fitted spectrum (see main body of the text), while the dashed curve corresponds to a nonresonance background.

For the ratio of the branching fractions of these decays, we obtained

$$\frac{\mathrm{Br}[\Lambda(1520) \to \Lambda\gamma]}{\mathrm{Br}[\Lambda(1520) \to pK^-]} = (4.54 \pm 0.94)\times 10^{-2}. \quad (4)$$

By using the world-average values from [15] for the branching ratio $\mathrm{BR}[\Lambda(1520) \to pK^-]$ and for the total width $\Gamma_{\mathrm{tot}}[\Lambda(1520)]$, we can evaluate the branching ratio and the radiative width for the decay process in (1):

$$\mathrm{Br}[\Lambda(1520) \to \Lambda\gamma] = (1.02 \pm 0.21) \times 10^{-2}, \quad (5)$$
$$\Gamma[\Lambda(1520) \to \Lambda\gamma] = 159 \pm 35\ \mathrm{keV}.$$

Only statistical errors are quoted in these results. Many systematic effects cancel, as usually occurs in the case of relative measurements. In the present case, this concerns the efficiencies associated with the trigger and with the reconstruction of charged particles. The main systematic errors arise in simulating the photon-detection efficiency. The total systematic error does not exceed 15%. It can be reduced in the course of further investigations.

4. CONCLUSION

The partial width with respect to the radiative decay $\Lambda(1520) \to \Lambda\gamma$ has been determined on the basis of measurements at the SPHINX facility. The value obtained in this way agrees with the experimental result reported previously in [6], but it disagrees with the result from [7, 8]. In the future, we are going to perform a more detailed analysis of the systematic errors of our present measurement and to study the possibilities for measuring the radiative decay $\Lambda(1520) \to \Sigma^0\gamma$.

The results presented in this article were reported at the session of the Department of Nuclear Physics of Russian Academy of Sciences (Institute of Theoretical and Experimental Physics, Moscow, March 1–5, 2004) devoted to the 100th anniversary of the birth of the outstanding experimental physicist Academician Abram Isaakovich Alikhanov, one of the pioneers of nuclear and elementary-particle physics in our country. Some of the present authors had worked with Alikhanov for many years, being his disciples; in their further studies, they have tried to follow the scientific enthusiasm of Alikhanov and his keenness on new phenomena in physics. It is a great honor to us to publish this article in the issue of the *Physics of Atomic Nuclei* that is dedicated to his memory.

ACKNOWLEDGMENTS

We are grateful to Professor R. Bertini for a discussion on the data reported in [7, 8].

This work was supported in part by the Russian Foundation for Basic Research (project nos. 99-02-18252, 02-02-16086).

REFERENCES

1. L. G. Landsberg, Phys. Rep. **128**, 301 (1985).
2. M. Zielinski, Acta Phys. Pol. B **18**, 455 (1987).
3. D. Burkert, Int. J. Mod. Phys. E **1**, 421 (1992).
4. B. Krusche and S. Schadmand, Prog. Part. Nucl. Phys. **51**, 399 (2003); nucl-ex/0306023.
5. L. G. Lansberg, Yad. Fiz. **59**, 2161 (1996) [Phys. At. Nucl. **59**, 2080 (1996)].
6. T. S. Mast *et al.*, Phys. Rev. Lett. **21**, 1715 (1968).
7. R. Bertini *et al.*, *Contribution NM18 of Heidelberg–Saclay–Strasbourg Collab. at PANIC-84 (Particles and Nuclei of the 10th International Conference), Heidelberg, 1984*.
8. R. Bertini, Nucl. Phys. B **279**, 49 (1987).
9. SPHINX Collab. (D. V. Vavilov *et al.*), Yad. Fiz. **57**, 241 (1994) [Phys. At. Nucl. **57**, 227 (1994)].
10. SPHINX Collab. (V. A. Bezzubov *et al.*), Yad. Fiz. **59**, 2199 (1996) [Phys. At. Nucl. **59**, 2117 (1996)].
11. SPHINX Collab. (Yu. M. Antipov *et al.*), Yad. Fiz. **65**, 2131 (2002) [Phys. At. Nucl. **65**, 2070 (2002)].
12. Yu. M. Antipov *et al.*, Nucl. Phys. B (Proc. Suppl.) **44**, 206 (1995).
13. A. P. Kozhevnikov *et al.*, Nucl. Instrum. Methods Phys. Res. A **433**, 164 (1999).
14. Yu. M. Antipov *et al.*, Prib. Tekh. Éksp., No. 1, 45 (1991).
15. K. Hagiwara *et al.* (Particle Data Group), Phys. Rev. D **66**, 010001 (2002).

Translated by A. Isaakyan

Physics of Atomic Nuclei, Vol. 68, No. 3, 2005, pp. 385–397. Translated from Yadernaya Fizika, Vol. 68, No. 3, 2005, pp. 414–426.

Spin Physics in High-Energy Hadron Interactions

V. V. Abramov[*]

Institute for High Energy Physics, Protvino, Moscow oblast, 142281 Russia

Received May 24, 2004; in final form, August 25, 2004

Abstract—Data on single-spin asymmetry (A_N) in high-energy hadron—hadron collisions are discussed. The data are classified according to the beam and target types. The single-spin asymmetry A_N is considered as a function of kinematical variables and the sort of participant particles. Data from the PROZA and FODS facilities operating in beams of the IHEP accelerator are presented. The origin of a large single-spin asymmetry is briefly considered. © *2005 Pleiades Publishing, Inc.*

1. INTRODUCTION

The spin is one the fundamental quantum features of the microcosm. It manifests itself at the level atoms, nuclei, and elementary particles. The observation of a large single-spin asymmetry A_N and a large transverse polarization P_N of hyperons in hadron—hadron collisions is some kind of challenge to QCD. Perturbative QCD predicts small polarization effects in such interactions owing to the vector nature of gluons and a low current-quark mass [1].

Basic experiments aimed at studying single-spin asymmetry at high energies were reported in [2—32]. It should be emphasized that physicists from the Institute for High Energy Physics (IHEP, Protvino) have participated in obtaining the majority of data in this realm of physics. The most spectacular manifestations of single-spin asymmetry were observed in the E704 experiment [19—25], where, owing to a rather high energy of the polarized beam used and a high accuracy of the measurements, the data exhibited simple dependences on kinematical variables and on the sort participant particles. Data obtained at the PROZA [10—16] and FODS-2 [17, 18] facilities, as well as the first data from the STAR [28—30] and PHENIX [31, 32] setups at the Relativistic Heavy-Ion Collider (RHIC) at the Brookhaven National Laboratory (BNL) at $\sqrt{s} = 200$ GeV, significantly extended the kinematical domain for the reactions being studied. In those experiments, it is planned to obtain new, more precise data for various reactions and in various kinematical regions (that is, in the central region and in the beam- and target-fragmentation regions). This will make it possible to make considerable advances toward obtaining deeper insight into the mechanism of the emergence of a large transverse single-spin asymmetry.

This article is organized as follows. Reactions to be studied are specified in Section 2. The notion of single-spin asymmetry is introduced in Section 3. The exact properties of single-spin asymmetry that follow from the symmetry properties of strong interactions are considered in Section 4. Basic properties of single-spin reactions are formulated in Section 5 on the basis of an analysis of the entire body of available experimental data. Sections 6 and 7 are devoted to describing the PROZA and FODS-2 experiments in beams of the IHEP accelerator. Theoretical models proposed for explaining single-spin polarization effects are considered in Section 8. The basic conclusions are summarized in Section 9.

2. REACTIONS UNDER STUDY

The following three classes of reactions are considered:

$$A^{\uparrow} + B \to C + X, \tag{1}$$

$$A + B^{\uparrow} \to C + X, \tag{2}$$

$$A + B \to C^{\uparrow} + X. \tag{3}$$

In reactions of the first class, use is made of polarized beams of particles $A^{\uparrow}$ (proton or antiproton beams). Particles $A^{\uparrow}$ are transversely polarized in their rest frame. Polarized protons (antiprotons) are obtained by means of their acceleration (with the aid of the RHIC collider at BNL) or (as in the E704 and FODS experiments) from decays of Λ hyperons.

In the second class of reactions, one employs polarized targets containing polarized protons. If use is made of so-called frozen polarized targets (as in the PROZA experiment), protons are polarized by means of a dynamical high-frequency pumping of polarization. The target used is placed in a uniform magnetic

---

[*] E-mail: `abramov_v@mx.ihep.su`

field, and a low temperature is maintained in it. An overview of available data on the transverse single-spin asymmetry in reactions of the types in (1) and (2) can be found in [33–35].

In the third class of reactions, colliding hadrons A and B are not polarized; as to the polarization of particle $C^{\uparrow}$ (usually, this is a hyperon), it is determined from the angular distribution of its decay products. Hadrons detected in reactions belonging to the type in (3) include Λ, $\Sigma^{\pm}$, Σ^0, Ξ^0, Ξ^-, Ω^-, p, $\tilde{\Lambda}$, $\tilde{\Sigma}^-$, and $\tilde{\Xi}^+$. A survey of available data on the transverse polarization of hadrons in reactions of the type in (3) is given in [35, 36]. The polarization of antibaryons is of particular interest here. Within many models, it must be zero, but a sizable polarization was obtained in a number of experiments. New, high-precision measurements are required for clarifying this situation.

Experiments with a polarized beam are advantageous in relation to experiments employing a polarized target, since the former yield a higher measured ("raw") asymmetry owing to the fact that, in this case, interactions on polarized protons are not diluted with more numerous interactions on nuclei of the working substance of the target. The possibility of a fast reverse of the beam porarization (in order to reduce the systematic errors of the measurements) and the possibility of employing various (solid-state nuclear and cryogenic hydrogen) targets are further advantages of experiments with polarized beams. On the other hand, a polarized target makes it possible to harness various beams, including meson ones, and this is of interest from the physical point of view.

3. SINGLE-SPIN ASYMMETRIES IN HADRON–HADRON INTERACTIONS

The cross section for the production of particle C in a reaction of the type in (1) or (2) (it is a scalar quantity) can be expressed in terms of two axial vectors $\mathbf{S}$ and $\mathbf{n}$ directed, respectively, along the polarization vector of one of the colliding particles ($A^{\uparrow}$ or $B^{\uparrow}$) and along the normal to the reaction plane. We define a unit axial vector $\mathbf{S}$ aligned with the polarized-nucleon spin and the normal $\mathbf{n} = [\mathbf{p}^A \times \mathbf{p}^C]/|\mathbf{p}^A \times \mathbf{p}^C|$ to the reaction plane, where $\mathbf{p}^A$ and $\mathbf{p}^C$ are the momenta of particles A and C, respectively. The differential cross section for the production of particle C can then be represented in the form

$$\sigma^C \equiv Ed^3\sigma/d^3p = \sigma_0 + \mathbf{S}\cdot\mathbf{n}\cdot\sigma_1 \tag{4}$$
$$= \sigma_0(1 + \cos\varphi\sigma_1/\sigma_0) = \sigma_0(1 + A_N\cos\varphi),$$

where φ is the azimuthal angle between the axial vectors $\mathbf{S}$ and $\mathbf{n}$ and A_N is the single-spin asymmetry in the respective reaction or the analyzing power. If the degree of polarization of the beam or the target is different from unity (we denote it by P), then, instead of (4), we have

$$\sigma^C = \sigma_0(1 + A_N P\cos\varphi), \tag{5}$$

where σ_0, σ_1, and A_N are in general functions of three independent kinematical variables—for example, the well-known Mandelstam variables

$$s = (p^A + p^B)^2, \quad t = (p^A - p^C)^2, \tag{6}$$
$$u = (p^B - p^C)^2.$$

Here, A, B, and C label quantities referring to respective particles in reactions (1)–(3). The experimental raw asymmetry is defined as

$$A_N^{\text{raw}} = [N(\uparrow) - N(\downarrow)]/[N(\uparrow) + N(\downarrow)] \tag{7}$$
$$= [\sigma^C(\varphi) - \sigma^C(\pi - \varphi)]/[\sigma^C(\varphi) + \sigma^C(\pi - \varphi)]$$
$$= A_N P\cos\varphi,$$

where $N(\uparrow)$ and $N(\downarrow)$ are the numbers of recorded particles C whose spins are directed upward and downward, respectively, these numbers being normalized to the number of beam particles $A^{\uparrow}$ that traversed the target. Thus, there is a nonzero azimuthal asymmetry (5) in single-spin reactions of the type in (1) or (2) [37]. In the following, we assume that $A_N > 0$ if, in the case where the spin of beam particles $A^{\uparrow}$ is directed along $\mathbf{S}$ upward and where $\varphi = 0$, the number of particles C produced on the left in the reaction plane spanned by the momenta of particles $A^{\uparrow}$ and C is greater.

For reactions of type (3), the transverse polarization of a secondary particle $C^{\uparrow}$ is directed along the only axial vector $\mathbf{n}$ that is normal to the reaction plane [37].

In the present study, we will not consider two-spin asymmetries or reactions involving leptons (for an overview dealing with these issues, the interested reader is referred to [35]).

4. EXACT PROPERTIES OF SINGLE-SPIN ASYMMETRY

The exact properties of single-spin asymmetry that follow from the symmetry properties of strong interactions are listed below.

In strong interactions, secondary particles C originating from reactions of the type in (3) cannot have a longitudinal polarization. The presence of a longitudinal polarization $P_L \propto \mathbf{S}^C \cdot \mathbf{p}^C$ would violate the parity-conservation law.

In strong interactions, the single-spin asymmetry for a longitudinal polarization of a beam or a target in reactions of the type in (1) or (2), respectively, is zero. A nonzero correlation of the form $A_L \propto \mathbf{S}^A \cdot \mathbf{p}^A$ would violate the parity-conservation law. For this reason, one studies transverse single-spin asymmetries in hadron–hadron interactions. A longitudinal asymmetry or polarization in reactions of the types in (1), (2), and (3) can arise as a manifestation of weak interactions, which violate the parity-conservation law.

The asymmetry A_N and the polarization P_N vanish at zero value of the product-particle transverse momentum, $p_T^C = 0$ (the emission angle of particle C in the reaction c.m. frame is $\theta^C_{\text{c.m.}} = 0$), since, in this case, there is no particular direction (associated with a normal $\mathbf{n}$ to the reaction plane).

For collisions of identical unpolarized particles ($A \equiv B$), $P_N(-x_\text{F}) = -P_N(x_\text{F})$ in reactions of the type in (3) by virtue of invariance under the rotation of the coordinate system through an angle of 180° about the normal $\mathbf{n}$ to the reaction plane. As a consequence, we have $P_N(x_\text{F} = 0) = 0$.

In collisions of identical particles one of which is transversely polarized, the asymmetry $A_N(x_\text{F} = 0)$ can be different from zero in reactions of the type in (1) or (2), since the initial state is not fully symmetric with respect to the interchange of particles A and B. Nevertheless, the equality $A_N(x_\text{F} = 0) = 0$ does not contradict the symmetry properties of strong interactions and can hold in some reactions.

The above exact properties of single-spin asymmetry impose constraints on the possible form of its dependence on kinematical variables. Further constraints arise from the experimentally established properties of single-spin asymmetry that are considered below.

5. POLARIZATION EFFECTS AT HIGH AND INTERMEDIATE ENERGIES

According to the E704 experiment, the dependence of the properties of the single-spin asymmetry at 200 GeV on the quantum numbers and kinematical variables is especially simple. In Fig. 1*a*, the dependence of A_N on x_F is displayed for the reactions $p^\uparrow + p \to \pi^{\pm,0} + X$ [19, 21]. The asymmetry A_N for π^+ and π^- mesons at 200 GeV possesses mirror symmetry within the errors. For π^0 mesons, A_N is positive and is approximately one-half as large as that for π^+ mesons. In the region $x_\text{F} \geq 0.25$, the dependence of A_N on x_F is nearly linear. The dependence of A_N on x_F for the reactions $\bar{p}^\uparrow + p \to \pi^{\pm,0} + X$ is shown in Fig. 1*b* [20, 25]. The sign of A_N for π^+ and π^- mesons is reversed upon the replacement of a proton beam by an antiproton one; at the same time, the asymmetry A_N for π^0 mesons remains positive. This behavior of A_N is consistent with the $SU(6)$ symmetry of quarks in nucleons and with charge symmetry.

The dependence of the asymmetry A_N on quantum numbers and kinematical variables is more complicated at intermediate energies. In the experiment reported in [5] and performed at a proton-beam momentum of 11.75 GeV/c, the asymmetry A_N was studied as a function of two independent variables, p_T and x_F. In the majority of experiments, A_N was measured at one or two fixed values of the laboratory angle θ^C of secondary-particle emission, and it was difficult, for this reason, to separate the p_T and the x_F dependence. The dependences of A_N on p_T and x_F for π^+ mesons are shown, respectively, in Fig. 1*c* and in Fig. 1*d* [5]. At low transverse momenta, the sign of A_N and its dependence on x_F differ from those at high energies (see Fig. 1*d*). If one selects $p_T \geq 0.7$ GeV/c events, the x_F dependence of A_N will be close to that observed at 200 GeV. A more detailed analysis of the dependence of the asymmetry on kinematical variables can be found in [33, 34].

The transverse polarization of hyperons in reactions of the type in (3) exhibits many properties peculiar to a single-spin asymmetry, and this can be indicative of the similarity of the mechanisms that generate polarization effects. The polarization of Λ hyperons is negative; it increases in magnitude with increasing x_F and is independent of the beam energy within the accuracy of data [38–40]. A review of data on polarization can be found in [35, 36].

From Fig. 1 and from data of other experiments, we can draw the following conclusions on the dependence of the asymmetry A_N and polarization of hyperons on kinematical variables:

(i) In the region $p_T^C \leq p_T^0 \approx 0.2$–$2$ GeV/c, the asymmetry A_N and the polarization P_N grow with increasing transverse momentum of particle C [34, 35]. As can be seen from Fig. 1*c*, the asymmetry A_N tends to zero as p_T^C decreases.

(ii) In the region of polarized-particle fragmentation, the asymmetry $|A_N|$ grows, as a rule, with increasing Feynman variable $x_\text{F} = p_z^C / p_{\text{max}}^C$, where p_z^C and p_{max}^C are, respectively, the longitudinal component and the maximum possible magnitude of the momentum of particle C in the c.m. frame. In the region of fragmentation of unpolarized beam protons, the polarization $|P_N|$ grows similarly, as a rule, with increasing x_F [35, 36].

(iii) In the region of beam-hadron fragmentation, there is an approximate scale invariance for the polarization of hyperons [35, 36]. The polarization P_N in the c.m. frame is generally a function of three independent variables—for example, s, t, and u. If

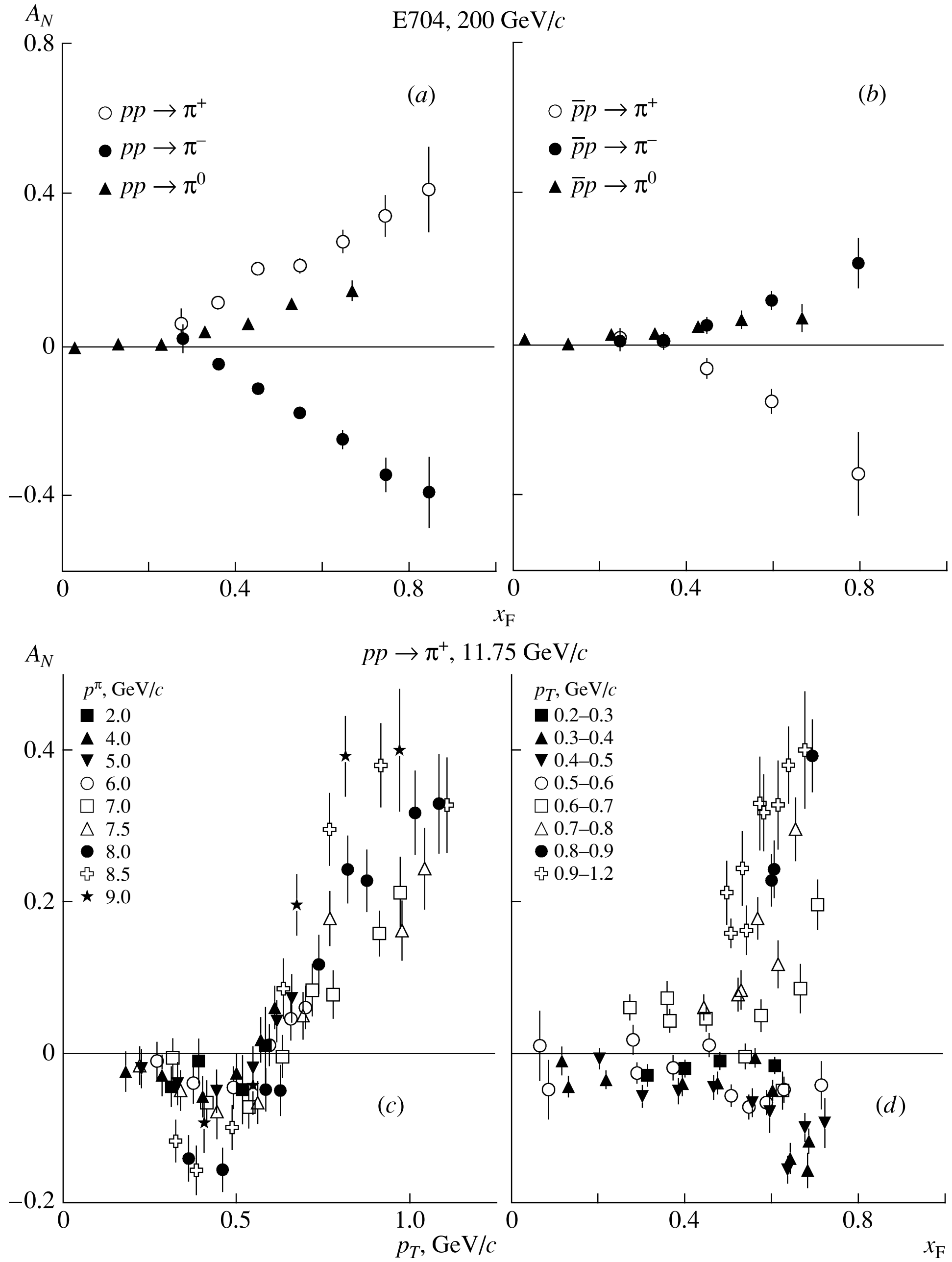

Fig. 1. Asymmetry A_N as a function of x_F for the reactions $(a)\, p^\uparrow + p \to \pi^{\pm,0} + X$ [19, 21] and $(b)\, \bar{p}^\uparrow + p \to \pi^{\pm,0} + X$ [20, 25], (c) as a function of p_T for the reaction $p^\uparrow + p \to \pi^+ + X$ [5], and (d) as a function of x_F for the reaction $p^\uparrow + p \to \pi^+ + X$ [5].

the above scale invariance holds, P_N depends only on two variables—for example, p_T and x_F—but it does not depend on the beam energy. This approximate scaling, $P_N\,(s, t, u) \approx P_N\,(p_T, x_F)$, is observed in the fragmentation region for Λ hyperons. The quantities P_N and A_N are dimensionless observables, which are bounded in absolute value. On the basis of a dimensional analysis, one can assume that they depend on the bounded dimensionless variables $x_A = -u/s$ and $x_B = -t/s$ and, by virtue of property (i), on p_T/p_T^0 as well, where p_T^0 is a dimensional parameter characteristic of the reaction being considered. At high energies, we have approximately $x_A = (x_R + x_F)/2$ and $x_B = (x_R - x_F)/2$, where $x_R = p^C/p^C_{\max}$ is a radial variable (in the c.m. frame). The variables x_A and x_B range between 0 and 1 and are convenient for describing the regions of fragmentation of hadrons A and B, respectively. In the central region ($x_F = 0$), we have $x_A = x_B = x_R/2 \leq 0.5$. In general, it follows from a data analysis that, for the single-spin asymmetry and for the polarization of hyperons, the relation $A_N(s, t, u) \approx A_N\,(p_T\,, x_A, x_B)$ holds approximately,

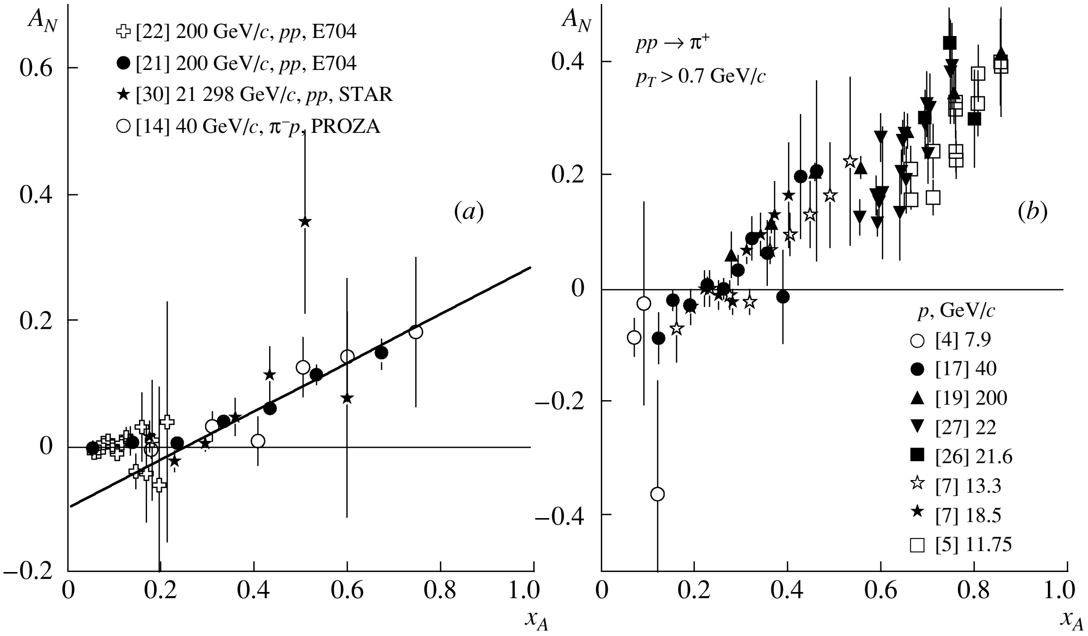

Fig. 2. Asymmetry A_N as a function of x_A for (*a*) the reactions $p^\uparrow + p \to \pi^0 + X$ [21, 22, 30] and $\pi^- p^\uparrow + p \to \pi^0 + X$ [14] in the region of polarized-proton fragmentation (the straight line represents a fit to the STAR data from [30]) and (*b*) the reaction $p^\uparrow + p \to \pi^+ + X$ (particles of transverse momentum in the region $p_T \geq 0.7$ GeV/c are selected).

where one can explicitly see the symmetry of the contributions from hadrons A and B [36]. It should be noted that a similar variable ($x = E^C/E^A$, where E^C and E^A are the laboratory energies of particles C and A, respectively) was previously used to describe the scale-invariance properties discovered at the IHEP accelerator for the differential cross sections for the production of secondary hadrons (π, K, $\bar{p}$, $\bar{n}$) [41].

(iv) In the region of polarized-proton fragmentation, the asymmetry A_N depends only slightly on the quantum numbers of target particles B [14]. This can be considered as an indication that single-spin polarization effects arise precisely in the process of fragmentation (hadronization) of quarks after their hard scattering in hadron collisions. A specific formulation of this hypothesis can have a scaling form or a form that violates scaling. Data from the E704 experiment [21, 22] ($p^A = 200$ GeV/c) for the reaction $p^\uparrow + p \to \pi^0 + X$ and data from the PROZA experiment [14] for the reaction $\pi^- + p^\uparrow \to \pi^0 + X$ ($p^A = 40$ GeV/c) are shown in Fig. 2*a* versus x_A. In the latter case, the data correspond to the region of polarized-proton fragmentation ($B \equiv p^\uparrow$). The same figure displays data from the STAR experiment [30] that were obtained at RHIC for the reaction $p^\uparrow + p \to \pi^0 + X$ at $\sqrt{s} = 200$ GeV, which, in the rest frame of B, corresponds to $p^A = 21$ TeV/c. Within the errors, the data on A_N can be described by a unified function of x_A. In order to determine the value $x_A = x_0$ at which A_N vanishes, the data from [30] were approximated by the linear function $A_N = A_0 \cdot (x_A - x_0)$. A fit to this form yielded the values of $A_0 = 0.38 \pm 0.13$ and $x_0 = 0.251 \pm 0.023$, this corresponding to the c.m. π^0-meson energy of $E_0 \sim 25$ GeV for $\sqrt{s} = 200$ GeV. So large a value of E_0 is somewhat at odds with the hypothesis of Mochalov *et al.* [42] that the threshold energy for π mesons has a universal value in the range $E_0 = 1.5$–2 GeV. From Fig. 2*a*, one can see that the agreement with the hypothesis that x_0 is independent of the beam energy over a broad range from 40 GeV to 21 TeV is quite good. For π^+ mesons, A_N is also described by a unified function of the variable x_A, provided that particles are selected from the transverse-momentum region $p_T \geq 0.7$ GeV/c (see Fig. 2*b*). In the case of this event selection, which ensures that the process being considered is rather hard, data in the energy range between 8 and 200 GeV, including the FODS data [17] in the central region $x_\mathrm{F} \approx 0$ [33, 34], are described by a unified dependence on x_A. It should be noted that the selection of $p_T \geq 0.7$ GeV/c events corresponds to distances of $r \leq r_0 = 0.3$ fm, where r_0 is on the order of the constituent-quark size [43]. Thus, we can state that scaling reveals itself in the behavior of the single-spin asymmetry as soon as we begin to see the internal structure of hadrons.

(v) In comparing the magnitudes and signs of A_N for π^+, π^-, and π^0 mesons in the region of

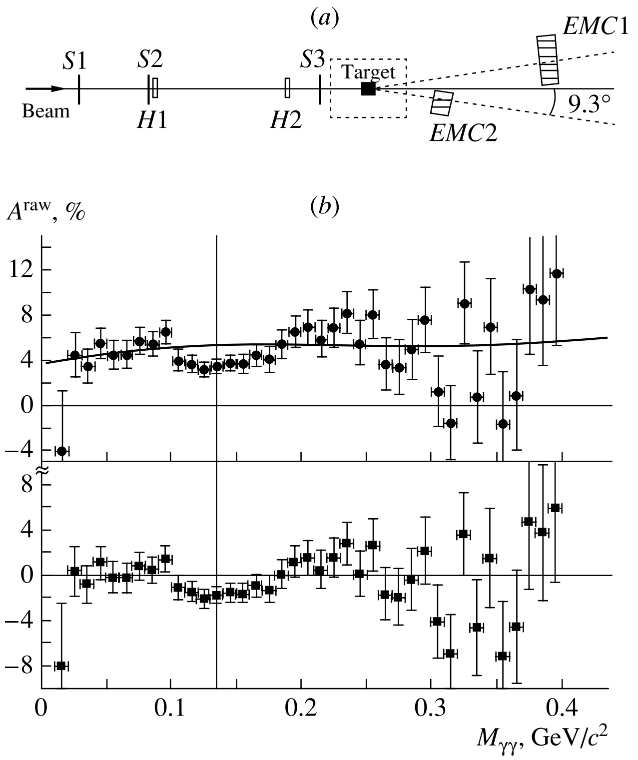

Fig. 3. (*a*) Layout of the PROZA-M facility. (*b*) Raw asymmetry as a function of the two-photon mass (upper panel) and result obtained upon subtracting the spurious asymmetry of the background (lower panel), the solid curve representing the spurious asymmetry obtained by approximating the raw asymmetry beyond the region of the neutral-pion mass peak.

polarized-proton (polarized-antiproton) fragmentation, it should be borne in mind that the main contribution to π^+ production comes from valence u quarks and that the main contribution to π^- production comes from d quarks. The process of π^0-meson production is also dominated by u quarks. According to $SU(6)$ symmetry, the u quarks in the proton have a positive polarization, while the d quarks there have a negative polarization. In view of this, it natural to expect a positive asymmetry in the fragmentation processes $p \to \pi^+$, $p(\bar{p}) \to \pi^0$, and $\bar{p} \to \pi^-$. Similarly, it is natural to expect a negative asymmetry in the fragmentation processes $\bar{p} \to \pi^+$ and $p \to \pi^-$. In view of $SU(6)$ symmetry for quarks and charge symmetry, one should expect an approximate fulfillment of the relations $A_N(p \to \pi^+) \approx -A_N(p \to \pi^-)$, $A_N(p \to \pi^+) \approx A_N(\bar{p} \to \pi^-)$, and $A_N(p \to \pi^0) \approx A_N(\bar{p} \to \pi^0)$. As can be seen from Figs. 1*a* and 1*b*, these relations do indeed hold within the errors [19, 20, 25].

We will now consider in greater detail the results coming from the PROZA and FODS-2 facilities, which operate in beams from the IHEP accelerator.

6. EXPERIMENTS AT THE PROZA FACILITY

Over the last 15 years, measurements of the single-spin asymmetry in the inclusive production of π^0 and η mesons have been performed at the PROZA setup in various kinematical regions by using a 40-GeV π^--meson beam [10–14] and a 70-GeV proton beam [15, 16].

A frozen-type polarized hydrogen target of mean polarization 80% was the hub of the apparatus. For a working substance, use was made of propanediol ($C_3H_8O_2$), where polarized protons constituted 11% of the total number of target nucleons. On average, the polarization was reversed once every two days.

An electromagnetic calorimeter that consisted of radiator counters from TF-1 lead glass, which were 38 × 38 × 50 mm in size, was used to detect photons from π^0-meson decay. Figure 3*a* shows one of the last configurations of the PROZA setup for measuring the asymmetry A_N in the central region of the reaction $p + p^\uparrow \to \pi^0 + X$ at a beam energy of 70 GeV. In addition to 480- and 144-channel calorimeters (EMC1, EMC2), this configuration included beam counters and hodoscopes. The number of beam particles hitting the target was determined by three scintillation counters ($S1$–$S3$). The coordinates of particles incident on the target were determined by two hodoscopes ($H1$, $H2$). The number of calorimeters, their positions, and the number of channels in them were adjusted to the physics problem at hand. These parameters are indicated below for each specific realization of the experiment.

In measuring asymmetry with a one-arm detector, there can arise an additional spurious asymmetry associated with the jitter of trigger electronics, monitor miscounts, or some other factors. With allowance for this, the measured asymmetry is the sum of the true asymmetry of π^0 mesons and the background asymmetry A_{BG}; that is,

$$A^{meas}(2\gamma) = kA^{raw}(\pi^0) + A_{BG}, \qquad (8)$$

where k is the relative number of π^0 mesons, which depends on the two-photon mass. In order to get rid of spurious asymmetry, a method was developed that is based on the assumption that the physical background asymmetry vanishes in the region beyond the π^0-meson mass peak [14]. This assumption relies on the results obtained in the previous experiments PROZA-M and E704. An example of the calculation of $A^{raw}(\pi^0)$ is illustrated in Fig. 3*b*.

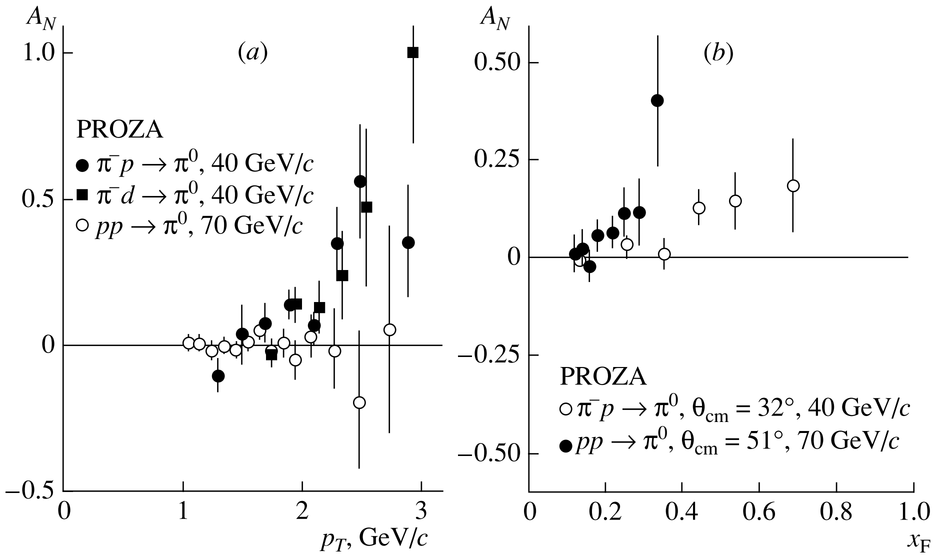

Fig. 4. Asymmetry A_N as a function of (*a*) p_T for the reactions $\pi^- p(d)^\uparrow + p \to \pi^0 + X$ [12, 13] and $p + p^\uparrow \to \pi^0 + X$ [15] in the central region and (*b*) x_F for the reactions $\pi^- p^\uparrow + p \to \pi^0 + X$ [14] and $p + p^\uparrow \to \pi^0 + X$ [16] in the region of polarized-proton fragmentation.

6.1. Measurement of A_N in the Central Region of the Reaction $\pi^- + p^\uparrow(d) \to \pi^0 + X$ at an Energy of 40 GeV

Photon pairs from π^0-meson decays were detected by two 144-channel electromagnetic calorimeters arranged at an angle of 12.3° on the two sides of the beam. The energy resolution of the calorimeters was $\Delta E/E = 15\%/\sqrt{E}$.

The measurement of A_N in the reaction $\pi^- + p^\uparrow(d) \to \pi^0 + X$ at an energy of 40 GeV revealed the presence of a large (up to 0.4 or 0.5) asymmetry for $-0.2 \leq x_F \leq 0.2$ at transverse momenta in the range $1.6 \leq p_T \leq 3.2$ GeV/c [12, 13]. The dependence of A_N on p_T is shown in Fig. 4*a*. Here and in the figures that follow, the sign of the asymmetry and of x_F is given in accordance with the data in Fig. 1, where the z axis is aligned with the polarized-proton momentum in the reaction c.m. frame. Figure 4*a* also displays data for a polarized deuterium target. There is a slight distinction between data obtained with hydrogen and deuterium targets, which is due primarily to the point at $p_T = 1.7$ GeV/c. The mean value of the asymmetry for $1.7 \leq p_T \leq 2.9$ GeV/c is $A_N = 0.145 \pm 0.033$ in the case of a hydrogen target and $A_N = 0.058 \pm 0.030$ in the case of a deuterium target.

6.2. Measurement of A_N in the Central Region of the Reaction $p + p^\uparrow \to \pi^0 + X$ at an Energy of 70 GeV

The single-spin asymmetry in the reaction $p + p^\uparrow \to \pi^0 + X$ for $-0.2 \leq x_F \leq 0.2$ was independently measured by two electromagnetic calorimeters arranged at an angle of 9.3° on the two sides of the beam (see Fig. 3*a*). Protons of energy 70 GeV were extracted with the aid of a bent single crystal. In the transverse-momentum range $1.0 \leq p_T \leq 3.0$ GeV/c, the asymmetry A_N is zero within the errors [15] (see Fig. 4*a*). This is consistent with the results obtained at the Fermi National Accelerator Laboratory (FNAL) for an energy of 200 GeV [22]. Comparing the results presented here with those measured in the same kinematical region at 40 GeV for π^--meson scattering, we can conclude that the asymmetry in the central region depends on the sort of interacting particles.

6.3. Measurement of A_N in the Reaction $\pi^- + p^\uparrow \to \pi^0 + X$ at 40 GeV in the Region of Polarized-Target Fragmentation

Photon pairs from π^0-meson decays were detected by one 720-channel electromagnetic calorimeter arranged at an angle of 40° on the right of the beam. The mean value of the asymmetry was $A_N = 0.138 \pm 0.038$ for $0.4 \leq x_F \leq 0.8$ and $1 \leq p_T \leq 2$ GeV/c [14]. For $0.1 \leq x_F \leq 0.4$ and $0.5 \leq p_T \leq 1.5$ GeV/c, the asymmetry was compatible with zero within the errors (see Fig. 4*b*). The asymmetry A_N behaves similarly in the region of polarized-proton fragmentation for this reaction and for the data of the E704 and STAR experiments (reaction $p^\uparrow + p \to \pi^0 + X$) at equivalent polarized-beam energies of 200 GeV [21] and 21 TeV [28, 30], respectively. Thus, we can conclude that A_N depends only slightly on energy and on the quantum numbers of an unpolarized particle involved in collisions.

6.4. Measurement of A_N in the Reaction $p + p^\uparrow \to \pi^0 + X$ at 70 GeV in the Region of Polarized-Target Fragmentation

The asymmetry was measured over the kinematical region specified by the inequalities $0.1 \le x_F \le 0.4$ and $0.9 \le p_T \le 2.5$ GeV/c. Photon pairs from π^0-meson decays were detected by one 720-channel electromagnetic calorimeter arranged at an angle of 21.5° on the right of the beam. The asymmetry is close to zero in the range $0.1 \le x_F \le 0.2$ and grows in magnitude with increasing x_F, reaching a value of 0.106 ± 0.032 at $\langle x_F \rangle \approx 0.3$ [16]. The dependence of A_N on x_F in Fig. 4*b* is consistent within the experimental errors with the behavior of A_N observed for different energies and reactions in the region of polarized-proton fragmentation [14, 21, 30].

Experiments at the PROZA facility revealed that, in the region of polarized-proton fragmentation, the asymmetry A_N depends only slightly on the quantum numbers of an unpolarized particle involved in collisions. In the central region, there is a sharp difference in A_N for the reactions $\pi^- + p^\uparrow \to \pi^0 + X$ and $p + p^\uparrow \to \pi^0 + X$. Mochalov *et al.* [42] indicated that, for different reactions, A_N begins growing in absolute value at the same c.m. π-meson energy E_0 ranging between 1.5 and 2.0 GeV. The hypothesis that E_0 is independent of the beam energy is likely to have a bounded applicability range in energy and is manifestly violated at the RHIC energy (see Fig. 2*a*), where $E_0 = 25$ GeV.

7. EXPERIMENTS AT THE FODS-2 FACILITY

The FODS-2 facility is a two-arm magnetic spectrometer that was created for studying hard processes in proton and π^--meson beams. The layout of the facility is shown in Fig. 5*a*. A spectrometric magnet, a system of drift chambers (DC) for determining the directions of tracks after the magnet, a ring-image Cherenkov spectrometer (SCOCH) for identifying charged hadrons ($\pi^\pm$, $K^\pm$, p, $\bar{p}$), and scintillation counters (S) and hadron calorimeters (HCAL) for developing a trigger that responds to high-energy hadrons are the main elements of the apparatus. Additionally, atmospheric-air threshold Cherenkov counters (Č) placed within the magnet are used to identify particles. An absorber made of copper and tungsten for beam particles that traversed the target without undergoing interaction is also arranged within the magnet. The apparatus has two arms, which can be rotated about the target installed in front of the magnet. In this way, one can change the angle of secondary-particle detection. The square of the mass of a particle, M^2, could be determined by measuring its velocity in the RICH spectrometer and its momentum in the magnetic spectrometer. A typical distribution with respect to M^2 is shown in Fig. 5*b* for particles of momentum ranging between 2 and 27 GeV/c.

The investigation of the single-spin asymmetry in the inclusive production of charged hadrons at the FODS-2 facility began in 1994. The apparatus is arranged in beamline-22, to which up to 10^{13} protons per spill at an energy of 60 to 70 GeV are directed by means of a slow extraction. A primary target (T), where Λ hyperons and other particles are produced, is mounted in the head part of beamline-22 (see Fig. 5*c*) in order to form a polarized beam. A purifying magnet $MH1$ deflects all charged particles to an absorber $P1$. Polarized protons from Λ-hyperon decays are selected in momentum and are focused onto the secondary target $T1$ of the FODS-2 facility. A transverse polarization is obtained with the aid of a collimator $K4$, which selects protons flying at an angle of ≈90° to the beam in the Λ-hyperon rest frame. At the end of beamline-22, there are two correcting magnets (MV1, 2) that compensate the shift of the beam for two values of its polarization. Various intensity and beam-position monitors based on ionization chambers and two threshold Cherenkov counters ($C1$, $C2$) for particle identification (not shown in Fig. 5*c*) are also placed there. In the beam and at the inlet of the magnet, there are hodoscopes (H) for measuring particle coordinates (see Fig. 5*a*).

The nominal momentum of polarized protons was 40 GeV/c, $\Delta p/p = \pm 4.5\%$; the mean beam polarization was $(39 \pm 2)\%$; the intensity of the beam was up to 3×10^7 protons per spill; and the polarization was reversed every 18 min for 30 days.

The asymmetry A_N for charged hadrons in the region of low x_F for a hydrogen target was measured during the run of 1994 [17]. Below, these data are compared with those obtained with nuclear targets.

The asymmetry A_N in reactions on nuclear targets (C, Cu) was measured during two runs of 2003. In this article, we present preliminary data based on part of the statistics (55%) that were obtained in the central region; we give no data here that are associated with different kinematical regions and which are being presently processed. The measurements in the region specified by the inequalities $-0.15 \le x_F \le 0.2$ and $1 \le p_T \le 4$ GeV/c were performed for a symmetric orientation of the apparatus arms at an angle of 160 mrad. The averaging of the results from the two arms made it possible to compensate in part

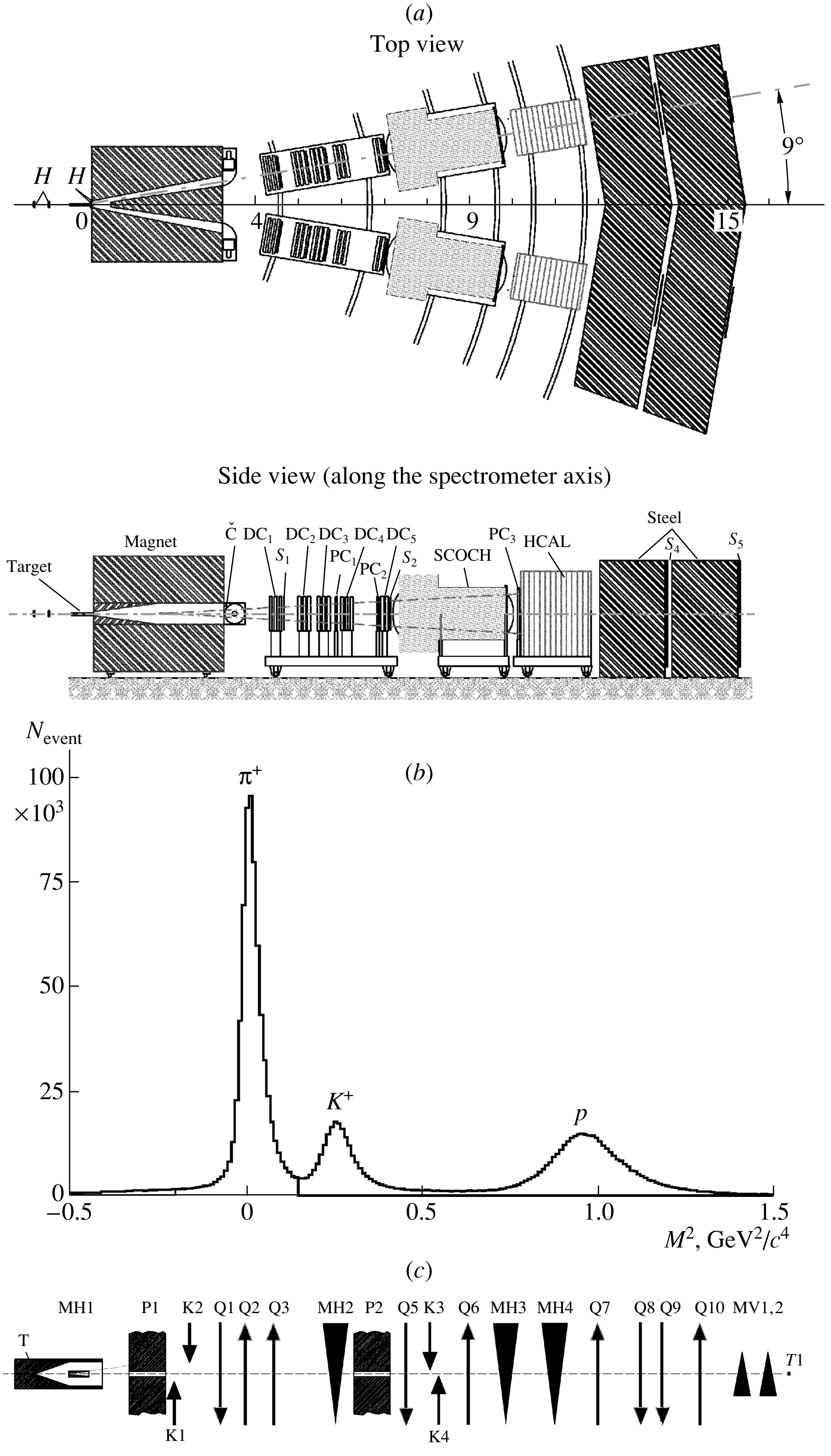

Fig. 5. (*a*) Layout of the FODS-2 facility. (*b*) Distribution of the number of events with respect to M^2 in the SCOCH spectrometer. (*c*) Layout of the polarized-proton channel.

for systematic errors associated with changes in the position of the beam in the vertical direction and with the drift of the beam-intensity monitors and of the equipment in the spectrometer arms.

7.1. Measurement of A_N in the Reaction $p^\uparrow + p(A) \to \pi^+ + X$

Figure 6*a* shows the asymmetry A_N in pp, pC, and pCu collisions for the region specified by the inequalities $-0.15 \le x_{\rm F} \le 0.2$ and $1 \le p_T \le 4$ GeV/c. Within the errors, there is no difference in A_N for C and Cu targets. The mean asymmetry for nuclear targets in the range $1.7 \le p_T \le 4$ GeV/c is 0.058 ± 0.004 for carbon and 0.062 ± 0.006 for copper. Within the range $1 \le p_T \le 2$ GeV/c, the asymmetry is about 0.05 higher for nuclear targets than for a hydrogen target. For the central region, this distinction can be associated with a smaller fraction of u quarks in a nuclear target, which contains neutrons. The cross section receives contributions both from the fragmentation $u \to \pi^+$ of u quarks entering into the composition of polarized beam protons and from the fragmentation of target u quarks. Since the target is not polarized, its significant contribution to the cross section in the central region reduces the measured asymmetry. In the case of a nuclear target, the contribution of u quarks is smaller. In the high-$x_{\rm F}$ region, which is dominated by the fragmentation of beam u quarks, there is no reason to expect a significant distinction between the asymmetries in pp and pA collisions.

7.2. Measurement of A_N in the Reaction $p^\uparrow + p(A) \to \pi^- + X$

Figure 6*b* shows the asymmetry A_N for pp, pC, and pCu collisions for the region specified by the inequalities $-0.15 \le x_{\rm F} \le 0.2$ and $1 \le p_T \le 4$ GeV/c. In the range $1.7 \le p_T \le 4$ GeV/c, the mean asymmetry for nuclear targets is -0.004 ± 0.008 for carbon and -0.009 ± 0.007 for copper. Over the range $1 \le p_T \le 1.5$ GeV/c, the asymmetry is about 0.05 higher for nuclear targets than for a hydrogen target.

7.3. Measurement of A_N in the Reaction $p^\uparrow + p(A) \to K^+ + X$

Figure 6*c* displays the asymmetry A_N in pp, pC, and pCu collisions for the region specified by the inequalities $-0.04 \le x_{\rm F} \le 0.17$ and $1.2 \le p_T \le 3.2$ GeV/c. The mean asymmetry for C and Cu targets in the range $1.7 \le p_T \le 4.0$ GeV/c is 0.065 ± 0.007 and 0.077 ± 0.011, respectively. Over the range $1.2 \le p_T \le 1.8$ GeV/c, the asymmetry is 0.07 higher for nuclear targets than for a hydrogen target.

7.4. Measurement of A_N in the Reaction $p^\uparrow + p(A) \to K^- + X$

In Fig. 6*d*, the asymmetry A_N in pp, pC, and pCu collisions is shown for the region specified by the inequalities $-0.04 \le x_{\rm F} \le 0.17$ and $1.2 \le p_T \le 3.2$ GeV/c. Within the errors, there are no significant distinctions between the A_N values for all three targets (p, C, Cu). The mean asymmetry for nuclear targets is close to zero over the range $1.7 \le p_T \le 3.0$ GeV/c: 0.023 ± 0.016 for carbon and 0.022 ± 0.022 for copper. In some models, an asymmetry close to zero is expected for K^- mesons, since they do not contain valence quarks from a polarized proton.

7.5. Measurement of A_N in the Reaction $p^\uparrow + p(A) \to p + X$

In Fig. 6*e*, one can see the asymmetry A_N in pp, pC, and pCu collisions for the region specified by the inequalities $-0.09 \le x_{\rm F} \le 0.22$ and $1.2 \le p_T \le 3.7$ GeV/c. Within the range $1.2 \le p_T \le 1.8$ GeV/c, the asymmetry is about 0.07 higher for nuclear targets than for a hydrogen target. The mean asymmetry for nuclear targets is close to zero over the range $1.7 \le p_T \le 3.7$ GeV/c: 0.022 ± 0.004 for carbon and 0.032 ± 0.005 for copper. For the central region, other experiments also yielded an asymmetry close to zero [4, 7, 25]. In the region of polarized-proton fragmentation, a significant asymmetry of neutrons was observed in the PHENIX experiment: $A_N = -0.108 \pm 0.009$ [32]. The sign and the scale of A_N for neutrons are identical to those for protons in pp collisions.

7.6. Measurement A_N in the Reaction $p^\uparrow + p(A) \to \bar{p} + X$

Figure 6*e* displays the asymmetry A_N in pp, pC, and pCu collisions for the region specified by the inequalities $-0.09 \le x_{\rm F} \le 0.19$ and $1.2 \le p_T \le 3.1$ GeV/c. Within the errors, there are no significant distinctions between the A_N values for the three targets (p, C, Cu). The mean asymmetry for nuclear targets is close to zero over the range $1.2 \le p_T \le 3.1$ GeV/c: 0.008 ± 0.015 for carbon and 0.029 ± 0.013 for copper. Asymmetry values close to zero that were obtained for antiprotons and K^- mesons can serve as an upper limit on the possible spurious asymmetry in the experiment being discussed (≤ 0.04).

The single-spin asymmetry measured for $\pi^\pm$ mesons in the central region is significantly smaller in absolute value than that in the region of polarized-proton fragmentation [19, 25]. In the central region, the asymmetry for π^+ and K^+ mesons is different

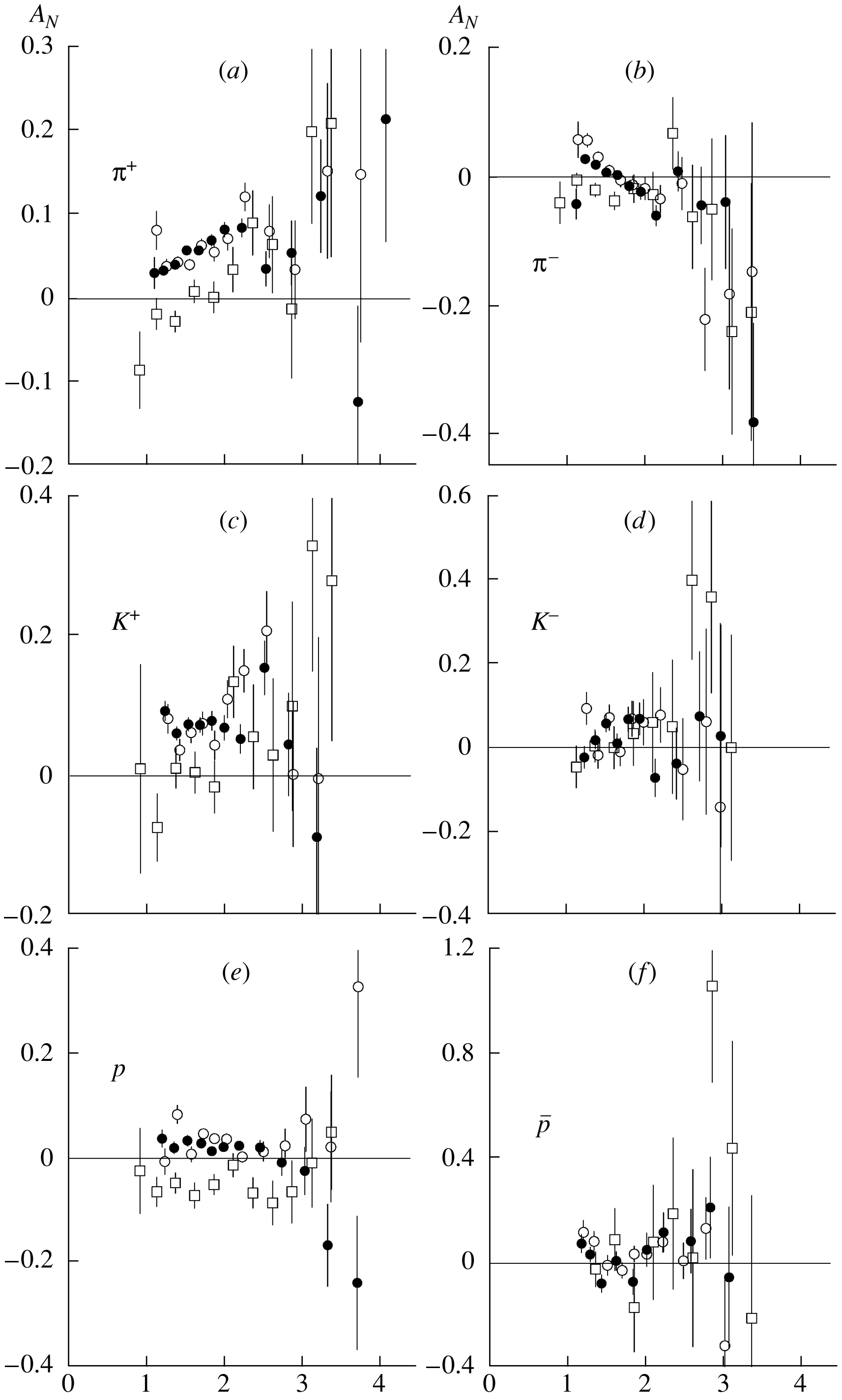

Fig. 6. Asymmetry A_N as a function of p_T in the reactions $p^\uparrow + p(A) \to h + X$, where $h = (a)\,\pi^+, (b)\,\pi^-, (c)\,K^+, (d)\,K^-$, $(e)\,p$, and $(f)\,\bar{p}$, on (□) proton, (○) copper, and (●) carbon targets.

from zero, which is likely to be due to a dominant contribution of u quarks to their production. The asymmetries measured for the first time on nuclear targets (C and Cu) do not differ within the experimental errors. The A_N values measured for hydrogen and nuclear targets differ by 0.05 to 0.07 for hadrons containing valence quarks of a polarized proton. The asymmetry A_N for K^- mesons and antiprotons, which do not feature valence quarks from a polarized proton, is zero on average. Measurements of A_N for antiprotons were performed for the first time.

8. POSSIBLE ORIGIN OF SINGLE-SPIN ASYMMETRY

As was indicated above, single-spin asymmetries are low within perturbative QCD [1]. The single-spin asymmetry is given by

$$A_N \sim \mathrm{Im}(F_{nf}F_f^*), \tag{9}$$

where F_{nf} is the non-helicity-flip amplitude and F_f is the helicity-flip amplitude. The phases of the amplitudes F_{nf} and F_f must be different. In [1], it was shown that, according to QCD, the helicity-flip amplitude is of order m/E^q, where m is the quark mass and $E^q \sim p_T$ is the quark-interaction energy in the c.m. frame. The presence of the phase difference requires considering the second order (in the factor α_s) and higher orders of perturbation theory. This yields

$$A_N \sim \alpha_s m/p_T, \tag{10}$$

where α_s is the strong-interaction coupling constant [44]. The asymmetry in (10) is low at a current quark mass of $m \sim 6$ MeV/c^2 and $p_T \sim 1$ GeV/c.

The results of the PROZA-M [10–16], E704 [19–25], and FODS-2 [17] experiments, which were performed by research groups including physicists from IHEP, contributed greatly to developing models that were proposed in the past decade to explain large single-spin asymmetries by associating them with

(i) the introduction of an additional quark transverse momentum k_T;

(ii) the absence of symmetry of the quark-density distribution in the initial state with respect to the proton polarization (Sivers mechanism) [45–47];

(iii) the absence of symmetry of quark fragmentation functions in the final state with respect the proton polarization (Collins mechanism) [48];

(iv) the contribution of higher twists [49–54];

(v) the effect of the orbital angular momentum of valence quarks (Berlin model) [55, 56] or current quarks in a constituent quark (U-matrix model) [57];

(vi) the interaction of the quark chromomagnetic moment with a chromomagnetic field [36, 58];

(vii) the formation of resonances or excited states [59].

A survey of these models is given in [35, 44, 60]. In the higher twist model, as well as in the Sivers and Collins models, it is implied that hard processes of quark and gluon scattering and soft processes associated with structure functions and fragmentation functions factorize. The accuracy of existing data gives no way to choose between specific models and mechanisms. It is necessary to compare model predictions with the entire body of available data rather than with data from one especially precise experiment [61].

9. CONCLUSIONS

An analysis of experimental data on single-spin effects in the inclusive production of hadrons in hadron–hadron collisions has given surprising results, as frequently occurs in spin physics. Although the dynamics of hard scattering with allowance for spin is rather simple, experiments disclosed an unexpected and rich pattern of physical phenomena that have yet to be understood [61]. The main conclusions from the above analysis of experimental data can be summarized as follows:

Single-spin polarization effects remain on the same order of magnitude at c.m. energies ranging between 6 and 200 GeV, this being indicative of an approximate scaling of the form $A_N(s, t, u) \approx A_N(p_T, x_A, x_B)$ in the region $p_T \geq 0.7$ GeV/c.

In the region of polarized-proton fragmentation, the single-spin asymmetry depends only slightly on the quantum numbers of an unpolarized particle involved in collisions.

In the central region, A_N depends on the sort of unpolarized particle involved in collisions.

In the central region, the asymmetry A_N does not show any significant dependence on the target charge number. There is a distinction of 0.05 to 0.07 in A_N between the data obtained for hydrogen and nuclear targets. This may be due to the different quark content in the proton and nuclei.

New, more precise data over a broad kinematical domain and for various reactions are required for unambiguously choosing a specific mechanism that generates a single-spin asymmetry. Such measurements would make it possible to refine the structure of hadrons and the dynamics of interaction of structural components (quarks and gluons) everywhere, including the confining region, where the theory of strong interactions has yet to be developed conclusively.

ACKNOWLEDGMENTS

I am indebted to A.M. Zaitsev and V.I. Kryshkin for permanent attention to this study. I am also grateful to P.I. Goncharov, A.V. Korablev, and V.V. Talov for assistance in data processing and to A.N. Vasiliev and V.V. Mochalov for enlightening discussions.

REFERENCES

1. G. Kane, J. Pumplin, and W. Repko, Phys. Rev. Lett. **41**, 1689 (1978).
2. L. Dick *et al.*, Phys. Lett. B **57B**, 93 (1975).
3. D. S. Ayres *et al.*, Phys. Rev. D **15**, 1826 (1977).
4. D. G. Aschman *et al.*, Nucl. Phys. B **142**, 220 (1978).
5. W. H. Dragoset *et al.*, Phys. Rev. D **18**, 3939 (1978).
6. J. Antille *et al.*, Phys. Lett. B **94B**, 523 (1980).
7. S. Saroff *et al.*, Phys. Rev. Lett. **64**, 995 (1990).

8. B. E. Bonner *et al.*, Phys. Rev. D **38**, 729 (1988).
9. B. E. Bonner *et al.*, Phys. Rev. D **41**, 13 (1990).
10. V. D. Apokin *et al.*, Yad. Fiz. **49**, 156 (1989) [Sov. J. Nucl. Phys. **49**, 97 (1989)].
11. V. D. Apokin *et al.*, Yad. Fiz. **49**, 165 (1989) [Sov. J. Nucl. Phys. **49**, 103 (1989)].
12. N. S. Amaglobeli *et al.*, Yad. Fiz. **50**, 695 (1989) [Sov. J. Nucl. Phys. **50**, 432 (1989)].
13. V. D. Apokin *et al.*, Phys. Lett. B **243**, 461 (1990).
14. A. N. Vasil'ev *et al.*, Preprint No. 2003-21, IFVÉ (Inst. of High Energy Phys., Protvino, 2003); A. Davidenko *et al.*, hep-ex/0312014.
15. A. N. Vasil'ev *et al.*, Preprint No. 2003-22, IFVÉ (Inst. of High Energy Phys., Protvino, 2003); V. Mochalov *et al.*, hep-ex/0312009.
16. A. N. Vasiliev, V. N. Grishin, A. M. Davidenko, *et al.*, *Report Presented at the Conference of the Section of Nuclear Physics, Department of General Physics, Russian Academy of Sciences, March 2004* (preliminary results were reported by V. V. Abramov).
17. V. V. Abramov *et al.*, Nucl. Phys. B **492**, 2 (1997); hep-ex/0110011.
18. V. V. Abramov, P. I. Goncharov, V. I. Kryshkin *et al.*, *Report Presented at the Conference of the Section of Nuclear Physics, Department of General Physics, Russian Academy of Sciences, March 2004.*
19. D. L. Adams *et al.*, Phys. Lett. B **264**, 462 (1991).
20. D. L. Adams *et al.*, Phys. Lett. B **261**, 201 (1991).
21. D. L. Adams *et al.*, Z. Phys. C **56**, 181 (1992).
22. D. L. Adams *et al.*, Phys. Rev. D **53**, 4747 (1996).
23. D. L. Adams *et al.*, Nucl. Phys. B **510**, 3 (1998).
24. A. Bravar *et al.*, Phys. Rev. Lett. **75**, 3073 (1995).
25. A. Bravar *et al.*, Phys. Rev. Lett. **77**, 2626 (1996).
26. K. Krueger *et al.*, Phys. Lett. B **459**, 412 (1999).
27. C. E. Allgower *et al.*, Phys. Rev. D **65**, 092008 (2002).
28. L. C. Bland, AIP Conf. Proc. **675**, 98 (2003); hep-ex/0212013.
29. A. Bazilevsky *et al.*, AIP Conf. Proc. **675**, 584 (2003).
30. J. Adams *et al.*, Phys. Rev. Lett. **92**, 171801 (2004); hep-ex/0310058.
31. K. Okada (PHENIX Collab.), AIP Conf. Proc. **675**, 395 (2003).
32. G. Bunce, in *Proceedings of the X International Workshop on High Energy Spin Physics (SPIN-2003), Dubna, Russia, 2003.*
33. V. V. Abramov, Preprint No. 98-84, IFVÉ (Inst. of High Energy Phys., Protvino, 1998); hep-ph/0110152.
34. V. V. Abramov, Eur. Phys. J. C **14**, 427 (2000).
35. E. Leader, *Spin in Particle Physics* (Cambridge Univ. Press, Cambridge, 2001), Vol. 15, p. 382.
36. V. V. Abramov, Preprint No. 2001-13, IFVÉ (Inst. of High Energy Phys., Protvino, 2001); hep-ph/0111128.
37. L. D. Landau and E. M. Lifshitz, *Quantum Mechanics: Non-Relativistic Theory* (Nauka, Moscow, 1974; Pergamon, Oxford, 1977).
38. K. Heller *et al.*, Phys. Rev. Lett. **41**, 607 (1978).
39. B. Lundberg *et al.*, Phys. Rev. D **40**, 3557 (1989).
40. E. J. Ramberg *et al.*, Phys. Lett. B **338**, 403 (1994).
41. Yu. B. Bushnin *et al.*, Phys. Lett. **29**, 48 (1969).
42. V. V. Mochalov, S. M. Troshin, and A. N. Vasiliev, in *Proceedings of the X International Workshop on High Energy Spin Physics (SPIN-2003), Dubna, Russia, 2003*; hep-ph/0310224; hep-ex/0312007; hep-ex/0312010.
43. V. V. Anisovich, in *Proceedings of XIV Winter School of Leningrad Institute of Nuclear Physics, Leningrad, 1979*, Vol. 3, p. 3.
44. M. Anselmino, Czech. J. Phys., Suppl. C **52**, C13 (2002); hep-ph/0201150.
45. D. Sivers, Phys. Rev. D **41**, 83 (1990).
46. D. Sivers, Phys. Rev. D **43**, 261 (1991).
47. T. T. Chou and C. N. Yang, Nucl. Phys. B **107**, 1 (1976).
48. J. C. Collins, Nucl. Phys. B **396**, 161 (1993).
49. A. V. Efremov and O. V. Teryaev, Yad. Fiz. **36**, 242 (1982) [Sov. J. Nucl. Phys. **36**, 140 (1982)]; Yad. Fiz. **36**, 950 (1982) [Sov. J. Nucl. Phys. **36**, 557 (1982)]; **39**, 1517 (1984) [**39**, 962 (1984)]; A. V. Efremov and O. V. Teryaev, Phys. Lett. B **150B**, 383 (1985).
50. A. V. Efremov, V. M. Korotkiyan, and O. V. Teryaev, Phys. Lett. B **348**, 577 (1995).
51. J. W. Qiu and G. Sterman, Phys. Rev. Lett. **67**, 2264 (1991); Nucl. Phys. B **378**, 52 (1992).
52. A. Shäfer, L. Mankiewicz, P. Gonicki, and S. Güllenstern, Phys. Rev. D **47**, R1 (1993); B. Ehrnsperger, A. Schäfer, W. Greiner, and L. Mankiewicz, Phys. Lett. B **321**, 121 (1994).
53. J. W. Qiu and G. Sterman, Phys. Rev. D **59**, 014004 (1999); hep-ph/9806356.
54. Y. Kanazawa and Y. Koike, Phys. Lett. B **490**, 99 (2000); hep-ph/0007272.
55. Meng Ta-Chung, in *Proceedings of the 4th Workshop on High Energy Spin Physics "Spin-91", Protvino, Russia, 1991* (IHEP, Protvino, 1992), p. 112.
56. Zuo-tang Liang and C. Boros, Int. J. Mod. Phys. A **15**, 927 (2000); hep-ph/0001330.
57. S. M. Troshin and N. E. Tyurin, Phys. Rev. D **52**, 3862 (1995); **54**, 838 (1996).
58. M. G. Ryskin, Yad. Fiz. **48**, 1114 (1988) [Sov. J. Nucl. Phys. **48**, 708 (1988)].
59. G. Musulmanbekov and M. Tokarev, in *Proceedings of the 6th Workshop on High Energy Spin Physics "Spin-95", Protvino, Russia, 1995* (Protvino, 1996), p. 132.
60. M. Anselmino *et al.*, Int. J. Mod. Phys. A **18**, 1237 (2003); hep-ph/0201076.
61. P. G. Ratcliffe, AIP Conf. Proc. **675**, 176 (2003); hep-ph/0211232.

Translated by A. Isaakyan

Physics of Atomic Nuclei, Vol. 68, No. 3, 2005, pp. 398–403. Translated from Yadernaya Fizika, Vol. 68, No. 3, 2005, pp. 427–432.
Original Russian Text Copyright © 2005 by Beloglazov, Kovalev, Kruglov, Novinsky, Sumachev, Trautman, Filimonov, Shchedrov, Alekseev, Budkovsky, Zhurkin, Kanavets, Koroleva, Morozov, Nesterov, Ryltsov, Svirida, Sulimov, Bazhanov, Bunyatova.

Program of Measurement of the Asymmetry P at the Minima of the Differential Cross Section for Elastic π^+p Scattering

Yu. A. Beloglazov[1], A. I. Kovalev[1], S. P. Kruglov[1], D. V. Novinsky[1]*, V. V. Sumachev[1], V. Yu. Trautman[1], E. A. Filimonov[1], V. A. Shchedrov[1], I. G. Alekseev[2], P. E. Budkovsky[2], V. V. Zhurkin[2], V. P. Kanavets[2], L. I. Koroleva[2], B. V. Morozov[2], V. M. Nesterov[2], V. V. Ryltsov[2], D. N. Svirida[2], A. D. Sulimov[2], N. A. Bazhanov[3], and E. I. Bunyatova[3]

Received May 24, 2004; in final form, September 3, 2004

Abstract—A program of measurement of the polarization parameter P in elastic π^+p interaction in the resonance region of backward pion scattering is presented. This program is aimed at determining the bifurcation points of the trajectory of zeros of the pion–nucleon amplitude and, hence, at unambiguously reconstructing the amplitude of πN scattering in the second resonance region. It is planned to perform a relevant experiment in a pion beam from the accelerator of the Institute of Experimental and Theoretical Physics (ITEP, Moscow). © *2005 Pleiades Publishing, Inc.*

1. INTRODUCTION

Over the past few years, a collaboration of physicists from the Petersburg Nuclear Physics Institute (PNPI, Gatchina) and the Institute of Theoretical and Experimental Physics (ITEP, Moscow)—below, it is referred to as the PNPI–ITEP Collaboration—has conducted experiments devoted to measuring polarization parameters in the second resonance region of elastic pion–nucleon (πN) interaction. These experiments were aimed at unambiguously reconstructing the amplitude of πN scattering. In particular, measurement of the spin-rotation parameters A and R in π^+p scattering at a pion momentum above 1000 MeV/c [1] made it possible for the first time to resolve part of the discrete ambiguities in existing partial-wave analyses (PWA) for the amplitude of isospin $I = 3/2$. The available PWA predicted different values for the parameters A and R. Presently, there are three global PWA: KH80 (KA84) [2]; CMB80 [3]; and the modern analysis of the G. Washintgton University group (USA), FA02 [4]. The previous analyses of this group are known as SM90 [5] and SM95 [6]. On the basis of experimental data, PWA reconstruct the energy dependence of the amplitude of πN scattering, whereupon one extracts information about resonance states and all observables from this dependence. A theoretical analysis that employs the method of the trajectory of zeros of the transverse amplitudes [7] permits revealing kinematical regions where there are discrete ambiguities in the πN amplitude. Owing to this, one can plan an experiment in such a way as to resolve the aforementioned ambiguities within an optimal data-acquisition time.

The new PWA FA02 incorporated the experimental results of the PNPI–ITEP Collaboration on the spin-rotation parameter A [1]. It turned out that, in the FA02 analysis, the point of intersection of the corresponding trajectory of zeros with a unit circle (the bifurcation region of the trajectory) was shifted by more than 250 MeV/c along the momentum axis and by more than 30° in angle in relation to the previous analysis SM95. A more detailed analysis revealed that this discrepancy can be due to the lack of sufficient experimental information about the polarization parameter P in the pion-momentum interval $p_\pi = 750$–1000 MeV/c. A direct measurement of the polarization P in this region of p_π in elastic π^+p scattering would make it possible to refine the actual position of the bifurcation region. There is yet another reason why it is of importance to solve this problem: so far, the predictions of all existing PWA have been coincident with the predictions of SM95 for the position of the bifurcation region for this trajectory of zeros.

2. ZEROS OF THE TRANSVERSE AMPLITUDES

The main objective of experimentally studying πN interaction is to perform a PWA with the aim of un-

---

[1] Petersburg Nuclear Physics Institute, Russian Academy of Sciences, Gatchina, 188350 Russia.

[2] Institute of Theoretical and Experimental Physics, Bol'shaya Cheremushkinskaya ul. 25, Moscow, 117259 Russia.

[3] Joint Institute for Nuclear Research, Dubna, Moscow oblast, 141980 Russia.

* E-mail: `dimanov@pnpi.spb.ru`

ambiguously reconstructing the πN amplitude. Generally, only a complete experiment—that is, systematic measurements of all observables in all kinematical regions—enables one to reconstruct unambiguously the amplitudes in question. Such systematic measurements are overly cumbersome and expensive; therefore, they have been performed only for specific bounded regions of kinematical variables. Incompleteness of experimental results leads to discrete ambiguities in the reconstruction of the amplitude of πN scattering. The formalism of the trajectory of zeros of the transverse amplitudes makes it possible to separate the regions of such ambiguities. In this way, one can fill the gap in data by measuring additional observables only in some, so-called critical, regions of kinematical variables.

The underlying idea is to compare the trajectories of zeros of the πN amplitude constructed on the basis of the predictions of existing PWA. Upon determining the trajectory of zeros following a bifurcation (intersection with the physical region or reflections from it) for each PWA, one can plan experiments aimed at measuring polarization parameters required for unambiguously reconstructing the amplitude.

The matrix of elastic πp scattering is usually represented in the form

$$M = f + ig(\boldsymbol{\sigma} \cdot \mathbf{n}), \tag{1}$$

where f and g are the complex-valued non-spin-flip and spin-flip scattering amplitudes, respectively; $\boldsymbol{\sigma}$ is the Pauli matrix; and $\mathbf{n}$ is the unit vector normal to the plane of elastic πp scattering. The transverse amplitudes F^+ and F^- are defined as linear combinations of the amplitudes f and g:

$$F^+ = f + ig, \quad F^- = f - ig. \tag{2}$$

The observables of elastic πN scattering (the total cross section σ_{tot} and the differential cross section $d\sigma/d\Omega$, as well as the polarization parameters P, R, and A) can be expressed in terms of the above transverse amplitudes [1]. The cross section and the polarization parameter P determine only the absolute values of the amplitudes F^+ and F^-. Their relative phase can be determined only by measuring the spin-rotation parameters A and R. Similarly to the generally adopted partial-wave expansion (in Legendre polynomials) of the amplitudes f and g, the amplitudes F^+ and F^- can be expanded in a series in $\cos\theta_{\text{c.m.}}$ and $\sin\theta_{\text{c.m.}}$ ($\theta_{\text{c.m.}}$ is the pion scattering angle in the c.m. frame). Further, we introduce the variable $\omega = \exp(i\theta_{\text{c.m.}})$ [7], so that $\cos\theta_{\text{c.m.}} = (\omega + \omega^{-1})/2$ and $\sin\theta_{\text{c.m.}} = (\omega - \omega^{-1})/2i$. The transverse amplitudes can then be expanded in a series in ω as

$$F^{\pm}(\omega) = \frac{1}{\omega^n} \sum_{l=1}^{2L_{\max}} a_l \omega^l, \tag{3}$$

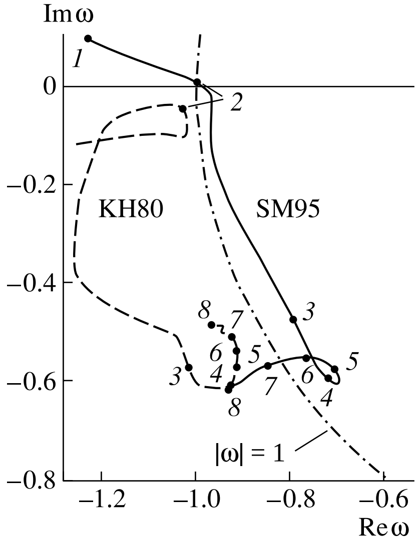

Fig. 1. Trajectories of zeros of the transverse amplitudes according to the predictions of the PWA (dashed curve) KH80 [2] and (solid curve) SM95 [6].

where $L_{\max}$ is the maximum orbital angular momentum, ω_l is a variable for each partial wave, and a_l is an expansion coefficient. Equating $F^{\pm}$ to zero, we obtain the roots of the polynomial in (3). The resulting solutions are referred to as the zeros of the transverse amplitudes. There is a one-to-one correspondence between the scattering amplitude and its zeros [7] for each value of the pion-beam momentum.

The zeros of the scattering amplitude move in the complex plane of ω in response to a variation in the incident-pion energy (momentum). Figure 1 displays the trajectories of zeros according to the predictions of the PWA (solid curve) SM95 and (dashed curve) KH80. The physical region in the complex plane is the circle $|\omega| = 1$ (dash-dotted curve). The angle between the real axis and the line connecting the coordinate origin with the running point on the trajectory corresponds to the pion scattering angle in the c.m. frame. For π^+ momenta below 750 MeV/c, both trajectories lie on the same side of the circle. As the pion momentum (energy) increases—that is, as the trajectory approaches the physical region—it either is reflected from the circle (KH80) or intersects it (SM95). It was shown previously (see, for example, [8]) that the discrete ambiguities in the πN amplitude for $p_\pi > 750$ MeV/c (that is, the position of the trajectories on different sides of the physical region) cannot be removed without new measurements of the spin-rotation parameters A and R. These measurements were performed for three momentum values [1], and it was shown that the branch of the PWA solution corresponding to the SM95 analysis is correct for $p_\pi \geq 800$ MeV/c.

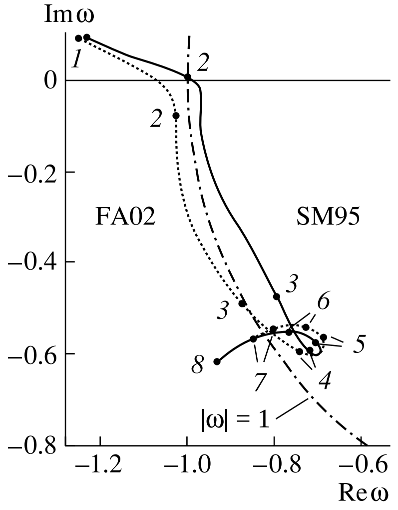

Fig. 2. Trajectories of zeros of the transverse amplitudes according to the predictions of the PWA (dotted curve) FA02 [4] and (solid curve) SM95 [6].

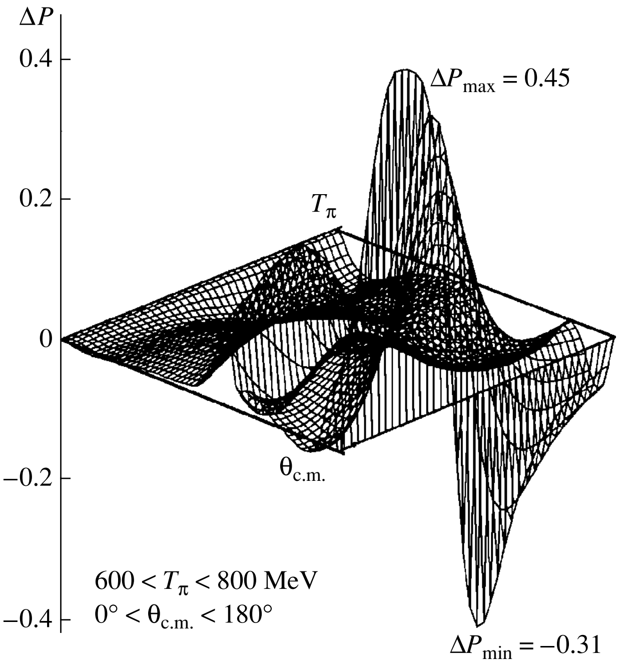

Fig. 3. Difference of the predictions of the PWA FA02 and SM95 for the polarization parameter P, $\Delta P = P(\text{FA02}) - P(\text{SM95})$, in the region of bifurcation of the trajectory of zeros for the pion-energy interval $T_\pi = 600$–800 MeV.

3. NEED FOR MEASURING THE POLARIZATION PARAMETER P AT MOMENTA OF $p_\pi \geq 800$ MeV/c

From the data obtained by the PNPI–ITEP Collaboration for the parameters A and R [1], it was found that the correct branch of the PWA solution corresponds to the trajectory of zeros that traverses the physical region. It turned out that the point of intersection of the trajectory with the unit circle can also be shifted. Figure 2 displays the trajectories of zeros according to the predictions of the (solid curve) SM95 and (dotted curve) FA02 analyses. It is clear from this figure that, in the momentum interval $p_\pi = 750$–1000 MeV/c, the trajectories lie on different sides of the physical region. From the formalism of the trajectory of zeros, we know that the intersection of the trajectory with the physical region means that the spin-rotation parameters vanish at this point; concurrently, the polarization P assumes the values of ± 1, while the differential cross section has a minimum. In the regions where the trajectory of zeros lies in the vicinity of the circle $|\omega| = 1$, the observables have special features similar to those described just above. It is clear from Fig. 2 that the trajectories in which we are interested are close to the physical region.

The actual position of the bifurcation region can be determined only from an experiment. In this study, we propose measuring the polarization parameter P in the interval of c.m. scattering angles where the PWA predict the minimum of the differential cross section. The procedure for planning a relevant experiment consists in determining the regions of kinematical variables where there are significant distinctions between the PWA predictions for the polarization value. Figure 3 shows the differences of the PWA predictions for the parameter P for π^+-meson energies in the range $T_\pi = 600$–800 MeV (the respective momentum range is $p_\pi \sim 725$–930 MeV/c) for the whole angular range of the pion scattering. It is clear from the figure that the differences are maximal at angles $\theta_{\text{c.m.}}$ close to 180°. The cross section has a minimum in the region $\theta_{\text{c.m.}} > 160°$ (for example, at a momentum of $p_\pi \sim 800$ MeV/c—see Fig. 4*a*). The optimum momentum for a polarization measurement corresponds to the maximum differences of the predictions of all PWA. We would like to emphasize yet another point, which directly follows from the difference in the position of the bifurcation region. The KH80 analysis [2] predicts a maximum in the polarization parameter P, $P_{\max} \approx 0.95$, at a scattering angle of $\theta_{\text{c.m.}} \approx 172°$ (Fig. 4*b*); as the scattering angle increases further, the polarization tends fast to zero. All other analyses predict a smoother angular dependence of the polarization. Figure 4*b* also displays the experimental results from [9], which were obtained for angles smaller than $\theta_{\text{c.m.}} \approx 160°$. The results are only in satisfactory agreement with the PWA predictions, the discrepancy between the measured values and the predictions of all PWA increasing with the angle.

There are other kinematical regions of elastic $\pi^+ p$ interaction where a similar situation is possible. Let

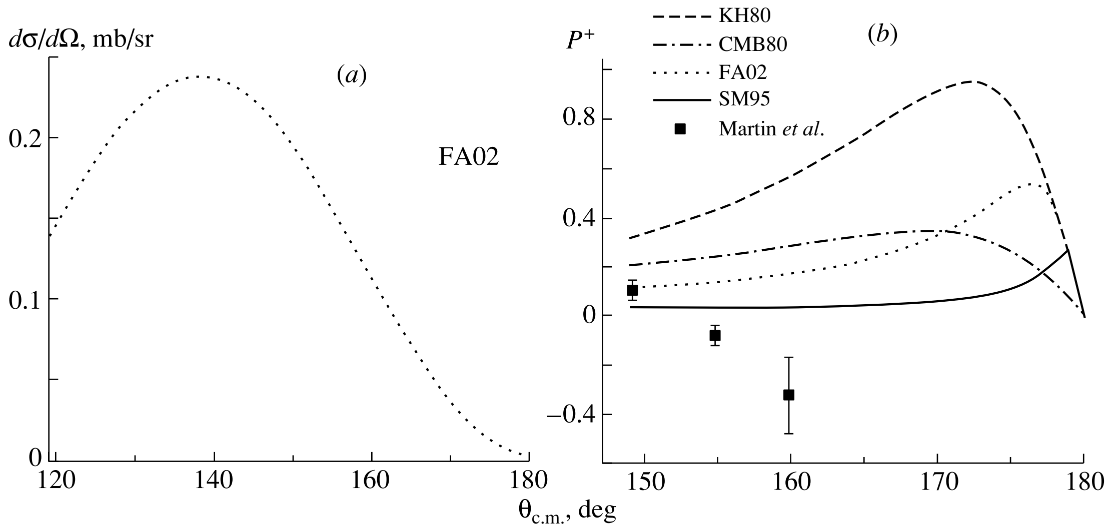

Fig. 4. Predictions of PWA for the observables at the pion momentum of $p_\pi = 800$ MeV/c: (a) differential cross section in the angular interval $\theta_{\rm c.m.} = 120°{-}180°$ (FA02 [4]); (b) polarization P in the angular interval $\theta_{\rm c.m.} = 150°{-}180°$ (KH80 [2], CMB80 [3], FA02 [4], and SM95 [6]), closed boxes representing the experimental data [9] at a pion momentum of 803 MeV/c.

us consider the region of higher momenta, where the trajectories of zeros according to the predictions of the PWA SM95 and FA02 intersect the unit circle outward. We see from Fig. 2 that this intersection occurs at momenta that differ by more than 100 MeV/c. For example, point 7, which corresponds to the momentum value of $p_\pi = 1860$ MeV/c, lies on different sides of the physical region in the two analyses being considered. This means that, in the momentum interval $p_\pi \sim 1790{-}1930$ MeV/c, the trajectory has an instability that leads to the difference in the predictions of the two analyses. Figure 5 shows the difference of the predictions of the PWA FA02 and SM95 for the polarization P in the energy interval $T_\pi = 1600{-}1800$ MeV (the respective momentum interval is $p_\pi \sim 1740{-}1940$ MeV/c) over the whole region of pion-scattering angles, $\theta_{\rm c.m.} = 0°{-}180°$. This region of kinematical variables is also interesting for studying the position of the bifurcation region for the trajectory of zeros.

4. EXPERIMENTAL FACILITY

The experiment in question consists in measuring the asymmetry of protons in elastic pion scattering on polarized target protons. The proton polarization vector in the target is normal to the scattering plane. It is necessary to collect the same statistics for positive and negative polarizations. The SPIN-P facility (Fig. 6), which includes a polarized target, tracking detectors, and scintillation counters, is placed in the pion channel of the ITEP synchrotron, which makes it possible to extract beams of charged particles (protons and π mesons) in the momentum interval 800–2100 MeV/c. An extracted π^+ beam also contains a proton contamination. The particles are separated by the time of flight between the first and the second

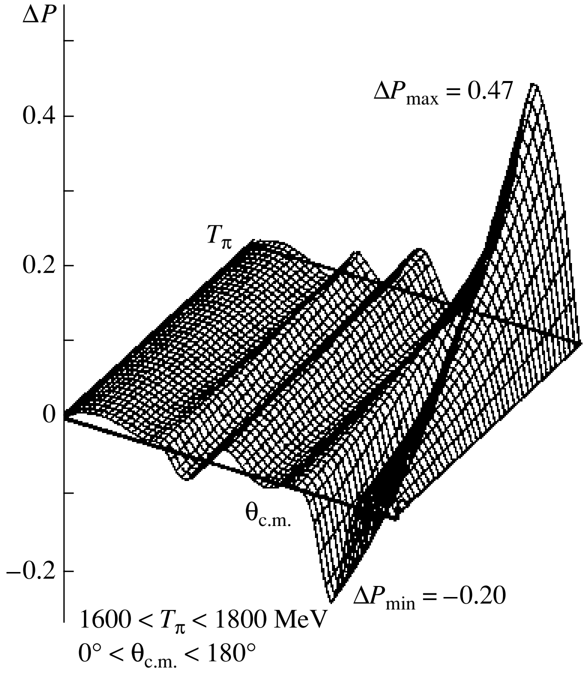

Fig. 5. Difference of the predictions of the PWA FA02 and SM95 for the polarization parameter P in the possible region of bifurcation of the trajectory of zeros in the pion energy interval $T_\pi = 1600{-}1800$ MeV.

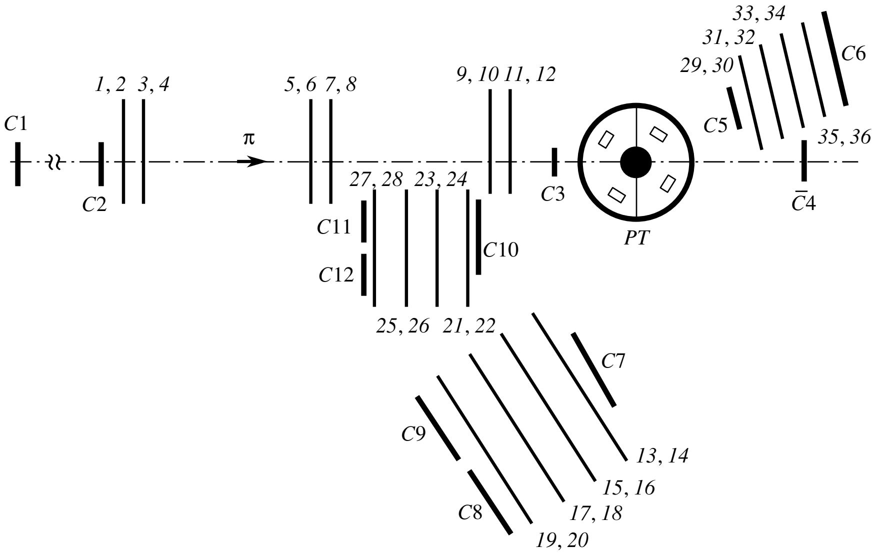

Fig. 6. Layout of the SPIN-P facility: (PT) polarized proton target in a superconductor solenoid, the proton spin being oriented vertically; (*1–36*) two-coordinate track detectors; and ($C1$–$C12$) scintillation counters.

channel focus over a base of ~20 m (counters $C1$ and $C2$ in Fig. 6).

The experiment employs a polarized proton target (PT), the polarization vector of free protons being oriented vertically in a target material. The target material is a compound of pentavalent chromium (Cr^V) in propanediol ($C_3O_2H_8$). The container, which is a cylinder 30 mm high whose base is 30 mm in diameter, is placed in the magnetic field generated by a pair of superconductor Helmholtz coils. The magnetic-field strength is 2.5 T, its relative nonuniformity in the container volume being less than 4×10^{-4}. The target is cooled to a temperature 0.5 K by evacuating ^{3}He in the cryostat. The degree of target polarization is 70–75%; it is permanently measured during the experiment to a precision of ±2%. The polarization is reversed approximately once every 24 hours.

Events are reconstructed with the aid of magnetostriction-data-readout two-coordinate (x and y) spark wire chambers. Three chamber assemblies (the counter sets *1–4*, *5–8*, and *9–12* in Fig. 6) are used to determine incident-pion tracks. Two assemblies each containing four chambers (counters *13–20* and *21–28*) determine the tracks of scattered pions. This makes it possible to cover the pion-scattering angle interval $\theta_{\mathrm{c.m.}} \sim 150^\circ$–$173^\circ$. Recoil protons are detected by an assembly of chambers (counters *29–36*) positioned in such a way as to detect protons kinematically related to scattered pions. The triggering pulse that initiates data readout from all chambers is formed by the coincidence of pulses from the scintillation counters ($C1$–$C12$); that is, the presence of signals from the incident pion and from one of two assemblies for the scattered pion and the recoil proton is required for trigger formation. The monitoring of the setup efficiency control and the primary discrimination of events during the experiment are performed in the on-line mode. The on-line code package ensures the readout of information and its accumulation in the buffer memory and subsequent transmission to a computer that writes it on the disk and further to an archiving facility. Information about the degree of target polarization comes from the computer that controls the operation of the target.

5. CONCLUSIONS

An unambiguous reconstruction of the amplitude for πN scattering requires measuring the polarization parameter P in kinematical regions where there are no such data at the present time. The method of zeros of the transverse amplitudes makes it possible to plan an experiment as to minimize the accelerator-operation time necessary for resolving the existing discrete ambiguities in PWA. The main conclusions of the present analysis are the following:

(i) The actual position of the region where the trajectory of zeros intersects the physical region (bifurcation region) can be determined only from experiments. This method for resolving discrete ambiguities in PWA will be implemented for the first time.

(ii) The nearest task is to measure the polarization parameter P in the region where, according to the predictions of the PWA SM95, the trajectory of zeros undergoes bifurcations—that is, for momenta of about 800 MeV/c and c.m. angles in excess of 160°.

The measured parameter P would specify the PWA that provides a correct prediction.

(iii) Similar measurements are required in all critical regions where the data in question are absent or have a low accuracy.

(iv) Presently, the setup of the PNPI–ITEP Collaboration is the only facility in the world where such measurements can be performed.

ACKNOWLEDGMENTS

We are grateful to our colleagues from the G. Washington University who provided the possibility of employing the SAID code.

This work was supported by the Russian Foundation for Basic Research (project no. 04-02-16335-a).

REFERENCES

1. I. G. Alekseev, P. E. Budkovsky, V. P. Kanavets, *et al.*, Yad. Fiz. **65**, 244 (2002) [Phys. At. Nucl. **65**, 220 (2002)].
2. G. Höhler, *Pion–Nucleon Scattering* (Springer-Verlag, Berlin, 1980), p. 405.
3. R. E. Cutkosky, R. E. Hendrick, J. W. Alcock, *et al.*, Phys. Rev. D **20**, 2804 (1979).
4. R. A. Arndt, W. J. Briscoe, I. I. Strakovsky, and R. L. Workman, Phys. Rev. C **69**, 035213 (2004).
5. R. A. Arndt, Z. Li, D. Roper, *et al.*, Phys. Rev. D **43**, 2131 (1991).
6. R. A. Arndt, I. I. Strakovsky, and R. L. Workman, Phys. Rev. C **52**, 2120 (1995).
7. E. Barellet, Nuovo Cimento A **8**, 331 (1972).
8. D. N. Svirida, Candidate's Dissertation in Mathematics and Physics (Moscow, 1998).
9. J. E. Martin, J. C. Sleeman, R. M. Brown, *et al.*, Nucl. Phys. B **89**, 253 (1975).

Translated by M. Kobrinsky

Physics of Atomic Nuclei, Vol. 68, No. 3, 2005, pp. 404–413. From Yadernaya Fizika, Vol. 68, No. 3, 2005, pp. 433–442.
Original English Text Copyright © 2005 by Tokarev, Dedovich.

Verification of z Scaling at RHIC and Tevatron[*]

M. V. Tokarev[**] **and T. G. Dedovich**

Joint Institute for Nuclear Research, Dubna, Moscow oblast, 141980 Russia

Received May 24, 2004

Abstract—The concept of z scaling reflecting the general features of high-p_T particle production is reviewed. Properties of data z presentation are discussed. New data on high-p_T particle spectra obtained at the RHIC and Tevatron are analyzed in the framework of z presentation. It was shown that these experimental data confirm z scaling. The change in the anomalous fractal dimensions of colliding objects ("δ jump") is considered as a signature of new physics. The kinematic ranges preferable for searching for z-scaling violation are established. *© 2005 Pleiades Publishing, Inc.*

1. INTRODUCTION

The primary goal of all new accelerators is to discover new physics phenomena. They can give an impulse to development of physics theory and extend our understanding of the micro and macro worlds. Some puzzles of nature are particle structure at small scales; distributions of mass, charge, and spin in spacetime; features of particle-to-particle transitions; and others. Therefore, the search for scaling regularities in high-energy particle collisions is a subject of intense investigations [1–10].

Properties of particle formation are believed to reveal themselves more clearly at high energy $\sqrt{s}$ and transverse momenta. It is considered also that partons produced in hard scattering retain information about primary collisions during hadronization. It is known that the mechanism of particle formation is modified by the nuclear medium and can be sensitive to the phase transition of nuclear matter. Therefore, the features of high-p_T single inclusive particle spectra of hadron–hadron and hadron–nucleus collisions are of interest in searching for new physics phenomena in elementary processes (quark compositeness, fractal spacetime, extra dimensions), signatures of exotic states of nuclear matter (phase transitions, quark–gluon plasma), and complementary restrictions on the theory (nonperturbative QCD effects, physics beyond the Standard Model).

The universal phenomenological description (z scaling) of high-p_T particle production cross sections in inclusive reactions is developed in [11, 12]. The approach is based on properties of particle structure, their constituent interaction, and particle formation such as locality, self-similarity, and fractality. The scaling function ψ and scaling variable z are expressed via experimental quantities such as the inclusive cross section $Ed^3\sigma/dp^3$ and the multiplicity density of charged particles $dN/d\eta$. Data z presentation is found to reveal symmetry properties (energy and angular independence, A and F dependence, power law of $\psi(z)$). The properties of ψ at high z are assumed to be relevant to the structure of spacetime at small scales [13–15]. The function $\psi(z)$ is interpreted as the probability density to produce a particle with a formation length z.

In this report, we present the results of analysis of new data on high-p_T particle spectra obtained at the RHIC and Tevatron. The results in the framework of z presentation are compared with other ones based on the data obtained at lower collision energy $\sqrt{s}$ at the U70, ISR, and Tevatron (Run I). The obtained results are shown to confirm z scaling. The possibility of searching for the scaling violation at the RHIC, Tevatron, and LHC is discussed.

2. z SCALING

In the section underlying ideas of z scaling, a general scheme of data z presentation and the physical meaning of the scaling function $\psi(z)$ and the scaling variable z are discussed.

2.1. Basic Principles: Locality, Self-Similarity, Fractality

The idea of z scaling is based on the assumptions [6] that the gross feature of inclusive particle distribution of the process

$$M_1 + M_2 \to m_1 + X \qquad (1)$$

---

[*] This article was submitted by the authors in English.

[**] e-mail: `tokarev@sunhe.jinr.ru`

at high energies can be described in terms of the corresponding kinematic characteristics of the constituent subprocess written in the symbolic form

$$(x_1M_1) + (x_2M_2) \to m_1 + (x_1M_1 + x_2M_2 + m_2) \tag{2}$$

satisfying the condition

$$(x_1P_1 + x_2P_2 - p)^2 = (x_1M_1 + x_2M_2 + m_2)^2. \tag{3}$$

The equation is the expression of locality of hadron interaction at the constituent level. The x_1 and x_2 are the fractions of the incoming momenta P_1 and P_2 of the colliding objects with the masses M_1 and M_2. They determine the minimum energy that is necessary for production of the secondary particle with the mass m_1 and the four-momentum p. The parameter m_2 is introduced to satisfy the internal conservation laws (for baryon number, isospin, strangeness, and so on).

Equation (3) reflects minimum-recoil-mass hypothesis in the elementary subprocess. To connect kinematic and structural characteristics of the interaction, the quantity Ω is introduced. It is chosen in the form

$$\Omega(x_1, x_2) = m(1-x_1)^{\delta_1}(1-x_2)^{\delta_2}, \tag{4}$$

where m is a mass constant and δ_1 and δ_2 are factors relating to the anomalous fractal dimensions of the colliding objects. The fractions x_1 and x_2 are determined to maximize the value of $\Omega(x_1, x_2)$, simultaneously fulfilling the condition (3):

$$\left.\frac{d\Omega(x_1, x_2)}{dx_1}\right|_{x_2 = x_2(x_1)} = 0. \tag{5}$$

The fractions x_1 and x_2 are equal to unity along the phase-space limit and cover the full phase space accessible at any collision energy.

Self-similarity is a scale-invariant property connected with dropping of certain dimensional quantities out of the physical picture of the interactions. It means that dimensionless quantities for the description of physical processes are used. The scaling function $\psi(z)$ depends in a self-similar manner on the single dimensionless variable z. It is expressed via the invariant cross section $Ed^3\sigma/dp^3$ as follows:

$$\psi(z) = -\frac{\pi s}{(dN/d\eta)\sigma_{\text{in}}} J^{-1} E\frac{d^3\sigma}{dp^3}. \tag{6}$$

Here, s is the center-of-mass collision energy squared, σ_{in} is the inelastic cross section, and J is the corresponding Jacobian. The factor J is a known function of the kinematic variables, the momenta and masses of the colliding and produced particles.

The function $\psi(z)$ is normalized as follows:

$$\int\limits_0^\infty \psi(z)dz = 1. \tag{7}$$

This relation allows us to interpret the function $\psi(z)$ as a probability density to produce a particle with the corresponding value of the variable z.

The principle of fractality states that variables used in the description of the process diverge in terms of the resolution. This property is characteristic for the scaling variable

$$z = z_0\Omega^{-1}, \tag{8}$$

where

$$z_0 = \sqrt{\hat{s}_\perp}/(dN/d\eta). \tag{9}$$

The variable z has the character of a fractal measure. For the given production process (1), its finite part z_0 is the ratio of the transverse energy released in the binary collision of constituents (2) and the average multiplicity density $dN/d\eta|_{\eta=0}$. The divergent part Ω^{-1} describes the resolution at which the collision of the constituents can be singled out of this process. The quantity $\Omega(x_1, x_2)$ represents the relative number of all initial configurations containing the constituents that carry fractions x_1 and x_2 of the incoming momenta. δ_1 and δ_2 are the anomalous fractal dimensions of the colliding objects (hadrons or nuclei). The momentum fractions x_1 and x_2 are determined in a way to minimize the resolution $\Omega^{-1}(x_1, x_2)$ of the fractal measure z with respect to all possible subprocesses (2) subjected to the condition (3). The variable z was interpreted as a particle formation length.

The scaling function of high-p_T particle production, as shown below, is described by the power law $\psi(z) \sim z^{-\beta}$. Both quantities, ψ and z, are scale dependent. Therefore, we consider the high-energy hadron—hadron interactions as interactions of fractals. In the asymptotic region, the internal structure of particles, the interactions of their constituents, and the mechanism of real particle formation manifest self-similarity over a wide-scale range.

2.2. Properties of Data z Presentation

In this section we, recall properties of data z presentation for particle (hadrons, direct photons, jets) production at high p_T. These properties are the energy and angular independence and the power law of the scaling function $\psi(z)$. Other properties, A and F dependence of z scaling, were discussed elsewhere [11].

The energy independence of data z presentation means that the scaling function $\psi(z)$ has the same shape for different $\sqrt{s}$ over a wide p_T range.

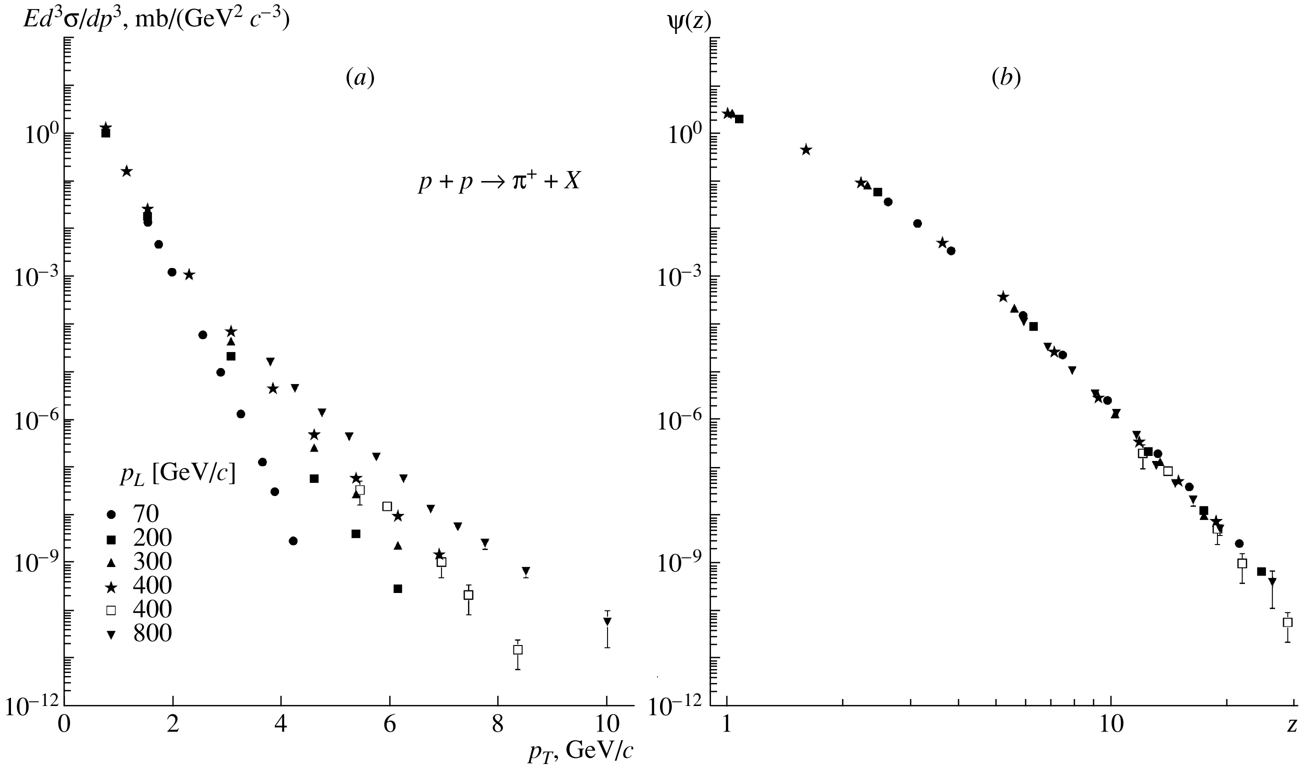

Fig. 1. (a) The inclusive cross section of π^+ mesons produced in pp collisions at $p_L = 70, 200, 300, 400$, and 800 GeV/c and $\theta_{\rm c.m.} \simeq 90°$ as a function of the transverse momentum. Experimental data are taken from [16–18]. (b) The corresponding scaling function $\psi(z)$.

Figure 1a shows the dependence of the cross section of the π^+ mesons produced in pp collisions on transverse momentum p_T at the incident proton momentum p_L = 70, 200, 300, 400, and 800 GeV/c and the angle $\theta_{\rm c.m.} \simeq 90°$. The data [16–18] cover a wide transverse-momentum range, $p_T = 1$–10 GeV/c. The figure demonstrates the typical power high-p_T particle spectra characterized by strong dependence on collision energy. Figure 1b shows z presentation of the same data sets revealing the energy independence of the scaling function $\psi(z)$ over a wide energy and transverse-momentum range at $\theta_{\rm c.m.} \simeq 90°$.

The other property of data z presentation, the angular independence, means that the scaling function $\psi(z)$ has the same shape for different values of angle θ of a produced particle over a wide p_T range. Figure 2 illustrates p_T and z presentations of data [19] of π^0-meson production in pp collisions at $\sqrt{s} = 53$ GeV and the angular range $\theta_{\rm c.m.} = 5°$–$90°$.

It was established [11] that the scaling function $\psi(z)$ for different species of produced particles (hadrons, direct photons, and jets) at high z reveals the power behavior $\psi(z) \sim z^{-\beta}$. The slope parameter β was found to be independent of collision energy over a wide p_T range. The existence of the power law, $\psi(z) \sim z^{-\beta}$, is considered as an indication that the mechanism of particle formation reveals self-similar and fractal properties.

3. z SCALING AT RHIC

In this section, we analyze new data obtained by the STAR and PHENIX Collaborations at the RHIC in pp collisions at $\sqrt{s} = 200$ GeV and compare them with our previous results. The comparison is a new test of z scaling.

The high-p_T spectra of charged particles produced in pp and AuAu collisions at energy $\sqrt{s} = 200$ GeV within $|\eta| < 0.5$ were measured by the STAR Collaboration [20]. The results are presented in Fig. 3a. The p_T distribution of charged hadrons produced in AuAu collisions were measured at different centralities. The shape of the cross section drastically changes as centrality increases. The spectrum for pp collisions is similar to the spectrum observed in peripheral AuAu collisions. The STAR data [20] for pp collisions correspond to the nonsingle diffraction cross section. Other experimental data correspond to the inelastic cross section. Therefore, in the analysis, the multiplicity particle density $dN/d\eta$ for nonsingle diffraction interaction for STAR data was used. The RHIC

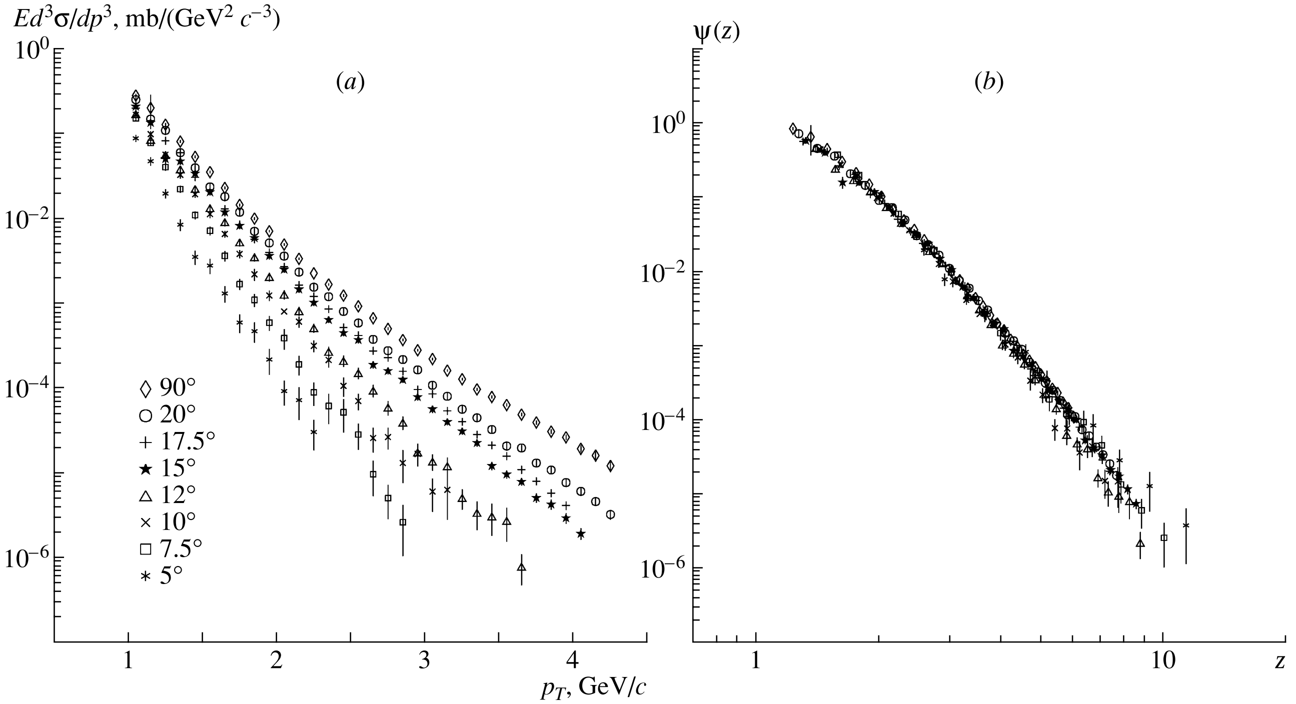

Fig. 2. (a) The inclusive cross section of π^0 mesons produced in pp collisions at $\sqrt{s} = 53$ GeV and $\theta_{\text{c.m.}} = 5°-90°$ as a function of the transverse momentum. Experimental data are taken from [19]. (b) The corresponding scaling function $\psi(z)$.

data and other data for pp collisions obtained at the U70 [16], Tevatron [17, 18], and ISR [21] are shown in Fig. 3b. The charged-hadron spectra were measured over a wide kinematic range $\sqrt{s} = 11.5-200$ GeV and $p_T = 0.5-9.5$ GeV/c. The strong energy dependence and the power behavior of the particle p_T spectrum are found to be clear. The energy independence of data z presentation shown in Fig. 3c is confirmed. It is of interest to verify the asymptotic behavior of ψ at $\sqrt{s} = 200$ GeV and reach values of z up to 30 or more.

New data on p_T spectra of neutral strange particles (K^0_S, Λ, $\bar{\Lambda}$) produced in pp collisions at $\sqrt{s} = 200$ GeV are presented by STAR in [22]. We compare the data for K^0_S-meson cross sections with data for K^+ mesons obtained at the U70 [16], Tevatron [17, 18], and ISR [21] at lower energies 11.5, 19.4, 23.8, 27.4, 38.8, and 53 GeV. The data p_T and z presentations are shown in Figs. 4a and 4b. As seen from Fig. 4a, the energy dependence of the cross section is enhanced with p_T. The difference between values of the cross section at $\sqrt{s} = 11.5$ and 200 GeV at the momentum $p_T = 4$ GeV/c is about four orders of magnitude. The shape of the scaling function for K^0_S mesons coincides with a similar one for K^+ mesons in the range $z = 0.2-3.0$. It means that mechanism of neutral and charged strange K-meson formation reveals the property of self-similarity. A similar feature is observed for neutral and charged π-meson production [11].

New data on the inclusive cross section of π^+ mesons produced in pp collisions at $\sqrt{s} = 200$ GeV in the central rapidity range are presented by the PHENIX Collaboration in [23]. The transverse momentum of pions is measured up to 2.2 GeV/c. Data p_T and z presentation are shown in Fig. 5. They are compared with data obtained at the U70 [16], Tevatron [17, 18], and ISR [21] at lower energies 11.5, 19.4, 23.8, 27.4, 38.8, and 53 GeV. As seen from Fig. 5b, the scaling function corresponding to data [23] is in agreement with our results obtained previously [11]. We would like to note that, to perform a more detailed comparison with available results for behavior of the scaling function $\psi(z)$ for π^+ mesons in the asymptotic region, the transverse momentum $p_T \simeq 15$ GeV/c corresponding to $z = 20$ at $\sqrt{s} = 200$ GeV should be reached.

New data on η-meson spectra in pp collisions at $\sqrt{s} = 200$ GeV in the range $p_T = 1.2-8.5$ GeV/c are presented by the PHENIX Collaboration in [24]. The η/π^0 ratio is found to be 0.54 ± 0.05 in the range $p_T = 3.5-9$ GeV/c. This value is in agreement with existing data. We compare the data with other data obtained at $\sqrt{s} = 30$, 31.6, 38.8, 53, and 63 GeV [25, 26]. Data p_T and z presentations are shown in Fig. 6. As seen from Fig. 6b, the results of our new analysis

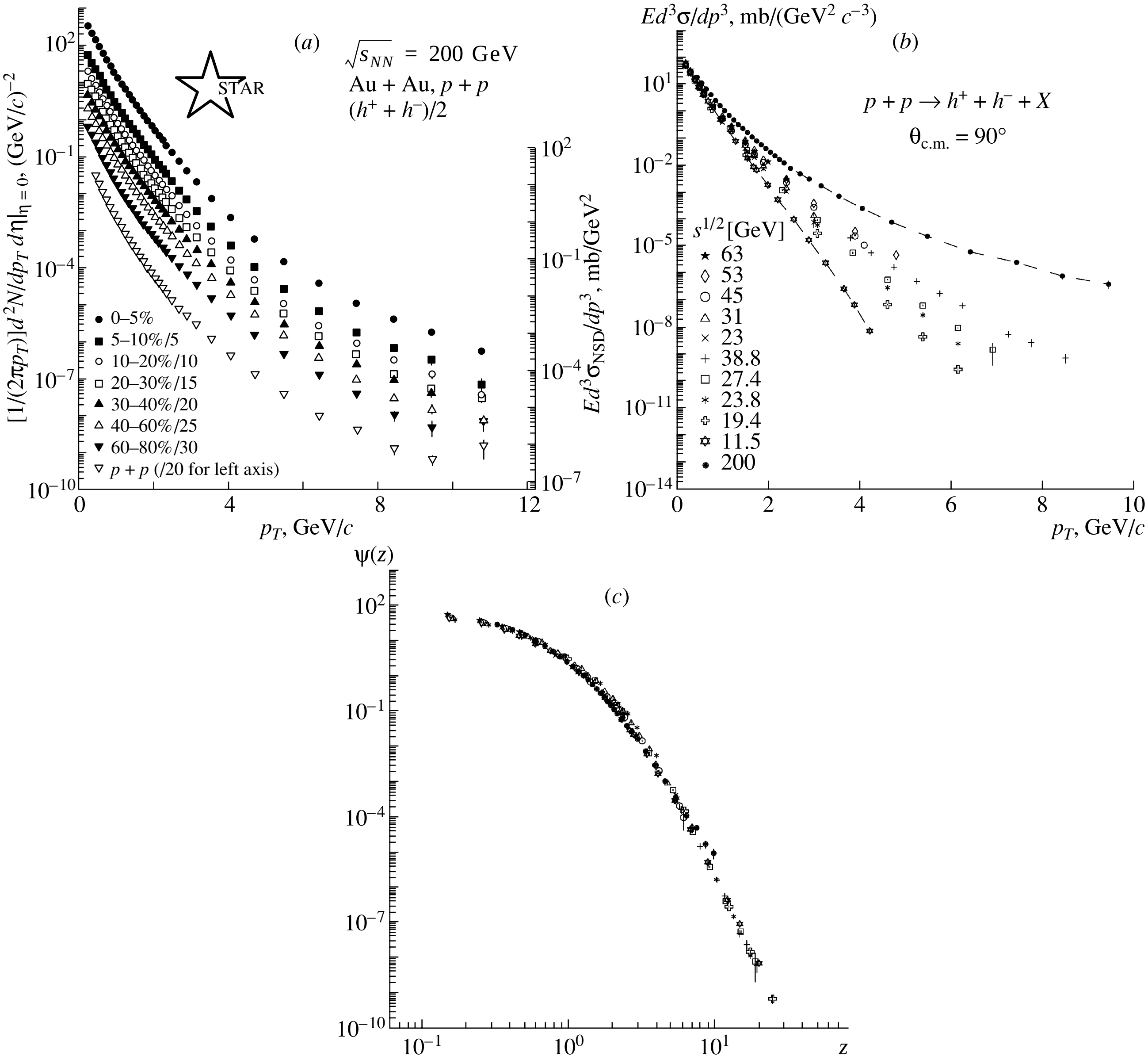

Fig. 3. (a) The inclusive cross section of charged hadrons produced in AuAu and pp collisions at $\sqrt{s} = 200$ GeV and $\theta_{\mathrm{c.m.}} \simeq 90°$ as a function of the transverse momentum. Experimental data are taken from [20]. Data (b) p_T and (c) z presentation of experimental data taken from [16–18, 21] and [20].

confirm the energy independence of the scaling function for η-meson production in pp collisions over a wide $\sqrt{s}$ and p_T range. Note that the new result on the η/π^0 ratio indicates flavor independence of a scaling function at high z.

4. z SCALING AT TEVATRON

In this section, we analyze new data on the inclusive cross section of jet production in $\bar{p}p$ collisions at $\sqrt{s} = 1960$ GeV obtained by the D0 and CDF Collaborations at the Tevatron in Run II and compare them with our previous results [11].

The production of hadron jets at the Tevatron probes the highest momentum-transfer region currently accessible and thus potentially sensitive to a wide variety of new physics. The information on the inclusive jet cross section in the high-transverse-momentum range is the basis to test QCD, in particular, to extract the strong coupling constant $\alpha_s(Q^2)$ and the parton distribution functions and to constrain uncertainties for the gluon distribution in the high-x range. In Run II, as mentioned in [27], the measurement of jet production and the sensitivity to new physics will profit from the large integrated luminosity

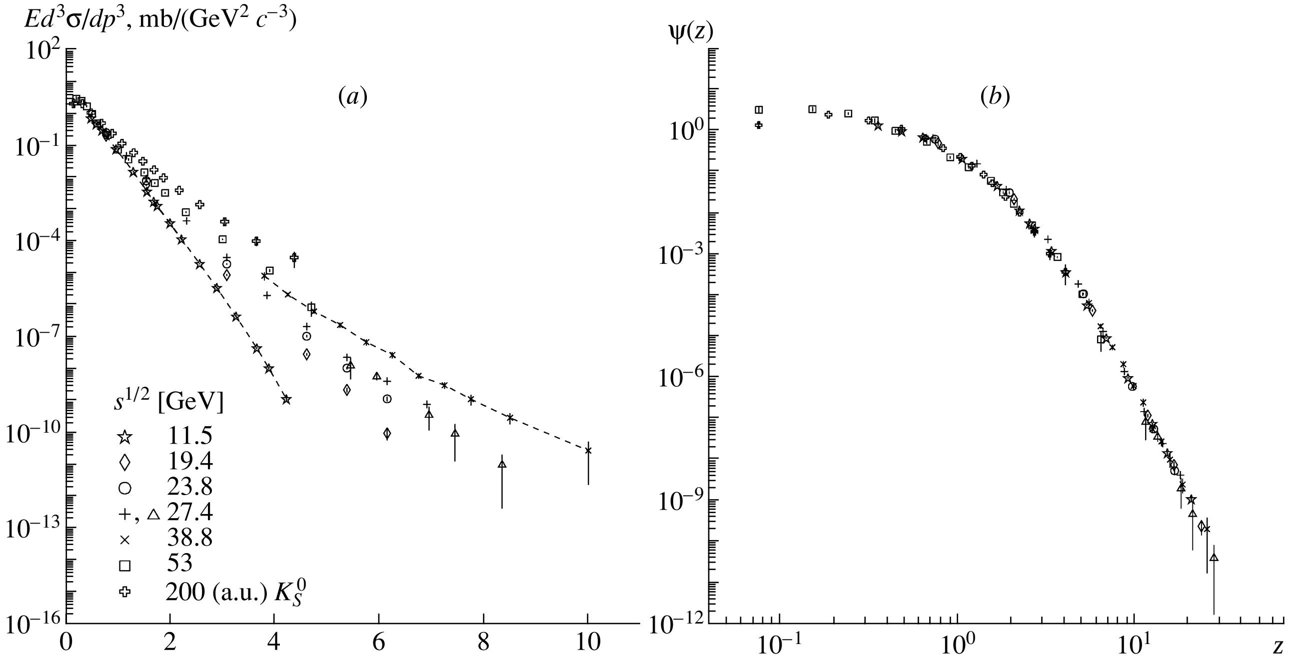

Fig. 4. (*a*) The inclusive cross section of K^+ and K_S^0 mesons produced in pp collisions in the central rapidity range as a function of the transverse momentum at $\sqrt{s} = 11.5$, 19.4, 23.8, 27.4, 38.8, 53, and 200 GeV, respectively. Experimental data are taken from [16–18, 21] and [22]. (*b*) The corresponding scaling function $\psi(z)$.

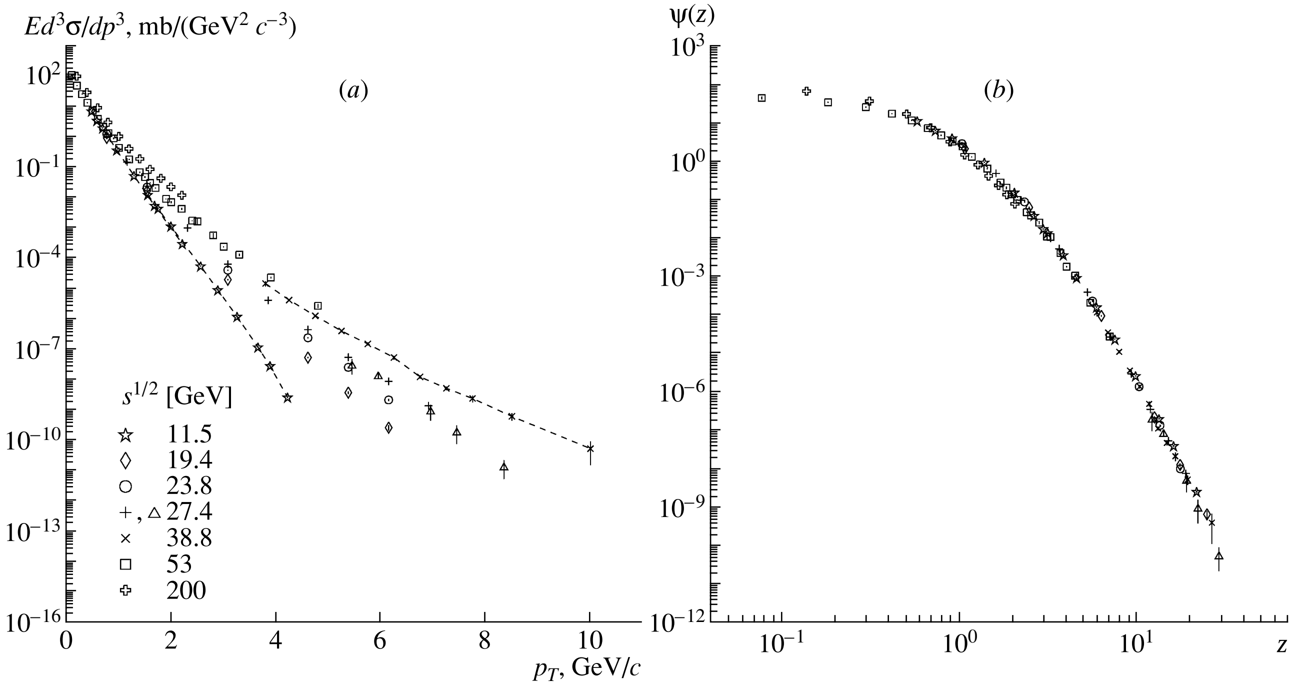

Fig. 5. (*a*) The inclusive cross section for the π^+ mesons produced in pp collisions in the central rapidity range as a function of the transverse momentum at $\sqrt{s} = 11.5$, 19.4, 23.8, 27.4, 38.8, 53, and 200 GeV. Experimental data are taken from [16–18, 21] and [23]. (*b*) The corresponding scaling function $\psi(z)$.

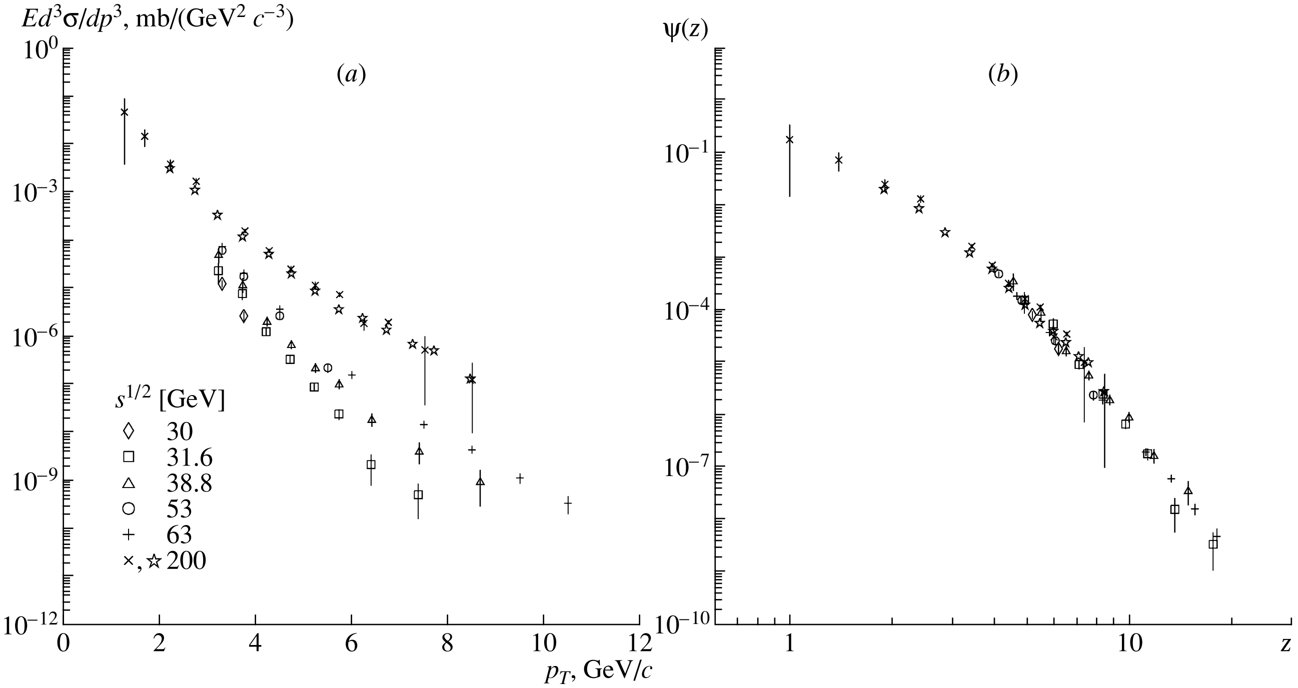

Fig. 6. (*a*) The inclusive cross section of η mesons produced in pp collisions in the central rapidity range as a function of the transverse momentum at $\sqrt{s} = 30$, 31.6, 38.8, 53, 63, and 200 GeV. Experimental data are taken from [25, 26] and [24]. (*b*) The corresponding scaling function $\psi(z)$.

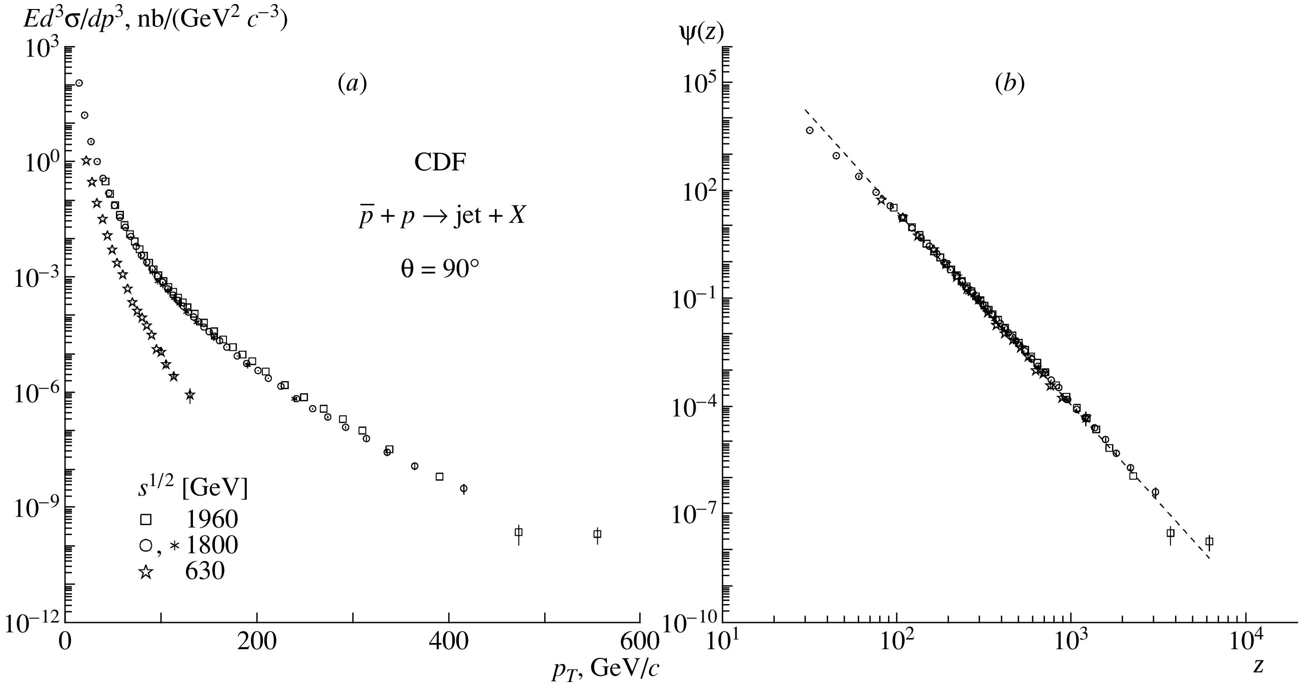

Fig. 7. (*a*) The inclusive cross section of one jets produced in $\bar{p}p$ collisions at $\sqrt{s} = 630$, 1800, 1960 GeV and $0.1 < |\eta| < 0.7$ as a function of the transverse momentum. Experimental data obtained by the CDF Collaboration are taken from [29] and [28]. (*b*) The corresponding scaling function $\psi(z)$. The dashed line is obtained by fitting the function taken in the form $\psi(z) = az^{-\beta}$.

and the higher cross section, which is associated with the increase in the center-of-mass energy from 1800 to 1960 GeV. Therefore, the test of z scaling for jet production in $\bar{p}p$ collisions in a new kinematic range is of great interest to verify scaling features established in our previous analysis [11].

The first Run II results of the inclusive one-jet cross section at $\sqrt{s} = 1960$ GeV in the central pseudorapidity region ($0.1 < |\eta| < 0.7$) are presented by the CDF Collaboration in [28]. We use the data in the present analysis. The dependence of the one-jet cross section on the transverse momentum of jet in $\bar{p}p$ collisions at $\sqrt{s} = 630$, 1800, and 1960 GeV is shown in Fig. 7*a*. The data [28, 29] cover the momentum range $p_T = 10{-}560$ GeV/c. The energy dependence of the jet cross section is observed to be strong from $\sqrt{s} =$ 630 to 1800 GeV and weak from 1800 to 1960 GeV. Data z presentation is shown in Fig. 7*b*. As seen from Fig. 7*b*, new data [28] are in agreement with other data obtained in Run I. The energy independence of $\psi(z)$ is observed up to $z \simeq 4000$. The asymptotic behavior of the scaling function is described by the power law $\psi(z) \sim z^{-\beta}$ (the dashed line in Fig. 7*b*). The slope parameter β is energy independent over a wide p_T range.

New data on inclusive cross sections of jet production in $\bar{p}p$ collisions obtained by the D0 Collaboration at the Tevatron in Run II are presented in [30]. The spectrum of jet production is measured at $\sqrt{s} = 1960$ GeV in the pseudorapidity and transverse-momentum ranges $|\eta| < 0.5$ and $p_T =$ 60–560 GeV/c, respectively. Data p_T and z presentations are shown in Fig. 8. Note that results of the present analysis of new D0 data are in good agreement with our results [11] based on the data [31] obtained by the same collaboration in Run I. The energy independence and the power law (the dashed line in Fig. 8*b*) of the scaling function $\psi(z)$ are found as well.

5. SEARCH FOR z-SCALING VIOLATION

A lot of experimental data used in analysis of z scaling confirm its general properties. Therefore, it is of interest to verify z scaling in the regions accessible at the RHIC, Tevatron, and future collider LHC. Note that the search for the scaling violation is possible at the U70 accelerator as well. The inclusive cross sections of charged hadrons ($\pi^{\pm}, K^{\pm}, p^{\pm}$) were measured at the accelerator up to $z = 20$ with high accuracy [16].

The scaling function $\psi(z)$ demonstrates the universality over a wide kinematic range for different species of produced particles. The scaling function reveals two modes of particle formation observed at higher energies. The first one reveals exponential behavior at low z and the second one is described by the power law $\psi(z) \sim z^{-\beta}$ at high z. The last property of data z presentation provides us arguments to believe that fractal properties of particles possess a general character. The properties at small scales have relevance to the fractal structure of spacetime [13–15]. The geometrical carrier of the physical properties of particles such as mass, charge, and spin is supposed to be fractal. It is characterized by anomalous fractal dimensions, hidden extra dimensions, and other topological irregularities. One can assume that a theory claiming to describe physics at small scales should account for this structure. The asymptotic behavior of the scaling function is described by the slope parameter β, which depends on the anomalous fractal dimension δ of colliding objects. We assume that new physics effects at small scales should be characterized by a change in the fractal dimension ("δ jump") and, consequently, another value of the slope parameter β at high z. To determine the kinematic range that is more preferable for experimental search for z-scaling violation, the $z - p_T$ plot can be used. Figure 9*a* shows the $z{-}p_T$ plot, the dependence of the variable z on the transverse momentum p_T of π^+ mesons produced in pp collisions at $\sqrt{s} = 24{-}14\,000$ GeV and $\theta_{\text{c.m.}} = 90°$. One can see from Fig. 9*a* that the value of the scaling function $\psi(z)$ at $z = 20$ can be reached at different values of the transverse momentum p_T corresponding to different values of collision energy $\sqrt{s}$. The corresponding values of the transverse momentum p_T at RHIC energies 200 and 500 GeV are equal to 16 and 24 GeV/c, respectively. The energy independence of $\psi(z)$ can be used to estimate particle yields at high p_T. Figure 9*b* demonstrates π^+-meson spectra at ISR, RHIC, and LHC energies.

6. CONCLUSIONS

New experimental data on inclusive cross section for high-p_T hadron and jet production in proton–proton and proton–antiproton collisions obtained at RHIC energy $\sqrt{s} = 200$ GeV and Tevatron energy $\sqrt{s} = 1960$ GeV were analyzed in the framework of z presentation.

In the presentation, the scaling function $\psi(z)$ and scaling variable z are expressed via the experimental quantities, the invariant inclusive cross section $Ed^3\sigma/dp^3$ and the multiplicity density of charged particles $\rho(s, \eta)$. The physical interpretation of the scaling function ψ as a probability density to produce a particle with the formation length z is argued. The quantity z has the property of fractal measure, and δ is the fractal dimension describing the intrinsic structure of the interacting constituents revealed at high energies.

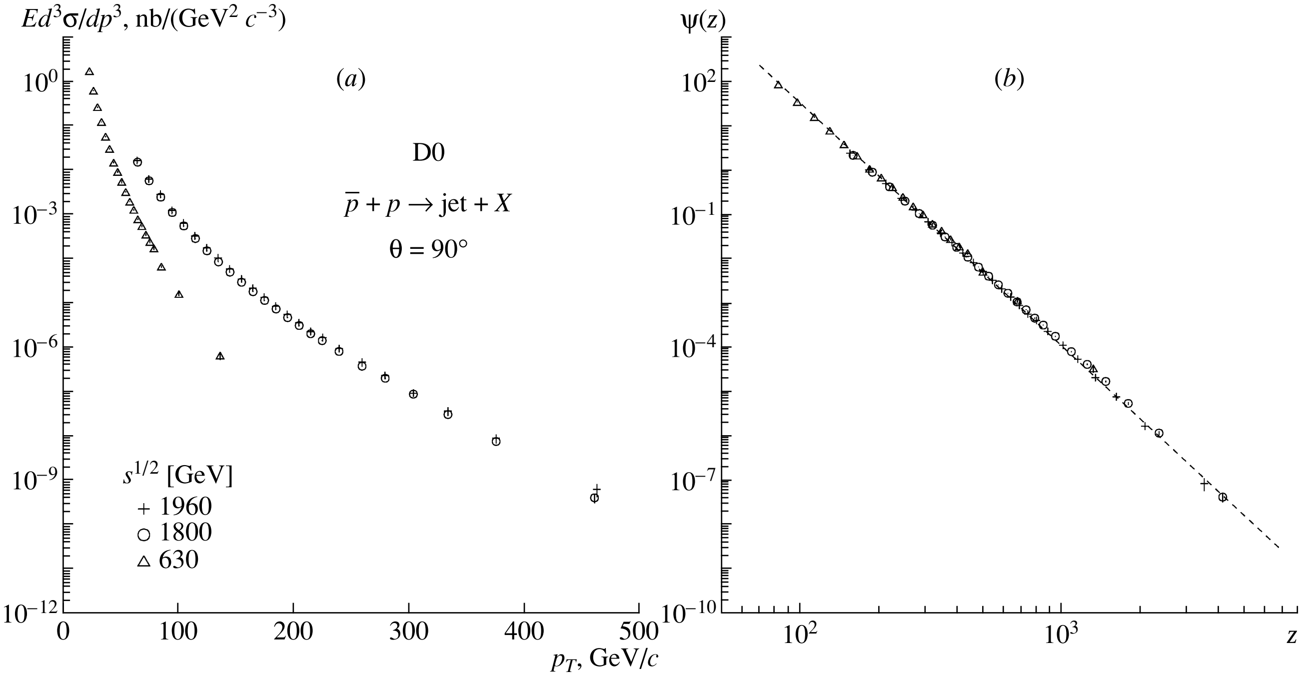

Fig. 8. (*a*) The inclusive cross section of one jets produced in $\bar{p}p$ collisions at $\sqrt{s} = 630$, 1800, and 1960 GeV in the central pseudorapidity range $|\eta| < 0.5$ as a function of the transverse momentum. Experimental data obtained by the D0 Collaboration are taken from [31] and [30]. (*b*) The corresponding scaling function $\psi(z)$. The dashed line is obtained by fitting the function taken in the form $\psi(z) = az^{-\beta}$.

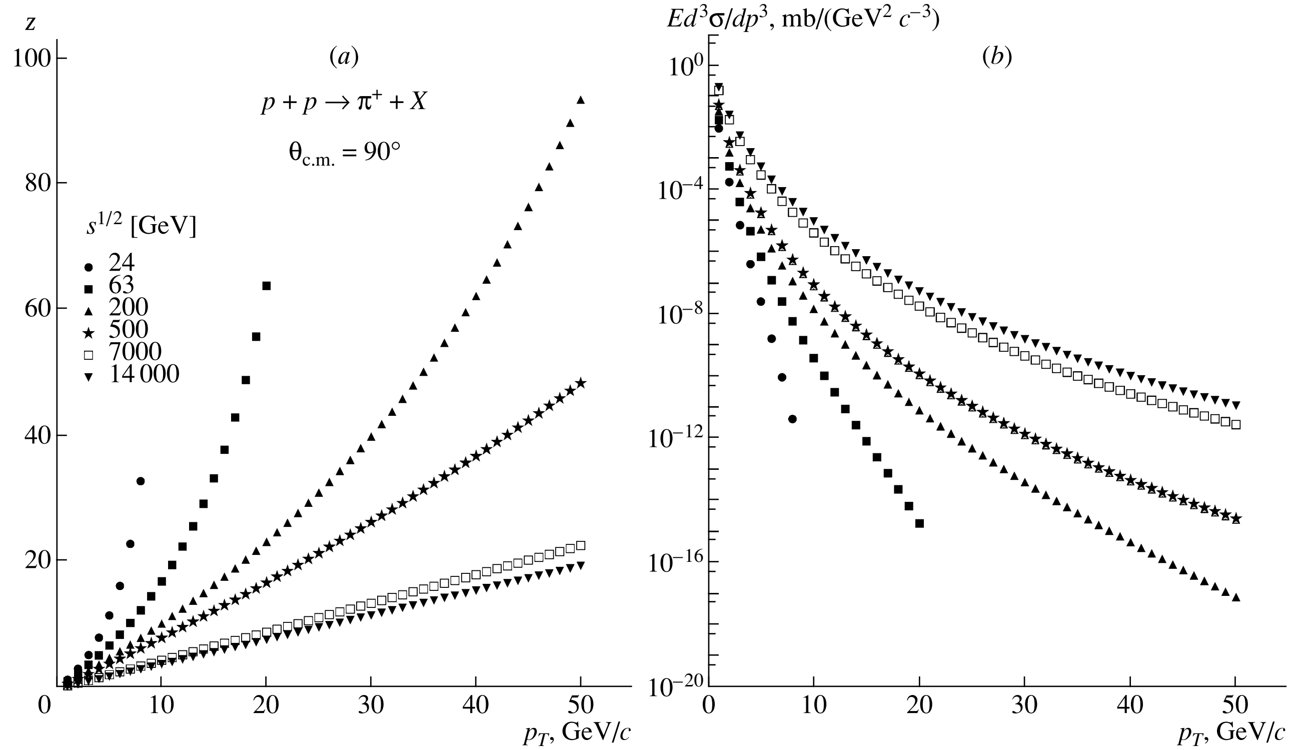

Fig. 9. (*a*) The dependence of *z* on the transverse momentum p_T and (*b*) the spectra of π^+ mesons produced in *pp* collisions at $\sqrt{s} = 24$–14 000 GeV and $\theta_{c.m.} = 90°$.

New RHIC and Tevatron data included in present analysis were shown to confirm the general properties of z scaling, such as the energy independence of the scaling function $\psi(z)$ and the power law $\psi(z) \sim z^{-\beta}$.

The change in the fractal dimension, "δ jump," is suggested for consideration as an indication of new physics phenomena. The kinematic regions preferable to search for z-scaling violation are established. High-p_T π^+-meson yields at RHIC and LHC energies are estimated.

Thus, the results of our analysis confirm the concept of z scaling and the possibility of its applicability to analysis of experimental high-p_T data and search for new physics phenomena at the RHIC, Tevatron, and LHC.

ACKNOWLEDGMENTS

We thank I. Zborovský, O. Rogachevski, and D. Toivonen for collaboration and many useful and stimulating discussions of the problem.

REFERENCES

1. R. P. Feynman, Phys. Rev. Lett. **23**, 1415 (1969).
2. J. D. Bjorken, Phys. Rev. **179**, 1547 (1969); J. D. Bjorken and E. A. Paschanos, Phys. Rev. **185**, 1975 (1969).
3. P. Bosted *et al.*, Phys. Rev. Lett. **49**, 1380 (1982).
4. J. Benecke *et al.*, Phys. Rev. **188**, 2159 (1969).
5. A. M. Baldin, Fiz. Élem. Chastits At. Yadra **8**, 429 (1977) [Sov. J. Part. Nucl. **8**, 175 (1977)].
6. V. S. Stavinsky, Fiz. Élem. Chastits At. Yadra **10**, 949 (1979) [Sov. J. Part. Nucl. **10**, 373 (1979)].
7. G. A. Leksin, Report No. ITEF-147 (1976); in *Proceedings of the XVIII International Conference on High Energy Physics, Tbilisi, Georgia, 1976*, Ed. by N. N. Bogolubov *et al.*, JINR Report No. D1, 2-10400 (1977), p. A6-3.
8. Z. Koba, H. B. Nielsen, and P. Olesen, Nucl. Phys. B **40**, 317 (1972).
9. V. A. Matveev, R. M. Muradyan, and A. N. Tavkhelidze, Sov. J. Part. Nucl. **2**, 7 (1971); Lett. Nuovo Cimento **5**, 907 (1972); **7**, 719 (1973).
10. S. Brodsky and G. Farrar, Phys. Rev. Lett. **31**, 1153 (1973); Phys. Rev. D **11**, 1309 (1975).
11. I. Zborovský, Yu. A. Panebratsev, M. V. Tokarev, and G. P. Škoro, Phys. Rev. D **54**, 5548 (1996); I. Zborovský, M. V. Tokarev, Yu. A. Panebratsev, and G. P. Škoro, Phys. Rev. C **59**, 2227 (1999); M. V. Tokarev and T. G. Dedovich, Int. J. Mod. Phys. A **15**, 3495 (2000); M. V. Tokarev, O. V. Rogachevski, and T. G. Dedovich, J. Phys. G **26**, 1671 (2000); Preprint No. E2-2000-90 (JINR, Dubna, 2000); M. V. Tokarev, Yu. A. Panebratsev, I. Zborovský, and G. P. Škoro, Int. J. Mod. Phys. A **16**, 1281 (2001); M. Tokarev, hep-ph/0111202; M. Tokarev and D. Toivonen, hep-ph/0209069; G. P. Škoro, M. V. Tokarev, Yu. A. Panebratsev, and I. Zborovský, hep-ph/0209071; M. V. Tokarev, G. L. Efimov, and D. E. Toivonen, Phys. At. Nucl. **67**, 564 (2004).
12. M. V. Tokarev, Preprint No. E2-98-92 (JINR, Dubna, 1998); Preprint No. E2-98-161 (JINR, Dubna, 1998); M. V. Tokarev and E. V. Potrebenikova, Comput. Phys. Commun. **117**, 229 (1999); M. Tokarev and G. Efimov, hep-ph/0209013.
13. L. Nottale, *Fractal Space-Time and Microphysics* (World Sci., Singapore, 1993).
14. B. Mandelbrot, *The Fractal Geometry of Nature* (Freeman, San Francisco, 1982).
15. I. Zborovský, hep-ph/0311306.
16. V. V. Abramov *et al.*, Yad. Fiz. **41**, 357 (1985) [Sov. J. Nucl. Phys. **41**, 227 (1985)].
17. J. W. Cronin *et al.*, Phys. Rev. D **11**, 3105 (1975); D. Antreasyan *et al.*, Phys. Rev. D **19**, 764 (1979).
18. D. Jaffe *et al.*, Phys. Rev. D **40**, 2777 (1989).
19. D. Lloyd Owen *et al.*, Phys. Rev. Lett. **45**, 89 (1980).
20. STAR Collab. (J. Adams *et al.*), Phys. Rev. Lett. **91**, 172302 (2003).
21. B. Alper *et al.*, Nucl. Phys. B **87**, 19 (1975).
22. STAR Collab. (J. Adams, M. Heinz, *et al.*), in *Proceedings of the Quark Matter 2004, Oakland, California, USA*; http://qm2004.lbl.gov/
23. PHENIX Collab. (M. Harvey *et al.*), in *Proceedings of the Quark Matter 2004, Oakland, California, USA*; http://qm2004.lbl.gov/
24. PHENIX Collab. (H. Hiejima *et al.*), in *Proceedings of the Quark Matter 2004, Oakland, California, USA*; http://qm2004.lbl.gov/
25. C. Kourkoumelis *et al.*, Phys. Lett. B **84B**, 277 (1979).
26. G. Alverson *et al.*, Phys. Rev. D **48**, 5 (1993); L. Apanasevich *et al.*, Phys. Rev. Lett. **81**, 2642 (1998); hep-ex/9711017; M. Begel *et al.*, in *Workshop "High-p_T Phenomena at RHIC", BNL, Nov. 1–2, 2001*.
27. CDF Collab. (M. Tönnesmann *et al.*), hep-ex/0310055.
28. CDF Collab. (A. Meyer *et al.*), Mod. Phys. Lett. A **18**, 1643 (2003).
29. CDF Collab. (F. Abe *et al.*), Phys. Rev. Lett. **62**, 613 (1989); **68**, 1104 (1992); **70**, 1376 (1993); **74**, 3538 (1995); **77**, 438 (1996); **80**, 3461 (1998).
30. D0 Collab. (M. Begel *et al.*), hep-ex/0305072.
31. D0 Collab. (B. Abbott *et al.*), Phys. Rev. D **64**, 032003 (2001).

Physics of Atomic Nuclei, Vol. 68, No. 3, 2005, pp. 414–419. Translated from Yadernaya Fizika, Vol. 68, No. 3, 2005, pp. 443–448.
Original Russian Text Copyright © 2005 by Barabash.

Investigation of Double-Beta-Decay Processes at the NEMO-3 Tracking Detector

A. S. Barabash[*]
The NEMO Collaboration

Institute of Theoretical and Experimental Physics,
Bol'shaya Cheremushkinskaya ul. 25, Moscow, 117259 Russia

Received May 24, 2004

Abstract—In order to investigate double-beta-decay processes with a sensitivity of up to about 10^{25} yr, the NEMO Collaboration created the NEMO-3 tracking detector consisting of Geiger counters for reconstructing tracks and plastic scintillators for measuring energy. A brief description of the NEMO-3 detector is given, and its main features are presented. The first preliminary results for ^{100}Mo, ^{82}Se, ^{116}Cd, and ^{150}Nd are quoted. © *2005 Pleiades Publishing, Inc.*

1. INTRODUCTION

Interest in neutrinoless double-beta decay has been quickened significantly in recent years by the fact that, from an analysis of the results obtained for atmospheric [1] and solar neutrinos [2–6], it was deduced that there exist neutrino oscillations (see, for example, the relevant discussion in [7–9]). This conclusion was recently confirmed in the KamLAND experiment with reactor antineutrinos [10] and in new measurements with the SNO detector [11]. This means that the neutrino has a mass. However, experiments studying neutrino oscillations are not sensitive to the nature of the neutrino mass (a Dirac versus a Majorana mass) and furnish no information about the absolute scale of the neutrino masses (since such experiments measure the quantity Δm^2). The detection and investigation of $2\beta(0\nu)$ decay may clarify the following problems of neutrino physics (see the relevant discussion in [12–14]):

(i) the nature of the neutrino mass (a Dirac versus a Majorana mass),

(ii) the absolute scale of the neutrino mass (measurement of m_1 or a limit on it),

(iii) the type of hierarchy (normal, inverse, or quasidegenerate one),

(iv) CP violation in the lepton sector (measurement of the Majorana CP-odd phase).

2. NEMO-3 EXPERIMENT

The main objective of the NEMO-3 experiment is to seek the $2\beta(0\nu)$ decay of various isotopes (^{100}Mo, ^{82}Se, etc.) with a sensitivity as high as about 10^{25} yr, which corresponds to a sensitivity to the effective mass of the Majorana neutrino at a level of 0.1 to 0.3 eV [15]. The planned sensitivity to decay involving Majoron emission is about 10^{23} yr (the sensitivity to the neutrino–Majoron coupling constant $\langle g_{ee}\rangle$ is about 10^{-5}). In addition, one of the tasks consists in studying, at a high level of precision, the $2\beta(2\nu)$ decay of a broad range of nuclei (such as ^{100}Mo, ^{82}Se, ^{116}Cd, ^{150}Nd, ^{130}Te, ^{96}Zr, and ^{48}Ca) and concurrently exploring all features of double-beta-decay processes.

The NEMO-3 experiment is a tracking experiment where, in contrast to experiments with ^{76}Ge [16, 17], one detects not only the total energy deposition but also the remaining parameters of the process, including the energy of individual electrons, their divergence angle, and the coordinate of an event in the source plane. Since June 2002, the NEMO-3 detector has operated at the Frejus underground laboratory (France) located at a depth of 4800 mwe.

Description of the NEMO-3 Detector

The NEMO-3 detector has a cylindrical structure and consists of 20 identical sectors (see Fig. 1). A thin (about 30–60 mg/cm^2) source containing 2β-decaying nuclei and having a total area of 20 m^2 and a weight of up to ~10 kg is placed at the detector center. Some of the sources (Cd and about one-third of Mo) are metallic foils, while the others

---

[*] E-mail: `Alexander.Barabash@itep.ru`

are foils manufactured from powders of corresponding isotopes according to special technologies. The list of isotopes that are being studied at the present time is given in Table 1. With the aim of determining the external background, part of the sources were manufactured from ultrapure natural materials (767 g of TeO_2 and 621 g of Cu). The level of radioactive admixtures in the sources was determined in dedicated measurements with low-background HPGe detectors.

The basic principles of detection of useful events in the NEMO-3 detector are as follows: the energy of the electrons is measured by plastic scintillators (1940 individual counters), while the tracks are reconstructed on the basis of information obtained in the planes of Geiger cells (6180 cells) surrounding the source on both sides. The tracking volume of the detector is filled with a mixture of composition 95% He + 4% spirit + 1% Ar at normal pressure. In addition, a magnetic field of strength about 30 G parallel to the detector axis is created in the sensitive volume by a solenoid surrounding the detector. The magnetic field is used to identify e^+e^- pairs and, hence, to suppress this source of background.

The main parameters of the detector are as follows: the energy resolution of the scintillation counters lies in the interval 14–17% (FWHM) for electrons of energy 1 MeV; the time resolution is 250 ps for an electron energy of 1 MeV; and the accuracy in reconstructing the vertex of $2e$ events is about 1 cm.

The main features of the detector are determined in dedicated calibration measurements. The energy calibration is performed with the aid of ^{207}Bi (by using conversion electrons of energy 0.482 and 976 MeV) and ^{90}Sr (the endpoint of the β spectrum is 2.283 MeV). The accuracy in reconstructing the vertex of a $2e$ event is determined in measurements with ^{207}Bi, while the time properties are found in measurements with ^{60}Co (two photons are emitted simultaneously) and ^{207}Bi (two electrons are emitted simultaneously).

The detector is surrounded by a passive shield consisting of 20 cm of steel and 35 cm of water (paraffin and wood are used instead of water above and below the detector). The level of radioactive admixtures in structural materials of the detector and in the passive shield was tested in measurements with low-background HPGe detectors.

From June to December 2002, a large number of calibrations and test measurements were performed, along with the first accumulation of data for studying double-beta decay. Since February 14, 2003, the detector has operated in the mode of continuous data acquisition. The calibrations with radioactive sources are performed at regular intervals of approximately 1.5 months.

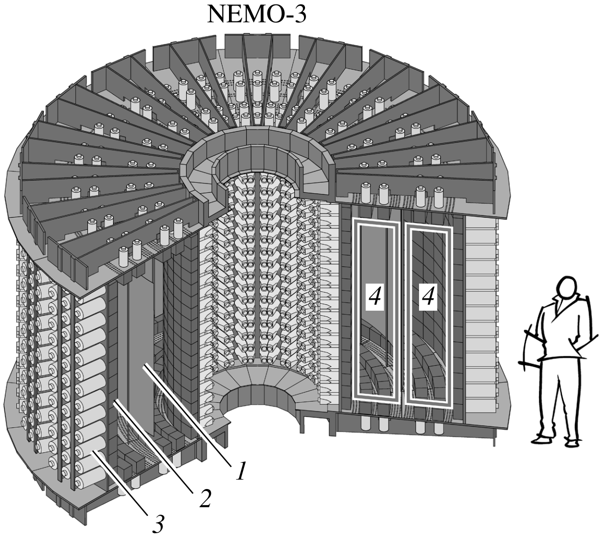

Fig. 1. Layout of the NEMO-3 detector: (*1*) source, (*2*) counters based on plastic scintillators, (*3*) low-background photomultiplier tubes, and (*4*) tracking volume (6180 Geiger cells).

A detailed description of the detector and its properties is given elsewhere [18].

3. EXPERIMENTAL RESULTS

This article reports on the first preliminary results obtained for ^{100}Mo, ^{82}Se, ^{116}Cd, and ^{150}Nd upon processing part of available data (3843 h of measurements). Data from 2919 h of measurements were processed in studying the double-beta decay of ^{100}Mo to an excited 0^+ state of ^{100}Ru.

3.1. Double-Beta Decay of ^{100}Mo

Events featuring two electrons were selected as $2e$ events of double-beta decay if these two electrons issued from a common vertex in the source. In seeking

Table 1. Isotopes studied at the NEMO-3 detector

Isotope	Enrichment, %	Isotope mass, g
^{100}Mo	95.14–98.95	6914
^{82}Se	96.82–97.02	932
^{116}Cd	93.2	405
^{130}Te	89.4	454
^{150}Nd	90.97	36.6
^{96}Zr	57.3	9.4
^{48}Ca	73.17	7.0

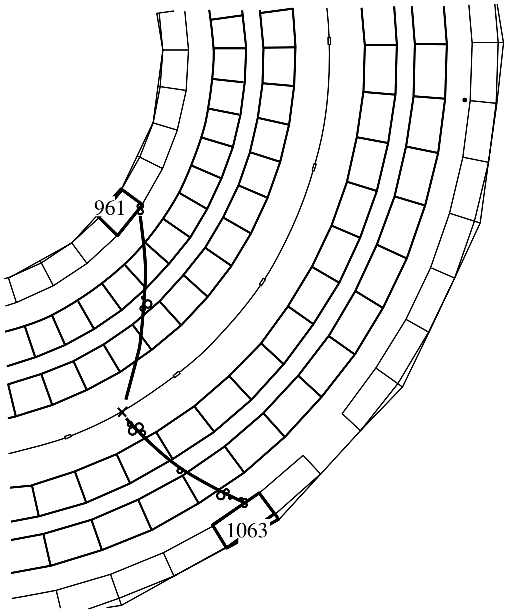

Fig. 2. Example of a $2e$ event. The total energy of the electrons was 2.024 MeV, and the energies of the individual electrons in the pair were 961 and 1063 keV.

$2e$ events, an electron was defined as a track that connected the source surface with a scintillation counter, the energy deposited in the counter being required to exceed 200 keV. The curvature of a track must correspond to a particle having a negative charge. Time-of-flight criteria must confirm that two electrons are emitted simultaneously from a common point in the source being considered. In order to suppress the background from ^{214}Bi, whose decay is accompanied by the appearance of delayed alpha particles from ^{214}Po decay, it is necessary that delayed actuations of Geiger counters (700 μ) in the vicinity of the vertex be absent. A typical $2e$ event is shown in Fig. 2.

Figure 3 displays the spectrum of $2\beta(2\nu)$ events in ^{100}Mo. The total number of useful events (upon background subtraction) was 75 535 at a signal-to-background ratio of 40/1. In the energy region $E_{2e} >$ 1 MeV, this ratio was 100; that is, the background was negligible. The detection efficiency for useful events was calculated by the Monte Carlo method. This was done for two different assumptions on the form of the single-electron spectrum. In the first case, use was made of a standard form of the spectrum (HSD mechanism—see [19]), while, in the second case, the spectrum was taken in the form obtained in [19] for the SSD mechanism, where the decay process proceeds through the ground (1^+) state of ^{100}Tc [20]. The efficiency was 5.3 and 4.8% in the first and the second case, respectively. As a result, the following half-life

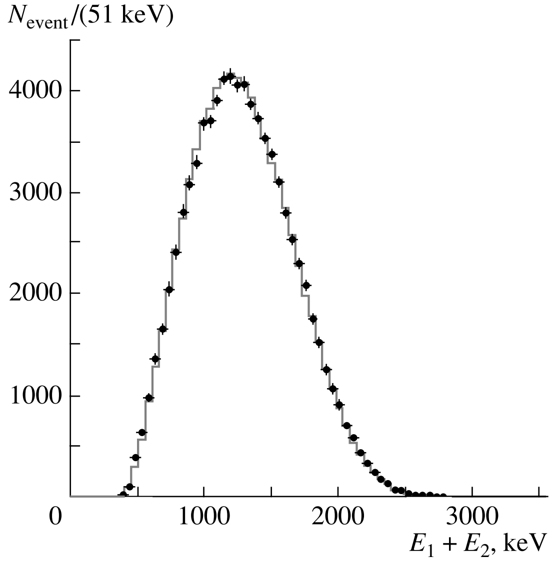

Fig. 3. Spectrum of $2\beta(2\nu)$ events in ^{100}Mo.

values were obtained:

$$T_{1/2} = [7.3 \pm 0.03\ (\text{stat.}) \pm 0.7\ (\text{syst.})] \times 10^{18}\ \text{yr}\ (\text{SSD mechanism}), \quad (1)$$

$$T_{1/2} = [8.2 \pm 0.03\ (\text{stat.}) \pm 0.8\ (\text{syst.})] \times 10^{18}\ \text{yr}\ (\text{HSD mechanism}). \quad (2)$$

A preliminary analysis of the spectrum of single electrons revealed that the SSD mechanism is in better agreement with experimental data. However, this issue requires a further thorough study, and definitive conclusions will be drawn later. Nevertheless, both values agree with the world-average value of $(8 \pm 0.7) \times 10^{18}$ yr [21, 22].

The same experiment involved seeking events peculiar to the $2\beta(2\nu)$ decay of ^{100}Mo to the 0^+ excited state of ^{100}Ru at 1130.29 keV. This search was performed by selecting $2e$ events accompanied by two photons, their energies being 540 and 590 keV. Data obtained over 2919 h of measurements were analyzed. Information from sectors not containing molybdenum was used to estimate the background. As a result, it was found that there is an excess of events in sources containing ^{100}Mo. Upon background subtraction, the effect amounted to 22.4 ± 5.6 events, which corresponds to the ^{100}Mo half-life of $T_{1/2} = 8.8^{+2.9}_{-1.7} \times 10^{20}$ yr with respect to decay to the 0^+ excited state of the daughter nucleus, this result not including the systematic error, which is about 20% in the case being considered. Within the errors, the above half-life value is compatible with the results of earlier experiments [23–25] (the world-average value is $(6.8 \pm 1.2) \times 10^{20}$ yr [26]).

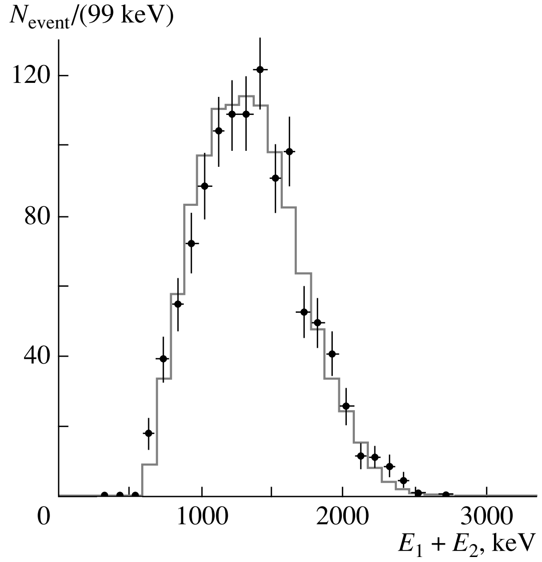

Fig. 4. Spectrum of $2\beta(2\nu)$ events in ^{82}Se.

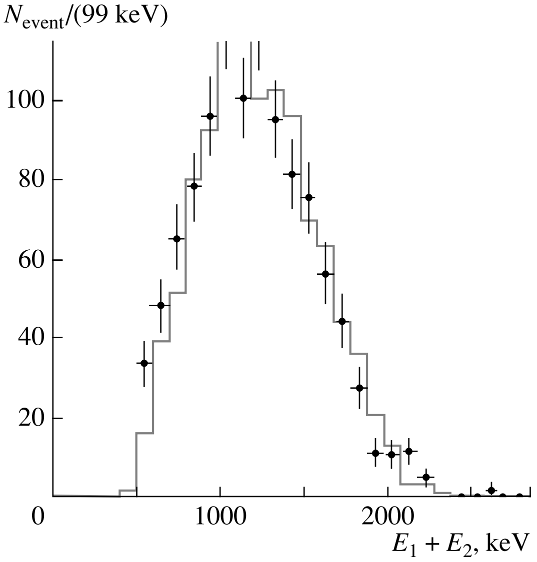

Fig. 5. Spectrum of $2\beta(2\nu)$ events in ^{116}Cd.

$0\nu\chi^0$ decay. The energy range 2.4–3.2 MeV was studied. The number of detected events was 218, while the expected contribution of $2\beta(2\nu)$ decay and of the background was 230. Taking into account the detection efficiency for useful events (2.3%), one obtains the following limit on ^{100}Mo 2β decay involving the emission of a standard Majoron: $T_{1/2} > 1.5 \times 10^{22}$ yr (at a 90% C.L.). This limit is more stringent than the best of the preceding ones ($T_{1/2} > 5.8 \times 10^{21}$ yr [27]). Employing the above limit and the values of the nuclear matrix elements from [28, 29], one can obtain a limit on the neutrino–Majoron coupling constant, $\langle g_{ee} \rangle < (0.5–0.9) \times 10^{-4}$. This result is among the best ones obtained thus far for $\langle g_{ee} \rangle$.

0ν decay. Events in the energy region above 2.75 MeV were investigated. The total number of events was 16, while the number of events where the energy was in excess of 2.8 MeV was 8, which is approximately coincident with the expected number of events (background + 2ν events). The detection efficiency was 11.5 and 9.8%, respectively. As a result, the following limit on ^{100}Mo 0ν decay was obtained: $T_{1/2} > 2.3 \times 10^{23}$ yr (at a 90% C.L.). This limit is more stringent than the best of the preceding results for ^{100}Mo ($T_{1/2} > 5.5 \times 10^{22}$ yr [30]). Employing the above limit and the values of the nuclear matrix elements from [28, 29], one can obtain a limit on the effective mass of the Majorana neutrino, $\langle m_\nu \rangle <$ 0.9–1.4 eV. This limit can be compared with the range of limits obtained in an experiment with ^{76}Ge [16, 31], $\langle m_\nu \rangle <$ 0.33–0.84 eV.

It is worth noting here that the use of information about the emission angles and energies of individual electrons in $2e$ events would make it possible to reduce the number of candidate events significantly and to improve thereby the sensitivity of the NEMO-3 experiment [32]. Such an analysis will be performed in the near future.

3.2. Double-Beta Decay of ^{82}Se

Figure 4 displays the spectrum of $2\beta(2\nu)$ events in ^{82}Se. In this case, the energy threshold for an individual electron was 300 keV. The total number of useful events (upon background subtraction) was 1100 at a signal-to-background ratio of 4/1. The detection efficiency for useful events was calculated by the Monte Carlo method (5.1%). As a result, the following half-life value was obtained:

$$T_{1/2} = [9.52 \pm 0.3\ (\mathrm{stat.}) \pm 0.9\ (\mathrm{syst.})] \times 10^{19}\ \mathrm{yr}. \tag{3}$$

Limits on $2\beta(0\nu)$ and $2\beta(0\nu\chi^0)$ decays were 1×10^{23} and 8×10^{21} yr, respectively; these are much more stringent than the results of previous experiments [33, 34]. Limits on $\langle m_\nu \rangle$ and $\langle g_{ee} \rangle$ were also calculated. The results are $\langle m_\nu \rangle <$ 1.7–3.7 eV and $\langle g_{ee} \rangle < (0.9–1.9) \times 10^{-4}$.

3.3. Double-Beta Decay of ^{116}Cd

Figure 5 shows the spectrum of $2\beta(2\nu)$ events in ^{116}Cd. In this case, the energy threshold for an individual electron was 300 keV. The total number

Table 2. Preliminary results for ^{100}Mo, ^{82}Se, ^{116}Cd and ^{150}Nd

Isotope	Time of measurements, h	Number of 2ν events	$T_{1/2}(2\nu)$, yr	$T_{1/2}(0\nu)$, yr (90%C.L.)	$T_{1/2}(0\nu\chi^0)$, yr (90% C.L.)
^{100}Mo	3834	75 535	$[7.3 \pm 0.03\ (\text{stat.}) \pm 0.7\ (\text{syst.})] \times 10^{18}$	$>2.3 \times 10^{23}$	$>1.5 \times 10^{22}$
$0^+-0^+_1$	2919	22.4	$8.8^{+2.9}_{-1.7} \times 10^{20}$		
^{82}Se	3834	1100	$[9.52 \pm 0.3\ (\text{stat.}) \pm 0.9\ (\text{syst.})] \times 10^{19}$	$>1 \times 10^{23}$	$>8 \times 10^{21}$
^{116}Cd	3834	810	$[3.1 \pm 0.2\ (\text{stat.}) \pm 0.3\ (\text{syst.})] \times 10^{19}$	$>1.6 \times 10^{22}$	$>1.7 \times 10^{21}$
^{150}Nd	3834	400	$[7.5 \pm 0.4\ (\text{stat.}) \pm 0.7\ (\text{syst.})] \times 10^{18}$	$>3.6 \times 10^{21}$	$>3.3 \times 10^{20}$

of useful events (upon background subtraction) was 810 at a signal-to-background ratio of 5.6/1. The detection efficiency for useful events was calculated by the Monte Carlo method (4%). As a result, the following half-life value was obtained:

$$T_{1/2} = [3.1 \pm 0.2\ (\text{stat.}) \pm 0.3\ (\text{syst.})] \times 10^{19}\ \text{yr}. \tag{4}$$

Limits on $2\beta(0\nu)$ and $2\beta(0\nu\chi^0)$ decays were 1.6×10^{22} and 1.7×10^{21} yr, respectively. At the present time, these are inferior to the best current limits [35], but we hope to improve our results in the future significantly.

3.4. Double-Beta Decay of ^{150}Nd

Figure 6 displays the spectrum of $2\beta(2\nu)$ events in ^{150}Nd. In this case, the energy threshold for an individual electron was 300 keV. The total number of useful events (upon background subtraction) was 400 at a signal-to-background ratio of 4/1. The detection efficiency for useful events was calculated by the Monte Carlo method (6.8%). As a result, the following half-life value was obtained:

$$T_{1/2} = [7.5 \pm 0.4\ (\text{stat.}) \pm 0.7\ (\text{syst.})] \times 10^{18}\ \text{yr}. \tag{5}$$

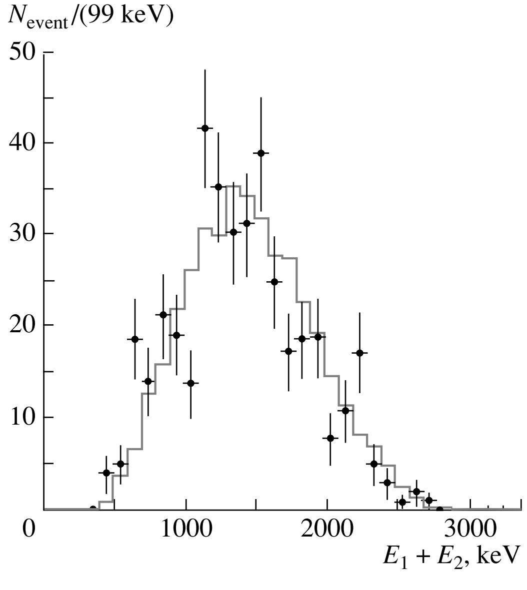

Fig. 6. Spectrum of $2\beta(2\nu)$ events in ^{150}Nd.

It is interesting to compare this value with the results obtained in two previous experiments. Specifically, the values of $T_{1/2} = [18.8^{+6.9}_{-3.9}$ (stat.) $\pm$ 1.9 (syst.)] $\times 10^{18}$ yr and $T_{1/2} = [6.75^{+0.37}_{-0.42}$ (stat.) $\pm$ 0.68 (syst.)] $\times 10^{18}$ yr were reported in [36] and [37], respectively. Thus, our result is in better agreement with the value from [37].

Limits on $2\beta(0\nu)$ and $2\beta(0\nu\chi^0)$ decays were 3.6×10^{21} and 3.3×10^{20} yr, respectively, which are more stringent than those in previous experiments [37, 38].

4. CONCLUSIONS

Thus, the NEMO-3 tracking detector has operated stably for more than a year in the mode of data acquisition. The first preliminary results have been obtained for ^{100}Mo, ^{82}Se, ^{116}Cd, and ^{150}Nd (see Table 2). It should be noted that the limits on the $2\beta(0\nu)$ and $2\beta(0\nu\chi^0)$ decays of ^{100}Mo, ^{82}Se, and ^{150}Nd are the best ones for these isotopes. As to the limits on $\langle m_\nu \rangle$ and $\langle g_{ee} \rangle$ from measurements with ^{100}Mo at NEMO-3, they are among the best ones in the world at the present time.

Work on improving the properties of the detector and the procedures for data processing and at reducing the level of background is still being continued. For example, it is planned to remove completely the background associated with the activity of ^{222}Rn in air around and within the passive shield.

New results for ^{100}Mo, ^{82}Se, ^{116}Cd, and ^{150}Nd and the first results for ^{96}Zr, ^{48}Ca, and ^{130}Te are expected in the near future.

ACKNOWLEDGMENTS

This work was supported in part by the INTAS foundation (project no. 03051-3431).

REFERENCES

1. H. Sobel *et al.*, Nucl. Phys. B (Proc. Suppl.) **91**, 127 (2001).
2. B. T. Cleveland *et al.*, Astrophys. J. **496**, 505 (1998).
3. S. Fukuda *et al.*, Phys. Rev. Lett. **86**, 5655 (2001); **86**, 5656 (2001).
4. V. N. Gavrin *et al.*, Nucl. Phys. B (Proc. Suppl.) **91**, 36 (2001).
5. M. Altman *et al.*, Phys. Lett. B **490**, 16 (2000).
6. Q. R. Ahmad *et al.*, Phys. Rev. Lett. **89**, 011301 (2002); **89**, 011302 (2002).
7. P. C. de Holanda and A.Yu. Smirnov, Phys. Rev. D **66**, 113005 (2002).
8. J. N. Bahcall *et al.*, J. High Energy Phys. **0207**, 054 (2002); hep-ph/0204314.
9. M. Maltoni *et al.*, Phys. Rev. D **67**, 013011 (2003); hep-ph/0207227.
10. K. Eguchi *et al.*, Phys. Rev. Lett. **90**, 021802 (2003).
11. S. N. Ahmed *et al.*, nucl-ex/0309004.
12. S. Pascoli and S. T. Petcov, Phys. Lett. B **544**, 239 (2002).
13. S. Pascoli, S. T. Petcov, and W. Rodejohann, Phys. Lett. B **558**, 141 (2003).
14. S. Pascoli and S. T. Petcov, Phys. Lett. B **580**, 280 (2004).
15. NEMO-3 Proposal, Preprint No. 94-29, LAL (Orsay, 1994).
16. H. V. Klapdor-Kleingrothaus *et al.*, Eur. Phys. J. A **12**, 147 (2001).
17. C. E. Aalseth *et al.*, Phys. Rev. D **65**, 092007 (2002).
18. R. Arnold *et al.*, Preprint No. 04-05, LAL (Orsay, 2004); physics/0402115.
19. F. Simkovic, P. Domin, and S. Semenov, J. Phys. G **27**, 2233 (2001).
20. J. Abad *et al.*, J. Phys. (France) **45**, 147 (1984); Ann. Fis. A **80**, 9 (1984).
21. V. D. Ashitkov *et al.*, Pis'ma Zh. Éksp. Teor. Fiz. **74**, 601 (2001) [JETP Lett. **74**, 529 (2001)].
22. A. S. Barabash, Czech. J. Phys. **52**, 567 (2002).
23. A. S. Barabash *et al.*, Phys. Lett. B **345**, 408 (1995).
24. A. S. Barabash *et al.*, Yad. Fiz. **62**, 2211 (1999) [Phys. At. Nucl. **62**, 2039 (1999)].
25. L. De Braeckeleer, M. Hornish, A. Barabash, *et al.*, Phys. Rev. Lett. **86**, 3510 (2001).
26. A. S. Barabash, Yad. Fiz. **66**, 486 (2003) [Phys. At. Nucl. **66**, 458 (2003)].
27. H. Ejiri *et al.*, Phys. Lett. B **531**, 190 (2002).
28. F. Simkovic *et al.*, Phys. Rev. C **60**, 055502 (1999).
29. S. Stoica and H. V. Klapdor-Kleingrothaus, Nucl. Phys. A **694**, 269 (2001).
30. H. Ejiri *et al.*, Phys. Rev. C **63**, 065501 (2001).
31. H. V. Klapdor-Kleingrothaus *et al.*, hep-ph/0103062.
32. R. Arnold *et al.*, Nucl. Instrum. Methods Phys. Res. A **503**, 649 (2003).
33. S. R. Elliott *et al.*, Phys. Rev. C **46**, 1535 (1992).
34. R. Arnold *et al.*, Nucl. Phys. A **636**, 209 (1998).
35. F. A. Danevich *et al.*, Phys. Rev. C **68**, 035501 (2003).
36. V. Artemiev *et al.*, Phys. Lett. B **345**, 564 (1995).
37. A. De Silva *et al.*, Phys. Rev. C **56**, 2451 (1997).
38. A. A. Klimenko *et al.*, Nucl. Instrum. Methods Phys. Res. B **17**, 445 (1986).

Translated by A. Isaakyan

Physics of Atomic Nuclei, Vol. 68, No. 3, 2005, pp. 420–438. Translated from Yadernaya Fizika, Vol. 68, No. 3, 2005, pp. 449–467.
Original Russian Text Copyright © 2005 by Dedenko, Zatsepin.

Cosmic Rays of Ultrahigh Energy

L. G. Dedenko[1] and G. T. Zatsepin[2]

Received May 24, 2004; in final form, September 15, 2004

Abstract—A new phenomenon—giant air showers of energy above 10^{20} eV, which lie beyond the Greisen–Zatsepin–Kuzmin cutoff—was discovered by various detection methods. The mechanism of particle acceleration to such high energies is still a puzzle. The arrival directions of giant showers do not contradict the hypothesis of their isotropic distribution. There are indications of their correlations with distant objects. It is obvious that only observations at new arrays can clarify the problem. The observed events must be reanalyzed within a more elaborate scheme. Verification of slight deviations from Lorentz invariance is possible. © *2005 Pleiades Publishing, Inc.*

1. INTRODUCTION

By convention, energies of primary-cosmic-ray particles in excess of 10^{19} eV will be referred to as ultrahigh energies. The flux I of such particles at the boundary of Earth's atmosphere is very low, $I \sim 1$ km^{-2} yr^{-1} sr^{-1}. In the atmosphere, a primary-cosmic-ray particle interacts with nuclei of air atoms, generating fluxes of secondary pions, kaons, and other hadrons, which in turn undergo multiple interactions with nuclei. Numerous photons, which arise predominantly from neutral-pion decays, generate electron–photon showers, while the decays of charged hadrons are sources of muons and neutrinos. If the energy of a primary-cosmic-ray particle is high—for example, $E > 10^{19}$ eV—then the number N of particles in the generated cascade is enormous, $N > 10^{10}$. Muons and electrons are scattered over a large area of $S \sim 3$–10 km^2 at Earth's surface, this being due to the transverse momentum $p_\perp$ of decayed hadrons and Coulomb interaction for the former and the latter, respectively. For this region, the emerging cascade of particles was called an extensive air shower. Showers from particles of ultrahigh energy are referred to as giant air showers. Extensive air showers are recorded by arrays of detector stations separated by distances of $d \sim 100$–1000 m. Use is made of both scintillation detectors, in which one measures energy depositions, and water tanks, where one records Cherenkov radiation from relativistic particles. Detectors of Cherenkov radiation from relativistic particles of extensive air showers are also applied in these realms. A procedure for detecting fluorescence light in the wavelength range between about 300 and 400 nm was developed about 20 years ago and is widely used at the present time. This light is emitted by nitrogen atoms excited by relativistic particles of a shower. Since the amount of light is proportional to the sum of the lengths of tracks of all particles in a shower, this method makes it possible to estimate the energy of the particle that generated the shower. However, this procedure, as well as that which employs Cherenkov light, can be applied only on clear moonless nights (about 10% of the total time of array operation). Since detector stations are separated by large distances d, an array of large effective area S can be created by using a relatively small number of stations. A shower is recorded if several stations are actuated almost simultaneously with allowance for delays associated with the arrival direction of the shower.

Extensive air showers were first discovered in 1939 in the experiments of the group headed by Auger [1]. Investigations in the Pamirs [2] revealed that an extensive air shower arises as a hadron cascade accompanied by secondary electrons and photons rather than as an electron–photon shower, as was thought previously. The first large array, Volcano Ranch, which had an effective detection area of about 8 km^2, was created in the United States of America by Linsley and Scarcey. A set of scintillation detector stations separated by a distance of $d \sim 880$ m was used in that array. Showers of ultrahigh energy were observed at the Volcano Ranch array a few years before the discovery of cosmic microwave background radiation and the prediction of Greisen [3] and Zatsepin and Kuz'min [4] that the flux of primary-cosmic-ray particles decreases sharply at energies above $(3$–$6) \times 10^{19}$ eV (Greisen–Zatsepin–Kuzmin effect) because of their interaction

---

[1] Department of Physics, Moscow State University, Vorob'evy gory, Moscow, 119992 Russia; e-mail: `ddn@dec1.sinp.msu.ru`

[2] Institute for Nuclear Research, Russian Academy of Sciences, pr. Shestidesyatiletiya Oktyabrya 7a, Moscow, 117312 Russia.

1063-7788/05/6803-0420$26.00 © 2005 Pleiades Publishing, Inc.

with photons of cosmic microwave background radiation. The energy of one such event was estimated at about 10^{20} eV [5]. A subsequent analysis [6] did not reveal any significant errors in the estimates of the energy of these showers. Thus, giant showers were discovered for the first time, which, according to later predictions [3, 4], are not expected to be observed if the sources of ultrahigh-energy particles are situated at large distances of $r \geq 100$ Mpc from the Earth. Another large array, Haverah Park, whose effective detection area was about 12 km^2, was created by Watson's group in England. In contrast to the American array, the Haverah Park array employed water tanks. Beginning in 1967, four events for which the original estimates of energy exceeded a value of about 10^{20} eV were observed over 20 years of array operation [7]. An analysis of these events within the currently accepted QGSJet version of the model of quark–gluon strings [8–11] reduced this estimate by about 30%, so that the maximum estimate of energy became about 8.6×10^{19} eV [12]. Two years after the cessation of investigations at the Haverah Park array, a shower of energy 1.2×10^{20} eV was recorded in the Soviet Union at the Yakutsk array for studying extensive air showers [13], its effective detection area being about 20 km^2 at that time. In addition to standard scintillation detector stations deployed on Earth's surface, use was made of detectors that were lowered into rock by about 2 m and which made it possible to measure muon fluxes. The Yakutsk array has yet another advantage of great importance. With the aid of Cherenkov detectors, the Cherenkov light flux, which is approximately proportional to the shower energy, is measured on clear moonless nights. Measurement of Cherenkov radiation permitted employing the calorimetric method for estimating the energy of primary-cosmic-ray particles [14]. In 1993, four years after the observation of the Yakutsk giant air shower, a shower of energy about 3×10^{20} eV was observed in the United States of America at the Fly's Eye array [15], where fluorescence light from excited nitrogen atoms was recorded for the first time. In the same year, a shower of energy about 2.7×10^{20} eV was detected in Japan at the AGASA (Akeno Giant Air Shower Array) facility [16]. The AGASA facility had a record area of about 111 km^2. As in Yakutsk, use was made of scintillation detector stations there. Muons of threshold energy 0.75 GeV were detected at the SUGAR (Sydney University Giant Airshower Recorder) array in Austalia, and giant air showers were also recorded [17].

Thus, different procedures for detecting extensive air showers yield consistent estimates for the energies of giant air showers, suggesting the existence of a new unique phenomenon—the presence of primary-cosmic-ray particles whose energy is about 10^{20} eV.

2. BRIEF REVIEW OF THE LATEST EXPERIMENTAL DATA

Although the area of the Yakutsk array for studying extensive air showers has been reduced to about 10 km^2 at the present time, the measurements there are being continued. A shower of energy about 5×10^{19} eV was recorded in 2002. The energy spectrum of primary-cosmic-ray particles in the energy range 10^{17}–10^{20} eV was presented in 2003 at the 28th International Cosmic Ray Conference [18]. It is given here in Fig. 1. For the sake of comparison, the data of the AGASA [19] and HiRes (USA) [20] groups are also displayed in this figure. From the figure, one can see that the intensity of primary-cosmic-ray particles according to data of the Yakutsk group is sizably higher than the intensity in [20], while the energy spectrum as measured in Yakutsk is somewhat steeper than the spectra from [19] and [20]. At the same time, Glushkov *et al.* [18] indicated that only one shower of energy in excess of 10^{20} eV was recorded at the Yakutsk array for studying extensive air showers,[3)] but that, on the basis of a comparison with the data of the AGASA group, one would expect about four events characterized by such energies. We note that a preliminary analysis [21] of the same events within the model of quark–gluon strings [10, 11] leads to precisely this number of events at energies above about 10^{20} eV. We also note that the data of the Yakutsk group that were obtained by using two different procedures (closed circles and triangles in Fig. 1) are poorly consistent with each other in the energy region around 5×10^{19} eV. We emphasize once again that the main advantage of the Yakutsk array is that one measures there Cherenkov radiation, which forms the basis of the calorimetric method for estimating the energy of showers. Indeed, the energy E of a primary-cosmic-ray particle is estimated by using the balance equation

$$E = E_{\rm s} + E_{\rm elphc} + E_{\mu\nu} + E_{\rm nucl}, \qquad (1)$$

where the component $E_{\rm s}$ is the energy scattered in the atmosphere above the observation level, $E_{\rm elphc}$ is the energy of the electron–photon component at the observation level, $E_{\mu\nu}$ is the energy carried away by muons and neutrino, and $E_{\rm nucl}$ is the energy spent into the disintegration of nuclei in hadron interactions. The energy $E_{\rm s}$, which is about 80% of the total

---

[3)] Yet another shower of energy above 10^{20} eV has been recorded there by now and two showers of energy have been added upon data processing.

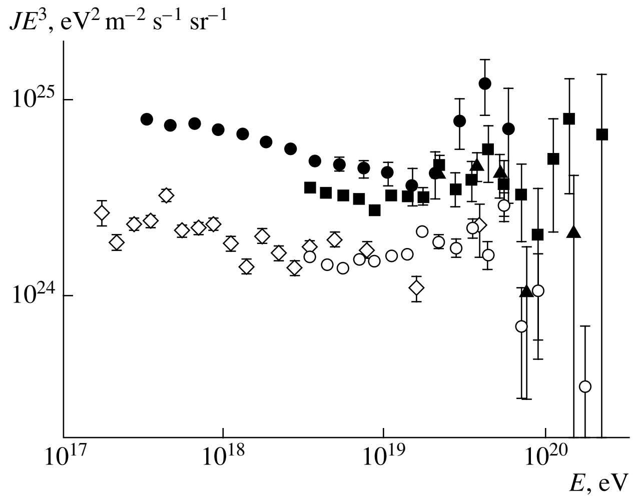

Fig. 1. Energy spectrum of primary-cosmic-ray particles according to data from [18] (closed circles and closed triangles). Also shown here are data from (closed boxes) [19] and (open diamonds and open circles) [20].

sum in (1), is estimated by using precisely Cherenkov radiation. The estimates of the remaining terms of the sum in (1) at a reference energy of 10^{18} eV according to the data of the Yakutsk group [14] and the data from [22] may be different, but, by and large, a very good balance holds and there are no discrepancies in estimating the first term, which is a dominant one. Apart from the detection of Cherenkov light, measurement of the fraction of muons with respect to the signal in detector stations deployed on Earth's surface is also of great importance. The results of such measurements for a distance of 600 m from the shower axis are given in Fig. 2 (circles) as a function of energy E. In this figure, curve *1* corresponds to a calculation with the Nishimura–Kamata–Greisen function [23]. Curve *2* there was obtained by using the modification of this function from [24], while curve *3* was constructed on the basis of the calculations performed in [25]. The estimates of energy from [21] were obtained from direct calculations with a modified Nishimura–Kamata–Greisen function that approximates well the experimental data shown in Fig. 2.

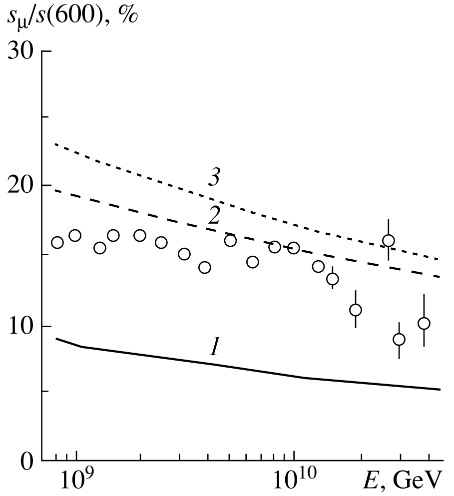

Fig. 2. Fraction of muons at a distance of 600 m from the shower axis versus the energy E (open circles) [14]. The curves correspond to (*1*) the calculation with the Nishimura–Kamata–Greisen function [23], (*2*) the calculation with the modified Nishimura–Kamata–Greisen function from [24], and (*3*) the calculation performed in [25].

Since the area of the AGASA facility is more than ten times larger than that of the Yakutsk array, the experimental-data sample from the former is much wider. First, the number of events in the energy region above 10^{20} eV is 11, as can be seen in Fig. 3, which shows the latest experimental data from [26]. The dashed curve there represents the spectrum expected in the case where cosmic-ray sources are distributed uniformly over the Universe and where the Greisen–Zatsepin–Kuzmin effect is taken into account. The figures by the points indicate the numbers of events in respective energy intervals. From this figure, it can be seen how dramatically the uniform-distribution model is violated. As in the case of the Yakutsk array, there arise questions concerning the procedure for estimating energy. In particular, Fig. 4 shows the so-called zenith-angle dependence of the parameter $s(600)$ [$s(600)$ is the energy-deposition density at a distance 600 m from the shower axis], this dependence being estimated by applying, to the spectra of showers characterized by preset values of this parameter, the method of sections along equal-intensity lines [27]. We can see that old (dotted curves) and new (solid curves) data differ significantly in the region of large zenith angles and ultrahigh energies (five

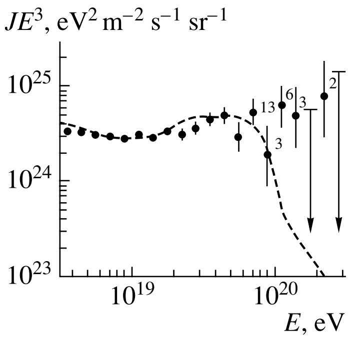

Fig. 3. Energy spectrum according to AGASA data from [26]. The dashed curve represents the expected spectrum for the case where cosmic-ray sources are uniformly distributed over the universe and where the Greisen–Zatsepin–Kuzmin effect is taken into account. The figures by the curves indicate the numbers of events in respective energy intervals.

figures on the right characterize the energies for the corresponding set of experimental points). As will be shown in Section 3, the zenith-angle dependence obtained in this way does not reflect actual particle absorption in a shower. We can indicate, however, that, if we use the dependences given in Fig. 4 up to zenith angles of about 60°, then the number of recorded events at energies in excess of 10^{20} eV increases to 17 [28]. The discovery of doublets and triplets, which are couples and triples of events observed, within an error of about 2.5° in measuring angles, in the same direction over the celestial sphere in the energy range $(4-5) \times 10^{19}$ eV, was quite unexpected. The estimated probability of an accidental observation of such events is given in Fig. 5*a* for couples and in Fig. 5*b* for triples [29]. It is about 10^{-3} for doublets and about 10^{-2} for triplets in the energy region mentioned above. Surprisingly, events of higher energy do not form clusters, although the trajectories of primary-cosmic-ray particles that have such energies are much less curved in intergalactic magnetic fields. Possibly, the available statistics of such events are insufficient. Figure 6, which was also borrowed from [29], displays the results of a correlation analysis for showers of energy not less than (*a*) 4×10^{19} and (*b*) 10^{19} eV. It can be seen that, in the first bins (of width about 3°), there is a considerable excess of events (Fig. 6*a*). We would like to note that a more thorough analysis of clustering by Tinyakov and Tkachev [30] reduced the probability of accidental clustering to a level of 6×10^{-6}. In view of the importance of the clustering phenomenon, it would be useful to perform an additional analysis where the widths of angular bins would be increased to about 5° for the AGASA data and to about 10° for the Yakutsk data in order to take into account more reliably the errors of the experiments in determining the arrival directions of showers. Obviously measurements at new arrays with a higher angular resolution would be of considerable interest.

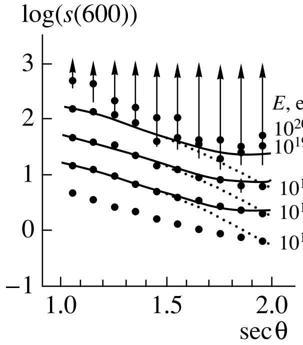

Fig. 4. Parameter $s(600)$ as a function of the zenith angle [27]: (dotted curves) older data and (solid curves) new data. The numbers on the right scale indicate the energy values for the corresponding set of experimental points.

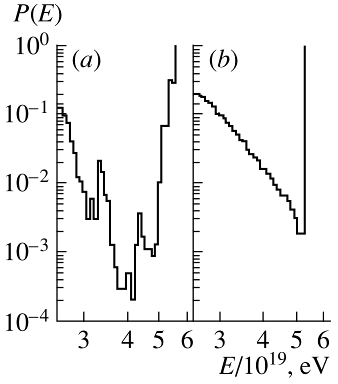

Fig. 5. Probability of an accidental observation of (*a*) doublets and (*b*) triplets [29].

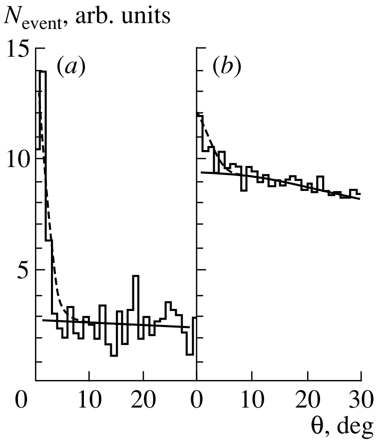

Fig. 6. Results of a correlation analysis for showers of energy not less than (*a*) 4×10^{19} and (*b*) 10^{19} eV [29]. The solid curves correspond to an isotropic distribution, while the dashed curves represent approximations of histograms.

Information about the chemical composition of primary-cosmic-ray particles is of paramount importance since it enables one to choose between many possible models of origin of cosmic rays that have ultrarelativistic energies. Figure 7 presents data of the AGASA group (points) from [31] on the density $s_{\mu}(1000)$ of muons at a distance of 1000 m from the shower axis, this density being dependent on the nature of primary-cosmic-ray particles, and the boundaries of standard-error intervals within ±1 for protons, iron nuclei, and photons. From this figure, one can see that almost all of the observed events are compatible with the assumption of the proton composition of primary-cosmic-ray particles at energies above 10^{19} eV. Since models involving topological defects [32], Z showers [33], and decay of hypothetical superheavy particles [34] are very popular, a possible upper limit on the ratio of the photon and proton fluxes

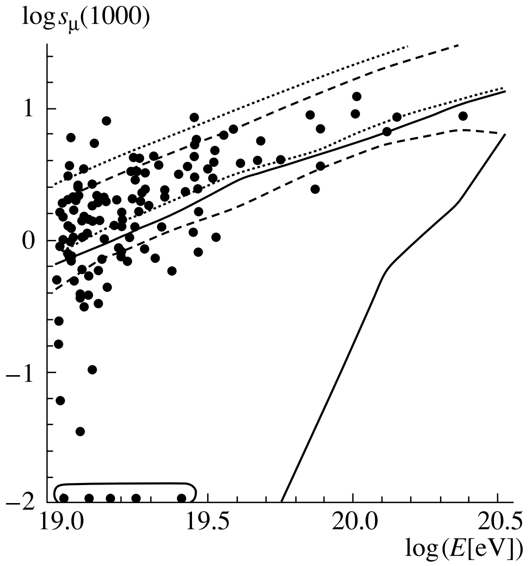

Fig. 7. Parameter $s_\mu(1000)$ as a function of energy E. Shown are data borrowed from [31] (points) and the boundaries of standard-error intervals within ±1 for (dashed curves) protons, (dotted curves) iron nuclei, and (solid curves) photons.

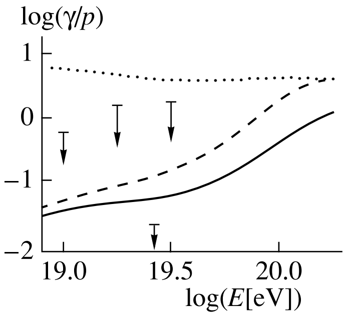

Fig. 8. Upper limit on the ratio of the photon and proton fluxes (arrows) and boundaries for models involving (solid curve) topological defects, (dashed curve) Z showers, and (dotted curve) superheavy particles for various bins in energy [31].

is of interest. These limits and boundaries for models involving topological defects, Z-showers, and superheavy particles for various bins in energy are given in Fig. 8, which was borrowed from [31]. A preliminary conclusion is that the displayed data rule out the model involving superheavy particles. We note that an upper limit of about 50% on the photon flux in the energy region around 10^{19} eV was set in [35]. This limit approximately corresponds to those in Fig. 8.

The arrival directions of primary-cosmic-ray particles on the celestial sphere at ultrahigh energies are of particular interest, since these directions may carry information about the sources of primary cosmic rays. Indeed, the deflection of a charged particle in random magnetic fields can be estimated by the formula

$$\delta\theta = 15^\circ \left(\frac{d}{d_0}\right)^{1/2} \left(\frac{D}{D_0}\right)^{1/2} \left(\frac{B}{B_0}\right) \left(\frac{E_0}{E}\right), \quad (2)$$

where $d_0 = 1$ Mpc characterizes the extension of a regular magnetic field, $D_0 = 16$ Mpc is the distance to a source, $B_0 = 10^{-9}$ G is the presumed magnetic-field strength, and $E_0 = 10^{19}$ eV is a constant. If the energy is $E \sim 5 \times 10^{19}$ eV and if the sources in question are situated rather closely—for instance, $D \sim D_0$—a simple estimation by formula (2) leads to $\delta\theta \sim 3^\circ$, which is nearly coincident with the angular resolution attained at the AGASA facility. Figure 9, which was borrowed from [36], shows, in terms of galactic coordinates, the arrival directions of 20 showers whose energies are above 5×10^{19} eV (boxes) and 16 showers whose energies lie in the range $(4-5) \times 10^{19}$ eV (diamonds). The dashed curve represents the Supergalaxy plane, while the dotted curve separates the shaded region, which is not observed at the AGASA facility in selecting showers whose zenith angles lie in the range $\theta \leq 45^\circ$. Although this statistical sample is rather small, it seems that the distribution obtained by the AGASA group and quoted in [36] is consistent with an isotropic one. This conclusion is of paramount importance, since it is virtually equivalent to ruling out models that involve nearby sources. Unfortunately, experiments at the AGASA facility were terminated at the end of 2003. At the present time—until new arrays (for example, Auger Observatory in Argentina) are commissioned—new expectations are associated with the operation of the HiRes facility, which replaced the earlier Fly's Eye. In Fig. 10, which was borrowed from [37], the energy spectra according to HiRes-2 (circles) and HiRes-1 (boxes) data, which were obtained in an independent mode, are displayed along with the AGASA data from [19] (triangles), which have already been considered. It can be seen that the statistics of events is still modest and that the errors are much larger than in the case of AGASA. Only one event of energy in excess of 10^{20} eV has so far been recorded at HiRes-1. In all probability, any conclusions concerning a corroboration of the observation of the Greisen–Zatsepin–Kuzmin effect by these data would be premature. Since the HiRes procedure makes it possible to observe a cascade curve and to estimate the depth $x_{\max}$ of the shower maximum, it is a method that enables one to determine the chemical composition of primary-cosmic-ray particles and which is alternative to that used at the AGASA facility, since this depth depends on the nature of a particle that initiated the shower being considered. In Fig. 11, which was borrowed from [38], the results obtained by measuring the average depth

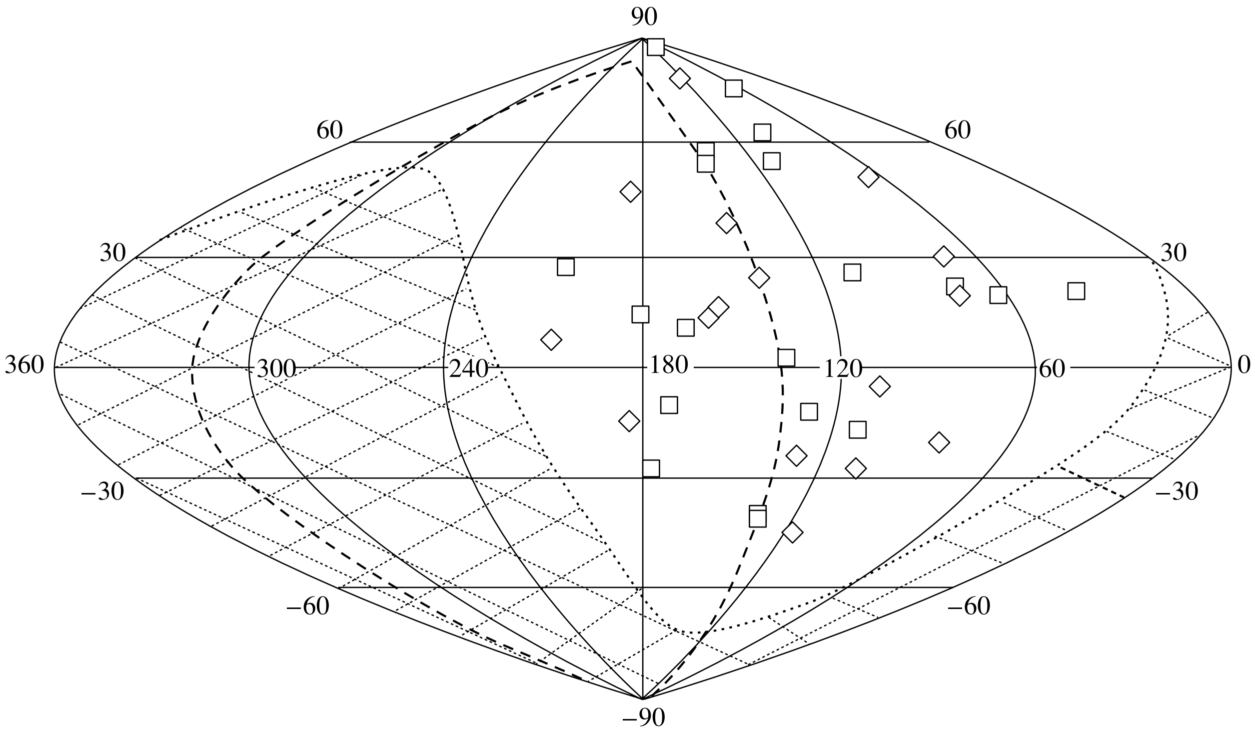

Fig. 9. Arrival directions of giant air showers [36] in the system of galactic coordinates for events of energy (open squares) not less than 5×10^{19} eV and (open diamonds) $(4\text{–}5) \times 10^{19}$ eV.

$\langle x_{\max} \rangle$ as a function of energy E for HiRes (triangles) and its prototype (asterisks) are given along with the results of calculations for primary protons and iron nuclei within the QGSJet (boxes) and SIBYLL (circles) models. From Fig. 11, one can see that, within the QGSJet model, primary-cosmic-ray particles consist predominantly of protons from an energy of about 10^{18} eV, this being consistent, in the region of ultrahigh energies, with the possible conclusions from AGASA data. The results of measurements of clustering in the energy region above 10^{19} eV also agree with the AGASA data. Figure 12 shows the function $W(\theta)$ characterizing the correlation between two events that were selected in a stereomode (in recording extensive air showers with the two detectors HiRes-1 and HiRes-2) at energies above 10^{19} eV [39]. The vertical dashes represent standard deviations for random fluctuations. From Fig. 12, one can see that, over the entire range of zenith angles, doublets, if any, are unnoticeable against the background of random fluctuations. It should be emphasized that, in the stereomode, the HiRes facility has a high energy resolution of about 0.9°.

Thus, about 14 to 20 showers of energy above 10^{20} eV have been observed so far. The arrival directions of these showers are consistent with an isotropic distribution and were not associated with any specific sources. Most likely, primary cosmic rays of ultrahigh energy are dominated by protons. In view of the obvious significance of all of these conclusions, further observations at new arrays—those that are already under construction (such as the Auger Observatory [40]), those whose construction will begin, according to plans, this year (Telescope Array (TA) [41]), or those that are only being discussed at the present time (EUSO project [42] and so on)—are mandatory both for significantly refining the above results and for, possibly, revealing absolutely few phenomena. It is also obvious that an additional analysis of all of the results obtained thus far and proposals of new lines of investigations are of great interest for future observations.

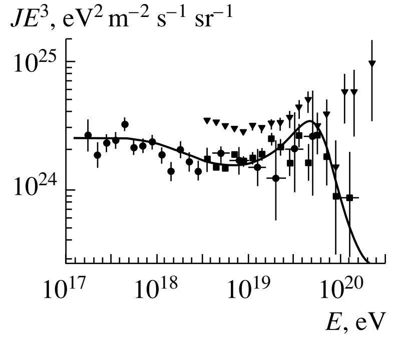

Fig. 10. Energy spectrum according to (closed boxes) HiRes-1 and (closed circles) HiRes-2 data [37]. Closed inverted triangles represent data from [19].

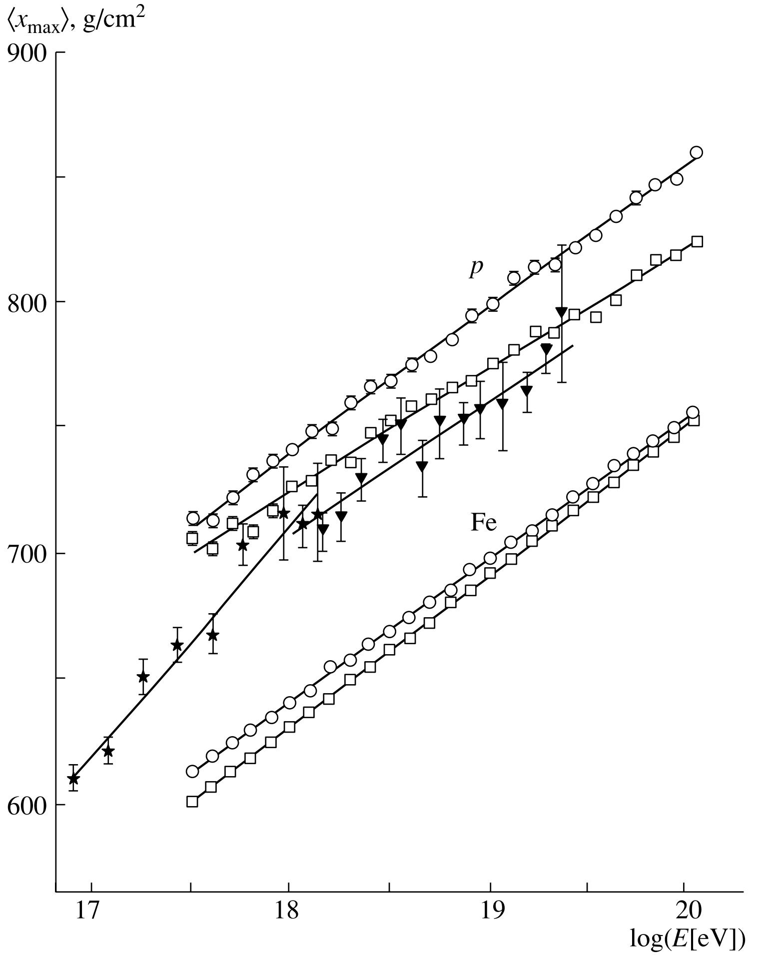

Fig. 11. Average depth $\langle x_{\max}\rangle$ of the shower maximum as a function of energy E: (stars and closed inverted triangles) data from [38]; (open circles and open boxes) results of calculations within, respectively, the SYBILL and QGSJet models for (upper points) protons and (lower points) iron nuclei.

3. STANDARD PROCEDURE FOR ESTIMATING ENERGY WITH THE AID OF THE PARAMETER $s(600)$

At the Yakutsk array for studying extensive air showers, as well as at the Haverah Park and AGASA facilities, the shower energy E is estimated by using the parameter $s_0(600)$, which is the density of the energy deposition in the detector in a vertical shower at the distance of 600 m from the shower axis, according to the formula

$$E = as_0^b(600), \tag{3}$$

where a and b are constants. This method was proposed by Hillas *et al.* [43] in 1971. In [18], the exponent in (3) was determined to be $b = 0.98 \pm 0.03$. In our opinion, this value of b is underestimated. Indeed, the shower maximum approaches the observation level with increasing energy E; therefore, an ever smaller number of particles is scattered over large distances from the shower axis, so that the exponent b must increase. For example, it is 1.02 in the case of the AGASA facility [26] (we note that the first estimate of the exponent for this facility was 0.9). Moreover, a procedure for rescaling the parameter $s(600)$ from the value measured for a shower that arrived at a zenith angle θ to the value that would be observed for a vertical shower is employed for all arrays. As was indicated above, the rescaling of this parameter is performed on the basis of its zenith-angle dependence, which is estimated experimentally by applying, to showers that have given values of the parameter $s(600)$, the method of sections of spectra with equal-intensity lines. This method was proposed by Clark [44] approximately 40 years ago for reconstructing a cascade curve on the basis of data coming from the Chacaltaya array in Bolivia. This array is situated at an altitude of about 5200 m above sea level; therefore, showers detected there are near the maximum of their development. Fluctuations are small in the vicinity of the maximum, so that an approximation of a cascade curve by some average dependence obtained as the result of observations of

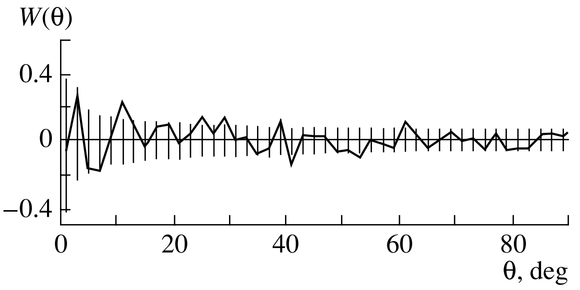

Fig. 12. Correlation function from [39].

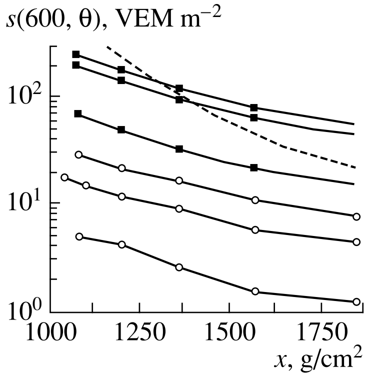

Fig. 13. Reconstructed cascade curves (closed boxes), data borrowed from [47] (closed circles), and average cascade curve (dashed curve). The explanation of VEM units in which we give values of the energy-deposition density $S(600)$ is given in Section 5.

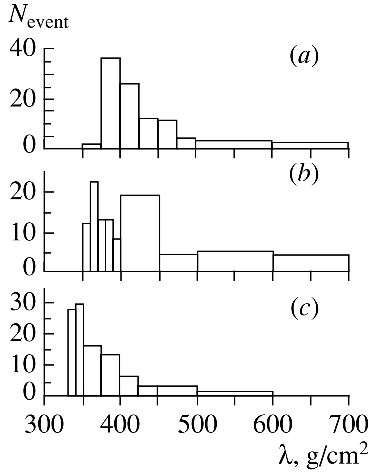

Fig. 14. Distributions of the absorption length λ for the energy values of (a) 3×10^{20}, (b) 3×10^{19}, and (c) 3×10^{18} eV.

many showers must not lead to a large error. Showers observed at sea level have already passed the maximum of their development. In this case, fluctuations of the shower parameters are great; therefore, the result obtained by approximating an individual cascade curve by some dependence may lead to sizable deviations from this curve. The idea of the method proposed in [44] and basic steps of its simulation [45, 46], which was performed in order to estimate errors, are as follows. At the observation level x_0, where the array used is deployed, one can measure the spectra of showers characterized by $s(600)$ values exceeding some threshold value $s_{\rm thr}(600)$ for various zenith-angle intervals $\Delta\theta_i = \theta_{i+1} - \theta_i$. For a given zenith-angle interval, the spectrum is given by

$$C(>s_{\rm thr}, \bar{\theta}_i) = A \int\limits_{\theta_i}^{\theta_{i+1}} d\theta_0 \int\limits_{y_{\rm min}}^{y_{\rm max}} e^{-\gamma y} dy \qquad (4)$$

$$\times \int\limits_{\theta_0 - 3\sigma}^{\theta_0 + 3\sigma} \psi(>s_{\rm thr}|\theta, y) f(\theta, \theta_0) d\theta,$$

where we have suppressed the label of the distance of 600 m to the shower axis on the parameter $s(600)$ and where

$$f(\theta, \theta_0) = \sin\theta e^{-(\theta_0 - \theta)^2/2\sigma^2},$$

A is a constant, θ is the shower zenith angle, σ is the error in measuring this angle, θ_0 is the measured value of the zenith angle, and $\bar{\theta}_i$ is the mean value for a bin of width $\Delta\theta_i$. It is assumed that θ_0 is distributed according to the normal law, with its mean value and standard deviation being $\bar{\theta}$ and σ, respectively. The function $\psi(>s_{\rm thr}|\theta, y)$ is the conditional probability of the distribution $s_{\rm thr}$ for given θ and y, where $y = \ln(E \text{ [eV]})$, E being the energy of the primary-cosmic-ray particle that generated the shower being considered. In (4), the average over the observation zenith angles within the bin $\Delta\theta_i$ is estimated in terms of the first integral, and it is associated with the mean value $\bar{\theta}_i$ for this interval. With the aid of the second integral, one estimates the average over the spectrum of primary-cosmic-ray particles, which is assumed to be power-law, its exponent being denoted by γ. The last integral takes into account errors in measuring zenith angles. Within the model of quark–gluon strings [10, 11], one first calculates the conditional probabilities $\psi(s_{\rm thr}|\theta, y)$. The total statistics of computed showers included about 10^5 events. After that, one calculates the functions $\psi(>s_{\rm thr}|\theta, y)$:

$$\psi(>s_{\rm thr}|\theta, y) = \int\limits_{s_{\rm thr}}^{\infty} \psi(s_{\rm thr}|\theta, y) ds. \qquad (5)$$

Finally, the spectra $C(>s_{\rm thr}, \bar{\theta}_i)$ of showers were calculated by formula (4) for various average values $\bar{\theta}_i$. In the case of observations, use is made of the same procedure for constructing the spectra of showers, with the only exception that events simulated by the Monte Carlo method are replaced by actual ones. Clark [44] assumed that the equal-intensity line $C = \text{const}$ corresponds to the same energy of a primary-cosmic-ray particle. Therefore, the cascade curve can be reconstructed by using the points of intersection of this line with spectra obtained for different $\bar{\theta}_i$. Indeed, each point of intersection specifies the abscissa $x_i = x_0/\cos\bar{\theta}_i$ and the ordinate s_i. By approximating the reconstructed cascade curve by an exponential dependence of the $e^{-x/\lambda}$ type, one can calculate the absorption length λ. Obviously, different values of energy correspond to different equal-intensity lines. The cascade curves given in Fig. 4, which were obtained from observations and which are referred to as zenith-angle dependences for the parameter $s(600)$, were constructed precisely in this way. An approximation of these zenith-angle curves by more complicated dependences cannot introduce anything new since the curves themselves are the result of many operations with various showers, this result not even being an average curve [see Eq. (5)]. By way of example, both the calculated curves (boxes) and the experimental data borrowed from [47] (circles) are displayed in Fig. 13. The dashed line is the ordinary cascade curve. Figure 13 shows how significant the distortion of the cascade-curve shape is. Quantitatively, this distortion manifests itself in the values of the absorption length λ—specifically, the absorption length is $\lambda \simeq 350$ g/cm^2 for the average curve, but it is $\lambda \simeq 540$ g/cm^2 for the reconstructed curve. As can be seen from Fig. 13, the experimental curves are parallel to their calculated counterparts and are characterized by an absorption-length value of $\lambda \simeq 520 \pm 60$ g/cm^2. Thus, it has strictly been shown that the zenith-angle dependences do not reflect the cascade curve adequately. Moreover, even the average curve describes an individual cascade poorly because of large fluctuations in the development of showers. The distributions of the absorption length λ for various energies of primary-cosmic-ray particles $y = \ln(E\,[\text{eV}])$ at a zenith angle of $\theta \simeq 45°$ are shown in Fig. 14 according to calculations by the Monte Carlo method. From this figure, one can see that, in individual showers, the absorption length λ fluctuates very widely, from about 330 to about 700 g/cm^2. Therefore, the estimate of the energy of an individual event with the aid of some fixed value of λ would not be reliable, the more so as this is not even the average value.

Methods for estimating the energy of a primary-cosmic-ray particle that are based on the assumptions put forth in [43, 44] have played a positive role. Various details on this subject can be found in the review article of Nagano and Watson [48]. However, there is the possibility of employing more elaborate procedures at the present time. We will begin by describing the procedure for estimating the arrival directions of showers.

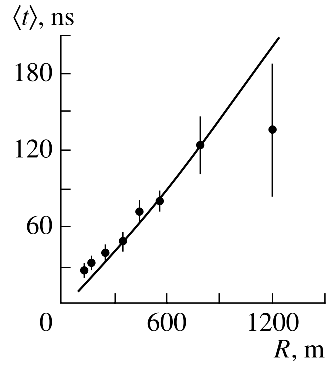

Fig. 15. Average time delay for muons, $\langle t \rangle$, as a function of the distance R to the shower axis and data borrowed from [52] (points).

4. ARRIVAL DIRECTIONS OF EXTENSIVE AIR SHOWERS

The arrival direction of showers is estimated on the basis of the delays of the time of signal detection in different detector stations. These time delays depend both on the shower arrival direction, which is determined by the zenith angle θ and the azimuthal angle φ, and on the spacetime structure of the shower front (shower disk). At the present time, this structure can be determined both experimentally and theoretically. At the Yakutsk array, use is made of the plane-front model, where all particles are concentrated in the same plane. Some modification of the Linsley model is employed in the case of the AGASA facility [49]. Obviously, the use of the spacetime structure obtained for a shower disk from calculations on the basis of some chosen model would be the optimum version. According to the calculations presented in [50], muons are the first to reach the detector. The time delay for a muon in a shower with respect to the first one is estimated by the simple formula

$$t = \frac{h_\mu}{c}\left(\frac{1}{\beta}\sqrt{1 + (R/h_\mu)^2} - 1\right), \qquad (6)$$

where h_μ is the altitude of the generation of a muon, β is its relative speed, c is the speed of light, and R is the distance from the shower axis. Naturally, time delays for all muons in a shower are estimated by the sum in (6) with the weights equal to the numbers of muons characterized by the corresponding parameters. In the approximation specified by Eq. (6), the calculations describe well experimental data [51]. The average time delays for muons, $\langle t \rangle$, as a function of the distance R to the shower axis are given in Fig. 15 along with data borrowed from [52]. There is good agreement between the results of the calculations and measurements. For the above distance fixed at the value of $R = 630$ m, Fig. 16 shows the dependence $\langle t \rangle$ on secθ. The results of the calculations are compatible with data from [52] in this case inclusive. Finally, Fig. 17 illustrates the dependence of the average muon-delay time at a distance of $R = 630$ m to the shower axis on the shower energy E. In this case, one can assume that, at an energy of $E \sim 4 \times 10^{18}$ eV, the data from [52] suggest a decrease in the average time delay. However, the errors are large, so that one can also assume that there are no significant discrepancies between the calculated and experimental values. Within the calculated structure of the shower front (disk), the arrival direction of showers (zenith angle θ and azimuthal angle φ) and the uncertainties in θ and φ can be estimated in a standard way by minimizing the χ^2 functional. The calculated arrival directions and the uncertainties in determining the angles θ and φ are given in the table according to the plane-front model, which is used by the Yakutsk group, and according to the calculated front. From the table, where No. is the ordinal number of a shower and $N_{\rm st}$ is the number of actuated stations, one can see that, in the case of a plane front, the uncertainties can be very large (about 20°). For the majority of showers, the uncertainty exceeds 6°, in which case it is very difficult to determine correlations with directions to some celestial objects. This uncertainty is due to a large error in measuring delay times ($\sigma \sim 60$–100 ns). In employing the computed front, the uncertainties are much smaller—in half of the cases, they are smaller than 5°. The analysis performed in [53] revealed that, as in the case of AGASA data, the distribution of the arrival directions of the 20 maximum-energy showers over the celestial sphere in galactic coordinates is compatible with an isotropic distribution. This conclusion can be considered as an indication that sources of primary-cosmic-ray particles having such energies are at cosmological distances from the Earth. In turn, this conclusion suggests that it is necessary to introduce new-physics events in the respective analysis. In particular, Farrar and Biermann [54] noticed a possible correlation of five showers with quasars. Virmani *et al.* [55] extended this correlation to 11 events. Uryson [56] indicated a possible correlation with Seifert galaxies. Tinyakov and Tkachev [57] found a correlation with objects of the BL Lacertae type. It is obvious that, if the number of objects is large, the correlation is observed. The main problem here consists in developing a mechanism of acceleration to ultrahigh energies and in proving the possibility of the implementation of this mechanism in objects with which a correlation was found.

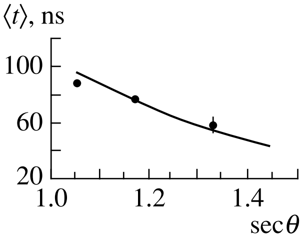

Fig. 16. Average time delay for muons, $\langle t \rangle$, as a function of sec$\,\theta$ for the distance of $R = 630$ m from the shower axis and data borrowed from [52] (points).

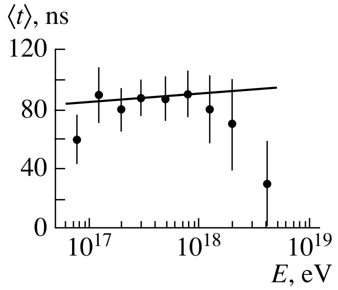

Fig. 17. Average time delay for muons, $\langle t \rangle$, as a function of energy for the distance of $R = 630$ m from the shower axis and data borrowed from [52] (points).

5. FIVE-STEP SCHEME FOR ESTIMATING ENERGIES

The next task after determining the arrival direction of a shower is to estimate its energy. Because of large fluctuations in the development of a shower, the procedure proposed 30 to 40 years ago [43, 44], which led to many interesting results, can be considered only as a first approximation. At the present time, it is possible to simulate events characterized by any number of parameters and arbitrary zenith angles. Since a simulation by the standard Monte Carlo method still presents a problem if the number of particles is about 10^{12}, it is necessary to introduce some simplifications. In view of this, Dedenko *et al.* [58, 59] proposed a five-step scheme that essentially consists in the following. Since individual events are observed, they must be interpreted on the basis of a computational scheme that makes it possible to simulate these events. Thus, one must take into account basic processes that lead to fluctuations in the development of showers. As was shown in [60, 61], variations in the depth of interactions and energy depositions of leading particles (that is, those that have the highest energies) are the main sources of fluctuations. Processes involving the propagation of a large number of secondary particles do not make a significant contribution to variations in the parameters of showers [62]. At the first step, it is therefore necessary to employ

Table

No.	Calculation with allowance for the shower front			Plane-front model		Experimental estimate		
	N_{st}	χ^2	θ/φ	χ^2	θ/φ	N_{st}	χ^2	θ/φ
1	9	4	40.2 ± 4.0	6.3	45.0 ± 4.6	8	5.4	45
			54.2 ± 3.5		55.0 ± 3.9			54.6
2	10	15.1	22.0 ± 3.3	20.2	20.0 ± 4.3	9	16.3	19
			2203 ± 13		165 ± 19			169
3	12	7.5	17.2 ± 2.0	10.3	16.0 ± 3.0	12	10.3	16
			7.4 ± 9.0		27.0 ± 11.0			27
4	19	39.7	29.6 ± 4.0	85	30 ± 10	14	14.1	29.2
			61.6 ± 5.0		66 ± 12			62.8
5	19	20.7	70 ± 7	49	65 ± 20	22	83.1	67.9
			135.4 ± 2.4		134.0 ± 3.7			132.7
6	12	18.5	23.8 ± 5.0	32.2	31.0 ± 6.6	11	27.6	24.2
			110 ± 9		104.0 ± 8.8			99.3
7	4	0.64	21.8 ± 1.3	4.7	16.5 ± 3.4	4	4.7	16.5
			311.0 ± 3.8		285.0 ± 17.0			285.6
8	8	2.8	24.0 ± 1.8	20.3	20.4 ± 5.6	8	20.3	20.4
			113.2 ± 2.6		109.7 ± 8.6			109.7
9	9	3.1	44.0 ± 2.2	18.3	48.0 ± 5.4	10	27.3	48.7
			145.4 ± 2.1		141.0 ± 4.4			147.5
10	30	11	57.6 ± 1.5	61	60.0 ± 4.0	17	39.1	58.7
			166.2 ± 1.4		165.0 ± 3.0			165.9
11	16	7.9	47.0 ± 3.8	26.1	53.0 ± 5.8	13	9.1	49.1
			223.4 ± 2.1		323.0 ± 3.2			320.3
12	5	4.1	26.4 ± 2.2	7	23.5 ± 4.0	5	7	23.5
			320.8 ± 8.0		288 ± 14			288.3
13	20	38	21.2 ± 2.9	96	20.0 ± 7.0	13	24.3	19.6
			230.8 ± 8.0		226 ± 19			229.3
14	11	11.5	30.2 ± 3.5	26	34.0 ± 5.5	11	25.9	34.2
			184.0 ± 5.4		189 ± 8			189.2
15	17	21	51 ± 4	31.1	55 ± 5	14	14.3	55.6
			237.4 ± 4.0		231 ± 4			233.3
16	15	31	56 ± 6	44.1	59.0 ± 6.4	12	5.8	57.4
			49 ± 4		51.0 ± 4.4			50.5
17	13	14.6	38 ± 4	22.3	42.0 ± 6.0	11	13.4	41
			230 ± 4		236.0 ± 5.0			234
18	20	27.6	26 ± 3	84.5	31.0 ± 6.5	15	36.2	27.4
			289 ± 7		284 ± 11			289.3

a standard Monte Carlo method for simulating the transport of leading particles, at least a primary particle. For this purpose, one can use the standard codes CORSIKA [63], AIRES [64], and COSMOS [65]. At the initial stage of shower development, each interaction of a leading particle results in the production of many tens or even hundreds of secondary particles. Fluctuations in the development of cascades from these particles are obviously compensated for the most part. As long as the energies E of secondary particles (hadrons) are sufficiently high—for example, $E \gg p_\perp c$—their transport in one-dimensional space can therefore be described by using a set of transport equations. Various numerical methods were proposed for solving such a set of integro-differential equations [66–69]. A scheme based on an integral representation of this set of equations was developed in [70–72]. The calculation of two to three successive iterations (generations) within this scheme makes it possible to obtain an estimate of the required solution to a precision of about 1%. The main task of the second step is to calculate source functions for hadrons of energy below a threshold of about 10^3 GeV and for photons originating predominantly from the decays of neutral pions.

Photons generate many electron–photon showers, which can be considered as one shower. If the energies of particles are rather high in such a shower—for example, $E \geq E_{\text{thr}}$ (where $E_{\text{thr}} \simeq 10$ GeV)—the transport of these particles in one-dimensional space can be described with the aid of a set of transport equations involving a term that takes into account the photon source function. These equations can also be solved by means of various numerical methods [73, 74]. The scheme proposed in [75] for solving the equations in questions employs an integral representation of the equations. At the third step, one solves these equations and calculates the source functions for electrons, positrons, and photons of energy below 10 GeV.

If the energies of the hadrons lie in the range $E \leq 10^3$ GeV, their propagation must be considered in three-dimensional space, since the scattering angles $\theta \sim p_\perp c/E$ are not small. However, there is no need for simulating the histories of all hadrons, the more so as their number in giant air showers is large (not less than 10^7). It is sufficient to create an input database of hadron showers (IDBHS). For this purpose, about 10^4 events are traced by the Monte Carlo method (with the aid of the standard codes CORSIKA, AIRES, or GEANT4 [76]) for all combinations of values of the zenith angle θ_i, the energy E_j, and the hadron-production depth x_k (where the indices i, j, and k run though the intervals dictated by the required accuracy), this being done for each combination of the indices. A simulation of each event makes it possible to calculate the parameters of showers for distances to the shower axis in the interval 10–2000 m.

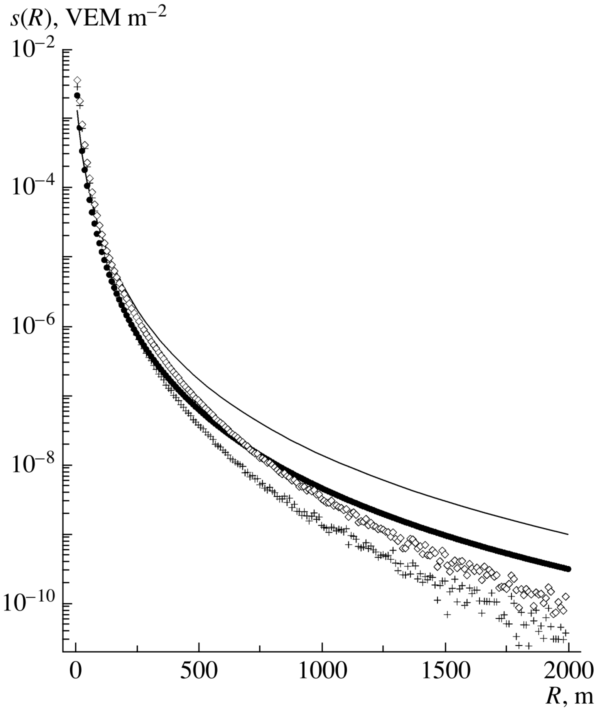

Fig. 18. Lateral distribution of (diamonds) signal s and (crosses) charged particles. The thin curve and closed circles represent, respectively, the Nishimura–Kamata–Greisen function and its modified counterpart.

If the ratio of the scattering energy E_{s} to the particle energy E in electron–photon showers is rather large ($E_{\text{s}}/E \geq 10^{-3}$), one must take into account the Coulomb scattering of electrons and consider the development of these showers in three-dimensional space with the aid of the code CORSIKA or EGS4. It is necessary to compute an input database of electron-photon showers (IDBEPS) in this case inclusive. For a grid of values of the zenith angle, energy, and shower-initiation depth (θ_i, E_j, and x_k, respectively), the shower parameters are also calculated for distances to the shower axis in the interval 10–2000 m. The calculation of the IDBHS and IDBEPS is the task of the fourth step of the global scheme.

Finally, the calculations must not end up in estimating shower parameters. Secondary particles (hadrons, muons, photons, electrons, and positrons) have different energies in the plane of detector stations and travel at different angles. These particles hit a detector of finite thickness (usually 3 to 5 cm in the case of scintillation detectors and about 1.2 m in the case of water tanks) and finite area (about a few m^2). The energy depositions in a detector and its effective area depend on the zenith angle. Moreover, the energies of all of these particles are different. They change from the threshold value of 1 MeV to a few hundred megaelectronvolts. The spectrum of positrons is harder than the spectrum of electrons. In the energy range $E \leq 30$ MeV, there is an excess of electrons, their number being severalfold greater than the number of positrons. The energy spectrum of photons is steeper than the spectrum of electrons (the former is characterized by a greater value of the exponent). Over the entire range of zenith angles and energies, the number of photons is more than ten times as great as the number of electrons. This means that, even in a scintillation detector—to say nothing of water tanks—the contribution to the signal from photons may exceed the energy losses of electrons. Thus, it is obvious that a correct interpretation requires calculating responses of detector stations to shower particles. These calculations constitute the last (fifth) step of the scheme described here. At the Yakutsk array for studying extensive air showers, use is made of plastic scintillation detectors based on polystyrene with luminiscent additions (n-terphenyl: about 2% PPP and about 0.02% POPO) in the form of blocks of thickness 5 cm and total area 2 m^2 [77–79]. The detector is arranged on a platform playing the role of a container whose lid from a sheet of duralimin has a thickness of 1.5 mm. The platform itself is installed within a wooden structure whose roof is covered with an aluminum dye. The following model of the detector is used: a plastic of density $\rho \sim 1$ g/cm^2 and thickness 5 cm covered with sheets of aluminum (2 mm thick) and wood (1 cm thick). There is also a fastening iron layer 0.2 mm thick. A particle that hits the detector can interact in its roof and undergo scattering; it can also generate a shower. Only energy depositions in the detector active layer of thickness 5 cm appear in the results of the calculations. For photons, electrons, positrons, and muons, the energy depositions in the detector were calculated by means of the standard code GEANT4 for a grid of energies (E_i) and angles (θ_j) of particle incidence to the detector. For each combination of the parameters (particle type and values of energy and zenith angle), the statistical sample contained 10^4 events. The total number of simulated events was about 10^8. About 50 years ago, extensive air showers were studied by employing hodoscopes that consisted of a large number of Geiger–Müller counters and which usually operated in the saturation mode and recorded charged particles. This fact was reflected in the terminology used: the concept of the charged-particle density at a given distance from the shower axis was introduced. In the early 1960s, Linsley and Scarcey used scintillation detectors of thickness about 7 cm. At the Yakutsk array for studying extensive air showers, as well as at the AGASA facility, the thickness of the detector was 5 cm. At the new Telescope Array, it is planned to use scintillation detectors of thickness 3 cm. There arises the natural question of how one can compare the readings of all of these detectors. Within a more correct formulation of the problem, it is necessary to take into account the design of the container housing the detector and of the structure for shielding it. At a typical energy of about 10 MeV, the number of photons in a shower is approximately 30 times larger than the number of electrons. The energies that are deposited in the detector are about 6 MeV in the case of electrons and about 0.7 MeV in the case of photons. The total energy losses of 10-MeV photons are approximately 3.5 times larger than the energy losses of electrons having the same energy. This simple example shows that it is necessary to introduce a new concept for the measured quantity and its unit. It is obvious that one does not deal here with a measurement of the charged-particle density. Since one measures energy deposited in the scintillation detector, it would be natural to use the notion of the deposited-energy density. Because the notion of a "particle" had always been conventional and, partly, because, at large distances from the shower axis, the muon contribution to the signal was known to be dominant, it was proposed, however, to adopt, for a unit of measurement, the energy that a muon moving in the vertical direction loses in the detector. According to the proposal of Watson [80, 81], this unit was called a VEM (vertical equivalent muon). This clear interpretation of a signal in terms of the number of vertical relativistic muons is convenient, but it should not lead one astray. The contribution to the signal from the electron–photon component is dominant at close distances from the shower axis. Moreover, it is obvious that the magnitude of a VEM unit depends on the material and thickness of the detector. The signal itself also depends on the material and design of the container and the structure housing it.

In the case of electron–photon showers, the contribution to the signal from photons is dominant at any distance from the shower axis. The lateral distribution of charged particles in a shower is frequently approximated by the Nishimura–Kamata–Greisen function involving the parameter R_{M}. On the basis of the calorimetric results for showers [14], a modification of this function was proposed where use is made of the parameter $\sim 0.5R_{\mathrm{M}}$ [22]. The results of calculations make it possible to determine the applicability range of the Nishimura–Kamata–Greisen approximation and to find out whether the use of the modified function is justifiable. For distances from the axis of a shower generated by a 10-TeV photon at a depth of 700 g/cm^2 that range between 10 and 2000 m, the lateral distributions of (crosses) charged particles and (diamonds) a signal expressed in VEM units are shown in Fig. 18 along with the standard Nishimura–Kamata–Greisen function and its modification. It can be seen from this figure that the standard Nishimura–Kamata–Greisen function describes, within an error of about 20%, the lateral distribution of charged particles up to distances of 200 to 300 m—that is, up to 2 to 3 Molière units—this corresponding to the claimed applicability range of the theory. At distances of $R > 500$ m, the discrepancy increases fast, exceeding an order of magnitude at a distance of 2 km from the shower axis. In accordance with the underlying ideas, the modified Nishimura–Kamata–Greisen function coincides with the lateral distribution of a signal at distances of about 600 m from the shower axis; therefore, it can be used in calculating the parameter $s(600)$ and in deriving preliminary estimates of the energy of extensive air showers (with allowance for the muon contribution). However, it can be seen from Fig. 18 that, both at small and at large distances from the shower axis, the lateral distribution of a signal differs markedly from the modified Nishimura–Kamata–Greisen function. In order to interpret responses of detector stations within a wide interval of distances from the shower axes, it is therefore necessary to use the calculated lateral distributions of the signal both from the electron–photon component of extensive air showers and from muons. An implementation of the fourth and fifth steps of the proposed scheme makes it possible to create a database that would include calculated lateral distributions of signals from partial showers. An example is given in Fig. 18.

Thus, the five-step scheme makes it possible to interpret responses of all actuated detector stations with allowance for fluctuations and to obtain more reliable estimates of the energy and arrival direction of giant air showers.

6. DEFLECTION OF MUONS BY THE GEOMAGNETIC FIELD IN INCLINED SHOWERS

In the case of inclined extensive air showers, it is necessary to consider that, since the trajectories of charged particles in the magnetic field of the Earth are curved, the lateral distributions of signals lose cylindrical symmetry even in the plane normal to the shower axis [82–88]. If the zenith angle θ exceeds a value of about 60°, it is predominantly muons and particles produced in their decay that are recorded at the observation level x_0. The electron–photon component of a shower is almost completely absorbed in the higher lying part of the atmosphere ($2x_0$). Positively and negatively charged muons are produced at a relatively high altitude and reach a detector upon traveling a distance of 10 to 20 km. If the angle between the shower axis and the direction of the geomagnetic field is not small, muons are considerably deflected by this field. For example, it was shown within a simple model [87] that, in the case of showers characterized by a very large inclination angle of about 80°, muons are separated in sign completely and that a strongly elongated image of the lateral distribution of muons is observed in the plane of detector stations. An inclined shower that has such an elongated image was detected at the Auger Observatory facility [88]. It is obvious that signals from such showers must be interpreted within a scheme that would take into account the geomagnetic field. A multigroup method that makes it possible to calculate the lateral distributions of both signals and muons with allowance for this field was developed in [82–85]. The direction of the muon-velocity vector $\mathbf{V}$ with respect to the shower axis is determined by the angle of deflection from this axis, α, and the azimuthal angle δ in the normal plane. All muons of an extensive air shower are divided into groups according to the energy intervals E_i–$(E_i + \Delta E_i)$, the angular intervals α_j–$(\alpha_j + \Delta\alpha_j)$ and δ_m–$(\delta_m + \Delta\delta_m)$, and the generation-altitude intervals h_k–$(h_k + \Delta h_k)$. To each group, one assigns the average values of energy, angles, and generation altitude ($\bar{E}_i$, $\bar{\alpha}_j$, $\bar{\delta}_m$, and $\bar{h}_k$). The numbers of positively and negatively charged muons, ΔN_μ^+ and ΔN_μ^-, with these average parameter values for each group, possible muon decays being taken into account, were considered as weight factors by which one multiplies the solution to the relativistic

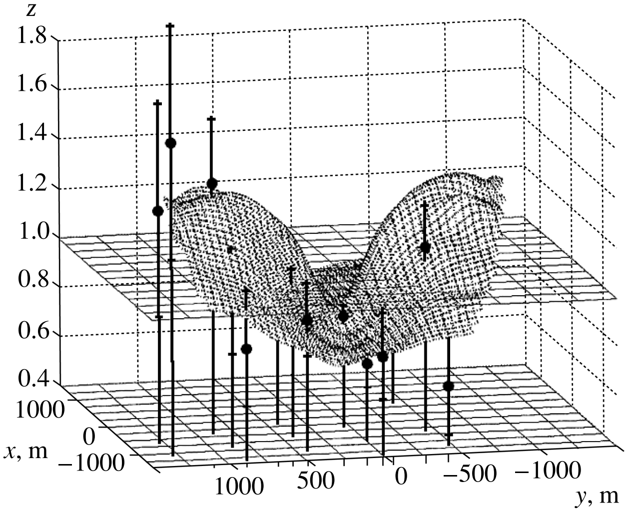

Fig. 19. Ratio z of the muon densities calculated with and without allowance for the magnetic field of the Earth along with the data borrowed from [13].

equation of motion for a single muon,

$$\gamma m_\mu \frac{d\mathbf{V}}{dt} = e[\mathbf{V} \times \mathbf{B}], \tag{7}$$

where m_μ is the muon mass, e is a unit charge, γ is the Lorentz factor, t is time, and $\mathbf{B}$ is the induction of the geomagnetic field. In solving Eq. (7), use was made of the standard second-order explicit scheme. The energy losses of muons in the atmosphere by ionization were taken into account. The time step h_t was determined from the condition requiring that the range within this time be about 120 m. The number of groups depends on the capacity of the computer used. We employed the partition where $\Delta\alpha$ and $\Delta\delta$ were about 1°, Δh was about 10 g/cm^2, and the energy interval was broken down into 20 subintervals. The results of the calculations are given in Fig. 19. In this figure, we present the ratio z of the muon density calculated with allowance for the geomagnetic field to the corresponding density calculated without taking this field into account (saddle-like surface). The displayed experimental data from [13] (circles with error bars) were also normalized to the densities calculated in the absence of the geomagnetic field. If the geomagnetic field had not affected the results, the calculated ratios would have singled out the $z = 1$ plane and the data would have concentrated around this plane. It can be seen from this figure that the data borrowed from [13] agree with the calculated saddle-like surface. As a matter of fact, it has been shown that, in this inclined shower, muons are partly separated in sign and that the estimated energy is 3×10^{20} eV, which is approximately three times higher than the original estimate [13]. Of course, additional investigations are required, as well as the interpretation of data within a model that would feature calculated signals.

7. SEARCHES FOR MANIFESTATIONS OF NEW PHYSICS

The correlation between the arrival directions of showers and distant objects and the observation of doublets and triplets lead to the assumption that particles that generate showers are neutral. The hypothesis of ultrahigh-energy neutrinos interacting with relic neutrinos in the vicinity of the Earth [89, 90] and producing Z showers is the simplest assumption of neutral primary particles that makes it possible to solve problems concerning both correlations with distant objects and the Greisen–Zatsepin–Kuzmin paradox. However, sources of such neutrinos must possess rather special properties [91]. Although the hypothesis of primary photons is compatible with the Fly's Eye, HiRes, and, partly, AGASA data, it must be considered with caution since the shower reported in [13] consists of muons exclusively and since the showers reported in [16] also involve muons. Various unusual ideas have long since been invoked in order to resolve the Greisen–Zatsepin–Kuzmin paradox. In particular, the idea based on the possible violation of Lorentz invariance at ultrahigh energies was first proposed more than 30 years ago in [92, 93]. In recent years, interest in these ideas and some other unusual assumptions has grown considerably (see, for example, [94–99]) in connection with a significant increase in the number of detected giant air showers whose energies are above 10^{20} eV. A new interesting possibility of testing Lorentz invariance on the basis of the results of observations of the longitudinal development of extensive air showers at energies of $E > 10^{19}$ eV was considered in [100–102]. As was shown in [99], neutral pions can be stable at energies exceeding the threshold

$$E = m_{\pi^0} / \sqrt{c_\gamma^2 - c_{\pi^0}^2}, \tag{8}$$

where c_γ and c_{π^0} are the maximally achievable speeds of photons and neutral pions, respectively. The following two assumptions were considered in [100–102]:

(1) $E > 10^{19}$ eV and $c_\gamma - c_{\pi^0} = 10^{-22}$;

(2) $E > 10^{18}$ eV and $c_\gamma - c_{\pi^0} = 10^{-20}$.

For the propagation of neutral pions over cosmological distances to be possible, neutral pions must not interact with photons of cosmic microwave background radiation. The reaction

$$\pi^0 + \gamma \to \omega(782), \tag{9}$$

whose threshold within standard theory,

$$E_{(\mathrm{thr})} = (m_{\omega(782)}^2 - m_{\pi^0}^2)/4\omega_\gamma \tag{10}$$

(where ω_γ is the photon energy), differs from the threshold energy for protons by 7%, can be kinematically forbidden within the assumptions put forth in [99], provided that

$$c_{\omega(782)} - c_{\pi^0} > 2\omega_\gamma^2/(m_{\omega(782)}^2 - m_{\pi^0}^2) \approx 1.86 \times 10^{-25} (\omega_\gamma/\omega_0)^2, \tag{11}$$

where $c_{\omega(782)}$ is the maximally achievable speed of the $\omega(782)$ meson and $\omega_0 = 2.35 \times 10^{-4}$ eV is the characteristic thermal energy of photon. Within the assumptions considered in [99], charged pions can similarly be stable at energies above the threshold value (if we neglect the neutrino mass)

$$E_{(\mathrm{thr})} = \sqrt{\frac{m_\pi^2 - m_\mu^2}{c_\mu^2 - c_\pi^2}} \approx 6.45 \times 10^{19} \left(\frac{10^{-24}}{c_\mu - c_\pi} \right)^{1/2}, \tag{12}$$

where c_π and c_μ are the maximally achievable speeds of pions and muons, respectively, and $E_{(\mathrm{thr})}$ is measured in eV. For the sake of simplicity, we additionally set $c_\mu = c_\nu$ in (12). Charged pions can propagate over cosmological distances if the reaction

$$\pi^\pm + \gamma \to \omega^\pm(770) \tag{13}$$

is kinematically forbidden. This occurs under the condition

$$c_{\omega(770)} - c_{\pi^\pm} > 2\omega_\gamma^2/(m^2_{\omega(770)} - m^2_\pi) \tag{14}$$
$$\approx 0.963 \times 10^{-25}(\omega_\gamma/\omega_0)^2,$$

which is similar to that in (11). Figure 20 shows the calculated dependences [100–102] of the average depth $\langle x_{\max}\rangle$ on the shower energy E for primary (dashed curves) protons and (dash-dotted curves) iron nuclei, along with the analogous dependences within hypothesis (1) and (2) for primary (solid curves in Fig. 20*a*) protons and (solid curves in Fig. 20*b*) pions and data borrowed from [15]. We note that the calculated parameters of giant air showers generated by pions do not contradict observation data. Since data from [15] agree, within approximately one standard deviation, with the calculated depth of the shower-development maximum for a primary proton, we can obtain an important constraint on the parameters violating Lorentz invariance. Namely, we must require that $c_\gamma - c_{\pi^0} < 10^{-22}$ [100]. We note that it is impossible to obtain a more stringent constraint since, at very small values of the difference $c_\gamma - c_{\pi^0}$, the results of the calculations become virtually independent of this difference. In order to rule out showers from primary charged pions, one needs the new constraint $c_\mu - c_\pi < 4 \times 10^{-26}$ because the shower energy is $E_0 \approx 3 \times 10^{20}$ eV. If the sources are situated at cosmological distances, the additional constraints $c_{\omega(782)} - c_{\pi^0} < 2 \times 10^{-23}$ and $c_{\omega(770)} - c_\pi < 10^{-23}$ for, respectively, neutral and charged pions are necessary [102, 103].

It is obvious that the parameters that could enable us to distinguish between showers generated by pions, protons, and nuclei are of interest. Since the ranges of different particles to the first interaction are different, it is natural to compare the distributions of these ranges. The depth x_1 at which the first interaction occurred can be defined as

$$x_1 = x_{\max} - \Delta x, \tag{15}$$

where $\Delta x = x_{\max} - x_1$. The depth $\langle x_{\max}\rangle$ can be determined from observations for each shower. The quantity Δx can be taken from calculations. The calculations performed in [102] show that the standard deviations Δx are about 1 to 1.5 g/cm^2 for pions and about 10 g/cm^2 for protons. Within the model in question, the quantity Δx can therefore be set to a constant—for example, to its average value $\overline{\Delta x}$. This value can be used to construct distributions of the depth x_1. As a result, one can obtain information about the nature of a primary particle.

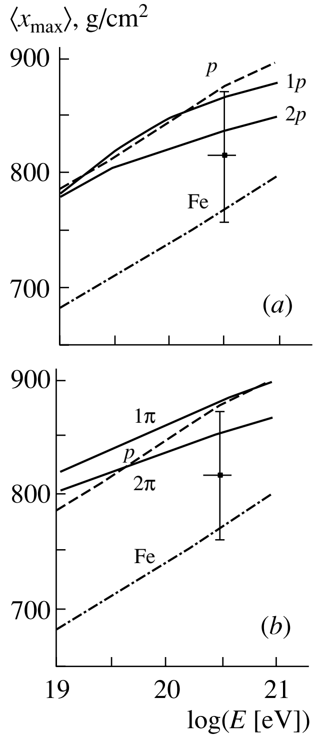

Fig. 20. Dependences of the average depth $\langle x_{\max}\rangle$ on the shower energy E within the standard model for primary (dashed curves) protons and (dash-dotted curves) iron nuclei, analogous dependences within hypotheses (1) and (2) for primary (solid curves in Fig. 20*a*) protons and (solid curves in Fig. 20*b*) pions, and data borrowed from [15].

Finally, the distributions of the altitudes (h_μ) or depths (x_μ) of the generation of high-energy (>10 GeV) muons are of particular interest. Figure 21 presents the distributions in the standard model for (dotted curve) a primary iron nucleus and (dashed curve) a primary proton and similar distributions according to hypotheses (1) and (2) for primary (curves $1p$ and $2p$) protons and (curves 1π and 2π) pions. It can be seen from this figure (the error of the calculations is less than 10 g/cm^2) that the peak of the distribution for protons occurs approximately 60 g/cm^2 deeper in the atmosphere than the peak of the distribution for iron nuclei. This makes it possible to distinguish primary nuclei from protons and to interpret more reliably the decrease in the depth $\langle x_{\max}\rangle$ in proton-generated showers as a manifestation of Lorentz invariance violation. In turn, the peak of the distribution for a primary proton is situated approximately 90 g/cm^2 higher in the

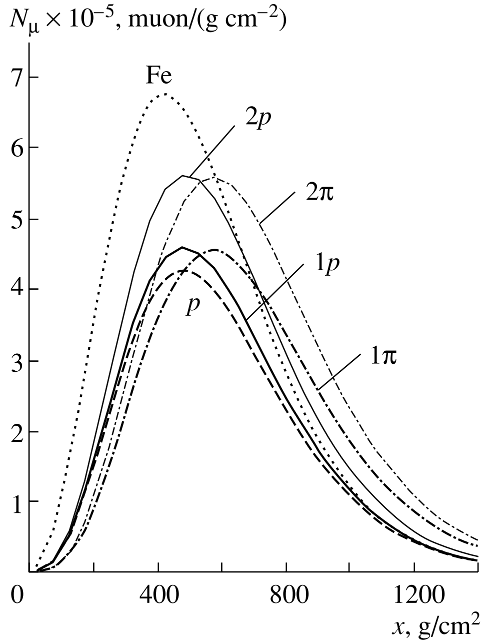

Fig. 21. Distributions of muon-production depths within the standard model for primary (dashed curve) protons and (dotted curve) iron nuclei and similar dependences within hypothesis (1) (solid curve $1p$ and dash-dotted curve 1π for a primary proton and a primary pion, respectively) and within hypothesis (2) (solid curve $2p$ and dash-dotted curve 2π for a primary proton and a primary pion, respectively).

atmosphere than the peak of the distribution for a primary pion, this making it possible to single out pions in the composition of primary cosmic rays. The methods used in [103], which enable one to determine the distributions of depths of high-energy-muon production, appear to be of particular importance.

8. CONCLUSIONS

Investigations performed at the Volcano Ranch [5], Haverah Park [7], Yakutsk [13], AGASA [16], SUGAR [17], Fly's Eye [15], and HiRes [20] arrays permitted making a fundamental discovery—giant air showers of energy in excess of 10^{20} eV. These energies are far beyond the cutoff of the energy spectrum of primary-cosmic-ray particles [3, 4] (Greisen–Zatsepin–Kuzmin effect). A specific mechanism owing to which particles can possess such high energies remains puzzling. The distribution of the arrival directions of primary-cosmic-ray particles that generate giant air showers is consistent with an isotropic distribution. It was indicated that the arrival directions of showers are correlated with quasars [54, 55] occurring at cosmological distances from the Earth and with objects of the BL Lacertae type [57] that also occur at extremely large distances from the Earth. Observations of doublets and triplets of showers arriving at the Earth from the same direction must be particularly highlighted [29]. These observations can be considered as a possible manifestation of pointlike sources and as an indication that primary-cosmic-ray particles are neutral.

Obviously, only observations at new arrays—HiRes (in the stereoregime), Auger Observatory, Telescope Array, EUSO, and so on—that will have a large effective detection area and a high angular resolution will make it possible to clarify the situation around giant air showers in the region of ultrahigh energies.

At the same time, it is necessary to develop further strategies of data interpretation. In particular, the above five-step scheme for simulating responses of detector stations makes it possible to obtain more reliable estimates of the energy and arrival directions of showers. In interpreting data for inclined showers, it is necessary to take into account the deflection of muon trajectories in the magnetic field of the Earth.

Within the hypothesis of an extremely weak violation of Lorentz invariance due to Coleman and Glashow [99], neutral and charged pions can be stable particles at energies higher than 10^{19} eV and can enter into the composition of primary cosmic rays in the region of ultrahigh energies. Observations of the depths $x_{\rm max}$ and x_1 and altitudes h_μ of muon generation would enable one to distinguish between primary nuclei, protons, and pions and to test Lorentz invariance at ultrahigh energies. At the same time, the interpretation of experimental data within the standard model yields new constraints on the parameters violating Lorentz invariance: $c_\gamma - c_{\pi^0} < 10^{-22}$ and $c_\mu - c_\pi < 4 \times 10^{-26}$ and, additionally, $c_{\omega(770)} - c_\pi < 10^{-23}$ and $c_{\omega(778)} - c_{\pi^0} < 2 \times 10^{-23}$ in the case of distant sources [100–102].

ACKNOWLEDGMENTS

We are grateful to T.M. Roganova and G.F. Fedorova for assistance in preparing the manuscript.

This work was supported in part by the foundation for support of leading scientific schools (grant no. 1782.2003.2) and by the Russian Foundation for Basic Research (project no. 03-02-16290).

REFERENCES

1. P. Auger *et al.*, Rev. Mod. Phys. **11**, 288 (1939).
2. G. T. Zatsepin, Dokl. Akad. Nauk SSSR **67**, 993 (1949).
3. K. Greisen, Phys. Rev. Lett. **16**, 748 (1966).
4. G. T. Zatsepin and V. A. Kuz'min, Pis'ma Zh. Éksp. Teor. Fiz. **4**, 78 (1966) [JETP Lett. **4**, 53 (1966)].
5. J. Linsley, Phys. Rev. Lett. **10**, 146 (1963).
6. A. J. Bower, G. Cunningham, J. Linsley, *et al.*, J. Phys. G **9**, L53 (1983).

7. G. Brooke, G. Cunningham, P. I. Eames, *et al.*, in *Proceedings of the 19th ICRC, La Jolla, 1985,* Vol. 2, p. 150.
8. A. B. Kaĭdalov and K. A. Ter-Martirosyan, Yad. Fiz. **39**, 1545 (1984) [Sov. J. Nucl. Phys. **39**, 979 (1984)].
9. A. B. Kaĭdalov, K. A. Ter-Martirosyan, and Yu. M. Shabel'skiĭ, Yad. Fiz. **43**, 1282 (1986) [Sov. J. Nucl. Phys. **43**, 822 (1986)].
10. N. N. Kalmykov and S. S. Ostapchenko, Yad. Fiz. **56** (3), 105 (1993) [Phys. At. Nucl. **56** (3), 346 (1993)].
11. N. N. Kalmykov, S. S. Ostapchenko, and A. I. Pavlov, Izv. Akad. Nauk, Ser. Fiz. **58** (12), 21 (1994).
12. M. Ave, J. A. Hinton, J. Knapp, *et al.*, in *Proceedings of the 27th ICRC, Hamburg, 2001*, Vol. 1, p. 381.
13. N. N. Efimov, T. A. Egorov, A. V. Glushkov, *et al.*, in *Proceedings of the International Workshop on Astrophysical Aspects of the Most Energetic Cosmic Rays, Kofu, 1990*, p. 20.
14. A. V. Glushkov *et al.*, in *Proceedings of the 20th ICRC, Moscow, 1987,* Vol. 5, p. 494.
15. D. J. Bird, S. C. Corbato, H. U. Dai, *et al.*, Astrophys. J. **424**, 491 (1994).
16. N. Hayashida, K. Honda, M. Honda, *et al.*, Phys. Rev. Lett. **73**, 3491 (1994).
17. M. M. Winn, J. Ulrichs, L. Horton, *et al.*, in *Proceedings of the 19th ICRC, La Jolla, 1985*, Vol. 9, p. 499.
18. A. V. Glushkov, V. P. Egorova, A. A. Ivanov, *et al.*, in *Proceedings of the 28th ICRC, Tsukuba, 2003*, Vol. 1, p. 389.
19. N. Sakaki, M. Chikawa, M. Fukushima, *et al.*, in *Proceedings of the 27th ICRC, Hamburg, 2001*, Vol. 1, p. 333.
20. T. Abu-Zayyad, G. C. Archbold, J. A. Bellido, *et al.*, astro-ph/0208301.
21. E. E. Antonov, L. G. Dedenko, G. F. Fedorova, *et al.*, in *Proceedings of the 26th ICRC, Salt Lake City, 1999*, Vol. 1, p. 423.
22. L. G. Dedenko, Izv. Akad. Nauk SSSR, Ser. Fiz. **55**, 720 (1991).
23. K. Greisen, *Wide Air Showers: Physics of Cosmic Rays*, Ed. by J. Wilson (Inostrannaya Literatura, Moscow, 1958), Vol. 3, p. 3.
24. L. G. Dedenko, N. M. Nesterova, S. I. Nikolsky, *et al.*, in *Proceedings of the 14th ICRC, Munchen, 1975*, Vol. 8, p. 2731.
25. A. I. Goncharov, A. K. Konopel'ko, A. A. Lagutin, *et al.*, Izv. Akad. Nauk SSSR, Ser. Fiz. **55**, 724 (1991).
26. M. Takeda, N. Sakaki, K. Honda, *et al.*, in *Proceedings of the 28th ICRC, Tsukuba, 2003*, Vol. 1, p. 381.
27. N. Sakaki, M. Chikawa, F. Fukushima, *et al.*, in *Proceedings of the 27th ICRC, Hamburg, 2001*, Vol. 1, p. 329.
28. M. Takeda, N. Sakaki, K. Honda, *et al.*, Astropart. Phys. **19**, 447 (2003).
29. M. Takeda, M. Chikawa, M. Fukushima, *et al.*, in *Proceedings of the 27th ICRC, Hamburg, 2001*, Vol. 1, p. 341.
30. P. G. Tinyakov and I. I. Tkachev, Pis'ma Zh. Éksp. Teor. Fiz. **74**, 3 (2001) [JETP Lett. **74**, 1 (2001)].
31. K. Shinozaki, M. Chikawa, M. Fukushima, *et al.*, in *Proceedings of the 28th ICRC, Tsukuba, 2003*, Vol. 1, p. 401.
32. V. Beresinsky, Nucl. Phys. B (Proc. Suppl.) **70**, 419 (1999).
33. T. J. Weiler, hep-ph/9710431.
34. V. Beresinsky, M. Kachelriess, and V. Vilenkin, Phys. Rev. Lett. **79**, 4302 (1997).
35. M. Ave, J. A. Hinton, R. A. Vazquez, *et al.*, Phys. Rev. D **65**, 063007 (2002).
36. N. Hayashida *et al.*, Astropart. Phys. **10**, 303 (1999).
37. D. R. Bergman (for the High Resolution Fly's Eye Collab.), in *Proceedings of the 28th ICRC, Tsukuba, 2003*, Vol. 1, p. 397.
38. G. Archbold and P. V. Sokolsky (for the HiRes Collab.), in *Proceedings of the 28th ICRC, Tsukuba, 2003*, Vol. 1, p. 405.
39. Chad B. Finley and Stefan Westerhoff (for the HiRes Collab.), in *Proceedings of the 28th ICRC, Tsukuba, 2003*, Vol. 1, p. 433.
40. M. Dova (for the Pierre Auger Observatory Collab.), in *Proceedings of the 27th ICRC, Hamburg, 2001*, Vol. 2, p. 699.
41. Y. Arai, J. Beltz, M. Chikawa, *et al.*, in *Proceedings of the 28th ICRC, Tsukuba, 2003*, Vol. 2, p. 1025.
42. M. Teshima, P. Lipari, and A. Santangelo, in *Proceedings of the 28th ICRC, Tsukuba, 2003*, Vol. 2, p. 1069.
43. A. M. Hillas *et al.*, in *Proceedings of the 12th ICRC, Hobart, 1971*, Vol. 3, p. 1007.
44. G. Clark *et al.*, in *Proceedings of the 8th ICRC, Jaipar, 1963*, Vol. 4, p. 65.
45. L. G. Dedenko, A. V. Glushkov, V. A. Kolosov, *et al.*, Izv. Ross. Akad. Nauk, Ser. Fiz. **66**, 1603 (2002).
46. E. E. Antonov, L. G. Dedenko, G. F. Fedorova, *et al.*, Comput. Phys. Commun. **147**, 484 (2002).
47. N. N. Efimov *et al.*, in *Proceedings of the 22nd ICRC, Dublin, 1991*, Vol. 4, p. 335.
48. B. Nagano and A. A. Watson, Rev. Mod. Phys. **72**, 689 (2000).
49. K. Honda *et al.*, Phys. Rev. D **56**, 3833 (1997).
50. A. M. Anokhina, L. G. Dedenko, G. F. Fedorova, *et al.*, Phys. Rev. D **60**, 033004 (1999).
51. E. E. Antonov, L. G. Dedenko, G. F. Fedorova, *et al.*, in *Proceedings of the 26th ICRC, Salt Lake City, 1999*, Vol. 1, p. 449.
52. A. V. Glushkov, L. G. Dedenko, V. B. Kosarev, *et al.*, in *Proceedings of the 26th ICRC, Salt Lake City, 1999*, Vol. 1, p. 387.
53. E. E. Antonov, I. L. Buylova, L. G. Dedenko, *et al.*, Comput. Phys. Commun. **147**, 480 (2002).
54. G. R. Farrar and P. L. Biermann, Phys. Rev. Lett. **81**, 3579 (1998).

55. A. Virmani, S. Bhattacharya, P. Jain, *et al.*, Astropart. Phys. **17**, 489 (2002).
56. A. Uryson, Pis'ma Astron. Zh. **27**, 901 (2001) [Astron. Lett. **27**, 775 (2001)].
57. P. G. Tinyakov and I. I. Tkachev, Pis'ma Zh. Éksp. Teor. Fiz. **74**, 499 (2001) [JETP Lett. **74**, 445 (2001)].
58. L. G. Dedenko, G. F. Fedorova, E. Yu. Fedunin, *et al.*, Comput. Phys. Commun. **122**, 329 (2002).
59. L. G. Dedenko, G. F. Fedorova, E. Yu. Fedunin, *et al.*, in *Proceedings of the 28th ICRC, Tsukuba, 2003*, Vol. 2, p. 643.
60. G. T. Zatsepin, in *Proceedings of 6th International Conference on Cosmic Rays, Moscow, USSR, 1960*, Vol. 2, p. 212.
61. L. G. Dedenko and G. T. Zatsepin, in *Proceedings of 6th International Conference on Cosmic Rays, Moscow, USSR, 1960*, Vol. 2, p. 222.
62. N. N. Kalmykov and V. P. Chistyakov, Izv. Akad. Nauk SSSR, Ser. Fiz. **29**, 1788 (1965).
63. D. Heck *et al.*, FZKA 6019 (Forschungszentrum Karlsruhe, 1998).
64. S. J. Sciutto, http://www.fisica.unpl.edu.ar/auger/aires
65. K. Kasahara, http://eweb.b6.kanagawa-u.ac.jp/kasahara
66. I. L. Rozental', Dokl. Akad. Nauk. SSSR **80**, 731 (1951).
67. G. T. Zatsepin and I. L. Rozental', Dokl. Akad. Nauk SSSR **99**, 369 (1954).
68. I. P. Ivanenko, Zh. Éksp. Teor. Fiz. **37**, 1046 (1959) [Sov. Phys. JETP **37**, 744 (1959)].
69. H. Fukuda, N. Ogita, and A. Ueda, Prog. Theor. Phys. **21**, 29 (1959).
70. L. G. Dedenko, Izv. Akad. Nauk SSSR, Ser. Fiz. **29**, 1722 (1965).
71. L. G. Dedenko, in *Proceedings of the 9th ICRC, London, 1966*, Vol. 2, p. 662.
72. L. G. Dedenko, Can. J. Phys. **46**, S178 (1968).
73. R. E. Streitmatter and S. A. Stephens, in *Proceedings of the 19th ICRC, La Jolla, 1985*, Vol. 7, p. 227.
74. S. Kawaguchi, A. Misaki, and N. Fujimaki, in *Proceedings of the 17th ICRC, Paris, 1981*, Vol. 11, p. 403.
75. L. G. Dedenko, in *Proceedings of the 15th ICRC, Plovdiv, 1977*, Vol. 8, p. 470.
76. The GEANT4 Collab., http://www.info.cern.ch/asd/geant4.html
77. T. A. Egorov, N. N. Efimov, D. D. Krasil'nikov, *et al.*, Izv. Akad. Nauk SSSR, Ser. Fiz. **29**, 1702 (1965).
78. T. A. Egorov, N. N. Efimov, D. D. Krasil'nikov, *et al.*, in *Cosmic Rays* (Nauka, Moscow, 1972), No. 13, p. 1.
79. A. V. Glushkov, O. S. Diminshtein, T. A. Egorov, *et al.*, in *Experimental Methods for Studying Ultrahigh-Energy Cosmic Rays* (YaF SO AN SSSR, Yakutsk, 1974), p. 52 [in Russian].
80. A. A. Watson, astro-ph/0112474.
81. A. A. Watson, Contemp. Phys. **43**, 181 (2002).
82. L. G. Dedenko, G. F. Fedorova, and A. A. Kirillov, in *Proceedings of the 24th ICRC, Roma, 1995*, Vol. 1, p. 309.
83. E. E. Antonov, L. G. Dedenko, A. V. Glushkov, *et al.*, Pis'ma Zh. Éksp. Teor. Fiz. **68**, 177 (1998) [JETP Lett. **68**, 185 (1998)].
84. E. E. Antonov, A. V. Glushkov, L. G. Dedenko, *et al.*, Pis'ma Zh. Éksp. Teor. Fiz. **69**, 614 (1999) [JETP Lett. **69**, 650 (1999)].
85. E. E. Antonov, L. G. Dedenko, G. F. Fedorova, *et al.*, Comput. Phys. Commun. **147**, 501 (2002).
86. Yu. N. Antonov, Yu. N. Vavilov, G. T. Zatsepin, *et al.*, Zh. Éksp. Teor. Fiz. **32**, 227 (1957) [Sov. Phys. JETP **5**, 172 (1957)].
87. M. Ave, R. A. Vazquez, E. Zas, *et al.*, Astropart. Phys. **14**, 109 (2000).
88. M. Ave (for the Pierre Auger Collab.), in *Proceedings of the 28th ICRC, Tsukuba, 2003*, Vol. 1, p. 365.
89. D. Fargion, B. Mele, and A. Salis, Astrophys. J. **517**, 725 (1999).
90. T. J. Weiler, Astropart. Phys. **11**, 303 (1999).
91. O. E. Kalashev, V. A. Kuzmin, D. V. Semikoz, *et al.*, Phys. Rev. D **65**, 103003 (2002).
92. D. A. Kirzhnits and V. A. Chechin, Pis'ma Zh. Éksp. Teor. Fiz. **14**, 261 (1971) [JETP Lett. **14**, 172 (1971)].
93. D. A. Kirzhnits and V. A. Chechin, Yad. Fiz. **15**, 1051 (1972) [Sov. J. Nucl. Phys. **15**, 585 (1972)].
94. J. Ellis, K. Farakos, N. E. Mavromatos, *et al.*, astro-ph/9907340.
95. T. Kifune, astro-ph/9904164.
96. B. E. Schaefer, Phys. Rev. Lett. **82**, 4964 (1999).
97. L. Gonzalez-Mestres, astro-ph/0011181.
98. G. Amelino-Camelia, J. Ellis, N. E. Mavromatos, *et al.*, Nature **393**, 763 (1998).
99. S. Coleman and S. L. Glashow, Phys. Rev. D **59**, 116008 (1999).
100. E. E. Antonov, L. G. Dedenko, A. A. Kirillov, *et al.*, Pis'ma Zh. Éksp. Teor. Fiz. **73**, 506 (2001) [JETP Lett. **73**, 446 (2001)].
101. L. G. Dedenko, G. F. Fedorova, E. Yu. Fedunin, *et al.*, Nucl. Phys. B (Proc. Suppl.) **122**, 321 (2003).
102. L. G. Dedenko, T. M. Roganova, G. F. Fedorova, *et al.*, Pis'ma Zh. Éksp. Teor. Fiz. **78**, 131 (2003) [JETP Lett. **78**, 101 (2003)].
103. G. Agnetta, M. Ambrosio, J. Beaman, *et al.*, Nucl. Instrum. Methods Phys. Res. A **359**, 596 (1995).

Translated by A. Isaakyan

Physics of Atomic Nuclei, Vol. 68, No. 3, 2005, pp. 439–454. From Yadernaya Fizika, Vol. 68, No. 3, 2005, pp. 468–483.

Search for $\Theta^+(1540)$ in Exclusive Proton-Induced Reaction $p + \mathrm{C}(N) \to \Theta^+\bar{K}^0 + \mathrm{C}(N)$ at the Energy of 70 GeV*,**

V. F. Kurshetsov[1]*, Yu. M. Antipov[1], A. V. Artamonov[1], V. A. Batarin[1], O. V. Eroshin[1], V. Z. Kolganov[2], A. S. Konstantinov[1], A. P. Kozhevnikov[1], A. E. Kushnirenko[1], L. G. Landsberg[1], V. M. Leontiev[1], G. S. Lomkatsi[2], V. V. Molchanov[1], V. A. Mukhin[1], A. F. Nilov[2], D. I. Patalakha[1], S. V. Petrenko[1], V. T. Smolyankin[2], D. V. Vavilov[1], and V. A. Victorov[1]**

The SPHINX Collaboration

Received July 21, 2004; in final form, September 20, 2004

Abstract—A search for narrow $\Theta^+(1540)$, a candidate for a pentaquark baryon with positive strangeness, has been performed in an exclusive proton-induced reaction $p + \mathrm{C}(N) \to \Theta^+\bar{K}^0 + \mathrm{C}(N)$ on carbon nuclei or quasifree nucleons at $E_{\mathrm{beam}} = 70$ GeV ($\sqrt{s} = 11.5$ GeV) studying nK^+, pK^0_S, and pK^0_L decay channels of $\Theta^+(1540)$ in four different final states of the $\Theta^+\bar{K}^0$ system. In order to assess the quality of the identification of the final states with neutron or K^0_L, we reconstructed $\Lambda(1520) \to nK^0_S$ and $\phi \to K^0_L K^0_S$ decays in the calibration reactions $p + \mathrm{C}(N) \to \Lambda(1520)K^+ + \mathrm{C}(N)$ and $p + \mathrm{C}(N) \to p\phi + \mathrm{C}(N)$. We found no evidence for a narrow pentaquark peak in any of the studied final states and decay channels. Assuming that the production characteristics of the $\Theta^+\bar{K}^0$ system are not drastically different from those of the $\Lambda(1520)K^+$ and $p\phi$ systems, we established upper limits on the cross-section ratios $\sigma(\Theta^+\bar{K}^0)/\sigma(\Lambda(1520)K^+) < 0.02$ and $\sigma(\Theta^+\bar{K}^0)/\sigma(p\phi) < 0.15$ at 90% C.L. and a preliminary upper limit for the forward-hemisphere cross section $\sigma(\Theta^+\bar{K}^0) < 30$ nb/nucleon. *© 2005 Pleiades Publishing, Inc.*

1. INTRODUCTION

Although the list of the experiments supporting the first observation [1] of the narrow Θ^+ baryon with exotic quantum numbers is impressive [2–13], its properties (spin, parity, total width, and production cross sections) are not established and even its mere existence is far from being proved. The experimental concerns about the Θ^+ baryon include the statistical significance of the observed peaks, the evident discrepancy in its mass measured in nK^+ and pK^0_S decay modes, and the physical meaning of cuts used to enrich and even to see the signal. Possible sources of the false peaks were proposed for the nK^+ final state [13, 14] as well as for the pK^0_S one [15]. The discussion of these questions can be found in [16, 17].

Recently, negative results in a search for $\Theta^+/\bar{\Theta}^-$ started to emerge [18–22], some of them still having the status of conference presentations. However, negative results come either from the study of specific processes (J/ψ and Z decays) or from high-energy inclusive nucleon–nuclei interactions, whereas positive ones come from $\gamma/K^+/\nu/e$ beams or relatively low energy proton reactions. A possible explanation why Θ^+ has been seen in some experiments and not in others was proposed in [23]. In any case, it is evident that more experiments are needed with different beams, targets, energies, and higher statistics to reject or confirm the existence of the Θ^+ baryon and establish its properties.

The SPHINX experiment has a long history of searches for exotic baryons and other exotic structures in various proton-induced exclusive and semi-inclusive reactions. As a result of the first stage of the experiment, we published upper limits for the productions of heavy ($M > 2.3$ GeV) narrow states in the $p\phi$, $\Lambda(1520)K^+$, pK^+K^-, and $\Sigma^0(1385)K^+$ systems [24] as well as in the $p\bar{p}$ and $pp\bar{p}$ systems [25]. Searches for the narrow $N_\phi(1960)$ baryon were also

---

*This article was submitted by the authors in English.

[1] Institute for High Energy Physics, Protvino, Moscow oblast, 142284 Russia.

[2] Institute of Theoretical and Experimental Physics, Bol'shaya Cheremushkinskaya ul. 25, Moscow, 117259 Russia.

**Based on talks given by V.F. Kurshetsov at the IHEP seminar (Protvino, IHEP, February 5, 2004) and at the session of the Nuclear Physics Department of the Russian Academy of Sciences (Moscow, ITEP, March 5, 2004).

***E-mail: `kurshetsov@mx.ihep.su`

negative [26]. At the same time, we found interesting structures in the Σ^0K^+, $\Sigma^+\bar{K}^0$, $\Sigma^0(1385)K^+$, and $p\eta$ systems in the 1.7–2.1-GeV mass region. The origin of these structures is uncertain, and they need further study and confirmation in other experiments. The status of the study of some of these structures can be found in [27–30].

The search for Θ^+ at SPHINX has its own history. After the publication of the paper by Diakonov, Petrov, and Polyakov [31] in 1997, the planning started and the hadron calorimeter was installed in 1998 with the idea to have additional capabilities to detect neutral hadrons. However, we always had in mind that, in a similar model, Weigel [32] predicted a much heavier (1580 vs. 1530 MeV) and much wider (100 vs. $\lesssim$15 MeV) exotic baryon. The relatively big width of the Weigel state could demand background subtraction. After a lengthy reconstruction of more than 600 million events recorded in 1998–1999, in 2001–2002 we made a first attempt to find the Θ^+ baryon using the final states without neutral hadrons. We looked at the reaction[3)]

$$p + N \to \Theta^+\bar{K}^{0*} + N, \quad (1)$$
$$\Theta^+ \to pK^0_S, \quad \bar{K}^{0*} \to K^-\pi^+,$$

where Θ^+ can be produced, and compared it to the reaction

$$p + N \to pK^0_S K^{0*} + N, \quad K^{0*} \to K^+\pi^-, \quad (2)$$

which can be used to estimate the background. Surprisingly enough, a narrow peak at $M = 1548$ MeV was found in the signal but not in the background reaction. However, it had a low significance (3–3.5 σ) and was found to be unstable against cuts. Later on, with a better understanding of the neutron reconstruction, we had a quick look at the same reaction with different final state

$$p + N \to \Theta^+\bar{K}^{0*} + N, \quad (3)$$
$$\Theta^+ \to nK^+, \quad \bar{K}^{0*} \to K^-\pi^+,$$

and did not find the expected signal. Currently, we consider an early peak to be a normal statistical fluctuation. The reactions (1)–(3) are still under study and the results will be available in the near future.

In this work, we present results of a search for the Θ^+ baryon in a simpler reaction

$$p + N \to \Theta^+\bar{K}^0 + N. \quad (4)$$

The basic idea of our approach is to study simultaneously all experimentally available final states of the $\Theta^+\bar{K}^0$ system, thus eliminating the influence of possible reflections and inevitable statistical fluctuations on the final judgment.

2. EXPERIMENTAL APPARATUS

The SPHINX spectrometer was operating in the proton beam of the IHEP accelerator with energy $E_p = 70$ GeV and intensity $I \simeq (2–4) \times 10^6$ p/spill in 1989–1999. During that time, several modifications of the detector were made. The data presented in this work were obtained with the last completely upgraded version of the SPHINX spectrometer [30]. A detailed description of the setup can be found in [33]. In brief, it included detectors of the primary proton beam; two targets (copper and carbon) inside the guard box; a wide-aperture magnetic spectrometer with proportional chambers, drift tubes, and scintillation hodoscopes; and a system of Cherenkov counters for identification of secondary particles including a RICH velocity spectrometer, lead-glass electromagnetic calorimeter ECAL, and hadron calorimeter HCAL.

The beam was produced diffractively off the main beam of the U-70 accelerator and had negligible momentum spread, small space dimensions (2 × 4 mm), and small angular divergence. A special trigger logic scheme allowed the construction of up to eight different kinds of triggers, using as primitive elements the signals from scintillation and veto counters, the multiplicity of hits in the hodoscopes and threshold Cherenkov counter, and the total energy sum in ECAL.

The data acquisition system was based on the MISS standard [34] developed at IHEP and could record up to 4000 events per 10-s spill of the accelerator.

The statistics used in this work were written during the last run of the SPHINX experiment in March–April 1999. More than 600 million trigger events were written, corresponding to 3×10^{11} live protons on targets.

3. DATA ANALYSIS

3.1. General Considerations

The $\Theta^+\bar{K}^0$ system in the reaction (4) can have the final states presented in Table 1. Typical energy of K^0_L for the processes under study is ∼15 GeV. The decay length of K^0_L was more than 450 m on average; thus, it can be regarded as a stable particle and reconstructed as a neutral cluster in ECAL or NCAL in the same way as a neutron. The last two final states in Table 1 have only one charged track and are unavailable at SPHINX due to trigger restrictions, while the others

---

[3)] Here and below, we use N instead of C(N) in the reaction notation. We do not distinguish the processes on C nuclei and quasifree nucleons in this work. However, they can be easily separated using the P_T^2 distribution.

Table 1. Possible final states of the $\Theta^+\bar{K}^0$ system in the reaction (4) (it is assumed that the Θ^+ baryon has only two modes of decay with equal probabilities; only $\pi^+\pi^-$ decays of K_S^0 meson are considered)

Physical states and branching ratio				Experimental final state	Total branching ratio	Available at SPHINX
1	1/2	1/4	1/8			
		$[nK^+]K_S^0$		$nK^+\pi^+\pi^-$	$(1/4)\cdot 0.69$	Yes
	$\Theta^+K_S^0$					
			$[pK_S^0]K_S^0$	$p\pi^+\pi^-\pi^+\pi^-$	$(1/8)\cdot 0.47$	Yes
		$[pK^0]K_S^0$				
			$[pK_L^0]K_S^0$	$pK_L^0\pi^+\pi^-$	$(1/8)\cdot 0.69$	Yes
$\Theta^+\bar{K}^0$						
			$[pK_S^0]K_L^0$	$pK_L^0\pi^+\pi^-$	$(1/8)\cdot 0.69$	Yes
		$[pK^0]K_L^0$				
			$[pK_L^0]K_L^0$		1/8	No
	$\Theta^+K_L^0$					
		$[nK^+]K_L^0$			1/4	No

were detected by three- and five-track triggers, which had the following structure (for notation, see Fig. 1 of [33]):

$$T_{(3)} = T_0 \times H_3(0\text{–}1) \times H_4(2\text{–}3) \times H_6(\equiv 3) \times H_7(1\text{–}3), \quad (5)$$

$$T_{(5)} = T_0 \times H_3(0\text{–}1) \times H_4(4\text{–}5) \times H_6(\equiv 5) \times H_7(3\text{–}6), \quad (6)$$

where pretrigger $T_0 = S_1S_2S_3S_4 \times (\overline{B_1B_2}) \times \bar{A}_{5-8}$ and $H_i(m_1 - m_2)$ means the multiplicity requirement between m_1 and m_2 for the number of hits in hodoscope H_i. For technical reasons, the five-track trigger was implemented not from the very beginning of the run, resulting in a lower luminosity for this kind of trigger. In addition, a simple beam trigger T_{beam}, which was a greatly prescaled ($\approx 16\,000$) fourfold coincidence $S_1S_2S_3S_4$, was written throughout the run.

Four experimentally available final states of the $\Theta^+\bar{K}^0$ initial state have different and to some extent complementary properties, which are (together with the simulated characteristics of the SPHINX detector) summarized below:

$[nK^+]K_S^0$: Definite strangeness, large branching ratio, moderate effective-mass resolution, $\Lambda(1520) \to nK_S^0$ calibration decay in the same final state, but neutron should be detected, background from $\Lambda(1520)$.

$[pK_S^0]K_L^0$: The best effective-mass resolution, moderate branching ratio, $\phi \to K_S^0K_L^0$ calibration decay in the same final state, but indefinite strangeness, K_L^0 should be detected, background from ϕ.

$[pK_L^0]K_S^0$: Moderate branching ratio, $\phi \to K_S^0K_L^0$ calibration decay in the same final state, but indefinite strangeness, worst effective-mass resolution, K_L^0 should be detected, background from ϕ.

$[pK_S^0]K_S^0$: No neutral particles in the final state (thus an additional constraint on the total energy in the event), moderate effective-mass resolution, no or small background from the known particles, but indefinite strangeness, small branching ratio and low efficiency (five tracks, two weak decays), lower luminosity.

For all but the $[pK_S^0]K_S^0$ final state, a neutral hadron (K_L or n) should be reconstructed. In the SPHINX detector, approximately 65% of neutrons and a somewhat lower fraction of K_L^0 interact in ECAL, giving highly fluctuating hadron showers with a typical visual energy release of $\sim 20\%$ of their total energy. All the others are totally absorbed in NCAL except for a small fraction ($\sim$5%), interacting in dead material in between. For neutral hadrons interacting in ECAL, only coordinates can be measured; the hadron energy should be calculated using the exclusivity of the event. On the contrary, for neutral hadrons in NCAL, both coordinates and energy can be measured in one detector, giving an additional constraint on the exclusivity of the event. However, it was found by the Monte Carlo (MC) simulation and verified with the study of $\Lambda(1520) \to nK^0_S$ decays that the method of neutral-hadron reconstruction in ECAL gives better effective-mass resolution for the nK^+ and pK^0_L systems due to the excellent ability of the SPHINX setup to isolate exclusive processes and negligible momentum spread of the diffractively produced proton beam. In addition, the sample of events with ECAL neutral hadrons is more than two times bigger. Only the sample of events with $n(K^0_L)$ in interacting ECAL is used in this work. The sample of events with $n(K^0_L)$ in NCAL was our strategic reserve and was planned to be used as a control one in the case of Θ^+ observation.

Being products of the decay of the same initial state, the experimental final states (Table 1) have different final particle sets and even different multiplicities. In order to have conclusive results, a careful relative normalization and calibration is needed for all reactions under study, including the reactions selected by different triggers. It was provided by studying the reactions

$$p + N \to \Lambda(1520)K^+ + N \tag{7}$$

and

$$p + N \to p\phi + N, \tag{8}$$

and then using different decay modes of the ϕ meson and especially those of the $\Lambda(1520)$ hyperon, which has a lot of well-measured decay modes [35] with quite different topologies and multiplicities. With all this in mind, the following strategy was adopted:

Step 1: Use beam trigger (minibias events) to investigate the ability of the setup to isolate exclusive processes, the ability of the MC simulation to reproduce trigger conditions for the main types of trigger. High-intensity reactions like $p + N \to p\pi^+\pi^- + N$ and $p + N \to p\pi^+\pi^-\pi^0 + N$ can be used for this study.

Step 2: Develop MC generators for the simulation of exclusive production of $\Lambda(1520)K^+$ and $p\phi$ systems [reactions (7), (8)] and adjust them to reproduce the experimentally measured kinematics for decay modes with large statistics, $\Lambda(1520) \to pK^-$ (21 k events) and $\phi \to K^+K^-$ (10 k events).

Step 3: Understand the ability of the setup to isolate and reconstruct exclusive reactions with neutral hadrons (n, K^0_L) in the final state. It can be done comparing the generated and reconstructed reactions with $\Lambda(1520) \to nK^0_S$ and $\phi \to K^0_S K^0_L$ decays.

Step 4: Understand the ability of the setup to isolate and reconstruct the exclusive reactions with five tracks in the final state using the decay $\Lambda(1520) \to \Lambda\pi^+\pi^-$.

Step 5: In addition, verify the ability of the setup to reconstruct as wide a set of the different topologies of the final state as possible by using generated and reconstructed decays of $\Lambda(1520)$ to $\Sigma^+\pi^-$, $\Sigma^0\pi^0$, and $\Sigma^-\pi^+$.

In other words, the plan was to study the whole set of calibration reactions,

$$\begin{aligned} p + N &\to p\pi^+\pi^- + N, \qquad (9)\\ p + N &\to p\pi^+\pi^-\pi^0 + N,\\ p + N &\to pK^+K^- + N,\\ p + N &\to [nK^0_S]K^+ + N,\\ p + N &\to p[K^0_S K^0_L] + N,\\ p + N &\to [\Lambda\pi^+\pi^-]K^+ + N,\\ p + N &\to [\Sigma^+\pi^-]K^+ + N,\\ p + N &\to [\Sigma^-\pi^+]K^+ + N,\\ p + N &\to [\Sigma^0\pi^0]K^+ + N, \end{aligned}$$

for different purposes and in a certain order. Only after steps 1–5 are successfully done should we start to look for Θ^+ in the set of signal reactions:

$$\begin{aligned} p + N &\to [nK^+]K^0_S + N, \qquad (10)\\ p + N &\to [pK^0_S]K^0_L + N,\\ p + N &\to [pK^0_L]K^0_S + N,\\ p + N &\to [pK^0_S]K^0_S + N, \end{aligned}$$

some of them being part of the calibration set. If existent and produced in the process under study, Θ^+ should emerge simultaneously in all four final states in accordance with their relative probabilities and efficiencies.

3.2. Study of Calibration Reactions

The first step in the analysis is illustrated by Fig. 1. All T_{beam} events were reconstructed with a standard tracking program requiring at least one track after the magnet. The events with exactly two positive and one negative track after the magnet were then selected, and this sample of unbiased events was used to study the efficiency of trigger elements and the trigger itself ($T_{(3)}$ in this case). The peak in total energy at 70 GeV corresponds to exclusive events mainly of the $p\pi^+\pi^-$ type, and the inelastic background after imposing trigger simulation cuts and simple additional ones is quite small. This figure also demonstrates that interactions in targets can be easily isolated with a small background. Only events with a primary vertex in the carbon target were used in further study. The sample

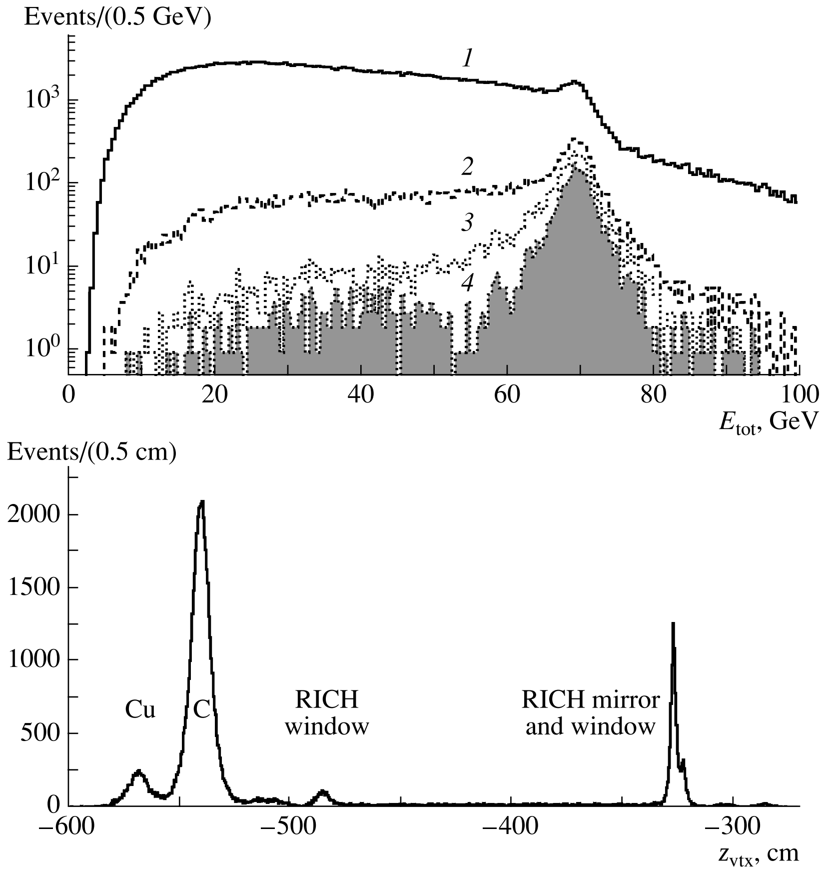

Fig. 1. Events from the beam trigger. (Upper panel) Total energy of secondary tracks for (*1*) all two-positive/one-negative-track events, (*2*) with trigger ($T_{(3)}$) simulation cuts, (*3*) no neutral clusters in ECAL, (*4*) good primary vertex in targets. (Lower panel) z Coordinate of good primary vertex for case *3* of the upper panel.

of events from the copper target was again left as a control one.

To study the production characteristics of reactions (7) and (8), which was the subject of the second step, the events of the reaction $p + N \to [pK^+K^-] + N$ were selected from the $T_{(3)}$ trigger sample using the following criteria:

two positive and one negative track after the magnet;

good primary vertex in the carbon target;

no neutral clusters with $E > 1$ GeV in ECAL;

energy balance, $65 < E_{\rm tot} = E_1 + E_2 + E_3 < 75$ GeV;

the momentum of any secondary particle >5 GeV/c;

identification in RICH as a pK^+K^- system.

The procedure of identification of the final state by the RICH detector was described in our previous publications (see [36] for details) and will not be discussed here. More than 160 000 events passed the selections cuts and results are presented in Fig. 2. The peaks from $\Lambda(1520) \to pK^-$ and $\phi \to K^+K^-$ decays can be clearly seen together with other well-known structures.

The events from $\Lambda(1520)$ and ϕ peaks after background subtraction were used to study the production characteristics of the $\Lambda(1520)K^+$ and $p\phi$ systems and to develop MC generators for the simulation of the reactions (7) and (8).

The simulation of signal and normalization processes in the SPHINX setup was done in the framework of the GEANT 3.21 package. This included, in particular,

detailed description of geometry and material of the setup including, for example, individual wires in drift tubes;

realistic simulation of the efficiencies of trigger elements;

simulation of experimentally measured inefficiency of tracking devices (PC and DT), including inefficiency in the beam region;

propagation of all secondary particles generated by GEANT, including electromagnetic and hadron showers in the γ spectrometer;

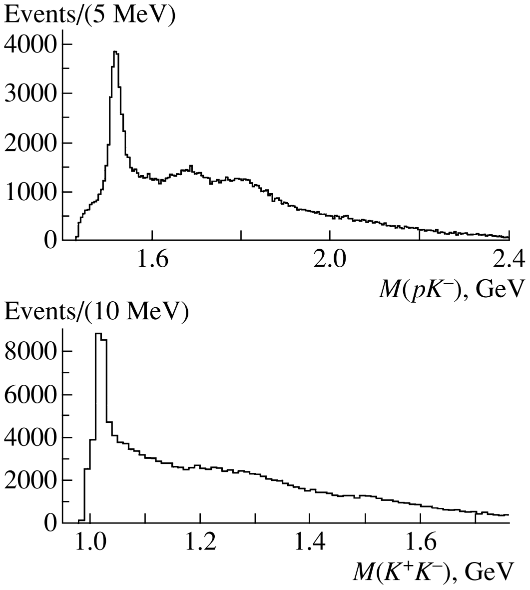

Fig. 2. Effective-mass distributions $M(pK^-)$ and $M(K^+K^-)$ for the reaction $p+N \to pK^+K^- + N$ after applying selection cuts described in the text.

simulation of the multibeam events with more than one beam particle within the ±600-ns time window of the main process and then realistic simulation of signal development in various detectors.

The simulation of the events was done up to the level of digitized detector responses so that they were processed in exactly the same way as real events.

After a few iterations, it was possible to reproduce the experimentally observed characteristics of $\Lambda(1520)K^+$ and $p\phi$ production with a reasonable accuracy. The variables studied were the mass M of the system $\Lambda(1520)K^+(p\phi)$, the transverse momentum squared P_T^2, and the angles (θ^*, ϕ^*) of $\Lambda(1520)(\phi)$ in the $\Lambda(1520)K^+(p\phi)$ rest frame (Gottfried–Jackson reference frame). The comparison of experimental and MC distributions (after passing the analysis chain) is presented in Fig. 3 for $\Lambda(1520)K^+$ production. The distributions for the $p\phi$ system are quite similar, as was already observed in our earlier work [24]. Both systems exhibit low-mass enhancement and distinct evidence for the coherent production on the carbon nuclei (see P_T^2 distribution). The most significant difference between the two systems is a $\cos\theta^*$ distribution, which for $p\phi$ is flatter. The detailed study showed, however, that the efficiency for the processes under study is quite insensitive to P_T^2 (up to $\approx 2\,\mathrm{GeV}^2/c^2$) and the production angles of the resulting $NK\bar{K}$ system. For example, for a flat $\cos\theta^*$ distribution for the production of the $\Lambda(1520)K^+$ system, the overall efficiency only changes from 10.5 to 11%.

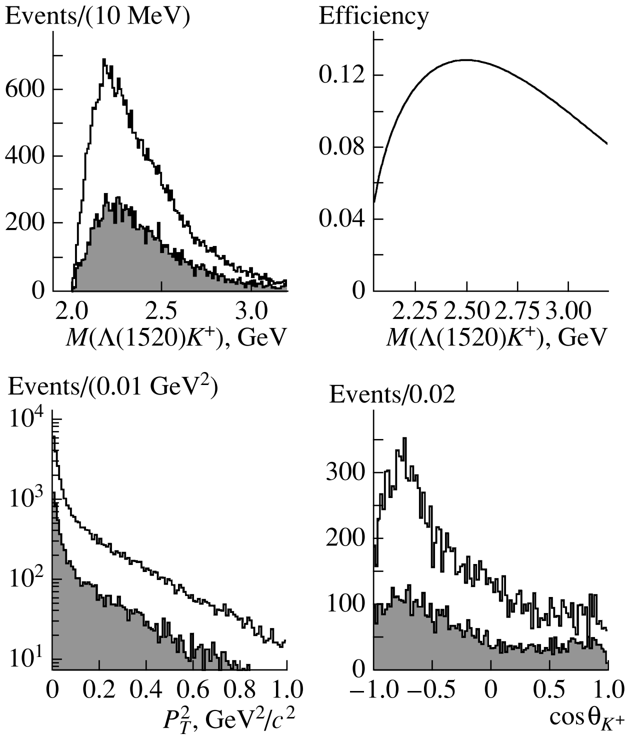

Fig. 3. A comparison of reconstructed and simulated distributions for the reaction $p+N \to \Lambda(1520)K^+ + N$ with $\Lambda(1520) \to pK^-$ decay. Open histogram represents data; hatched histogram, MC (only a small fraction of MC events are used in this picture). Also is shown the efficiency.

With generators at hand, it was then possible to simulate other decay channels of $\Lambda(1520)$ and ϕ and to compare the results of the simulation with experimental distributions.

The events corresponding to the reaction

$$p + N \to nK_S^0K^+ + N \qquad (11)$$

were selected from the three-track sample as follows:

A good secondary decay vertex lies in the allowed region: $-520 < z_{\mathrm{sec}} < -270$ cm.

A good primary vertex, composed of the vee vector, unpaired secondary track, and beam track, is in the carbon target: $-555 < z_{\mathrm{prim}} < -525$ cm.

$l/\sigma_z > 3$, where $l = z_{\mathrm{sec}} - z_{\mathrm{prim}}$ and σ_z is the calculated accuracy for this quantity.

Missing energy $E_{\mathrm{miss}} = E_{\mathrm{beam}} - E_{\pi^+} - E_{\pi^-} - E_{K^+} > 5$ GeV.

There is only one neutral cluster in ECAL with $E > 1$ GeV.

The momentum of the unpaired positive track is >5 GeV/c.

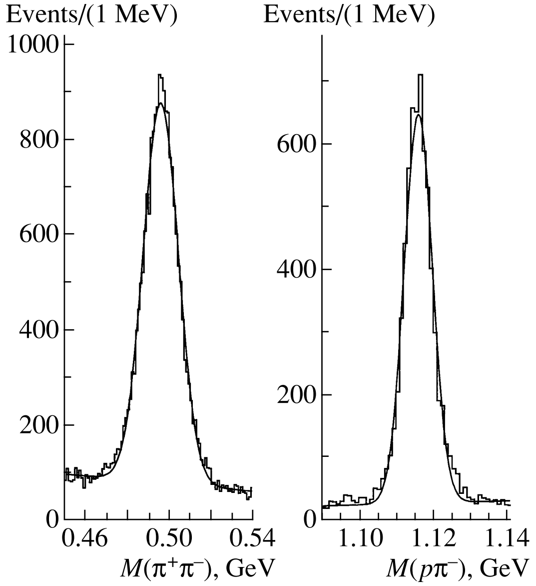

Fig. 4. Signals from decays of $K^0_S \to \pi^+\pi^-$ and $\Lambda \to p\pi^-$ in the reactions $p + N \to nK^0_S K^+ + N$ and $p + N \to \Lambda\pi^+\pi^-K^+ + N$. The fit gives $M(K^0_S) =$ 496 MeV, $\sigma(K^0_S) = 8.4$ MeV, $M(\Lambda) = 1116$ MeV, and $\sigma(\Lambda) = 3.8$ MeV.

RICH readings are consistent with the hypothesis that the negative and positive tracks forming the secondary vertex are pions and the remaining track is a kaon.

The effective mass $M(\pi^+\pi^-)$ is within $\pm 2.5\sigma$ of the K^0_S-peak value.

The events corresponding to the reaction

$$p + N \to pK^0_S K^0_L + N \tag{12}$$

were selected in exactly the same way with the evident exchange kaon ↔ proton in the identification requirement. Approximately 20 000 (30 000) events of $nK^0_S K^+ (pK^0_S K^0_L)$ type were thus selected. The mass spectrum $\pi^+\pi^-$ for the $nK^0_S K^+$ system before the final K^0_S selection cut is shown in Fig. 4.

The energy of n (or K^0_L, with the evident changes in formulas) is calculated as $E_n = E_{\text{beam}} - E_{K^0_S} - E_{K^+}$ and the direction of flight of the neutron is calculated using coordinates of the ECAL cluster and primary vertex. The effective mass of the nK^0_S system is then calculated using the tabular value of the K^0_S mass as

$$\begin{aligned} M(nK^0_S) &= M(n\pi^+\pi^-) \\ &- M(\pi^+\pi^-) + M(K^0_S). \end{aligned} \tag{13}$$

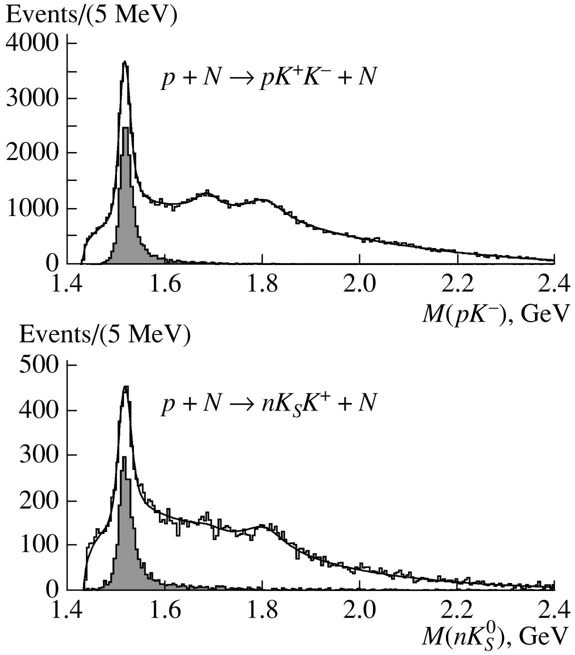

Fig. 5. Effective-mass distributions $M(pK^-)$ and $M(nK^0_S)$ for the reaction $p + N \to [N\bar{K}]K^+ + N$. MC-simulated signals for $\Lambda(1520)$ are shown hatched.

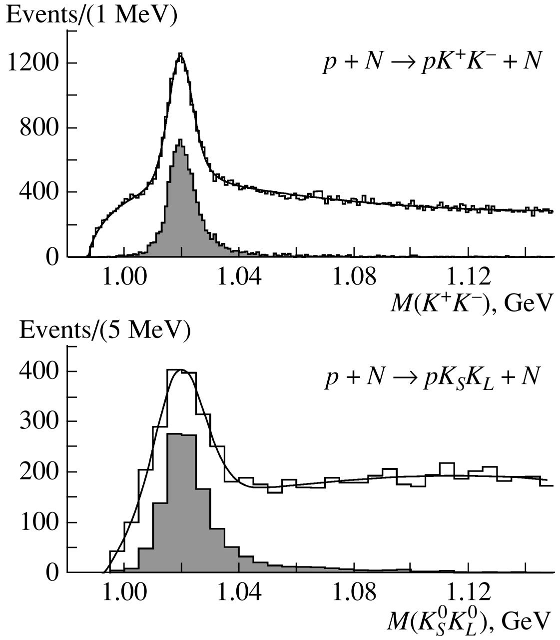

Fig. 6. Effective-mass distributions $M(K^+K^-)$ and $M(K^0_SK^0_L)$ for the reaction $p + N \to p[K\bar{K}] + N$. MC-simulated signals for ϕ are shown hatched.

In a threshold region, this gives an improvement in the resolution by 20–30%, in agreement with the MC simulation. The resulting mass spectra $M(nK^0_S)$ and $M(K^0_SK^0_L)$ are presented in Figs. 5 and 6. We observe a good qualitative agreement in the form of spectra for different final states and also between resonance sig-

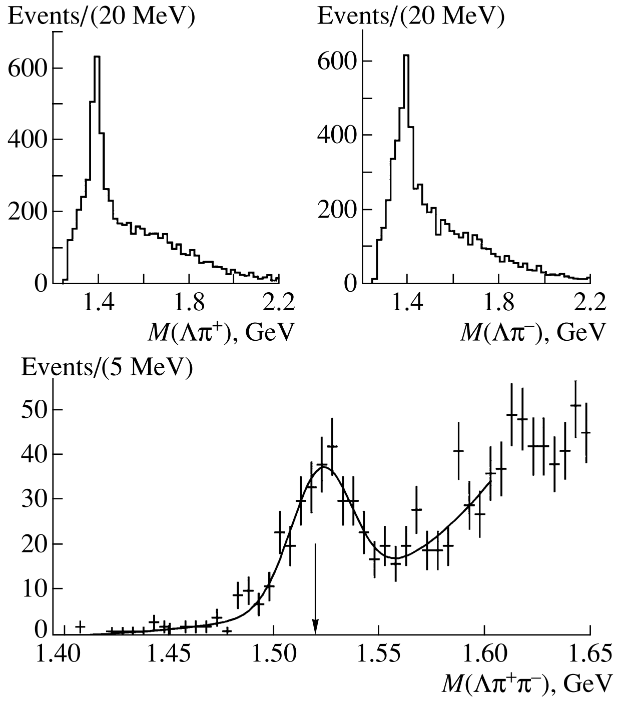

Fig. 7. Effective-mass distributions $M(\Lambda\pi^+)$, $M(\Lambda\pi^-)$, and $M(\Lambda\pi^+\pi^-)$ for the reaction $p + N \to \Lambda\pi^+\pi^-K^+ + N$. The peaks of $\Sigma^+(1385)$ and $\Sigma^-(1385)$ are clearly seen (upper pictures). The arrow shows the nominal mass of $\Lambda(1520)$.

nals in the data and MC simulation. The agreement is also good numerically, as will be shown later.

The reaction

$$p + N \to \Lambda(1520)K^+ + N, \ \ \Lambda(1520) \to \Lambda\pi^+\pi^- \tag{14}$$

is a main calibration process for the five-track trigger. It allows us to cross-check the simulation for three- and five-track events and connect the $pK_S^0K_S^0$ decay mode of the $\Theta^+\bar{K}^0$ system to all the others. The events were selected from the five-track trigger sample as follows:

Five secondary tracks with $\sum Q_i = 1$.

No neutral clusters with $E > 1$ GeV in ECAL.

The total energy of all five particles corresponds to the energy of the incident proton: $65 < E_{\text{tot}} < 75$ GeV.

Only one good secondary vertex in the allowed region.

A good primary vertex composed of vee tracks and three other tracks is in the carbon target.

$l/\sigma_z > 3$.

RICH readings are consistent with the hypothesis that one of the unpaired positive tracks with momentum >5 GeV is a kaon.

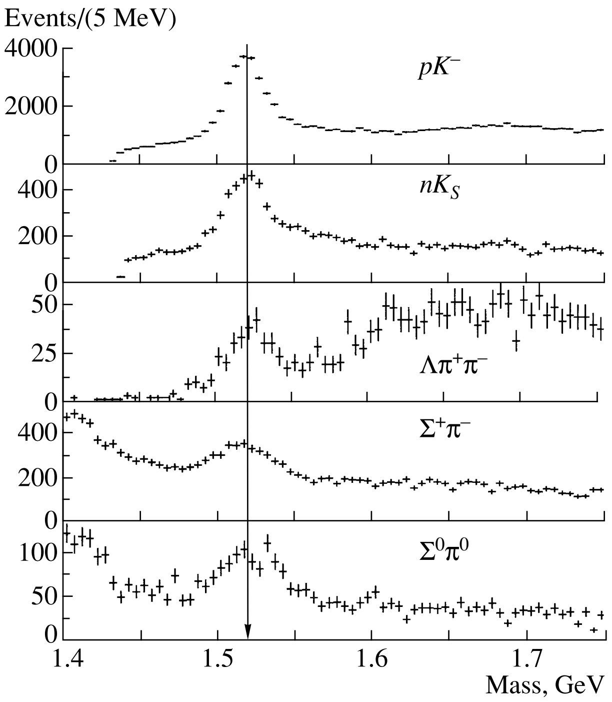

Fig. 8. Mass spectra for different decay modes of $\Lambda(1520)$ in the reaction $p + N \to \Lambda(1520)K^+ + N$. The arrow shows the nominal mass of $\Lambda(1520)$.

The effective mass of $p\pi^-$ combination is within $\pm 2.5\ \sigma$ of the Λ-peak value.

Events of the $pK_S^0K_S^0$ final state were selected in a similar way, demanding two (instead of one) different secondary vertices and the lone unpaired positive track identified as being consistent with the proton hypothesis. Both $\pi^+\pi^-$ combinations were then required to be within $\pm 2.5\ \sigma$ of the K_S^0-peak value.

The quality of the Λ signal for the $\Lambda\pi^+\pi^-K^+$ final state can be seen in Fig. 4 and mass spectra for some subsystems are shown in Fig. 7. The reaction is dominated by the production of the $\Sigma^{\pm}(1385)\pi^{\mp}K^+$ system. The peak from $\Lambda(1520)$ in the $\Lambda\pi^+\pi^-$ effective-mass spectrum is clearly seen and the number of events is sufficient to make quantitative conclusions. Figure 8 represents the summary of the results in the study of the $\Lambda(1520)K^+$ production in different decay modes. Two more decay modes are included, $\Lambda(1520) \to \Sigma^+\pi^-$ and $\Lambda(1520) \to \Sigma^0\pi^0$, with $\Sigma^+ \to p\pi^0$ and $\Sigma^0 \to \Lambda\gamma, \Lambda \to p\pi^-$ decays, corresponding to the topologies "kink + 2γ" and "vee + 3γ." The details of the data processing for these modes will not be discussed here. This figure can be used to estimate the systematics of the mass scale for quite different topologies and final particle sets.

Up to now, the results have been presented at a qualitative level. Now we turn to the discussion of

Table 2. Results of the fits of mass spectra in Figs. 5 and 6; also the efficiencies (assuming $\mathrm{BR}(K_S^0 \to \pi^+\pi^-) = 100\%$ for the decay modes with K_S^0) and experimental (Monte Carlo) resolution are shown (the number of events corresponds to fits with experimental resolution); for the meaning of cross section values see text

Particle	Final state	Events	ε, %	Resolution σ, MeV	$\sigma_{\mathrm{meas}}(\sigma_{\mathrm{corr}})$, nb/nucleon
$\Lambda(1520)$	$[pK^-]K^+$	$21\,200 \pm 300$	10.5	8.1(7.1)	1015(1400)
	$[nK_S^0]K^+$	2490 ± 90	3.8	9.8(8.8)	965
$\phi(1020)$	$[K^+K^-]p$	$10\,660 \pm 190$	12.1	3.4(3.5)	202(279*)
	$[K_S^0K_L^0]p$	1440 ± 80	3.7	7.8(6.6)	188

the numerical results for calibration processes. To estimate the number of events, the mass spectra in Figs. 5 and 6 were fitted by a sum of resonance and smooth background. The peaks of $\Lambda(1520)$ and ϕ were described by the relativistic Breit–Wigner function with orbital momenta $L = 2$ and $L = 1$ smeared by Gaussian resolution. Widths of the resonances were fixed by world average values. Two other peaks in the pK^- mass spectrum are known to contain a lot of Λ^*/Σ^* states and were described by two simple Breit–Wigner functions with free parameters for mass and width. The background was chosen to have the form of $P_1(\Delta M)^{P_2} \exp(-P_3\Delta M - P_4\Delta M^2)$ with free parameters P_i, $\Delta M = M - M_{\mathrm{thr}}$, and threshold mass $M_{\mathrm{thr}} = M_N + M_K$. The resolution parameter of the Gaussian function was either free or fixed by the MC value. The results of fits are presented in Table 2.

The errors in the number of events are statistical. The systematic uncertainties include an uncertainty associated with the background description (polynomial function instead of exponential with a smaller fitting range in mass), Gaussian resolution (experimental or MC), and uncertainties in the PDG parameters of the $\Lambda(1520)$ and ϕ resonant width. Added in quadrature, these do not exceed 4 (8)% for the modes with high (low) statistics.

As a first check of the consistency of the results, we can calculate the relative branching for different decay modes. For $\Lambda(1520)$, we have

$$\frac{\mathrm{BR}[\Lambda(1520) \to n\bar{K}^0]}{\mathrm{BR}[\Lambda(1520) \to pK^-]} \tag{15}$$

$$= \frac{2N[\Lambda(1520) \to nK_S^0]/\mathrm{BR}[K_S^0 \to \pi^+\pi^-]}{N[\Lambda(1520) \to pK^-]} \frac{\varepsilon_{pK^-}}{\varepsilon_{nK_S^0}}$$

$$= \frac{2 \cdot 2490/0.686}{21200} \frac{10.5}{3.8} = 0.94 \pm 0.08,$$

which is very close to unity, as it should be. For ϕ-meson decays, we have

$$\frac{\mathrm{BR}[\phi \to K_S^0K_L^0]}{\mathrm{BR}[\phi \to K^+K^-]} \tag{16}$$

$$= \frac{N[\phi \to K_S^0K_L^0]/\mathrm{BR}[K_S^0 \to \pi^+\pi^-]}{N[\phi \to K^+K^-]} \frac{\varepsilon_{K^+K^-}}{\varepsilon_{K_S^0K_L^0}}$$

$$= \frac{1440/0.686}{10660} \frac{12.1}{3.7} = 0.64 \pm 0.06,$$

which again is close to the tabular value 0.693 ± 0.018. We can conclude, therefore, that the processes with neutron and K_L^0 in the final state can be reproduced at SPHINX with a relative accuracy better than 10%. This is also true for other decay modes of $\Lambda(1520)$ not shown in the table, including the "five-track" calibration decay $\Lambda(1520) \to \Lambda\pi^+\pi^-$, however, with a little bit worse accuracy. It should be noted, in addition, that MC and experimental effective-mass resolutions are close to each other, the MC resolution being typically a little bit better. This is important in the search for narrow states, where the estimations rely heavily on the resolution.

Another question of major importance is the absolute calibration of cross sections. In most of the models, the cross section for the production of the Θ^+ baryon in a wide class of exclusive processes is directly proportional to its width, being governed by the same constant $g^2_{\Theta NK}$. The cross section for $\Lambda(1520)K^+$ and $p\phi$ production was calculated as $\sigma = (1/L)N/(\mathrm{BR} \cdot \varepsilon)$, where luminosity L per nucleon was estimated assuming $A^{2/3}$ dependence of the cross section on the mass number. The luminosity for the carbon target was found to be 884 events/nb for $T_{(3)}$ and 445 events/nb for $T_{(5)}$. The measured cross sections σ_{meas} can be found in Table 2. The data is preliminary, as not all corrections common to all processes and not influencing the relative quantities like (15) and (16) were included in efficiency calculations. These corrections include, for example,

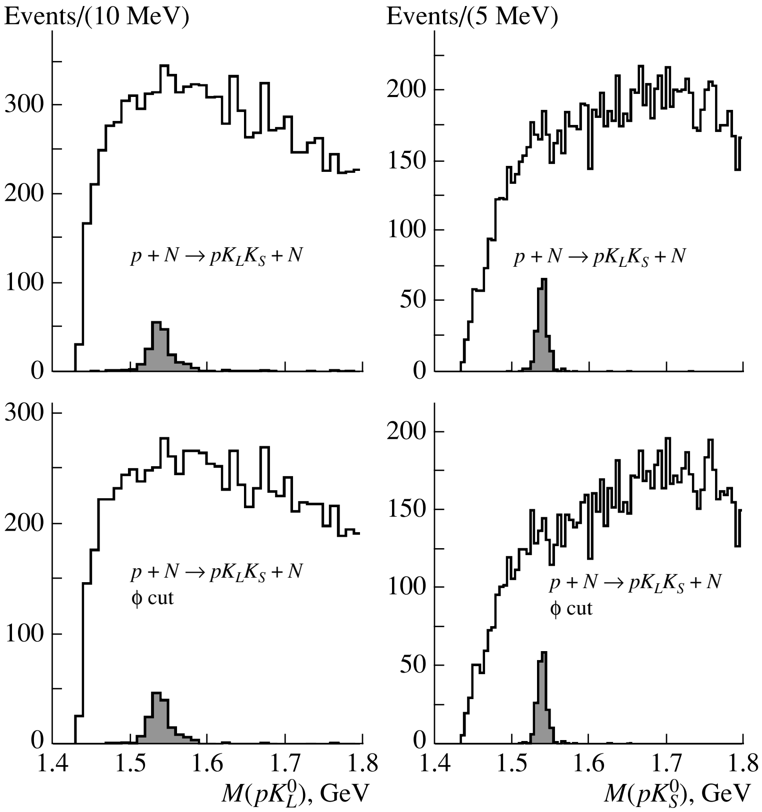

Fig. 9. Effective-mass spectra of pK_L^0 and pK_S^0 systems in the reaction $p+N \to pK_S^0K_L^0+N$ with ($M(K_S^0K_L^0) > 1.04$ GeV, lower row) and without (upper row) "ϕ cut." MC-simulated signals (hatched) correspond to $\sigma_{\Theta^+\bar{K}^0}/\sigma_{\Lambda(1520)K^+} = 0.1$.

rate-dependent accidentals in veto counters. In general, they are small and are under study now. Can we check the cross-section values from independent measurements? As far as we know, there are no data on the exclusive production of the $\Lambda(1520)K^+$ system in nucleon–nucleon (nucleus) interactions and our result seems to be the first one of this kind. The existing data for ϕ-meson production in the reaction $pp \to \phi pp$ are scarce and do not allow extrapolation to our energy. However, we can use the data for reaction $pp \to \omega pp$, which exist at higher as well as lower energies. The analysis done in [37] allows us to extrapolate to our energy, giving the value $(36 \pm 4)/2 = 18 \pm 2$ μb/nucleon for the ωp forward-hemisphere production cross section. Using then the cross-section ratio $\sigma_\phi/\sigma_\omega = (1.55 \pm 0.31) \times 10^{-2}$, measured in our study of the OZI rule [38], we arrived at the prediction for ϕp-production cross section $\sigma_{\phi p} = 279 \pm 64$ nb/nucleon. This value is close to, but somewhat higher than, $\sigma_{\text{meas}} = 202$ nb/nucleon (Table 2). Being conservative, we used this (higher) cross section as input. It is denoted by the asterisk in Table 2. The correction factor $k_{\text{corr}} = 279/202 = 1.38$ was used then to calculate the corrected cross section for the $\Lambda(1520)K^+$ production in Table 2. The same conservative correction factor will be used later in the estimations of the absolute cross section for the Θ^+ production.

3.3. Study of Signal Reactions

The calibration reactions (12) and (11) are at the same time the reactions where the Θ^+ baryon can be sought. Effective-mass spectra $M(pK_L^0)$ and $M(pK_S^0)$ for the reaction (12) are shown in Fig. 9 and mass spectrum $M(nK^+)$ for the reaction (11) is shown in Fig. 10. No evident structures can be seen in these distributions, except for a hint on a shoulder in the pK_S^0 mass spectrum at a mass of ≈1510 MeV. However, this structure is completely absent in the $M(pK_L^0)$ mass spectrum as well as in the $M(nK^+)$ mass spectrum. Thus, we do not see the signals for the Θ^+ baryon and only upper limits can be produced from these distributions.

We are searching for narrow signals and will assume that effective-mass distributions are completely dominated by experimental resolutions for each of the systems under study. This assumption is valid for the width (FWHM) of the Θ^+ baryon <6–10 MeV. A width like that or lower is indicated in most precise

Table 3. Upper limits for reactions $p + N \to \Theta^+\bar{K}^0 + N$ and $p + N \to \Theta^{++}K^- + N$ at $E_p = 70$ GeV (the number of events corresponds to the fit of the distributions with smooth background function plus Gaussian with $M = 1540$ MeV and MC resolution; the efficiencies were calculated assuming $\mathrm{BR}(K^0_S \to \pi^+\pi^-) = 100\%$)

Particle	Final state	Events	ε, %	Resolution (σ), MeV	σ_{corr} (90% C.L.) nb/nucleon
$\Theta^+(1540)$	$[nK^+]K^0_S$	55 ± 43	3.3	9.8	<32
		10 ± 33 (Λ_{1520} cut)	2.2	10.1	<26
	$[pK^0_S]K^0_L$	48 ± 29	3.0	5.8	<53
		26 ± 25 (ϕ cut)	2.7	5.5	<42
	$[pK^0_L]K^0_S$	6 ± 43	2.6	11.8	<54
		-14 ± 37 (ϕ cut)	2.3	11.3	<39
	$[pK^0_S]K^0_S$	-4 ± 7	0.9	7.5	<52
$\Theta^{++}(1540)$	$[pK^+]K^-$	-57 ± 100	10.0	8.0	<2

"positive evidence" experiments and the assumption does not seem to be limiting. To achieve the limits on the number of events and then on production cross sections, the resolution and efficiency for each of the final states are needed. These can be estimated only by MC simulation. However, the production mechanism for the Θ^+ baryon is unknown, so some model is needed to simulate its production. We simulate the production of the Θ^+K^0 system as being similar to that of the $\Lambda(1520)K^+$ and $p\phi$ systems (P_T^2 and $M(\Theta^+\bar{K}^0)$), and the distributions of the decay angles of the Θ^+K^0 system in the Gottfried–Jackson frame were assumed to be isotropic. The assumptions about production characteristics are not as limiting as they seem. The efficiencies demonstrate a very weak dependence on P_T^2 and decay angles (see the discussion about the simulation of the $\Lambda(1520)K^+$ production above), and only if Θ^+ is preferred to originate from the Θ^+K^0 system with very big mass ($\geq$3.5 GeV) and very high P_T would the efficiency for the Θ^+K^0-system detection be significantly overestimated.

The results of the simulation of an interesting case of the $pK^0_SK^0_S$ final state in comparison with the real data are shown in Fig. 11, and one-dimensional plots used to set the upper limits are shown in Fig. 12.

We also made a search for the $\Theta^{++}(1540)$ baryon in the reaction $p + N \to \Theta^{++}K^- + N, \Theta^{++} \to pK^+$. This state emerges as a partner of Θ^+ in some theoretical models. The study was a by-product of the investigation of the calibration reaction $p + N \to pK^+K^- + N$. The pK^+ effective-mass distributions are shown in Fig. 13 for all events, for the events with "$\Lambda(1520)$ cut" (the events with $1.50 < M(pK^-) < 1.55$ GeV were excluded), and for the events with combined "$(\Lambda(1520) + \phi)$ cut," where in addition the events with $1.01 < M(K^+K^-) < 1.03$ GeV were excluded. Neither distribution shows a statistically significant signal and only the upper limits can be set for the $\Theta^{++}K^-$ production.

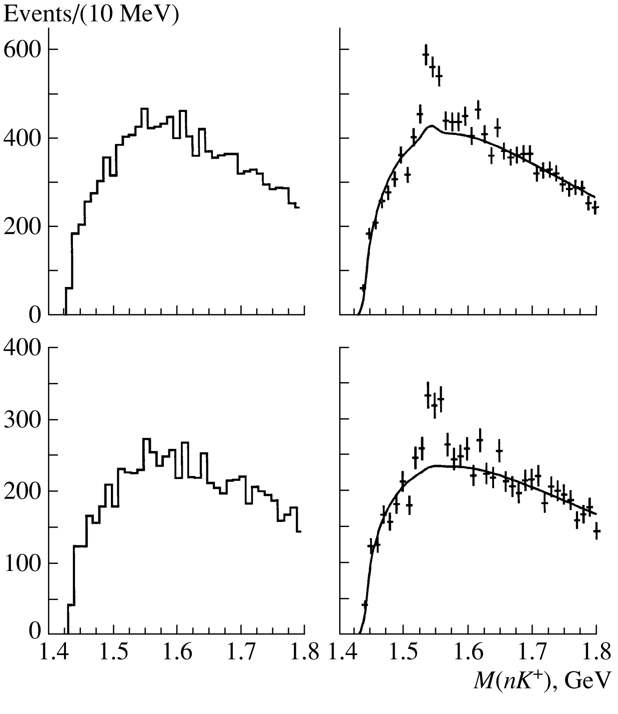

Fig. 10. Effective-mass spectrum of nK^+ in the reaction $p + N \to nK^+K^0_S + N$ with ($M(nK^0_S) > 1.55$ MeV, lower row) and without (upper row) "$\Lambda(1520)$ cut." Pictures on the right panel are the sums of real data and MC-simulated signals for $\sigma_{\Theta^+\bar{K}^0}/\sigma_{\Lambda(1520)K^+} = 0.1$. Curves in the right column are the results of the fit of left column distributions.

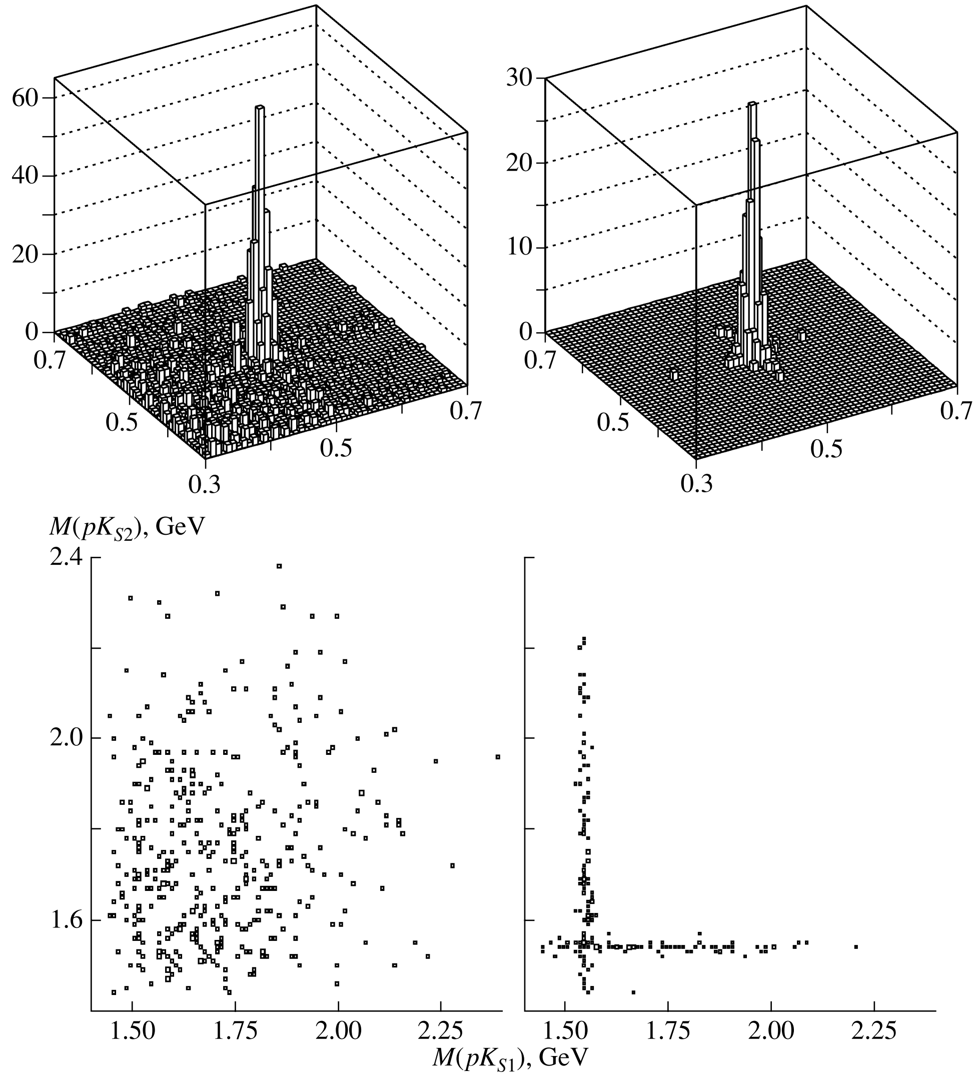

Fig. 11. Distributions for the reaction $p + N \to pK^0_S K^0_S + N$. (Upper row) $M(\pi_1^+\pi_2^-)$ vs. $M(\pi_3^+\pi_4^-)$ with all cuts but K^0_S selection cut. (Lower row) $M(pK^0_{S2})$ vs. $M(pK^0_{S1})$ after all cuts: (left column) data, (right column) MC simulation of reaction $p + N \to \Theta^+\bar{K}^0 + N$, $\Theta^+\bar{K}^0 \to [pK^0_S]K^0_S$.

To get the limit on the number of events from the distributions in Figs. 9, 10, 12, and 13, we tried two different methods. In the first method, the distributions were fitted by a smooth curve plus a Gaussian function with fixed mass and resolution determined by MC simulation for a particular final state. The 90%-C.L. upper limits for the number of events were then estimated in a usual way. In the second method, the events in the mass window near the presumed signal region were excluded from the fit and 90%-C.L. upper limits were calculated as $N = \max(0, \Delta n) + 1.28\sqrt{b}$ with Δn being the excess over the estimated background b. The mass window was from 20 MeV for the $[pK^0_S]K^0_L$ system to 40 MeV for the $[pK^0_L]K^0_S$ one. To understand the systematics, we varied the fitting range and background function. In the first method, we also made fits with MC resolution enlarged by 1 MeV. Both methods give similar results with no more than 20% difference in upper limits. In the rest of the paper, we use the results from the first method.

4. RESULTS

Our results in the search for narrow exotic baryons are presented in Table 3, where efficiencies, Gaussian resolutions, fitted number of events, and upper limits on cross section for the reactions $p + N \to \Theta^+\bar{K}^0 + N$ and $p + N \to \Theta^{++}K^- + N$ can be found.

The upper limits for production cross sections are preliminary. They were calculated from the upper limits on the number of events using the procedure de-

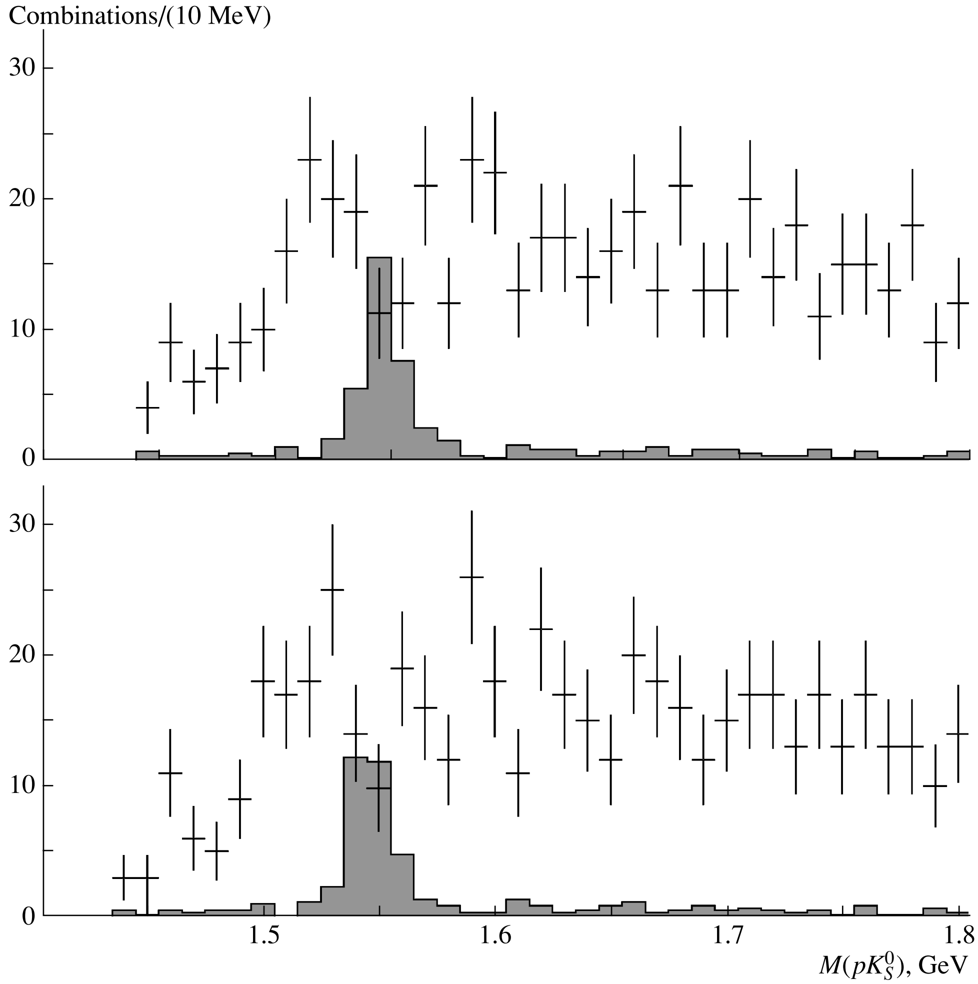

Fig. 12. Effective-mass spectrum of pK^0_S system for the reaction $p + N \rightarrow pK^0_S K^0_S + N$. Lower picture corresponds to bin shift by 5 MeV. The MC signal corresponds to the cross-section ratio $\sigma_{\Theta^+\bar{K}^0}/\sigma_{\Lambda(1520)K^+} = 0.1$.

scribed above for the calibration reactions. The measured values were corrected with the same correction factor $k_{\text{corr}} = 1.38$. The systematic errors for the production cross sections are estimated to be <25%.

Since different "positive" experiments reported different masses for the Θ^+ baryon, we made a scan in the effective mass for each of the different final states. The results of the scan are presented in Fig. 14. A poor upper limit for the $[pK^0_S]K^0_S$ final state in the mass range 1515–1530 MeV is a consequence of a bump in the pK^0_S mass spectrum, which is partly supported by a shoulder in the pK^0_S mass spectrum of the $[pK^0_S]K^0_L$ final state. However, an interpretation of this bump as a (relatively wide) Θ^+ baryon is absolutely excluded by nK^+ data. It is also possible that the one-star $\Sigma(1480)$ hyperon really exists, producing the irregularities in the pK^0_S mass spectrum (but why not in pK^0_L?).

We tried to apply additional cuts in order to find a signal. These cuts included, in particular,

cut on transverse momentum of the $NK\bar{K}$ system (coherent region $P_T^2 < 0.1$ GeV$^2/c^2$, high-P_T^2 region, etc.);

cut on transverse momentum of the NK system;

cut on the effective mass of the $NK\bar{K}$ system;

cuts on the decay angles $(\cos\theta^*, \phi^*)$ of the $[NK]\bar{K}$ system.

None of these cuts allowed us to see a statistically significant signal in the region of the Θ^+ baryon. In addition, we do not see any evidence for the existence of narrow structures in $NK\bar{K}$ effective-mass distributions, in particular, the state with $M \approx 2.4$ GeV, indicated by CLAS data [6]. It should be noted that, with the extreme values of cuts, when statistics start to be low, irregularities in different mass spectra begin to appear, sometimes at a mass of the Θ^+ baryon.

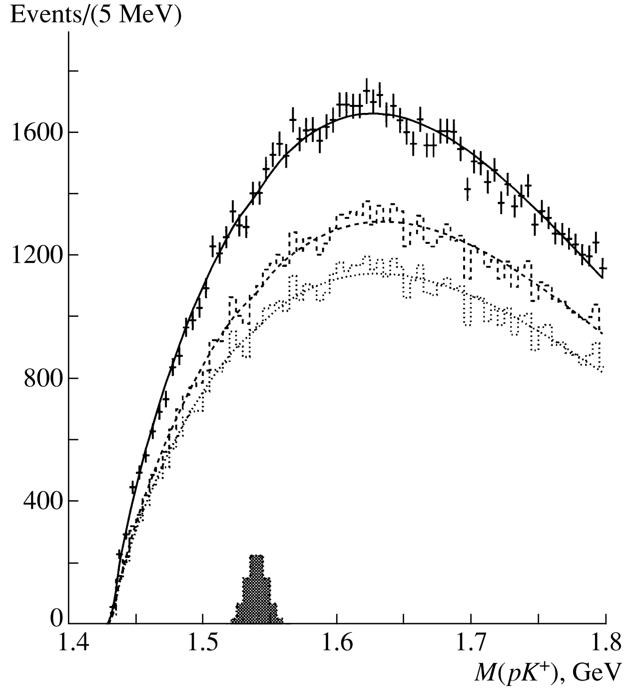

Fig. 13. Search for Θ^{++} baryon in the reaction $p + N \to \Theta^{++}K^- + N$; $\Theta^{++} \to pK^+$. The histograms are with no cuts (solid), with $\Lambda(1520)$ (dashed), and ($\Lambda(1520) + \phi$) (dotted) cuts. The curves are results of the fit described in the test. The MC signal from narrow Θ^{++} corresponds to the cross-section ratio $\sigma_{\Theta^{++}K^-}/\sigma_{\Lambda(1520)K^+} = 0.01$ and $\text{BR}(\Theta^{++} \to pK^+) = 100\%$.

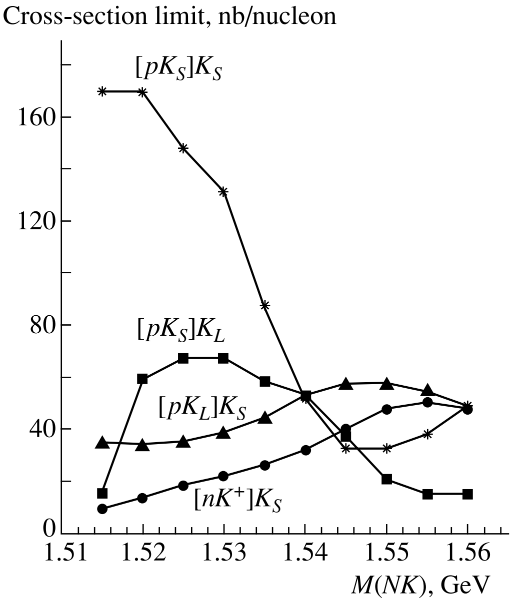

Fig. 14. Cross-section limits on the Θ^+-baryon production for different masses of Θ^+.

In our case, however, they never occurred simultaneously in the same place under the same cuts in more than one mass spectrum.

The relative yield $\Theta^+/\Lambda(1520)$ is the most commonly used variable to compare different experiments. In our case, it transforms to the cross-section ratio $\sigma(\Theta^+\bar{K}^0)/\sigma(\Lambda(1520)K^+)$. The best way to calculate this ratio is to use the $nK_S^0K^+$ final state, which is common to both systems. Many factors cancel in the ratio and we arrive at ($\Lambda^* \equiv \Lambda(1520)$)

$$R_{\Lambda^*} \equiv \frac{\sigma(\Theta^+\bar{K}^0)}{\sigma(\Lambda^*K^+)} \tag{17}$$

$$= \frac{N_\Theta}{N_{\Lambda^*}} \frac{\text{BR}(\Lambda^* \to N\bar{K})}{\text{BR}(\Theta^+ \to NK)} \frac{\varepsilon_{\Lambda^*}}{\varepsilon_{\Theta^+}} = 0.45 \frac{N_\Theta}{N_{\Lambda^*}} \frac{\varepsilon_{\Lambda^*}}{\varepsilon_{\Theta^+}},$$

where we used the PDG value $\text{BR}(\Lambda^* \to N\bar{K}) = 45\%$ and $\text{BR}(\Theta^+ \to NK)$ was assumed to be 100%. The number of events and efficiencies for corresponding decay modes can be read from Tables 2 and 3, and we finally get

$$R_{\Lambda^*} = 0.45 \frac{55 \pm 43}{2490 \pm 90} \frac{0.038}{0.033} = 0.011 \pm 0.007,$$

with an upper limit $R_{\Lambda^*} < 0.02$ at 90% C.L. for $M(\Theta^+) = 1540$ MeV. The mass dependence of this limit can be understood from the $[nK^+]K_S^0$ curve in Fig. 14. This estimate is free of any correction factors, and it is hard to imagine that the efficiency of the Θ^+ detection is significantly lower than that of $\Lambda(1520)$. Note that, for $\sigma(\Theta^+\bar{K}^0) \approx \sigma(\Lambda(1520)K^+)$ and $\varepsilon_{\Theta^+} \approx \varepsilon_{\Lambda^*}$, we should see as many as 5000 $\Theta^+ \to nK^+$ decays.

The ratio $R_\phi \equiv \sigma(\Theta^+\bar{K}^0)/\sigma(p\phi)$ can be estimated in the same way as R_{Λ^*}, and the result is $R_\phi < 0.15$ at 90% C.L.

Our result for R_{Λ^*} is based on a sample of ≈2500 $\Lambda(1520) \to nK_S^0$ decays or, equivalently, on ≈21 000 $\Lambda(1520) \to pK^-$ decays, corresponding to ≈ 900 k of $\Lambda(1520)$ produced in the reaction $p + N \to \Lambda(1520)K^+ + N$. With a somewhat smaller number of $\Lambda(1520)$, HERA-B [19] reports (preliminary) $R_{\Lambda^*} < 0.02$ for inclusive pA interactions at 920 GeV/c and mid-rapidity. A small value of R_{Λ^*} found by HERA-B and SPHINX in proton-induced reactions corresponds, however, to quite different physical processes and kinematical regimes. It is natural to assume that this value should hold for any proton (nucleon)-induced reactions.

Our upper limit on the absolute cross-section production of Θ^+ can be used to set the upper limit on its width, though in a model-dependent way. The forward-hemisphere cross section for the reaction $pp \to \Theta^+\bar{K}^0p$ was calculated in [39] using a hadronic Lagrangian with empirical coupling constants and form factors. The cross section was found to have a maximum of 13 μb at $\sqrt{s} \approx 4.5$ GeV. The last point in their figure at $\sqrt{s} = 7$ GeV gives the value $\approx$6.5 μb. We can extrapolate this value for $\sigma(\Theta^+\bar{K}^0)$ to our energy ($\sqrt{s} = 11.5$ GeV) using (conservatively) ($1/P^2_{\rm beam}$) dependence and find $\sigma(\Theta^+\bar{K}^0) \approx$ 900 nb. As both the cross section and the total width of Θ^+ are proportional to $g^2_{\Theta NK}$ and the width of Θ^+ was assumed to be $\Gamma[\Theta^+] = 20$ MeV in the calculations, our upper limit on the production cross section transforms to the upper limit on the width, $\Gamma[\Theta^+] < 20(32/900) = 0.7$ MeV (the limit from the nK^+ decay mode was used). This result is in good agreement with constraints on $\Gamma[\Theta^+]$ deduced from K^+N and K^+d data [40].

5. CONCLUSION

In a high-statistics experiment with the SPHINX facility at the IHEP accelerator, we have searched for the production of the Θ^+ baryon in the exclusive reaction $p + N \to \Theta^+\bar{K}^0 + N$ at an energy of 70 GeV. For the first time, the search was done simultaneously in all possible decay modes of Θ^+. We did not see statistically significant signals and found that the production of the $\Theta^+\bar{K}^0$ system is very small (if any) compared to the production of the $\Lambda(1520)K^+$ system and small (if any) compared to OZI-suppressed production of the $p\phi$ system.

The work is under way in the search for Θ^+ in the reaction $p + N \to \Theta^+K^-\pi^+ + N$. In the search for the exotic mechanisms for Θ^+ production, we also plan to study the final states with baryon–antibaryon pairs, like $p + N \to \Theta^+\Sigma^+\bar{p} + N$.

Searches for new phenomena and new states of hadronic matter every time elicited great interest on the part of the outstanding physicist Academician A.I. Alikhanov. And it is a great honor for us to have the possibility of presenting our work on the searcher for pentaquark states at the session of the Nuclear Physics Department of the Russian Academy of Sciences (ITEP, 1–5 of March 2004) and in a special issue of *Yadernaya Fizika* dedicated to the memory of A.I. Alikhanov in connection with the 100-year anniversary of his birth.

ACKNOWLEDGMENTS

It is a pleasure to express our gratitude to the staff of the IHEP accelerator and especially A.A. Aseev for the invaluable help with the beam adjustment in the critical moments of data taking, and to A.M. Zaitsev for useful discussions.

This work was partly supported by Russian Foundation for Basic Research (project nos. 99-02-18252 and 02-02-16086).

REFERENCES

1. T. Nakano *et al.* (LEPS Collab.), Phys. Rev. Lett. **91**, 012002 (2003); hep-ex/0301020.
2. V. V. Barmin *et al.* (DIANA Collab.), Yad. Fiz. **66**, 1763 (2003) [Phys. At. Nucl. **66**, 1715 (2003)]; hep-ex/0304040.
3. S. Stepanyan *et al.* (CLAS Collab.), Phys. Rev. Lett. **91**, 252001 (2003); hep-ex/0307018.
4. J. Barth *et al.* (SAPHIR Collab.), hep-ex/0307083.
5. A. E. Asratyan, A. G. Dolgolenko, and M. A. Kubantsev, hep-ex/0309042.
6. V. Kubarovsky *et al.* (CLAS Collab.), Phys. Rev. Lett. **92**, 032001 (2004); **92**, 049902 (E) (2004); hep-ex/0311046.
7. R. Togoo *et al.*, Proc. Mongolian Acad. Sci. **4**, 2 (2003).
8. A. Airapetian *et al.* (HERMES Collab.), Phys. Lett. B **585**, 213 (2004); hep-ex/0312044.
9. A. Aleev *et al.* (SVD Collab.), hep-ex/0401024.
10. M. Abdel-Bary *et al.* (COSY-TOF Collab.), hep-ex/0403011.
11. P. Z. Aslanyan, V. N. Emelyanenko, and G. G. Rikhkvitzkaya, hep-ex/0403044.
12. S. Chekanov *et al.* (ZEUS Collab.), hep-ex/0403051.
13. A. R. Dzierba, D. Krop, M. Swat, *et al.*, Phys. Rev. D **69**, 051901 (2004); hep-ph/0311125.
14. J. L. Rosner, Phys. Rev. D **69**, 094014 (2004); hep-ph/0312269.
15. M. Zavertyaev, hep-ph/0311250.
16. Q. Zhao and F. E. Close, hep-ph/0404075.
17. E. Klempt, hep-ph/0404270.
18. J. Z. Bai *et al.* (BES Collab.), hep-ex/0402012.
19. K. T. Knopfle, M. Zavertyaev, and T. Zivko (HERA-B Collab.), hep-ex/0403020.
20. C. Pinkenburg (for the PHENIX Collab.), nucl-ex/0404001.
21. P. Hansen (for ALEPH Collab.), Talk at *DIS 2004*, http://www.saske.sk/dis04/talks/C/hansen.pdf
22. Throsten Wengler (DELPHI Collab.), Talk at *Moriond'04 QCD*, http://moriond.in2p3.fr/QCD/2004/WednesdayAfternoon/Wengler.pdf
23. M. Karliner and H. J. Lipkin, hep-ph/0405002.
24. M. Y. Balats *et al.* (SPHINX Collab.), Z. Phys. C **61**, 223 (1994); SPHINX Collab. (V. A. Dorofeev *et al.*), Yad. Fiz. **57**, 241 (1994) [Phys. At. Nucl. **57**, 227 (1994)].
25. D. V. Vavilov *et al.* (SPHINX Collab.), Yad. Fiz. **57**, 2046 (1994) [Phys. At. Nucl. **57**, 1970 (1994)].
26. M. Y. Balats *et al.* (SPHINX Collab.), Z. Phys. C **61**, 399 (1994).
27. S. V. Golovkin *et al.* (SPHINX Collab.), Eur. Phys. J. A **5**, 409 (1999).
28. D. V. Vavilov *et al.* (SPHINX Collab.), Yad. Fiz. **63**, 1469 (2000) [Phys. At. Nucl. **63**, 1391 (2000)].
29. L. G. Landsberg, Phys. Rep. **320**, 223 (1999).
30. Y. M. Antipov *et al.* (SPHINX Collab.), Yad. Fiz. **65**, 2131 (2002) [Phys. At. Nucl. **65**, 2070 (2002)].

31. D. Diakonov, V. Petrov, and M. V. Polyakov, Z. Phys. A **359**, 305 (1997); hep-ph/9703373.
32. H. Weigel, Eur. Phys. J. A **2**, 391 (1998); hep-ph/9804260.
33. D. V. Vavilov *et al.*, Yad. Fiz. **68** (3), 407 (2005) [Phys. At. Nucl. **68**, 378 (2005)].
34. S. I. Bityukov *et al.*, IFVE-94-101.
35. K. Hagiwara *et al.*, Phys. Rev. D **66**, 010001 (2002).
36. A. Kozhevnikov, V. Kubarovsky, V. Molchanov, *et al.*, Nucl. Instrum. Methods Phys. Res. A **433**, 164 (1999).
37. M. W. Arenton, D. S. Ayres, R. Diebold, *et al.*, Phys. Rev. D **25**, 22 (1982).
38. S. V. Golovkin *et al.* (SPHINX Collab.), Z. Phys. A **359**, 435 (1997).
39. W. Liu and C. M. Ko, Phys. Rev. C **68**, 045203 (2003); nucl-th/0308034.
40. S. Nussinov, hep-ph/0307357; R. W. Gothe and S. Nussinov, hep-ph/0308230; R. A. Arndt, I. I. Strakovsky, and R. L. Workman, Phys. Rev. C **68**, 042201 (2003); nucl-th/0308012; nucl-th/0311030; J. Haidenbauer and G. Krein, hep-ph/0309243; R. N. Cahn and G. H. Trilling, hep-ph/0311245; A. Casher and S. Nussinov, Phys. Lett. B **578**, 124 (2004); hep-ph/0309208; A. Sibirtsev, J. Haidenbauer, S. Krewald, and U. G. Meissner, hep-ph/0405099.

Physics of Atomic Nuclei, Vol. 68, No. 3, 2005, pp. 455–465. Translated from Yadernaya Fizika, Vol. 68, No. 3, 2005, pp. 484–494.

Topology of "White Stars" in the Relativistic Fragmentation of Light Nuclei

N. P. Andreeva[1], V. Bradnova[2], S. Vokal[2],[3], A. Vokalova[2], A. Sh. Gaitinov[1], S. G. Gerasimov[4], L. A. Goncharova[4], V. A. Dronov[4], P. I. Zarubin[2]*, I. G. Zarubina[2], A. D. Kovalenko[2], A. Kravchakova[3], V. G. Larionova[4], O. V. Levitskaya[5], F. G. Lepekhin[5], A. I. Malakhov[2], A. A. Moiseenko[6], G. I. Orlova[4], N. G. Peresadko[4], N. G. Polukhina[4], P. A. Rukoyatkin[2], V. V. Rusakova[2], N. A. Salmanova[4], V. R. Sarkisyan[6], B. B. Simonov[5], E. Stan[2],[7], R. Stanoeva[2],[8], M. M. Chernyavsky[4], M. Haiduc[7], S. P. Kharlamov[4], I. Tsakov[8], and T. V. Schedrina[2]

The BECQUEREL Collaboration

Received May 24, 2004; in final form, August 27, 2004

Abstract—Experimental observations of the multifragmentation of relativistic light nuclei by means of emulsions are surveyed. Events that belong to the type of "white stars" and in which the dissociation of relativistic nuclei is not accompanied by the production of mesons and target-nucleus fragments are considered. An almost complete suppression of the binary splitting of nuclei to fragments of charge in excess of two, $Z > 2$, is a feature peculiar to charge topology in the dissociation of Ne, Mg, Si, and S nuclei. An increase in the degree of nuclear fragmentation manifests itself in the growth of the multiplicity of singly and doubly charged fragments ($Z = 1, 2$) as the charge of the unexcited fragmenting-nucleus part (which is the main part) decreases. Features of the production of systems formed by extremely light nuclei α, d, and t are studied in the dissociation of the stable isotopes of Li, Be, B, C, N, and O to charged fragments. Manifestations of ^{3}He clustering can be observed in "white stars" in the dissociation of neutron-deficient isotopes of Be, B, C, and N. *© 2005 Pleiades Publishing, Inc.*

INTRODUCTION

The charge topology of fragments in peripheral interactions of light nuclei at a primary energy in excess of 1 GeV per nucleon may serve as an efficient characteristic of nuclear multifragmentation. In this energy region, one reaches the regime of limiting nuclear fragmentation—that is, the spectrum of fragments becomes independent of the collision energy and of the composition of target nuclei.

In studying multifragmentation in the region of relativistic energies, the possibilities of observation and of spectroscopy of final states of a product system formed by charged fragments are determined by the accuracy achieved in measuring angles. Owing to the best spatial resolution (0.5 μm), nuclear emulsions provide an angular resolution of about 10^{-5} rad for tracks of relativistic fragments. This ensures complete observability of all possible decays of excited nuclear states to fragments. By way of example, we indicate that, over a length of 1 mm, one can distinguish with confidence the process ^{8}Be $\to 2\alpha$, which manifests itself at a momentum of 4.5 GeV/c per nucleon as a pair of tracks within an angular cone of about 2×10^{-3} rad. Such narrow decays are rather frequently observed in the fragmentation of relativistic oxygen and heavier nuclei.

Topological features of events involving the dissociation of light nuclei in peripheral interactions were investigated in emulsions for ^{12}C [1–6], ^{22}Ne [7–12], ^{24}Mg [13], ^{28}Si [14–16], ^{16}O [17, 18], ^{6}Li [19–22], and ^{10}B [23–25] nuclei at energies of about a

---

[1] Institute for Physics and Technology, Kazakh Academy of Sciences, Almaty, Republic of Kazakhstan.

[2] Joint Institute for Nuclear Research, Dubna, Moscow oblast, 141980 Russia.

[3] P.J. Šafárik University, Košice, Slovak Republik.

[4] Lebedev Institute of Physics, Russian Academy of Sciences, Leninskii pr. 53, Moscow, 117924 Russia.

[5] Petersburg Nuclear Physics Institute, Russian Academy of Sciences, Gatchina, 188350 Russia.

[6] Yerevan Physic Institute, ul. Brat'ev Alikhanyan 2, Yerevan, 375036 Armenia.

[7] Institute of Space Sciences, Bucharest-Maguerele, Romania.

[8] Institute for Nuclear Research and Nuclear Energy, Bulgarian Academy of Sciences, Blvd. Tsarigradsko chausse 72, BG-1784 Sofia, Bulgaria.

*E-mail: `zarubin@lhe.jinr.ru`

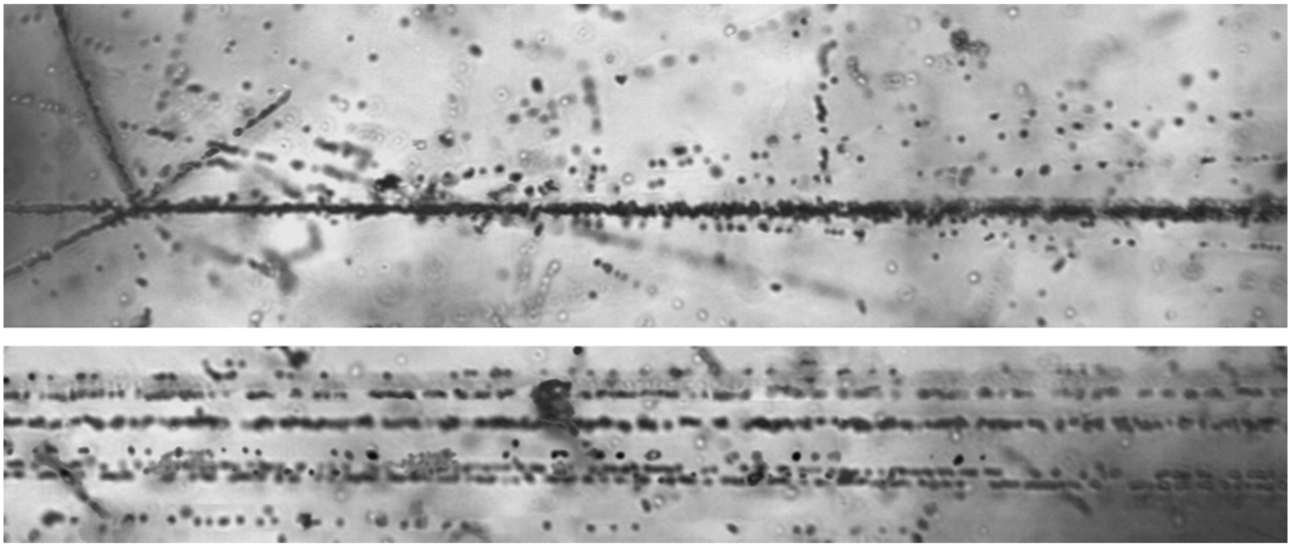

Fig. 1. Event of the fragmentation of a ^{28}Si nucleus having an energy of 3.65 GeV per nucleon and participating in a peripheral interaction with an emulsion nucleus. The upper photograph shows the interaction vertex and a jet of fragments within a narrow angular cone, along with four accompanying singly charged particles within a broad cone and three target-nucleus fragments. Upon a shift in the direction of the jet of fragments (lower photograph), one can distinguish three H and five He fragments. An intense track on the lower photograph (the third one from top to bottom) is identified as a pair of $Z = 2$ fragments that occurs in very narrow angular cone and which corresponds to the decay of a ^{8}Be nucleus. The three-dimensional image of events was reconstructed as a plane projection with the aid of an automated microscope entering into the composition of the PAVIKOM complex at the Lebedev Institute of Physics (Moscow).

few gigaelectronvolts per nucleon. The dissociation of ^{16}O and ^{32}S nuclei was investigated at an energy of 200 GeV per nucleon [17, 26, 27]. These results are complete and highly reliable and can be useful in planning investigations of nuclear multifragmentation that are characterized by a high statistical significance.

In this article, we present data on dissociation channels for a broad range of light nuclei in events belonging to the "white star" type. Experimental data on the branching fractions of observed nuclear-dissociation channels give an idea both of the general regularities of the nuclear-fragmentation process and of the special features of fragmentation that are associated with the structure of individual nuclei. For ^{24}Mg, ^{14}N, and ^{7}Be nuclei, the results in question are given for the first time. Data on the other nuclei discussed below were obtained on the basis of events from experimental results published previously that had passed more stringent selection criteria. The irradiation at energies of about a few gigaelectronvolts per nucleon was performed at the synchrophasotron and nuclotron of the Joint Institute for Nuclear Research (JINR, Dubna, Russia), while the irradiation at the energy of 200 GeV per nucleon was conducted at CERN (Switzerland).

In order to illustrate the criteria of event selection, an event of silicon-nucleus multifragmentation at a momentum of 4.5 GeV/c per nucleon is displayed in Fig. 1. A group of projectile fragments that travel within a narrow cone of angle about a few degrees and having the total charge of $Z = 13$ is of particular interest. The size of the cone is determined by the ratio of the transverse Fermi momentum to the projectile momentum per nucleon. The tracks of relativistic fragments remain within a single emulsion layer for a long time, and this is sufficient for reconstructing a continuous three-dimensional image of this group of tracks. Within emulsions, a mass identification of relativistic hydrogen and helium isotopes can be performed by using the mean angle of scattering of tracks and the total momentum associated with this angle.

The longitudinal momenta of fragments per nucleon are equal, to within a few percent, to the momenta of projectile nucleons. The excitation energy of the system of fragments is determined by their multiplicity and angles of divergence. This energy can be determined as the difference of the invariant mass of the fragmenting system and the projectile mass and is about 1 MeV per fragment nucleon. Angular correlations of fragments reflect the angular momentum of the product system. Minimum-ionization tracks of product mesons are seen within a broader cone in Fig. 1. In addition, tracks from strongly ionizing target-nucleus fragments of energy about a few tens of megaelectronvolts are present in the interaction vertex. Thus, the separation of the kinematical regions of fragmentation of colliding nuclei clearly manifests itself in the interaction being considered.

Multifragmentation in White Stars

In accumulating statistics of multifragmentation of nuclei, one selects events featuring no charged particles emitted between the projectile- and target-fragmentation regions. As a rule, the projectile charge is completely transferred in such events to the narrow angular cone of fragmentation. The interpretation is the clearest for events that do not involve target fragments either. They are produced in the case of a minimum energy transfer to the fragmenting nucleus. Events of this type are referred to as "white stars." Their fraction among the total number of inelastic events is about a few percent. This term reflects not only a general view of the tracks of such events but also a sharp decrease in ionization losses (by the factor Z in the limiting case) upon going over from the projectile track to the narrow cone of secondary tracks. White stars are formed in the electromagnetic interactions of target nuclei with virtual photons and in diffractive scattering on perpheral target neutrons.

The requirement of charge conservation is a circumstance of practical convenience in seeking events of this type, since this makes it possible to exclude the contribution from an admixture of lighter particles in the beam that have a close charge-to-mass ratio. This is of importance in exposing emulsions to secondary beams of radioactive nuclei, because the composition of such beams is rather complex. We note that the above criteria for selecting white stars can be used, along with the condition requiring the energy-flux conservation in the fragmentation cone, in future experiments aimed at studying global special features of the fragmentation of heavy nuclei in processes of peripheral dissociation.

Loosely Bound Cluster Systems

The objective of our experiments was to study, in the vicinity of the thresholds for the reactions being discussed, the pattern of the phase transition of nuclear matter from the state of a quantum liquid to the state of a quantum gas consisting of a large number of nucleons and extremely light nuclei. By extremely light nuclei, we mean deuterons, tritons, and ^{3}He and ^{4}He nuclei—that is, stable systems that do not have excited states below the threshold for their decay to nucleons.

Current interest in studying phase transitions in nuclear systems is motivated by the prediction of such states as loosely bound cluster systems [28–30]. The spatial extension of such systems may exceed the fragment sizez significantly {Efimov's states [28] in the vicinity of the threshold for the decay of a three-body system, light nuclei of molecular-type structure (for an overview, see [29]), or a Bose condensate of a dilute gas of alpha particles in $N\alpha$ nuclei [30]}. The multifragmentation process involving adiabatic excitation transfer can be interpreted in terms of the disappearance of the Coulomb barrier owing to a simultaneous increase in the distance between charged clusters.

Investigation of multiparticle states on scales that are characteristic of the nucleon and cluster structure of a nucleus is of interest for nuclear astrophysics. By way of example, we indicate that, owing to a significant decrease in Coulomb repulsion in extended nuclear systems, such states may play the role of intermediate states in the processes of nuclear fusion in stars. The topologies found here may prove to be useful for clarifying versions of nuclear fusion as the process inverse to nuclear fragmentation.

SPECIAL FEATURES OF THE FRAGMENTATION OF Mg, Ne, Si, AND S NUCLEI

Multifragmentation of ^{24}Mg Nuclei

Searches for white stars in the dissociation of ^{24}Mg nuclei with a kinetic energy of 3.65 GeV per nucleon were performed by following the projectile track up to an interaction vertex with the aid of microscopes (see, for example, [25]). This resulted in finding 83 events of the type in question, where almost all of the secondary tracks were within a cone of angle not larger than 4° with respect to the primary-track direction. The charge of a particle that generated a track in the emulsion used was determined on the basis of the density of gaps and the number of delta electrons. The distribution of events with respect to the charge topology of fragments is given in Table 1. The charge of a $Z > 2$ fragment, the number of singly charged fragments, the number of doubly charged fragments, and the observed number of events that have this topology are quoted in each column of the table in the rows from top to bottom. The efficiency of the observation of events characterized by $11 + 1$ charge topology is estimated at 50% because of the screening of singly charged tracks by secondary tracks of high ionization.

Table 1 presents data concerning channels of the production of white stars that cover the cases from the separation of singly and doubly charged fragments from a cold nuclear residue of the primary nucleus to its complete breakup to extremely light nuclei. None of such events involves more than one track from a $Z > 2$ relativistic fragment. An obvious special feature of the processes being considered is that they do not produce events of the binary or ternary

Table 1. Charge-topology distribution of white stars in the dissociation of ^{24}Mg nuclei with an energy of 3.65 GeV per nucleon

Z_f	11	10	10	9	9	8	8	8	7	7	6	5	5	5	4	4	3	–	–	–
$N_{Z=1}$	1	2	–	3	1	4	2	–	3	1	2	5	3	1	6	4	5	6	4	2
$N_{Z=2}$	–	–	1	–	1	–	1	2	1	2	2	1	2	3	1	2	2	3	4	5
N_{ev}	10	14	8	5	9	1	7	4	4	2	4	2	1	1	2	1	3	1	2	2

Table 2. Charge-topology distribution of white stars in the dissociation of ^{22}Ne nuclei with an energy of 3.3 GeV per nucleon

Z_f	9	8	8	7	6	6	5	5	$5+3$	4	$4+3$	–	–
$N_{Z=1}$	1	–	2	1	–	2	1	3	–	–	3	2	–
$N_{Z=2}$	–	1	–	1	2	1	2	1	1	3	–	4	5
N_{ev}	22	51	6	7	5	2	1	1	1	2	1	1	3

Table 3. Charge-topology distribution of white stars in the dissociation of ^{28}Si nuclei with an energy of 3.65 GeV per nucleon

Z_f	13	12	12	11	11	10	10	10	9	9	9	8	8	8	7	7	7	6	6	6	6	5	5	4	–	–	–
$N_{Z=1}$	1	–	2	1	3	–	2	4	1	3	5	6	2	4	3	5	7	2	4	6	8	3	5	2	2	8	10
$N_{Z=2}$	–	1	–	1	–	2	1	–	2	1	–	–	2	1	2	1	–	3	2	1	–	3	2	4	6	3	2
N_{ev}	9	3	15	11	6	2	7	2	2	8	3	2	5	6	1	3	3	3	5	8	1	1	3	1	1	2	3

splitting of light nuclei to fragments heavier than the alpha particle, this being indicative of a crucial role of the multifragmentation process here. Previously, only one event of the disintegration process $\text{Mg}^* \to \text{B} + \text{N}$ without an additional emission of charged particles was found in analyzing 1666 interactions [31]. The dominance of multifragmentation processes despite high energy thresholds for them can be explained by a high density of multiparticle states.

It is planned to perform an analysis of events of a complete breakup of Mg nuclei on the basis of substantially vaster statistics and to identify simultaneously extremely light nuclei originating from this breakup. This would provide the possibility of reconstructing the invariant mass of a decaying system and its subsystems (for example, $N\alpha$-particle ones). Two events of the decay of magnesium nuclei to six helium nuclei have been found so far. One of these was identified as a $5^4\text{He} + {}^3\text{He}$ event. Since these events are accompanied by single target-nucleus fragments, they were not included in the data presented in Table 1. Nevertheless, their existence provides sufficient grounds to continue seeking 6α configurations over a large length of primary tracks of ^{24}Mg nuclei.

Multifragmentation of ^{22}Ne Nuclei

We will compare special features of the fragmentation of ^{24}Mg nuclei with data on neighboring nuclei, in which case we have vast statistics of interactions at our disposal. Table 2 displays the charge-topology distribution of 103 white stars generated by ^{22}Ne nuclei of energy 3.3 GeV per nucleon and selected among 4100 inelastic events [7]. There are no events of binary splitting in this case inclusive. Bogdanov *et al.* [31], who used a different sample of 4155 events, did not observe the binary splitting of ^{22}Ne either.

A much more pronounced role of helium isotopes in the fragmentation of ^{22}Ne nuclei may be due to the fact that, in contrast to the symmetric magnesium nucleus, the nucleus in question involves a pair of extra outer neutrons. In initiating multiparticle dissociation via the knockout of external neutrons, this circumstance can be used for a more efficient generation and detection of systems containing a large number of alpha particles. Three events of the decay of ^{22}Ne nuclei to five helium nuclei whose tracks are within a cone of 3° were found (Table 2). In two of these events, all tracks are even within 1°. These observations indicate once again that nuclear emulsions provide unique possibilities in studying multiparticle systems consisting of extremely light nuclei that have minimum relative 4-velocities (relative Lorentz factors).

Multifragmentation of ^{28}Si and ^{32}S Nuclei

A sample of 116 white stars generated by ^{28}Si nuclei of energy 3.65 GeV per nucleon exhibits the same regularity—a transition to multifragmentation (Table 3) without binary splitting [14]. In [31], only one event of the process $\mathrm{Si}^* \rightarrow \mathrm{O} + \mathrm{C}$ was observed in a different sample of 1900 inelastic interactions. It is interesting to note that the transition to the complete breakup of ^{28}Si nuclei is accompanied by an increase in the contribution to the final states of hydrogen isotopes in relation to helium isotopes. It is desirable to find out whether this is a consequence of a decrease in the degree of alpha-particle clustering in nuclei with increasing A. The results in Table 3 represent an improved sample of events from data obtained previously in [7, 14]. We note that those articles contain rich information, which may be of use in planning experiments where the degree of inelasticity of selected collisions is varied.

We will also present results obtained by irradiating emulsions with ^{32}S nuclei accelerated to an energy of 200 GeV per nucleon. In this case, the angular size of the fragmentation cone is 0.5°. Table 4 demonstrates that the channels of hydrogen-isotope separation are dominant. Although the data sample used is insufficiently vast, multifragmentation manifests itself in the topology of 193 white stars.

It is of interest to study the topology of white stars for heavy nuclei. Single events of a complete breakup of lead nuclei were observed in emulsions irradiated at CERN with ultrarelativistic lead nuclei of energy 160 GeV per nucleon. However, a detailed investigation of heavy nuclei within the fragmentation cone is beyond the potential of even the emulsion method. In all probability, this can be done in intense relativistic beams of heavy nuclei by measuring total ionization and energy fluxes in a complete solid angle.

SPECIAL FEATURES OF THE FRAGMENTATION OF C, O, B, AND N NUCLEI

Multifragmentation of ^{12}C and ^{16}O Nuclei

The probabilities of the production and the properties of systems consisting of a small number of $Z = 1$, 2 fragments can be studied by selecting white stars in the fragmentation of B, C, N, and O isotopes. Detailed information about the multifragmentation of nuclei belonging to this group may form a basis for understanding corresponding processes in heavier nuclei. The dissociation of B and C nuclei to three-particle systems can proceed either via the separation of extremely light nuclei (alpha particles, deuterons, tritons, and ^{3}He nuclei) from the core in the form of the unstable nucleus ^{8}Be or via a direct fragmentation to hydrogen and helium isotopes.

The white stars from the process $^{12}\mathrm{C}^* \rightarrow 3\alpha$ at an energy of 3.65 GeV per nucleon were studied in [4–6]. These investigations resulted in demonstrating the role of the channel involving a ^{8}Be nucleus and in drawing the conclusion that, with increasing total energy of the system of three alpha particles, there occurs a transition to direct multifragmentation. In [31], no event of binary splitting through the only possible channel $^{12}\mathrm{C}^* \rightarrow {}^6\mathrm{Li} + {}^6\mathrm{Li}$ was observed in the statistical sample of 2757 inelastic interactions.

In [18], the white stars from the process $^{16}\mathrm{O}^* \rightarrow 4\alpha$ were studied at a high statistical level (641 events). The analysis of angular correlations that was performed there suggested that there is angular-momentum transfer to fragment systems and that the role of cascade decays through ^{8}Be and $^{12}\mathrm{C}^*$ is insignificant. Tables 5 and 6 present the results obtained by selecting white stars in the sample of 2159 interactions of ^{16}O nuclei at energies of 3.65 (72 stars) and 200 GeV (86 stars) per nucleon.

Multifragmentation of ^{10}B Nuclei

The study of the deuteron contributions to the decays of odd–odd nuclei ^{6}Li [19–22], ^{10}B [23–25], and ^{14}N was a continuation of the investigation into the multifragmentation of light even–even nuclei that involves dissociation only to alpha particles. The role of a deuteron as a cluster was the most pronounced in the white stars from ^{6}Li nuclei at an energy of 3.65 GeV per nucleon (the branching fraction of the decays $^6\mathrm{Li}^* \rightarrow d\alpha$, $^6\mathrm{Li}^* \rightarrow {}^3\mathrm{He}t^*$ and $^6\mathrm{Li}^* \rightarrow tdp$ are, respectively, 74, 13, and 13% [21]).

The topology of white stars for ^{10}B nuclei was studied at an energy of 1 GeV per nucleon. Table 7 presents the charge-topology distribution of 41 white stars, where the secondary tracks are within the angular cone of 15°. The fraction of the decays $^{10}\mathrm{B}^* \rightarrow d\alpha\alpha$ among events of $2+2+1$ charge topology was 40%. The contribution of the channel $^{10}\mathrm{B}^* \rightarrow {}^8\mathrm{Be}d \rightarrow d\alpha\alpha$ was estimated at a level of $18 \pm 3\%$. The decay of an unstable nucleus ^{9}B is not the main source of events having this topology. This is suggested by a low probability of $4+1$ topology in the decay $^{10}\mathrm{B}^* \rightarrow {}^9\mathrm{Be}p$ and by a moderately small contribution of ^{8}Be to the decay $^{10}\mathrm{B} \rightarrow {}^8\mathrm{Be}p$. We can conclude that direct three-body decays having the $2+2+1$ configuration of white stars play a

Table 4. Charge-topology distribution of white stars in the dissociation of ^{32}S nuclei with an energy of 200 GeV per nucleon

Z_f	15	14	14	13	13	12	12	11	11	10	10	10	9	8	8	7 + 3	7	5 + 3
$N_{Z=1}$	1	–	2	1	3	2	4	3	5	2	4	6	3	–	6	4	3	4
$N_{Z=2}$	–	1	–	1	–	1	–	1	–	2	1	–	2	4	1	1	3	2
N_{ev}	99	11	48	7	6	3	4	4	1	1	2	1	1	1	1	1	1	1

decisive role. Thus, the decay $^{10}\text{B}^* \to d\alpha\alpha$ is similar in topology to the decay $^{12}\text{C}^* \to 3\alpha$.

In order to refine our ideas of the relationship between the direct three-body decay and decays through ^{8}Be, we irradiated emulsions with relativistic ^{9}Be nuclei. A beam of ^{9}Be nuclei that have a momentum of 2 GeV/c per nucleon was formed at the JINR nuclotron in the fragmentation process $^{10}\text{B} \to {}^9\text{Be}$. The formation of white stars involving two alpha particles is initiated in the fragmentation process accompanied by the stripping of one neutron. An analysis of data would make it possible to assess the degree of clustering in the ^{9}Be nucleus and the probability of the formation of a ^{8}Be nucleus. This must be manifested in the yield of alpha-particle pairs through the excitation of n–^{8}Be and α–n–α configurations.

Multifragmentation of ^{14}N Nuclei

It is of interest to reveal the role of three-body decays here, which was established for the processes $^{10}\text{B}^* \to d\alpha\alpha$, $^{12}\text{C}^* \to 3\alpha$, and $^{16}\text{O}^* \to 4\alpha$, and to extend the concepts of clustering in nuclei that involves deuterons. For this, we irradiated emulsions with ^{14}N nuclei of energy 2.1 GeV per nucleon. The main objective here was to study $^{14}\text{N}^* \to d\alpha\alpha\alpha$ white stars in the forward cone of angular size up to 8°. The statistics of 540 interactions of nitrogen nuclei with photoemulsion nuclei, including 25 white stars, have been accumulated thus far. The charge-topology distribution of these events is given in Table 8. There is an indication of an important role of the $2+2+2+1$ configuration, which is associated with the decay $^{14}\text{N}^* \to d\alpha\alpha\alpha$. The $6+1$ configuration seems to contribute considerably, which is analogous to what we have in events involving the separation of $Z = 1$ fragments in the dissociation of heavier symmetric nuclei.

Table 5. Charge-topology distribution of white stars in the dissociation of ^{16}O nuclei with an energy of 3.65 GeV per nucleon

Z_f	7	6	6	5	5	4	4	–	–
$N_{Z=1}$	1	2	–	3	1	–	2	–	2
$N_{Z=2}$	–	–	1	–	1	2	1	4	3
N_{ev}	18	7	21	2	10	1	1	9	3

Table 6. Charge-topology distribution of white stars in the dissociation of ^{16}O nuclei with an energy of 200 GeV per nucleon

Z_f	7	6	6	5	5	4	3	3	–	–	–
$N_{Z=1}$	1	–	2	1	3	2	1	3	–	2	4
$N_{Z=2}$	–	1	–	1	–	1	2	1	4	3	2
N_{ev}	49	6	10	5	1	3	2	2	2	4	2

Clustering That Involves Tritons

Investigation of white stars generated by light odd–even stable nuclei (^{7}Li, ^{11}B, ^{15}N, and ^{19}F) can create a basis for including tritons in a general pattern. It was established that the contributions from various channels to white stars generated by relativistic ^{7}Li nuclei were the following: 50% from $^7\text{Li}^* \to t\alpha$, 30% from $^7\text{Li}^* \to dn\alpha$, and 20% from $^7\text{Li}^* \to pnn\alpha$ [25]. As a further step in our investigations, we implemented an irradiation with ^{11}B nuclei of energy 1.2 GeV per nucleon and began an analysis of their dissociation. The main objective of the experiment is to study $^{11}\text{B}^* \to t\alpha\alpha$ white stars.

PROSPECTS FOR STUDYING NEUTRON-DEFICIENT ISOTOPES OF C, B, N, AND Be

Searches for the "Ternary He Processes" in the Decays of ^{11}C, ^{10}C, and ^{9}C

The ^{11}B nucleus is the daughter nucleus in the beta decay of the mirror nucleus ^{11}C. Upon studying $^{11}\text{B}^* \to t\alpha\alpha$ and $^{11}\text{B}^* \to {}^7\text{Li}\alpha$ white stars, it would therefore be of interest to clarify the role of ^{3}He in the decay of ^{11}C. The decays through the channels

Table 7. Charge-topology distribution of white stars in the dissociation of ^{10}B nuclei with an energy of 1 GeV per nucleon

Z_f	4	3	–	–
$N_{Z=1}$	1	–	3	1
$N_{Z=2}$	–	1	1	2
$N_{\rm ev}$	1	5	5	30

Table 8. Charge-topology distribution of white stars in the dissociation of ^{14}N nuclei with an energy of 2.1 GeV per nucleon

Z_f	6	5	5	4	3	3	–	–
$N_{Z=1}$	1	–	2	1	4	2	3	1
$N_{Z=2}$	–	1	–	1	–	1	2	3
$N_{\rm ev}$	6	3	2	1	1	1	1	10

^{11}C$^* \to$ ^{3}He$\alpha\alpha$ and ^{11}C$^* \to$ ^{7}Beα may be analogous to the channels ^{12}C$^* \to 3\alpha$ and ^{12}C$^* \to$ ^{8}Beα. Clustering in the decays ^{12}C$^* \to 3\alpha$ reflects the well-known ternary α process in nucleosynthesis in stars. Observation of the cluster decays ^{11}C$^* \to$ ^{3}He$\alpha\alpha$ would provide a basis for studying the possible role of the ternary He process in nucleosynthesis in stars via ^{3}He$\alpha\alpha$ fusion—that is, in helium media characterized by a mixed composition of helium isotopes.

The ^{10}C nucleus is formed from the ^{9}C nucleus via the addition of one neutron. However, the addition of a neutron is unlikely to result in the formation of deuteron or ^{3}He clusters in the ground state of ^{10}C. The formation of two-cluster structures in the form of ^{7}Be and ^{3}He nuclei or in the form of a ^{8}B nucleus and a deuteron is improbable because of a high binding energy of such clusters in the ^{10}C nucleus. In the case of one outer proton, the unstable nucleus ^{9}B may be a core of the ^{10}C nucleus. In a different possible structure featuring two outer protons, the core of the ^{10}C nucleus is formed by the ^{8}Be nucleus, which is also unstable. In all probability, such structures are similar to borromean structures of neutron-rich nuclei. In the case being considered, outer protons prevent the ^{10}C nucleus from decaying to fragments.

It is of interest to obtain experimental information about the channels ^{10}C$^* \to$ ^{3}He^{3}Heα and ^{10}C$^* \to$ ^{7}Be^{3}He, since this would make it possible to construct a generalization of the ternary He process. In the aforementioned irradiation of emulsions with ^{10}B nuclei, we have already observed two white stars interpreted in terms of the processes ^{10}B$^* \to$ ^{3}He$\alpha t \to (^{10}$C$^*)\pi^- \to \alpha^3$He^{3}Heπ^-. They suggest the existence of the mode of three-cluster excitation of the ^{10}C nucleus. By way of example, we also note that, in studying the charge-exchange process $t \to$ ^{3}He on photoemulsion nuclei, a high reliability of its observation was established in [22].

The dissociation of a ^{10}C nucleus may proceed via a cascade involving the production of unstable intermediate nuclei ^{9}B, ^{8}Be, and ^{6}Be in the intermediate state. In such decays, four charged fragments are formed in each final state. Thus, it is possible to study the decays of unstable nuclei ^{9}B, ^{8}Be, and ^{6}Be.

Table 9. Charge-topology distribution of white stars in the dissociation of ^{7}Be nuclei of energy 1.23 GeV per nucleon

Z_f	3	–	–	–
$N_{Z=1}$	1	4	2	–
$N_{Z=2}$	–	–	1	2
$N_{\rm ev}$	7	2	38	28

The beta-decay processes ^{11}C $\to$ ^{11}B and ^{10}C $\to$ ^{10}B lead to the formation of stable boron isotopes. In view of this, the participation of an extended ternary He process may affect the abundances of the isotopes of this element in cosmic rays and in matter. At the present time, it is generally believed that boron originates from the disintegration of heavier nuclei.

It is planned to form beams of ^{11}C and ^{10}C nuclei at the JINR nuclotron and to irradiate emulsions with them. The charge-exchange processes ^{11}B $\to$ ^{11}C and ^{10}B $\to$ ^{10}C rather than the fragmentation of heavier nuclei are chosen for their generation in order to suppress the contribution of nuclei close to those in ionization that they produce.

Of all nuclei considered here, the ^{9}C nucleus has the highest ratio of the number of protons to the number of neutrons. It has one extra proton in relation to the ^{8}B nucleus. The binding energy of this proton is much higher than the binding energy of the outer proton in the ^{8}B nucleus. This may be a manifestation of the interaction of the two protons, which is similar to the interaction of the two outer neutrons in the ^{6}He nucleus. Investigation of the probability of the decays ^{9}C$^* \to$ ^{3}He^{3}He^{3}He is of particular interest and importance in relation to ^{9}C$^* \to$ ^{8}Bp, ^{7}Bepp and other decay channels. It should be noted that the greater the ratio Z/N in the nucleus being studied, the more pronounced the advantages of the emulsion procedure in studying white stars. This is due to the possibility of more comprehensively observing nucleons originating from the fragmenting nucleus.

The fusion process ^{3}He^{3}He^{3}He $\to$ ^{6}Be^{3}He $\to$ ^{9}C is yet another version of a ternary He process. Its beta decay to the mirror nucleus ^{9}B, which is not bound, leads to the prompt decay $^9\mathrm{B} \to p\alpha\alpha$. Thus, we see that, in a stellar medium originally containing only ^{3}He, there can occur the production of ^{4}He. Under certain astrophysical conditions, the product nucleus ^{9}C can participate in the further fusion process ^{4}He^{9}C $\to$ ^{13}N(β^+) $\to$ ^{13}C.

In the fragmentation process $^9\mathrm{C} \to {}^8\mathrm{C}$, the intersection of the proton drip line occurs. There then arises the possibility of studying nuclear resonance states in the multiparticle decay channels $^8\mathrm{C} \to$ ^{3}He^{3}Hepp, ^{4}He$pppp$, which possess clear-cut signatures. We cannot rule out the possibility that their investigation may give new impetus to the development of the physics of loosely bound nuclear systems.

A beam of secondary nuclei that have a magnetic rigidity that corresponds to the ratio $Z/A = 2/3$ was formed at the JINR nuclotron in accelerating ^{12}C nuclei of momentum 2 GeV/c per nucleon at an intensity of about 10^9 nuclei per spill. Data for an analysis of the interaction of ^{9}C nuclei in emulsions were obtained.

Clustering in the Decays of ^{8}B Nuclei

A uniquely low binding energy of one of the protons is a feature peculiar to the ^{8}B nucleus. Therefore, it is the most probable that the ^{8}B nucleus has a core in the form of a ^{7}Be nucleus and a loosely bound proton, whose spatial distribution determines, to a considerable extent, the radius of the ^{8}B nucleus.

The structural features of light neutron-deficient nuclei may underlie the so-called fast rp processes of proton capture. For example, the presence of a state belonging to the proton-halo type [32] (a proton far off the nuclear core) may increase the rate of synthesis of light radioactive nuclei along the proton drip line, which decay to stable isotopes. In particular, the halo of ^{8}B reduces the Coulomb repulsion in the ^{3}Heαp fusion of nuclei in mixtures of stable isotopes of H and He in astrophysical systems. The product ^{8}B nucleus can either “wait” for β^+ decay or, within certain astrophysical scenarios, participate in the fusion processes α^8B $\to$ ^{12}N(β^+) $\to$ ^{12}C. A much longer lifetime of ^{8}B is a feature that distinguishes this process from the synthesis of ^{12}C through ^{8}Be nuclei.

A beam of secondary nuclei that have a magnetic rigidity that corresponds to the ratio $Z/A = 5/8$ was formed in accelerating, at the JINR nuclotron, ^{10}B nuclei of momentum 1 GeV/c per nucleon and intensity about 10^8 nuclei per spill (the fragmentation process $^{10}\mathrm{B} \to$ ^{8}B, as was proposed in [25]). Results of irradiation for ^{8}B interactions in emulsion were obtained. It is planned to determine the probabilities of the formation of $^8\mathrm{B} \to$ ^{7}Bep, α^3Hep, ^{6}Lipp, αdpp white stars. In the fragmentation process $^8\mathrm{B} \to$ ^{7}B, the intersection of the proton drip line also occurs. Here, it becomes possible to study the decay channels $^7\mathrm{B} \to$ ^{3}He^{3}Hep (analog of ^{9}B), ^{4}Heppp. In order to study the structure of ^{12}N and to clarify the role of ^{8}B in this nucleus, it is planned to irradiate emulsions with a beam of nuclei produced in the charge-exchange reaction $^{12}\mathrm{C} \to$ ^{12}N. In turn, the decays of yet another nucleus beyond the proton drip line can be studied in the fragmentation process $^{12}\mathrm{N} \to$ ^{11}N.

Clustering in the Decays of ^{7}Be Nuclei

It is of interest to study the fragmentation of a ^{7}Be nucleus, since this nuclear species can form a core in the ^{8}B nucleus. It would be instructive to employ a unified approach to compare, on the basis of the probabilities of white-star formation in the α^3He and ^{6}Lip channels, the cluster structure of this nucleus with those in ^{6}Li [21] and ^{7}Li nuclei, which are close to it in structure [25].

An emulsion was irradiated with ^{7}Be nuclei of energy 1.23 GeV per nucleon. The beam of these nuclei was formed at the JINR nuclotron on the basis of the charge-exchange reaction $^7\mathrm{Li} \to$ ^{7}Be. The procedure of following all primary tracks made it possible to find 75 white stars, where the total charge of secondary tracks within the cone of angular size 15° was $Z = 4$. Examples of such stars for $2+2$ topology with and without target excitation, as well as for $3+1$ and $1+1+1+1$ topologies, are given in Fig. 2. Table 9 presents the charge-topology distribution of these stars. One observes here a channel involving the separation of a singly charged fragment that is unambiguously interpreted as ^{6}Lip. As a special feature, one can indicate two cases of a complete breakup of the nucleus in question to singly charged fragments. For 36 events of $2+1+1$ topology, the method for assessing total momentum on the basis of multiple scattering made it possible to identify 20 $Z = 2$ tracks as ^{3}He and the remaining 16 tracks as ^{4}He. In the mass separation of He nuclei, use was made of $P\beta = 5.1$ GeV/c as the boundary value of the total momentum of fragments. As a continuation of our investigations, it is of interest to analyze the channel $^7\mathrm{Be} \to$ ^{6}Be(n) $\to$ ^{4}He$pp(n)$, which is accompanied by target-nucleus fragmentation induced by a neutron.

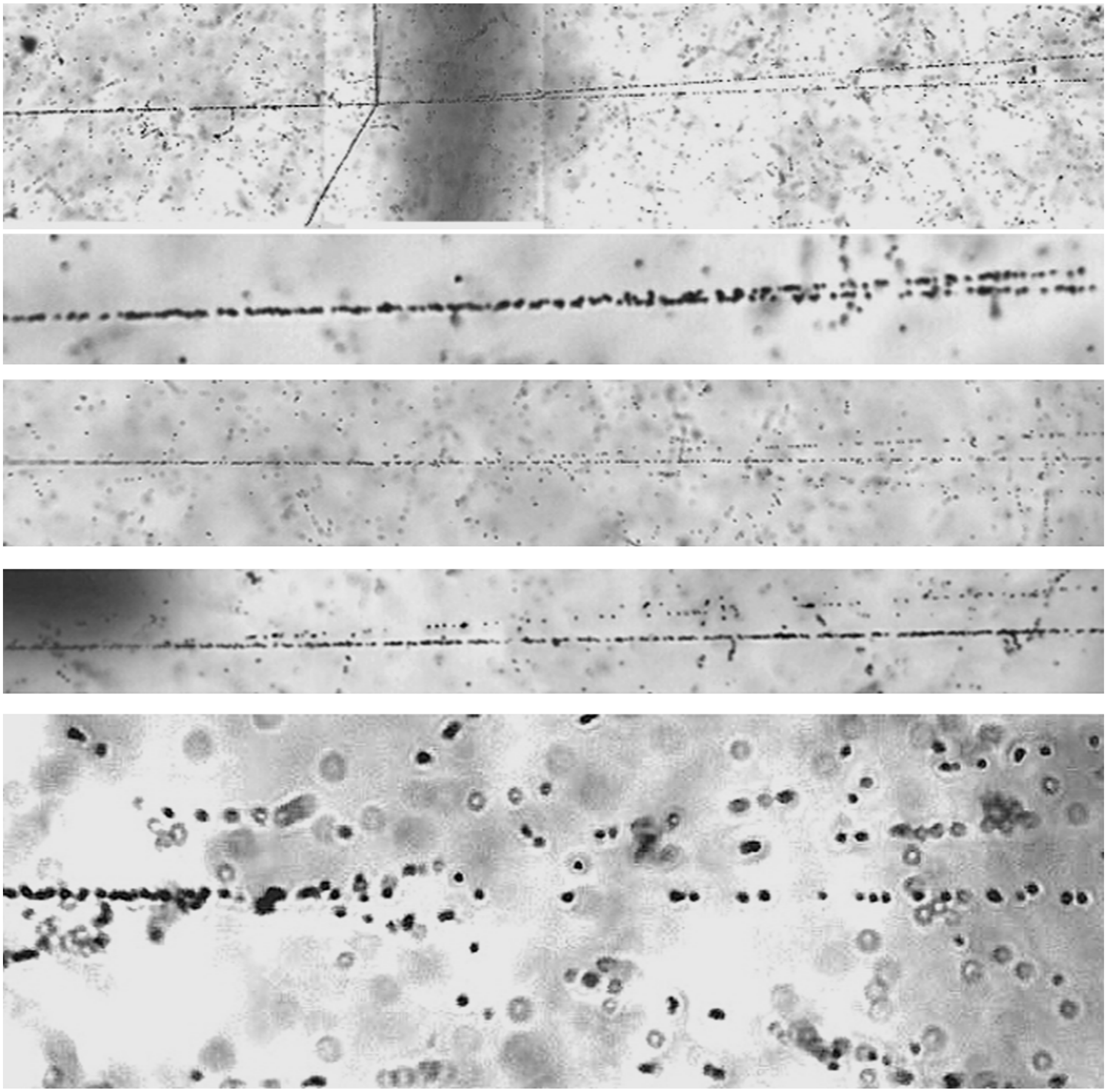

Fig. 2. Examples of events of the peripheral dissociation of ^{7}Be nuclei with an energy of 1.23 GeV per nucleon in emulsion. The upper photograph shows the process in which splitting to two He fragments is accompanied by the formation of two target fragments. The lower photographs show in succession white stars corresponding to splitting into two helium fragments, one helium fragment and two hydrogen fragments, one lithium and one hydrogen fragment, and four hydrogen fragments.

In Fig. 3, two-particle decays are represented by points whose coordinates are defined as the total momenta $P\beta$ of $Z = 2$ fragments—more specifically, the maximum and the minimum value of $P\beta$ in an event are taken for the ordinate and the abscissa, respectively. The distribution is clearly seen to be anisotropic. The decay $^7\text{Be}^* \to \alpha^3\text{He}$, proceeding at a minimal excitation above the decay threshold, is dominant in 22 events of $2 + 2$ topology in relation to other channels. Within this topology, five events were identified as those of the decay $^7\text{Be}^* \to (n)^3\text{He}^3\text{He}$. Thus, clustering accompanied by the production of a ^{3}He nucleus clearly manifests itself in white stars generated by ^{7}Be nuclei. This conclusion gives sufficient grounds to pose the question of clustering in neighboring neutron-deficient nuclei.

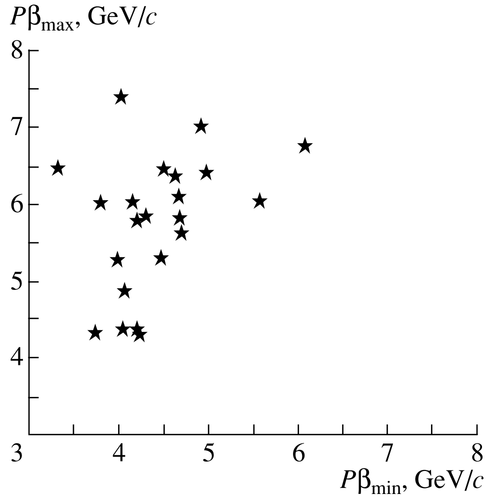

Fig. 3. Distribution of white stars generated by ^{7}Be nuclei of energy 1.23 GeV per nucleon for decays to two helium fragments in terms of the minimum and maximum momenta.

CONCLUSIONS

A review of experimental observations of the multifragmentation of light relativistic nuclei by means of emulsions has been given. Events of the white-star type that involve only tracks of fragments of a relativistic nucleus and which do not contain tracks of charged mesons or tracks of target-nucleus fragments have been selected. The topology of multifragmentation has been considered for these events.

An almost complete suppression of the binary splitting of nuclei to fragments of charge in excess of two, $Z > 2$, is a feature peculiar to charge topology in the fragmentation of Ne, Mg, Si, and S nuclei. Processes involving the separation of single fragments and proceeding at minimal excitation energies are dominant here. An increase in the degree of nuclear fragmentation manifests itself in the growth of the multiplicity of $Z = 1$ and 2 fragments as the charge of the unexcited part of the fragmenting nucleus (this is its main part) decreases.

Special features of the formation of systems of extremely light nuclei α, d, and t have been established in the multifragmentation of stable Li, B, C, N, and O isotopes. For example, nucleon clustering in the form of deuterons in the decays of ^{6}Li and ^{10}B and in the form of tritons in the decays of ^{7}Li has been found in addition to alpha-particle clustering. Moreover, the important role of multiparticle dissociation has been proven for these nuclei.

A manifestation of ^{3}He clustering can be discovered in white stars from the dissociation of neutron-deficient isotopes of Be, B, and C. An analysis of white stars from ^{7}Be nuclei shows a manifestation of ^{3}He clustering.

Emulsions provide a unique basis for reconstructing relativistic multiparticle systems. Some of such systems can play the role of initial or loosely bound intermediate states in the fusion of more than two nuclei in nucleosynthesis in stars. The observational basis described in the present article can be used in searches for such states.

ACKNOWLEDGMENTS

In conclusion, we would like to recall our supervisors in investigations with relativistic nuclei, who, unfortunately, passed away. The basis of investigations along these lines was laid by Academician A.M. Baldin. For many years, M.I. Adamovich, V.I. Ostroumov, Z.I. Solov'eva, K.D. Tolstov, M.I. Tret'yakova, and G.M. Chernov were the leaders of investigations performed by the nuclear-emulsion method in beams from the JINR synchrophasotron.

The results presented here are based to a considerable extent on painstaking visual searches and measurements, which could hardly be possible without the generous contribution from technicians including A.V. Pisetskaya (Lebedev Institute of Physics); L.N. Tkach (Petersburg Nuclear Physics Institute); and N.A. Kachalova, I.I. Sosul'nikova, A.M. Sosul'nikova, and G.V. Stel'makh (JINR). I.I. Mar'in (JINR) ensured the maintenance of the microscopes used. A high-quality development of emulsions was performed by the Chemical Group of the V.I. Veksler and A.M. Baldin Laboratory of High Energies at JINR. Specialists from this laboratory who ensured a stable operation of the JINR nuclotron made a valuable contribution to our study. We are indebted to the Directorate of the G.N. Flerov Laboratory of Nuclear Reactions (JINR) for support in timely purchasing emulsions.

This work was supported by the Russian Foundation for Basic Research (project nos. 96-1596423, 02-02-164-12a, 03-02-16134, 03-02-17079, 04-02-16593, and 04-02-17151); the Agency for Science at the Ministry for Education of the Slovak Republic and Slovak Academy of Sciences (grant VEGA no. 1/9036/02); and grants from the plenipotentiaries of the Slovak Republic, Czech Republic, and Romania at JINR in 2002 and 2003.

REFERENCES

1. M. I. Adamovich *et al.*, JINR Commun., No. E1-10838 (Dubna, 1977).
2. A. Marin *et al.*, Yad. Fiz. **32**, 1387 (1980) [Sov. J. Nucl. Phys. **32**, 716 (1980)].
3. U. A. Abdurazakova, R. A. Bondarenko, U. G. Gulyamov *et al.*, Yad. Fiz. **39**, 272 (1984) [Sov. J. Nucl. Phys. **39**, 169 (1984)].

4. V. V. Belaga *et al.*, Yad. Fiz. **58**, 2014 (1995) [Phys. At. Nucl. **58**, 1905 (1995)].
5. V. V. Belaga *et al.*, Pis’ma Zh. Éksp. Teor. Fiz. **62**, 385 (1995) [JETP Lett. **62**, 395 (1995)].
6. A. I. Bondarenko *et al.*, Yad. Fiz. **61**, 263 (1998) [Phys. At. Nucl. **61**, 214 (1998)].
7. N. P. Andreeva *et al.*, JINR Commun., No. P1-85-692 (Dubna, 1985).
8. M. Karabova *et al.*, Acta Phys. Slov. **36**, 238 (1986).
9. N. P. Andreeva *et al.*, Yad. Fiz. **47**, 157 (1988) [Sov. J. Nucl. Phys. **47**, 102 (1988)].
10. N. P. Andreeva *et al.*, Pis’ma Zh. Éksp. Teor. Fiz. **47**, 20 (1988) [JETP Lett. **47**, 23 (1988)].
11. A. El-Naghy *et al.*, J. Phys. G **14**, 1125 (1988).
12. A. El-Naghy *et al.*, JINR Commun., No. E1-85-547 (Dubna, 1985).
13. A. I. Bondarenko, V. V. Rusakova, Dzh. A. Salomov, and G. M. Chernov, Sov. Phys. J. **34**, 400 (1991).
14. S. A. Krasnov *et al.*, JINR Commun., No. P1-88-252 (Dubna, 1988).
15. Collab. (B. U. Ameeva *et al.*), Yad. Fiz. **51**, 1047 (1990) [Sov. J. Nucl. Phys. **51**, 669 (1990)].
16. M. I. Adamovich *et al.*, Z. Phys. A **351**, 311 (1992).
17. M. I. Adamovich *et al.*, Z. Phys. C **55**, 235 (1992).
18. F. A. Avetyan *et al.*, Yad. Fiz. **59**, 110 (1996) [Phys. At. Nucl. **59**, 102 (1996)].
19. F. G. Lepekhin, D. M. Seliverstov, and B. B. Simonov, Yad. Fiz. **58**, 881 (1995) [Phys. At. Nucl. **58**, 816 (1995)].
20. F. G. Lepekhin *et al.*, Eur. Phys. J. A **1**, 137 (1998).
21. M. I. Adamovich *et al.*, Yad. Fiz. **62**, 1461 (1999) [Phys. At. Nucl. **62**, 1378 (1999)].
22. M. I. Adamovich *et al.*, Part. Nucl. Lett. **110**, 29 (2003); nucl-ex/0206013.
23. V. Bradnova *et al.*, Few-Body Syst., Suppl. **14**, 241 (2003).
24. V. Bradnova *et al.*, Yad. Fiz. **66**, 1694 (2003) [Phys. At. Nucl. **66**, 1646 (2003)].
25. M. I. Adamovich *et al.*, Yad. Fiz. **67**, 533 (2004) [Phys. At. Nucl. **67**, 514 (2004)].
26. G. Baroni *et al.*, Nucl. Phys. A **516**, 673 (1990).
27. G. Baroni *et al.*, Nucl. Phys. A **540**, 646 (1992).
28. V. Efimov, Phys. Lett. B **32B**, 563 (1970).
29. F. Nunes, Comptes Rendus Physique **4**, 489 (2003).
30. P. Schuck, H. Horiuchi, G. Röpke, and A. Tohsaki, Comptes Rendus Physique **4**, 537 (2003).
31. V. G. Bogdanov *et al.*, Pis’ma Zh. Éksp. Teor. Fiz. **44**, 306 (1986) [JETP Lett. **44**, 391 (1986)].
32. W. Schwab *et al.*, Z. Phys. A **350**, 283 (1995).

Translated by A. Isaakyan

Physics of Atomic Nuclei, Vol. 68, No. 3, 2005, pp. 466–470. Translated from Yadernaya Fizika, Vol. 68, No. 3, 2005, pp. 495–499.

Measurement of Inclusive Pion Double Charge Exchange on ^{16}O at $T_0 \geq 0.5$ GeV with the SKS Spectrometer at KEK

A. P. Krutenkova[1], **O. Hashimoto**[2], **T. Watanabe**[2], **H. Noumi**[3], **P. K. Saha**[3], **D. Abe**[2], **A. B. Kaidalov**[1], **V. V. Kulikov**[1], **T. Nagae**[3], **M. Nakamura**[4], **T. Takahashi**[2], **H. Tamura**[2], and **Y. Fujii**[2]

Received May 24, 2004

Abstract—The inclusive cross section for pion double charge exchange on ^{16}O at $T_0 = 0.5$ and 0.75 GeV was measured with the superconducting kaon spectrometer (SKS) at KEK in a joint ITEP/KEK experiment. The result shows a relatively weak energy dependence of the measured cross section, which is in contradiction with its rapid drop predicted within the conventional model of two sequential single charge exchanges. The data of this experiment agree with the results that were obtained previously from similar measurements at ITEP and which are indicative of a significant contribution from the mechanism of inelastic Glauber rescatterings for $T_0 \gtrsim 0.6$ GeV. *© 2005 Pleiades Publishing, Inc.*

1. INTRODUCTION

Investigation of exclusive pion double charge exchange (DCX) at an incident-pion kinetic energy of $T_0 \simeq 1$ GeV has long been considered as a promising tool [1] for seeking two-nucleon correlations in nuclei, since DCX is a process that involves only two intranuclear nucleons. For $T_0 \lesssim 0.5$ GeV, the energy dependence of the experimental cross section for exclusive DCX on nuclei can be reasonably described [2] within the model of two sequential single charge-exchange interactions $\pi^{\mp} \to \pi^0 \to \pi^{\pm}$ (SSCX mechanism). There is no relevant experimental data at high energies; at the same time, the cross section for forward DCX according to the calculations in [2] within the SSCX mechanism decreases by approximately two orders of magnitude in the energy range $T_0 \approx 0.5$–1 GeV. It was expected [1, 2] that the contribution from other possible DCX mechanisms (in particular, those associated with two-nucleon correlations) could be revealed against the background of so fast a decrease in the cross section.

At the Institute of Theoretical and Experimental Physics (ITEP, Moscow), inclusive DCX processes (which have larger cross sections than their exclusive counterparts, so that their detection does not require a high momentum resolution of the spectrometer) were studied in the energy range 0.6–1.1 GeV [3]. A high-energy section of the emitted-pion spectrum near its endpoint, where the DCX process is pure owing to the impossibility of additional-pion production, which is forbidden by the energy-conservation law, was selected in that experiment.

It turned out [3] that, as the energy T_0 grows from 0.6 to 1.1 GeV, the cross section for forward DCX decreases by a factor of 2.5 to 3, while the calculation within the SSCX mechanism predicts a decrease in the inclusive cross section by a factor of 25 to 30. Thus, it was shown that other mechanisms can make a dominant contribution to DCX reactions in this energy region. Inelastic rescatterings provide a natural candidate for such a mechanism [4]. A substantiation of this effect within the Gribov–Glauber formalism was given in [5], and a method for estimating it within the one-pion-exchange model was proposed in [6]. The resulting estimate confirmed, in principle, the possibility of explaining the experimental data in question within this theoretical mechanism.

The objective of the joint ITEP/KEK investigation was to measure inclusive DCX cross sections in the energy region accessible to the superconducting magnetic spectrometer (SKS) with an accuracy higher than that attainable in less intense beams at ITEP and within a somewhat different procedure.

2. DESCRIPTION OF THE EXPERIMENT

Pion double charge exchange was studied in the K6 beam of negatively charged pions from the 12-GeV KEK proton synchrotron at energies of $T_0 = 0.5$ and 0.75 GeV. The measurements in question

---

[1] Institute of Theoretical and Experimental Physics, Bol'shaya Cheremushkinskaya ul. 25, Moscow, 117259 Russia.

[2] Tohoku University, Sendai, 980-77 Japan.

[3] KEK, 1-1 Oho, Tsukuba-shi, Ibaraki-ken 305, Japan.

[4] University of Tokyo, 7-3-1 Hongo, Bunkyo-ku, Tokyo 113, Japan.

1063-7788/05/6803-0466$26.00 © 2005 Pleiades Publishing, Inc.

were performed within the experiment described in [7] (see Fig. 1). The beam intensity was (1–2) × 10^6 particles/s at a spill duration of about 1 s. The beam spectrometer involved a magnetic system of the $QQDQQ$ type, four sets of drift chambers ($BDC1$–$BDC4$) with 24 planes of sensitive wires for momentum vector reconstruction, and three trigger counters [a gas Cherenkov counter GC filled with freon and two hodoscopes of scintillation counters ($BH1$ and $BH2$)]. A negatively charged pion that traversed the beam spectrometer interacted with a target 5 cm long filled with water. A positive particle emitted from the target in the forward direction as the result of the reaction

$$\pi^- + A \to (e^+, \pi^+, p) + X \qquad (1)$$

was analyzed in the SKS magnetic field [8]. The SKS apparatus was comprised of a superconducting dipole magnet supplemented with four sets of drift chambers ($SDC1$–$SDC4$ involving 22 planes of sensitive wires) intended for reconstructing linear momenta, and the trigger counters of TOF (scintillation) and LC (Cherenkov) hodoscopes. Data acquisition was initiated by a trigger that was generated by the coincidence of signals from the counters ($BH1 \times BH2 \times \overline{GC} \times TOF \times LC$). In order to extend the momentum acceptance for an emitted particle, the measurements were performed at two values of the spectrometer magnetic field for each initial energy ($I_{\text{SKS}} = 145$ and 175 A at $T_0 = 0.5$ GeV and $I_{\text{SKS}} = 272$ and 320 A at $T_0 = 0.75$ GeV).

The procedures for data acquisition and data processing were described in detail elsewhere [9–11]. We selected events for which the tracks of the beam and emitted particles were measured in all chamber planes and were successfully reconstructed in space. In order to suppress the background, we imposed cuts on the position of the event vertex along the beam axis (this removes interactions in the magnet material and in other parts of the facility) and on the time of flight between the BH2 and TOF hodoscopes (this suppresses protons).

The positron background, which arises both from the interactions of electrons in the target that are admixed to the beam and from the decays of π^0 produced in the target, was preliminary measured by the EAC Cherenkov counter (which was not used in data acquisition) [11]. The correction R to the cross section due to the positron admixture was $R = N(\pi^-, e^+)_{\text{true}}/(N(\pi^-, e^+)_{\text{true}} + N(\pi^-, \pi^+)_{\text{true}}) = 0.54 \pm 0.08$ and 0.35 ± 0.06 at $T_0 = 0.5$ and 0.75 GeV, respectively.

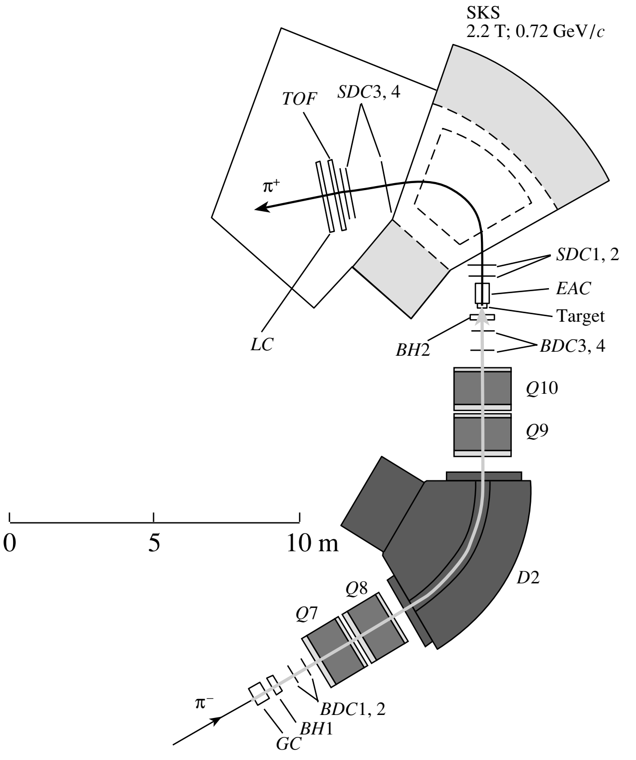

Fig. 1. Layout of the experimental facility used.

3. SPECTRA OF EMITTED PIONS

In Fig. 2, the differential cross section for the reaction

$$\pi^- + {}^{16}\text{O} \to \pi^+ + X \qquad (2)$$

at $T_0 = 0.5$ and 0.75 GeV in the angular range $4° \geq \theta \geq 6°$ for two values of the magnetic field at each energy value is shown as a function of $\Delta T = T_0 - T$, where θ and T are the emission angle of the positively charged pion and its kinetic energy, respectively. It is clear from the figure that the results for the different currents in the SKS are consistent within the statistical errors and can be averaged. The systematic error, which includes the uncertainty of calibration of the ΔT scale, does not exceed 10%.

In Fig. 2, the spectra obtained here are compared with (a) LAMPF data [12] for the reaction

$$\pi^+ + {}^{16}\text{O} \to \pi^- + X \qquad (3)$$

at $T_0 = 0.5$ GeV and $\theta = 5°$ and (b) ITEP results [3] at $T_0 = 0.75$ GeV and $\theta \approx 5°$. The solid and the dashed curve represent the results of the calculations from [3] on the basis of the SSCX model [13] that were performed, respectively, without and with allowance for the in-medium modification of the amplitude for pion single charge exchange [2].

At $T_0 = 0.75$ GeV, the slope of the spectrum changes in the region $\Delta T \sim 150$ MeV, this being due

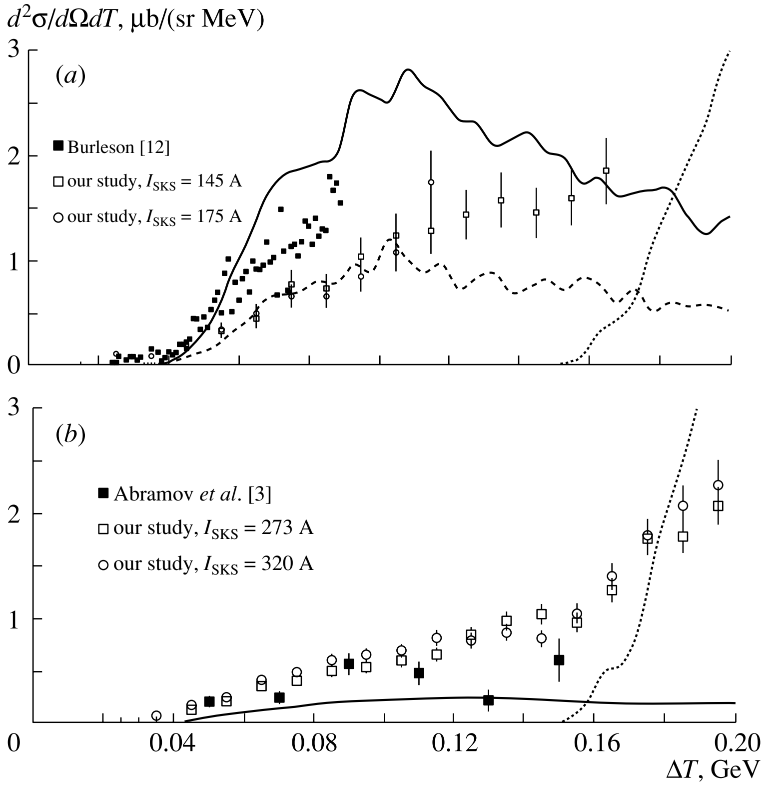

Fig. 2. Differential cross section for the reaction $\pi^{-16}\mathrm{O} \to \pi^+X$ in the angular range $\theta = 4°{-}6°$ as a function of $\Delta T = T_0 - T$ at the initial energies of $T_0 =$ (*a*) 0.5 and (*b*) 0.75 GeV. The solid and dashed curves were calculated within the cascade model for the SSCX mechanism (solid curve) without and (dashed curve) with allowance for the in-medium modification of the amplitude for pion single charge exchange. The dotted curve represents the cross section for the production of an additional pion.

to the threshold for the reaction of additional-pion production on an intranuclear proton in the nucleus. The cross section for this reaction was obtained on the basis of the cascade model and is shown in Fig. 2*b* by the dotted curve. However, this curve ascends more sharply than the measured cross section. This is likely to be caused by a far extrapolation of experimental data that is embedded in the cascade model (because of the lack of experimental data on pion production at $T_0 \sim 0.75$ GeV).

At $T_0 = 0.5$ GeV, our experimental data are systematically below the LAMPF cross sections. At $\Delta T \leq 110$ MeV, the present data are described within the SSCX model allowing for the in-medium modification of the amplitude for pion single charge exchange (dashed curve). At $T_0 = 0.75$ GeV, the results obtained here are in good agreement with the ITEP data from [3] and systematically exceed the predictions of the SSCX model even without allowance for the aforementioned modification of the amplitude for pion single charge exchange.

4. ENERGY DEPENDENCE OF THE CROSS SECTION

In order to obtain the energy dependence of the DCX cross section, we integrated the differential cross sections presented in Fig. 2 with respect to the ΔT from 0 to 140 MeV ($\langle d\sigma/d\Omega\rangle_{140}$). Figure 3 displays the resulting energy dependences averaged over $I_{\rm SKS}$ (closed circles). Figure 3 also shows the results obtained in [14] at $T_0 = 0.18$, 0.21, and 0.24 GeV and $\theta = 25°$ (open circles) and the ITEP results from [3] for T_0 values between 0.6 and 1.1 GeV (asterisks). The solid curve in the figure represents the cross section $\langle d\sigma/d\Omega\rangle_{140}$ for reaction (2) according to calculations within the SSCX model (that is, with π^0 in the intermediate state).

We see from the figure that the SKS data are in good agreement with the results from [3] and confirm the conclusion that the decrease in the cross section for the reaction under study is anomalously slow in the energy interval 0.6–1.1 GeV. This suggests the existence of a significant contribution from other possible DCX mechanisms in this region. As was shown in [5], the calculations at $T_0 \gtrsim 0.6$ GeV must take into account Glauber inelastic rescatterings (IR) in the intermediate state (first of all, two-pion rescatterings). By way of example, we indicate that, in [6], the cross section for reaction (2) was represented as the sum of two contributions: that which corresponds to intermediate π^0 and that which corresponds to an intermediate two-pion state. The latter contribution was estimated in the Gribov—Glauber approximation for the one-pion-exchange model. The dashed and dotted curves in Fig. 3 show the upper and the lower bound on this theoretical estimate, respectively. According to [6], the cross section must approach the upper bound for $T_0 \lesssim 1$ GeV and the lower bound for $T_0 \gtrsim 2$ GeV.

Thus, the preliminary results of the experiment that are presented in Fig. 3 suggest a significant contribution of the inelastic-rescattering mechanism to inclusive DCX at $T_0 \gtrsim 0.6$ GeV and highlight the importance of measuring the cross section at $T_0 \geq 1.1$ GeV, where the data show a maximum deviation from the SSCX prediction. It is worth noting that the inclusive DCX reaction for $T_0 \simeq 1$–5 GeV is presently the only process where the inelastic-rescattering mechanism is likely to be dominant. We recall that its contribution to the total pion—nucleus cross sections is as small as a few percent [15].

Interest in the IR mechanism is motivated by the following circumstances. First, this mechanism is fully disregarded in the existing cascade models. Second, inelastic rescatterings that produce intermediate hadron systems of high masses play a significant role in high-energy hadron—nucleus and nucleus—nucleus collisions (see, for example, [16, 17]). They result, in particular, in a sizable decrease in the multiplicity of hadrons (per rapidity unit) produced in these processes. For example, the inclusive cross sections for the hadron production at the RHIC energy decrease by a factor of about 2 in relation to the prediction of the Glauber model [17—19]. From the point of view of QCD, these phenomena correspond to the shadowing of soft partons in colliding nuclei [20, 21] and, at ultrahigh energies, lead to saturation [22].

5. CONCLUSION

The measurements of the inclusive pion double charge exchange on ^{16}O at $T_0 = 0.5$ and 0.75 GeV with higher statistics by means of SKS confirmed the previously observed anomalously slow decrease in the cross section for this process with energy for $T_0 \gtrsim 0.6$ GeV. The resulting data are indicative of a small contribution from a one-pion intermediate state in the model of two sequential charge exchanges and furnish evidence for a dominant contribution of Glauber inelastic rescatterings to the cross section for the process. In principle, we cannot rule out effects of a strong in-medium modification of the pion—nucleon amplitude like that in [23].

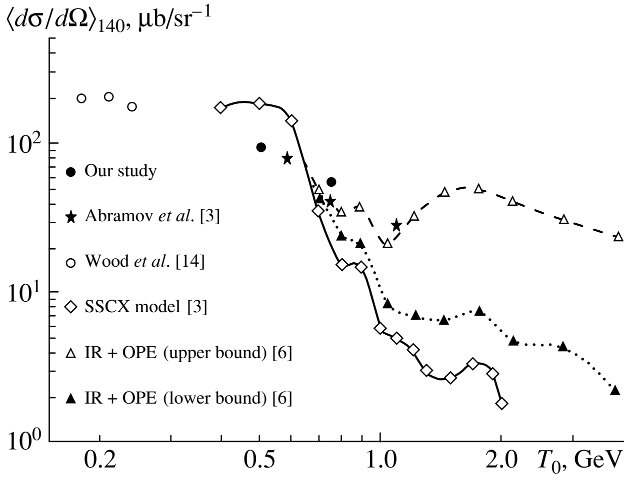

Fig. 3. Energy dependence of the $\pi^{-16}\mathrm{O} \to \pi^+ X$ cross section integrated with respect to ΔT from 0 to 140 MeV.

ACKNOWLEDGMENTS

We are grateful to all services of the KEK proton synchrotron for providing a stable operation of the accelerator and SKS apparatus throughout the experiment. A.P. Krutenkova thanks the KEK and the Tohoku University management for hospitality kindly extended to her.

This work was supported in part by the Federal Target-Oriented Scientific and Technological Program (grant no. 40.052.1.1.1113), the Program for Support of Leading Scientific Schools (grant no. 1867.2003.02), and the Russian Foundation for Basic Research (project no. 01-02-17383).

REFERENCES

1. O. Hashimoto, Preprint No. INS-844, Tokyo University (Tokyo, 1990); in *Perspectives of Meson Science* (North-Holland, Amsterdam, 1992), Chap. 19, p. 547.
2. E. Oset and D. Strottman, Phys. Rev. Lett. **70**, 146 (1993); E. Oset, D. Strottman, H. Toki, and J. Navarro, Phys. Rev. C **48**, 2395 (1993).
3. B. M. Abramov *et al.*, Nucl. Phys. A **723**, 389 (2003); Yad. Fiz. **65**, 253 (2002) [Phys. At. Nucl. **65**, 229 (2002)]; **59**, 399 (1996) [**59**, 376 (1996)].
4. O. D. Dal'kapov, private communication (1994).
5. A. B. Kaidalov and A. P. Krutenkova, Yad. Fiz. **60**, 1334 (1997) [Phys. At. Nucl. **60**, 1206 (1997)].
6. A. B. Kaidalov and A. P. Krutenkova, J. Phys. G **27**, 893 (2001).
7. H. Noumi *et al.*, Phys. Rev. Lett. **89**, 072301 (2002).
8. T. Fukuda *et al.*, Nucl. Instrum. Methods Phys. Res. A **361**, 485 (1995).
9. P. K. Saha, Dr. Thesis, Sokendai (KEK Report No. 2001-17).
10. M. Nakamura, Master Thesis (University of Tokyo, 2001).

11. T. Watanabe, Master Thesis (Tohoku University, 2001).
12. G. R. Burleson, in *Proceedings of the Second LAMPF Workshop on Pion–Nucleus Double Charge Exchange, Los Alamos, New Mexico, USA* (World Sci., Singapore, 1990), p. 79.
13. M. J. Vicente Vacas, M. Kh. Khankhasayev, and S. G. Mashnik, nucl-th/9412023.
14. S. A. Wood *et al.*, Phys. Rev. C **46**, 1903 (1992).
15. V. V. Anisovich, P. E. Volkovitsky, and L. G. Dakhno, Phys. Lett. B **42B**, 224 (1972); A. B. Kaidalov and L. A. Kondratyuk, Nucl. Phys. B **56**, 90 (1973); V. A. Karmanov and L. A. Kondratyuk, Pis'ma Zh. Éksp. Teor. Fiz. **18**, 451 (1973) [JETP Lett. **18**, 266 (1973)].
16. A. B. Kaidalov, Nucl. Phys. A **525**, 39c (1991).
17. A. Capella, A. B. Kaidalov, and J. Tran Thanh Van, Heavy Ion Phys. **9**, 169 (1999).
18. A. B. Kaidalov, Surveys High Energy Phys. **16**, 267 (2001).
19. N. Armesto *et al.*, Eur. Phys. J. C **29**, 531 (2003).
20. L. McLerran and R. Venuqopalan, Phys. Rev. D **49**, 2233 (1994); **49**, 3352 (1994); **50**, 2225 (1994); A. Ayala *et al.*, Phys. Rev. D **53**, 458 (1996).
21. A. H. Mueller, Nucl. Phys. B **558**, 285 (1999); hep-ph/0208278.
22. *QCD Perspectives on Hot and Dense Matter*, Ed. by J.-P. Blaizot and E. Iancu (Kluwer Acad. Publ., 2002).
23. Ye. S. Golubeva, L. A. Kondratyuk, and W. Cassing, Nucl. Phys. A **625**, 832 (1997).

Translated by M. Kobrinsky

Physics of Atomic Nuclei, Vol. 68, No. 3, 2005, pp. 471–473. Translated from Yadernaya Fizika, Vol. 68, No. 3, 2005, pp. 500–502.
Original Russian Text Copyright © 2005 by Dubinina, Egorenkova, Krotkova, Pozharova, Smirnitsky.

Intergroup Azimuthal Correlations of Secondary Particles in the Interaction between ^{56}Fe Nuclei of Momentum 2.5 GeV/c per Nucleon and Photoemulsion Nuclei

V. V. Dubinina, N. P. Egorenkova, V. I. Krotkova, E. A. Pozharova, and V. A. Smirnitsky

Institute of Theoretical and Experimental Physics,
Bol'shaya Cheremushkinskaya ul. 25, Moscow, 117259 Russia

Received May 11, 2004

Abstract—Angular correlations between secondary particles emitted in the interaction between ^{56}Fe nuclei of momentum 2.5 GeV/c per nucleon and photoemulsion nuclei were measured. These secondaries are partitioned into four groups: s, g, b, and f. For particles from each pair of the above groups, the average values of the collinearity factor and of the asymmetry parameter, as well as the parameter η of the function $a(1 + \eta \cos\varepsilon)$ approximating the distribution of azimuthal-angle differences ε, were calculated.

1. INTRODUCTION

Investigation of azimuthal correlations provides information about the properties of nucleus–nucleus interactions. This problem was thoroughly considered in [1–4]. In nucleus–nucleus interactions, correlations are measured both within various groups of particles and for particles belonging to different groups (so-called intergroup correlations (ij)). In [1, 2], one can find a detailed list of references and a detailed investigation of azimuthal correlations without transforming nucleus–nucleus interactions to a common nuclear-reaction plane. In this study, we consider intergroup azimuthal correlations for various combinations of b, g, s, and f particles produced in the interaction between ^{56}Fe nuclei of momentum 2.5 GeV/c per nucleon and photoemulsion nuclei (FeEm) for the case where one performs a transformation of nuclear reactions to a common plane [5]. In accordance with the photoemulsion procedure [6], slow target-nucleus fragments whose kinetic energy rescaled to protons is $T_p \leq 26$ MeV (the range in emulsion is $R \leq 3$ mm) and whose velocity satisfies the condition $\beta \leq 0.23$ are identified as b particles. Predominantly, these are evaporated protons. Fast singly charged particles emitted from a target nucleus that have a kinetic energy rescaled to protons in the range $26 < T_p \leq 400$ MeV, a relative ionization of $I/I_0 > 1.4$ (I_0 is the ionization density of singly charged relativistic particles), and a velocity in the range of $0.23 < \beta \leq 0.7$ are taken to be g particles. As to s particles, they have a relative ionization of $I/I_0 < 1.4$ and $\beta > 0.7$, which corresponds to $T_p > 400$ MeV. Among s particles, there are pions, interacted projectile protons, and singly charged particles from a target nucleus. Relativistic multiply charged ($Z \geq 2$) and singly charged particles emitted within the fragmentation cone [6] are classified as projectile-nucleus fragments (f particles).

Intergroup azimuthal correlations depend on several parameters, including the asymmetry parameter (A_{ij}) and the collinearity factor (B_{ij}) [1, 2],

$$A_{ij} = (N(\varepsilon_{ij} \geq \pi/2) - N(\varepsilon_{ij} < \pi/2))/N(0 \leq \varepsilon_{ij} < \pi); \quad (1)$$

$$B_{ij} = (N(\varepsilon_{ij} < \pi/4) + N(\varepsilon_{ij} \geq 3\pi/4) - N(\pi/4 \leq \varepsilon_{ij} < 3\pi/4))/N(0 \leq \varepsilon_{ij} < \pi). \quad (2)$$

Here, ε_{ij} is the azimuthal-angle difference (pair azimuthal angle) for the case where one particle is taken from group i, while the other is taken from group j of the same interaction. The coefficients A_{ij} and B_{ij} are equal to zero for a uniform distribution of pair azimuthal angles and are nonzero if the particles being considered tend to escape either in the same direction or in opposite directions. The method of azimuthal correlation functions was considered in [1–3]. The probability distribution $W(\varepsilon_{ij})_{\text{corr}}$ for angles ε_{ij} between the transverse momenta of particles from two different groups (i, j) is defined as

$$W(\varepsilon_{ij})_{\text{corr}} = a(1 + \eta \cos\varepsilon_{ij}). \quad (3)$$

To rule out the instrumental anisotropy, one can consider the ratio

$$C(\varepsilon_{ij}) = W(\varepsilon_{ij})_{\text{corr}}/W(\varepsilon_{ij})_{\text{uncorr}}, \quad (4)$$

Correlation coefficients A_{ij} and B_{ij} and parameter η for various pairs of particles

Particle pair	η	χ^2/n.d.f.	χ^2/n.d.f., $C(\varepsilon_{ij}) = \text{const}$	A_{ij}	B_{ij}
	$C(\varepsilon_{ij}) = a(1+\eta\cos\varepsilon_{ij})$				
gs	0.26 ± 0.03	1.0	4.6	-0.12 ± 0.02	0.05 ± 0.02
fs	-0.29 ± 0.04	1.9	6.1	0.18 ± 0.03	-0.11 ± 0.06
fg	-0.11 ± 0.05	2.9	4.3	0.09 ± 0.03	-0.05 ± 0.03
fb	0.09 ± 0.03	2.4	1.6	-0.02 ± 0.02	0.02 ± 0.02
bs	0.09 ± 0.03	2.4	1.9	-0.08 ± 0.03	0.08 ± 0.05
bg	0.13 ± 0.04	1.2	2.1	-0.07 ± 0.02	0.06 ± 0.02

where $W(\varepsilon_{ij})_{\text{uncorr}}$ is determined from mixed events where particles belonging to groups i and j are taken from different interactions. In the case where there are no correlations, the distribution $C(\varepsilon_{ij})$ must be uniform ($\eta = 0$).

2. EXPERIMENTAL PROCEDURE AND RESULTS

Intergroup azimuthal correlations were studied within an experiment aimed at investigating azimuthal anisotropy in the interaction of ^{56}Fe nuclei with photoemulsion nuclei (FeEm) [5]. The emulsion chamber used was assembed from nuclear-photoemulsion layers of the BR-2 type. It was irradiated by a beam of ^{56}Fe nuclei accelerated to momentum of 2.5 GeV/c per nucleon at the Berkeley accelerator (Lawerence Berkeley Laboratory). Nucleus–nucleus interactions were sought by following projectile-nucleus tracks. To rule out edge effects (flat-chamber effect), we rejected events that occurred near the upper and lower surfaces of the developed emulsion layer (specifically, at distances less than 30 μm). For our analysis, we selected interactions involving more than three fragments of charge $Z \geq 2$. The details of event selection for FeEm and of a determination of nuclear-reaction planes are described in [5]. The particle emission angles were determined by measuring the coordinates of grains on tracks. The support program provided the necessary operator–computer dialogue and, hence, the on-line monitoring of the results of our measurements. The accuracy in measuring angular angles was about 1 mrad for singly charged particles.

The pair azimuthal angles ε_{ij} were measured for various combinations of particles. From the results of these measurements, we calculated the correlation coefficients A_{ij} and B_{ij} by Eqs. (1) and (2), the distribution $C(\varepsilon_{ij})$ by Eq. (4), and χ^2/n.d.f. for the case of $C(\varepsilon_{ij}) = \text{const}$. The table, gives the correlation coefficients A_{ij} and B_{ij}, the parameter η obtained from a fit to the distribution $C(\varepsilon_{ij})$ for various particles, and the corresponding values of χ^2/n.d.f. for n.d.f. = 17.

3. DISCUSSION OF THE RESULTS

The results obtained by measuring intergroup azimuthal correlations suggest the presence of a correlated flux of particles from different groups (i, j) in nucleus–nucleus interactions. In particular groups, we observed a simultaneous emission of particles either in the same direction or in opposite directions. Negative values of η indicate that fragments (f) and g and s particles escape in opposite directions. For b particles, there is a trend toward emission in the same direction with s and b particles. The emission of b particles simultaneously with s and f particles is virtually uncorrelated [see the values of χ^2/n.d.f. for $C(\varepsilon_{ij}) = \text{const}$ in the table], while their correlation with g particles is insignificant. The collinearity factor differs from zero only negligibly for all pairs of particles (the maximum value is $B_{ij} \cong 1$).

In events where the nuclear-reaction planes are made to be coincident, it is necessary to compare the results of measurements of the azimuthal anisotropy and correlation measurements with the results of calculations performed with various theoretical approaches to the mechanism of nucleus–nucleus interactions. The intergroup correlations observed here are not corroborated by calculations based on the cascade–evaporation model. Maybe, this phenomenon will be explained in terms of the hydrodynamic model, which takes into account collective flows of nuclear matter.

ACKNOWLEDGMENTS

We are grateful to V.A. Sheinkman for assistance in the irradiation of test samples of nuclear photoemulsion at the accelerator of the Institute of Theoretical and Experimental Physics (ITEP, Moscow) and V.V. Shamanov for his help in the organization of computer-aided data processing.

REFERENCES

1. A. I. Bondarenko, Doctoral Dissertation in Mathematics and Physics (Dubna, 1997).
2. S. Vokal, Doctoral Dissertation in Mathematics and Physics (Dubna, 2001).
3. S. Wang *et al.*, Phys. Rev. C **44**, 1091 (1991).
4. W. K. Wilson *et al.*, Phys. Rev. C **45**, 738 (1992).
5. V. V. Dubinina, N. P. Egorenkova, V. I. Krotkova, *et al.*, Yad. Fiz. **67**, 537 (2004) [Phys. At. Nucl. **67**, 518 (2004)].
6. C. F. Powell, P. H. Fowler, and D. H. Perkins, *The Study of Elementary Particles by the Photographic Method* (Pergamon, London, 1959; Inostrannaya Literatura, Moscow, 1962).

Translated by V. Bukhanov

Physics of Atomic Nuclei, Vol. 68, No. 3, 2005, pp. 474–480. Translated from Yadernaya Fizika, Vol. 68, No. 3, 2005, pp. 503–509.

Quasielastic Deuteron and Triton Knockout from Lithium Isotopes by Intermediate-Energy Pions

B. M. Abramov, Yu. A. Borodin, S. A. Bulychjov, I. A. Dukhovskoy,
A. P. Krutenkova, V. V. Kulikov*, M. A. Martemianov,
M. A. Matsyuk, V. E. Tarasov, E. N. Turdakina, and A. I. Khanov

Institute of Theoretical and Experimental Physics,
Bol'shaya Cheremushkinskaya ul. 25, Moscow, 117259 Russia

Received May 24, 2004; in final form, September 3, 2004

Abstract—Quasielastic deuteron and triton knockout from ^{6}Li and ^{7}Li nuclei that was induced by a π^--meson beam of momentum $p_0 = 0.72$ and 0.88 GeV/c was studied under conditions of full kinematics. The experiment was performed at the Institute of Theoretical and Experimental Physics (ITEP, Moscow) by using a 3-m magnetic spectrometer equipped with spark chambers. The distributions with respect to the momenta of quasideuteron and quasitriton internal motion, the excitation-energy spectra of residual nuclei, and the effective numbers of quasideuterons in ^{6}Li and ^{7}Li nuclei were obtained. © *2005 Pleiades Publishing, Inc.*

1. INTRODUCTION

The quasielastic knockout of fragments from nuclei is an efficient method for studying the cluster structure of light nuclei. If one measures the kinematical features of both the knock-on fragment and the scattered beam particle (that is, under conditions of full kinematics), this method makes it possible to determine, within the pole mechanism, the momentum of fragment intranuclear motion and the energy of the residual nucleus by using data on the missing energy and momentum. In order to separate the effects of the cluster structure of a nucleus from those associated with the special features of the reaction mechanism, it is desirable to have relevant experimental data for various projectile particles. There are data obtained with electron and proton beams. Our experiment was aimed at extending the range of these particles by applying pion beams. It should be noted that a lower intensity of pion beams and an almost two orders of magnitude smaller cross section for pion–deuteron scattering into the backward hemisphere in relation to protons complicate the implementation of an experiment with pions considerably. In the experiment reported in [1], our group employed pions for the first time to study quasielastic deuteron knockout in the reaction

$$\pi^- + {}^6\text{Li} \to d + \pi^- + {}^4\text{He}. \qquad (1)$$

In performing an analysis of the results of those measurements, which was based on the αd model of the ^{6}Li nucleus, the ground state of the residual nucleus was singled out by using its excitation energy.

In the present study, we analyze the entire excitation-energy spectrum of residual nuclei both for ^{6}Li and for ^{7}Li targets. Unexpectedly, it turned out that the statistics of our experiment are sufficient for observing quasielastic pion–triton scattering on these nuclei, and we were able to obtain the first data on the parameters of quasitriton clusters.

2. DESCRIPTION OF THE EXPERIMENT

The experiment was performed in beams of 0.72- and 0.88-GeV/c negatively charged pions from the 10-GeV proton synchrotron of the Institute of Theoretical and Experimental Physics (ITEP, Moscow). Use was made of a 3-m magnetic spectrometer equipped with spark chambers situated in a magnetic field (see, for example, [1, 2]). A target was placed near the center of the magnet. Owing to this and to a large volume covered by the magnetic field ($3 \times 0.5 \times 1$ m) we could perform a full kinematical analysis of the respective reaction—that is, to measure the momenta of the deuteron (triton) knocked out in the forward direction and the beam pion and the pion scattered in the backward directions and to determine the residual-nucleus energy to a precision of about 10 MeV. The targets used in the present experiment—those from ^{6}Li of isotopic composition 90.4% ^{6}Li and 9.6% ^{7}Li and those from ^{7}Li of natural isotopic composition (7.52% ^{6}Li and 92.48% ^{7}Li)—were

---

*E-mail: `kulikov@itep.ru`

1063-7788/05/6803-0474$26.00 © 2005 Pleiades Publishing, Inc.

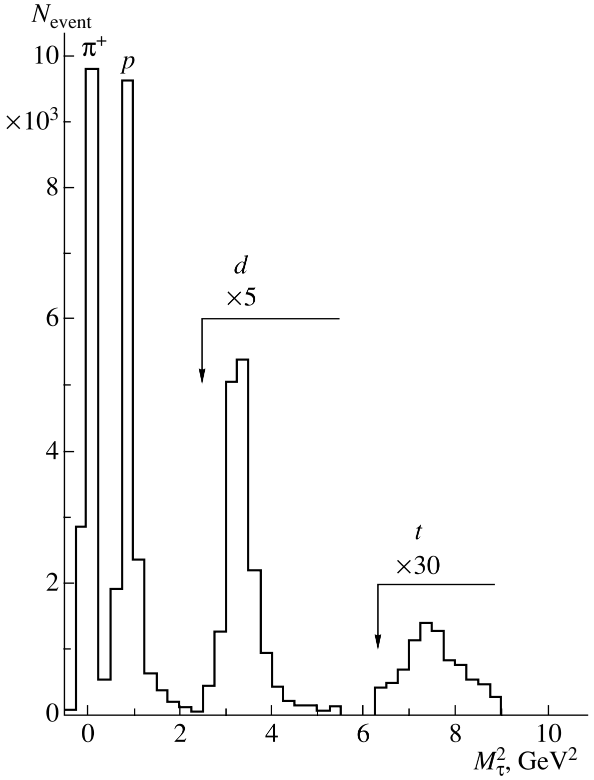

Fig. 1. Distribution of events with respect to the square of the mass (M_τ^2) of a particle emitted in the forward direction in the reactions $\pi^- + A \to (\pi^+, p, d, t) + X$.

manufactured in the form of solid cylinders 9.5 cm long and 8 cm in diameter that were enclosed by 0.1-mm-thick walls from stainless steel. All targets were mounted on a disk whose rotation made it possible to expose the required target to the beam.

The time of flight of a positively charged particle emitted from the target in the forward direction in the reactions

$$\pi^- + A \to (p, d, t) + \pi^- + X \qquad (2)$$

was determined over a base of about 6 m by using a system of hodoscopic scintillation counters of area 0.7×2.1 m^2. The distribution of events with respect to the square of the mass (M_τ^2) of a particle emitted in the forward direction is displayed in Fig. 1 according to calculations on the basis of the measured momentum and time of flight. The reactions involving deuteron and triton knockout were separated with the aid of the criteria $2.5 \le M_\tau^2 \le 5.5$ GeV^2 and $6.3 \le M_\tau^2 \le 8.9$ GeV^2, respectively. For the separated events, we calculated the momentum of quasideuteron (quasitriton) intranuclear motion as

$$\mathbf{p}_{\text{F}} = \mathbf{p}_0 - \mathbf{p}_d(\mathbf{p}_t) - \mathbf{p}_{\pi^-} \qquad (3)$$

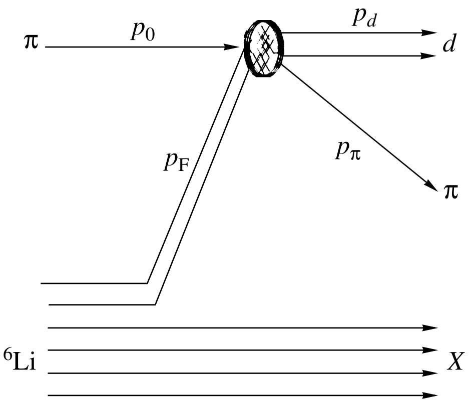

Fig. 2. Diagram of the plane-wave impulse approximation.

and the missing energy (or the excitation energy of the residual nucleus X) as

$$E_{\text{miss}} = T_0 - T_d(T_t) - T_{\pi^-} - T_X, \qquad (4)$$

where T is the kinetic energy; the indices 0, π, $d(t)$, and X label quantities referring to the primary pion, the final pion, the deuteron (triton), and the residual nucleus X, respectively; and $T_X = (\mathbf{p}_{\text{F}})^2/2M$, M being the residual-nucleus mass. A further analysis was performed in the plane-wave impulse approximation (PWIA), the corresponding pole diagram being given in Fig. 2 for the reaction in (1).

3. DEUTERON KNOCKOUT

3.1. Knockout of Deuterons from ^{6}Li

Figure 3 shows the distribution of recorded events of the reaction

$$\pi^- + {}^6\text{Li} \to d + \pi^- + X \qquad (5)$$

with respect to the missing energy E_{miss} at $p_0 = 0.72$ GeV/c. As was shown in [3], this spectrum reduces to a delta function at $E_{\text{miss}} = 1.5$ MeV, this corresponding to the knockout of a deuteron cluster [$X = {}^4\text{He}_{\text{g.s.}}$, reaction (1)], and is continuous for $E_{\text{miss}} \ge 22$ MeV, this corresponding to deuteron knockout from an alpha-particle cluster and the breakup of the residual nucleus ($X = {}^4\text{He}_{\text{e.s.}}$; see also [1]).

Events of reaction (5) for $X = {}^4\text{He}_{\text{g.s.}}$ populate predominantly the range $-0.020 \le E_{\text{miss}} \le 0.015$ GeV, while events corresponding to deuteron knockout from an alpha-particle cluster ($X = dd$, dnp) fall within the interval $0.015 \le E_{\text{miss}} \le 0.070$ GeV. The distributions of events from these intervals with respect to the momentum of intranuclear motion (see Figs. 4a and 4b, respectively) were described in terms of Gaussian functions $\exp(-p_{\text{F}}^2/\kappa^2)$.

Table 1. Parameter κ of quasideuteron internal motion [in the $\exp(-p_{\rm F}^2/\kappa^2)$ parametrization] and the effective number n_d of quasideuterons in ^{6}Li for various excitations of the residual nucleus according to calculations in the plane-wave impulse approximation

T_0, GeV	a	$a + ^6\mathrm{Li} \to d + a + ^4\mathrm{He}_{\rm g.s.}$		$a + ^6\mathrm{Li} \to d + a + ^4\mathrm{He}_{\rm e.s.}$		References
		κ, MeV/c	n_d	κ, MeV/c	n_d	
0.59	π^-	56 ± 8	0.60 ± 0.06	102 ± 16	1.3 ± 0.1	Our study
0.59	p	73.0 ± 1.6	0.78 ± 0.10			[8]
0.67	p	51.5 ± 2.5	0.83 ± 0.08	133 ± 10	0.9 ± 0.1	[4]
0.48	e	46.1	0.73 ± 0.07			[3]

For a comparison with data obtained with a proton beam to be more convenient, fits were constructed over $p_{\rm F}$ regions from zero to 100 or 150 MeV, which were approximately the regions that were used in [4]. For the first interval, the fitting procedure yields $\kappa = 56 \pm 8$ MeV/c; the respective value for the second interval is substantially greater, $\kappa = 102 \pm 16$ MeV/c.

The distribution with respect to $E_{\rm miss}$ was approximated by the sum of the contributions from three final states $X = {}^4\mathrm{He}_{\rm g.s.}$, *dd*, *dpn*, where the last two are associated with a continuous spectrum. This spectrum was simulated here as the sum of the contributions from the *dd* and *dpn* states of an alpha cluster. In doing this, the ^{6}Li wave function was taken in the cluster form in accordance with [5], the parameters of cluster wave functions being borrowed from [6]. The calculation was performed by the Monte Carlo method with allowance for the parameters of the facility used. The contributions of all three final states $X = {}^4\mathrm{He}_{\rm g.s.}$, *dd*, and *dpn* are represented in Fig. 3 by, respectively, the dashed, the dotted, and the dash-dotted curve. One can see that these processes describe well the entire $E_{\rm miss}$ spectrum; they also describe well the $p_{\rm F}$ spectra.

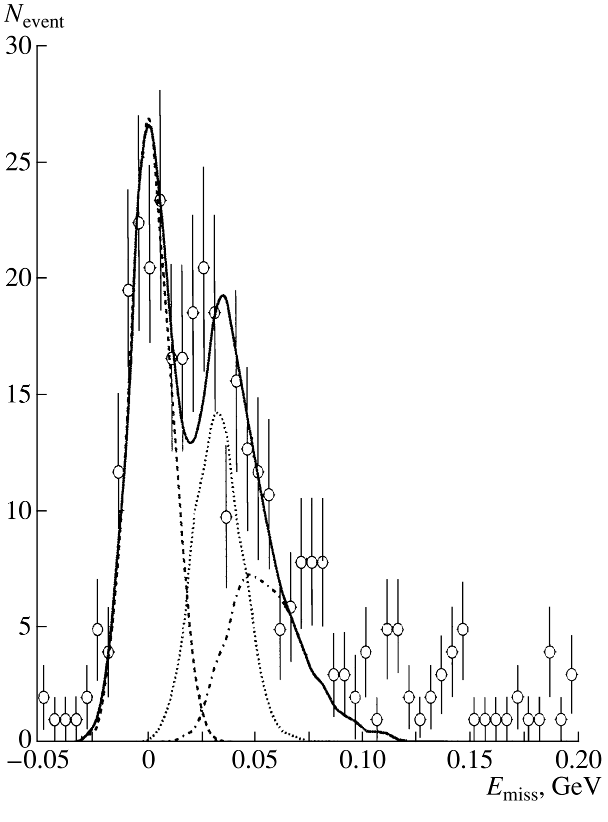

Fig. 3. Missing-energy ($E_{\rm miss}$) distribution for the reaction $\pi^- + {}^6\mathrm{Li} \to d + \pi^- + X$ at 0.72 GeV/c. The dashed, dotted, and dash-dotted curves correspond to the final states $X = {}^4\mathrm{He}_{\rm g.s.}$, *dd*, and *dpn*, respectively, while the solid curve corresponds to their sum.

Our simulation made it possible to determine, for each of these processes individually, the product $n_d \times d\sigma/d\Omega$, where n_d is the effective number of quasideuterons in ^{6}Li that are involved in reaction (5) and $d\sigma/d\Omega$ is the differential cross section for elastic pion scattering on a free deuteron in the backward direction in the c.m. frame. The values obtained in this way for n_d are, respectively, 0.6, 0.65, and 0.65, the error being about 0.06. The values of κ and n_d are given in Table 1 for $X = {}^4\mathrm{He}_{\rm g.s.}$ and $X = {}^4\mathrm{He}_{\rm e.s.}$ individually, the sum of n_d for $X = dd$ and *dpn* being taken as the value of n_d for the latter.

3.2. Knockout of Deuterons from ^{7}Li

Figure 5 displays the distributions of recorded events of the reactions

$$\pi^- + {}^7\mathrm{Li} \to d + \pi^- + X \qquad (6)$$

with respect to the missing energy $E_{\rm miss}$ at 0.72 GeV/c. The distributions of events with respect to intranuclear-motion momenta are shown in Figs. 6*a* and 6*b*. The values of the parameter κ for the intervals $-0.020 \le E_{\rm miss} \le 0.015$ GeV ($X = {}^5\mathrm{He}_{\rm g.s.}$) and $0.015 \le E_{\rm miss} \le 0.070$ GeV ($X =$

Table 2. Parameter κ of quasideuteron intranuclear motion [in the $\exp(-p_F^2/\kappa^2)$ parametrization] and effective number n_d of quasideuterons in ^{7}Li for various excitations of the residual nucleus according to calculations in the plane-wave impulse approximation

T_0, GeV	a	$a + ^7\mathrm{Li} \to d + a + ^5\mathrm{He}_{\mathrm{g.s.}}$		$a + ^7\mathrm{Li} \to d + a + ^5\mathrm{He}_{\mathrm{e.s.}}$		References
		κ, MeV/c	n_d	κ, MeV/c	n_d	
0.59	π^-	82 ± 11	0.55 ± 0.07	119 ± 19	1.0 ± 0.1	Our study
0.67	p	75 ± 10	1.96 ± 0.17	140 ± 21		[7]
0.67	p	75 ± 10	1.7 ± 0.10	130 ± 17	0.79 ± 0.08	[9]

$^5\mathrm{He}_{\mathrm{e.s.}}$) are, respectively, 82 ± 11 and 119 ± 19 MeV/c (see Table 2). These values are somewhat greater than their counterparts in the corresponding energy intervals for ^{6}Li. Unfortunately, there is no dominant cluster configuration for ^{7}Li; therefore, we used two approaches to construct a phenomenological description of the E_{miss} spectrum that we obtained. Within the first approach, we assumed, following the analysis performed in [7], the presence of the $^7\mathrm{Li} = d + ^5\mathrm{He}$ configuration, where the binding energy was 9.5 MeV. The knockout of a deuteron from ^{5}He was described by an exponential function decreasing from the threshold (26 MeV) for the reaction involving $X = td$ production, the slope parameter being fitted. Within the second approach, we wanted to assess the extent to which the assumption of a sizable contribution of ^{5}He is significant for describing the E_{miss} spectrum. In order to do this, we replaced the delta function

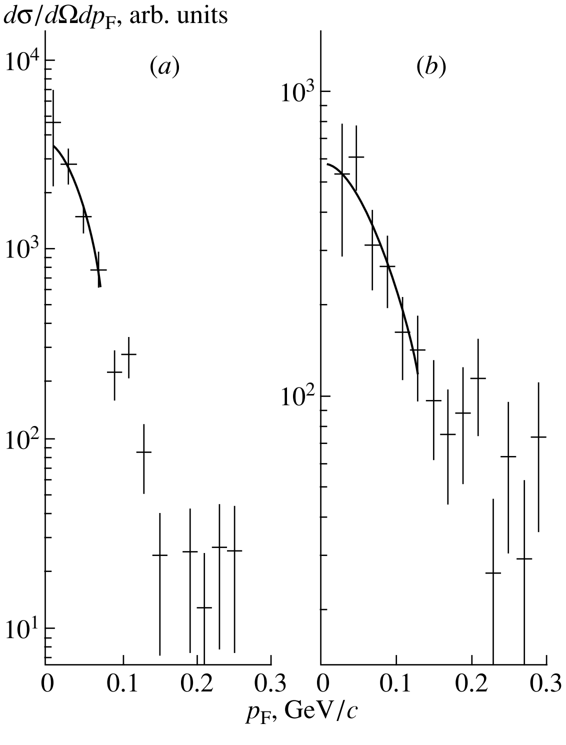

Fig. 4. Distributions of events with respect to the momentum of quasideuteron internal motion in the reactions $\pi^- + ^6\mathrm{Li} \to d + \pi^- + X$ for the intervals (a) $-0.020 \le E_{\mathrm{miss}} \le 0.015$ GeV and (b) $0.015 \le E_{\mathrm{miss}} \le 0.070$ GeV. The curves correspond to Gaussian distributions $\exp(p_F^2/\kappa^2)$.

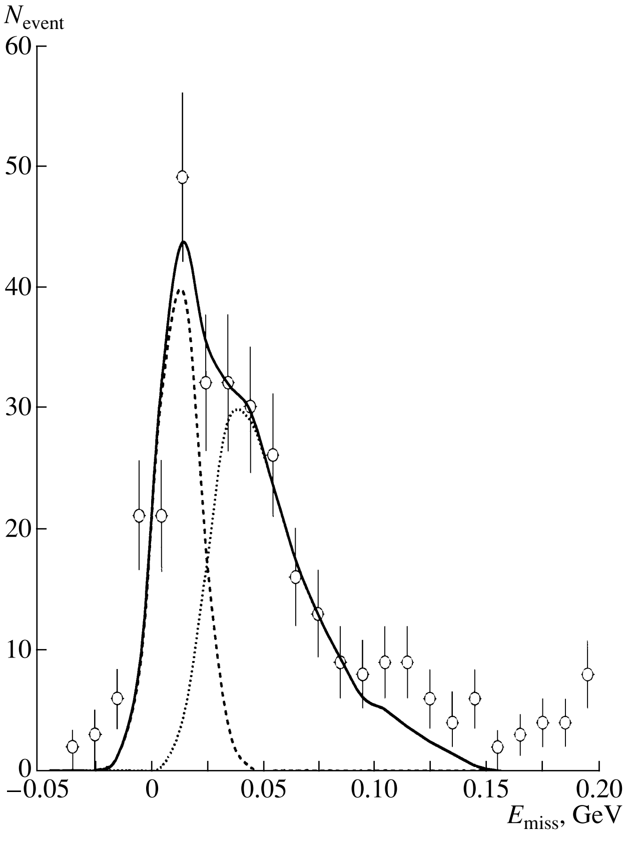

Fig. 5. Missing-energy (E_{miss}) distributions for the reactions $\pi^- + ^7\mathrm{Li} \to d + \pi^- + X$ at 0.72 GeV/c. The dashed curve corresponds to the $X = ^5\mathrm{He}$ state (delta function at 9.5 MeV), while the dotted curve corresponds to the continuous spectrum [exponential decreasing from the threshold for $X = td$ production (26 MeV)]; the solid curve is the sum of these two curves.

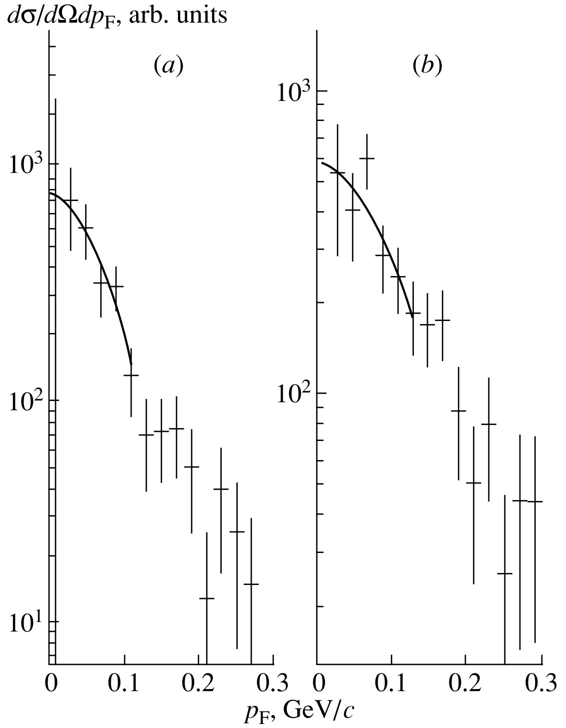

Fig. 6. Distributions of events with respect to the momentum of quasideuteron intranuclear motion in the reactions $\pi^- + {}^7\text{Li} \to d + \pi^- + X$ for the intervals (*a*) $-0.020 \le E_{\text{miss}} \le 0.015$ GeV and (*b*) $0.015 \le E_{\text{miss}} \le 0.070$ GeV. The curves correspond to Gaussian distributions $\exp(p_F^2/\kappa^2)$.

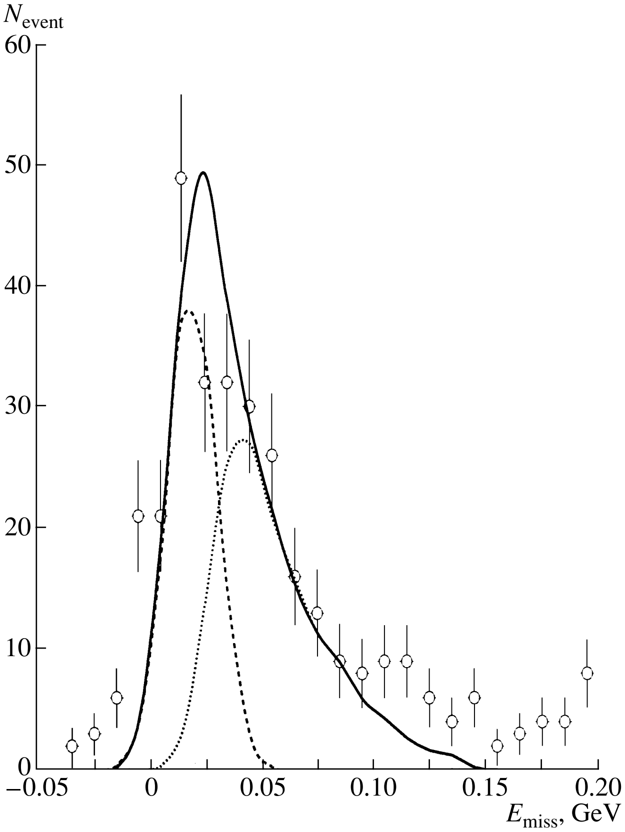

Fig. 7. Missing-energy (E_{miss}) distributions for the reactions $\pi^- + {}^7\text{Li} \to d + \pi^- + X$ at 0.72 GeV/*c*. The dashed curve corresponds to a uniform distribution between $X = n^4\text{He}$ (threshold at 8.7 MeV) and $X = td$ (threshold at 26 MeV), while the dotted curve corresponds to a continuous spectrum from the $X = td$ threshold (decreasing exponential); the solid curve is sum of these two curves.

corresponding to the contribution of ^{5}He by a uniform distribution from the threshold of the reaction for $X = n^4\text{He}$ (8.7 MeV) to the threshold of the reaction for $X = td$ (26 MeV). In either case, we simulated the operation of our facility. The descriptions of the spectra are given in Figs. 5 and 7. The first approach provides a better description with $\chi^2/\text{n.d.f.} = 18/12$, while the second proved to be much inferior to it, $\chi^2/\text{n.d.f.} = 32.9/12$. Thus, our data favor the hypothesis of a dominant role of the d^5He configuration in the knockout of deuterons from ^{7}Li with low energy losses. The effective numbers of quasideuterons for the corresponding final states are 0.55 and 1.00 (with an error of ±0.1) within the first approach and 0.6 and 0.9 (with an error of ±0.1) within the second approach, and they agree with each other within the errors. Naturally, the total effective number of quasideuterons takes the same value within the two approaches. Table 2 gives the values obtained on the basis of the first approach.

In addition to our present data, Tables 1 and 2 present results obtained in other studies at close energies with different beams. One can see that, both for ^{6}Li and for ^{7}Li, the parameter κ of quasideuteron intranuclear motion is approximately two times greater for the excited than for the ground state. For each final state individually, there is general agreement between the different measurements both for κ and for n_d. However, the experiment reported in [8] yields a markedly greater value of κ than all other experiments, while the experiment analyzed in [7, 9] leads to a nearly three times greater value of n_d for the ^{5}He (final state in the case of ^{7}Li) than the results of our measurements. As a matter of fact, the last conclusion is based on the result of a single study with a proton beam (since the article of Konz *et al.* [9] and the article of Ero *et al.* [7] report on somewhat different treatments of the same statistics) and the present study with a pion beam. Here, one cannot rule out the possibility that deuterons are knocked out via different mechanisms in proton and pion beams, to say nothing of experimental errors.

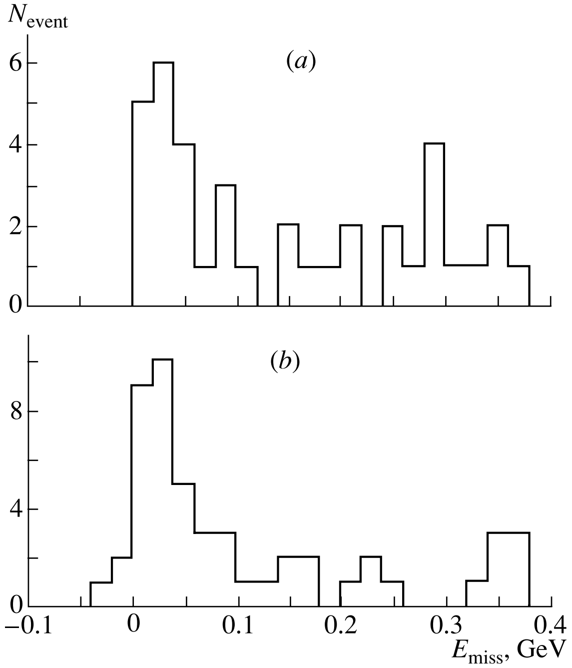

Fig. 8. Missing-energy ($E_{\rm miss}$) distributions in the reactions $\pi^- + {}^{6,7}\mathrm{Li} \to t + \pi^- + X$ for the total statistics accumulated at $p_0 = 0.72$ and 0.88 GeV/c for (a) ^{6}Li and (b) ^{7}Li.

4. TRITON KNOCKOUT

The first, as-yet-preliminary, data were obtained for the reactions

$$\pi^- + {}^{6,7}\mathrm{Li} \to t + \pi^- + X. \qquad (7)$$

The distributions of corresponding events with respect to $E_{\rm miss}$ are displayed in Fig. 8 for total statistics that were accumulated at $p_0 = 0.72$ and 0.88 GeV/c. It can be seen that a signal from quasielastic triton knockout is present for both isotopes. For ^{7}Li, it is more pronounced, which is indicative of a higher yield of tritons from ^{7}Li than from ^{6}Li. This suggests the presence of a more significant quasitriton component in the ^{7}Li nucleus. The experimental resolution in $E_{\rm miss}$ was $\sigma = 15{-}18$ MeV, while the step of the histogram in Fig. 8 was determined by statistics.

The distributions of events with respect to the momentum of quasitriton intranuclear motion are shown in Fig. 9. The values of the parameter κ for the interval $-0.010 \le E_{\rm miss} \le 0.050$ GeV proved to be $\kappa = 149 \pm 56$ MeV/c for ^{6}Li (Fig. 9a) and $\kappa = 93 \pm 18$ MeV/c for ^{7}Li (Fig. 9b). These results also suggest the presence of a stronger triton component in the ^{7}Li nucleus. The experiment reported in [10] and performed in a full kinematics by using a 590-MeV proton beam incident on a ^{6}Li target was the only study devoted to exploring quasifree triton knockout from lithium nuclei. The results of that experiment yielded a value of $\kappa = 100 \pm 20$ MeV/c, which agrees with our present result.

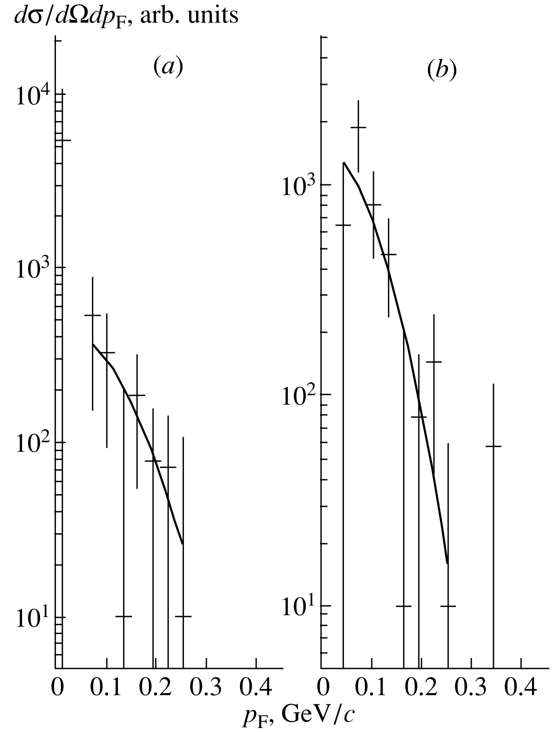

Fig. 9. Distributions of events with respect to the momentum of quasitriton intranuclear motion in the reactions $\pi^- + {}^{6,7}\mathrm{Li} \to t + \pi^- + X$ in the interval $-0.010 \le E_{\rm miss} \le 0.050$ GeV for (a) ^{6}Li, $\kappa = 149 \pm 56$ MeV/c, and (b) ^{7}Li, $\kappa = 93 \pm 18$ MeV/c. The curves correspond to Gaussian distributions $\exp(p_F^2/\kappa^2)$.

5. CONCLUSIONS

Quasifree deuteron and triton knockout from ^{6}Li and ^{7}Li nuclei has been studied in a full kinematics by using beams of $p_0 = 0.72$- and 0.88-GeV/c π^- mesons. The distributions of events with respect to the momenta of quasideuteron and quasitriton intranuclear motion, the excitation-energy spectra of residual nuclei, and the effective numbers of quasideuterons in the ^{6}Li and ^{7}Li nuclei have been obtained. The values of the parameter κ of intranuclear motion that have been deduced here for a quasideuteron and a quasitriton are in reasonably good agreement with the results of measurements in different beams. At the same time, there is a serious discrepancy between the values of n_d that were determined in a proton beam and in pion beam here for the reaction $^7\mathrm{Li}(\pi, \pi d)^5\mathrm{He}$. For other final states in the reactions on both lithium isotopes, there is in general good agreement between the results of our measurements (in a pion beam) and the results obtained with proton and electron beams.

ACKNOWLEDGMENTS

We gratefully acknowledge the assistance of the personnel of the 3-m spectrometer and the personnel of the ITEP accelerator in performing this experiment. We are also indebted to L.A. Kondratyuk and A.E. Kudryavtsev for stimulating discussions.

This work was supported in part by the Russian Foundation for Basic Research (project no. 03-02-17470), the Program for Support of Leading Scientific Schools (grant no. 1867.2003.02) and the Federal Target-Oriented Scientific and Technological Program (grant no. 40.052.1.1.112).

REFERENCES

1. B. M. Abramov *et al.*, Pis'ma Zh. Éksp. Teor. Fiz. **74**, 504 (2001) [JETP Lett. **74**, 449 (2001)].
2. B. M. Abramov *et al.*, Nucl. Phys. A **723**, 389 (2003).
3. R. Ent *et al.*, Phys. Rev. Lett. **57**, 2367 (1986).
4. D. Albrecht *et al.*, Nucl. Phys. A **338**, 477 (1980).
5. Yu. A. Kudeyarov *et al.*, Nucl. Phys. A **163**, 316 (1971).
6. A. Foursat *et al.*, Nucl. Phys. A **392**, 399 (1983).
7. J. Ero *et al.*, Nucl. Phys. A **372**, 317 (1981).
8. P. Kitching *et al.*, Phys. Rev. C **11**, 420 (1975).
9. P. Konts *et al.*, Preprint No. R1-80-780, OIYaI (Joint Inst. for Nucl. Res., Dubna, 1980).
10. W. Dollhopf *et al.*, Phys. Rev. C **8**, 877 (1973).

Translated by A. Isaakyan

Physics of Atomic Nuclei, Vol. 68, No. 3, 2005, pp. 481–487. Translated from Yadernaya Fizika, Vol. 68, No. 3, 2005, pp. 510–516.

Correlation Femtoscopy in Neutron–Carbon Interactions at Average Neutron Energy of 51 GeV

A. N. Aleev, N. S. Amaglobeli[†1)], V. P. Balandin, O. V. Bulekov[2)], I. M. Geshkov[3)], E. A. Goudzovski, D. K. Guriev, D. D. Emelianov, S. V. Eremin[2)*], A. I. Zinchenko, Z. M. Ivanchenko, I. M. Ivanchenko, R. A. Kvatadze[1)], V. D. Kekelidze, Z. I. Kozhenkova, M. V. Kopadze[1)], I. G. Kosarev, N. A. Kuzmin, A. A. Loktionov[4)], N. L. Lomidze[1)], A. L. Ljubimov, D. T. Madigozhin, V. G. Maznyj, V. V. Micin, N. A. Molokanova, R. E. Pismenyj, I. A. Polenkevich, A. K. Ponosov[2)], Yu. K. Potrebenikov, F. M. Sergeev[2)], L. A. Slepets, P. Z. Hristov[5)], and S. N. Shkarovsky

The EXCHARM Collaboration

Joint Institute for Nuclear Research, Dubna, Moscow oblast, 141980 Russia

Received May 24, 2004

Abstract—Correlations of pairs of Λ hyperons, neutral kaons, and charged pions having a low relative momentum are analyzed on the basis of data obtained at the EXCHARM facility in neutron–carbon interactions at an average neutron energy of 51 GeV. Preliminary results of this analysis are presented. *© 2005 Pleiades Publishing, Inc.*

1. INTRODUCTION

Experiments studying correlations between hadrons of low relative momenta (correlation femtoscopy) make it possible to study the spacetime properties of the hadron-production region and the parameters of hadron–hadron scattering both for identical and for nonidentical particles [1–3]. Narrow pair correlations between protons emitted from nuclei play an important role in obtaining deeper insight into the mechanism of cumulative processes [4].

An effect is observed in comparing experimental distributions in the difference of the particle momenta with their calculated counterparts where there are no correlations. The ratio of these distributions (correlation function) at low relative momenta differs from unity.

Correlation femtoscopy of strange particles is in the stage of development. In recent years, the first data on correlations between Λ hyperons of low relative momenta were obtained in experiments at LEP [5] and KEK [6]. By studying correlations of Λ-hyperon pairs produced in an intranuclear cascade, the authors of [6] were able to measure the ΛΛ scattering length. In that experiment, they explored kaon (K^-, K^+) double charge exchange on carbon nuclei at a primary momentum of 1.65 GeV/c, detecting two Λ hyperons.

On the basis of data obtained by the EXCHARM Collaboration [7], we perform here a systematic analysis of correlations between pions, kaons, and Λ hyperons having low relative momenta [8] and originating from neutron–carbon interactions at an average neutron energy of 51 GeV.

The effect of the $f_0(980)$ resonance is a feature peculiar to the observation of correlations between pairs of neutral kaons having a low relative momentum. This resonance can decay to $K\bar{K}$, significantly distorting the correlation function.

2. EXPERIMENTAL CONDITIONS

2.1. Experimental Facility

The EXCHARM spectrometer is situated in the 5N neutron channel of the U-70 accelerator installed at the Institute for High Energy Physics (IHEP,

---

[†] Deceased.

[1)] High Energy Physics Institute, Universitetskaya ul. 9, Tbilisi State University, GE-380086 Tbilisi, Republic of Georgia.

[2)] Moscow State Engineering Physics Institute (State University), Kashirskoe sh. 31, Moscow, 115409 Russia.

[3)] Institute for Nuclear Research and Nuclear Energy, Blvd. Tsarigradsko chausse 72, BG-1784 Sofia, Bulgaria.

[4)] Institute for Physics and Technology, Kazakh Academy of Sciences, Almaty, Republic of Kazakhstan.

[5)] CERN, CH-1211 Genève, Switzerland.

[*] E-mail: `eremin@hyperon.mephi.ru`

1063-7788/05/6803-0481$26.00 © 2005 Pleiades Publishing, Inc.

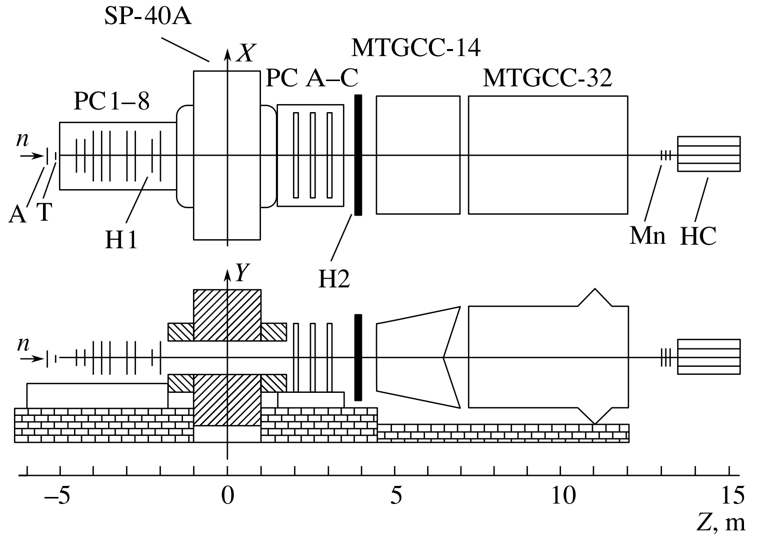

Fig. 1. Layout of the EXCHARM spectrometer (see main body of the text for explanations).

Protvino). A neutron beam is produced upon the interaction of protons circulating in the accelerator ring with the internal beryllium target and is formed by a system of collimators arranged along the axis that is nearly parallel to incident protons. The transverse dimensions of the beam in the vicinity of the target is approximately 4 × 6 cm.

The energy spectrum of beam neutrons had a maximum around 58 GeV and a width of about 12 GeV. In order to reduce the admixture of photons, a lead filter of variable thickness (from 0 to 20 cm, depending the position along the beam) was installed in the beam. The admixture of charged particles was removed by the deflecting magnets of the accelerator and the SP-129 magnet, which was arranged in the nose part of the experimental region.

The intensity of the neutron beam during an accelerator spill was about 6×10^6 neutrons per 5×10^{11} protons dumped onto the internal target. The arrangement of basic units of the spectrometer is displayed in Fig. 1. This apparatus includes the following elements:

(i) a carbon target (T) of diameter 9 cm and thickness 1.3 g/cm^2 along the beam (the Z coordinate of the target is -460 cm);

(ii) an analyzing magnet (SP-40A) having an aperture of 274 × 49 cm and generating a magnetic field of maximum strength 0.79 T (the system of the magnet power supply provides the possibility of a fast reversal of its polarity);

(iii) a system of 11 multiwire proportional chambers (PC) [9, 10] (25 signal planes) positioned upstream and downstream of the magnet (the maximum dimensions of the chambers were 100 × 60 cm upstream and 200 × 100 cm downstream of the magnet);

(iv) hodoscopes (H1, H2) of scintillation counters (these hodoscopes were used to develop a signal triggering the facility);

(v) a neutron-beam monitor (Mn);

(vi) a hadronic calorimeter (HC), which is used to measure the energy spectrum of beam neutrons;

(vii) a 14-channel (MTGCC-14) and a 32-channel (MTGCC-32) threshold gas Cherenkov counter [11, 12], which are used to identify charged particles (the former and the latter are filled with, respectively, Freon-12 and air, at atmospheric pressure in either case).

The system of triggering the spectrometer in the problem being discussed requires that not less than four charged particles traverse the main units of the apparatus.

A detailed description of the EXCHARM apparatus is given elsewhere [13].

In this study, we use the statistics sample of approximately 172×10^6 primary nC interactions recorded on a tape.

2.2. Selection of Events

Correlations of identical particles were studied in the reactions

$$n + \mathrm{C} \longrightarrow \pi^{\pm}\pi^{\pm} + X, \tag{1}$$

$$n + \mathrm{C} \longrightarrow K^0_S K^0_S + X, \tag{2}$$

$$n + \mathrm{C} \longrightarrow \Lambda\Lambda + X. \tag{3}$$

In selecting pairs of identical particles, we imposed general requirements on the geometric position of the vertex of an event—the pair-production

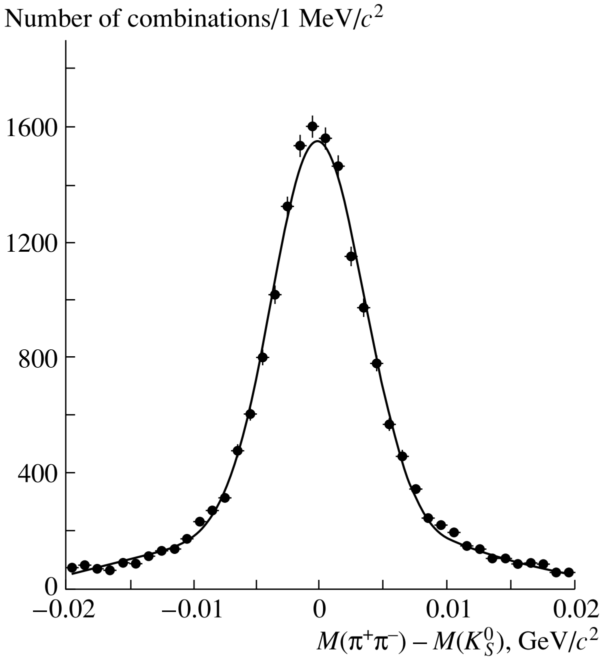

Fig. 2. Effective-mass spectrum of the $\pi^+\pi^-$ system.

region must be within the target. In order to identify pions, charged kaons, and protons, we used data from the Cherenkov detectors. In selecting likely charged pions in reaction (1), tracks associated with reconstructed neutral particles were excluded from our consideration. Pairs of charged pions accompanied by neutral strange particles were analyzed separately. For a further analysis, we selected approximately 148 000 events of the type in (1), 6000 events of the type in (2), and 1190 events of the type in (3).

As the result of a methodological investigation, we formulated the following optimum criteria for selecting neutral-kaon pairs [reaction (2)]:

The minimum distance between tracks should be less than 0.5 cm, this corresponding to a tripled experimental resolution in this parameter.

The decay vertex should occur within the decay volume of a neutral vee, $V^0 \in [-448, -270]$ cm, this volume beginning at a distance of 12 cm from the target edge along the Z axis.

Vees V^0 having common tracks of secondary particles were rejected.

The ratio of the absolute value of the positive-track momentum to the absolute value of the negative-track momentum should be less than five, this making it possible to exclude a large number of vees V^0 corresponding to a Λ^0 hyperon.

In order to exclude electron–positron pairs, the constraint $M_{e^+e^-} > 100$ MeV/c^2 was imposed on the effective mass of the pair.

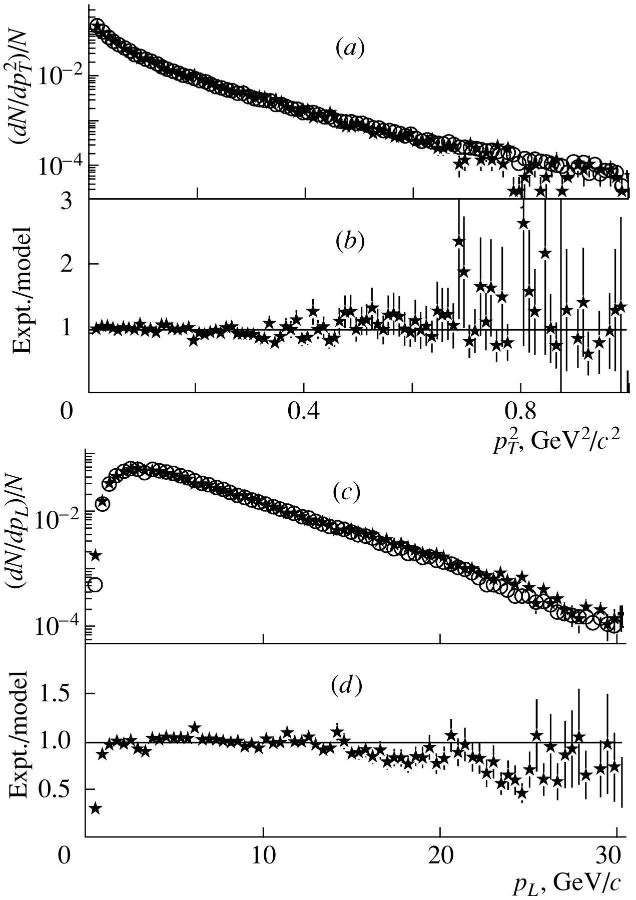

Fig. 3. Experimental and simulated distributions with respect to kinematical variables: (a, c) distributions with respect to the transverse momentum squared and the longitudinal momentum squared of negatively charged pions (open circles and stars represent, respectively, the experimental data and the results of a simulation); (b, d) ratios of the experimental and simulated spectra.

The effective mass of the $\pi^+\pi^-$ system was required to be within ±4.5 MeV/c^2 around the tabular value of the K^0_S mass, this approximately corresponding to the tripled value of the experimental resolution in this quantity (about 1.5 MeV/c^2).

The minimum distance between the reconstructed trajectories of two K^0_S particles in the event being considered should not exceed 0.5 cm.

The coordinates X of the vertex of a reconstructed pair should be within the range $-1 < X < 2$ cm.

The coordinates Y of the vertex of a reconstructed pair should be within the range $-2.5 < Y < 2$ cm.

The event vertex composed of the reconstructed pair of K^0_S should be within ±5 cm around the target center along the beam axis (the spectrometer resolution in the coordinate Z was about 1 cm).

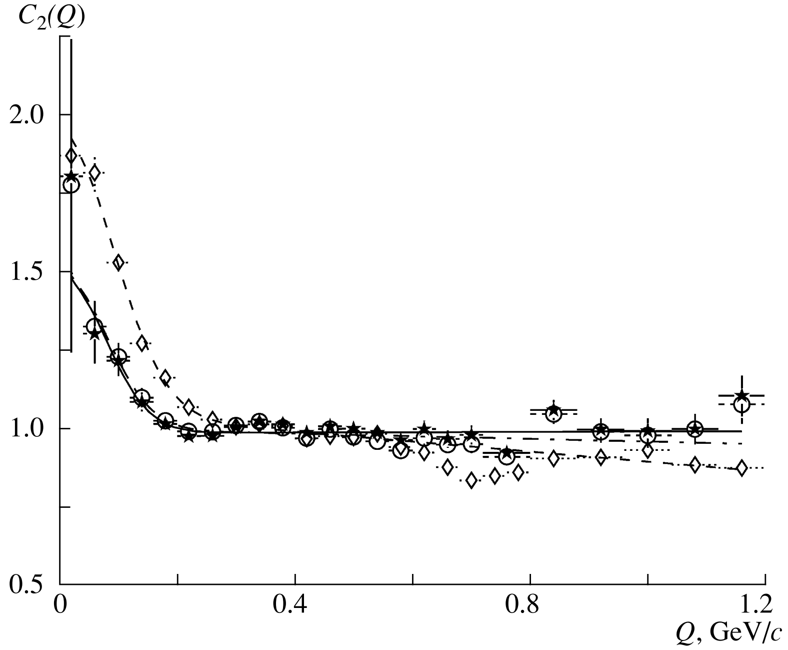

Fig. 4. Correlation functions for π-meson pairs for the cases where the background distribution was obtained (diamonds) by using unlikely charged pions, (circles) via a simulation, and (stars) on the basis of the double-ratio procedure. The curves represent the result of an approximation by a Gaussian function and a first-degree polynomial.

Figure 2 shows the $M(\pi^+\pi^-) - M_{\rm tabl}(K^0_S)$ distribution for events selected with allowance for the cuts listed above. The presence of a clear-cut signal in this distribution makes it possible to study its features. The parameters of the signal in the $M(\pi^+\pi^-)$ spectrum were determined by approximating this spectrum and the background by, respectively, a Gaussian function and a second-order polynomial. The solid curve in Fig. 2 represents the result of this approximation. The background function describes well the $M(\pi^+\pi^-)$ spectrum off the region of the signal.

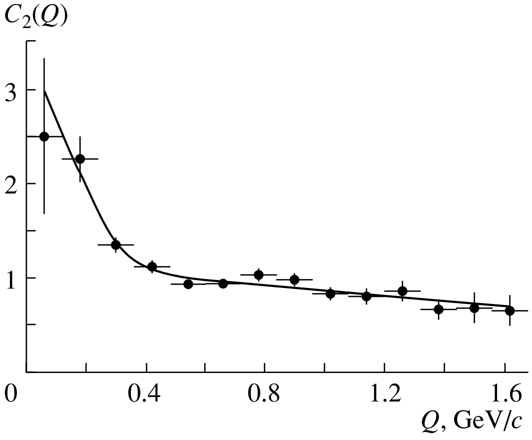

Fig. 5. Correlation function for pairs of K^0_S mesons. The background distribution was obtained by the double-ratio method. The curve represents the result of an approximation by a Gaussian function and a first-degree polynomial.

The above approximation yielded a mass value of $M(K^0_S) = 497.56 \pm 0.04$ MeV/c^2, which, within the error of 0.1 MeV/c^2, agrees with the tabular value. The resulting value of $\sigma = 3.67 \pm 0.05$ MeV/c^2 corresponds to the kaon-mass resolution obtained in detecting the inclusive production of K^0_S. In order to determine the number of product K^0_S pairs, we constructed the two-dimensional distribution of $\pi^+\pi^-$ effective masses, which was approximated by a combination of a two-dimensional and two one-dimensional Gaussian functions (representing correlated and uncorrelated kaon production, respectively) and a second-order polynomial representing the background. As a result, the number of correlated K^0_S pairs proved to be 5780 ± 107. The background to these events was approximately 15% of the signal. Two-thirds of background events were due to the production of K^0_S accompanied by random $\pi^+\pi^-$ pairs, while one-third stemmed from events where $\pi^+\pi^-$ pairs were not products of K^0_S-meson decay.

Our method for selecting and analyzing Λ-hyperon pairs [reaction (3)] was described in detail elsewhere [8].

Fitted values of the parameters in the approximations of the correlation functions $C_2(Q)$

$N^{\text{data}}/N^{\text{BG}}$	λ	R, fm	χ^2/n.d.f.
Charged pions			
$N^{\pi\pi}/N^{\pi^+\pi^-}$	0.85 ± 0.05	1.54 ± 0.05	1.4
$N^{\pi\pi}/N^{\pi\pi}_{\text{FRITIOF}}$	0.5 ± 0.12	1.79 ± 0.2	1.7
$(N^{\pi\pi}/N^{\pi\pi}_{\text{mix}})^{\text{data}}/(N^{\pi\pi}/N^{\pi\pi}_{\text{mix}})^{\text{FRITIOF}}$	0.52 ± 0.12	1.85 ± 0.2	1.2
Charged pions produced in association with K^0_S and Λ			
$N^{\pi\pi}/N^{\pi^+\pi^-}$	0.99 ± 0.21	1.26 ± 0.15	0.95
$N^{\pi\pi}/N^{\pi\pi}_{\text{FRITIOF}}$	0.47 ± 0.17	1.26 ± 0.3	0.7
$(N^{\pi\pi}/N^{\pi\pi}_{\text{mix}})^{\text{data}}/(N^{\pi\pi}/N^{\pi\pi}_{\text{mix}})^{\text{FRITIOF}}$	0.73 ± 0.18	1.20 ± 0.19	0.7
Λ hyperons			
$N^{\Lambda\Lambda}/N^{\Lambda\Lambda}_{\text{FRITIOF}}$	-0.47 ± 0.14	0.39 ± 0.08	0.3
$(N^{\Lambda\Lambda}/N^{\Lambda\Lambda}_{\text{mix}})^{\text{data}}/(N^{\Lambda\Lambda}/N^{\Lambda\Lambda}_{\text{mix}})^{\text{FRITIOF}}$	-0.45 ± 0.16	0.4 ± 0.1	0.4

3. ANALYSIS OF TWO-PARTICLE CORRELATIONS AND DISCUSSION OF THE RESULTS

In order to analyze our experimental data, we used the two-particle correlation function

$$C_2(p_1, p_2) = \frac{N_2(p_1, p_2)}{N_1(p_1)N_1(p_2)},$$

where p_1 and p_2 are the 4-momenta of the particles involved and N_1 and N_2 are, respectively, the single- and two-particle distribution densities.

We investigated the dependence of the correlation function C_2 on the invariant variable $Q^2 = -(p_1 - p_2)^2$.

For this correlation function, the model of independently emitting single-particle sources that obey a Gaussian spacetime distribution in the volume of a static sphere leads to the Goldhaber parametrization [14],

$$C_2(Q) = 1 + \lambda \exp(-R^2Q^2),$$

where λ is a parameter that characterizes the amplitude of correlations and which is sensitive to the presence of an admixture of misidentified particles and of resonances and R is a parameter that is proportional to the root-mean-square radius of the spherically symmetric production region in the rest frame of the pair of particles ($R^2 = \langle r^2 \rangle/3$).

The correlation function is determined as the ratio of the experimental distribution normalized to unity and the so-called reference (background) distribution (normalized in the same way) that reproduces, by and large, the features of the experimental distribution, but which does not contain interference correlations; that is,

$$C_2(Q) = \frac{1/N_{\text{exp}} \cdot dN_{\text{exp}}(Q)/dQ}{1/N_{\text{ref}} \cdot dN_{\text{ref}}(Q)/dQ}.$$

In constructing the distributions for charged particles, we take into account final-state Coulomb interaction with the aid of the Gamow factor [1].

In studying correlations of identical charged particles, three types of distributions—the distribution of pairs of unlikely charged particles, the distribution obtained via a simulation, and the distribution obtained by the method of mixing (where particles are taken from different events)—can be taken for the background distribution. Frequently, a straightforward application of the method of mixing can introduce, because of the violation of the energy- and momentum-conservation laws, kinematical correlations in the distributions, with the result that it becomes impossible to obtain a correct correlation function. Therefore, a double ratio—that is, the ratio of the experimental and simulated correlation functions, each being the ratio of the distribution of identical pairs to the background distribution obtained with the aid of the method of mixing—is usually used in such cases. In this study, we use double ratios.

In analyzing correlations of identical pions, we employed a background distribution obtained by using $\pi^+\pi^-$-meson pairs. The region of the ρ meson was excluded in constructing the relevant approximation.

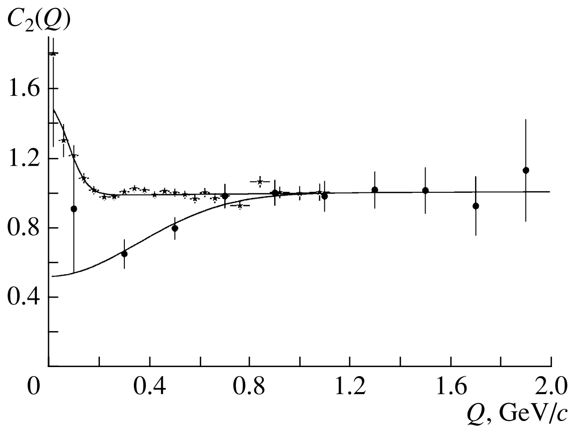

Fig. 6. Correlation functions for pairs of (stars) charged pions and (closed circles) Λ hyperons. The background distribution was obtained by the double-ratio method. The curves represent the result of approximations by a Gaussian function and a first-degree polynomial.

For a generator of secondary particles, we choose the FRITIOF package [15], which is intended for describing soft hadron processes at c.m. energies of colliding particles not less than 10 GeV. In order to take into account the detection efficiency of the setup, we used the package presented in [16] and based on the GEANT-3 system [17].

A comparison of the experimental distributions of charged pions with respect to kinematical variables with their counterparts obtained on the basis of our simulations showed satisfactory agreement (Fig. 3).

The correlation functions averaged over positive and negative pion pairs are displayed in Fig. 4 for various types of background distributions. The curves represent the result of an approximation by a Gaussian function, the fitted values of the parameters of the approximation being given in the table. It can be seen from the table that, within the errors, the results for all three forms of the background distribution are compatible.

We have also studied the effect of the associated production of pions and neutral strange particles on the dimensions of the pion-production region. For this, we analyzed the correlation function constructed from pairs of identical pions selected from events involving at least one neutral strange particle. The results of the approximation are also given in the table. One can see the trend toward a decrease in the dimensions of the pion-production region in the presence of accompanying strange particles. The values given in the table for the parameters characterizing the dimensions of the pion-production region are in good agreement with the results of the AFS experiment [18], which studied pp interactions at a c.m. energy of 63 GeV ($R = 1.4 \pm 0.2$ fm).

The correlation function for $K^0_S K^0_S$ pairs is depicted in Fig. 5. The parameter characterizing the region of neutral-kaon production is $R = 0.78 \pm 0.09$ fm. The amplitude of the correlations is larger than that allowed by the theory, and this can be due to the effect of the decay of the $f_0(980)$ resonance, which was disregarded in the simulation. In order to introduce the respective correction in the correlation function, measurement of the parameters of the $f_0(980)$ resonance in its decay to two pions and of the cross section for its production are presently being performed.

Figure 6 shows the correlation functions for pairs of charged pions and Λ hyperons. One can observe constructive correlations for meson pairs and destructive correlations for hyperon pairs. A nonmonotonic behavior of the correlation function for pions after the first maximum corroborates the interference nature of the observed correlations. It can be seen that the dimensions of the region of hyperon-pair production are significantly smaller than those for pion-pair production.

4. CONCLUSIONS

Pair correlations of charged pions, neutral kaons, and Λ hyperons in neutron—carbon interactions have been studied. Preliminary data have been obtained for the characteristics of the particle-production region. From the data given in the table, it can be concluded that the dimensions of the production region decrease with increasing mass of the particles under study. Indications that the associated production of pions and strange particles also reduces the dimensions of the pion-production region have been found.

ACKNOWLEDGMENTS

We are grateful to R. Lednicky and G.A. Leksin for interest in this study and stimulating discussions.

This work was supported by the program Universities of Russia (project no. UR.02.01.009) and by the Russian Foundation for Basic Research (project no. 03-07-90385).

REFERENCES

1. R. Lednitskiĭ and V. L. Lyuboshits, Yad. Fiz. **35**, 1316 (1982) [Sov. J. Nucl. Phys. **35**, 770 (1982)].
2. R. Lednicky, V. L. Lyuboshits, B. Erazmus, and D. Nouais, Phys. Lett. B **373**, 30 (1996).
3. R. Lednicky, Phys. At. Nucl. **67**, 72 (2004).
4. G. A. Leksin, Soros Obraz. Zh., No. 11, 70 (1997).
5. G. Alexander *et al.*, Phys. Lett. B **452**, 159 (1999).
6. A. Ohnishi *et al.*, Nucl. Phys. A **670**, 297 (2000).
7. A. N. Aleev *et al.*, Instrum. Exp. Tech. **38**, 425 (1995).

8. A. N. Aleev *et al.*, Preprint No. P1-2003-191, OIYaI (Joint Inst. for Nucl. Res., Dubna, 2003).
9. A. N. Aleev *et al.*, Prib. Tekh. Eksp., No. 1, 50 (1991)
10. A. N. Aleev *et al.*, Prib. Tekh. Eksp., No. 4, 8 (1995).
11. M. N. Voĭchishin *et al.*, Prib. Tekh. Eksp., No. 3, 71 (1985).
12. A. N. Aleev *et al.*, Preprint No. P13-94-520, OIYaI (Joint Inst. for Nucl. Res., Dubna, 1994).
13. A. N. Aleev *et al.*, Prib. Tekh. Eksp., No. 4, 52 (1999). [Instrum. Exp. Tech. **42**, 481 (1991)].
14. G. Goldhaber *et al.*, Phys. Rev. **120**, 300 (1960).
15. Pi Hong, Comput. Phys. Commun. **82**, 74 (1992).
16. G. A. Aralbaeva *et al.*, Preprint No. P1-93-85, OIYaI (Joint Inst. for Nucl. Res., Dubna, 1993).
17. R. Brun *et al.*, Cern Program Library W 5013 (1994).
18. T. Akesson *et al.* (AFS), Z. Phys. C **36**, 517 (1987).

Translated by A. Isaakyan

Physics of Atomic Nuclei, Vol. 68, No. 3, 2005, pp. 488–490. From Yadernaya Fizika, Vol. 68, No. 3, 2005, pp. 517–519.
Original English Text Copyright © 2005 by Bargholtz, Chernyshev, Gerén, Grebenev, Gurov, Höistad, Laukhin, Lindberg, Sandukovsky, Shafigullin, Tegnér.

A Search for Deeply Bound Pionic States of Xenon Produced in the ^{136}Xe(d, ^{3}He)^{135}Xe$_{\pi\text{-bound}}$ Reaction*

Chr. Bargholtz[1], B. A. Chernyshev[2], L. Gerén[1], V. N. Grebenev[2], Yu. B. Gurov[2], B. Höistad[3], I. V. Laukhin[2], K. Lindberg[1], V. G. Sandukovsky[4], R. R. Shafigullin[2], and P.-E. Tegnér[1]

Received May 24, 2004; in final form, July 19, 2004

Abstract—A search for deeply bound pionic states of xenon produced in the ^{136}Xe(d, ^{3}He)^{135}Xe$_{\pi\text{-bound}}$ reaction at $E_d = 500$ MeV is reported. The population of the 1s pionic-atom state of ^{135}Xe is observed on the predicted level of the cross section ∼40 μb/sr. The binding energy of the 1s state, $B = 2.9 \pm 0.5$ MeV, however, is lower than theoretically predicted. *© 2005 Pleiades Publishing, Inc.*

Bound states of negatively charged pions and nuclei, pionic atoms, have been investigated by detecting X rays emitted in the electromagnetic deexcitation of atomic levels. These studies have provided valuable information regarding the pion optical potential in light- and medium-mass nuclei. Due to the competition from absorption by the nucleus, however, deeply bound states cannot be studied with this technique. The existence of relatively narrow deeply bound pionic states in heavy nuclei was predicted theoretically by Toki and Yamazaki [1]. Their calculations show that the repulsive strong interaction decreases the probability for the pion to be inside the nucleus, making the width of the 1s state considerably smaller than the level spacing, even in nuclei as heavy as lead. Numerous experimental and theoretical efforts have been made to find an efficient method for the population of such states. Until now, only the (d, ^{3}He) pickup reaction was found to be a suitable tool. The existence of the deeply bound pionic states of lead [2, 3] and tin [4] isotopes and also natural xenon [5] was observed experimentally in this reaction. These results open new possibilities to acquire information on the local s-wave part of the potential. Another important aspect of these studies regards the behavior of hadrons in the nuclear medium. The question as to how hadron properties change inside nuclear matter is important from the point of view of QCD [6].

The relative population of atomic states depends on the target nuclei. For example, in the case of a lead target, the probability to populate atomic 2p states is large compared to that for populating the 1s state, due to the lack of s-state neutrons in the outer nuclear shell. For xenon, the 50–82 neutron outer shell contains s-state neutrons and a relative increase in the population probability of the 1s state of the pionic atom is expected. The closed-shell nucleus ^{136}Xe is suggested, by Umemoto *et al.* [7], to be a particularly good candidate as a target for the study of the deeply bound 1s state. At a beam energy of 500 MeV the experimental spectrum is expected to be dominated by a single peak due to pickup from the $s_{1/2}$ neutron state. Also, xenon offers the possibility to do the experiment in a storage ring with a thin internal target that does not affect the resolution of the experiment.

In our previous work [5], counting rates and experimental conditions were studied using a natural xenon target. Here, we report on a pilot study of pionic-atom production on an isotopically pure target in the ^{136}Xe(d, ^{3}He)^{135}Xe$_{\pi\text{-bound}}$ reaction. The experiment was carried out in the accelerator and storage ring CELSIUS [8] with similar conditions as in the previous experiment. An electron-cooled deuteron beam with a momentum resolution $\Delta p/p \sim 4 \times 10^{-4}$ and a current of approximately 1 mA interacted with the internal cluster-jet target. The beam energy was chosen to be 499.8 MeV in order to optimize the conditions for recoilless kinematics. The thickness of the windowless xenon target was approximately 4×10^{12} atom/cm^2. The accelerator was operated in cycles, 900 s long, defined by injection of deuterium ions, acceleration, cooling, data taking for 800 s, and finally dumping of the beam. The luminosity during

---

*This article was submitted by the authors in English.

[1] Stockholm University, Sweden.

[2] Moscow Engineering Physics Institute, Kashirskoe sh. 31, Moscow, 125080 Russia.

[3] Uppsala University, Sweden.

[4] Joint Institute for Nuclear Research, Dubna, Moscow oblast, 141980 Russia.

1063-7788/05/6803-0488$26.00 © 2005 Pleiades Publishing, Inc.

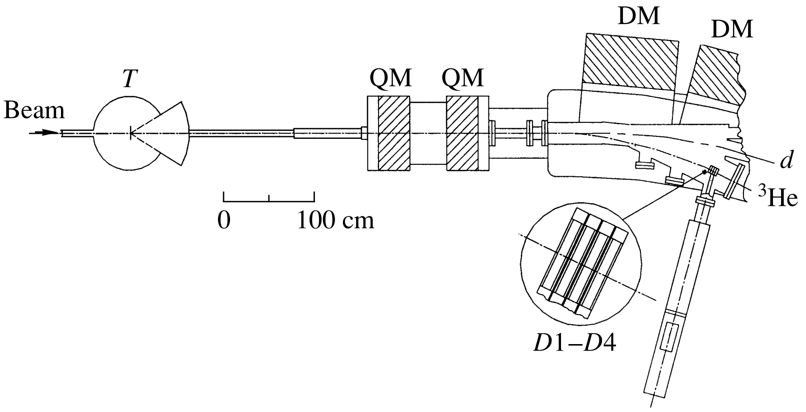

Fig. 1. Part of the fourth quadrant of CELSIUS and the zero-degree spectrometer, comprising target (T), quadrupole magnets (QM), dipole magnets (DM), and solid-state detectors ($D1$–$D4$).

data taking was approximately 1.3×10^{28} cm^{-2} s^{-1}. The spectrometer [9] consists of the magnetic elements of the CELSIUS ring which follow the cluster-jet target (cf. Fig. 1). The detector telescope, which comprised four germanium detectors cooled to liquid-nitrogen temperature, was installed in the second dipole magnet of the bend, 6.1 m away from the target. The diameter of the detector sensitive area was 32 mm and detector thickness ranged between 5 and 11 mm. The total thickness of the detectors was $\sim$30 mm and the corresponding ^{3}He energy range covered by the telescope extended up to $\sim$420 MeV. The intrinsic energy resolution of the telescope for 360 MeV ^{3}He ions was estimated to be approximately 900 keV. The center of the detector telescope was positioned approximately 150 mm from the beam in order to detect ^{3}He particles from the ^{136}Xe(d, ^{3}He)^{135}Xe$_{\pi\text{-bound}}$ reaction.

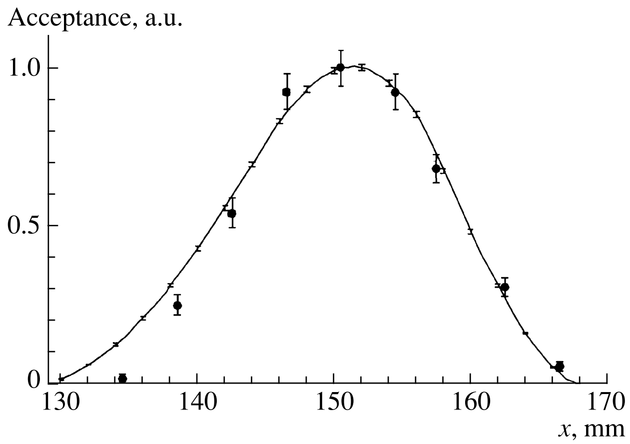

Fig. 2. The measured acceptance (dots) for the H(d, ^{3}He)π^0 reaction as a function of the horizontal distance from the beam. The solid curve corresponds to results of simulations.

The energy calibration of the setup was carried out by means of the ^{1}H(d, ^{3}He)π^0 reaction with the same beam energy as for the xenon target. To make sure that the measurement conditions were the same for the two targets, the accelerator systems were not switched off during target change. The ^{1}H(d, ^{3}He)π^0 reaction corresponds to the elementary process behind the pionic-atom formation. It provides a pro-

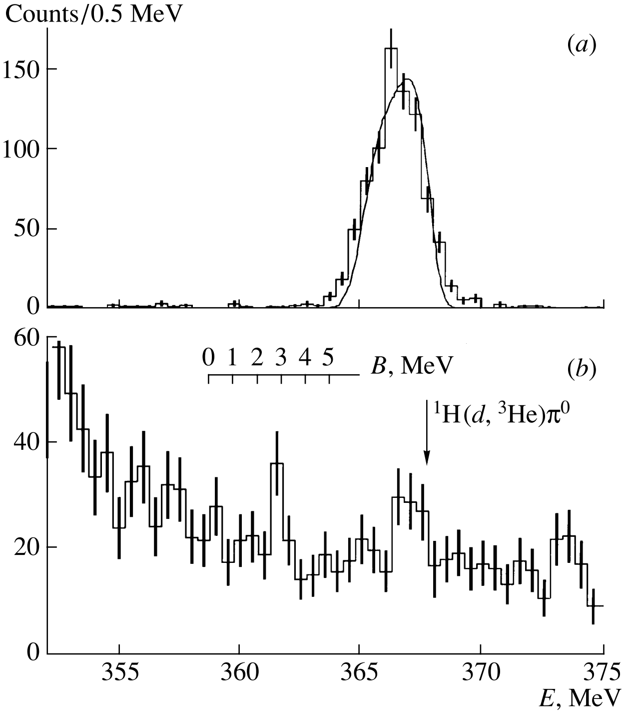

Fig. 3. ^{3}He energy spectrum in the (a) H(d, ^{3}He)π^0 and (b) ^{136}Xe(d, ^{3}He)X reactions, $E_d = 500$ MeV. The binding energy axis B corresponds to the resulting $1s$ binding energy assuming a nuclear excitation of 0.29 MeV.

nounced, however kinematically broadened, peak for the precise relative calibration of the energy of the deeply bound pionic states. In addition, the acceptance as a function of the horizontal distance between the center of the telescope and the beam was measured in order to control the experimental geometry. The peak shape, as well as the counting rate and acceptance, was compared with the results of simulations (cf. Figs. 2 and 3*a*). The simulations reproduced the experimental data well assuming a vertical shift of the beam with respect to the central trajectory in the target region (∼9 mm). The beam displacement increased the peak width in the ^{1}H(d, ^{3}He)π^0 reaction in comparison with zero shift by a factor of ∼2 and reduced the effective counting rate by a factor of ∼3 for both the ^{1}H(d, ^{3}He)π^0 and ^{136}Xe(d, ^{3}He)^{135}Xe$_{\pi\text{-bound}}$ reactions. The overall uncertainty of the energy calibration is estimated to be ∼0.5 MeV.

The measured ^{3}He spectrum from the ^{136}Xe(d, ^{3}He)X reaction is shown in Fig. 3*b*. These data correspond to approximately 75 h of data taking. Two peaks are observed at approximately 363 and 367 MeV. The wider peak at 367 MeV corresponds to the ^{1}H(d, ^{3}He)π^0 reaction on a small admixture of hydrogen arising from the pumping system. The narrower peak at ∼363 MeV corresponds to the production of the deeply bound pionic 1s state in the ^{136}Xe(d, ^{3}He)^{135}Xe$_{\pi\text{-bound}}$ reaction. The number of events in the peak (∼25) is in good agreement with the expected one for a reaction cross section of 40 μb/sr [7]. However, the binding energy deduced for the pionic 1s state, $B = 2.9 \pm 0.5$ MeV, is lower than theoretically predicted, $B = 4.17$ MeV [7].

The results of this experiment show that, with a well-tuned CELSIUS beam, it probably requires 160 h of beam on target to reach ∼250 events in the peak corresponding to the production of the 1s state of ^{135}Xe$_{\pi\text{-bound}}$. We expect that, together with a new telescope with better energy resolution (∼500 keV), this will allow a significantly improved precision in the determination of the binding energy and, in addition, a determination of the width of the 1s pionic state.

We thank the staff at the Svedberg Laboratory for their continuous efforts in making this experiment possible.

This work was supported by the Royal Swedish Academy of Sciences, the Russian Foundation for Basic Research (project no. 01-02-17264), the CRDF project (grant no. MO-011-0), and the Swedish Research Council.

REFERENCES

1. H. Toki and T. Yamazaki, Phys. Lett. B **213**, 129 (1988).
2. T. Yamazaki *et al.*, Z. Phys. A **355**, 219 (1996).
3. A. Geissel *et al.*, Nucl. Phys. A **663–664**, 206 (2000).
4. K. Suzuki *et al.*, Prog. Theor. Phys. Suppl. **149**, 32 (2003).
5. M. Andersson *et al.*, Phys. Rev. C **66**, 022203 (2002).
6. T. Yamazaki *et al.*, Phys. Lett. B **418**, 246 (1998).
7. Y. Umemoto *et al.*, Prog. Theor. Phys. **103**, 337 (2000).
8. D. Reistad *et al.*, in *Proceedings of the 14th International Conference on Cyclotrons and Their Applications*, *Cape Town, South Africa, 1995*, p. 350.
9. Chr. Bargholtz *et al.*, Nucl. Instrum. Methods Phys. Res. A **390**, 160 (1997).

Physics of Atomic Nuclei, Vol. 68, No. 3, 2005, pp. 491–497. Translated from Yadernaya Fizika, Vol. 68, No. 3, 2005, pp. 520–526.
Original Russian Text Copyright © 2005 by Gurov, Aleshkin, Behr, Lapushkin, Morokhov, Pechkurov, Poroshin, Sandukovsky, Tel'kushev, Chernyshev, Tschurenkova.

Spectroscopy of Superheavy Hydrogen Isotopes in Stopped-Pion Absorption by Nuclei

Yu. B. Gurov[*], **D. V. Aleshkin**, **M. N. Behr**, **S. V. Lapushkin**,
P. V. Morokhov, **V. A. Pechkurov**, **N. O. Poroshin**, **V. G. Sandukovsky**,
M. V. Tel'kushev, **B. A. Chernyshev**, and **T. D. Tschurenkova**

Moscow State Engineering Physics Institute (State University),
Kashirskoe sh. 31, Moscow, 115409 Russia

Received May 24, 2004

Abstract—The structure of levels of superheavy hydrogen isotopes $^{4-6}$H is analyzed on the basis of a record statistics of experimental data on the absorption of negatively charged pions by light nuclei. Qualitatively new experimental data are obtained for the spectroscopy of the superheavy hydrogen isotopes ^{5}H and ^{6}H. Peaks due to four resonance states of ^{5}H are observed in the missing-mass spectra for the reaction channels ^{9}Be(π^-, pt)X and ^{9}Be(π^-, dd)X. A structure that is associated with four resonance states of ^{6}H is observed in the missing-mass spectra for the reaction channels ^{9}Be(π^-, pd)X and ^{11}B(π^-, p^4He)X. On the basis of the results presented for ground-state parameters, it can be concluded that the binding energy of superheavy hydrogen isotopes decreases as the number of neutrons increases. Excited levels of the isotopes ^{5}H and ^{6}H are observed for the first time. On the energy scale, all of these states lie above the threshold for decay to free nucleons. *© 2005 Pleiades Publishing, Inc.*

1. INTRODUCTION

In recent years, much attention has been given to experimentally studying light nuclei in the vicinity of the nucleon drip line, since such nuclei possess unique properties deviating from known regularities. The superheavy hydrogen isotopes ^{n}H ($n \geq 4$) are of particular interest since their nuclei feature a record excess of neutrons, $N/Z = 6$ for ^{7}H [1]. In this connection, spectroscopic data on superheavy hydrogen isotopes are of importance for answering the question of whether there can exist purely neutron nuclei. At the same time, a microscopic description of superheavy hydrogen isotopes is quite feasible owing to a small number of nucleons in their nuclei, this rendering them an appropriate testing ground for theoretical nuclear models.

At the present time, the existence of the isotope ^{4}H is reliably established [2–12] (references to earlier studies can be found in [13, 14]). In nuclear reactions of various types, it was shown experimentally that ^{4}H is a nucleus that is unstable with respect to nucleon emission; however, data on the resonance energy and width of this state are not always consistent. Excited levels of ^{4}H were observed in [2, 9, 15–17].

The situation around the investigation of the isotope ^{5}H is contradictory. The early experiments of our group that were devoted to studying stopped-pion absorption on ^{9}Be [6] and ^{6,7}Li [7] nuclei furnished indications of the existence of a broad loosely bound state of ^{5}H at $E_r > 7$ MeV (E_r is the energy above the threshold for the breakup to a triton and neutrons). In [18], a level at $E_r \approx 5.2$ MeV was observed in the heavy-ion reaction ^{7}Li(^{6}Li, ^{8}B)X. Recent measurements in beams of radioactive nuclei have not clarified the situation. In experiments performed at Dubna, the formation of a narrow state (of width less than 0.5 MeV) in ^{5}H at $E_r \approx 1.8$ MeV was observed in the reaction p(^{6}He, pp)X [19] and in the reactions $t(t, ptn)n$ and d(^{6}He, ^{3}He)X [12]. An indication of the formation of a narrow state at $E_r = 2.7$ MeV was obtained in the reaction $t(t, ptn)n$. At the same time, only a broad structure that has a maximum at $E_r \sim$ 3 MeV and a width of about 6 MeV (FWHM) was observed in the experiment performed in GSI [11] to study the proton-knockout reaction C(^{6}He, $2nt$)X.

Experimental information about the ^{6}H isotope is still scarcer [20]. The state at $E_r \approx 2.7$ MeV was observed in the reactions ^{7}Li(^{7}Li, ^{8}B)X [21] and ^{9}Be(^{11}B, ^{14}O)X [22], but the statistical significance of the results was rather low in either of these two studies.

The question of whether there exist heavier hydrogen isotopes is still open. An indication of the forma-

---

[*] E-mail: `Gurov@axpk40.mephi.ru`

tion of ^{7}H in the reaction $p(^8\mathrm{He}, pp)X$ was obtained quite recently [1].

Thus, experimental information is much poorer for superheavy hydrogen isotopes, especially for excited states, than for heavy helium and lithium isotopes (see, for example, [20]). No systematic regularities can be revealed for the former because of a small number of reaction channels subjected to investigation and because of a low statistical significance of some of the results. It is hardly reasonable to use, with the aim of filling this gap, spectroscopic results for heavier elements, since, among all nuclei in the vicinity of the nucleon drip line, only hydrogen isotopes involve an unfilled proton $1s$ shell. In particular, the frequently used assumption that the character of the dependence of the binding energy in hydrogen isotopes on the number of neutrons is similar to that in helium and lithium isotopes was not confirmed by the theoretical results obtained in [23].

In view of the aforesaid, it is of paramount importance to perform systematic studies of superheavy isotopes. In recent years, we obtained data on the structure of levels in the isotopes ^{4}H [17], ^{5}H [24], and ^{6}H [25], which were produced upon the absorption of stopped negatively charged pions by nuclei in the reactions

$$^9\mathrm{Be}(\pi^-, dt)^4\mathrm{H},$$

$$^9\mathrm{Be}(\pi^-, pt)^5\mathrm{H}, \quad ^9\mathrm{Be}(\pi^-, dd)^5\mathrm{H},$$

$$^9\mathrm{Be}(\pi^-, pd)^6\mathrm{H}, \quad ^{11}\mathrm{B}(\pi^-, p^4\mathrm{He})^6\mathrm{H}.$$

Below, these results are analyzed with the aim of revealing general regularities.

2. DESCRIPTION OF THE EXPERIMENT

In this article, we present results obtained within an experiment aimed at studying the production of neutron-rich isotopes in stopped-pion absorption on the $1p$-shell nuclei ^{9}Be, ^{10,11}B, and ^{12,14}C. The experiment was performed in a beam of low-energy pions (LEP) at the Los Alamos Meson Physics Facility (LAMPF) with the aid of a multilayer semiconductor spectrometer [24]. A beam of 30-MeV pions was transmitted through a beryllium moderator and was then stopped in a thin target of thickness about 24 mg/cm^2. Charged secondaries formed upon pion absorption by nuclei were detected by two silicon telescopes arranged at an angle of 180° with respect to each other. Each telescope ensured identification of charged particles and measurement of their energy up to the kinematical boundaries of the reaction. In the spectra given below, the threshold energies are 10, 12, 14, and 34 MeV for p, d, t, and ^{4}He, respectively. The energy resolution for hydrogen (p, d, t) and helium (^{3,4}He) ions was 0.5 and 1.0 MeV, respectively.

The reactions $^{11}\mathrm{B}(\pi^-, dt)^6\mathrm{He}$ [26], $^{10}\mathrm{B}(\pi^-, pt)^6\mathrm{He}$, $^{10}\mathrm{B}(\pi^-, dd)^6\mathrm{He}$, $^{11}\mathrm{B}(\pi^-, pd)^8\mathrm{He}$ [26], $^{12}\mathrm{C}(\pi^-, pd)^9\mathrm{Li}$ [27], and $^{12}\mathrm{C}(\pi^-, p^4\mathrm{He})^7\mathrm{He}$ were used to determine the energy resolution with respect to the missing mass (MM) in correlation measurements. The ground states and the widths of product helium and lithium isotopes were reliably determined in [20, 28]. An analysis of the results revealed that the energy resolution with respect to the missing masses was 1 MeV for event where one recorded pairs of hydrogen ions and between 2.0 and 2.5 MeV for events where one recorded pairs of hydrogen and helium ions. The resolution for events involving ^{3,4}He ions is poorer since the losses of their energy by ionization in the target are greater than those of singly charged particles. The error in the absolute calibration of the energy scale did not exceed 0.1 MeV.

With the aim of monitoring the possible time variations in the energy resolution and in calibration, use was made of the three-body reaction $^9\mathrm{Be}(\pi^-, tt)t$ on a ^{9}Be target [24] and the three-body reaction $^{11}\mathrm{B}(\pi^-, pd)^8\mathrm{He}$ on a ^{11}B target. The absence of time variations in the properties of the spectrometer was proven by the invariability of the shapes of the peaks in the missing-mass spectra for various parts of accumulated statistics.

Searches for peaks corresponding to known two-body reactions on nuclei of possible admixtures in targets were performed in to order assess the level of such admixtures quantitatively. For a ^{11}B target, ^{12}C is a dominant admixture (8%). The contribution of other (uncontrollable) admixtures in ^{11}B and ^{9}Be targets did not exceed 1%.

A more detailed description of the spectrometer and of the experimental procedure used is given elsewhere [29].

3. RESULTS

Figure 1 shows the missing-mass spectrum for the reaction $^9\mathrm{Be}(\pi^-, dt)^4\mathrm{H}$. The sum of the triton and neutron masses is taken for a zero point here. In order to separate ^{4}H states responsible for the formation of the observed peak, we used the method of least squares in describing the experimental spectra by the sum of n-particle distributions over the phase space ($n \geq 4$) and Breit–Wigner distributions. It was assumed that ^{4}H states are p-wave resonances parametrized as in [30]. The angular and energy distributions of the spectrometer and the background of random coincidences were taken into account in the data and in the calculations described below.

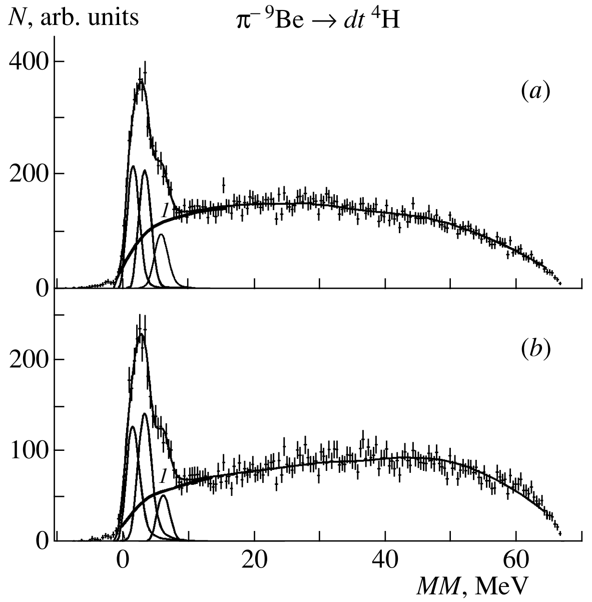

Fig. 1. Missing-mass spectra for the reaction ^{9}Be(π^-, dt)X: (a) measured spectrum and (b) measured spectrum for the case where the undetected-residue momentum is subjected to the cut $P_X \leq 100$ MeV/c. The thin solid curves represent the Breit–Wigner distribution and a total description; curve *1* correspond to the total distribution according to the phase-space model.

A satisfactory description of the spectrum in Fig. 1a (χ^2/n.d.f. = 0.95) was achieved by including, in the description, two resonance states of ^{4}H that are characterized by the following parameter values:

$$E_{\text{g.s.}} = 2.0 \pm 0.2 \text{ MeV}, \quad \Gamma_{\text{g.s.}} = 1.2 \pm 0.2 \text{ MeV};$$

$$E_{1r} = 5 \pm 1 \text{ MeV}, \quad \Gamma_{1r} = 1.3 \pm 0.2 \text{ MeV}.$$

It should be noted that, visually, there is a structure in the spectrum around $MM \cong 1$ MeV, but the statistical significance of the indication that there can exist a ^{4}H state of higher binding energy is insufficiently high.

A additional possibility of verifying the stability of these data on the spectroscopy of ^{4}H can be based on the fact that quasifree processes not involving directly residual-nucleus nucleons contribute significantly to three-body channels of pion-absorption reactions. With the aim of attaining a relative enrichment of the measured spectra in such events, we subjected the residual-nucleus momentum to the cut $P_X < 100$ MeV/c, where the boundary momentum value obviously does not exceed the value expected for the Fermi momentum of an intranuclear cluster. This cut also makes it possible to suppress the contribution of the final-state interaction between the recorded particles and neutrons [25]. The missing-mass spectra obtained in this way are displayed in Fig. 1b. In describing these spectra, the parameters of the Breit–Wigner distributions used were set to the values indicated above. The resulting value of χ^2/n.d.f. = 1.0 is compatible with the hypothesis that the isotope ^{4}H has two resonance states.

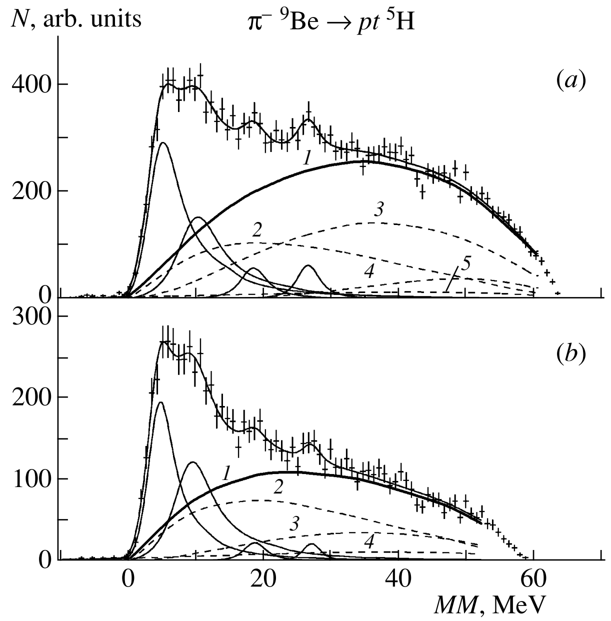

Fig. 2. Missing-mass spectra for the reaction ^{9}Be(π^-, pt)X: (a) measured spectrum and (b) measured spectrum for the case where the undetected-residue momentum is subjected to the cut $P_X \leq 100$ MeV/c. The thin solid curves represent the Breit–Wigner distributions and a total description; curve *1* corresponds to the total distribution according to the phase-space model; the dashed curves *2*, *3*, and *4* are four-, five-, and six-particle distributions over the phase space, while the dashed curve *5* represents the background of random coincidences.

Our results are in the best agreement with the data presented in [9], where two resonance states at $E_r = 2.0 \pm 0.3$ and 5.2 ± 0.5 MeV were observed in the reaction $d(^6\text{He}, \alpha)X$. At the same time, only one state of rather large width was observed in recent experiments with radioactive beams, that of width $\Gamma = 3.28(12)$ MeV at $E_r = 2.67(9)$ MeV in [11] and that of width $\Gamma = 4.1 \pm 0.3$ MeV at $E_r = 3.3 \pm 0.2$ MeV in [12]. Possibly, the peaks observed in those measurements are manifestations of more than one state of ^{4}H.

Figures 2 and 3 show the missing-mass spectra for the reaction channels ^{9}Be(π^-, pt)X and ^{9}Be(π^-, dd)X, respectively. The sum of the masses of the triton and two neutrons is taken here for a zero point. In the region of positive values of the missing mass, either spectrum features structures that

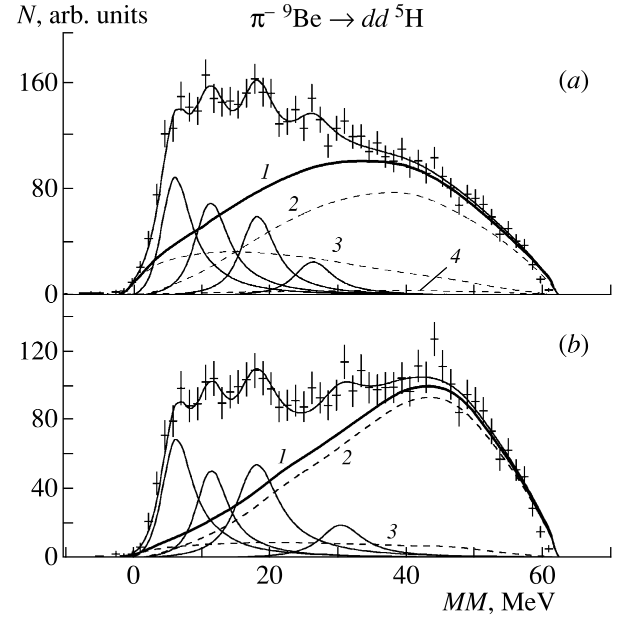

Fig. 3. Missing-mass spectra for the reaction ^{9}Be(π^-, dd)X: (a) measured spectrum and (b) measured spectrum for the case where the undetected-residue momentum is subjected to the cut $P_X \leq 100$ MeV/c. The thin solid curves represent Breit–Wigner distributions and a total description; curve *1* corresponds the total distribution according to the phase-space model; the dashed curves *2* and *3* are four- and five-particle distributions over the phase space, while the dashed curve *4* is the background of random coincidences.

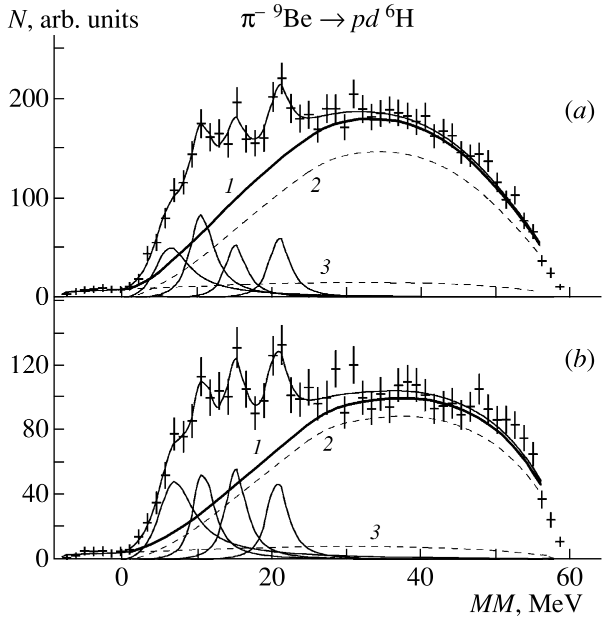

Fig. 4. Missing-mass spectra for the reaction ^{9}Be(π^-, pd)X: (a) measured spectrum and (b) measured spectrum for the case where the undetected-residue momentum is subjected to the cut $P_X \leq 100$ MeV/c. The thin solid curves represent Breit–Wigner distributions and a total description; curve *1* corresponds to the total distribution according to the phase-space model; the dashed curve *2* is the four-particle distribution over the phase space, while the dashed curve *3* represents the background of random coincidences.

can be associated with the production of resonance states. The missing-mass spectra for the reactions ^{9}Be(π^-, pt)X and ^{9}Be(π^-, dd)X in Figs. 2a and 3a are satisfactorily described (the respective values of χ^2 per degree of freedom are 1.05 and 0.94) by four resonance states of ^{5}H and the sum of n-particle distributions over the phase space ($4 \leq n \leq 6$). The weighted-mean values of the parameters of these distributions are given in Table 1. The quantities Γ are defined as the full widths at half-maximum for the peaks displayed in the figures. The relative errors in the channel yields range between 10 and 30%. Since the manifestations of two highly excited states are less pronounced, two hypotheses according to which the spectra were described in terms of three resonance states, the levels at $E_r = 18.5$ and 26.7 MeV being successively excluded, were tested on the basis of the χ^2 criterion. Both hypothesis can be rejected at a 10% confidence level. The spectra corresponding to the above cut on the residual-nucleus momentum were described with the values of the parameters of Breit–Wigner distributions from Table 1. The resulting values of χ^2/n.d.f., 1.2 for pt events and 1.1 for dd events, are compatible with the hypothesis that there exist four resonance states of the isotope ^{5}H.

For the ^{5}H state that is observed in our measurements and which is characterized by the highest binding energy, the resonance-energy value is consistent with experimental results reported in [18] and the results of the theoretical calculations from [23], but it is above ($\Delta E \sim 2.5$–3.8 MeV) the values obtained in the experiments with radioactive beams in [12, 18, 19] and the results of the theoretical calculations from [31, 32]. In our opinion, the discrepancies between the experimental data from the different studies are quite sizable.

Figure 4a shows the missing-mass spectrum for the reaction ^{9}Be(π^-, pd)X. The sum of the triton mass and the masses of three neutrons are taken here for a zero point. In the region of positive values of the missing mass, the spectrum displays structures that can be associated with the production of resonance states. In describing the spectrum in terms of the sum of Breit–Wigner distributions and n-particle distributions over the phase space, we took into account all possible $n \geq 4$ final states, including reaction channels that lead to the production of ^2n, ^{4}H, and ^{5}H systems.

Table 1. Values of the resonance parameters for the isotope ^{5}H

^{9}Be(π^-, pt)^{5}H, ^{9}Be(π^-, dd)^{5}H		^{7}Li(^{6}Li, ^{8}B)X [18]		p(^{6}He, pp)X [19]		d(^{6}He, ^{3}He)X, t(t, ptn)n [12]		C(^{6}He, $2nt$)X [11]	
E_r, MeV	Γ, MeV	E_r, MeV	Γ, MeV	E_r, MeV	Γ, MeV	E_r, MeV	Γ, MeV	E_r, MeV	Γ, MeV
5.5 ± 0.2	5.4 ± 0.5	5.2 ± 0.4	≈ 4	1.7 ± 0.3	1.9 ± 0.4	1.8 ± 0.1	< 0.5	≈ 3	≈ 6
10.6 ± 0.3	6.8 ± 0.5					2.7 ± 0.1	< 0.5		
18.5 ± 0.4	4.8 ± 1.3								
26.7 ± 0.4	3.6 ± 1.3								

Table 2. Values of the resonance parameters for the isotope ^{6}H

^{9}Be(π^-, pd)X		^{11}B(π^-, p^4He)^{6}H		^{7}Li(^{7}Li, ^{8}B)X [21]		^{9}Be(^{11}B, ^{14}O)X [22]	
E_r, MeV	Γ, MeV	E_r, MeV	Γ, MeV	E_r, MeV	Γ, MeV	E_r, MeV	Γ, MeV
6.6 ± 0.7	5.5 ± 2.0	7.3 ± 1.0	5.8 ± 2.0	2.7 ± 0.4	1.8 ± 0.5	2.6 ± 0.5	1.3 ± 0.5
10.7 ± 0.7	4 ± 2						
15.3 ± 0.7	3 ± 2	14.5 ± 1.0	5.5 ± 2.0				
21.3 ± 0.4	3.5 ± 1.0	22.0 ± 1.0	5.5 ± 2.0				

As can be seen from Fig. 4*a*, distributions over the phase space cannot reproduce the structure observed for $MM < 25$ MeV. We note that, here, the main contribution to the total distribution comes from the five-particle phase space featuring a dineutron in the final state ($d + p +^2 n + t + n$). A satisfactory description (χ^2/n.d.f. = 0.95) of the experimental spectrum is attained only upon introducing four resonance states of ^{6}H that are characterized by the parameter values in Table 2. The relative errors in the channel yields lie in the range 20–30%. For the spectrum obtained at the residual-nucleus momentum subjected to the aforementioned cut (Fig. 4*b*), the description with the same values of the parameters of Breit–Wigner distributions also proves to be quite satisfactory (χ^2/n.d.f. = 1.01).

In the measurements with a ^{11}B target, the search for the isotope ^{6}H was performed in the reaction ^{11}B(π^-, p^4He)X. The ^{11}B target used contained an ^{12}C admixture; therefore, we subtracted, from the measured spectrum (Fig. 5*a*), the corresponding contribution from the reactions ^{12}C(π^-, p^4He)X. The contribution of these spectra (Fig. 5*b*) was determined by normalizing, to the relative fraction of the admixture (8%), the spectra measured on a ^{12}C target in the same experimental run. The spectrum obtained by applying this procedure is given in Fig. 5*c*.

The spectrum measured for ^{11}B was analyzed by two methods. First, the spectrum was described with the values derived for the parameters of the ^{6}H resonance states by using ^{9}Be. In this case, the value of χ^2 per degree of freedom proved to be 0.88, which is compatible with the hypothesis that the isotope ^{6}H has four energy levels. Further, the position and width of the levels and their number were treated as free parameters in describing the spectrum. In this case, the spectrum for the reaction ^{11}B(π^-, p^4He)X (Fig. 5*c*) can be described (χ^2/n.d.f. = 0.87) by using only three resonance states whose parameters are set to the values in Table 2. We note that, within the errors, the values of these parameters agree with the results obtained in the reaction ^{9}Be(π^-, pd)X.

An analysis of data has demonstrated the absence of contradictions between the results obtained for two targets. In relation to measurements with ^{9}Be, however, the energy resolution for data on ^{11}B and their statistical significance are poorer, which complicates the observation of ^{6}H states. In this connection, we can assume that the data obtained in the reaction ^{9}Be(π^-, pd)X reproduce the structure of levels of the isotope ^{6}H more adequately.

The resonance energy of the ground state of the isotope ^{6}H is much higher than the experimental results obtained previously in [21, 22]. In addition, it should be emphasized that the statistical significance of our data is an order of magnitude higher. Our result

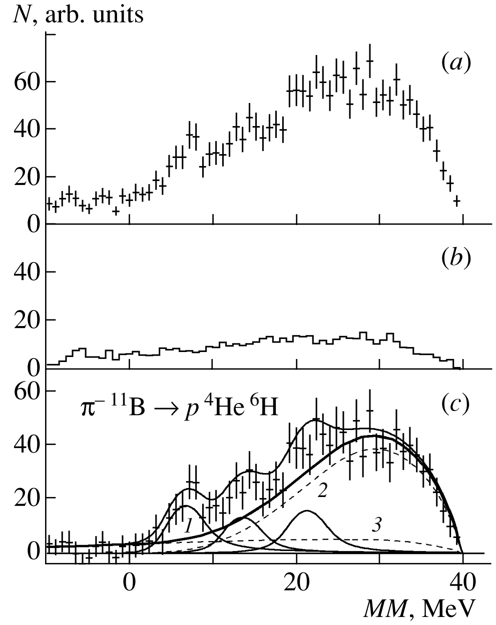

Fig. 5. Missing-mass spectrum for the reaction ^{11}B(π^-, p^4He)X: (*a*) spectrum measured for a ^{11}B target, (*b*) spectrum measured for the reaction ^{12}C(π^-, p^4He)X and normalized to the fraction of the ^{12}C admixture in the ^{11}B target, and (*c*) spectrum obtained upon the subtraction of the background contribution. The notation for the curves is identical to that in Fig. 4.

is in good agreement with theoretical predictions of Sidorchuk *et al.* [12].

4. DISCUSSION

Our analysis of available experimental information revealed that data on the spectroscopy of superheavy hydrogen isotopes (heavier than ^{4}H) are very scarce and contradictory. In particular, the discrepancy between data on the ground-state energy of ^{5}H exceeds considerably the quoted experimental errors. This may be associated with the effect of the structure of participant nuclei on the population of levels of the isotope ^{5}H. In [11, 19], it was assumed that, in the ground state of ^{5}H, neutrons fill the same orbitals as in nuclei of the ^{6}He beam. The difference in the wave functions of the intranuclear cluster ^{5}H in ^{6}He and ^{9}Be may indeed prove to be significant, but it cannot explain the observed discrepancy between the results reported in [11] and [12, 19].

In view of the scarcity of experimental data, the problem of revealing regularities of the changes in the properties of superheavy hydrogen isotopes with increasing number of neutrons is rather vague. For example, measurements performed at the Laboratory of Nuclear Reactions at the Joint Institute for Nuclear Research (JINR, Dubna) indicate that the binding energy of ^{5}H is higher than that of ^{4}H [12], while the data obtained at GSI suggest an approximate equality of the binding energies for these isotopes; as to our results, they demonstrate that the binding energy of ^{5}H is lower.

Nevertheless, we believe that there are a few arguments in support of considering our results as a basis for a systematic analysis of the spectroscopy of superheavy hydrogen isotopes. These include (i) the maximum number of isotopes studied at the state-of-the-art level; (ii) a high statistical significance of the results; (iii) the discovery of isotopes in several reaction channels simultaneously; and (iv) a broad interval of missing masses measured in our experiment, this suppressing the phase-space effect on the results. In addition, it should be noted that all of the experimental results, including those for reaction channels used for calibration, were obtained within the same experimental run, whereby the possible errors are minimized.

On the basis of our data obtained in reactions of stopped-pion absorption by light nuclei, one can conclude that the binding energies of the ground states of superheavy hydrogen isotopes decrease with increasing number of neutrons: $B(^4\mathrm{H}_{\mathrm{g.s.}}) = 6.5 \pm 0.2$ MeV, $B(^5\mathrm{H}_{\mathrm{g.s.}}) = 3.0 \pm 0.2$ MeV, and $B(^6\mathrm{H}_{\mathrm{g.s.}}) = 1.9 \pm 0.7$ MeV. However, we cannot rule out the possibility that this result is caused by the structure of the target nuclei ^{9}Be and ^{11}B.

States lying above the threshold for the breakup of isotopes to free nucleons have been observed for the first time in the excitation spectrum of the isotopes ^{5}H and ^{6}H. The excitations of these systems of free nucleons prove to be rather high, reaching a value of about 18 MeV (or 3.6 MeV/nucleon). The origin of such states and the mechanism of their formation are unclear. An analysis of a compilation of data on the spectroscopy of light nuclei [20, 28] revealed that such high excitations were observed only for He and Li isotopes in [3]. The levels observed in that study at the excitation energy of 35.7 MeV for ^{5}He and at the excitations energies of 32.0 and 35.7 MeV for ^{6}He are possibly isobaric analogs of, respectively, the level at $E_r = 18.5$ MeV in ^{5}H and the levels at $E_r = 10.7$ and 15.3 MeV in ^{6}H.

In conclusion, we would like to emphasize that a continuation of investigations into superheavy hydrogen isotopes remains a problem of topical interest. At the present time, we further pursue our analysis of experimental data with the aim of seeking the isotope ^{7}H in the reactions ^{9}Be(π^-, pp)X and ^{11}B(π^-, p^3He)X. On the basis of experimental data that we obtained, we also plan to perform searches for isobaric-analog states in the excitation spectra of the helium isotopes $^{5-7}$He.

ACKNOWLEDGMENTS

This work was supported by CRDF (grant no. NMO-011-0), the Russian Foundation for Basic Research (project no. 00-02-17511), and the program "Universities of Russia" (grant no. 02.02.007).

REFERENCES

1. A. A. Korsheninnikov *et al.*, Phys. Rev. Lett. **90**, 082501 (2003).
2. U. Sennhauser *et al.*, Phys. Lett. B **103B**, 1 (1981).
3. R. Franke *et al.*, Nucl. Phys. A **433**, 351 (1985).
4. A. V. Belozyorov *et al.*, Preprint No. E7-85-966, JINR (Dubna, 1985).
5. D. Miljanic *et al.*, Phys. Rev. C **33**, 2204 (1986).
6. M. G. Gornov *et al.*, Pis'ma Zh. Éksp. Teor. Fiz. **45**, 205 (1987) [JETP Lett. **45**, 252 (1987)].
7. A. I. Amelin *et al.*, Pis'ma Zh. Éksp. Teor. Fiz. **51**, 67 (1990) [JETP Lett. **51**, 688 (1990)].
8. S. Blagus *et al.*, Phys. Rev. C **44**, 325 (1991).
9. D. V. Aleksandrov *et al.*, Pis'ma Zh. Éksp. Teor. Fiz. **62**, 18 (1995) [JETP Lett. **62**, 18 (1995)].
10. Yu. Ts. Oganesyan *et al.*, Izv. Akad. Nauk, Ser. Fiz. **66**, 619 (2002).
11. M. Meister *et al.*, Nucl. Phys. A **723**, 13 (2003).
12. S. I. Sidorchuk *et al.*, Nucl. Phys. A **719**, 229c (2003).
13. S. Fiarman and W. E. Meyerhof, Nucl. Phys. A **206**, 1 (1973).
14. D. R. Tilley, H. R. Weller, and G. M. Hale, Nucl. Phys. A **541**, 1 (1992).
15. T. A. Tombrello, Phys. Rev. **143**, 772 (1966).
16. R. C. Minehart *et al.*, Phys. Rev. **177**, 225 (1969).
17. M. G. Gornov *et al.*, in *LI Conference on Nuclear Spectroscopy and Structure of Atomic Nucleus, Sarov, Russia, 2001*, p. 142.
18. D. V. Aleksandrov *et al.*, in *Proceedings of the International Conference on Exotic Nuclei and Atomic Masses (ENAM-95), Arles, France, 1995* (Editions Frontières, Gif-sur-Yvette, 1995), p. 329.
19. A. A. Korsheninnikov *et al.*, Phys. Rev. Lett. **87**, 092501 (2001).
20. D. R. Tilley *et al.*, Nucl. Phys. A **708**, 3 (2002).
21. D. V. Aleksandrov *et al.*, Yad. Fiz. **39**, 513 (1984) [Sov. J. Nucl. Phys. **39**, 323 (1984)].
22. A. V. Belozyorov *et al.*, Nucl. Phys. A **460**, 352 (1986).
23. A. M. Gorbatov, V. L. Skopich, P. Yu. Nikishov, *et al.*, Yad. Fiz. **50**, 1551 (1989) [Sov. J. Nucl. Phys. **50**, 962 (1989)].
24. M. G. Gornov *et al.*, Pis'ma Zh. Éksp. Teor. Fiz. **77**, 412 (2003) [JETP Lett. **77**, 344 (2003)].
25. Yu. B. Gurov *et al.*, Pis'ma Zh. Éksp. Teor. Fiz. **78**, 219 (2003) [JETP Lett. **78**, 183 (2003)].
26. M. G. Gornov *et al.*, Izv. Akad. Nauk, Ser. Fiz. **62**, 1781 (1998).
27. M. G. Gornov *et al.*, Phys. Rev. Lett. **81**, 4325 (1998).
28. F. Ajzenberg-Selove, Nucl. Phys. A **490**, 1 (1988).
29. M. G. Gornov *et al.*, Nucl. Instrum. Methods Phys. Res. A **446**, 461 (2000).
30. A. M. Lane and R. G. Thomas, Rev. Mod. Phys. **30**, 257 (1958).
31. B. Shul'gina *et al.*, Phys. Rev. C **62**, 014312 (2000).
32. P. Descouvemont and A. Kharbach, Phys. Rev. C **63**, 027001 (2001).

Translated by A. Isaakyan

Physics of Atomic Nuclei, Vol. 68, No. 3, 2005, pp. 498–507. Translated from Yadernaya Fizika, Vol. 68, No. 3, 2005, pp. 527–536.
Original Russian Text Copyright © 2005 by Korenchenko.

Deviation from the Standard Model in the Decay $\pi^+ \to e^+\nu\gamma$

S. M. Korenchenko*
The PIBETA Collaboration(1)
Joint Institute for Nuclear Research, Dubna, Moscow oblast, 141980 Russia

Received May 24, 2004

Abstract—A precise investigation of radiative pion decay ($\pi^+ \to e^+\nu\gamma$) in a pion beam from the meson factory of the Paul Scherrer Institute (Switzerland) was performed by the PIBETA Collaboration with the aid of the PIBETA detector. This resulted in finding 41 601 events of radiative pion decay in three kinematical regions. The absolute values of the branching ratio for radiative pion decay were determined in each of these regions. To a precision approximately four times higher than that known previously, the ratio of the axial-vector to the vector form factor was found to be $\gamma \equiv F_A/F_V = 0.443\,(15)$, the latter being fixed at $F_V = 0.0259$. The number of events found in the kinematical region specified by photon energies of $E_\gamma > 55.6$ MeV, positron energies of $E_e > 20.0$ MeV, and angles of $\theta_{\gamma,e} > 40^\circ$ between the momenta of the corresponding particles (B region) was 5233. In region B, the measured branching ratio for radiative pion decay, $R_{\pi\to e\nu\gamma}(\text{expt}) = 11.6(3) \times 10^{-8}$, proved to be smaller by eight standard deviations than that which follows from the Standard Model, $R_{\pi\to e\nu\gamma}(\text{theor}) = 14.34(1) \times 10^{-8}$. *© 2005 Pleiades Publishing, Inc.*

INTRODUCTION

At the present time, determination of the applicability limits of the Standard Model and searches for phenomena beyond it, which would suggest the presence of new physics, are among the most important objectives of experimental elementary-particle physics. This was among the goals pursued in creating ever more high-energy accelerators. A alternative way to new physics consists in an ever more precise measurement of known processes, including very rare ones. Radiative pion decay ($\pi^+ \to e^+\nu\gamma$) is one of such processes.

Radiative pion decay was first observed in 1963 [1]. Four more experiments had been performed before 1989 [2–5], the total number of radiative-pion-decay events observed in all experiments being 1300.

The main contribution to radiative pion decay comes from internal bremsstrahlung (IB) in accordance with the IB diagrams in Fig. 1. However, the structure-dependent part of radiative pion decay (diagrams V and A in Fig. 1) is of greatest interest. According to the $V-A$ version of weak interactions, this part is described by the vector and axial-vector form factors (F_V and F_A, respectively), which are determined by the hadronic structure of the pion [6]. From the conserved-vector-current (CVC) hypothesis [7, 8], it follows that the vector form factor is determined by the π^0-meson mass and lifetime, $F_V = 0.0259(5)$ [9]. In experiments, one therefore measures, as a rule, only the axial-vector form factor—more precisely, the ratio $\gamma \equiv F_A/F_V$.

All of the preceding experiments, with the exception of the latest ISTRA experiment at the Institute for Nuclear Research (INR, Moscow) [5], involved detecting the decays of positively charged pions stopped in a target. These decays were recorded in a bounded phase-space region specified by those

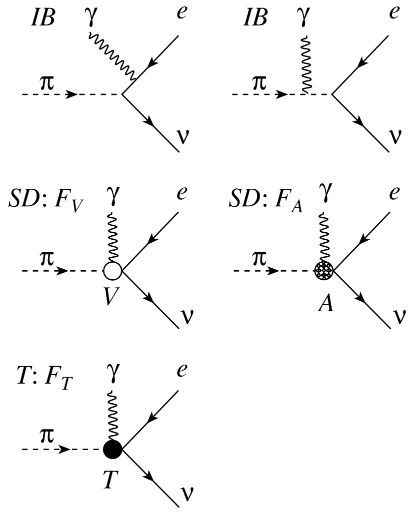

Fig. 1. Diagrams of the decay $\pi^+ \to e^+\nu\gamma$: (IB) internal-bremsstrahlung diagrams and (V, A, and T) structure-dependent-radiation diagrams.

---

[1] `http://pibeta.web.psi.ch` or `http://pibeta.phys.virginia.edu`

*E-mail: `spkoren@jinr.ru`

cases where the emitted positron and photon traveled nearly in opposite directions and where their energies exceeded 40 to 50 MeV. This kinematics is preferable for studying the structure-dependent part of radiative pion decay since the contribution of internal bremsstrahlung is suppressed to a considerable extent in this phase-space region, while the contribution of the structure-dependent part is close to its maximum value. It should be noted that the choice of kinematical conditions in [2–4] was also dictated by the potential of the experimental procedures available at that time. Since the yield of structure-dependent radiation in radiative pion decay (it is determined by the parameter γ) is proportional to the square of γ, experiments gave two γ values different in sign and in magnitude. In [3, 4], where radiative pion decay was detected in a rather large phase-space region, it was found, owing to this, that a positive solution for γ is severalfold preferable. The same conclusion was drawn by Egli *et al.* [10], who studied the decay $\pi \rightarrow 3e\nu$. Other studies yielded positive γ values ranging between 0.4 and 0.5.

In the ISTRA experiment [5], which was devoted to studying the radiative decay of negatively charged pions in flight, radiative pion decay was detected in a phase-space region larger than those in previous experiments. Upon an analysis of experimental data obtained in [5], it was concluded that the resulting total yield of radiative pion decay is approximately 30% less than that which was expected. So low a yield could not be explained by radiative corrections [11]. The authors of [5] assumed that this anomaly could be due to the presence of an additional tensor current in the radiative-pion-decay amplitude, this current being characterized by the tensor form factor $F_T \approx -0.0056 \pm 0.0017$ [5, 12].

Further attempts at theoretically justifying, on the basis of known extensions of the Standard Model, the presence of the tensor current on this order of magnitude were not successful [13–15]. Nevertheless, there was the general consensus among all researchers that a further, more thorough, investigation of radiative pion decay is necessary.

The particular problem of determining the phase-space region where a destructive anomaly associated with the possible presence of the tensor current in the radiative-pion-decay amplitude must manifest itself most strongly was considered by Chernyshev *et al.* [16].

Recently, Poblaguev [17] proposed a method for revealing, in a model-independent way, new admixtures in the radiative-pion-decay amplitude.

The mechanism that could be responsible for the appearance of the tensor current in radiative pion decay (and not only there) and which was proposed in [18] is worthy of note. This mechanism implies the existence of a new family of particles (chiral bosons) that reverse helicity upon interaction with matter. The presence of such particles explains, in a natural way, a number of special features concerning, in particular, the decays $\pi^+ \rightarrow e^+\nu\gamma$ and $K^+ \rightarrow \pi^0 e^+\nu$, the axial-vector meson resonance $b_1(1235)$, and the hadron resonances ρ and a_1. In [19], the last two were considered as prototypes of photons and weak bosons.

The possibility of a new precision investigation of radiative pion decay appeared upon the creation of the unique PIBETA spectrometer [20, 21], which was used to perform precision measurements of the pion-beta-decay branching ratio [22]. In this article, we present a description of the PIBETA spectrometer and the results of radiative-pion-decay studies conducted with it by the PIBETA Collaboration [23].

PIBETA DETECTOR

The same runs of PIBETA operation involved collecting experimental data on radiative pion decay and statistics of pion beta decays. The investigations in question were performed in a π^+-meson beam from the πE5 channel of the meson factory at the Paul Scherrer Institute (PSI, Switzerland). The channel was tuned to obtaining a pion beam of intensity $\lesssim 10^6 \pi^+/c$ and momentum 113.4 MeV/c ($\Delta p/p < 1.3\%$) that has a muon admixture of $(\mu^+) < 0.13\%$ and a positron admixture of $(e^+) < 0.37\%$. Pions were moderated in an active degrader and were stopped in a segmented target positioned at the detector center, whereupon they decayed in the target. The degrader and the target were manufactured from a fast scintillation plastic.

The layout of the PIBETA detector is shown in Fig. 2. The main elements of the setup are the following:

(1) beam counters (BC, AC1, AC2), an active degrader (AD3), and segmented active target that stops pions (AT);

(2) two thin-wall cylindrical multiwire proportional chambers (MWPC1, MWPC2) surrounding the central target, which are intended for detecting the tracks of charged particles [24];

(3) cylindrical hodoscope (CH) consisting of 20 plastic scintillation counters that are positioned around the proportional chambers;

(4) segmented fast shower total-absorption calorimeter (CsI) manufactured in a spherical form with two windows on the beam axis (the beam enters through the first, and light and electric signals from detectors situated at the setup center go out through the second) and deployed around the scintillation hodoscope;

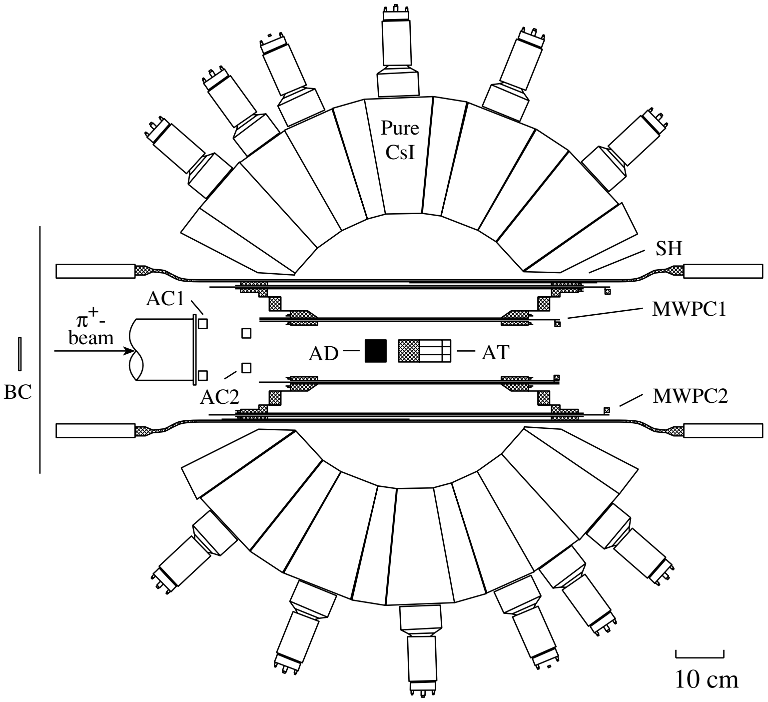

Fig. 2. Schematic representation of the cross section of the PIBETA setup. The main elements given in a scaled form are the following: (BC) beam counter, (AD) active degrader, (AT) active target, (AC1, AC2) active collimators, (MWPC1, MWPC2) cylindrical multiwire proportional chambers, (SH) scintillation hodoscope, and (pure CsI) calorimeter from pure CsI crystals.

(5) cosmic-veto counters placed above the setup and intended for the suppression of the background from cosmic rays.

The calorimeter is manufactured from pure CsI crystals. The setup includes 240 truncated hexagonal and pentagonal pyramids.The length of the CsI crystals is 22 cm, which is equivalent to 12 radiation-length units. The radius of the outer spherical surface of the calorimeter is 48 cm. The use of fast ($\tau \sim 40$ ns) counters from pure CsI ensures unique properties of the spectrometer and makes it possible to operate under conditions of a high intensity of pion stoppings; this in turn furnishes high statistics of radiative-pion-decay events. The time resolution of the calorimeter is about 0.7 ns. Particles from radiative pion decay are detected within a solid angle of $\Omega = 0.77 \times 4\pi$ sr. The resolution of the calorimeter in photon and positron energies is approximately 5 to 6% (FWHM). The angular resolution is approximately 2°. The total weight of CsI counters is about 1.6 t, and the total volume is about 0.346 m^3.

The entire setup is placed within a temperature-controlled house equipped with thermal stabilization. The house is surrounded by a Pb shield and cosmic-veto detectors.

Signals from all detector counters are analyzed with the aid of the amplitude and time decoders. The extraction of experimental information and the monitoring the setup operation is performed with the aid of the original flexible Maximum Integration Data-Acquisition System (MIDAS), which makes it possible to trace the experiment and to execute an on-line control over it from any remote computer through the global net Ethernet. The MIDAS performs a parallel recording of experimental data on magnetic tapes in the DLT standard both in a local tape recorder and in the central archive of PSI through the local net Fast Ethernet. In combination with buffering by means of high-capacity disk drives, this ensures extremely high reliability of storage of information and a convenient assess to it.

DESCRIPTION OF THE EXPERIMENT

The trigger of the PIBETA setup made it possible to detect simultaneously various processes occurring in the detector and differing from one another in time, energy, or logical parameters. In all, 12 types of trigger were used. They ensured the detection of single hits and double coincidences of signals in the calorimeter at a low and at a high level of energy deposited in crystals separately. Concurrently, events coinciding with the instant of pion stopping in the target and events delayed with respect to this instant were separated. A channel detecting triple coincidences and a channel for recording random signals in the detector that are not associated with any factor other than cosmic radiation were also organized. It was possible to transfer, to the total trigger, one of 2^n arriving signals rather than each signal arising in an individual specific channel (trigger rescaled by a factor 2^n).

The experimental data on pion beta decays and radiative pion decays [$\pi^+ \to \pi^0 e^+ \nu$ and $\pi^+ \to e^+ \nu \gamma$, respectively] were accumulated by means of exposures in the pion beam for many months from 1999 to 2001. The resulting statistics involved 2.2×10^{13} pion decays in the target. The detection efficiency for particles producing minimum ionization (positrons) was traced continuously and was 93.7% for the inner MWPC, 97.9% for the outer MWPC, and 98.9% for the hodoscope. Thus, the total inefficiency of distinguishing between charged and neutral particles was about 1.5×10^{-5}. The energy losses in the hodoscope made it possible to discriminate between protons and positrons. Photons, as well as charged particles, were detected in the calorimeter (the detection efficiency was approximately 100%), and the energies of the particles were measured there.

A precision measurement of the branching ratio for pion beta decay ($\pi^+ \to \pi^0 e^+ \nu$) was the main original objective of the PIBETA Collaboration. As a result, the following result was obtained for this quantity: $\mathrm{BR} \approx [1.038 \pm 0.004(\mathrm{stat}) \pm 0.007(\mathrm{syst})] \times 10^{-8}$ [22]. From the Standard Model and the conserved-vector-current hypothesis, it follows that this branching ratio is determined by the matrix element V_{ud} of the Cabibbo–Kobayashi–Maskawa mixing matrix and is, according to the Particle Data Group [9], $\mathrm{BR} = (1.038\text{–}1.041) \times 10^{-8}$ (at a 90% C.L.). Thus, there is perfect agreement here between the theoretical and experimental values. The experimental value obtained previously for the pion-beta-decay branching ratio was $\mathrm{BR} \approx (1.026 \pm 0.039) \times 10^{-8}$ [25].

Events of the decay $\pi \to e\nu\gamma$ ($\pi e2\gamma$) were detected in three kinematical regions that differ by constraints on the particle energies:

(region A) $E_\gamma > 51.7$ MeV for the photon energy, and $E_e > 51.7$ MeV for the positron energy;

(region B) $E_\gamma > 55.6$ MeV for the photon energy, and $E_e > 20.0$ MeV for the positron energy;

(region C) $E_\gamma > 20.0$ MeV for the photon energy, and $E_e > 55.6$ MeV for the positron energy.

In all three regions, the relative particle-divergence angle $\theta_{\gamma,e}$ was required to satisfy the cut $\theta_{\gamma,e} > 40°$. Because of the trigger logic, this angle was always $\gtrsim 140°$ in region A.

The number of events found in region A was 30 670 (the statistical error was 0.6%). These events were obtained according to the master trigger of beta decay. It separated those events where two signals of energy in excess of 51.7 MeV were coincident in the calorimeter (two-arm trigger), the requirements that these signals came from opposite detector hemispheres within the time gate of about 150 ns, which is specified by pion stopping in the target, being imposed.

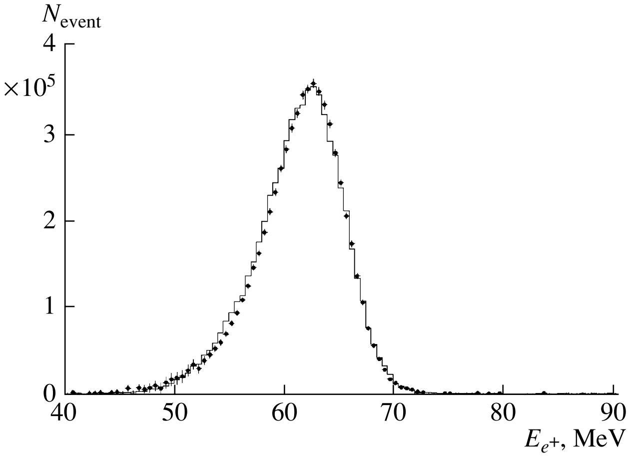

Fig. 3. Energy spectrum detected in the case of stopping of monochromatic positrons (of energy about 70 MeV) in the calorimeter that originate from the decay $\pi^+ \to e^+ \nu_e$: (points) experimental data and (histogram) results of Monte Carlo calculations.

In regions B and C, 5233 and 5698 events were detected with statistical uncertainties of 1.7 and 1.5%, respectively. The systematic errors were 1.8% in region A (mainly because of the subtraction of the background from pion beta decay) and 2.3 and 3.1% in regions B and C (mainly, because of the uncertainties in the estimates of the detection efficiency), respectively. The events in regions B and C were recorded according to the trigger organized for detecting the decay $\pi \to e\nu$ ($\pi e2$). All processes recorded in the detector were normalized to this decay. Figure 3 shows the detected energy spectrum that is obtained upon the stopping of monochromatic positrons ($E_e \sim 70$ MeV) in the calorimeter that originate from $\pi e2$ decay.

The total statistical sample of $\pi e2$ decays included about 2×10^8 events. The estimated absolute value of the branching ratio for this decay is fully consistent, within the systematic error of the measurement (about 0.5%), with the Standard Model predictions.

The generation of the $\pi e2$ trigger implied that, in the calorimeter, there arose at least one signal of energy in excess of 55.6 MeV within the time gate determined by pion stopping in the target (one-arm

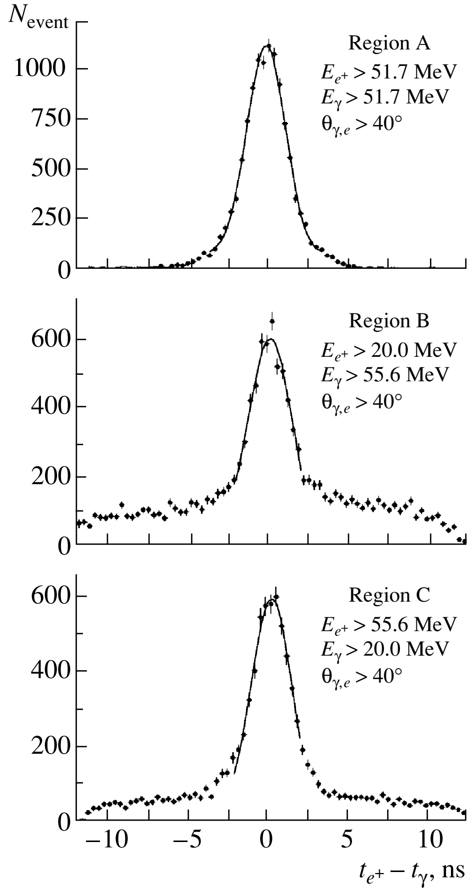

Fig. 4. Number of events of the decay $\pi^+ \to e^+\nu\gamma$ as a function of the time difference between the arrival of a positron signal and the arrival of a photon signal for regions A, B, and C.

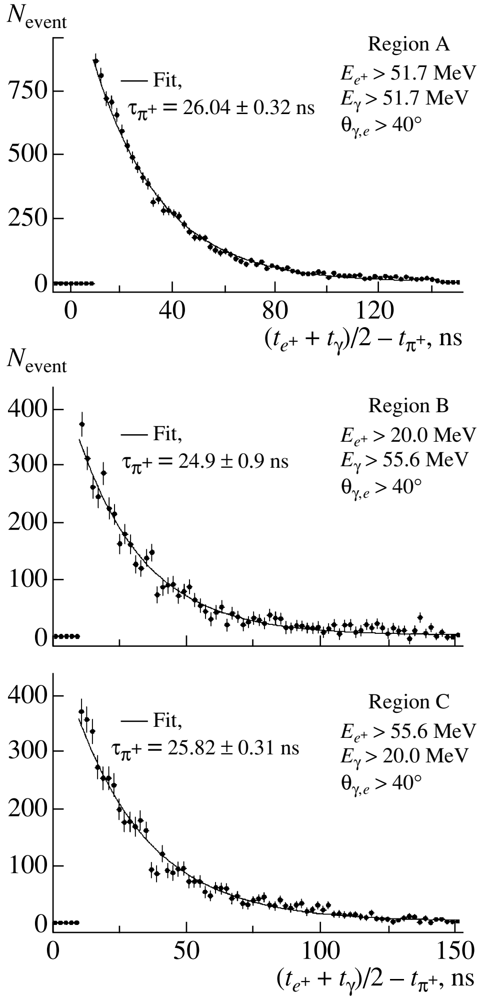

Fig. 5. Number of events of the decay $\pi^+ \to e^+\nu\gamma$ as a function of the time after pion stopping in regions A, B, and C.

trigger). Since these were predominantly single signals, their number was large; therefore, use was made of the trigger rescaled with the coefficients of 8 or 16 in various exposures. The question of whether the detected particles are charged or neutral was addressed later in processing information from the proportional chambers and scintillation hodoscope. Region B is characterized by the presence of a high-energy photon and a charged particle of lower energy in an event, while region C is characterized by the presence of a high-energy positron and a neutral particle of lower energy.

Curves that represent the dependence of the number of events of the decay $\pi^+ \to e^+\nu\gamma$ on the time difference between the arrival of a positron signal and the arrival of a photon signal are shown in Fig. 4 for regions A, B, and C. It can be seen that, in region A, there is virtually no background from random coincidences. In regions B and C, the signal-to-background ratio is 3.8 : 1 and 7.6 : 1, respectively. Figure 5 displays curves that represent the dependence of the number of radiative-pion-decay events (upon the the subtraction of the background due to random coincidences) on the time after pion stopping. All of them are in accord with the pion lifetime (about 26 ns). Figure 6 presents the invariant-mass (approximately 140 MeV) distribution of radiative-pion-decay events in regions A, B, and C.

The branching ratio for radiative pion decay can be calculated by using the expression

$$R_{\pi e2\gamma} = \frac{N_{\pi e2\gamma} p_{\pi e2\gamma}}{N_{\pi^+} g_\pi A_{\pi e2\gamma} \eta \varepsilon_{\pi e2\gamma}}, \tag{1}$$

where $N_{\pi e2\gamma}$ is the number of detected radiative-pion-decay events, $p_{\pi e2\gamma}$ is the corresponding prescaling factor of the trigger (if it appears), N_π is the number of decaying pions,

$$g_\pi = \int\limits_{t_1}^{t_2} \exp(-t/\tau_{\pi^+})dt$$

is the fraction of pion decays falling within the time gate specified by pion stopping, $A_{\pi e2\gamma}$ is the efficiency of detection of radiative pion decay by the detector (acceptance) with allowance for all adopted cuts, η is the coefficient taking into account the detector-dead-time fraction associated with the need for extracting information upon each generation of the trigger, and $\varepsilon_{\pi e2\gamma}$ is the efficiency of charged-particle detection (it is determined by the efficiency of the proportional chambers and scintillation hodoscope). A similar expression can be written for $R_{\pi e2}$. On the basis of these two expressions, we obtain

$$R_{\pi e2\gamma} = R_{\pi e2}\frac{N_{\pi e2\gamma}p_{\pi e2\gamma}}{N_{\pi e2}p_{\pi e2\gamma}}\frac{A_{\pi e2}}{A_{\pi e2\gamma}}\frac{\varepsilon_{\pi e2}}{\varepsilon_{\pi e2\gamma}}. \qquad (2)$$

The efficiency of detection of the process being studied depends both on the features of the process itself and on the properties of the detector. It was calculated by the Monte Carlo method. The GEANT [26] simulation of the PIBETA detector response took into account (i) the detailed geometry of the active part of the detector and passive structural materials, (ii) the experimentally measured dependences of the energy and time resolutions, (iii) event generators for the decays of pions and muons with allowance for measured random pileup event rates, and (iv) the photoabsorption reactions in the CsI crystals (these are incorporated in the GEANT code). A comparison of the experimentally observed processes with those calculated within the Monte Carlo model shows that the detector model describes all of the occurring processes to a precision on the order of a few tenths of a percent.

Within the Standard Model, the expression for the differential rate of radiative pion decay ($R_{\pi e2\gamma}$) has the form [27]

$$\frac{d\Gamma_{\pi\to e\nu\gamma}}{dxdy} = \frac{\alpha}{2\pi}\Gamma_{\pi\to e\nu}\Bigg\{IB(x,y) + \left(\frac{F_V m_\pi^2}{2f_\pi m_e}\right)^2 \qquad (3)$$

$$\times\left[(1+\gamma)^2 SD^+(x,y) + (1-\gamma)^2 SD^-(x,y)\right]$$

$$+\left(\frac{F_V m_\pi}{f_\pi}\right)\left[(1+\gamma)\,S^+_{\text{int}}(x,y) + (1-\gamma)\,S^-_{\text{int}}(x,y)\right]\Bigg\},$$

where $\alpha = 1/137$; IB and SD are terms that depend on the kinematical variables $x = 2E_\gamma/m_\pi$ and $y = 2E_e/m_\pi$; E_γ and E_e are the photon and the positron energy, respectively; m_π is the pion mass; $\gamma = F_A/F_V$; F_V is the pion vector form factor; F_A is the pion axial-vector form factor; and $f_\pi = 130.7 \pm 0.4$ MeV is the pion-decay constant [9].

In calculating the absolute differential rate of radiative pion decay, data were normalized to the value of $R_{\pi e2}/R_{\text{tot}} = 1.230(4) \times 10^{-4}$. To the calculated values, we have added integrated radiative corrections: −1.0% in region A, −1.4% in region B, and −3.3% in region C [28]. In fitting the experimental distributions, we have used two-dimensional distributions in E_γ and E_e.

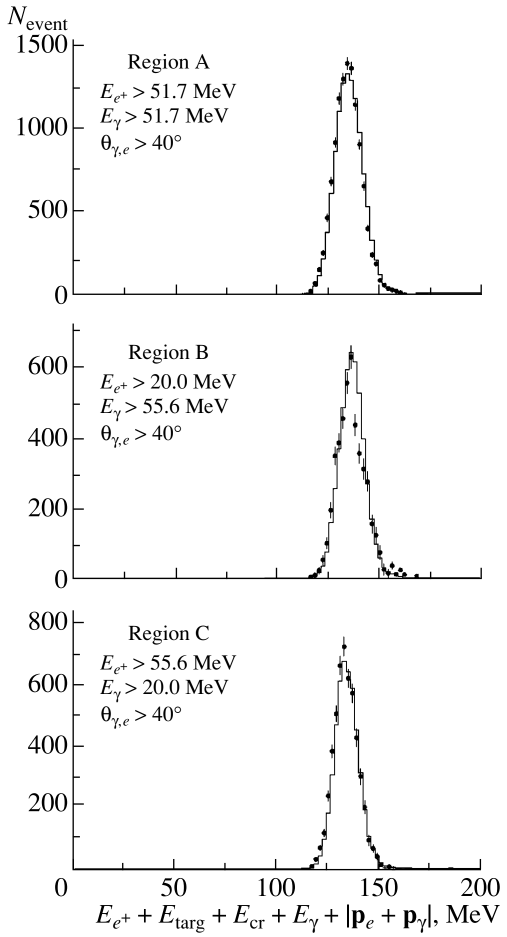

Fig. 6. Invariant-mass distribution of events of the decay $\pi^+ \to e^+\nu\gamma$ for regions A, B, and C: (points) experimental data and (histogram) results of Monte Carlo calculations.

The theoretical dependence of the radiative-pion-decay branching ratio as a function of the quantity γ and the corresponding experimental dependence measured in region A are shown in Fig. 7 (upper panel of the figure). Two possible solutions are seen here. If we additionally use the data from regions B and C (lower panel of the figure), the solution where γ is positive obviously appears to be preferable since the χ^2 value for this solution is approximately 50 times smaller than that for the solution where this parameter is negative. From the data in region A, one obtains $\gamma = 0.480(16)$. If use is made of the data from all regions, we have $\gamma = 0.443(15)$ and, hence, $F_A = 0.0115(4)$, this value of F_A being in agree-

Results of fitting the experimental distributions in regions A, B, and C (the first column indicates the number of a fit; the fourth, fifth, and sixth columns contain the radiative-pion-decay branching ratios measured in experimentally, R_{expt}, and calculated on the basis of the form factors in the corresponding fit, R_{theor}; fit 2 corresponds to the Standard Model, while fit 3 corresponds to the model involving a tensor current)

No.	Parameters		$R, 10^{-8}$			χ^2
	fixed	fitted	region A	region B	region C	
1	PDG $F_V = 0.017(8)$	No	$R_{\text{expt}} = 2.83(5)$	$R_{\text{expt}} = 13.0(4)$	$R_{\text{expt}} = 54.1(18)$	580
	PDG $F_A = 0.0116(16)$		$R_{\text{theor}} = 1.656(1)$	$R_{\text{theor}} = 12.73(1)$	$R_{\text{theor}} = 35.45(1)$	
2	conservation of vector current $F_V = 0.0259(5)$	$F_A = 0.0115(3)$	$R_{\text{expt}} = 2.71(5)$	$R_{\text{expt}} = 11.6(3)$	$R_{\text{expt}} = 39.1(13)$	76
	$F_T = 0$		$R_{\text{theor}} = 2.583(1)$	$R_{\text{theor}} = 14.34(1)$	$R_{\text{theor}} = 37.83(1)$	
3	conservation of vector current $F_V = 0.0259(5)$	$F_A = 0.0133(4)$	$R_{\text{expt}} = 2.58(5)$	$R_{\text{expt}} = 12.4(4)$	$R_{\text{expt}} = 37.0(13)$	0.02
		$F_T = -0.00267(37)$	$R_{\text{theor}} = 2.575(1)$	$R_{\text{theor}} = 12.44(1)$	$R_{\text{theor}} = 37.13(1)$	

ment, within the errors, with the preceding result. The values found here for γ agree with the results of previous measurements within the large statistical and systematic errors of the latter. The new value of γ was determined with an error four times smaller than that in previous experiments and is in agreement with the results of the calculations based on the chiral Lagrangian model [29–31].

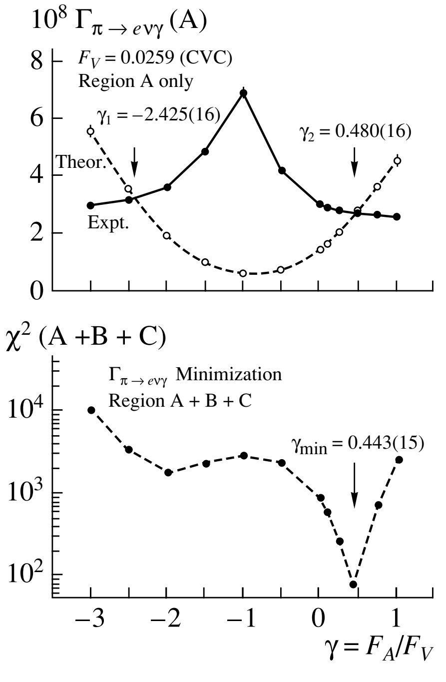

Fig. 7. Branching ratio for radiative pion decay as a function of the ratio $\gamma \equiv F_A/F_V$ in the kinematical region A (upper panel) [the theoretical decay curve (parabola) was calculated on the basis of the $V-A$ version of the theory. Distribution of minimum χ^2 values obtained by fitting the entire data set from all kinematical regions (A + B + C) (lower panel).

Results obtained by fitting the experimental distributions are presented in the table. The fits were constructed both on the basis of the Standard Model and under the assumption that there is a hypothetical tensor interaction. In the table, we present the most probable values of the pion form factors and the radiative-pion-decay branching ratios calculated on their basis and measured experimentally (R_{theor} and R_{expt}, respectively) in regions A, B, and C .

It can be seen that, on the whole, the results obtained in regions A and C are compatible with their counterparts calculated within the Standard Model. It turned out, however, that, in region B, the absolute value of the radiative-pion-decay branching ratio is smaller than that calculated on the basis of the Standard Model by about eight standard deviations (fit 2, row 5). In other words, the Standard Model fails to describe the experimental data on radiative pion decay in region B. This is a very important conclusion. It would be natural to verify whether this result is not a consequence of some error.

It was indicated above that the branching ratios obtained in the PIBETA experiment for the decays $\pi^+ \to \pi^0 e^+ \nu$ and $\pi^+ \to e^+ \nu$ agree within the accuracy of the measurements (about 0.5 to 0.8%) with the Standard Model calculations. However, the high energy (up to about 70 MeV) of decaying particles is a feature peculiar to these decays. But in region B, the positron energy extends to a value about 20 MeV. It would be reasonable to assume that the observed

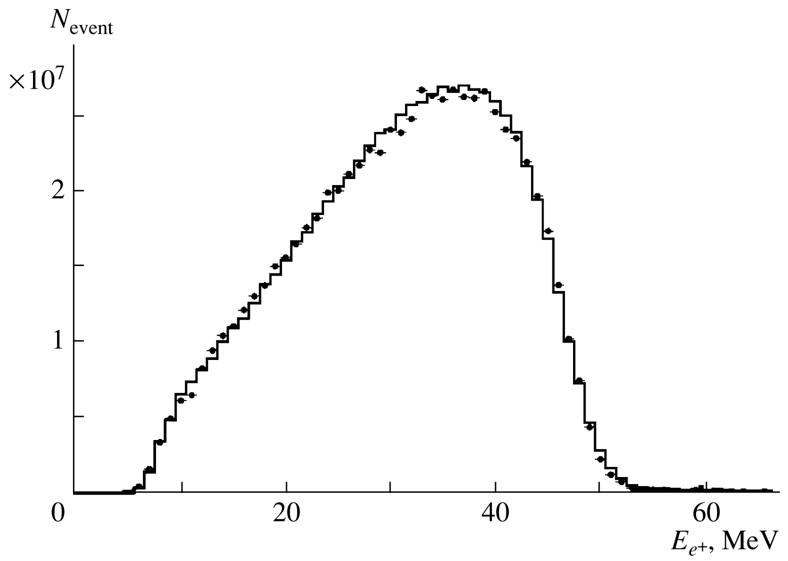

Fig. 8. Positron energy spectrum measured in the decay $\mu^+ \to e^+\nu\nu$ (Michel spectrum). The histogram represents the results of calculations based on the Monte Carlo method.

discrepancy can be due to an erroneous definition of the positron energy scale in the region of low energies. The muon decay $\mu^+ \to e^+\nu\nu$ is a process that involves low-energy positrons. Figure 8 shows the measured spectrum of positrons in this decay (Michel spectrum) and the spectrum simulated by the Monte Carlo method. It can be seen that there are no discrepancies between these spectra.

The radiative muon decay $\mu^+ \to e^+\nu\nu\gamma$ is yet another process that can be adequately described within the Standard Model. In this decay, positrons have predominantly low energies. In the kinematical region that is defined by the inequality $\theta_{\gamma,e} > 40°$ for the angle between the photon and positron momenta and the inequality $E_{\gamma,e} > 10$ MeV for the photon and positron energies, approximately 80 000 events of radiative muon decay were detected and analyzed. These data are described well within the Standard Model [32]. It was found that, in the kinematical region specified above, the radiative-muon-decay branching ratio is $R_{\mu\to e\nu\nu\gamma} \approx [2.563 \pm 0.050(\text{stat}) \pm 0.050(\text{syst})] \times 10^{-2}$. According to the Standard Model predictions, this quantity is $R_{\mu\to e\nu\nu\gamma} \approx 2.584 \times 10^{-2}$. The new value of $\bar{\eta} = 0.00(5)$ was obtained. The parameter $\bar{\eta}$ does not vanish in the presence of deviation from the pure $V-A$ version in weak interaction. According to the Standard Model, $\bar{\eta} \equiv 0$. Previously, the value of $\bar{\eta} = 0.02 \pm 0.08$ was obtained experimentally.

It should be noted that radiative corrections could also be one of the possible sources of the above discrepancy. The corrections given above in this article were derived on the basis of the last theoretical investigations of this issue [28], which were performed at the request of the authors. These corrections were negligible, but they were taken into account in the present analysis.

A comparison of all results of investigations of the various processes for which the experimental data were obtained in common runs of data acquisition and a detailed crosscheck of the possible errors in the determination of the properties of the detector or in the codes for simulating the apparatus revealed that there are no such errors. This means that the deficit of radiative-pion-decay events in the kinematical region B is an experimentally established fact rather than a consequence of some errors or of a deficit of statistics.

In order to compare the experimental data with the results of the calculations, it is convenient to use the kinematical variable λ,

$$\lambda = (2E_e/m_\pi)\sin^2(\theta_{\gamma,e}/2) \equiv (x + y - 1)/x. \quad (4)$$

All quantities appearing in this expression were defined above.

The spectrum of radiative-pion-decay events that was obtained experimentally for regions A, B, and C is shown in Fig. 9 versus the kinematical variable λ. The dashed curve was calculated within the Standard Model at $F_V = 0.0259$ and $F_A = 0.0115$ (the best fit obtained from a minimization for the entire data set over the three regions). The solid curve corresponds to the radiative-pion-decay distribution calculated by the Monte Carlo model under the assumption that there exists a tensor current. The curve was calculated at the following values of the form factors: $F_V = 0.0259$, $F_A = 0.0133$, and $F_T = -0.00267$. It

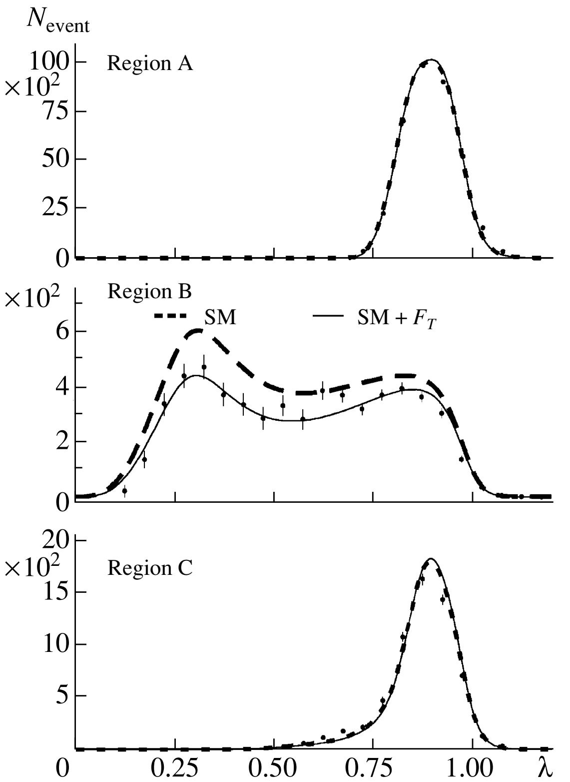

Fig. 9. Experimental distribution of events in regions A, B, and C versus the kinematical variable $\lambda = (2E_e/m_\pi)\sin^2(\theta_{\gamma,e}/2)$. The dashed curve was calculated within the Standard Model at the form-factor values of $F_V = 0.0259$ and $F_A = 0.0115$ (the best fit obtained via a minimization for the entire data set over the three regions). The solid curve was calculated at the form-factor values of $F_V = 0.0259$, $F_A = 0.0133$, and $F_T = -0.00267$.

can be seen that, in regions A and C, the dashed and the solid curve are nearly coincident. In region B, however, the description based on the Standard Model is unsatisfactory. The hypothesis that there exists a tensor current makes it possible to describe well the spectrum of radiative-pion-decay events in region B.

In calculating the contribution to radiative pion decay from the hypothesized tensor current, we took its amplitude in the form [16]

$$M_T = -i\frac{eG_{\mathrm{F}}V_{ud}}{\sqrt{2}}e^\mu q^\nu F_T\bar{\psi}_e\sigma_{\mu\nu}(1-\gamma_5)\psi_\nu. \quad (5)$$

Correspondingly, the differential rate of radiative pion decay is given by

$$\frac{d\Gamma_{\pi\to e\nu\gamma}}{dx d\lambda} = \frac{\alpha}{2\pi}\Gamma_{\pi\to e\nu}\left\{IB(x,\lambda) + \left(\frac{F_V m_\pi^2}{2f_\pi m_e}\right)^2\right. \quad (6)$$
$$\times\left[(1+\gamma)^2 SD^+(x,\lambda) + (1-\gamma)^2 SD^-(x,\lambda)\right]$$
$$+\left(\frac{F_V m_\pi}{f_\pi}\right)\left[(1+\gamma)S^+_{\text{int}}(x,\lambda) + (1-\gamma)S^-_{\text{int}}(x,\lambda)\right]$$
$$\left. + \left(\frac{F_T m_\pi^2}{f_\pi m_e}\right)T_1(x,\lambda) + \left(\frac{F_T m_\pi^2}{f_\pi m_e}\right)^2 T_2(x,\lambda)\right\},$$

where the terms representing internal bremsstrahlung (IB), the structure-dependent amplitudes ($SD^\pm$), the interference of the IB and $SD^\pm$ terms, and the contribution of the tensor term (F_T) have the form

$$IB(x,\lambda) = \frac{1-\lambda}{\lambda}\frac{1+(1-x)^2}{x}, \quad (7)$$
$$SD^+(x,\lambda) = \lambda^2 x^3(1-x),$$
$$SD^-(x,\lambda) = (1-\lambda)^2 x^3(1-x),$$
$$S^+_{\text{int}}(x,\lambda) = (1-\lambda)\frac{1-x}{x},$$
$$S^-_{\text{int}}(x,\lambda) = (1-\lambda)\left[1-x+\frac{x}{\lambda}\right],$$
$$T_1(x,\lambda) = (1-\lambda)x, \quad T_2(x,\lambda) = \lambda(1-\lambda)x^3.$$

It is obvious that the problem of radiative pion decay is of particular interest. We are going to perform new precision investigations of this process.

ACKNOWLEDGMENTS

The PIBETA experiment was supported by grants from the U.S. National Science Foundation, the U.S. Department of Energy, the Russian Foundation for Basic Research (project nos. 98-02-16506, 01-02-16412), and the Paul Scherrer Institute.

REFERENCES

1. P. Depommier *et al.*, Phys. Lett. **7**, 285 (1963).
2. A. Stetz *et al.*, Nucl. Phys. B **138**, 285 (1978).
3. A. Bay *et al.*, Phys. Lett. B **174**, 445 (1986).
4. L. E. Piilonen *et al.*, Phys. Rev. Lett. **57**, 1402 (1986).
5. V. N. Bolotov *et al.*, Phys. Lett. B **243**, 308 (1990).
6. D. A. Bryman *et al.*, Phys. Rep. **88**, 151 (1982).
7. S. S. Gershteĭn and I. B. Zel'dovich, Zh. Éksp. Teor. Fiz. **29**, 698 (1955) [Sov. Phys. JETP **2**, 576 (1955)].
8. R. P. Feynman and M. Gell-Mann, Phys. Rev. **109**, 193 (1958).
9. K. Hagivara *et al.*, Phys. Rev. D **66**, 010001 (2002).
10. S. Egli *et al.*, Phys. Lett. B **222**, 533 (1989).
11. I. N. Nikitin, Yad. Fiz. **54**, 1029 (1991) [Sov. J. Nucl. Phys. **54**, 621 (1991)].
12. A. A. Poblaguev, Phys. Lett. B **238**, 108 (1990).
13. V. M. Beliayev and I. I. Kogan, Phys. Lett. B **280**, 238 (1992).
14. M. B. Voloshin, Phys. Lett. B **283**, 120 (1992).
15. P. Herczeg, Phys. Rev. D **49**, 247 (1994).
16. A. V. Chernyshev *et al.*, Mod. Phys. Lett. A **12**, 1669 (1997).

17. A. A. Poblaguev, Phys. Rev. D **68**, 054020 (2003).
18. M. V. Chizhov, Mod. Phys. Lett. A **8**, 2753 (1993); hep-ph/0307100; hep-ph/0310203; hep-ph/0402105; hep-ph/0401217.
19. S.Weinberg, hep-ph/0401010.
20. E. Frlež *et al.*, hep-ex/0312017.
21. É. Frlezh *et al.*, Preprint No. P13-2003-102, OIYaI (Joint Inst. for Nucl. Res., Dubna, 2003).
22. D. Počanić *et al.*, hep-ex/0312030.
23. E. Frlež *et al.*, hep-ex/0312029.
24. V. V. Karpukhin, I. V. Kisel, A. S. Korenchenko, *et al.*, Nucl. Instrum. Methods Phys. Res. A **418**, 306 (1998).
25. W. K. McFarlane, L. B. Auerbach, F. C. Gaille, *et al.*, Phys. Rev. D **32**, 547 (1985).
26. R. Brun *et al.*, GEANT 3.21, CERN (Geneva, 1994).
27. D. A. Bryman *et al.*, Phys. Rep. **88**, 151 (1982).
28. E. A. Kuraev and Y. M. Bystritsky, hep-ph/0310275.
29. C. Q. Geng *et al.*, hep-ph/0306165.
30. B. R. Holstein, Phys. Rev. D **33**, 3316 (1986).
31. J. Bijnens and P. Talavera, Nucl. Phys. B **489**, 387 (1997).
32. E. Frlež *et al.* (in press).

Translated by A. Isaakyan

Physics of Atomic Nuclei, Vol. 68, No. 3, 2005, pp. 508–520. From Yadernaya Fizika, Vol. 68, No. 3, 2005, pp. 537–549.
Original English Text Copyright © 2005 by Dremin.

Wavelets: Mathematics and Applications*

I. M. Dremin**

Lebedev Physical Institute, Russian Academy of Sciences, Leninskii pr. 53, Moscow, 117924 Russia

Received April 19, 2004; in final form, October 11, 2004

Abstract—The notion of wavelets is defined. It is briefly described what wavelets are, how to use them, when we do need them, why they are preferred, and where they have been applied. Then one proceeds to the multiresolution analysis and fast wavelet transform as a standard procedure for dealing with discrete wavelets. It is shown what specific features of signals (functions) can be revealed by this analysis, but cannot be found by other methods (e.g., by the Fourier expansion). Finally, some examples of practical application are given. Rigorous proofs of mathematical statements are omitted, and the reader is referred to the corresponding literature. *© 2005 Pleiades Publishing, Inc.*

1. INTRODUCTION

Let us define wavelets as a complete orthonormal system of functions with a compact support obtained with the help of dilations and translations. Sometimes a wider class of functions is also called "wavelets" if the properties of completeness and/or orthonormality are not required. In what follows, we will use so-called discrete wavelets satisfying the above rigorous definition.

Wavelets have become a necessary mathematical tool in many investigations. They are used in those cases when the result of the analysis of a particular signal[1)] should contain not only the list of its typical frequencies (scales), but also definite knowledge of the particular local coordinates, where these properties are important. Thus, analysis and processing of different classes of nonstationary (in time) or inhomogeneous (in space) signals is the main field of applications of wavelet analysis.

In particle physics, wavelets can be used for analysis of multiparticle production processes, for separation of close overlapping resonances, for revealing small fluctuations over huge background, etc. The inhomogeneity of the secondary-particle distributions in the available phase space is one of the fields of wavelet applications, as demonstrated below. Besides their application to analysis of experimental data, wavelets can be successfully used for computer solution of nonlinear equations, because they provide a very effective and stable basis, especially for expansions in equations containing many varying scales.

The wavelet basis is formed by using dilations and translations of a particular function defined on a finite interval. Its finiteness is crucial for the locality property of the wavelet analysis. Commonly used (so-called discrete) wavelets generate a complete orthonormal system of functions with a finite support constructed in such a way. That is why, by changing the scale (dilations), they can distinguish the local characteristics of a signal at various scales and, by translations, they cover the whole region in which it is studied. Due to the completeness of the system, they also allow for the inverse transformation to be done properly. In the analysis of nonstationary signals, the locality property of wavelets gives a substantial advantage over the Fourier transform, which provides only information on the global frequencies (scales) of the object under investigation, because the system of the basic functions used (sine, cosine, or imaginary exponential functions) is defined over an infinite interval.

The literature devoted to wavelets is very extensive, and one can easily get a lot of references by sending the corresponding request to Internet web sites. Mathematical problems are treated in many monographs in detail (e.g., see [1–5]). Introductory courses on wavelets can be found in [6–9]. Review papers adapted for physicists and practical users were published in the journal *Physics-Uspekhi* [10, 11] and are available from web site www.ufn.ru (see also www.awavelet.ru). In particular, this paper is based on the talk delivered at the session of the Russian Academy of Sciences, which, in turn, was mainly based on the review paper [11].

It has been proven that any function can be written as a superposition of wavelets, and there exists a

---

[*] This article was submitted by the author in English.

[**] e-mail: `dremin@lpi.ru`

[1)] The notion of a signal is used here for any ordered set of numerically recorded information about some processes, objects, functions, etc. The signal can be a function of some coordinates, be it the time, the space, or any other (in general, n-dimensional) scale.

numerically stable algorithm to compute the coefficients for such an expansion. Moreover, these coefficients completely characterize the function, and it is possible to reconstruct it in a numerically stable way if these coefficients have been determined. Because of their unique properties, wavelets were used in functional analysis in mathematics; in studies of (multi)fractal properties, singularities, and local oscillations of functions; for solving some differential equations; for investigation of inhomogeneous processes involving widely different scales of interacting perturbations; for noise analysis; for pattern recognition; for image and sound compression; for digital geometry processing; and for solving many problems of physics, biology, medicine, engineering, etc. (see the recently published books [12–15]). This list is by no means exhaustive.

The codes exploiting the wavelet transform are widely used now not only for scientific research but for commercial projects as well. Some of them have been even described in books (see, e.g., [16]). At the same time, the direct transition from pure mathematics to computer programming and applications is nontrivial and often asks for an individual approach to the problem under investigation and for a specific choice of wavelets used. Our main objective here is to describe in a suitable way the bridge that relates mathematical wavelet constructions to practical signal processing. Practical applications considered by Grossman and Morlet [17, 18] have led to fast progress of the wavelet theory related to the work of Meyer [1, 3, 4], Daubechies [2], and others.

The main group of papers dealing with practical applications of wavelet analysis uses so-called discrete wavelets, which will be our main concern here. Discrete wavelets look strange to those accustomed to analytical calculations, because they cannot be represented by analytical expressions (except for the simplest one) or by solutions of some differential equations, and instead are given numerically as solutions of definite functional equations containing rescaling and translations. Moreover, in practical calculations, their direct form is not even required, and only the numerical values of the coefficients of the functional equation are used. Thus the wavelet basis is defined by the iterative algorithm of the dilation and translation of a single function. This leads to a very important procedure called multiresolution analysis, which gives rise to the multiscale local analysis of the signal and fast numerical algorithms. Each scale contains an independent nonoverlapping set of information about the signal in the form of wavelet coefficients, which are determined from an iterative procedure called the fast wavelet transform. In combination, they provide its complete analysis and simplify the diagnostics of the underlying processes.

After such an analysis has been done, one can compress (if necessary) the resulting data by omitting some inessential part of the encoded information. This is done with the help of the so-called quantization procedure, which commonly allocates different weights to various wavelet coefficients obtained. In particular, it helps to erase some statistical fluctuations and, therefore, increase the role of the dynamical features of a signal. This can, however, falsify the diagnostics if the compression is done inappropriately. Usually, accurate compression gives rise to a substantial reduction of the required computer storage memory and transmission facilities, and, consequently, to a lower expenditure. The number of vanishing moments of wavelets is important at this stage. Unfortunately, the compression introduces unavoidable systematic errors. The mistakes one has made will consist of multiples of the deleted wavelet coefficients, and, therefore, the regularity properties of a signal play an essential role. Reconstruction after such compression schemes is then no longer perfect. These two objectives (compression and reconstruction quality) are clearly antagonistic. Nevertheless, when one tries to reconstruct the initial signal, the inverse transformation (synthesis) happens to be rather stable and reproduces its most important characteristics if proper methods are applied. The regularity properties of wavelets used also become crucial at the reconstruction stage. The distortions of the reconstructed signal due to quantization can be kept small, although significant compression ratios are attained. Since the part of the signal that is not reconstructed is often called noise, in essence, what we are doing is denoising the signals. Namely, at this stage, the superiority of discrete wavelets becomes especially clear.

Thus, the objectives of signal processing consist in accurate analysis with the help of the transform, effective coding, fast transmission, and, finally, careful reconstruction (at the transmission destination point) of the initial signal. Sometimes, the first stage of signal analysis and diagnosis is sufficient for the problem to be solved and the anticipated goals to be achieved.

One should, however, stress that, even though this method is very powerful, the goals of wavelet analysis are rather modest. This helps us describe and reveal some features otherwise hidden in a signal, but it does not pretend to explain the underlying dynamics and physical origin, although it may give some crucial hints to it. Wavelets present a new stage in optimization of this description, providing, in many cases, the best known representation of a signal. With the help of wavelets, we merely see things a little more clearly.

However, one should not underestimate the significance of information obtained by this analysis. It often provides such new knowledge of processes, otherwise hidden but underlying the crucial dynamics, which cannot be found from traditional approaches. This helps further to introduce models assumed to be driving the mechanisms generating the observations and, therefore, to get deeper insight into the dynamics of the processes.

To define the optimality of the algorithms of the wavelet transform, some (still debatable!) energy and entropy criteria have been developed. They are internal to the algorithm itself. However, the choice of the best algorithm is also tied to the objective goal of its practical use, i.e., to some external criteria. That is why, in practical applications, one should submit the performance of a “theoretically optimal algorithm” to the judgements of experts and users to estimate its advantage over the previously developed ones.

Despite very active research and impressive results, the versatility of wavelet analysis implies that these studies are presumably not in their final form yet. We shall try to describe the situation in its status nascendi.

2. WAVELETS FOR BEGINNERS

Every signal can be characterized by its averaged (over some intervals) values (trend) and by its variations around this trend. Let us call these variations fluctuations independently of their nature, be they of dynamic, stochastic, psychological, physiological, or any other origin. When processing a signal, one is interested in its fluctuations at various scales because from these one can learn about their origin. The goal of wavelet analysis is to provide tools for such processing.

Actually, physicists dealing with experimental histograms analyze their data at different scales when averaging over different size intervals. This is a particular example of a simplified wavelet analysis treated in this section. To be more definite, let us consider the situation when an experimentalist measures some function $f(x)$ within the interval $0 \leq x \leq 1$, and the best resolution obtained with the measuring device is limited to 1/16 of the whole interval. Thus, the result consists of 16 numbers representing the mean values of $f(x)$ in each of these bins and can be plotted as a 16-bin histogram shown in the upper part of Fig. 1. It can be represented by the following formula

$$f(x) = \sum_{k=0}^{15} s_{4,k}\varphi_{4,k}(x), \tag{1}$$

where $s_{4,k} = f(k/16)/4$, and $\varphi_{4,k}$ is defined as a steplike block of the unit norm (i.e., of height 4 and width 1/16, with normalization fixed by $\int dx|\varphi_{4,k}|^2 = 1$) different from zero only within the kth bin. For an arbitrary j, one imposes the condition $\int dx|\varphi_{j,k}|^2 = 1$, where the integral is taken over the intervals of the lengths $\Delta x_j = 1/2^j$ and, therefore, $\varphi_{j,k}$ have the following form: $\varphi_{j,k} = 2^{j/2}\varphi(2^j x - k)$ with φ denoting a steplike function of unit height over such an interval. The label 4 is related to the total number of such intervals in our example. At the next, coarser, level, the average over the two neighboring bins is taken as is depicted in the histogram just below the initial one in Fig. 1. Up to the normalization factor, we will denote it as $s_{3,k}$ and the difference between the two levels shown to the right of this histogram as $d_{3,k}$. To be more explicit, let us write down the normalized sums and differences for an arbitrary level j as

$$s_{j-1,k} = \frac{1}{\sqrt{2}}[s_{j,2k} + s_{j,2k+1}]; \tag{2}$$
$$d_{j-1,k} = \frac{1}{\sqrt{2}}[s_{j,2k} - s_{j,2k+1}],$$

or for the backward transform (synthesis)

$$s_{j,2k} = \frac{1}{\sqrt{2}}(s_{j-1,k} + d_{j-1,k}); \tag{3}$$
$$s_{j,2k+1} = \frac{1}{\sqrt{2}}(s_{j-1,k} - d_{j-1,k}).$$

Since, for the dyadic partition considered, this difference has opposite signs in the neighboring bins of the previous fine level, we introduce the function ψ, which is 1 and -1, correspondingly, in these bins, and the normalized functions $\psi_{j,k} = 2^{j/2}\psi(2^j x - k)$. This allows us to represent the same function $f(x)$ as

$$f(x) = \sum_{k=0}^{7} s_{3,k}\varphi_{3,k}(x) + \sum_{k=0}^{7} d_{3,k}\psi_{3,k}(x). \tag{4}$$

One proceeds further in the same manner to the sparser levels 2, 1, and 0 with averaging done over the interval lengths 1/4, 1/2, and 1, respectively. This is shown in the subsequent drawings in Fig. 1. The sparsest level with the mean value of f over the whole interval denoted as $s_{0,0}$ provides

$$\begin{aligned} f(x) = {} & s_{0,0}\varphi_{0,0}(x) + d_{0,0}(x)\psi_{0,0}(x) \\ & + \sum_{k=0}^{1} d_{1,k}\psi_{1,k}(x) + \sum_{k=0}^{3} d_{2,k}\psi_{2,k}(x) \\ & + \sum_{k=0}^{7} d_{3,k}\psi_{3,k}(x). \end{aligned} \tag{5}$$

The functions $\varphi_{0,0}(x)$ and $\psi_{0,0}(x)$ are shown in Fig. 2. The functions $\varphi_{j,k}(x)$ and $\psi_{j,k}(x)$ are normalized by the conservation of the norm, dilated, and translated versions of them. In the next section, we will give explicit formulas for them in a particular case of Haar

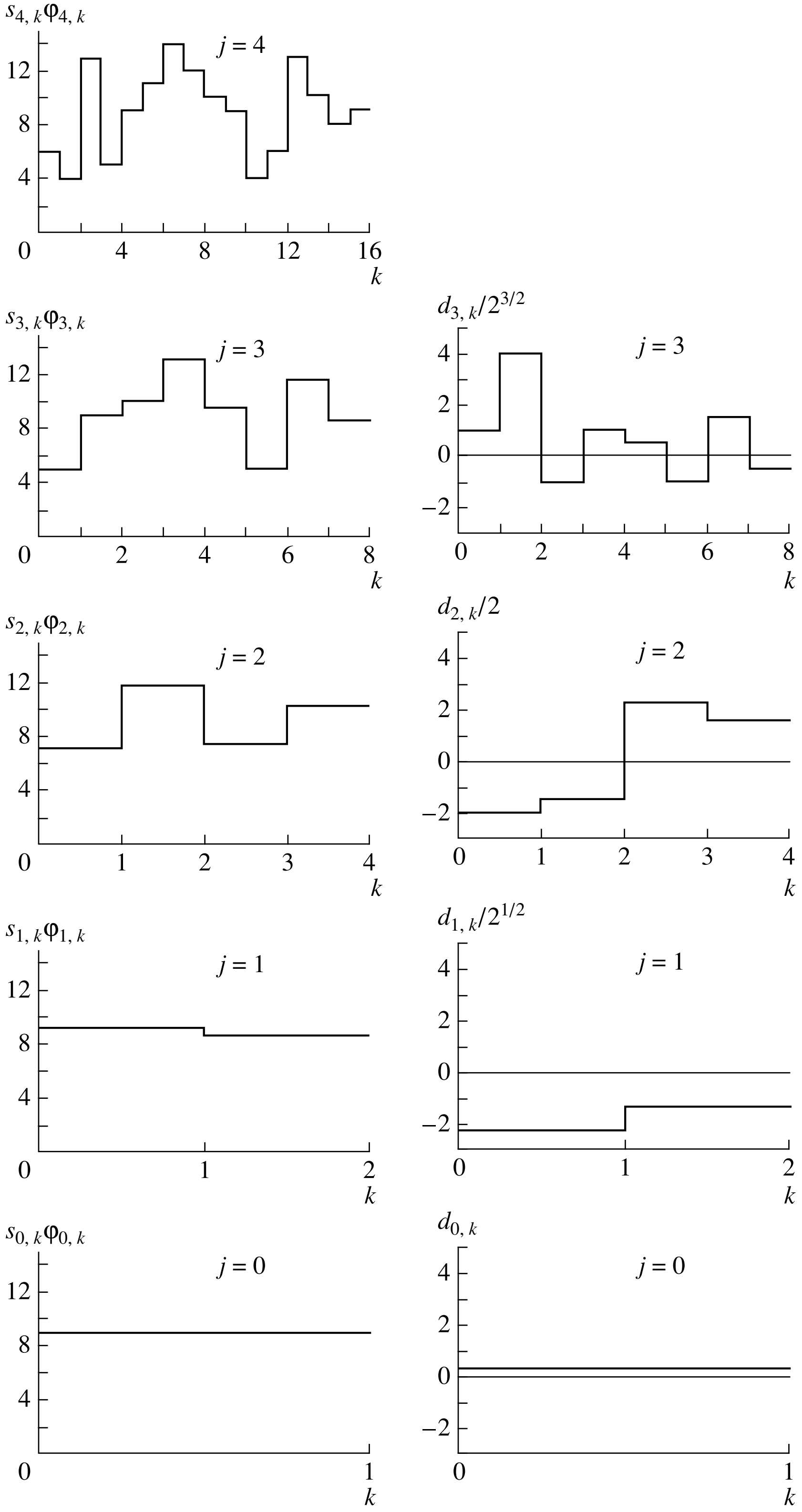

Fig. 1. A histogram and its wavelet decomposition. The initial histogram is shown in the upper part of the figure. It corresponds to the level $j = 4$ with 16 bins (Eq. (1)). The intervals are labeled on the abscissa axis on their left-hand sides. The next level $j = 3$ is shown below. The mean values over two neighboring intervals of the previous level are shown on the left-hand side. They correspond to eight terms in the first sum in Eq. (4). On the right-hand side, the wavelet coefficients $d_{3,k}$ are shown. Other graphs for the levels $j = 2, 1, 0$ are obtained in a similar way.

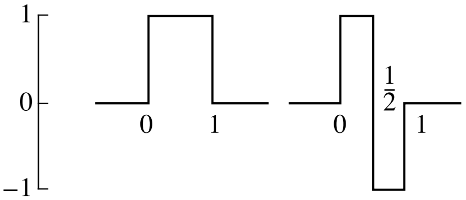

Fig. 2. The Haar scaling function $\varphi_H(x) \equiv \varphi_{0,0}(x)$ (to the left) and "mother" wavelet $\psi_H(x) \equiv \psi_{0,0}(x)$ (to the right).

scaling functions and wavelets. In practical signal processing, these functions (and more sophisticated versions of them) are often called low- and high-path filters, correspondingly, because they filter the large- and small-scale components of a signal. The subsequent terms in Eq. (5) show the fluctuations (differences $d_{j,k}$) at finer and finer levels with larger j. In all the cases (1)–(5), one needs exactly 16 coefficients to represent the function. In general, there are 2^j coefficients $s_{j,k}$ and $2^{j_n} - 2^j$ coefficients $d_{j,k}$, where j_n denotes the finest resolution level (in the above example, $j_n = 4$).

All the above representations of the function $f(x)$ [Eqs. (1)–(5)] are mathematically equivalent. However, the latter one representing the wavelet-analyzed function directly reveals the fluctuation structure of the signal at different scales j and various locations k present in a set of coefficients $d_{j,k}$, whereas the original form (1) hides the fluctuation patterns in the background of a general trend. The final form (5) contains the overall average of the signal depicted by $s_{0,0}$ and all its fluctuations with their scales and positions well labeled by 15 normalized coefficients $d_{j,k}$, while the initial histogram shows only the normalized average values $s_{j,k}$ in the 16 bins studied. Moreover, in practical applications, the latter wavelet representation is preferred, because, for rather smooth functions strongly varying only at some discrete values of their arguments, many of the high-resolution d coefficients in relations similar to Eq. (5) are close to zero (compared to the "informative" d coefficients) and can be discarded. Bands of zeros (or close-to-zero values) indicate those regions where the function is fairly smooth.

At first sight, this simplified example looks somewhat trivial. However, for more complicated functions and more data points with some elaborate forms of wavelets, it leads to a detailed analysis of a signal and to possible strong compression with subsequent good quality restoration. This example also provides an illustration of the very important feature of the whole approach with successive coarser and coarser approximations to f, called multiresolution analysis and discussed in more detail below.

3. BASIC NOTIONS AND HAAR WAVELETS

To analyze any signal, one should, first of all, choose the corresponding basis, i.e., the set of functions to be considered as "functional coordinates." In most cases, we will deal with signals represented by square integrable functions defined on the real axis. They form the infinite-dimensional Hilbert space $L^2(R)$. For nonstationary signals, e.g., the location of that moment when the frequency characteristics have abruptly been changed is crucial. Therefore, the basis should have a compact support. Wavelets are just such functions that span the whole space by translation of the dilated versions of a definite function. That is why every signal can be decomposed in a wavelet series (or integral). Each frequency component is studied with a resolution matched to its scale.

Let us try to construct functions satisfying the above criteria. An educated guess would be to relate the function $\varphi(x)$ to its dilated and translated version. The simplest linear relation with $2M$ coefficients is

$$\varphi(x) = \sqrt{2} \sum_{k=0}^{2M-1} h_k \varphi(2x - k), \qquad (6)$$

with the dyadic dilation 2 and integer translation k. At first sight, the chosen normalization of the coefficients h_k with the "extracted" factor $\sqrt{2}$ looks somewhat arbitrary. Actually, it is defined a posteriori by the traditional form of fast algorithms for their calculation [see Eqs. (34) and (35) below] and normalization of functions $\varphi_{j,k}(x), \psi_{j,k}(x)$. It is used in all the books cited above. However, sometimes (see [2], Chap. 7) it is replaced by $c_k = \sqrt{2}h_k$.

For discrete values of the dilation and translation parameters, one gets discrete wavelets. The value of the dilation factor determines the size of cells in the lattice chosen. The integer M defines the number of coefficients and the length of the wavelet support. They are interrelated, because, from the definition of h_k for orthonormal bases,

$$h_k = \sqrt{2} \int dx \varphi(x) \bar{\varphi}(2x - k), \qquad (7)$$

it follows that only finitely many h_k are nonzero if φ has a finite support. The normalization condition is chosen as

$$\int_{-\infty}^{\infty} dx \varphi(x) = 1. \qquad (8)$$

The function $\varphi(x)$ obtained from the solution to this equation is called a scaling function.[2)] If the scaling

---

[2)] It is often also called a "father wavelet," but we will not use this term.

function is known, one can form a "mother" wavelet (or a basic wavelet) $\psi(x)$ according to

$$\psi(x) = \sqrt{2}\sum_{k=0}^{2M-1} g_k \varphi(2x-k), \tag{9}$$

where

$$g_k = (-1)^k h_{2M-k-1}. \tag{10}$$

The simplest example would be for $M = 1$ with two nonzero coefficients h_k equal to $1/\sqrt{2}$, i.e., the equation leading to the Haar scaling function $\varphi_{\mathrm{H}}(x)$:

$$\varphi_{\mathrm{H}}(x) = \varphi_{\mathrm{H}}(2x) + \varphi_{\mathrm{H}}(2x-1). \tag{11}$$

One easily gets the solution to this functional equation

$$\varphi_{\mathrm{H}}(x) = \theta(x)\theta(1-x), \tag{12}$$

where $\theta(x)$ is the Heaviside step function equal to 1 at positive arguments and 0 at negative ones. The additional boundary condition is $\varphi_{\mathrm{H}}(0) = 1, \varphi_{\mathrm{H}}(1) = 0$. This condition is important for the simplicity of the whole procedure of computing the wavelet coefficients, when two neighboring intervals are considered.

The "mother" wavelet is

$$\psi_{\mathrm{H}}(x) = \theta(x)\theta(1-2x) - \theta(2x-1)\theta(1-x), \tag{13}$$

with boundary values defined as $\psi_{\mathrm{H}}(0) = 1$, $\psi_{\mathrm{H}}(1/2) = -1$, $\psi_{\mathrm{H}}(1) = 0$. This is the Haar wavelet [19] known since 1910 and used in functional analysis. Both the scaling function $\varphi_{\mathrm{H}}(x)$ and the "mother" wavelet $\psi_{\mathrm{H}}(x)$ are shown in Fig. 2. This is the first one of a family of compactly supported orthonormal wavelets ${}_M\psi$: $\psi_{\mathrm{H}} = {}_1\psi$. It possesses the locality property, since its support $2M - 1 = 1$ is compact. Namely, this example has been considered in the previous section for the histogram decomposition. It is easily seen that each part of a histogram is composed of a combination of a scaling function and a wavelet with corresponding weights considered at a definite scale.

The dilated and translated versions of the scaling function φ and the "mother" wavelet ψ,

$$\varphi_{j,k} = 2^{j/2}\varphi(2^j x - k), \tag{14}$$

$$\psi_{j,k} = 2^{j/2}\psi(2^j x - k), \tag{15}$$

form the orthonormal basis as can be (easily for Haar wavelets) checked.[3] The choice of 2^j with the integer-valued j as a scaling factor leads to a unique and self-consistent procedure of computing the wavelet coefficients. Integer values of j explain the name "discrete" used for this set of wavelets.

The Haar wavelet oscillates so that

$$\int_{-\infty}^{\infty} dx\psi(x) = 0. \tag{16}$$

This condition is common for all wavelets. It is called the oscillation or cancellation condition. From it, the origin of the name "wavelet" becomes clear. One can describe a "wavelet" as a function that oscillates within some interval like a wave but is then localized by damping outside this interval. This is a necessary condition for wavelets to form an unconditional (stable) basis. We conclude that, for special choices of coefficients h_k, one gets the specific forms of "mother" wavelets, which give rise to orthonormal bases.

One may decompose any function f of $L^2(R)$ at any resolution level j_n in a series

$$f = \sum_k s_{j_n,k}\varphi_{j_n,k} + \sum_{j \geq j_n,k} d_{j,k}\psi_{j,k}. \tag{17}$$

At the finest resolution level $j_n = j_{\max}$, only s coefficients are left, and one gets the scaling-function representation

$$f(x) = \sum_k s_{j_{\max},k}\varphi_{j_{\max},k}. \tag{18}$$

In the case of Haar wavelets, it corresponds to the initial experimental histogram with the finest resolution. Since we will be interested in its analysis at varying resolutions, this form is used as an initial input only. The final representation of the same data (17) shows all the fluctuations in the signal. The wavelet coefficients $s_{j,k}$ and $d_{j,k}$ can be calculated as

$$s_{j,k} = \int dx f(x)\varphi_{j,k}(x), \tag{19}$$

$$d_{j,k} = \int dx f(x)\psi_{j,k}(x). \tag{20}$$

However, in practice their values are determined from the fast wavelet transform described below.

In reference to the particular case of the Haar wavelet considered above, these coefficients are often referred to as sums (s) and differences (d), which are thus related to mean values and fluctuations.

Only the second term in (17) is often considered, and the result is often called the wavelet expansion. For the histogram interpretation, the neglect of the first sum would imply that one is not interested in average values but only in the histogram shape determined by fluctuations at different scales. Any function can be approximated to a precision $2^{j/2}$ (i.e., to an arbitrarily high precision at $j \to -\infty$) by a finite linear combination of Haar wavelets.

---

[3] We return back to the general case and therefore omit the index "H" because the same formula will be used for other wavelets.

4. MULTIRESOLUTION ANALYSIS AND DAUBECHIES WAVELETS

Although Haar wavelets provide a good tutorial example of an orthonormal basis, they suffer from several deficiencies. One of them is the bad analytic behavior with the abrupt change at the interval bounds, i.e., its bad regularity properties. By this, we mean that all finite-rank moments of the Haar wavelet are different from zero; only its zeroth moment, i.e., the integral (16) of the function itself, is zero. This shows that this wavelet is not orthogonal to any polynomial apart from a trivial constant. The Haar wavelet does not have good time–frequency localization. Its Fourier transform decays like $|\omega|^{-1}$ for $\omega \to \infty$.

The goal is to find a general class of those functions which would satisfy the requirements of locality, regularity, and oscillatory behavior. They should be simple enough in the sense that they are sufficiently explicit and regular to be completely determined by their samples on the lattice defined by the factors 2^j.

The general approach that respects these properties is known as the multiresolution approximation. A rigorous mathematical definition is given in the above-cited monographs. One can define the notion of wavelets so that the functions $2^{j/2}\psi(2^jx-k)$ are wavelets (generated by the "mother" ψ) possessing the regularity, localization, and oscillation properties. By varying j, we can resolve signal properties at different scales, while k shows the location of the analyzed region.

We just show how the program of the multiresolution analysis works in practice when applied to the problem of finding the coefficients of any filter h_k and g_k. They can be directly obtained from the definition and properties of the discrete wavelets. These coefficients are defined by relations (6) and (9),

$$\varphi(x) = \sqrt{2}\sum_k h_k\varphi(2x-k); \tag{21}$$

$$\psi(x) = \sqrt{2}\sum_k g_k\varphi(2x-k),$$

where $\sum_k |h_k|^2 < \infty$. The orthogonality of the scaling functions, defined by the relation

$$\int dx\varphi(x)\varphi(x-m) = 0, \tag{22}$$

leads to the following equation for the coefficients:

$$\sum_k h_k h_{k+2m} = \delta_{0m}. \tag{23}$$

The orthogonality of wavelets to the scaling functions,

$$\int dx\psi(x)\varphi(x-m) = 0, \tag{24}$$

gives the equation

$$\sum_k h_k g_{k+2m} = 0, \tag{25}$$

having a solution of the form

$$g_k = (-1)^k h_{2M-1-k}. \tag{26}$$

Thus the coefficients g_k for wavelets are directly defined by the scaling function coefficients h_k.

Another condition of the orthogonality of wavelets to all polynomials up to the power $(M-1)$ (thus, to any noise described by such polynomials), defining their regularity and oscillatory behavior

$$\int dx x^n\psi(x) = 0, \quad n = 0,\ldots,M-1, \tag{27}$$

provides the relation

$$\sum_k k^n g_k = 0, \tag{28}$$

giving rise to

$$\sum_k (-1)^k k^n h_k = 0 \tag{29}$$

when formula (26) is taken into account.

The normalization condition

$$\int dx\varphi(x) = 1 \tag{30}$$

can be rewritten as another equation for h_k:

$$\sum_k h_k = \sqrt{2}. \tag{31}$$

Let us write Eqs. (23), (29), (31) for $M = 2$ explicitly:

$$\begin{gathered} h_0h_2 + h_1h_3 = 0, \\ h_0 - h_1 + h_2 - h_3 = 0, \\ -h_1 + 2h_2 - 3h_3 = 0, \\ h_0 + h_1 + h_2 + h_3 = \sqrt{2}. \end{gathered}$$

The solution to this system is

$$h_3 = \frac{1}{4\sqrt{2}}(1 \pm \sqrt{3}), \quad h_2 = \frac{1}{2\sqrt{2}} + h_3, \tag{32}$$

$$h_1 = \frac{1}{\sqrt{2}} - h_3, \quad h_0 = \frac{1}{2\sqrt{2}} - h_3,$$

which, in the case of the minus sign for h_3, corresponds to the well-known filter

$$h_0 = \frac{1}{4\sqrt{2}}(1+\sqrt{3}), \quad h_1 = \frac{1}{4\sqrt{2}}(3+\sqrt{3}), \tag{33}$$

$$h_2 = \frac{1}{4\sqrt{2}}(3-\sqrt{3}), \quad h_3 = \frac{1}{4\sqrt{2}}(1-\sqrt{3}).$$

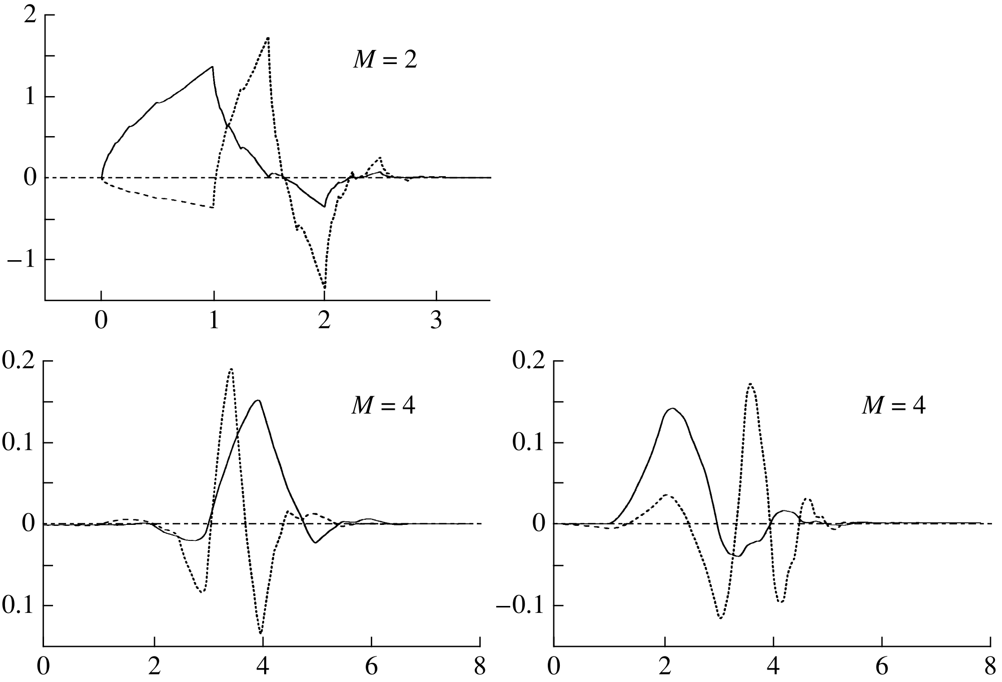

Fig. 3. Daubechies scaling functions (solid curves) and wavelets (dotted curves) for $M = 2, 4$.

These coefficients define the simplest D^4 (or ${}_2\psi$) wavelet from the famous family of orthonormal Daubechies wavelets with finite support. It is shown in the upper part of Fig. 3 by the dotted curve with the corresponding scaling function shown by the solid curve. Some other higher rank wavelets are also shown there. It is clear from this figure (especially for D^4) that wavelets are smoother at some points than at others.

For the filters of higher order in M, i.e., for higher rank Daubechies wavelets, the coefficients can be obtained in an analogous manner. The wavelet support is equal to $2M - 1$. It is wider than that for Haar wavelets. However, the regularity properties are better. The higher order wavelets are smoother compared to D^4, as seen in Fig. 3.

5. FAST WAVELET TRANSFORM

The coefficients $s_{j,k}$ and $d_{j,k}$ carry information about the content of the signal at various scales and can be calculated directly using formulas (19), (20). However, this algorithm is inconvenient for numerical computations, because it requires many (N^2) operations, where N denotes the number of sampled values of the function. In practical calculations, the coefficients h_k are used only without referring to the shapes of wavelets.

In real situations with digitized signals, we have to deal with finite sets of points. Thus, there always exists the finest level of resolution, where each interval contains only a single number. Correspondingly, the sums over k will get finite limits. It is convenient to reverse the level indexation, assuming that the label of this fine scale is $j = 0$. It is then easy to compute the wavelet coefficients for sparser resolutions $j \geq 1$.

Multiresolution analysis naturally leads to an hierarchical and fast scheme for the computation of the wavelet coefficients of a given function. The functional equations (6), (9) and the formulas for the wavelet coefficients (19), (20) give rise, in the case of Haar wavelets, to relations (2) or, for the backward transform (synthesis), to (3).

In general, one can get the iterative formulas of the fast wavelet transform

$$s_{j+1,k} = \sum_m h_m s_{j,2k+m}, \tag{34}$$

$$d_{j+1,k} = \sum_m g_m s_{j,2k+m}, \tag{35}$$

where

$$s_{0,k} = \int dx f(x)\varphi(x-k). \tag{36}$$

These equations yield a fast (so-called pyramid) algorithm for computing the wavelet coefficients, asking now just for $O(N)$ operations to be done. Starting from $s_{0,k}$, one computes all other coefficients, provided the coefficients h_m, g_m are known. The explicit shape of the wavelet is not used in this case anymore.

The remaining problem lies in the initial data. If an explicit expression for $f(x)$ is available, the coefficients $s_{0,k}$ may be evaluated directly according to (36). But this is not so in the situation when only discrete values are available. In the simplest approach, they are chosen as $s_{0,k} = f(k)$.

6. THE FOURIER AND WAVELET TRANSFORMS

The wavelet transform is superior to the Fourier transform, first of all, due to the locality property of wavelets. The Fourier transform uses sine, cosine, or imaginary exponential functions as the main basis. It is spread over the entire real axis, whereas the wavelet basis is localized. An attempt to overcome these difficulties and improve time localization, while still using the same basis functions, is made by the so-called windowed Fourier transform. The signal $f(t)$ is considered within some time interval (window) only. However, all windows have the same width.

In contrast, the wavelets ψ automatically provide the time (or spatial location) resolution window adapted to the problem studied, i.e., to its essential frequencies (scales). Namely, let t_0, δ and ω_0, δ_ω be the centers and the effective widths of the wavelet basic function $\psi(t)$ and its Fourier transform. Then for the wavelet family $\psi_{j,k}(t)$ (15) and, correspondingly, for wavelet coefficients, the center and the width of the window along the t axis are given by $2^j(t_0 + k)$ and $2^j\delta$. Along the ω axis, they are equal to $2^{-j}\omega_0$ and $2^{-j}\delta_\omega$. Thus, the ratios of widths to the center position along each axis do not depend on the scale. This means that the wavelet window resolves both the location and the frequency in fixed proportions to their central values. For the high-frequency component of the signal, it leads to quite a large frequency extension of the window, whereas the time-location interval is squeezed so that the Heisenberg uncertainty relation is not violated. That is why wavelet windows can be called Heisenberg windows. Correspondingly, the low-frequency signals do not require small time intervals and admit a wide window extension along the time axis. Thus, wavelets localize well the low-frequency “details” on the frequency axis and the high-frequency ones on the time axis. This ability of wavelets to find a perfect compromise between the time localization and the frequency localization by automatically choosing the widths of the windows along the time and frequency axes well adjusted to their centers’ location is crucial for their success in signal analysis. The wavelet transform cuts up the signal (functions, operators, etc.) into different frequency components and then studies each component with a resolution matched to its scale, providing a good tool for time–frequency (position–scale) localization. That is why wavelets can zoom in on singularities or transients (an extreme version of very short lived high-frequency features!) in signals, whereas windowed Fourier functions cannot. In terms of traditional signal analysis, the filters associated with the windowed Fourier transform are constant-bandwidth filters, whereas the wavelets may be seen as constant relative-bandwidth filters, whose widths in both variables linearly depend on their positions.

The wavelet coefficients are negligible in the regions where the function is smooth. That is why wavelet series with plenty of nonzero coefficients represent really pathological functions, whereas “normal” functions have “sparse” or “lacunary” wavelet series and are easy to compress. On the other hand, the Fourier series of the usual functions have a lot of nonzero coefficients, whereas “lacunary” Fourier series represent pathological functions.

7. WAVELETS AND OPERATORS

The study of many operators acting on a space of functions or distributions becomes simple when suitable wavelets are used, because these operators can be approximately diagonalized with respect to this basis. Orthonormal wavelet bases provide a unique example of a basis with nontrivial diagonal, or almost-diagonal, operators. That is why wavelets, used as a basis set, allow us to solve differential equations characterized by widely different length scales found in many areas of physics and chemistry.

It is extremely important that it is sufficient to first calculate the matrix elements at some (jth) resolution level. All other matrix elements can be obtained from it using the standard recurrence relations. As an example, we write the explicit equation for the nth order differentiation operator:

$$\begin{aligned} r_k^{(n)} &= \left\langle \varphi(x) \left| \frac{d^n}{dx^n} \right| \varphi(x-k) \right\rangle \qquad (37) \\ &= \sum_{i,m} h_i h_m \left\langle \varphi(2x+i) \left| \frac{d^n}{dx^n} \right| \varphi(2x+m-k) \right\rangle \\ &= 2^n \sum_{i,m} h_i h_m r_{2k-i-m}^{(n)}. \end{aligned}$$

It leads to a finite system of linear equations for r_k (the index n is omitted):

$$2^{-n} r_k = r_{2k} + \sum_m a_{2m+1}(r_{2k-2m+1} + r_{2k+2m-1}), \qquad (38)$$

where both r_k and $a_m = \sum_i h_i h_{i+m}$ ($a_0 = 1$) are rational numbers in the case of Daubechies wavelets. The wavelet coefficients can be found from these equations up to a normalization constant. The normalization condition reads

$$\sum_k k^n r_k = n!. \tag{39}$$

For the support region of the length L, the coefficients r_k differ from zero for $-L+2 \leq k \leq L-2$, and the solution exists for $L \geq n+1$. These coefficients possess the following symmetry properties:

$$r_k = r_{-k} \tag{40}$$

for even n and

$$r_k = -r_{-k} \tag{41}$$

for odd values of n.

At the end, two brief remarks are in order.

The analysis of any signal includes finding the regions of its regular and singular behavior. One of the main features of wavelet analysis is its capacity of doing a very precise local analysis of the regularity properties of functions. Combined with studies of the Poisson equation, this approach was used for determination of a very singular potential of interaction of two uranium nuclei (see [11]).

Wavelets are well suited to reveal fractal signals. In terms of wavelet coefficients, it implies that their higher moments behave in a powerlike manner with the scale changing. It is well known [20] that this problem is important for multiparticle production processes, which show the multifractal distribution of secondary particles in the phase space.

More detailed information about these problems can be found in [11].

8. APPLICATIONS

Wavelets have become widely used in many fields. Here, we describe just two examples of wavelet application to analysis of very high multiplicity events in multihadron production and of a one-dimensional curve describing the pressure variation in gas turbines.

In multihadron production, wavelets provide a completely new way for an event-by-event analysis, which is impossible with other methods, because now one can distinguish specific local features of particle correlations within the available phase space. Pattern recognition at different scales becomes possible.

High-energy collisions of elementary particles result in production of many new particles in a single event. Each newly created particle is depicted kinematically by its momentum vector, i.e., by a dot in the three-dimensional phase space. Different patterns formed by these dots in the phase space would correspond to different dynamics. Understanding this dynamics is a main goal of all studies done at accelerators and in cosmic rays. Especially intriguing is the problem of quark–gluon plasma, the state of matter with deconfined quarks and gluons, which could exist during extremely short time intervals. One hopes to create it in collisions of high-energy nuclei. At present, data on PbPb collisions are available, where, in a single event, more than 1000 charged particles are produced. New data from the RHIC accelerator in Brookhaven with multiplicities up to about 6000 charged particles have been already recorded. The LHC in CERN will provide events with up to 20 000 new particles created. However, we do not yet know what patterns will be drawn by nature in individual events. Therefore, the problem of phase-space pattern recognition in an event-by-event analysis becomes meaningful.

In [21], so-called continuous MHAT wavelets were first applied to analyze patterns formed in the phase space of the accelerator data on individual high-multiplicity events of PbPb interaction at an energy of 158 GeV per nucleon. The resulting pattern showed that there exist events where many particles are concentrated close to some value of the polar angle, i.e., reveal the ringlike structure in the target diagram. The interest in such patterns is related to the fact that they can result from so-called gluon Cherenkov radiation [22, 23] or, more generally, from gluon bremsstrahlung at a finite length within the quark–gluon medium (plasma, in particular). A cosmic-ray event earlier observed in [24] initiated the discussion of this problem.

More elaborate two-dimensional analysis with Daubechies (D^8) wavelets has been done in [25]. It confirmed these conclusions with jet regions tending to lie within some ringlike formations. Large wavelet coefficients have been found for the large-scale particle fluctuations. After the event analysis was done, only the resolution levels $6 \leq j \leq 10$ were left to store the long-range correlations in the events and get rid of short-range ones and background noise. Then the inverse restoration was done to get the event images with only these dynamic correlations left, and this is what is seen in Fig. 4. Any dot corresponds to the location of a single secondary particle on a two-dimensional polar plot, where its pseudorapidity is described by the radius and its azimuthal angle is defined around the center, as usual. The dark spots correspond to long-range correlated groups of particles (jets) restored by the above-mentioned analysis. The dashed rings denote those regions of pseudorapidities which were previously suspected for some peaks in inclusive pseudorapidity distributions. It directly demonstrates that the large-scale correlations chosen have a ringlike (ridge) pattern. With larger statistics, one will be able to say whether

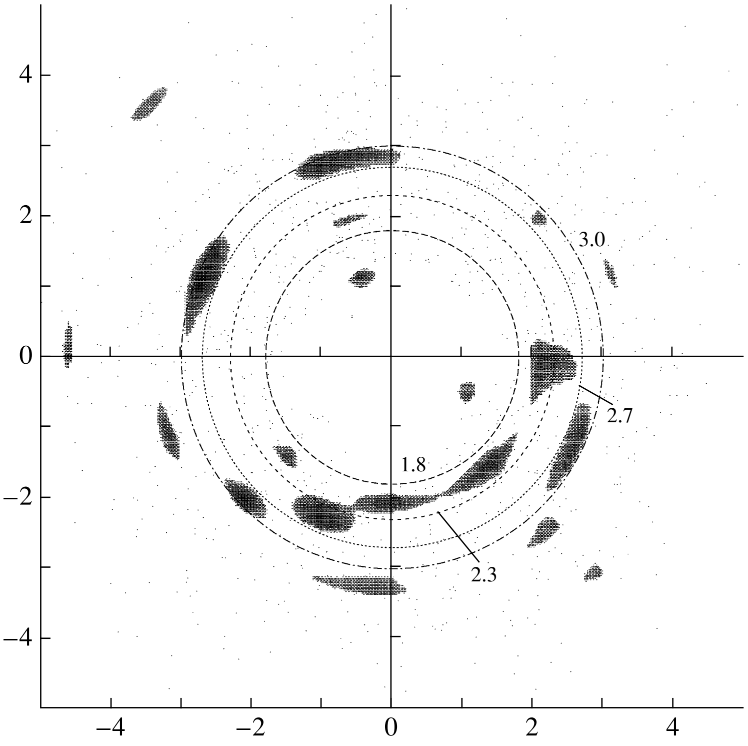

Fig. 4. The restored image of long-range correlations (dark regions) on an experimental plot of points in polar coordinates corresponding to pseudorapidities and azimuthal angles of 1029 charged particles produced in a single event of central PbPb interaction at 158 GeV. It clearly displays the typical ringlike structure of jetty spots. The dashed rings are drawn according to preliminary guesses based on spikes in the inclusive pseudorapidity distribution for this event. The two rings correspond to two symmetrical forward–backward regions in the center-of-mass system. One would interpret this image as jets that tend to be emitted by both colliding nuclei at the same (in the corresponding hemispheres) fixed polar angle that is typical for Cherenkov radiation.

they correspond to theoretical expectations. However, preliminary results favor positive conclusions [25]. It is due to the two-dimensional wavelet analysis that, for the first time, the fluctuation structure of an event is shown in a way similar to the target diagram representation of events on the two-dimensional plot.

Let me briefly mention that some more curious patterns have been observed, which, in particular, provide information about the higher order Fourier coefficients of the azimuthal decomposition, not yet observed anywhere else.

This type of analysis has also been used in attempts to unravel in individual high-multiplicity events a so-called elliptic flow, which corresponds to their azimuthal asymmetry (the second Fourier coefficient different from zero). It happened that the analysis of NA49 data revealed such an asymmetry. However, it was mainly due to inhomogeneous acceptance of the detector in this experiment. This cannot be cured in event-by-event analysis, and physical results cannot be obtained in this way. Nevertheless, this analysis has shown that it can be used for understanding some technical problems of a particular experiment.

Another example [26] of successful application of wavelet analysis is provided by the analysis of time variation of the pressure in an aircraft compressor, shown in Fig. 5. The aim of the analysis of this signal is motivated by the desire to find the precursors of a very dangerous effect (stall + surge) in engines leading to their destruction. It happened that the dispersion of the wavelet coefficients shown by the dashed line in Fig. 5 drops before the dangerous high pressure appears in the compressor of the engine. This drastic change in the dispersion can serve as a precursor of engine destruction. No such drop is seen in the upper dash-dotted line, which shows a similar dispersion for the random signal obtained from the initial one by shuffling its values at different time. These curves show the internal correlations at the different scales existing in the primary signal, possessing a very complicated structure. Even more important is the fact that the precursor helped find the physical nature of this effect. The decline of the dispersion is attributed to the dominance of a particular scale (frequency). The specific resonance is to be blamed for it. Thus, methods of preventing engine destruction have been proposed and patented.

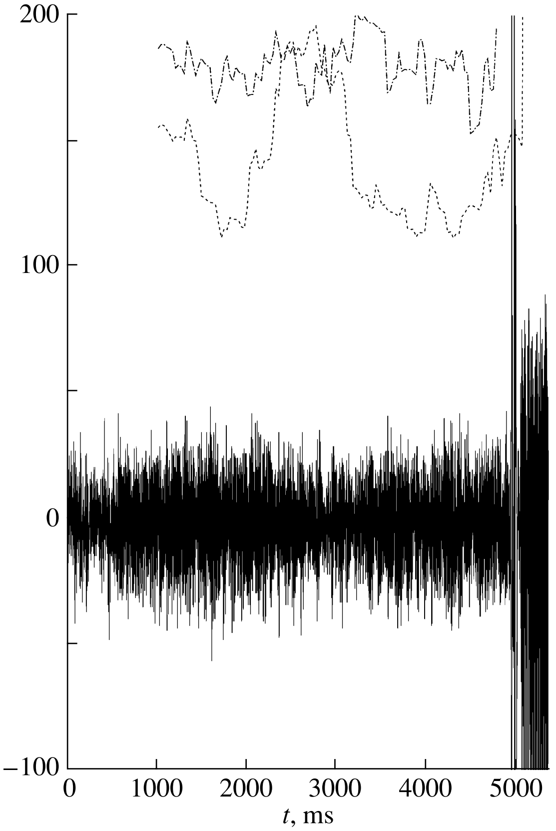

Fig. 5. The pressure variation in the compressor of a gas turbine measured each millisecond for 5 s with a drasic increase at the end. The signal of the pressure sensor is shown by the quite irregular solid line. The time dependence of the pressure in the engine compressor has been wavelet-analyzed. The dispersion of the wavelet coefficients (dashed line) shows the maximum and the remarkable drop about 1 s prior to the drastic increase in the pressure, providing the precursor of this malfunction. The shuffled set of data does not show such an effect for the dispersion of the wavelet coefficients (dash-dotted line), pointing to its dynamic origin.

Let us mention that a similar procedure has been quite successful in analysis of heartbeat intervals and diagnosis of heart disease [27–29].

The property of wavelet coefficients to be small for smooth images and large for strongly contrasting ones has been used for the automatic focusing of microscopes [11] and corresponding deciphering of some bad-quality blood samples in medical research.

Both direct and inverse wavelet transforms have to be applied for image compression, its further transmission, and restoration. This becomes especially important if the capacity of the transmission line is rather low. One of the examples of such a procedure and its comparison with the windowed Fourier transform are demonstrated in [11].

Many other examples can be found in the cited literature and on web sites.

9. CONCLUSIONS

The beauty of the mathematical construction of the wavelet transformation and its utility in practical applications attract researchers from both pure and applied science. We especially emphasize here that wavelet analysis of multiparticle events in high-energy particle and nucleus collisions proposes a completely new approach to the effective event-by-event study of patterns formed by secondary-particle locations within the available phase space. The newly found patterns have already shown some specific dynamical features not discovered before. One can expect other surprises when very high multiplicity events obtained in detectors with good acceptance become available for analysis.

Moreover, the commercial outcome of this research has become quite important. We have outlined a minor part of the activity in this field. However, we hope that the general trends in the development of this subject become comprehended and appreciated.

ACKNOWLEDGMENTS

This work has been supported in part by the Russian Foundation for Basic Research, project nos. 02-02-16779, 03-02-16134, NSH-1936.2003.2.

REFERENCES

1. Y. Meyer, *Wavelets and Operators* (Cambridge Univ. Press, Cambridge, 1992).
2. I. Daubechies, *Ten Lectures on Wavelets* (SIAM, Philadelphia, 1991).
3. Y. Meyer and R. Coifman, *Wavelets, Calderon–Zygmund and Multilinear Operators* (Cambridge Univ. Press, Cambridge, 1997).
4. Y. Meyer, *Wavelets: Algorithms and Applications* (SIAM, Philadelphia, 1993).
5. *Progress in Wavelet Analysis and Applications*, Ed. by Y. Meyer and S. Roques (Editions Frontières, Gif-sur-Yvette, 1993).
6. C. K. Chui, *An Introduction to Wavelets* (Academic, San Diego, 1992).
7. K. Hernandez and G. Weiss, *A First Course on Wavelets* (CRC, Boca Raton, 1997).
8. G. Kaiser, *A Friendly Guide to Wavelets* (Birkhauser, Boston, 1994).
9. *Wavelets: An Elementary Treatment of Theory and Applications*, Ed. by T. Koornwinder (World Sci., Singapore, 1993).
10. N. M. Astafyeva, Usp. Fiz. Nauk **166**, 1145 (1996) [Phys.–Usp. **39**, 1085 (1996)].
11. I. M. Dremin, O. V. Ivanov, and V. A. Nechitailo, Usp. Fiz. Nauk **171**, 465 (2001) [Phys. Usp. **44**, 447 (2001)].
12. *Wavelets in Physics*, Ed. by J. C. Van den Berg (Cambridge Univ. Press, Cambridge, 1998).

13. S. Mallat, *A Wavelet Tour of Signal Processing* (Academic Press, New York, 1998).
14. G. Erlebacher, M. Y. Hussaini, and L. M. Jameson, *Wavelets Theory and Applications* (Oxford Univ. Press, Oxford, 1996).
15. *Wavelets in Medicine and Biology*, Ed. by A. Aldroubi and M. Unser (CRC, Boca Raton, 1994).
16. R. Carmona, W.-L. Hwang, and B. Torresani, *Practical Time-Frequency Analysis* (Academic Press, San Diego, 1998).
17. A. Grossman and J. Morlet, in *Mathematica + Physics, Lectures on Recent Results*, Ed. by L. Streit (World Sci., Singapore, 1985), Vol. 1.
18. J. Morlet, G. Arens, E. Fourgeau, and D. Giard, Geophysics **47**, 203 (1982); **47**, 222 (1982).
19. A. Haar, Math. Ann. **69**, 331 (1910).
20. E. A. De Wolf, I. M. Dremin, and W. Kittel, Phys. Rep. **270**, 1 (1996).
21. N. M. Astafyeva, I. M. Dremin, and K. A. Kotelnikov, Mod. Phys. Lett. A **12**, 1185 (1997).
22. I. M. Dremin, Pis'ma Zh. Éksp. Teor. Fiz. **30**, 152 (1979) [JETP Lett. **30**, 140 (1979)].
23. I. M. Dremin, Yad. Fiz. **33**, 1357 (1981) [Sov. J. Nucl. Phys. **33**, 726 (1981)].
24. A. V. Apanasenko, N. A. Dobrotin, I. M. Dremin, *et al.*, Pis'ma Zh. Éksp. Teor. Fiz. **30**, 157 (1979) [JETP Lett. **30**, 145 (1979)].
25. I. M. Dremin, O. V. Ivanov, S. A. Kalinin, *et al.*, Phys. Lett. B **499**, 97 (2001).
26. I. M. Dremin, V. I. Furletov, O. V. Ivanov, *et al.*, Control Engineering Practice **10**, 599 (2002).
27. S. Thurner, M. C. Feurstein, and M. C. Teich, Phys. Rev. Lett. **80**, 1544 (1998).
28. L. A. N. Amaral, A. L. Goldberger, P. C. Ivanov, *et al.*, Phys. Rev. Lett. **81**, 2388 (1998).
29. P. C. Ivanov, L. A. N. Amaral, A. L. Goldberger, *et al.*, Nature **399**, 461 (1999).

Physics of Atomic Nuclei, Vol. 68, No. 3, 2005, pp. 521–523. Translated from Yadernaya Fizika, Vol. 68, No. 3, 2005, pp. 550–552.
Original Russian Text Copyright © 2005 by Okun.

Elusive Neutrinos[1]

L. B. Okun[*]

Received May 26, 2004

Abstract—A brief review of neutrino physics is presented. A.I. Alikhanov was a pioneer in searches for the neutrino mass. After the death of Alikhanov, his disciples at the Institute of Theoretical and Experimental Physics (ITEP, Moscow) have continued seeking elusive-neutrino effects. At the present time, the problem of the neutrino mass is one of the key points in elementary-particle physics, astrophysics, and cosmology. *© 2005 Pleiades Publishing, Inc.*

Beginning in the mid-1930s, Abram Isaakovich Alikhanov and his colleagues (A.I. Alikhanyan, V.P. Dzhelepov, S.Ya. Nikitin) performed a number of subtle experiments in order to study beta spectra in nuclear decays. The results that they obtained by exploring the spectra of electrons near their maximum energy with the aim of revealing the spectrum-shape distortion caused by a finite neutrino mass were published in 1938 [1, 2]. This possibility was previously indicated by Fermi [3] and Perrin [4]. In [1], it was concluded that, in RaE, the spectrum is consistent with $m_\nu = 0.3m_e$, where m_e is the electron mass, rather than with $m_\nu = 0$. But in [2] (an article that appeared in the same year), it was shown that, in the spectrum of ThC, $m_\nu = 0.8m_e$, whence it followed that the observed anomalies were due to some disregarded background effect rather than to the neutrino mass. [It should be recalled that RaE is an astatine isotope ($^{85}\mathrm{At}_{222}$), while ThC is a radon isotope ($^{86}\mathrm{Rn}_{222}$).] In the early 1940s, Alikhanov conducted searches for neutrinos by studying the spectrum of ^{7}Li in electron capture from the K shell in ^{7}Be. These experiments were interrupted by the war. A similar experiment was performed by J. Allen in 1943.

In 1958, Alikhanov, together with G.P. Eliseev and V.A. Lyubimov, was one of the first who measured the longitudinal polarization of electrons in nuclear beta decays. In 1976, after the death of Alikhanov, Lyubimov proposed employing E.F. Tretyakov's unique spectrometer in searches for manifestations of the neutrino mass in the spectrum of electrons in tritium beta decay [5, 6]. The discovery of an anomaly at about 20 eV (the previous record of accuracy was 50 eV [7]) caused great interest among physicists and astrophysicists, including Ya.B. Zeldovich. The current upper limit on the antineutrino mass from the spectrum of tritium is 3 eV. In the future, it is planned to reach an accuracy of 0.35 eV [in the KArlsruher TRItium Neutrino (KATRIN) experiment].

At the same time, neutrino masses manifested themselves in experiments devoted to studying neutrino oscillations, whose searches were first proposed by B. Pontecorvo.

As is well known, the existence of only three neutrino flavors—ν_e, ν_μ, and ν_τ—was established at the LEP collider. They are superpositions of three massive neutrinos: ν_1, ν_2, and ν_3.

The mass difference between ν_1 and ν_2 was measured in the oscillations of solar neutrinos: $|\Delta m^2_{12}| = |m^2_2 - m^2_1| \simeq 6 \times 10^{-5}$ eV^2. The mass difference between ν_2 and ν_3 was measured in oscillations of atmospheric neutrinos: $|\Delta m^2_{23}| = |m^2_3 - m^2_2| \simeq 3 \times 10^{-2}$ eV^2.

At the present time, it is not clear which neutrino flavor is heavier, ν_2 or ν_3. The hierarchy $m_3 > m_2 > m_1$ is referred to as a direct hierarchy, while $m_2 > m_1 > m_3$ is known as an inverse hierarchy. The KATRIN experiment would make it possible to choose between these two possibilities and establish the absolute scale of neutrino masses.

Up to 2003, all neutrino oscillations were observed only for neutrinos "supplied" by nature itself. The LSND experiment performed recently at the Los Alamos accelerator was the only exception to this rule. However, there is no consensus on the results of that experiment among physicists involved in research in these realms. Various exotic phenomena, such as CPT violation and the existence of sterile neutrinos, were invoked to interpret those results.

The first results of the KamLAND [8] and K2K [9] experiments appeared in 2003. In the first of these,

---

[1] This report was presented at the session of Russian Academy of Sciences that was held at the Institute of Theoretical and Experimental Physics (ITEP, Moscow) on March 4, 2004, and which was dedicated to the 100th anniversary of the birth of A.I. Alikhanov, who was the founding father of ITEP.

[*] E-mail: `okun@itep.ru`

antineutrinos from all Japanese nuclear reactors (of total power 180 GW) were detected by observing the reaction $\bar{\nu}_e + p \to n + e^+$ in 1 kt of a liquid scintillator. Eighty percent of the antineutrino flux came from reactors situated at a distance of 140 to 210 km from the KamLAND detector. The number of respective events detected over the first 145 days of observations (from March to September 2002) was 54 versus 87 ± 6 expected in the absence oscillations. This result agrees with data on solar neutrinos.

In the K2K experiment, neutrinos from the 12-GeV proton accelerator at KEK find their way to 50 kt of water in the SuperKamiokande detector (the figure "2" in the name of the experiment stands for the preposition "to": from KEK to Kamioka), which is situated at a distance of 250 km. The "disappearance" of neutrinos in the muon-neutrino (ν_μ) flux was observed here (in the absence of oscillations, one would expect 44 muon events, their observed number being 29). In perfect agreement with $\nu_\mu \to \nu_\tau$ oscillations in atmospheric neutrinos, the experiment being discussed has not recorded any $\nu_\mu \to \nu_e$ transitions.

Searches for double beta decay ($2\beta 0\nu$) are of particular interest: the probability of such decays in the absence of right-handed currents is determined by the quantity

$$m_{ee} = \left| \sum_{k=1}^{3} U_{ek}^2 m_k e^{i\phi_k} \right|,$$

where m_k stands for the masses of the three neutrino mass eigenstates, U_{ek} are elements of the Pontecorvo–Maki–Nakagawa–Sakata matrix [10, 11] that are responsible for charged currents involving electrons, and ϕ_k are three CP-violating phases. For $2\beta 0\nu$ decay to occur, it is necessary that at least one of the three neutrinos be a Majorana neutrino. So far, we have considered only neutral bosons (of the photon type), but, now, there may appear for the first time a truly neutral fermion. The best upper limit on m_{ee} from searches for the decay $^{76}\mathrm{Ge} \to ^{76}\mathrm{Se} + 2e$ is 0.35–0.50 eV [12] ($T_{1/2}(2\beta 0\nu) \geq 1.55 \times 10^{25}$ yr at a 90% C.L., although some members of the Moscow–Heidelberg Collaboration, which obtained this limit, stated that they saw a positive signal [13]).

It should be emphasized that the discovery of a Majorana neutrino would obviously lead us beyond the Standard Model. At the same time, Dirac neutrino masses fit well in the Standard Model framework, which, as is well known, contains singlet right-handed neutrinos (however, as if behind the scene). Of course, the smallness of the corresponding Yukawa constants, $m_\nu/m_e \lesssim 10^{-8}$, remains unexplained here; yet, m_e/m_t is also very small ($\sim 10^{-6}$).

The discovery of neutrinoless double beta decay would in principle make it possible to obtain information about those two of the three CP-violating phases ϕ_k that do not appear in the standard expression for the Pontecorvo–Maki–Nakagawa–Sakata matrix. This could contribute to understanding the phenomenon of CP violation.

Searches for the neutrino magnetic (and electric) dipole moment are planned in a number of laboratory experiments at a precision level of $10^{-10}\mu_\mathrm{B}$, which is poorer than the corresponding upper limits from astrophysical observations. This could be justified by the remnants of the skeptical attitude to astrophysicists, who, as Landau used to say, "are always in error and never in doubt." In recent years, the improved accuracy of astrophysical observations and calculations leaves an ever smaller room for such skepticism.

It should be noted that a close upper limit (0.2 to 0.3 eV) for the quasidegenerate case of $m_1 \approx m_2 \approx m_3$ comes from an analysis of the cosmological data obtained by WMAP [14]. The proximity of the dark-energy scale $(2 \times 10^{-3}\ \mathrm{eV})^4$ and the neutron-mass-splitting scale $[\delta m_\nu^2 \sim (10^{-2}\ \mathrm{eV})^2]$ gave rise to speculations about the connection between these two phenomena [15].

In conclusion, I would like to dwell upon one psychological problem. The opinion that, in experiments performed thus far to study neutrino oscillations, a neutrino of specific flavor—for example, a muon neutrino—is produced in the form of a superposition of three massive neutrinos that have equal momenta p and, hence, somewhat different energies, $E_k = p + m_k^2/2p$, is widespread in the literature. In fact, the situation is diammetrically opposite, since atomic nuclei have firmly established energies in massive neutrino detectors and oscillations are measured with rulers rather than with a watch [16–18]. Three massive neutrinos have identical energies and slightly different momenta, $p_k = E - m_k^2/2E$.

Since the neutrino masses are much smaller than the neutrino energies, their speed being close to the speed of light c, both approaches yield nearly identical numerical results,

$$(p_i - p_k)x \approx \frac{m_k^2 - m_i^2}{2E}x,$$

$$(E_i - E_k)t \approx \frac{m_i^2 - m_k^2}{2pc}x,$$

but they describe totally different physical phenomena: oscillations in space versus oscillations in time. The agreement between two numerical results does not imply the equivalence of two theoretical approaches. The hypothesis of equal momenta is incorrect. The use of this hypothesis in the literature (especially in textbooks) is caused exclusively by mental inertia.

REFERENCES

1. A. I. Alichanian, A. I. Alichanov, and B. S. Dzhelepov, Phys. Rev. **53**, 766 (1938); Dokl. Akad. Nauk SSSR **19**, 375 (1938).
2. A. I. Alichanian and S. J. Nikitin, Phys. Rev. **53**, 767 (1938).
3. E. Fermi, Ricerca Scient. **2**, 12 (1933); Z. Phys. **88**, 161 (1934).
4. F. Perrin, C. R. Acad. Sci. **197**, 1625 (1933).
5. E. F. Tretyakov, Izv. Akad. Nauk SSSR, Ser. Fiz. **39**, 583 (1975).
6. E. F. Tretyakov *et al.*, Izv. Akad. Nauk SSSR, Ser. Fiz. **40** (10), 1 (1976).
7. K. E. Bergquist, Nucl. Phys. B **39**, 317 (1972).
8. KamLAND Collab. (K. Eguchi *et al.*), Phys. Rev. Lett. **90**, 021802 (2003).
9. M. H. Ahn *et al.* (K2K Collab.), Phys. Rev. Lett. **90**, 041801 (2003).
10. B. Pontecorvo, Zh. Éksp. Teor. Fiz. **33**, 549 (1957); **34**, 247 (1958) [Sov. Phys. JETP **7**, 172 (1958)].
11. Z. Maki, M. Nakagawa, and S. Sakata, Prog. Theor. Phys. **28**, 870 (1962).
12. A. M. Bakalyarov *et al.*, hep-ex/0309016.
13. H. V. Klapdor-Kleingrothaus *et al.*, Mod. Phys. Lett. A **16**, 2409 (2001).
14. D. N. Spergel *et al.*, Astrophys. J., Suppl. Ser. **148**, 175 (2003); astro-ph/0302209.
15. D. B. Kaplan, A. E. Nelson, and N. Weiner, hep-ph/0401099.
16. L. Stodolsky, Phys. Rev. D **58**, 036006 (1998).
17. H. Lipkin, hep-ph/0212093; hep-ph/0312292.
18. L. B. Okun, M. S. Rotaev, M. G. Schepkin, and I. S. Tsukerman, hep-ph/0312151; hep-ph/0312280.

Translated by A. Isaakyan

Physics of Atomic Nuclei, Vol. 68, No. 3, 2005, pp. 524–527. From Yadernaya Fizika, Vol. 68, No. 3, 2005, pp. 553–556.
Original English Text Copyright © 2005 by V. L. Lyuboshitz, V. V. Lyuboshitz.

Lifetime and Path Length of the Virtual Particle[*]

V. L. Lyuboshitz and V. V. Lyuboshitz[**]

Joint Institute for Nuclear Research, Dubna, Moscow oblast, 141980 Russia

Received May 24, 2004; in final form, July 13, 2004

Abstract—The concepts of the lifetime and path length of a virtual particle are introduced. It is shown that, near the mass surface of the real particle, these quantities constitute a 4-vector. At very high energies, the virtual particle can propagate over considerable (even macroscopic) distances. The formulas for the lifetime and path length of an ultrarelativistic virtual electron in the process of bremsstrahlung in the Coulomb field of a nucleus are obtained. The lifetime and path length of the virtual photon at its conversion into an electron–positron pair are discussed. The connection between the path length of the virtual particle and the coherence length (formation length) is analyzed. © *2005 Pleiades Publishing, Inc.*

1. LOCALIZATION OF A VIRTUAL PARTICLE IN TIME AND SPACE

It is known that internal lines of Feynman diagrams play the role of intermediate states, or virtual particles [1]. The definite 4-momentum $P = \{E, \mathbf{P}\}$ outside the mass surface of the real particle corresponds to the virtual particle. Here, E is the energy of the virtual particle, and $\mathbf{P}$ is its 3-momentum (we use the unit system in which $\hbar = c = 1$). The magnitude

$$M = \sqrt{P^2} \equiv \sqrt{E^2 - \mathbf{P}^2} \tag{1}$$

has the meaning of the mass of the virtual particle. When P is the timelike 4-momentum, then the virtual particle has positive mass, as well as the real particle. In this case, $M \neq m$, where m is the mass of the real particle. When P is the spacelike 4-momentum, then the imaginary mass ($M^2 < 0$) formally corresponds to the virtual particle.

The lifetime T of the virtual particle, characterizing the time scale of the considered process, can be defined on the basis of the uncertainty principle for energy and time: $T = |\Delta E|^{-1}$, where

$$\Delta E = \sqrt{\mathbf{P}^2 + m^2} - \sqrt{\mathbf{P}^2 + M^2}$$

is the difference of energies of the real and virtual particles with the same 3-momentum $\mathbf{P}$. As a result, we obtain

$$T = \frac{E + \widetilde{E}}{|m^2 - M^2|}. \tag{2}$$

Here, E is the energy of the virtual particle, and $\widetilde{E} = \sqrt{E^2 + m^2 - M^2}$ is the energy of the real particle. Relation (2) can be rewritten in the form

$$T = \frac{E}{|m^2 - M^2|}\left(\sqrt{1 + \frac{m^2 - M^2}{E^2}} + 1\right). \tag{3}$$

Analogously, the space dimensions L of the region of propagation of the virtual particle, characterizing the space scale of the given process, can be defined on the basis of the uncertainty principle for momenta and coordinates: $L = |\Delta \mathbf{P}|^{-1}$, where

$$|\Delta \mathbf{P}| = \sqrt{E^2 - m^2} - \sqrt{E^2 - M^2}$$

is the difference of momenta of the real and virtual particles moving along the direction of the momentum vector $\mathbf{P}$ with the same energy E. It is easy to see that

$$L = \frac{|\mathbf{P}| + |\widetilde{\mathbf{P}}|}{|m^2 - M^2|}. \tag{4}$$

Here, $|\widetilde{\mathbf{P}}| = \sqrt{\mathbf{P}^2 - m^2 + M^2}$ is the absolute value of momentum of the real particle. We can also write

$$L = \frac{|\mathbf{P}|}{|m^2 - M^2|}\left(\sqrt{1 - \frac{m^2 - M^2}{\mathbf{P}^2}} + 1\right). \tag{5}$$

At small differences of masses of the virtual and real particles, when

$$|m^2 - M^2| \ll E^2, \quad |m^2 - M^2| \ll |\mathbf{P}|^2,$$

it follows from Eqs. (2) and (3) that

$$T = \frac{2E}{|m^2 - M^2|}, \quad L = \frac{2|\mathbf{P}|}{|m^2 - M^2|}. \tag{6}$$

---

[*] This article was submitted by the authors in English.

[**] e-mail: `Valery.Lyuboshitz@jinr.ru`

Under these conditions, the quantities T and $\mathbf{L} = 2\mathbf{P}/|m^2 - M^2|$ constitute the 4-vector [2]

$$\{T, \mathbf{L}\} = \frac{2P}{|m^2 - M^2|}. \qquad (7)$$

All the relations presented above are valid for any 4-momentum of the virtual particle (both timelike and spacelike). In the case of the timelike 4-momentum P, the quantity $\mathbf{L}$ can be clearly interpreted as the vector of path length of the virtual particle moving with the velocity $\mathbf{v} = \mathbf{P}/E < 1$; in this case, the path length and lifetime of the virtual particle are connected by the standard equation $\mathbf{L} = \mathbf{v}T$.[1)]

When the mass M of the virtual particle is close to the mass m of the real particle, the lifetime T of the virtual particle increases strongly and its path length $L = |\mathbf{L}|$ may considerably exceed the interatomic distances. The same takes place also at ultrarelativistic energies $E \gg |M|$, $E \gg m$, when the velocity of the virtual particle approaches the velocity of light. In the limit of very high energies, the path length of the virtual particle can reach even macroscopic values. That leads to the coherent effects observed in the interaction of very high energy particles with matter [3–6].

2. LIFETIME AND PATH LENGTH OF THE RELATIVISTIC VIRTUAL ELECTRON IN ELECTRON BREMSSTRAHLUNG

Using the Born approximation, the bremsstrahlung of the electron in the Coulomb field of a heavy nucleus is described by two Feynman diagrams (see Fig. 1). Let us denote the 4-momenta of the initial electron, final electron, and photon, respectively, as $p_1 = \{E_1, \mathbf{p}_1\}$, $p_2 = \{E_2, \mathbf{p}_2\}$, and $k = \{\omega, \mathbf{k}\}$. Taking into account that energy transfer to the heavy nucleus is absent, the equality $E_2 = E_1 - \omega$ is valid, and the energy component of the spacelike 4-momentum of the virtual photon $q = \{0, \mathbf{q}\}$ is equal to zero (here, $\mathbf{q}$ is the 3-momentum transferred to the nucleus) [1].

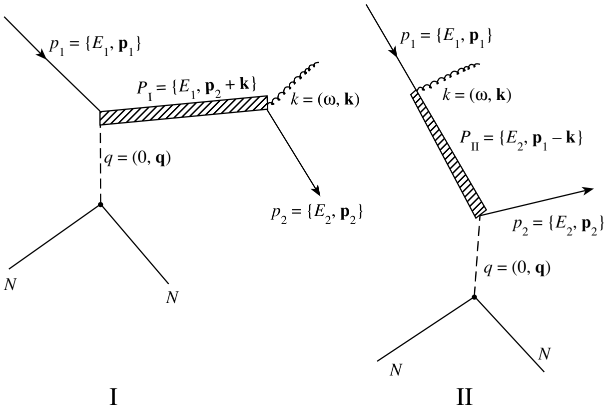

Fig. 1. Feynman diagrams for bremsstrahlung in the Coulomb field of a nucleus.

Then the 4-momentum of the virtual electron, corresponding to diagram I, is

$$P_{\rm I} = p_2 + k = \{E_1, \mathbf{p}_2 + \mathbf{k}\},$$

and the 4-momentum of the virtual electron, corresponding to diagram II, is

$$P_{\rm II} = p_1 - k = \{E_2, \mathbf{p}_1 - \mathbf{k}\}.$$

It is evident that the square of mass of the virtual electron for diagram I has the form

$$M_{\rm I}^2 = (p_2 + k)^2 = m^2 + 2p_2k$$
$$= m^2 + 2E_2\omega(1 - v_2\cos\theta),$$

where m is the electron mass, θ is the angle between the final electron momentum $\mathbf{p}_2$ and the photon momentum $\mathbf{k}$, and $v_2 = |\mathbf{p}_2|/E_2$ is the velocity of the final electron. According to Eq. (6), the lifetime and path length of the virtual electron under the condition $E_1^2 \gg E_2\omega(1 - v_2\cos\theta)$ are determined by the following formulas:

$$T_{\rm I} = \frac{E_1}{E_2\omega(1 - v_2\cos\theta)}; \qquad (8)$$
$$L_{\rm I} = \frac{|\mathbf{p}_2 + \mathbf{k}|}{E_2\omega(1 - v_2\cos\theta)}.$$

Analogously, in the case of diagram II, we have

$$M_{\rm II}^2 = (p_1 - k)^2 = m^2 - 2p_1k$$
$$= m^2 - 2E_1\omega(1 - v_1\cos\widetilde{\theta}),$$

where $\widetilde{\theta}$ is the angle between the initial electron momentum $\mathbf{p}_1$ and the photon momentum $\mathbf{k}$, and $v_1 = |\mathbf{p}_1|/E_1$ is the velocity of the initial electron. In accordance with Eq. (6), we obtain, under the condition $E_2^2 \gg E_1\omega(1 - v_1\cos\widetilde{\theta})$, the following expressions for the lifetime and path length of the virtual

---

[1)] In the usual unit system, formulas (3), (5), (6), and (7) have the following form:

$$T = \frac{\hbar E}{|m^2 - M^2|c^4}\left(\sqrt{1 + \frac{(m^2 - M^2)c^4}{E^2}} + 1\right); \qquad (3a)$$

$$L = \frac{\hbar|\mathbf{P}|}{|m^2 - M^2|c^2}\left(\sqrt{1 - \frac{(m^2 - M^2)c^2}{\mathbf{P}^2}} + 1\right); \qquad (5a)$$

$$T = \frac{2\hbar E}{|m^2 - M^2|c^4}, \quad L = \frac{2\hbar|\mathbf{P}|}{|m^2 - M^2|c^2}; \qquad (6a)$$

$$\{cT, \mathbf{L}\} = \frac{2\hbar P}{|m^2 - M^2|c^2}. \qquad (7a)$$

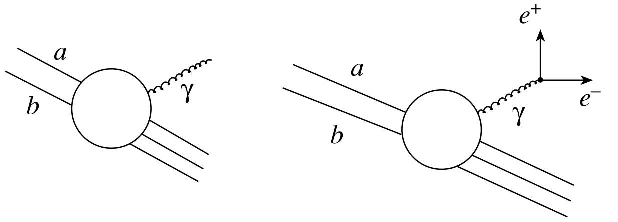

Fig. 2. Conversion of the virtual photon into an electron–positron pair.

electron:

$$T_{\rm II} = \frac{E_2}{E_1\omega(1 - v_1\cos\widetilde{\theta})}; \tag{9}$$

$$L_{\rm II} = \frac{|\mathbf{p}_1 - \mathbf{k}|}{E_1\omega(1 - v_1\cos\widetilde{\theta})}.$$

At ultrarelativistic energies $E_1 \gg m$, $E_2 \gg m$ and small angles $\theta \ll 1$, $\widetilde{\theta} \ll 1$, one can write

$$1 - v_2\cos\theta \approx 1 - v_2 + v_2\frac{\theta^2}{2}$$

$$\approx \frac{1}{2\gamma_2^2}(1 + \gamma_2^2\theta^2),$$

$$1 - v_1\cos\widetilde{\theta} \approx 1 - v_1 + v_1\frac{\widetilde{\theta}^2}{2}$$

$$\approx \frac{1}{2\gamma_1^2}(1 + \gamma_1^2\widetilde{\theta}^2),$$

where $\gamma_1 = E_1/m$ and $\gamma_2 = E_2/m$ are the Lorentz factors of the initial and final electrons, respectively ($\gamma_1 \gg 1$, $\gamma_2 \gg 1$). Under these conditions, taking into account the approximate equalities $|\mathbf{p}_2 + \mathbf{k}| \approx E_1$ and $|\mathbf{p}_1 - \mathbf{k}| \approx E_2$, relations (8) and (9) give

$$T_{\rm I} \approx L_{\rm I} \approx \frac{2\gamma_1\gamma_2}{\omega(1 + \gamma_2^2\theta^2)}, \tag{10}$$

$$T_{\rm II} \approx L_{\rm II} \approx \frac{2\gamma_1\gamma_2}{\omega(1 + \gamma_1^2\widetilde{\theta}^2)}.$$

The main contribution to the process of the bremsstrahlung of an ultrarelativistic electron in the Coulomb field of a heavy nucleus arises from the region of small angles $\theta <\sim 1/\gamma_2$, $\widetilde{\theta} <\sim 1/\gamma_1$. As a result, the effective path length of an ultrarelativistic electron in the bremsstrahlung in the Coulomb field has a magnitude of the order of

$$L \sim L_{\rm I} \sim L_{\rm II} \sim \frac{\gamma_1\gamma_2}{\omega}. \tag{11}$$

In the usual unit system, $L_{\rm I} \sim L_{\rm II} \sim \hbar c\gamma_1\gamma_2/(E_1 - E_2)$. For example, for an electron with energy $E_1 \approx E_2 = 100$ GeV and photon energy $\omega = 10$ MeV, the effective path length L of the virtual electron amounts to $\sim 8 \times 10^{-2}$ cm ~ 1 mm (the virtual electron lifetime T equals $\sim 3 \times 10^{-12}$ s).

3. CONVERSION OF THE VIRTUAL PHOTON INTO AN ELECTRON–POSITRON PAIR

Any process with the emission of a photon may be accompanied by another process in which the virtual photon is converted into an e^+e^- pair (see Fig. 2). In this case, the virtual photon has the timelike 4-momentum $P = \{E_+ + E_-, \mathbf{p}_+ + \mathbf{p}_-\}$, and its mass is given by the formula

$$M^2 = 2m^2 + 2E_+E_-(1 - v_-v_+\cos\phi),$$

where m is the mass of the positron and electron; $\mathbf{p}_+$, E_+, and v_+ are the momentum, energy, and velocity of the positron, respectively; $\mathbf{p}_-$, E_-, and v_- are the same for the electron; and ϕ is the angle between the electron and positron momenta. According to Eq. (6), under the condition $E^2 = (E_+ + E_-)^2 \gg M^2$, the lifetime and path length of the virtual photon at the conversion into an e^+e^- pair amount to

$$T \approx L = \frac{2E}{M^2}. \tag{12}$$

For narrow electron–positron pairs, when $\phi \approx 0$, $M^2 \approx 4m^2$, and $E_+ \approx E_-$, we obtain

$$T \approx L \approx \frac{E_+ + E_-}{2m^2} \approx \frac{\gamma}{m},$$

where γ is the Lorentz factor of the positron and electron. In the usual unit system, $T \approx \hbar\gamma/mc^2$ and $L \approx \hbar\gamma/mc$. For example, at $\gamma = 10^6$ (the energies of the ultrarelativistic electron and positron amount to $E_+ \approx E_- \approx 500$ GeV), the lifetime and the path length of the virtual photon reach the values $T \approx 1.3 \times 10^{-15}$ s and $L \approx 3.8 \times 10^{-5}$ cm, respectively. These magnitudes are not macroscopic, but they, nevertheless, strongly exceed the characteristic atomic scale.

4. CONNECTION BETWEEN THE PATH LENGTH OF THE VIRTUAL PARTICLE AND THE COHERENCE LENGTH

When the momentum $\mathbf{q}$ is transferred to atoms (nuclei) during the propagation of a particle in matter, the difference of phases for the amplitudes of emission from two points is $\phi = \mathbf{q}\cdot\mathbf{R}$, where $\mathbf{R}$ is the distance between these points. Thus, it follows from here that constructive (positive) interference of amplitudes of emission from different points takes place within the length $l \sim 1/|q|$. In the case when the process takes place mainly at the minimal momentum transfer to the target, the quantity $L_{\text{coh}} \sim 1/q_{\min}$ has the meaning of the coherence length (formation length) for the considered reaction [1, 3–6]. It is just such a situation that holds in the case of the bremsstrahlung of a relativistic electron on the nucleus [1]. In this case, the minimal transferred momentum corresponds to the forward direction, when the momenta of both the final electron and photon are parallel to the momentum of the initial electron. It is clear that

$$\begin{aligned} q_{\min} &= \sqrt{E_1^2 - m^2} - \sqrt{E_2^2 - m^2} - \omega \\ &= \sqrt{E_1^2 - m^2} - \sqrt{E_2^2 - m^2} - (E_1 - E_2) \\ &\approx \frac{m^2}{2E_2} - \frac{m^2}{2E_1} = \frac{m^2}{2}\frac{E_1 - E_2}{E_1 E_2} = \frac{\omega}{2\gamma_1\gamma_2} \end{aligned}$$

(all the notation is the same as in Section 2). So, we obtain

$$L_{\text{coh}} \sim \frac{2\gamma_1\gamma_2}{\omega}. \tag{13}$$

Thus, the path length L of the virtual ultrarelativistic electron [see Eq. (11)] coincides, in order of magnitude, with the coherence length L_{coh}.

The relation $L \sim L_{\text{coh}}$ is valid for any process in which the transition of a real particle into a virtual one, or the reverse transition, takes place with very low momentum transfer to a nucleus. That is connected with the fact that, in this case, both the inverse path length of the virtual particle and the minimal transferred momentum are proportional to the difference of mass squares $|M^2 - m^2|$.

5. SUMMARY

(i) The concepts of the lifetime T and path length L of a virtual particle are introduced. On the basis of the uncertainty principle for energy and time and the uncertainty principle for momenta and coordinates, the general expressions for T and L are obtained.

(ii) Using the example of the ultrarelativistic electron bremsstrahlung in the Coulomb field of a heavy nucleus, it is shown that, at very high energies, the virtual particle can propagate over considerable (even macroscopic) distances.

(iii) The connection between the path length of a virtual particle and the coherence length at the interaction of ultrarelativistic particles with nuclei is analyzed.

ACKNOWLEDGMENTS

The work is supported by Russian Foundation for Basic Research (project no. 03-02-16210).

REFERENCES

1. V. B. Berestetsky, E. M. Lifshitz, L. P. Pitaevsky, *Quantum Electrodynamics* (Nauka, Moscow, 1989), §§ 79, 93.
2. S. S. Kozlovskaya, G. I. Kopylov, V. L. Lyuboshitz, *et al.*, Yad. Fiz. **24**, 621 (1976) [Sov. J. Nucl. Phys. **24**, 326 (1976)].
3. M. L. Ter-Mikaelyan, Zh. Éksp. Teor. Fiz. **25**, 289 (1953).
4. M. L. Ter-Mikaelyan, Zh. Éksp. Teor. Fiz. **25**, 296 (1953).
5. E. L. Feinberg, Zh. Éksp. Teor. Fiz. **50**, 202 (1966) [Sov. Phys. JETP **23**, 132 (1966)].
6. E. L. Feinberg, Usp. Fiz. Nauk **132**, 255 (1980) [Sov. Phys. Usp. **23**, 629 (1980)].

Physics of Atomic Nuclei, Vol. 68, No. 3, 2005, pp. 528–529. Translated from Yadernaya Fizika, Vol. 68, No. 3, 2005, pp. 557–558.
Original Russian Text Copyright © 2005 by Kiselev.

On the Geometric Properties of the Dispersionless Toda Equation

A. V. Kiselev*
Moscow State University, Vorob'evy gory, Moscow, 119899 Russia

Received May 24, 2004

Abstract—The problem of constructing exact solutions, Noether symmetries, and conservation laws for the $(2+1)$-dimensional dispersionless Toda equation $u_{xy} = \exp(-u_{zz})$ is considered. © *2005 Pleiades Publishing, Inc.*

In this paper, algebraic methods in the geometry of equations of mathematical physics [1] are used to study the properties of the $(2+1)$-dimensional dispersionless Toda equation [2] $\mathcal{E} = \{F \equiv u_{xy} - \exp(-u_{zz}) = 0\}$, which is employed in many models of contemporary field theory—for example, in Yang–Mill theory [3] or in studying the anti-self-dual vacuum Einstein equations and their instanton solutions [4]. The structure of the generators of the classical-symmetry Lie algebra for the equation $\mathcal{E}$ allows one to obtain a large set of its exact solutions and to reconstruct classes of conserved currents assigned to the Noether symmetries of this equation.

We start with the following definition. Let $\varphi(u, \ldots, u_\sigma)$ be a symmetry of a differential equation $\mathcal{E} = \{F = 0\}$; that is, let φ be a solution to the linearized system $\sum_{i,\sigma} D_\sigma(\varphi^i)\,\partial F/\partial u^i_\sigma = 0$ on $\mathcal{E}$, where $u_\sigma = \partial^{|\sigma|}u/\partial(x^1)^{\sigma_1}\ldots\,\partial(x^n)^{\sigma_n}$ is the derivative of the dependent variable u for any multi-index σ. Suppose that there exists a flow $A_\tau\colon u(x,0) \mapsto u(x,\tau)$ of the symmetry φ. The flow is defined on the solutions to the evolution equation $u_\tau = \varphi$. It maps the solutions $s(x) = u(x,\tau)|_{\tau=0}$ of the equation $\mathcal{E}$ to solutions of the same equation for any $\tau > 0$. A solution $s(x)$ is called a φ-invariant solution if it is a stationary solution of the evolution equation $u_\tau = \varphi(u, \ldots, u_\sigma)$.

The generators φ_i of the classical-symmetry Lie algebra for the equation $\mathcal{E}$ are known [2, 5]. Namely, the solutions $\varphi(x, y, z, u, u_x, u_y, u_z)$ to the determining equation $\bar{D}_{xy}(\varphi) + \exp(-u_{zz})\,\bar{D}^2_z(\varphi) = 0$ (here, $\bar{D}_\sigma$ is the total derivative D_σ restricted to the equation $\mathcal{E}$ and f, g, q, and r are arbitrary smooth functions) have the following form: $\varphi_1[f(x)] = \left(u_x - \frac{1}{2}z^2\,\bar{D}_x\right) f(x)$ and $\bar{\varphi}_1[g(y)] = \left(u_y - \frac{1}{2}z^2\,\bar{D}_y\right) g(y)$ are conformal symmetries; $\varphi_2 = -\frac{1}{2}zu_z + u - \frac{1}{2}z^2$ is a scaling symmetry; $\varphi_3 = u_z$ is a translation along z; and, finally, $\varphi_4[q(x)] = q(x)\,z$ and $\varphi_5[r(x)] = r(x)$ are two shifts of the variable u.

1. Consider the symmetry $\varphi_1 = \varphi_1[f(x)] + \bar{\varphi}_1[g(y)]$ of the equation $\mathcal{E}$, express the invariance condition $\varphi_1 = 0$ in the characteristic form, and treat the variable z as a parameter. Thence, we obtain the first integrals $t = \int^x dx/f(x) - \int^y dy/g(y)$ and $C_2(z) = \frac{1}{2}z^2 \ln[f(x)g(y)] - u$. A solution $u(x,y,z)$ is defined implicitly by the relation $\Pi(t, C_2(z)) = 0$. Solving it with respect to u, we obtain $u = \frac{1}{2}z^2 \ln[f(x)g(y)] + \Phi(t,z)$, where the function Φ satisfies the $(1+1)$-dimensional dispersionless Toda equation $\varepsilon = \{\Phi_{tt} + \exp(-\Phi_{zz}) = 0\}$. The classical-symmetry structure of this equation provides the following property of its solutions. Suppose that $\Phi(t,z)$ is a propagating wave. Let $(a:b) \in \mathbb{RP}^1$ be a point of the projective line. Substituting the function $\Phi(z - (a:b)t)$ into the equation ε, we arrive at the algebraic equation $(a:b)^2\,\Psi = -\exp(-\Psi)$, where Ψ denotes the second derivative Φ'' with respect to the argument $w = z - (a:b)\,t$. Now, we see the obstacle to the equation ε to admit solutions that would propagate at low velocities, $-\sqrt{e} < (a:b) < \sqrt{e}$. Indeed, there are the critical (minimal) velocity $|a:b| = \sqrt{e}$ and the wave solution $\Phi = -\frac{1}{2}\left(z \pm \sqrt{e}\,t\right)^2 + \alpha\left(z \pm \sqrt{e}\,t\right) + \beta$, where α, $\beta \in \mathbb{R}$. For any greater velocity, $\sqrt{e} < |a:b| < \infty$, the equation ε admits two wave solutions $\Phi = \frac{1}{2}\Psi_{1,2}\cdot w^2 + \alpha w + \beta$ simultaneously, where $\Psi_{1,2}$ is the pair of distinct roots and the constants $\alpha, \beta \in \mathbb{R}$ are arbitrary.

2. Constructing φ_2-invariant solutions to the equation $\mathcal{E}$ reduces to solving the auxiliary ordinary

---

*e-mail: `arthemy@mccme.ru`

1063-7788/05/6803-0528$26.00 © 2005 Pleiades Publishing, Inc.

differential equation $\varphi_2 = 0$ and the hyperbolic Liouville equation. Indeed, substituting the expression $u = \left(\gamma(x,y) - \frac{1}{2}\ln z^2\right) z^2$ into the equation $u_{xy} = \exp(-u_{zz})$ and making the transformation $\mathcal{X} = x\,\exp(3/2)$, $\mathcal{Y} = y\,\exp(3/2)$, we obtain the Liouville equation $\gamma_{\mathcal{X}\mathcal{Y}} = \exp(-2\gamma)$, whose solutions (which are also invariant with respect to its conformal symmetries) are known to have the form

$$\gamma(\mathcal{X},\mathcal{Y}) = -\frac{1}{2}\ln[-f'(\mathcal{X})g'(\mathcal{Y})/\{\mathbf{Q}([f(\mathcal{X}) + g(\mathcal{Y})]^2)\}^2],$$

where the mapping $\mathbf{Q}$ is either $\sin$, sinh, or the identity. The physical interpretation of the corresponding class of solutions,

$$u = \frac{z^2}{2}\ln\frac{\{\mathbf{Q}\big([f(e^{3/2}x) + g(e^{3/2}y)]^2\big)\}^2}{-z^2 f'(e^{3/2}x)g'(e^{3/2}y)},$$

for the dispersionless Toda equation $\mathcal{E}$ was given in [5]: the functions $u(x,y,z)$ provide the particle-type (instanton) solutions to the vacuum Einstein equations [4].

3. The symmetries φ_1, φ_3, φ_4, and φ_5 are known [2] to be the Noether symmetries of the Lagrangian with the density $\frac{1}{2}u_{xz}u_{yz} + \exp(-u_{zz})$. By Noether's theorem (see [1]), nontrivial conservation laws for the equation $\mathcal{E}$ are assigned to these symmetries. Moreover, these classes of conservation laws can be reconstructed explicitly by using the modern technique of the generating sections of conservation laws [1]. The resulting expressions [2] are very cumbersome and quite nontrivial. In particular, a dispersionless analog of the holomorphic component of the energy—momentum tensor for the two-dimensional Toda systems $u_{xy} = \exp(Ku)$ [3] is assigned to the conformal symmetry $\varphi_1[f(x)]$ of the limit equation $u_{xy} = \exp(-u_{zz})$.

ACKNOWLEDGMENTS

I am grateful to I.S. Krasil'shchik and A.M. Verbovetskii for stimulating discussions and constructive criticisms. I am also indebted to M.A. Parinov, V. Rosenhaus, and E.V. Ferapontov for enlightening comments.

The work was supported in part by a scholarship of the Government of the Russian Federation and by INTAS (grant no. YS 2001/2-33).

REFERENCES

1. A. V. Bocharov, A. M. Verbovetskiĭ, A. M. Vinogradov *et al.*, *Symmetry and Conservation Laws of Mathematical Physics Equations* (Factorial, Moscow, 1997).
2. A. V. Kiselev, Matematika i ee Prilozheniya **1**, 69 (2004).
3. M. V. Savel'ev, Teor. Mat. Fiz. **92**, 457 (1992).
4. C. P. Boyer and J. D. Finley, J. Math. Phys. (N.Y.) **23**, 1126 (1982).
5. E. Alfinito, G. Soliani, and L. Solombrino, Lett. Math. Phys. **41**, 379 (1997).

Translated by A. Kiselev

Physics of Atomic Nuclei, Vol. 68, No. 3, 2005, pp. 530–535. From Yadernaya Fizika, Vol. 68, No. 3, 2005, pp. 559–563.
Original English Text Copyright © 2005 by Nefediev.

QCD String in the Schwinger–Dyson Approach to Heavy–Light Quarkonia[*]

A. V. Nefediev
Institute of Theoretical and Experimental Physics,
Bol'shaya Cheremushkinskaya ul. 25, Moscow, 117218 Russia

Received May 24, 2004; in final form, September 16, 2004

Abstract—The kernel of the Schwinger–Dyson equation for a heavy–light quarkonium is studied in the limit of potential quark dynamics, and the string correction to the quark–antiquark potential is derived in agreement with the results of the quantum-mechanical QCD string approach. Possible ways of further improvement of the method are outlined and discussed. © *2005 Pleiades Publishing, Inc.*

1. INTRODUCTION

QCD is believed to be a string theory at large distances, such a picture of color confinement being strongly supported by lattice calculations—the most reliable source of information about gluonic contents of the QCD vacuum. In the meantime, most of the analytical and numerical calculations of hadronic properties and reactions are performed in the framework of quark models, which, in spite of their long history, remain one of the main tools for studies of the nonperturbative effects in QCD. In the simplest versions of the quark models, the confining interaction has to be constructed phenomenologically and then built into the system in the form of the interquark potential (for example, the Cornell linear plus Coulomb potential, known to be successful in heavy quarkonia). More sophisticated approaches, such as the QCD string approach [1], allow one to have the quark Lagrangian and the interquark-interaction form that come in one pocket, starting from the fundamental QCD Lagrangian and without extra ad hoc assumptions. The gluonic contents of the theory are then encoded in a nontrivial form of the interaction between quarks at large distances, which cannot be described in terms of local potentials [1, 2]. A challenge for theorists is to "marry" the quantum-mechanical approaches to quarkonia, which easily incorporate such a nonpotential dynamics, with the field-theory-based methods, which prove to be very efficient in studies of chiral properties of the theory. In the present work, we take a step in this direction and identify the string correction, coming from the proper dynamics of the QCD string in a heavy–light quark–antiquark system, in the kernel of the quark current–current interaction. The paper is organized as follows. In Section 2, we give a necessary introduction to the Schwinger–Dyson approach to a heavy–light system and briefly discuss the results obtained in this approach. Section 3 is devoted to the details of the quantum-mechanical model for the QCD string with quarks at the ends and to the discussion of the proper dynamics of the string. In Section 4, the string correction to the interquark interaction is identified in the kernel of the aforementioned Schwinger–Dyson equation, and in the concluding Section 5, we discuss the results and give a brief discussion of possible further developments of the method.

2. SCHWINGER–DYSON APPROACH TO A HEAVY–LIGHT SYSTEM

2.1. Modified Fock–Schwinger Gauge and Schwinger–Dyson Equation

Recently, a new approach to heavy–light quarkonia was suggested [3] to study the interquark interaction and the chiral symmetry breaking in such a system. The system containing the static antiquark, placed at the origin, and a light quark was considered in the modified Fock–Schwinger gauge [4],

$$\mathbf{x}\cdot\mathbf{A}^a(x_0,\mathbf{x})=0,\quad A_0^a(x_0,\mathbf{0})=0, \tag{1}$$

and the equation for the quark–antiquark Green's function (in the Euclidean spacetime),

$$S(x,y)=\frac{1}{N_c}\int D\psi D\psi^+ DA_\mu \tag{2}$$
$$\times\exp\left[-\frac{1}{4}\int d^4z(F^a_{\mu\nu})^2\right.$$
$$\left.+\int d^4z\psi^+(i\hat{\partial}+im+\hat{A})\psi\right]$$
$$\times\psi^+(x)S_{\bar{Q}}(x,y|A)\psi(y),$$

---

[*] This article was submitted by the author in English.

was derived [3]:

$$(-i\hat{\partial}_x - im)S(x,y) \qquad (3)$$
$$- i\int d^4zM(x,z)S(z,y) = \delta^{(4)}(x-y).$$

A considerable simplification was achieved due to the gauge condition (1), since, in this gauge, the infinitely heavy antiquark decouples from the system, its Green's function being simply

$$S_{\bar{Q}}(x,y|A) \qquad (4)$$
$$= S_{\bar{Q}}(x,y) = i\frac{1-\gamma_4}{2}\theta(x_4-y_4)e^{-M(x_4-y_4)}$$
$$+ i\frac{1+\gamma_4}{2}\theta(y_4-x_4)e^{-M(y_4-x_4)}.$$

The mass operator $-iM(x,z)$ in Eq. (3) is given by the expressions [3]

$$-iM(x,z) = K_{\mu\nu}(x,z)\gamma_\mu S(x,z)\gamma_\nu, \qquad (5)$$

$$S(x,y) = \frac{1}{N_c}\langle\psi^\beta(x)\psi^+_\beta(y)\rangle,$$

where $S(x,y)$ plays the role of the Green's function of the light quark attached, via a string, to the static antiquark, and $K_{\mu\nu}(x,z)$ is the kernel of the interaction, which can be related to the irreducible bilocal gluonic correlator [5],

$$\langle F^a_{\mu\nu}(x)F^b_{\lambda\rho}(y)\rangle = \delta^{ab}\frac{2N_c}{N_c^2-1} \qquad (6)$$
$$\times D(x_0-y_0,|\mathbf{x}-\mathbf{y}|)(\delta_{\mu\lambda}\delta_{\nu\rho}-\delta_{\mu\rho}\delta_{\nu\lambda}) + \Delta^{(1)}.$$

Such a relation is a specific feature of the so-called coordinate gauges (see, for example, [6] and references therein), and, in the gauge (1), it reads ($\tau = x_0 - y_0$)

$$\begin{cases} K_{44}(\tau,\mathbf{x},\mathbf{y}) = (\mathbf{x}\cdot\mathbf{y})\int\limits_0^1 d\alpha\int\limits_0^1 d\beta D(\tau,|\alpha\mathbf{x}-\beta\mathbf{y}|), \\ K_{i4}(\tau,\mathbf{x},\mathbf{y}) = K_{4i}(\tau,\mathbf{x},\mathbf{y}) = 0, \\ K_{ik}(\tau,\mathbf{x},\mathbf{y}) = ((\mathbf{x}\cdot\mathbf{y})\delta_{ik} - y_ix_k)\int\limits_0^1 \alpha d\alpha\int\limits_0^1 \beta d\beta D(\tau,|\alpha\mathbf{x}-\beta\mathbf{y}|). \end{cases} \qquad (7)$$

The term $\Delta^{(1)}$ in Eq. (6) has a perturbative nature and will be disregarded below. The string tension is given as a double integral of the correlator profile D:

$$\sigma = 2\int\limits_0^\infty d\tau\int\limits_0^\infty d\lambda D(\tau,\lambda). \qquad (8)$$

The Schwinger–Dyson equation (3) is derived in the bilocal approximation to QCD, where correlators of the higher orders, $K_{\mu\nu\lambda},\ K_{\mu\nu\lambda\sigma},\ldots$, are neglected. Such an approximation is known to have a good accuracy [5] and is checked on the lattice with high precision [7]. Interested readers can find the details and applications of the method, as well as many references on the subject, in a recent review [8].

2.2. *Lorentz Nature of Confinement and Spin-Dependent Corrections*

The Schwinger–Dyson equation (3) was studied by a number of authors [3, 9–11] and a scheme of linearization of this equation was suggested, for the case of a sufficiently heavy quark, via the substitution of the free Green's function $S_0(x,z)$ instead of $S(x,z)$ with a consequent expansion of the mass operator (5) in terms of the inverse powers of the quark mass m. The resulting one-particle Dirac-type equation reads, in Minkowski space,

$$(\alpha\cdot\hat{\mathbf{p}} + \gamma_0 m + \gamma_0\hat{M})\psi = E\psi, \qquad (9)$$

with operator $\hat{M}$ given by

$$\hat{M}(\mathbf{x},\mathbf{z}) = -i\int\limits_0^\infty d\tau K_{\mu\nu}(\tau,\mathbf{x},\mathbf{z}) \qquad (10)$$
$$\times\int\frac{d^3k}{(2\pi)^3}e^{i\mathbf{k}\cdot(\mathbf{x}-\mathbf{z})}$$
$$\times\left\{\gamma_\mu\frac{i\gamma_4\varepsilon+\boldsymbol{\gamma}\cdot\mathbf{k}+im}{2\varepsilon}\gamma_\nu e^{-(\varepsilon-E)\tau}\right.$$
$$\left.+\gamma_\mu\frac{-i\gamma_4\varepsilon+\boldsymbol{\gamma}\cdot\mathbf{k}+im}{2\varepsilon}\gamma_\nu e^{-(\varepsilon+E)\tau}\right\},$$

where $\varepsilon = \varepsilon(\mathbf{k}) = \sqrt{\mathbf{k}^2+m^2}$ and the γ matrices are Euclidean ($\gamma_{4\mathrm{E}} = \gamma_{0\mathrm{M}},\ \gamma_{\mathrm{E}} = -i\gamma_{\mathrm{M}}$). Further expansion allows one to define the effective confining interaction V_{conf},

$$\hat{M}_0(\mathbf{x},\mathbf{z}) = \delta^{(3)}(\mathbf{x}-\mathbf{z})V_{\mathrm{conf}}(\mathbf{x}), \qquad (11)$$

$$V_{\mathrm{conf}}(\mathbf{x}) = \int\limits_0^\infty d\tau K_{\mu\nu}(\tau,\mathbf{x},\mathbf{x}) \qquad (12)$$

$$\times \left\{ \gamma_\mu \frac{1+\gamma_4}{2} \gamma_\nu + \gamma_\mu \frac{1-\gamma_4}{2} \gamma_\nu e^{-2m\tau} \right\}.$$

Since the decrease in the correlator $K_{\mu\nu}(\tau, \mathbf{x}, \mathbf{x})$ in time—as well as in the spatial directions, due to O_4 invariance of the vacuum—is defined by the gluonic correlation length T_g (lattice calculations give for T_g a value of around 0.3 fm [12]), then the two cases should be considered separately [3, 9–11]: $mT_g \ll 1$ and $mT_g \gg 1$. It was demonstrated [10] that the first case leads to a nonpotential quark dynamics because the corrections to the leading regime diverge as $mT_g \to 0$. Then the full nonlinearized equation (3) has to be solved. The two-dimensional model for QCD [13] is an example of the theory in which the Schwinger–Dyson equation, similar to Eq. (3), is exact and can be treated in its nonlinear form, reproducing the one-body limit of the well-known 't Hooft bound-state equation [14].

The case of $mT_g \gg 1$ brings no difficulties and one easily finds for the confining potential at large interquark distances

$$V_{\text{conf}}(r) = \left(\frac{5}{6} + \frac{1}{6}\gamma_0 \right) \sigma r, \tag{13}$$

which, together with the spin-dependent terms, gives, after the Foldy–Wouthuysen rotation, the interaction [9, 10]

$$V(r) = \sigma r - \frac{\sigma}{2m^2 r} \mathbf{S} \cdot \mathbf{L}, \tag{14}$$

in agreement with the general Eichten–Feinberg–Gromes results [15]. In the meantime, an important ingredient is missing in the effective interquark interaction (14)—namely, the proper dynamics of the QCD string. In the next section, we give a brief insight into the QCD string approach and remind the reader how the string correction [1, 16] to the confining potential emerges.

3. HAMILTONIAN OF A QUARK–ANTIQUARK MESON AND THE STRING CORRECTION

We start from the Lagrangian of the spinless quark–antiquark pair connected by the straight-line Nambu–Goto string,

$$L = -m_1 \sqrt{\dot{x}_1^2} - m_2 \sqrt{\dot{x}_2^2} - \sigma \int_0^1 d\beta \sqrt{(\dot{w} w')^2 - \dot{w}^2 w'^2}, \tag{15}$$

$$w_\mu(t, \beta) = \beta x_{1\mu}(t) + (1-\beta) x_{2\mu}(t),$$

and introduce einbeins $\mu_{1,2}$ to get rid of the square roots in the kinetic energies of the quarks [17] and the continuous einbein field $\nu(\beta)$ for the string term [1, 18]. Then one can proceed to the Hamiltonian of the system,

$$H = \sum_{i=1}^{2} \left[\frac{p_r^2 + m_i^2}{2\mu_i} + \frac{\mu_i}{2} \right] + \int_0^1 d\beta \left[\frac{\sigma^2 r^2}{2\nu} + \frac{\nu}{2} \right] + \frac{\hat{L}^2}{2r^2 [\mu_1 (1-\zeta)^2 + \mu_2 \zeta^2 + \int_0^1 d\beta \nu (\beta - \zeta)^2]}, \tag{16}$$

$$\zeta = \frac{\mu_1 + \int_0^1 d\beta \nu \beta}{\mu_1 + \mu_2 + \int_0^1 d\beta \nu},$$

where $m_1 = M$ and $m_2 = m$ are the masses of the heavy and light particle, respectively. For heavy quarks, einbeins $\mu_{1,2}$ almost coincide with the current quark masses, whereas in the case of light quarks they appear to be on the order of the interaction scale—much larger than the current quark masses—and play the role of the effective masses of the quarks [19].

The last summand in the denominator of the angular-momentum-dependent term in Eq. (16) describes the proper inetria of the rotating string. The influence of this extra contribution over the mesonic spectra was studied in detail in [1, 2, 18, 20, 21], and it was demonstrated that it brings the Regge trajectory (inverse) slope to the correct value of $2\pi\sigma$ for the light–light system and $\pi\sigma$ for the heavy–light one [1, 2, 18, 20], and it is important to reproduce the experimental spectra of D and B mesons [21].

Expansion of the Hamiltonian (16) for $M \to \infty$ and $\sqrt{\sigma} \ll m$ gives

$$H \approx M + m + \frac{\mathbf{p}^2}{2m} + \sigma r - \frac{\sigma \hat{L}^2}{6m^2 r} + \ldots, \tag{17}$$

which should be complemented by the nonperturbative spin–orbit interaction,

$$V_{\text{so}}^{\text{np}} = -\frac{\sigma}{2r} \left(\frac{\mathbf{S}_1 \cdot \mathbf{L}}{\mu_1^2} + \frac{\mathbf{S}_2 \cdot \mathbf{L}}{\mu_2^2} \right) \approx -\frac{\sigma}{2m^2 r} \mathbf{S} \cdot \mathbf{L}, \tag{18}$$

following from derivatives applied to the averaged Wilson loop formed by the quark and antiquark trajectories [22].

From Eqs. (17) and (18), one can extract the effective interquark interaction induced by the string,

$$V_{\text{string}}(r) = \sigma r - \frac{\sigma}{2m^2 r} \mathbf{S} \cdot \mathbf{L} - \frac{\sigma \hat{L}^2}{6m^2 r}, \tag{19}$$

which differs from the potential (14) in the last term—the string correction. Although quark models using the potential (14) (i.e., without the string correction), also supplied by the perturbative Coulomb interaction with the running or fixed strong coupling constant, prove to be rather successful in describing the mesonic spectra [23], we find it important to implement the string dynamics in the effective interaction. As mentioned above, this is necessary to have the correct Regge trajectories, and it is also important for merging the two complementary approaches: the quantum-mechanical approach of the QCD string with quarks at the ends and the field-theory-inspired Schwinger–Dyson approach. Therefore, in the next section, we return back to the Schwinger–Dyson equation for the heavy–light quarkonium, paying special attention to the rotation of the string and, as a result, restoring the missing term in Eq. (14).

4. STRING DYNAMICS IN THE SCHWINGER–DYSON APPROACH TO HEAVY–LIGHT QUARKONIA

As mentioned above, only the case of $mT_g \gg 1$ admits a self-consistent linearization of Eq. (3), so we neglect all the terms suppressed in this limit and start from the simplified version of Eq. (12) for the effective spin-independent confining potential in Minkowski space,

$$V_{\mathrm{conf}}(r) = \gamma_\mu \frac{1+\gamma_0}{2}\gamma_\nu \int\limits_0^\infty d\tau K_{\mu\nu}(\tau,\mathbf{x},\mathbf{y})_{|\mathbf{y}\to\mathbf{x}}. \tag{20}$$

Immediate substitution $\mathbf{y}=\mathbf{x}$ in (20) leads to the linear confinement (13). Meanwhile, such a substitution corresponds to the straight-line trajectory of the quark. As a result, angular-momentum-dependent terms in the Hamiltonian appear only from the kinetic energy of quarks, whereas all such terms coming from the kernel—the string correction being the leading one—are lost. On the other hand, it is clear that, in spite of the aforementioned immediate substitution, we still reproduce the spin-dependent terms in the Hamiltonian, in the order $1/m^2$, correctly. Indeed, all spin-dependent corrections appear from $(\boldsymbol{\gamma}\cdot\mathbf{k})/\varepsilon \sim 1/m$ terms in Eq. (10) and, being proportional to a nondiagonal γ matrices, they acquire an extra $1/m$ suppression after the Foldy–Wouthuysen transformation. Thus, the ultimate result already has the order $1/m^2$ [see Eq. (14)], so that allowance for the non-straight-line form of the light-quark trajectory will lead to even higher order corrections, which we do not consider. In the meantime, in the same order in $1/m$ expansion, such corrections must be taken into account in the diagonal terms in Eq. (10), proportional to γ_0 and unity matrices [24]. To this end, we follow the path-integral ideology and consider the trajectory of the quark, $\mathbf{r}(t)$, such that the two consequent positions of the latter are $\mathbf{y}=\mathbf{r}(t_1)$ and $\mathbf{x}=\mathbf{r}(t_2)$. Therefore, for close t_1 and t_2, one can use the expansion

$$\begin{aligned}\mathbf{x} = \mathbf{r}(t_2) = \mathbf{r}(t_1+\tau) &\approx \mathbf{r}(t_1) + \dot{\mathbf{r}}(t_1)\tau \\ &= \mathbf{y} + \frac{\mathbf{p}}{m}\tau,\end{aligned} \tag{21}$$

where $\mathbf{p}$ is the momentum of the quark. Due to the rotational invariance of the vacuum, the function D from Eq. (6) actually depends on a certain combination of its arguments, $D(\tau,\lambda) = D(\tau^2+\lambda^2)$. In our case, $\tau = t_2 - t_1$ and $\lambda = |\alpha\mathbf{x} - \beta\mathbf{y}|$, so that, with the help of the expansion (21), one easily finds

$$\begin{aligned}\tau^2+\lambda^2 &= \tau^2 + \left[(\alpha-\beta)\mathbf{r} + \alpha\tau\frac{\mathbf{p}}{m}\right]^2 \\ &= \left[1+\frac{\alpha^2p^2}{m^2}\right](\tau-\tau_0)^2 \\ &+ \frac{(\alpha-\beta)^2}{1+\alpha^2p^2/m^2}\left[r^2+\alpha^2\frac{L^2}{m^2}\right],\end{aligned} \tag{22}$$

where $\mathbf{r}\equiv\mathbf{y}$, $\mathbf{L}$ is the angular momentum, $\mathbf{L} = [\mathbf{r}\times\mathbf{p}]$, and the constant $\tau_0 = \frac{\alpha(\beta-\alpha)(\mathbf{r}\cdot\mathbf{p})}{m(1+\alpha^2p^2/m^2)}$ can be excluded using an appropriate shift of the time variable τ, so we omit it below. Using relations (7), one can easily calculate that

$$\begin{aligned}\int\limits_0^\infty d\tau K_{00}(\tau,\mathbf{x},\mathbf{y})_{|\mathbf{y}\to\mathbf{x}} &= r^2\int\limits_0^\infty d\tau\int\limits_0^1 d\alpha \\ &\times \int\limits_0^1 d\beta D\left(\tau\sqrt{1+\frac{\alpha^2p^2}{m^2}}, (\alpha-\beta)\right. \\ &\times \left.\sqrt{\frac{r^2+\alpha^2L^2/m^2}{1+\alpha^2p^2/m^2}}\right) \underset{r\gg T_g}{\approx} r \\ &\times \left(2\int\limits_0^\infty d\tau'\int\limits_0^\infty d\lambda D(\tau',\lambda)\right) \\ &\times \int\limits_0^1 \frac{d\alpha}{\sqrt{1+\alpha^2L^2/(m^2r^2)}} \approx \sigma r - \frac{\sigma L^2}{6m^2r},\end{aligned} \tag{23}$$

and, similarly,

$$\int\limits_0^\infty d\tau K_{ik}(\tau,\mathbf{x},\mathbf{y})_{|\mathbf{y}\to\mathbf{x}} \approx (\delta_{ik} - n_in_k) \tag{24}$$

$$\times\left(\frac{1}{3}\sigma r-\frac{\sigma L^2}{10m^2r}\right),$$

where the definition of the string tension (8) was used, as well as the case $n = 0$ of the general formula

$$\int\limits_0^1 d\alpha\int\limits_0^1 d\beta f(\alpha,\beta)(\alpha-\beta)^n$$

$$\times D(\tau,|\alpha-\beta|a)\underset{a\gg 1}{\approx}\frac{2}{a^{n+1}}\int\limits_0^\infty d\lambda D(\tau,\lambda)$$

$$\times\int\limits_0^1 d\alpha f(\alpha,\alpha),$$

which holds for an arbitrary function $f(\alpha, \beta)$, provided $f(\alpha, \alpha) \neq 0$.

Therefore, according to the relation (20), the confining interaction, in the limit $mT_g \gg 1$, becomes [24]

$$V_{\text{conf}}(r)=\left(\frac{5}{6}+\frac{1}{6}\gamma_0\right)\sigma r-\left(\frac{11}{10}-\frac{1}{10}\gamma_0\right)\frac{\sigma\hat{L}^2}{6m^2r}, \tag{25}$$

or, after the Foldy–Wouthuysen rotation, this corresponds to the confining potential

$$V_{\text{conf}}^{\text{FW}}(r)=\sigma r-\frac{\sigma\hat{L}^2}{6m^2r}, \tag{26}$$

in agreement with expression (17). It is also instructive to trace the coefficient 1/6 in the string correction, which appears as a product $\frac{1}{2}\cdot\frac{1}{3}$, with 1/2 coming from the expansion of the square root and 1/3 coming from the integral $\int_0^1 d\beta\beta^2$ for the internal string parameter β in the Hamiltonian (16) and, for the confining potential (20), from the same integral for the gauge parameter α (or β) introduced in Eq. (7). This identification emphasizes the deep connection between the modified Fock–Schwinger gauge and the straight-line QCD string developed between the light quark and the static antiquark.

5. DISCUSSION

In this paper, we demonstrate how an accurate $1/m$ expansion of the interaction kernel in the Schwinger–Dyson equation for the heavy–light system allows one to reproduce corrections to the confining potential due to the proper dynamics of the QCD string. Therefore, we conclude that, indeed, the string correction accompanies the linear confinement potential, whatever approach is used to derive the latter, provided the string picture of confinement is adopted. Still we find the approach developed above rather inconvenient for further investigations of the confining interaction in the approach of the Schwinger–Dyson nonlinear equation (3). On the other hand, a promising step is made in [6], where a contour gauge is introduced, which generalizes the gauge condition (1) for the case of an arbitrary trajectory of the heavy particle. Formally, Eqs. (3) and (5) remain valid, though the kernel of the interaction becomes contour-dependent. In the meantime, the form of the contour depends on the trajectory of the heavy particle (that is, it is defined dynamically), and the problem becomes self-consistent. Consequent expansion of the aforementioned contour around the straight-line form may provide a way of systematically accounting for the $(1/m)^n$ and $(1/M)^n$ corrections in this approach.

ACKNOWLEDGMENTS

Useful discussions with Yu.A. Simonov and Yu.S. Kalashnikova are acknowledged.

This work is supported by the grant NS-1774.2003.2 and by the Federal Program of the Russian Ministry of Industry, Science, and Technology no. 40.052.1.1.1112.

REFERENCES

1. A. Yu. Dubin, A. B. Kaidalov, and Yu. A. Simonov, Phys. Lett. B **323**, 41 (1994); **343**, 310 (1995).
2. V. L. Morgunov, A. V. Nefediev, and Yu. A. Simonov, Phys. Lett. B **459**, 653 (1999).
3. Yu. A. Simonov, Yad. Fiz. **60**, 2252 (1997) [Phys. At. Nucl. **60**, 2069 (1997)].
4. I. I. Balitsky, Nucl. Phys. B **254**, 166 (1985).
5. H. G. Dosch and Yu. A. Simonov, Phys. Lett. B **205**, 339 (1988).
6. V. I. Shevchenko and Yu. A. Simonov, Phys. Lett. B **437**, 146 (1998).
7. L. Del Debbio, A. Di Giacomo, and Yu. A. Simonov, Phys. Lett. B **332**, 111 (1994).
8. A. Di Giacomo, H. G. Dosch, V. I. Shevchenko, and Yu. A. Simonov, Phys. Rep. **372**, 319 (2002).
9. N. Brambilla and A. Vairo, Phys. Lett. B **407**, 167 (1997); P. Bicudo, N. Brambilla, E. Ribeiro, and A. Vairo, Phys. Lett. B **442**, 349 (1998).
10. Yu. S. Kalashnikova and A. V. Nefediev, Phys. Lett. B **414**, 149 (1997).
11. Yu. A. Simonov and J. A. Tjon, Phys. Rev. D **62**, 094511 (2000).
12. M. Campostrini, A. Di Giacomo, and G. Mussardo, Z. Phys. C **25**, 173 (1984); A. Di Giacomo and H. Panagopoulos, Phys. Lett. B **285**, 133 (1992).
13. G. 't Hooft, Nucl. Phys. B **75**, 461 (1974).
14. Yu. S. Kalashnikova and A. V. Nefediev, Yad. Fiz. **62**, 359 (1999) [Phys. At. Nucl. **62**, 323 (1999)]; Usp. Fiz. Nauk **45**, 378 (2002) [Phys. Usp. **45**, 347 (2002)].

15. E. Eichten and F. L. Feinberg, Phys. Rev. D **23**, 2724 (1981); D. Gromes, Z. Phys. C **26**, 401 (1984).
16. J. Merlin and J. Paton, J. Phys. G **11**, 439 (1985).
17. L. Brink, P. Di Vecchia, and P. Howe, Nucl. Phys. B **118**, 76 (1977); Yu. S. Kalashnikova and A. V. Nefediev, Yad. Fiz. **60**, 1529 (1997) [Phys. At. Nucl. **60**, 1389 (1997)].
18. C. Olson, M. G. Olsson, and D. La Course, Phys. Rev. D **49**, 4675 (1994).
19. Yu. A. Simonov, Nucl. Phys. B **307**, 512 (1988); Yu. A. Simonov and J. A. Tjon, Ann. Phys. (N. Y.) **228**, 1 (1993).
20. M. G. Olsson, Phys. Rev. D **55**, 5479 (1997).
21. A. V. Nefediev and Yu. S. Kalashnikova, Phys. Lett. B **492**, 91 (2000); **530**, 117 (2002); A. V. Nefediev, Yu. S. Kalashnikova, and Yu. A. Simonov, Phys. Rev. D **64**, 014037 (2001).
22. Yu. A. Simonov, Nucl. Phys. B **324**, 67 (1989).
23. D. R. Stanley and D. Robson, Phys. Rev. Lett. **45**, 235 (1980); P. Cea, G. Nardulli, and G. Preparata, Z. Phys. C **16**, 135 (1982); Phys. Lett. B **115**, 310 (1982); J. Carlson *et al.*, Phys. Rev. D **27**, 233 (1983); N. Isgur and S. Godfrey, Phys. Rev. D **32**, 189 (1985).
24. A. V. Nefediev, Pis'ma Zh. Éksp. Teor. Fiz. **78**, 801 (2003) [JETP Lett. **78**, 349 (2003)].

Physics of Atomic Nuclei, Vol. 68, No. 3, 2005, pp. 536–540. From Yadernaya Fizika, Vol. 68, No. 3, 2005, pp. 564–568.
Original English Text Copyright © 2005 by Narodetskii, Semay, Silvestre-Brac, Simonov, Trusov.

Pentaquarks in the Jaffe–Wilczek Approximation*

I. M. Narodetskii[1], C. Semay[2], B. Silvestre-Brac[3], Yu. A. Simonov[1], and M. A. Trusov[1]

Received May 20, 2004; in final form, September 13, 2004

Abstract—The masses of $uudd\bar{s}$, $uudd\bar{d}$, and $uuss\bar{d}$ pentaquarks are evaluated in a framework of both the effective Hamiltonian approach to QCD and the spinless Salpeter equation using the Jaffe–Wilczek diquark approximation and the string interaction for the diquark–diquark–antiquark system. The pentaquark masses are found to be in the region above 2 GeV. That indicates that the Goldstone boson exchange effects may play an important role in the light pentaquarks. The same calculations yield the mass of $[ud]^2\bar{c}$ pentaquark ~3250 MeV and $[ud]^2\bar{b}$ pentaquark ~6509 MeV. *© 2005 Pleiades Publishing, Inc.*

1. INTRODUCTION

Recently, the LEPS Collaboration [1] reported the observation of a very narrow peak in the K^+n and K^0p invariant mass distribution, whose existence has been confirmed by several experimental groups in various reaction channels [2]. These experimental results were motivated by the pioneering paper on the chiral soliton model [3]. The reported mass determinations for Θ are very consistent, falling in the range 1540 ± 10, with the width smaller than the experimental resolution of 20 MeV for the photon- and neutrino-induced reactions and of 9 MeV for the ITEP $K^+\mathrm{Xe} \to K^0p\mathrm{Xe}'$ experiment.

From the soliton point of view, Θ is nothing exotic compared with other baryons—it is just a member of the $\overline{\mathbf{10}}_F$ multiplet with $S = +1$. However, in the sense of the quark model, the $\Theta^+(1540)$ baryon with positive amount of strangeness is manifestly exotic—its minimal configuration cannot be satisfied by three quarks. The positive strangeness requires an $\bar{s}$ and $qqqq$ (where q refers to the lightest quarks (u,d)) are required for the net baryon number, thus making a pentaquark $uudd\bar{s}$ state as the minimal "valence" configuration. Later, the NA49 Collaboration at CERN SPS [4] announced evidence for an additional narrow $udus\bar{s}$ resonance with $I = 3/2$, a mass of 1.862 ± 0.002 GeV, and a width below the detector resolution of about 18 MeV,[4] and the H1 Collaboration at HERA [5] found a narrow resonance in $D^{*-}p$ and $D^{*+}\bar{p}$ invariant mass combinations at $3.099 \pm 0.033_{\mathrm{stat}} \pm 0.005_{\mathrm{syst}}$ GeV and a measured Gaussian width of $12 \pm 3_{\mathrm{stat}}$ MeV, compatible with the experimental resolution. The later resonance is interpreted as an anticharmed baryon with a minimal constituent quark composition of $uudd\bar{c}$, together with the charge conjugate. The discoveries of the first manifestly exotic hadrons mark the beginning of a new and rich spectroscopy in QCD and provide an opportunity to refine our quantitative understanding of nonperturbative QCD at low energy.

The Θ hyperon has hypercharge $Y = 2$ and a third component of isospin $I_3 = 0$. The apparent absence of $I_3 = +1$, Θ^{++} in K^+p argues against $I = 1$; therefore, Θ is usually assumed to be an isosinglet. The other quantum numbers are not established yet.

As to the theoretical predictions, we are faced with a somewhat ambiguous situation in which exotic baryons may have been discovered, but there are important controversies with theoretical predictions for masses of pentaquark states. The experimental results triggered a vigorous theoretical activity and put a renewed urge in the need to understand how baryon properties are obtained from QCD.

All attempts at theoretical estimations of the pentaquark masses can be subdivided into following four categories: (i) dynamical calculations using the sum rules or lattice QCD [6, 7], (ii) the phenomenological analyses of the hyperfine splitting in the quark model [8, 9], (iii) phenomenological analyses of the $SU(3)_F$ mass relations, and (iv) dynamical calculations using the chiral $SU(3)$ quark model [10].

The QCD sum rules predict a negative parity Θ^+ of mass $\simeq$1.5 GeV, while no positive-parity state was found [6]. The lattice QCD study also predicts that the parity of the lowest Θ hyperon is most likely negative [7].

---

*This article was submitted by the authors in English.

[1] Institute of Theoretical and Experimental Physics, Bol'shaya Cheremushkinskaya ul. 25, Moscow, 117259 Russia.

[2] Groupe de Physique Nucléaire Théorique, Université de Mons-Hainaut, Académie Universitaire Wallonie-Bruxelles, Mons, Belgium.

[3] Laboratoire de Physique Subatomique et de Cosmologie, Grenoble-Cedex, France.

[4] NA49 also reports evidence for a $\Xi^0(1860)$ decaying into $\Xi(1320)\pi$.

1063-7788/05/6803-0536$26.00 © 2005 Pleiades Publishing, Inc.

The naive quark models, in which all constituents are in a relative S wave, naturally predict the ground-state energy of a $J^P = 1/2^-$ pentaquark to be lower than that of a $J^P = 1/2^+$ one. However, using the arguments based on both Goldstone boson exchange between constituent quarks and color-magnetic exchange, it was mentioned that the increase in hyperfine energy in going from negative- to positive-parity states can be quite sufficient to compensate the orbital excitation energy ∼200 MeV. However, existing dynamical calculations of pentaquark masses using the chiral $SU(3)$ quark model (see, e.g., [10]) are subject to significant uncertainties and cannot be considered as conclusive.

Pentaquark baryons are unexpectedly light. Indeed, a naive quark model with quark mass ∼350 MeV predicts Θ^+ at about $350 \times 5 = 1750$ MeV plus ∼150 MeV for strangeness plus ∼200 MeV for the P-wave excitation. A natural remedy would be to decrease the number of constituents. This leads one to consider dynamical clustering into subsystems of diquarks like $[ud]^2\bar{s}$ [11] and/or triquarks like $[ud][ud\bar{s}]$ [9], which amplify the attractive color-magnetic forces. In particular, in [11], it has been proposed that the systematics of exotic baryons can be explained by diquark correlations.

The quark constituent model has not yet been derived from QCD. Therefore, it is tempting to consider the Effective Hamiltonian (EH) approach in QCD (see, e.g., [12]), which, on one hand, can be derived from QCD and, on the other hand, leads to results for the $\bar{q}q$ mesons and $3q$ baryons that are equivalent to the quark-model ones with some important modifications. The EH approach contains the minimal number of input parameters: current (or pole) quark masses, the string tension σ, and the strong coupling constant α_s; it does not contain fitting parameters as, e.g., the total subtraction constant in the Hamiltonian. It should be useful and attractive to consider expanding this approach to include diquark degrees of freedom with appropriate interactions. A preview of this program was done in [13]. It is based on the assumption that chiral and short-range gluon-exchange forces are responsible for the formation of ud diquarks in Θ, while the strings are mainly responsible for binding constituents in Θ. In this paper, we review and extend application of the EH approach to the Jaffe–Wilczek model of pentaquarks.

In this model, inside $\Theta(1540)$ and other $q^4\bar{q}$ baryons, the four quarks are bound into two scalar, singlet isospin diquarks. Diquarks must couple to $\mathbf{3}_c$ to join in a color singlet hadron. In the quark model, five quarks are connected by seven strings. In the diquark approximation, the short legs on this figure shrink to points and the five-quark system effectively reduces to the three-body one, studied within the EH approach in [14, 15]. In total, there are six flavor symmetric diquark pairs $[ud]^2$, $[ud][ds]_+$, $[ds]^2$, $[ds][su]_+$, $[su]^2$, and $[su][ud]_+$ combining with the remaining antiquark, which give 18 pentaquark states in $\mathbf{8}_F$ plus $\overline{\mathbf{10}}_F$. All these states are degenerate in the $SU(3)_F$ limit.

2. THE EH APPROACH AND THE RESULTS

The EH for the three constituents has the form

$$H = \sum_{i=1}^{3}\left(\frac{m_i^2}{2\mu_i} + \frac{\mu_i}{2}\right) + H_0 + V, \tag{1}$$

where H_0 is the kinetic energy operator and V is the sum of the perturbative one-gluon-exchange potentials and the string potential V_{string}.

The dynamical masses μ_i (analogues of the constituent ones) are expressed in terms of the current quark masses m_i from the condition of the minimum of the hadron mass $M_H^{(0)}$ as a function of μ_i:[5)]

$$\frac{\partial M_H^{(0)}(m_i,\mu_i)}{\partial \mu_i} = 0, \tag{2}$$
$$M_H^{(0)} = \sum_{i=1}^{3}\left(\frac{m_i^2}{2\mu_i} + \frac{\mu_i}{2}\right) + E_0(\mu_i),$$

where $E_0(\mu_i)$ is the eigenvalue of the operator $H_0 + V$. Quarks acquire constituent masses $\mu_i \sim \sqrt{\sigma}$ due to the string interaction in (1). As of today, the EH in the form of (1) does not include chiral-symmetry-breaking effects. A possible interplay with these effects should be carefully clarified in the future.

The physical mass M_H of a hadron is

$$M_H = M_H^{(0)} + \sum_i C_i. \tag{3}$$

The (negative) constants C_i have the meaning of the constituent self-energies and are explicitly expressed in terms of string tension σ [18]:

$$C_i = -\frac{2\sigma}{\pi\mu_i}\eta_i, \tag{4}$$

where

$$\eta_q = 1, \quad \eta_s = 0.88, \quad \eta_c = 0.234, \quad \eta_b = 0.052. \tag{5}$$

[5)] Technically, this is done using the auxiliary-field approach to get rid of the square-root term in the Lagrangian [16, 17]. Applied to the QCD Lagrangian, this technique yields the EH for hadrons (mesons, baryons, pentaquarks) depending on auxiliary fields μ_i. In practice, these fields are finally treated as c numbers determined from (2).

In Eq. (5) η_s, η_c, and η_b are the correction factors due to nonvanishing current masses of the strange, charm, and bottom quarks, respectively. The self-energy corrections are due to constituent spin interaction with the vacuum background fields and equal zero for any scalar constituent.

Accuracy of the EH method for the three-quark systems is ~100 MeV or better [14, 15]. One can expect the same accuracy for the diquark–diquark–antiquark system.

Consider a pentaquark consisting of two identical diquarks with current mass $m_{[ud]}$ and an antiquark with current mass $m_{\bar{q}}$ $(q = d, s, c)$. In the hyperspherical formalism, the wave function $\psi(\boldsymbol{\rho}, \boldsymbol{\lambda})$ expressed in terms of the Jacobi coordinates $\boldsymbol{\rho}$ and $\boldsymbol{\lambda}$ can be written in symbolic shorthand as

$$\psi(\boldsymbol{\rho}, \boldsymbol{\lambda}) = \sum_K \psi_K(R) Y_{[K]}(\Omega), \tag{6}$$

where $Y_{[K]}$ are eigenfunctions (the hyperspherical harmonics) of the angular-momentum operator $\hat{K}(\Omega)$ on the six-dimensional sphere: $\hat{K}^2(\Omega) Y_{[K]} = -K(K+4) Y_{[K]}$, with K being the grand orbital momentum. For identical diquarks, like $[ud]^2$, the lightest state must have a wave function antisymmetric under diquark space exchange. There are two possible pentaquark wave functions antisymmetric under diquark exchange, the first one (with lower energy) corresponding to the total orbital momentum $L = 1$ and the second one (with higher energy) corresponding to $L = 0$. For a state with $L = 1$, $l_\rho = 1$, $l_\lambda = 0$, the wave function in the lowest hyperspherical approximation $K = 1$ reads

$$\psi = R^{-5/2} \chi_1(R) u_1(\Omega), \tag{7}$$

$$u_1(\Omega) = \sqrt{\frac{8}{\pi^2}} \sin\theta \cdot Y_{1m}(\hat{\boldsymbol{\rho}}),$$

where $R^2 = \boldsymbol{\rho}^2 + \boldsymbol{\lambda}^2$. Here, one unit of orbital momentum between the diquarks is with respect to the $\boldsymbol{\rho}$ variable, whereas the $\boldsymbol{\lambda}$ variable is in an S state. The Schrödinger equation for $\chi_1(R)$ written in terms of the variable $x = \sqrt{\mu} R$, where μ is an arbitrary scale of mass dimension which drops off in the final expressions, reads

$$\frac{d^2\chi_1(x)}{dx^2} + 2\left[E_0 + \frac{a_1}{x} - b_1 x - \frac{35}{8x^2}\right]\chi_1(x) = 0, \tag{8}$$

with the boundary condition $\chi_K(x) \sim \mathcal{O}(x^{7/2})$ as $x \to 0$ and the asymptotic behavior $\chi_1(x) \sim \mathrm{Ai}((2b_1)^{1/3} x)$ as $x \to \infty$. In Eq. (8),

$$a_1 = R\sqrt{\mu} \int V_{\mathrm{C}}(\mathbf{r}_1, \mathbf{r}_2, \mathbf{r}_3) u_1^2 d\Omega, \tag{9}$$

$$b_1 = \frac{1}{R\sqrt{\mu}} \int V_{\text{string}}(\mathbf{r}_1, \mathbf{r}_2, \mathbf{r}_3) u_1^2 d\Omega,$$

where

$$V_{\mathrm{C}}(\mathbf{r}_1, \mathbf{r}_2, \mathbf{r}_3) = -\frac{2}{3}\alpha_s \sum_{i<j} \frac{1}{r_{ij}}, \tag{10}$$

and

$$V_{\text{string}}(\mathbf{r}_1, \mathbf{r}_2, \mathbf{r}_3) = \sigma l_{\min} \tag{11}$$

is proportional to the total length of the strings, i.e., to the sum of the distances of (anti)quark or diquarks from the string-junction point. In the Y shape, the strings meet at 120° in order to insure the minimum energy. This shape moves continuously to a two-leg configuration, where the legs meet at an angle larger than 120°. An explicit expression of $V_{\text{string}}(\mathbf{r}_1, \mathbf{r}_2, \mathbf{r}_3)$ in terms of Jacobi variables is given in [19].

The mass of Θ^+ obviously depends on $m_{[ud]}$ and m_s. The current masses of the light quarks are relatively well known: $m_{u,d} \approx 0$, $m_s \approx 170$ MeV. The only other parameter of strong interactions is the effective mass of the diquark $m_{[ud]}$. In principle, this mass could be computed dynamically. Instead, one can tune $m_{[ud]}$ (as well as $m_{[us]}$ and $m_{[ds]}$) to obtain the baryon masses in the quark–diquark approximation. We shall comment on this point later on.

In what follows, we use $\sigma = 0.15$ GeV^2 and explicitly include the Coulomb-like interaction between quark and diquarks with $\alpha_s = 0.39$.

For the pedagogy, let us first assume $m_{[ud]} = 0$. This assumption leads to the lowest $uudd\bar{d}$ and $uudd\bar{s}$ pentaquarks. If the current diquark masses vanish, then the $[ud]^2\bar{d}$ pentaquark is dynamically exactly analogous to the $J^P = 1/2^-$ nucleon resonance and the $[ud]^2\bar{s}$ pentaquark is an analog of the $J^P = 1/2^-$ Λ hyperon, with one important exception. The masses of P-wave baryons calculated using the EH method acquire the (negative) contribution $3C_q$ for $J^P = 1/2^-$ nucleons and $2C_q + C_s$ for $J^P = 1/2^-$ hyperons. These contributions are due to the interaction of constituent spins with the vacuum chromomagnetic field. Using the results of Table 1 below, we get the mass of the P-wave nucleon resonance with the orbital $\boldsymbol{\rho}$ excitation of 1600 MeV and the mass of Λ hyperon of 1600 MeV that within 100 MeV agrees with the known P-wave N and Λ resonances.

However, the above discussion shows that the self-energies $C_{[ud]}$ equal zero for the scalar diquarks. This means that introducing any scalar constituent increases the pentaquark energy (relative to the N and Λ P-wave resonances) by $2|C_q| \sim 200$–300 MeV. Therefore, prior to any calculation,

Table 1. The pentaquark masses in the quark–diquark–diquark approximations (the masses of $[ud]^2\bar{q}$ states ($q = d, s$) for $J^P = 1/2^+$ pentaquarks are in GeV)

		$\mu_{[ud]}$	μ_q	M
$[ud]^2\bar{s}\frac{1}{2}^+$	AF	0.482	0.458	2.171
	SSE	0.463	0.468	2.070
$[ud]^2\bar{d}\frac{1}{2}^+$	AF	0.476	0.415	2.091
	SSE	0.469	0.379	1.934

we can set the lower bound for the pentaquark in the Jaffe–Wilczek approximation, $M(\Theta) \geq 2$ GeV.

The numerical calculation for $m_{[ud]} = 0$ yields the mass of $[ud]^2\bar{s}$ pentaquark ∼2100 MeV (see Table 1). Similar calculations yield the mass of $[ud]^2\bar{c}$ pentaquark ∼3250 MeV (for $m_c = 1.4$ GeV) and $[ud]^2\bar{b}$ pentaquark ∼6509 MeV (for $m_b = 4.8$ GeV) [20]. For illustration of the accuracy of the auxiliary field (AF) formalism in Table 1, the masses of $[ud]^2\bar{d}$ and $[ud]^2\bar{d}$ pentaquarks calculated using the spinless Salpeter equation (SSE) are also shown:

$$H_S = \sum_{i=1}^{3}\sqrt{\mathbf{p}_i^2 + m_i^2} + V,$$

$$M = M_0 - \frac{2\sigma}{\pi}\sum_{i=1}^{3}\frac{\eta_i}{\left\langle\sqrt{\mathbf{p}_i^2 + m_i^2}\right\rangle},$$

where V is the same as in Eq. (1), M_0 is the eigenvalue of H_S, $\left\langle\sqrt{\mathbf{p}_{[ud]}^2 + m_{[ud]}^2}\right\rangle$ and $\left\langle\sqrt{\mathbf{p}_{\bar{q}}^2 + m_{\bar{q}}^2}\right\rangle$ are the average kinetic energies of diquarks and an antiquark, and η_i are the correction factors given in (5). The numerical algorithm to solve the three-body SSE is based on an expansion of the wave function in terms of harmonic-oscillator functions with different sizes [21]. In fact to apply this techniques to the three-body SSE, we need to use an approximation of the three-body potential V_{string} by a sum of the two- and one-body potentials (see [22]). This approximation, however, introduces a marginal correction to the energy eigenvalues. The quantities $\mu_{[ud]}$ and μ_q denote either the constituent masses calculated in the AF formalism using Eq. (2) or $\left\langle\sqrt{\mathbf{p}_{[ud]}^2 + m_{[ud]}^2}\right\rangle$, $\left\langle\sqrt{\mathbf{p}_{\bar{q}}^2 + m_{\bar{q}}^2}\right\rangle$ found from the solution of the SSE. It is seen from Table 1 that these quantities agree with accuracy better than 5%. The pentaquark masses calculated by the two methods differ by ∼100 MeV for ($[ud]^2\bar{s}$) and ∼160 MeV for $[ud]^2\bar{d}$. The approximation of V_{string} mentioned above introduces a correction to the energy eigenvalues ≤30 MeV, so we conclude that the results obtained using the AF formalism and the SSE agree within ∼5%, i.e., the accuracy of the AF results for pentaquarks is the same as for the $q\bar{q}$ system (see, e.g., [23]).

Table 2. The $[ud]^2\bar{s}$ mass (in GeV) calculated using the SSE as a function of α_s with and without Goldstone boson exchange (GBE)

α_s	0.39	0.50	0.60
M (with GBE)	1.893	1.814	1.737
M (without GBE)	2.069	2.007	1.949

If we withdraw the assumption that $m_{[ud]} = 0$, then a possible way to estimate the current diquark masses is to tune $m_{[ud]}$, $m_{[us]}$, and $m_{[ds]}$ from the fit to the nucleon and hyperon masses (in the quark–diquark approximation). In this way, one naturally obtains larger pentaquark masses. We have performed such calculations using the SSE. We briefly investigated the sensitivity of the pentaquark-mass predictions to the choice of σ, strange-quark mass m_s, and diquark masses $m_{[ud]}$ and found $M([ud]^2\bar{d})$ in the range 2.2–2.4 GeV, $M([ud]^2\bar{s}) \sim 2.4$ GeV and $M([us]^2\bar{d}) \sim 2.5$ GeV.

Increasing α_s up to 0.6 (the value used in the Capstick–Isgur model [24]) decreases the $[ud]^2\bar{s}$ mass by ∼120 MeV (see Table 2). We have briefly investigated the effect of the hyperfine interaction due to the σ-meson exchange between diquarks and strange antiquark and found that it lowers the Θ^+ energy by ∼180 MeV for $g_\sigma^2/4\pi \sim 1$. As a result, we obtain the lower bound of $[ud]^2\bar{s}$ pentaquark $M([ud]^2\bar{s}) = 1740$ MeV (for $m_{[ud]} = 0$), which is still ∼200 MeV above the experimental value.

3. CONCLUSIONS

We therefore conclude that the string dynamics alone in its simplified form predicts overly high masses of pentaquarks. This may indicate a large role of the chiral-symmetry-breaking effects in light pentaquark systems. An "extremal" approach of the chiral soliton model totally neglects the confinement effects and concentrates on the pure chiral properties of baryons. Therefore, the existence of Θ, if confirmed, provides a unique possibility to clarify the interplay between the quark and chiral degrees of freedom in light baryons.

ACKNOWLEDGEMENTS

This work was supported by the Russian Foundation for Basic Research, project nos. 03-02-17345 and 04-02-17263, and the grant for Leading Scientific Schools no. 1774.2003.2. NATO is also greatly acknowledged for the grant no. PST.CLG.978710.

REFERENCES

1. T. Nakano *et al.* (LEPS Collab.), Phys. Rev. Lett. **91**, 012002 (2003); hep-ex/0301020.
2. V. V. Barmin *et al.* (DIANA Collab.), Yad. Fiz. **66**, 1763 (2003) [Phys. At. Nucl. **66**, 1715 (2003)]; hep-ex/0304040; S. Stepanyan (CLAS Collab.), hep-ex/0307018; V. Kubarovsky and S. Stepanyan (CLAS Collab.), hep-ex/0307088; J. Barth *et al.* (SAPHIR Collab.), Phys. Lett. B **572**, 127 (2003); hep-ex/0307083; A. E. Asratyan, A. G. Dolgolenko, and M. A. Kubantsev, hep-ex/0309042; A. Airapetian *et al.* (SAPHIR Collab.), hep-ex/0312044.
3. D. Diakonov, V. Petrov, and M. V. Polyakov, Z. Phys. A **359**, 305 (1997); hep-ph/9703373.
4. C. Alt *et al.* (NA49 Collab.), hep-ex/0310014.
5. H1 Collab., hep-ex/0403017.
6. R. Matheus *et al.*, hep-ph/0309001; J. Sugiyama, T. Doi, and M. Oka, hep-ph/0309271.
7. F. Csikor *et al.*, JHEP **0311**, 070 (2003); S. Sasaki, hep-lat/0310014.
8. Fl. Stancu and D. O. Riska, hep-ph/0307010.
9. M. Karliner and H. J. Lipkin, hep-ph/0307243.
10. F. Huang *et al.*, hep-ph/0310040.
11. R. L. Jaffe and F. Wilczek, hep-ph/0307341.
12. Yu. A. Simonov, in *Proceedings of the XVII Autumn School Lisboa, Portugal, 24 Sept.–4 Oct. 1999*, Ed. by L. Ferreira, P. Nogueira, and J. I. Silva-Marco (World Sci., Singapore, 2000), p. 60; hep-ph/9911237.
13. I. M. Narodetskii, Yu. A. Simonov, M. A. Trusov, and A. I. Veselov, Phys. Lett. B **578**, 318 (2004).
14. Yu. A. Simonov, Yad. Fiz. **66**, 363 (2003) [Phys. At. Nucl. **66**, 338 (2003)]; hep-ph/0205334.
15. I. M. Narodetskii and M. A. Trusov, Yad. Fiz. **67**, 783 (2004) [Phys. At. Nucl. **67**, 762 (2004)]; hep-ph/0307131.
16. A. M. Polyakov, *Gauge Fields and Strings* (Harwood Acad. Publ., Harwood, 1987).
17. C. Semay, B. Silvestre-Brac, and I. M. Narodetskii, Phys. Rev. D **69**, 014003 (2004).
18. Yu. A. Simonov, Phys. Lett. B **515**, 137 (2001).
19. I. M. Narodetskii, A. N. Plekhanov, and A. I. Veselov, Pis'ma Zh. Éksp. Teor. Fiz. **77**, 64 (2003) [JETP Lett. **77**, 58 (2003)].
20. A. I. Veselov, private communication.
21. P. Nunberg, D. Prosperi, and E. Pace, Nucl. Phys. A **285**, 58 (1977); B. Silvestre-Brac, R. Bonnaz, C. Semay, and F. Brau, Internal Report No. ISN-00-66, ISN (Grenoble, 2000).
22. B. Silvestre-Brac, C. Semay, I. M. Narodetskii, and A. I. Veselov, Eur. Phys. J. C **32**, 385 (2004).
23. V. L. Morgunov, A. V. Nefediev, and Yu. A. Simonov, Phys. Lett. B **459**, 653 (1999).
24. S. Capstick and N. Isgur, Phys. Rev. D **34**, 2809 (1986).

Physics of Atomic Nuclei, Vol. 68, No. 3, 2005, pp. 541–548. Translated from Yadernaya Fizika, Vol. 68, No. 3, 2005, pp. 569–576.
Original Russian Text Copyright © 2005 by Akhmetzyanova, Dolgopolov, Dubinin, Smirnov.

Light Higgs Boson in the Two-Doublet Model Featuring Explicit *CP* Violation

E. N. Akhmetzyanova[1)*], M. V. Dolgopolov[1)], M. N. Dubinin[2)], and I. A. Smirnov[1)***]**

Received May 14, 2004; in final form, September 15, 2004

Abstract—The most general form of an effective two-doublet Higgs potential whose parameters are complex-valued and whose CP invariance is violated explicitly in the minimal supersymmetric model caused by Higgs boson interaction with third-generation squarks is considered. Higgs boson states are obtained and their masses are calculated, along with the decay widths of the lightest Higgs boson and the cross section for its production, in the case of substantial mixing between the CP-even states h and H and the CP-odd state A. *© 2005 Pleiades Publishing, Inc.*

1. INTRODUCTION

Models involving an extended Higgs sector that are characterized by an explicit violation of the CP symmetry of the Higgs potential whose parameters are complex-valued are of great interest [1, 2]. The simplest example of such a situation is provided by an effective two-doublet potential in the minimal supersymmetric model (MSSM). With the proviso that CP symmetry is not broken spontaneously, this potential can be described by ten parameters, four of them being in general complex-valued [3]. Here, CP violation may be due to the mixing of CP-odd and CP-even Higgs bosons, which are well known in the MSSM in the case of real-valued parameters, in new mass eigenstates. This mixing leads to changes in their masses and couplings to fermions and gauge bosons. In the MSSM, significant complex parameters of the effective two-doublet potential can be generated by Higgs boson interaction with third-generation squarks.

Within the MSSM, we calculate here the mass and the decay widths of the physical state associated with the light Higgs boson from the two-doublet Higgs sector featuring CP violation. We also evaluate the cross section for the production of a light Higgs boson in the case of maximal CP mixing. Effects of explicit CP violation in the Higgs sector may be significant for experiments at the LHC collider or next-generation electron—positron colliders. The values obtained for the masses and decay widths are thoroughly compared with the results obtained with the package proposed in [4].

2. VIOLATION OF THE *CP* INVARIANCE OF THE TWO-DOUBLET POTENTIAL AND LIGHT HIGGS BOSON

The general two-Higgs-doublet model [3] involves two $SU(2)$ doublets of complex scalar fields that have nonzero vacuum expectation values. The most general Hermitian form of the renormalizable $SU(2) \times U(1)$-invariant Lagrangian for such a system of fields is

$$\mathcal{L} = (\mathcal{D}_\nu \Phi_1)^\dagger \mathcal{D}^\nu \Phi_1 + (\mathcal{D}_\nu \Phi_2)^\dagger \mathcal{D}^\nu \Phi_2 - U(\Phi_1, \Phi_2). \quad (1)$$

The potential $U(\Phi_1, \Phi_2)$ involving the real-valued parameters μ_1^2, μ_2^2, $\lambda_1, \ldots, \lambda_4$ and the complex-valued parameters μ_{12}^2, λ_5, λ_6, and λ_7 was considered in detail, for example, in [2]. We disregard mixing in the kinetic terms, which was discussed recently in the general (nonsupersymmetric) two-doublet model [5].

Presently, there are two basic approaches to constructing an effective two-doublet potential in the MSSM at an energy scale of about m_t. Within the first, so-called diagrammatic [1], approach, radiative corrections to the masses of scalar fields and their interaction vertices can be obtained by straightforwardly calculating one-loop diagrams involving two and four external lines and subsequently diagonalizing the mass matrix including the self-energies of the scalar fields in the one-loop approximation. Within the second approach, which is referred to as an effective-field-theory approach [6, 7], use is made of a one-loop effective potential belonging to the

---

[1)] Samara State University, ul. Akademika Pavlova 1, Samara, 443011 Russia.

[2)] Institute of Nuclear Physics, Moscow State University, Vorob'evy gory, Moscow, 119899 Russia; e-mail: `dubinin@theory.sinp.msu.ru`

[*] e-mail: `elza@ssu.samara.ru`

[**] e-mail: `dolg@ssu.samara.ru`

[***] e-mail: `ismi@pochta.ru`

Coleman–Weinberg type and involving all possible one-loop contributions. The expansion of the effective potential in inverse powers of $M_{\rm SUSY}$ determines radiative corrections to the parameters λ_i at the scale m_t that are fixed at the scale $M_{\rm SUSY}$ by the requirements of supersymmetry [8]. Thus, the parameters λ_i are expressed analytically in terms of the squark masses (which play the role of Pauli–Willars regulators) and the parameters μ and $A_{t,b}$ (where μ is the coefficient of the bilinear Higgsino term, while $A_{t,b}$ is the coefficient of the triple interaction between Higgs bosons and squarks). Calculations within the effective-potential method do not include self-energy contributions from scalar fields; therefore, it is necessary to calculate them separately [9]. The results are as follows: in the simple case of $A_t = A_b \equiv A_{t,b}$, the real and imaginary parts of the MSSM parameters $\lambda_{6,7}$ are determined by the phase $\varphi \equiv \arg(\mu A_{t,b})$; the real and imaginary parts of the MSSM parameter λ_5 are the doubled phase φ; and the complex-valued MSSM parameter μ_{12}^2 is fixed by the condition requiring that the potential take a minimum value [2].

It is well known that the components of the complex fields from the $SU(2)$ doublets Φ_1 and Φ_2 are not squared-mass eigenstates. Within the effective-potential approach, the masses and interaction vertices of the Higgs bosons are determined by diagonalizing the squared-mass matrix corresponding to the minimum of the potential. This problem was considered in [2] for complex-valued parameters μ_{12}^2 and $\lambda_{5,6,7}$ and zero phase of the vacuum expectation value and in [10] for nonzero relative phases of the vacuum expectation values ζ and of the doublets of the complex scalar fields ξ. The diagonalization at the minimum of the potential is performed in two steps. First, one performs a linear transformation of the components of the $SU(2)$ doublets Φ_1 and Φ_2 (the transformation used is parametrized by the rotation angles α in the h–H sector and $\tan\beta = v_2/v_1$ [11]) in order to determine the CP-even fields h and H, the CP-odd field A (pseudoscalar), and the Goldstone field G^0, which are the squared-mass eigenstates at $\varphi = 0$. The masses of CP-even charged Higgs bosons (in the CP-conserving limit, $\varphi = 0$) are given by

$$\begin{aligned} m_h^2 = s_{\alpha+\beta}^2 m_Z^2 + c_{\alpha-\beta}^2 m_A^2 - v^2(\Delta\lambda_1 s_\alpha^2 c_\beta^2 \\ + \Delta\lambda_2 c_\alpha^2 s_\beta^2 - 2(\Delta\lambda_3 + \Delta\lambda_4) c_\alpha c_\beta s_\alpha s_\beta \\ + \mathrm{Re}\Delta\lambda_5 (s_\alpha^2 s_\beta^2 + c_\alpha^2 c_\beta^2) - 2c_{\alpha+\beta}(\mathrm{Re}\Delta\lambda_6 s_\alpha c_\beta \\ - \mathrm{Re}\Delta\lambda_7 c_\alpha s_\beta)), \end{aligned} \tag{2}$$

$$\begin{aligned} m_H^2 = c_{\alpha+\beta}^2 m_Z^2 + s_{\alpha-\beta}^2 m_A^2 - v^2(\Delta\lambda_1 c_\alpha^2 c_\beta^2 \\ + \Delta\lambda_2 s_\alpha^2 s_\beta^2 + 2(\Delta\lambda_3 + \Delta\lambda_4) c_\alpha c_\beta s_\alpha s_\beta \\ + \mathrm{Re}\Delta\lambda_5 (c_\alpha^2 s_\beta^2 + s_\alpha^2 c_\beta^2) + 2s_{\alpha+\beta}(\mathrm{Re}\Delta\lambda_6 c_\alpha c_\beta \\ + \mathrm{Re}\Delta\lambda_7 s_\alpha s_\beta)), \end{aligned} \tag{3}$$

$$m_{H^\pm}^2 = m_W^2 + m_A^2 - \frac{v^2}{2}(\mathrm{Re}\Delta\lambda_5 - \Delta\lambda_4), \tag{4}$$

where $\Delta\lambda_i$ are the radiative corrections to the parameters at the scale m_t [10]. These corrections specify the effective low-energy model of the interaction of the scalar fields associated with the MSSM. If the phase φ is different from zero, then the parameters $\Delta\lambda_{5,6,7}$ develop imaginary parts. This gives rise to the mixed terms hA and HA, which depend only on the imaginary parts of the parameters $\Delta\lambda_{5,6,7}$, in the effective potential, whose CP invariance is violated explicitly, and, hence, to off-diagonal terms in the squared-mass matrix of the Higgs bosons. At the second step, one eliminates the off-diagonal terms hA and HA by performing an orthogonal transformation in order to express the fields h, H, and A in terms of the squared-mass eigenstates h_1, h_2, and h_3 of the Higgs bosons, these physical states not being CP eigenstates. The mass squared of the light Higgs boson is then given by

$$m_{h_1}^2 = 2\sqrt{(-q)}\cos\left(\frac{\theta + 2\pi}{3}\right) - \frac{a_2}{3}, \tag{5}$$

where

$$\theta = \arccos\frac{r}{\sqrt{(-q^3)}}, \quad r = \frac{1}{54}(9a_1a_2 - 27a_0 - 2a_2^3),$$

$$q = \frac{1}{9}(3a_1 - a_2^2),$$

$$a_1 = m_h^2 m_H^2 + m_h^2 m_A^2 + m_H^2 m_A^2 - c_1^2 - c_2^2,$$

$$a_2 = -m_h^2 - m_H^2 - m_A^2,$$

$$a_0 = c_1^2 m_H^2 + c_2^2 m_h^2 - m_h^2 m_H^2 m_A^2.$$

The components $a_{ij} = a'_{ij}/n_j$ of the squared-mass eigenstate of the light Higgs boson, $(h, H, A) = a_{ij}h_j$, are

$$a'_{11} = ((m_H^2 - m_{h_1}^2)(m_A^2 - m_{h_1}^2) - c_2^2),$$

$$a'_{21} = c_1c_2, \qquad a'_{31} = -c_1(m_H^2 - m_{h_1}^2),$$

where $n_i = \sqrt{(a'^2_{1i} + a'^2_{2i} + a'^2_{3i})}$ and c_1 and c_2 are the coefficients of the off-diagonal terms hA and HA [2].

The dependences of the Higgs boson masses on the phase $\varphi = \arg(\mu A_{t,b})$ are shown in Fig. 1. For the plot to be more illustrative, we choose (on the basis of an analysis of two-dimensional dependences) that domain in the parameter space in which the distinction between the present values of the mass and decay width of the physical Higgs boson (h_1) and the respective values at $\varphi = 0$ [$m_h(\varphi = 0)$ in the case of the mass] is maximal—that is, the domain

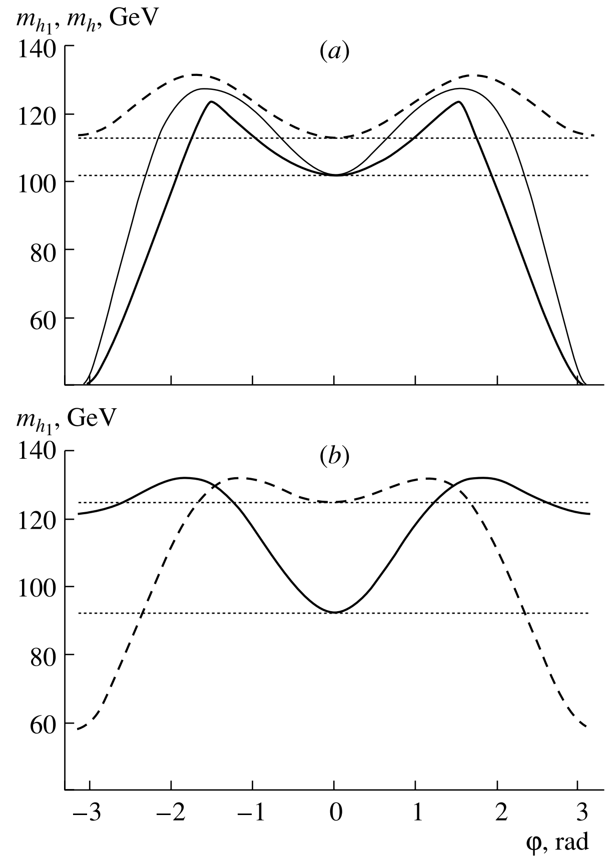

Fig. 1. Masses $m_{h_1}(\varphi)$ and $m_h(\varphi)$ at $\tan\beta = 5$, $M_{\rm SUSY} = 500$ GeV, and $\mu = 2000$ GeV: (*a*) $m_{h_1}(\varphi)$ (solid curve) and $m_h(\varphi)$ (fine curve) at $m_{H^\pm} = 180$ GeV and $m_{h_1}(\varphi)$ (dashed curve) at $m_{H^\pm} = 250$ GeV ($A_t = A_b = 1000$ GeV); (*b*) $m_{h_1}(\varphi)$ at (solid curve) $A_t = A_b = -1200$ and (dashed curve) 1300 GeV ($m_{H^\pm} = 300$ GeV). Here and in Figs. 2*a*, 3*a*, and 4*a*, the horizontal dotted lines represent the values of the respective functions in the *CP*-conserving limit $\varphi = 0$.

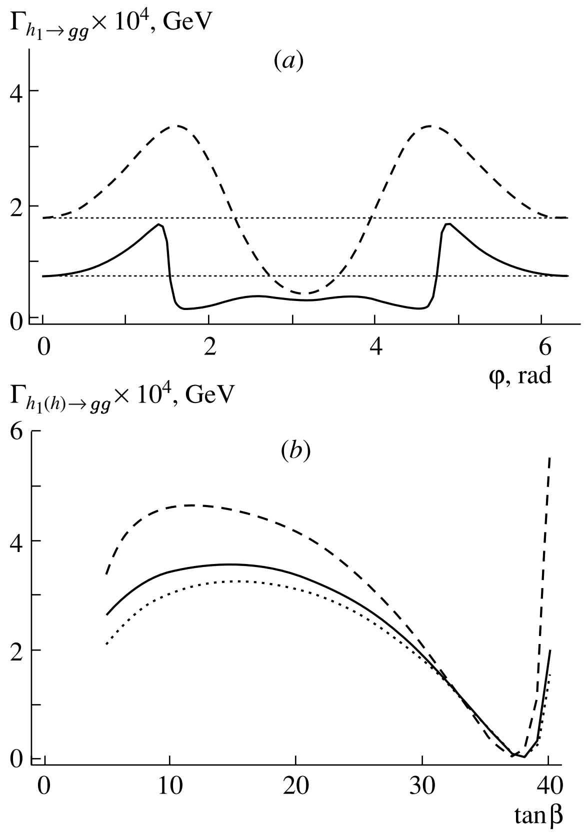

Fig. 2. Decay width $\Gamma_{h_1(h)\to gg}\times 10^4$ at $M_{\rm SUSY} = 500$ GeV, $A_t = A_b = 1000$ GeV, and $\mu = 2000$ GeV: (*a*) values of Γ_{h_1} at $m_{H^\pm} =$ (solid curve) 180 and (dashed curve) 250 GeV ($\tan\beta = 5$; (*b*) values of Γ_{h_1} at (solid curve) $\varphi = \pi/4$ and (dashed curve) $2\pi/3$ ($m_{H^\pm} = 300$ GeV) and (dotted curve) $\Gamma_h(\varphi = 0)$.

of maximal *CP* mixing. The distinction between the *CP* eigenstate $h(\varphi)$ and the mass eigenstate h_1 can be quite significant at low masses ($m_{H^\pm} < 250$ GeV) of the physical charged Higgs boson (see Fig. 1*a*, where solid thin and thick curves correspond to the *CP* eigenstate and the mass eigenstate of the h_1 Higgs boson, respectively). At high values of $m_{H^\pm}$, the distinction is much less.

Here we consider the parameter-space domain in which $M_{\rm SUSY} \sim 500$ GeV, $|\mu| \sim 2000$ GeV, and $|A_{t,b}| \sim 1000$ GeV and which corresponds to the so-called *CPX*-scenario [12]. In this case, the parameters of dimension GeV that are generated by mixing in the sfermion sectors are determined by the supersymmetry-breaking scale $M_{\rm SUSY}$—that is, $|\mu| = 4M_{\rm SUSY}$ and $|A_{t,b}| = 2M_{\rm SUSY}$. The remaining parameters ($\tan\beta$ and $m_{H^\pm}$) are varied within specific intervals. This scenario is based on the fact that *CP*-violating quantum effects in the neutral Higgs sector depend on the ratio ${\rm Im}(\mu A_t)/M^2_{\rm SUSY}$. From the point of view of reaching the maximal *CP* violation, the domain corresponding to the moderately small value of $M_{\rm SUSY} = 500$ GeV and rather large values of μ and $A_{t,b}$ is of greatest interest. By setting the mass of the charged Higgs boson to a modest value of $m_{H^\pm} \sim 200$ GeV, we go over to the intense-coupling regime corresponding to the maximal mixing of the physical Higgs bosons (in contrast to the decoupling regime whose scenario is similar to that in the Standard Model).

In the *CP*-symmetric case, some model-dependent constraints on the parameters μ, $A_{t,b}$, and $\tan\beta$ were obtained in [13]. Negative values of μ, as well as moderate positive values of μ at small $A_{t,b}$, are inconsistent with experimental data on the anomalous magnetic moment of the muon and on the rare decay $b \to s\gamma$; they are also inconsistent with constraints on the mass of the light Higgs boson. At large positive values of μ, one can single out domains at small

Table 1. Masses and decay widths of h_1 (in GeV) and its production cross section versus phase $\varphi = \arg(\mu A_{t,b})$ according to our present results and according to the results obtained in [4] by using the CPsuperH package at $\tan\beta = 5$, $|A_t| = |A_b| = 1000$ GeV, $|\mu| = 2000$ GeV, $m_{H^\pm} = 300$ GeV, $M_{\rm SUSY} = 500$ GeV, $\alpha_{\rm EM}(m_Z) = 0.7812 \times 10^{-2}$, $\alpha_s(m_Z) = 0.1172$, and $G_{\rm F} = 1.174 \times 10^{-5}$ GeV^{-2}

φ	m_{h_1}		m_{h_2}		m_{h_3}		$\Gamma_{h_1\to gg} \times 10^4$		$\Gamma_{h_1\to\gamma\gamma} \times 10^6$		$\Gamma_{h_1\to e\bar{e}} \times 10^{10}$		$\Gamma_{h_1\to\mu\bar{\mu}} \times 10^5$	
	our	[4]	our	[4]	our	[4]	our	[4]	our	[4]	our	[4]	our	[4]
0	115.4	106.8	295.5	302.2	297.1	302.3	2.103	1.878	7.470	5.796	0.460	0.345	0.212	0.157
$\pi/6$	118.7	109.0	289.6	297.8	299.5	304.4	2.355	1.964	8.371	6.287	0.440	0.335	0.204	0.152
$\pi/3$	125.9	113.9	279.7	290.9	300.4	305.0	3.024	2.107	10.832	7.605	0.394	0.310	0.179	0.141
$\pi/2$	131.4	117.4	269.3	282.2	299.9	304.5	3.643	1.961	13.321	8.996	0.365	0.329	0.166	0.137
$2\pi/3$	130.7	114.9	262.2	273.9	298.8	303.5	3.397	1.262	12.945	8.969	0.481	0.385	0.218	0.175
$5\pi/6$	125.2	105.7	259.8	268.3	297.6	302.4	2.412	0.503	10.274	7.223	0.672	0.529	0.304	0.240
π	122.0	99.4	259.6	264.4	297.1	302.0	1.889	0.263	8.887	6.101	0.672	0.592	0.341	0.269

φ	$\Gamma_{h_1\to\tau\bar{\tau}} \times 10^3$		$\Gamma_{h_1\to u\bar{u}} \times 10^8$		$\Gamma_{h_1\to d\bar{d}} \times 10^7$		$\Gamma_{h_1\to s\bar{s}} \times 10^5$		$\Gamma_{h_1\to c\bar{c}} \times 10^3$		$\Gamma_{h_1\to b\bar{b}} \times 10^2$		$\sigma_{e^+e^-\to Zh_1}$, fb
	our	[4]	our	[4]	our	[4]	our	[4]	our	[4]	our	[4]	
0	0.591	0.435	0.506	0.237	0.202	0.193	0.744	0.709	0.216	0.101	0.504	0.481	162
$\pi/6$	0.567	0.423	0.485	0.242	0.194	0.187	0.713	0.687	0.207	0.103	0.483	0.409	154
$\pi/3$	0.498	0.391	0.425	0.263	0.170	0.171	0.626	0.629	0.181	0.108	0.424	0.426	137
$\pi/2$	0.461	0.382	0.394	0.260	0.158	0.167	0.580	0.612	0.168	0.111	0.393	0.414	123
$2\pi/3$	0.607	0.485	0.520	0.251	0.208	0.212	0.764	0.780	0.222	0.107	0.518	0.528	124
$5\pi/6$	0.848	0.668	0.726	0.225	0.290	0.297	1.066	1.089	0.310	0.096	0.724	0.737	136
π	0.950	0.746	0.813	0.208	0.325	0.335	1.195	1.230	0.347	0.089	0.810	0.832	143

values of m_A and $\tan\beta$ that are forbidden by data on the decay $b \to s\gamma$.

Some numerical values obtained within our approach for the Higgs boson masses at various values of the phase φ are presented in Tables 1–3, along with the results derived by using the CPsuperH package [4], which is based on the precise calculation of the corrections to the masses in the one-loop approximation. The method used by the authors of CPsuperH to diagonalize the squared-mass matrix is different from ours. In particular, they do not introduce the mixing angle $\alpha(h, H)$; as a consequence, there are no squared-mass eigenstates in the *CP*-conserving limit; therewith, there appears the mixed mass term hH, which is absent in our approach. For this reason, the squared-mass matrices for the Higgs bosons differ: the condition $M_{12} = M_{21} = 0$ holds strictly in our approach, but it is not valid in the diagrammatic approach. The numerical results obtained in these two approaches are in qualitative agreement with each other, but a precise numerical comparison is complicated by the distinction between the approaches. In [14], it was indicated that, in the *CP*-symmetric case, there is significant disagreement between the results obtained within the MSSM by using the diagrammatic approach and the approach based on effective field theory.

In order to find the masses and decay widths in question, we first calculated the radiative corrections $\Delta\lambda_i$, which depend on the MSSM parameters. The

Table 2. Masses and decay widths (in GeV) of h_1 and its production cross section versus the phase $\varphi = \arg(\mu A_{t,b})$ according to our results along with the values obtained in [4] with the CPsuperH package at $m_{H^\pm} = 180$ GeV, the other parameters being identical to those in Table 1

φ	m_{h_1}		m_{h_2}		m_{h_3}		$\Gamma_{h_1\to gg} \times 10^4$		$\Gamma_{h_1\to\gamma\gamma} \times 10^6$		$\Gamma_{h_1\to e\bar{e}} \times 10^{10}$		$\Gamma_{h_1\to\mu\bar{\mu}} \times 10^5$	
	our	[4]	our	[4]	our	[4]	our	[4]	our	[4]	our	[4]	our	[4]
0	102.0	99.5	175.1	174.9	180.7	179.0	0.753	1.211	3.857	4.116	1.517	1.000	0.688	0.453
$\pi/6$	105.4	102.1	167.0	169.0	183.0	180.9	0.860	1.324	4.215	4.517	1.574	0.987	0.714	0.448
$\pi/3$	114.3	108.8	149.2	156.0	183.9	181.7	1.236	1.622	5.240	5.839	1.763	0.895	0.800	0.406
$\pi/2$	122.0	114.4	127.5	138.4	182.7	180.9	0.435	1.373	0.081	8.081	5.034	0.830	2.283	0.377
$2\pi/3$	91.2	93.9	138.4	136.0	180.2	179.0	0.250	0.098	0.501	3.296	3.446	2.463	1.564	1.112
$5\pi/6$	58.1	47.0	147.9	142.9	177.0	176.6	0.382	0.251	0.083	3.925	2.165	1.484	0.982	0.674
π	39.5	–	152.0	–	175.1	–	0.315	–	0.019	–	2.273	–	0.103	–

φ	$\Gamma_{h_1\to\tau\bar{\tau}} \times 10^3$		$\Gamma_{h_1\to u\bar{u}} \times 10^8$		$\Gamma_{h_1\to d\bar{d}} \times 10^7$		$\Gamma_{h_1\to s\bar{s}} \times 10^5$		$\Gamma_{h_1\to c\bar{c}} \times 10^3$		$\Gamma_{h_1\to b\bar{b}} \times 10^2$		$\sigma_{e^+e^-\to Zh_1}$, fb
	our	[4]	our	[4]	our	[4]	our	[4]	our	[4]	our	[4]	
0	0.191	1.260	1.638	0.185	0.655	0.566	2.406	2.078	0.699	0.079	1.629	1.406	160
$\pi/6$	0.198	1.244	1.700	0.191	0.680	0.556	2.498	2.042	0.726	0.081	1.691	1.382	150
$\pi/3$	0.222	1.128	1.904	0.211	0.761	0.499	2.797	1.831	0.813	0.089	1.896	1.241	123
$\pi/2$	0.635	1.047	5.437	0.226	2.175	0.459	7.989	1.685	2.321	0.096	5.417	1.141	7.3×10^{-3}
$2\pi/3$	0.434	3.105	3.722	0.089	1.489	1.407	5.469	5.170	1.589	0.038	3.698	3.499	47
$5\pi/6$	0.272	1.860	2.338	0.034	0.935	0.936	3.436	3.538	0.998	0.014	2.300	2.341	74
π	0.028	–	0.245	–	0.098	–	0.360	–	0.105	–	2.370	–	86

analytic expressions for $\Delta\lambda_i$ are given in [10], along with a discussion on various contributions to the effective parameters. Further, we use formula (2) for the mass of the light Higgs boson in the *CP*-conserving limit; in the case of complex-valued parameters, we performed a rotation in the (h,H,A) space and specified the h_1 mass in the form (5). The analytic expressions for two-body decays are presented in [10]. The decay widths $\Gamma_{h_1(h)\to gg} \times 10^4$ and $\Gamma_{h_1(h)\to\gamma\gamma} \times 10^6$ are plotted in Figs. 2 and 3, respectively. A comparison of numerical results for the decay widths of the Higgs boson and the cross section for its production in the process $e^+e^- \to Zh_1$ is illustrated in Tables 1–3. The cross sections for Higgs boson production in the process $e^+e^- \to h_1Z$ are also plotted in Fig. 4. From this plot, it can be concluded that the difference between the cross sections in the *CP*-invariant two-doublet model and the two-doublet model featuring *CP* violation is maximal at $\varphi \approx \pi/2$ and a moderate beam energy $E_{\text{c.m.}}$.

3. CONCLUDING REMARKS

In general, the potential of the two-doublet model is not *CP*-invariant, while the parameters μ_{12}^2 and $\lambda_{5,6,7}$ of the two-doublet effective potential in the MSSM Higgs sector are complex-valued. There is no reason to treat the parameters of the general two-doublet model as real-valued quantities, since this would imply fulfillment of the additional relations [2, 15]

$$\mathrm{Im}(\mu_{12}^4\lambda_5^*) = 0, \quad \mathrm{Im}(\mu_{12}^2\lambda_6^*) = 0,$$

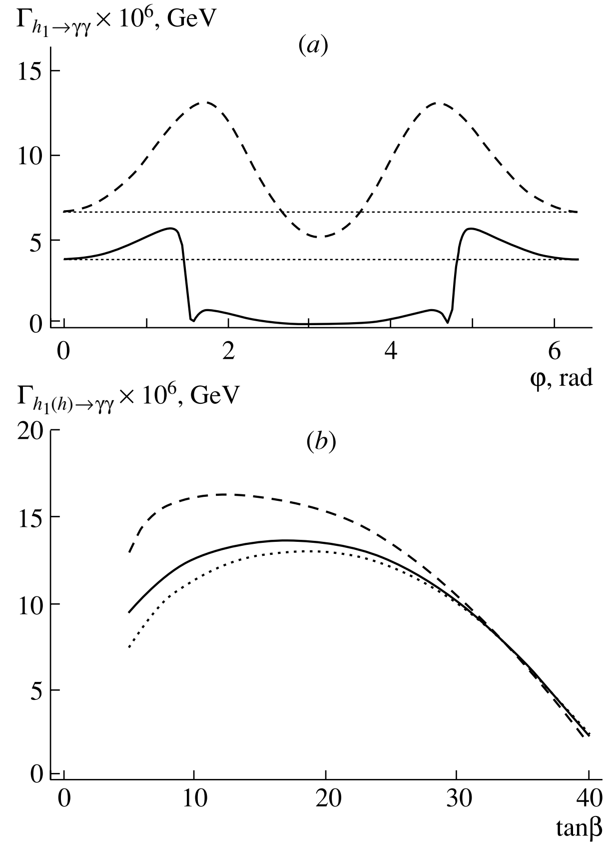

Fig. 3. Decay width $\Gamma_{h_1(h)\to\gamma\gamma}\times 10^6$. The notation for the curves and the values of the parameters are identical to those in Fig. 2.

$$\mathrm{Im}(\mu_{12}^2\lambda_7^*) = 0,$$

which do not have any physical grounds. Within the MSSM, the parameters of the effective Higgs potential may develop quite naturally complex values, provided that, in the squark sector, there arise mixings in way similar to the CKM mixing for three quark generations in the Standard Model. Of course, the mixing matrices in the fermion and sfermion sectors may differ substantially from each other. If these mixings give rise to a significant *CP* violation (scenarios of a slight violation of *CP* symmetry are discussed in [16]) and if the imaginary parts of the parameters μ_{12}^2 and $\lambda_{5,6,7}$ are rather large, then the predictions of the model involving *CP* violation can differ substantially from Standard Model signals of Higgs boson production at future colliders. Thus, *CP* violation can have a pronounced effect on the possibility of observing the Higgs boson in the $\gamma\gamma$, ttH, bbH, and other channels [17].

It is well known that supersymmetric models involving various types of *CP* violation admit large contributions to the electric dipole moments of the neutron and leptons [18]. Theoretical estimates of electric dipole moments are consistent with experimental limits on them if *CP*-violating phases are as small as $\mathcal{O}(10^{-2})$ or if the scale of supersymmetry breaking ranges up to a few TeV. The former case corresponds to a fine tuning of model parameters, whereas the latter case implies considerable difficulties in detecting supersymmetric particles even at the LHC energies [19]. In the space of MSSM parameters, the choice of domain that is different from any limiting case and which is allowed by available experimental data on electric dipole moments is of obvious physical interest in view of this. A comparison of the *CPX* scenario with experimental constraints indicates [20] that electroweak baryogenesis can naturally be included in the *CPX* scenario at moderate values of A_t $(0.2 \leq A_t/\tilde{M}_Q \leq 0.65)$, moderately large values of $\tan\beta \sim 20$, and values of the soft-sypersymmetry-breaking parameter $\tilde{M}_Q$ on the order of a few TeV.

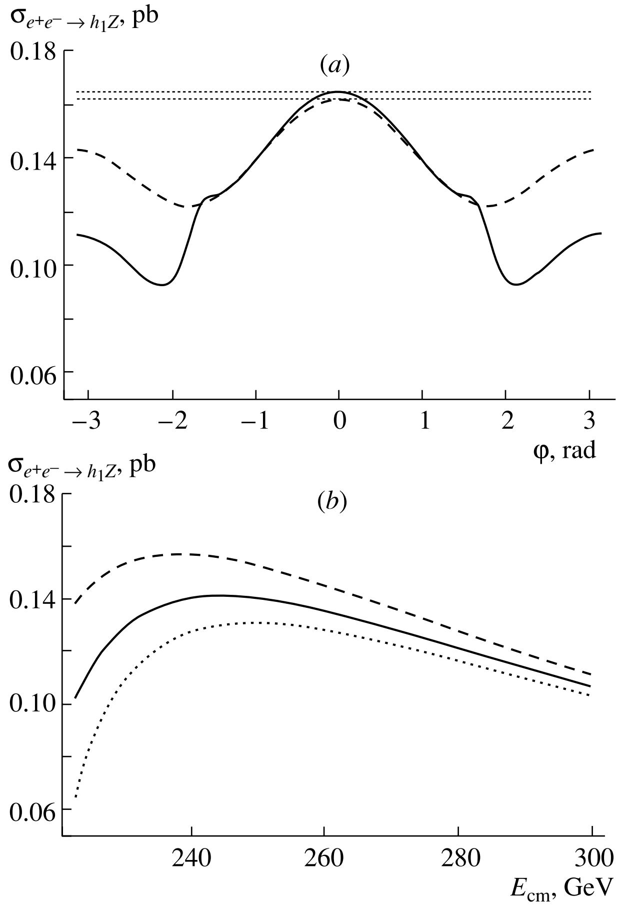

Fig. 4. Cross section for the process $\sigma_{e^+e^-\to h_1Z}$ at $\tan\beta = 5$, $M_{\rm SUSY} = 500$ GeV, and $\mu = 2000$ GeV: (*a*) results for (solid line) $m_{H^\pm} = 200$ GeV and (dashed line) $m_{H^\pm} = 300$ GeV at $E_{\rm c.m.} = 250$ GeV and $A_t = A_b = 1000$ GeV; (*b*) results for $\varphi =$ (solid line) $\pi/3$, (dashed line) $\pi/2$, and (dotted line) 0 at $m_{H^\pm} = 300$ GeV and $A_t = A_b = -500$ GeV.

Table 3. Masses and decay widths (in GeV) of h_1 and its production cross section versus the phase $\varphi = \arg(\mu A_{t,b})$ according to our present results and according to the results obtained in [4] with the CPsuperH package at $|\mu| = 1600$ GeV, the other parameters being identical to those in Table 1

φ	m_{h_1}		m_{h_2}		m_{h_3}		$\Gamma_{h_1\to gg} \times 10^4$		$\Gamma_{h_1\to\gamma\gamma} \times 10^6$		$\Gamma_{h_1\to e\bar{e}} \times 10^{10}$		$\Gamma_{h_1\to\mu\bar{\mu}} \times 10^5$	
	our	[4]	our	[4]	our	[4]	our	[4]	our	[4]	our	[4]	our	[4]
0	118.7	108.8	293.7	298.1	294.5	298.5	2.389	1.947	8.393	6.281	0.464	0.348	0.210	0.158
$\pi/6$	121.1	110.5	289.3	295.0	296.8	300.2	2.603	2.006	9.138	6.680	0.446	0.338	0.202	0.154
$\pi/3$	126.5	114.2	283.2	290.5	297.7	300.7	3.156	2.098	11.102	7.725	0.401	0.317	0.182	0.144
$\pi/2$	131.0	117.2	277.6	285.7	297.4	300.2	3.724	2.008	13.154	8.859	0.372	0.306	0.169	0.139
$2\pi/3$	131.8	116.8	274.5	282.0	296.4	299.0	3.869	1.593	13.667	9.227	0.417	0.341	0.189	0.155
$5\pi/6$	129.8	113.3	273.9	280.1	295.1	297.7	3.599	1.089	12.757	8.676	0.507	0.408	0.230	0.185
π	128.5	111.1	274.2	279.7	297.5	297.1	3.414	0.878	12.162	8.252	0.549	0.442	0.249	0.200

φ	$\Gamma_{h_1\to\tau\bar{\tau}} \times 10^3$		$\Gamma_{h_1\to u\bar{u}} \times 10^8$		$\Gamma_{h_1\to d\bar{d}} \times 10^7$		$\Gamma_{h_1\to s\bar{s}} \times 10^5$		$\Gamma_{h_1\to c\bar{c}} \times 10^3$		$\Gamma_{h_1\to b\bar{b}} \times 10^2$		$\sigma_{e^+e^-\to Zh_1}$, fb
	our	[4]	our	[4]	our	[4]	our	[4]	our	[4]	our	[4]	
0	0.585	0.438	0.501	0.241	0.200	0.194	0.736	0.712	0.214	0.103	0.499	0.482	154
$\pi/6$	0.562	0.427	0.482	0.245	0.193	0.188	0.708	0.692	0.205	0.105	0.480	0.468	149
$\pi/3$	0.505	0.399	0.433	0.254	0.173	0.175	0.636	0.644	0.185	0.108	0.431	0.436	136
$\pi/2$	0.468	0.386	0.401	0.260	0.161	0.169	0.589	0.619	0.171	0.111	0.400	0.420	124
$2\pi/3$	0.526	0.430	0.450	0.258	0.180	0.188	0.662	0.689	0.192	0.109	0.449	0.467	122
$5\pi/6$	0.639	0.515	0.547	0.247	0.219	0.226	0.804	0.829	0.234	0.105	0.545	0.562	127
π	0.693	0.557	0.593	0.240	0.237	0.245	0.872	0.901	0.253	0.103	0.591	0.610	130

Following the ideas proposed in [20], we conclude that experimental constraints on electric dipole moments are consistent with the *CPX* scenario at small $\tan\beta$: $4 < \tan\beta < 12$; this domain is of obvious interest for Higgs boson searches in collider experiments. At large values of $\tan\beta$ ($\tan\beta \approx 40$), there is good agreement with experimental limits on the neutron electric dipole moment d_n over a wide range of values of the parameter μ, whereas the theoretical estimate of the muon electric dipole moment exceeds experimental limits at small values of μ. A detailed analysis of the experimental constraints obtained for the model parameters from the thallium electric dipole moment $d_{^{205}\mathrm{Tl}}$, which can be represented as a superposition of the operator C_S and the electron electric dipole moment d_e, is also given in [20]. The constraints from $d_{^{205}\mathrm{Tl}}$ are more stringent than those from d_n. Nevertheless, these constraints can be substantially weakened by eliminating C_S and d_e. This may be done, for example, by reducing $\tan\beta$. This elimination of the operators C_S and d_e depends directly on the choice of $\arg(\mu A_t)$, $\arg(\mu m_{\tilde{g}})$, and $\arg(\mu m_{\tilde{W}})$. Thus, the *CP*-violating phases can be chosen in such a way that the domain of the parameters that corresponds to the *CPX* scenario becomes consistent with experimental constraints following from data on electric dipole moments.

ACKNOWLEDGMENTS

M.N. Dubinin and M.V. Dolgopolov acknowledge the support of the Russian Foundation for Basic

Research (project no. 04-02-17448). The work of Dubinin was supported by INTAS (grant no. 03-51-4007), the program Universities of Russia (grant no. 02.03.028), and the Program for Support of Leading Scientific Schools (grant no. 1685.2003.2). E.N. Akhmetzyanova acknowledges the support of the Dynasty Foundation and the International Center for Fundamental Physics in Moscow. I.A. Smirnov was supported by a grant for young scientists of the Samara oblast (no. 264 E 2.4 K).

REFERENCES

1. A. Pilaftsis and C. E. M. Wagner, Nucl. Phys. B **553**, 3 (1999); S. Y. Choi and J. S. Lee, Phys. Rev. D **61**, 015003 (2000); S. Y. Choi, M. Drees, *et al.*, Phys. Lett. B **481**, 57 (2000); S. Heinemeyer, Eur. Phys. J. C **22**, 521 (2001); M. Carena, J. Ellis, *et al.*, Nucl. Phys. B **625**, 345 (2002).
2. M. N. Dubinin and A. V. Semenov, Eur. J. Phys. C **28**, 223 (2003).
3. T. D. Lee, Phys. Rev. D **8**, 1226 (1973).
4. J. S. Lee, A. Pilaftsis, *et al.*, Comput. Phys. Commun. **156**, 283 (2004).
5. I. F. Ginzburg and M. Krawczyk, private communication.
6. H. E. Haber and R. Hempfling, Phys. Rev. D **48**, 4280 (1993).
7. Y. Okada, M. Yamaguchi, *et al.*, Phys. Lett. B **262**, 54 (1991); J. Ellis, G. Ridolfi, *et al.*, Phys. Lett. B **257**, 83 (1991); H. Haber and R. Hempfling, Phys. Rev. Lett. **66**, 1815 (1991); R. Barbieri, M. Frigeni, *et al.*, Phys. Lett. B **258**, 167 (1991).
8. K. Inoue, A. Kakuto, *et al.*, Prog. Theor. Phys. **67**, 1889 (1982); **68**, 927 (1982); **70**, 330 (1983); R. A. Flores and M. Sher, Ann. Phys. (N.Y.) **148**, 95 (1983).
9. E. Akhmetzyanova, M. Dolgopolov, and M. Dubinin, in *Proceedings of the International Workshop "Supersymmetries and Quantum Symmetries—SQS'03", Dubna, 2003*; in *Proceedings of the XVII Workshop on High Energy Physics and Quantum Field Theory (QFTHEP 2003), Samara–Saratov, 2003*.
10. E. Akhmetzyanova, M. Dolgopolov, and M. Dubinin, hep-ph/0405264.
11. J. Gunion, H. Haber, *et al., The Higgs Hunter's Guide* (Addison, Wesley, 1990).
12. M. Carena, J. R. Ellis, *et al.*, Nucl. Phys. B **586**, 92 (2000); Nucl. Phys. Lett. B **495**, 155 (2000).
13. J. R. Ellis, K. A. Olive, *et al.*, Phys. Lett. B **539**, 107 (2002).
14. M. Carena, H. E. Haber, *et al.*, Nucl. Phys. B **580**, 29 (2000).
15. J. F. Gunion and H. E. Haber, Phys. Rev. D **67**, 075019 (2003).
16. I. F. Ginzburg and M. V. Vychugin, in *Proceedings of the XVI Workshop on High Energy Physics and Quantum Field Theory (QFTHEP 2001),* p. 64.
17. S. Abdullin *et al.*, *Summary of the CMS Potential for the Higgs Boson Discovery,* CMS Note 2003/033.
18. J. Ellis, S. Ferrara, and D. V. Nanopoulos, Phys. Lett. B **114B**, 231 (1982); W. Buchmuller and D. Wyler, Phys. Lett. B **121B**, 321 (1983); J. Polchinski and M. B. Wise, Phys. Lett. B **125B**, 393 (1983); M. Dugan, B. Grinstein, *et al.*, Nucl. Phys. B **255**, 413 (1985); A. Sanda, Phys. Rev. D **32**, 2992 (1985); T. Kurimoto, Prog. Theor. Phys. **73**, 209 (1985); R. Garisto and J. D. Wells, Phys. Rev. D **55**, 1611 (1997); S. Weinberg, Phys. Rev. Lett. **63**, 2333 (1989); J. Dai, H. Dykstra, *et al.*, Phys. Lett. B **237**, 216 (1990); R. Arnowitt, J. Lopez, *et al.*, Phys. Rev. D **42**, 2423 (1990); P. Nath, Phys. Rev. Lett. **66**, 2565 (1991); Y. Kizukuri and N. Oshimo, Phys. Rev. D **46**, 3025 (1992).
19. T. Ibrahim and P. Nath, Phys. Rev. D **58**, 111301 (1998).
20. A. Pilaftsis, Nucl. Phys. B **644**, 263 (2002).

Translated by R. Rogalyov